PERMAFROST ENVIRONMENT CHANGES IN A WARMING CLIMATE

EDITED BY: Xiaodong Wu, Cuicui Mu and Wenxin Zhang
PUBLISHED IN: Frontiers in Environmental Science and
Frontiers in Earth Science

frontiers Research Topics

ISSN 1664-8714
ISBN 978-2-83250-756-8
DOI 10.3389/978-2-83250-756-8

About Frontiers

Frontiers is more than just an open-access publisher of scholarly articles: it is a pioneering approach to the world of academia, radically improving the way scholarly research is managed. The grand vision of Frontiers is a world where all people have an equal opportunity to seek, share and generate knowledge. Frontiers provides immediate and permanent online open access to all its publications, but this alone is not enough to realize our grand goals.

Frontiers Journal Series

The Frontiers Journal Series is a multi-tier and interdisciplinary set of open-access, online journals, promising a paradigm shift from the current review, selection and dissemination processes in academic publishing. All Frontiers journals are driven by researchers for researchers; therefore, they constitute a service to the scholarly community. At the same time, the Frontiers Journal Series operates on a revolutionary invention, the tiered publishing system, initially addressing specific communities of scholars, and gradually climbing up to broader public understanding, thus serving the interests of the lay society, too.

Dedication to Quality

Each Frontiers article is a landmark of the highest quality, thanks to genuinely collaborative interactions between authors and review editors, who include some of the world's best academicians. Research must be certified by peers before entering a stream of knowledge that may eventually reach the public - and shape society; therefore, Frontiers only applies the most rigorous and unbiased reviews.
Frontiers revolutionizes research publishing by freely delivering the most outstanding research, evaluated with no bias from both the academic and social point of view. By applying the most advanced information technologies, Frontiers is catapulting scholarly publishing into a new generation.

What are Frontiers Research Topics?

Frontiers Research Topics are very popular trademarks of the Frontiers Journals Series: they are collections of at least ten articles, all centered on a particular subject. With their unique mix of varied contributions from Original Research to Review Articles, Frontiers Research Topics unify the most influential researchers, the latest key findings and historical advances in a hot research area! Find out more on how to host your own Frontiers Research Topic or contribute to one as an author by contacting the Frontiers Editorial Office: frontiersin.org/about/contact

PERMAFROST ENVIRONMENT CHANGES IN A WARMING CLIMATE

Topic Editors:
Xiaodong Wu, Chinese Academy of Sciences (CAS), China
Cuicui Mu, Lanzhou University, China
Wenxin Zhang, Lund University, Sweden

Citation: Wu, X., Mu, C., Zhang, W., eds. (2022). Permafrost Environment Changes in a Warming Climate. Lausanne: Frontiers Media SA.
doi: 10.3389/978-2-83250-756-8

Table of Contents

frontiers | Frontiers in Environmental Science

TYPE Editorial
PUBLISHED 28 October 2022
DOI 10.3389/fenvs.2022.1053941

OPEN ACCESS

EDITED BY
Hong Liao,
Nanjing University of Information Science and Technology, China

REVIEWED BY
Nikita Tananaev,
Siberian Branch of the Russian Academy of Sciences (RAS), Russia

*CORRESPONDENCE
Xiaodong Wu,
wuxd@lzb.ac.cn

SPECIALTY SECTION
This article was submitted to Atmosphere and Climate, a section of the journal Frontiers in Environmental Science

RECEIVED 26 September 2022
ACCEPTED 14 October 2022
PUBLISHED 28 October 2022

CITATION
Wu X, Zhang W and Mu C (2022), Editorial: Permafrost degradation affects hydrology, ecology, and carbon cycle.
Front. Environ. Sci. 10:1053941.
doi: 10.3389/fenvs.2022.1053941

Editorial: Permafrost degradation affects hydrology, ecology, and carbon cycle

Xiaodong Wu[1,2]*, Wenxin Zhang[3,4] and Cuicui Mu[5]

[1]Cryosphere Research Station on the Qinghai-Tibet Plateau State Key Laboratory of Cryospheric Science, Northwest Institute of Eco-Environment and Resources, Chinese Academy of Sciences, Lanzhou, China, [2]College of Resources and Environment, University of Chinese Academy of Sciences, Beijing, China, [3]Department of Physical Geography and Ecosystem Science, Lund University, Lund, Sweden, [4]Center for Permafrost (CENPERM), Department of Geosciences and Natural Resource Management, University of Copenhagen, Copenhagen, Denmark, [5]Key Laboratory of Western China's Environmental Systems (Ministry of Education), College of Earth and Environmental Sciences, Lanzhou University, Lanzhou, China

KEYWORDS

permafrost, climate warming, hydrology, ecology, carbon cycle

Editorial on the Research Topic
Permafrost degradation affects hydrology, ecology, and carbon cycle

Permafrost regions account for about 22% of the exposed land area in the Northern Hemisphere (Obu et al., 2019). As one of physical characteristics in the cold environment, permafrost is sensitive to climate change. During the past decades, permafrost in high latitude and high-altitude regions shows obvious degradation, which is indicated by increasing ground temperature, deepening active layer, shrinking of permafrost area, and development of thermokarst features (Biskaborn et al., 2019).

Permafrost is distributed beneath the earth's surface. Permafrost can regulate the regional water cycle and ecology from several mechanisms. First, as a weak impermeable layer, permafrost can prevent water vertical infiltration and increase the surface soil water content. Second, the freeze-thaw cycles of the active layer can store excess water from summer rainfall as ice during winter, and the melting of this ice can supply soil water in the following summer. Third, ground ice melting can provide soil water for plant growth (Sugimoto et al., 2003). Permafrost regions also store a large amount of soil organic carbon, which is almost twice as the carbon currently contained in the atmosphere (Mishra et al., 2021). These carbon pools have been gradually accumulated and preserved during the past thousands of years due to the low-temperature limiting the microbial decomposition of organic matter. The permafrost degradation may remobilize these carbon pools by releasing greenhouse gases into the air. This process contributes one of the great uncertainties in the terrestrial carbon cycle feedback (Schuur et al., 2015). In addition, permafrost regions also store a large number of pollutants and heavy metals (e.g., mercury) which have been sequestrated for a long time. Permafrost degradation poses environmental risks

and thawing permafrost may release these biological or chemical substances that can affect human health (Schuster et al., 2018; Miner et al., 2021).

To address the issues on how permafrost environment is changing, to what extent the changing permafrost may affect the hydrology, ecology, carbon cycle, and pollutants, eleven multi-discipline studies are collected in this special topic on permafrost environment changes in a warming climate.

Permafrost regions have been warming at two to three times the global average (Hu et al., 2021). Using the monthly air temperature reanalysis dataset from the Climate Research Unit (CRU, University of East Anglia), it was found that the air freezing index in the Mongolian Plateau decreased by 4.1 C d yr^{-1}, and the air thawing index increased by 2.3 C d yr^{-1} during 1901–2019. The northern permafrost regions showed large variabilities in freezing and thawing index than the southern non-permafrost regions (Ma et al.). Based on the meteorological station records from 1957 to 2019, the annual mean air temperature has increased by 0.031–0.039°C yr^{-1} in the hinterland of the Qinghai-Tibet Plateau. The ground temperature within the active layer at 1 m depth increased at an average rate of 0.05°C yr^{-1} (Zhou et al.). Along with climate warming, frequency of extreme events also changed. On the Qinghai-Tibet Plateau, the warmth indices such as warm days, warm nights, summer days, and tropical nights increased at rates of 1.1, 1.6, 1.4 and 0.3 days per decade from 1960 to 2016. Meanwhile, cold indices including the number of cool days, cool nights, ice days, and frost days decreased significantly (Gong et al.). These results confirmed the rapid warming of the permafrost environment during the past decades and also provide useful data to understand the changing patterns and future projections of permafrost.

Three studies (i.e., Yang et al.; Rossi et al.; Polyakov et al.) examined the detecting permafrost and soil mapping method in permafrost regions. The equivalent anti-flux opposing coils were used to eliminate the blind area for the transient electromagnetic method, and the results showed that this method solved the problem of the shallow detection blind area, eliminated the interference caused by the primary field, and improved the horizontal and vertical resolutions (Yang et al.). In the Russian Arctic, geophysical and geocryological methods including landscape microzonation, borehole drilling, ground temperature measurements, and geoelectric surveys were employed to investigate the active layer thickness. The results showed that the multidisciplinary approach can be also useful for other areas (Rossi et al.). In permafrost regions, soil type is one of the most fundamental properties because it is an important parameter for Earth System Models as well as the carbon stocks estimation. However, due to the harsh natural conditions, field investigation of soil types is usually costly and difficult. Using the unmanned aerial vehicle (UAV) imaging data in the Lena River Delta, classical soil sections, geomorphological observation, and determination of the main chemical parameters of soils are presented. Although accurate mapping of soil types should be based on chemical analysis, this result suggests that the high-resolution soil-geomorphological maps based on the Geographic Information System and UAV data are useful for the mapping of soil types under the high variability of the watershed dan cryogenic landscapes (Polyakov et al.).

Permafrost significantly affects ecology and hydrology (Woo et al., 2008). A review paper in this topic summarizes that soil water potential is widely used to describe the energy state of liquid water. The movement of liquid water in the soil is mainly determined by soil matric potential. The process of ice lenses development in permafrost has been explained by mathematical models, however, existing models might be too simplified (Fu et al.). Therefore, new model development for ice formation for micro landscapes is still largely needed. To investigate the effects of hydrology on peat permafrost and carbon process, a process-based model, i.e., HPM-Arctic, was used the simulate the past and future changes in a peatland ecosystem in the Canadian Arctic. The results showed that the regional hydrology and basin characteristics strongly determined peat accumulation history and its future changes in organic carbon stocks under different climate scenarios (Treat et al.). For the carbon cycle in the Arctic permafrost, a pilot study showed that extensively grazing by large animals can cool the ground temperature by modifying ground cover properties. In addition, the soil organic carbon content is also higher in the extensively grazing sites than that of non-grazing sites, which is likely attributed to the higher carbon input (Windirsch et al.).

Heavy metals are anthropogenic contaminants that can be transported for long distances. Due to the atmospheric circulation and deposition, large heavy metals have been transported to the Arctic, Antarctic, as well as the Qinghai-Tibet Plateau. A review paper in this topic issue pointed out that heavy metals on the Qinghai-Tibet plateau are mainly from surrounding heavily-polluted regions. The shrinkage of the cryosphere may increase the release of these heavy metals in the future. This work highlights the importance of heavy metals in permafrost environments.

This special topic has collected the studies of permafrost regions located in the Arctic, Mongolia, and the Qinghai-Tibet Plateau. The results deepen our understanding of changing trends of climate and permafrost, interactions among permafrost, hydrology, ecology, carbon cycle, and risks of heavy metals. We hope this special topic could provide valuable references to the researchers with relevant interest and play an active role in promoting the research of permafrost changes and their environmental impacts.

Author contributions

All authors listed have made a substantial, direct, and intellectual contribution to the work and approved it for publication.

Funding

This work was supported by the National Natural Science Foundation of China (41941015, 32061143032), National Key Research and Development Program of China (2019YFA0607003), the State Key Laboratory of Cryospheric Science (SKLCS-ZZ-2022), and the West Light Foundation of the Chinese Academy of Sciences. WZ acknowledged grants of the Swedish Research Council VR 2020-05338.

Conflict of interest

The authors declare that the research was conducted in the absence of any commercial or financial relationships that could be construed as a potential conflict of interest.

Publisher's note

All claims expressed in this article are solely those of the authors and do not necessarily represent those of their affiliated organizations, or those of the publisher, the editors and the reviewers. Any product that may be evaluated in this article, or claim that may be made by its manufacturer, is not guaranteed or endorsed by the publisher.

References

Biskaborn, B. K., Smith, S. L., Noetzli, J., Matthes, H., Vieira, G., Streletskiy, D. A., et al. (2019). Permafrost is warming at a global scale. *Nat. Commun.* 10 (1), 264. doi:10.1038/s41467-018-08240-4

Hu, G., Zhao, L., Wu, T., Wu, X., Park, H., Fedorov, A., et al. (2021). Spatiotemporal variations and regional differences in air temperature in the permafrost regions in the Northern Hemisphere during 1980–2018. *Sci. Total Environ.* 197, 148358. doi:10.1016/j.scitotenv.2021.148358

Miner, K. R., D'Andrilli, J., Mackelprang, R., Edwards, A., Malaska, M. J., Waldrop, M. P., et al. (2021). Emergent biogeochemical risks from arctic permafrost degradation. *Nat. Clim. Chang.* 11 (10), 809–819. doi:10.1038/s41558-021-01162-y

Mishra, U., Hugelius, G., Shelef, E., Yang, Y., Strauss, J., Lupachev, A., et al. (2021). Spatial heterogeneity and environmental predictors of permafrost region soil organic carbon stocks. *Sci. Adv.* 7 (9), eaaz5236. doi:10.1126/sciadv.aaz5236

Obu, J., Westermann, S., Bartsch, A., Berdnikov, N., Christiansen, H. H., Dashtseren, A., et al. (2019). Northern hemisphere permafrost map based on TTOP modelling for 2000–2016 at 1 km^2 scale. *Earth-Science Rev.* 193, 299–316. doi:10.1016/j.earscirev.2019.04.023

Schuster, P. F., Schaefer, K. M., Aiken, G. R., Antweiler, R. C., Dewild, J. F., Gryziec, J. D., et al. (2018). Permafrost stores a globally significant amount of mercury. *Geophys. Res. Lett.* 45 (3), 1463–1471. doi:10.1002/2017gl075571

Schuur, E., McGuire, A. D., Schadel, C., Grosse, G., Harden, J. W., Hayes, D. J., et al. (2015). Climate change and the permafrost carbon feedback. *Nature* 520 (7546), 171–179. doi:10.1038/nature14338

Sugimoto, A., Naito, D., Yanagisawa, N., Ichiyanagi, K., Kurita, N., Kubota, J., et al. (2003). Characteristics of soil moisture in permafrost observed in east siberian taiga with stable isotopes of water. *Hydrol. Process.* 17 (6), 1073–1092. doi:10.1002/hyp.1180

Woo, M. K., Kane, D. L., Carey, S. K., and Yang, D. (2008). Progress in permafrost hydrology in the new millennium. *Permafr. Periglac. Process.* 19 (2), 237–254. doi:10.1002/ppp.613

frontiers in Earth Science

REVIEW
published: 10 February 2022
doi: 10.3389/feart.2022.826961

Water Migration and Segregated Ice Formation in Frozen Ground: Current Advances and Future Perspectives

Ziteng Fu[1,2,3], *Qingbai Wu*[1,2,3]*, *Wenxin Zhang*[4,5], *Hailong He*[6] *and Luyang Wang*[1,2,3]

[1]State Key Laboratory of Frozen Soil Engineering, Northwest Institute of Eco-Environment and Resources, Chinese Academy of Sciences, Lanzhou, China, [2]College of Resources and Environment, University of Chinese Academy of Sciences, Beijing, China, [3]Beiluhe Observation Station of Frozen Soil Environment and Engineering, Northwest Institute of Eco-Environment and Resources, Chinese Academy of Sciences, Lanzhou, China, [4]Department of Physical Geography and Ecosystem Science, Lund University, Lund, Sweden, [5]Center for Permafrost (CENPERM), University of Copenhagen, Copenhagen, Denmark, [6]College of Natural Resources and Environment, Northwest A&F University, Yangling, China

OPEN ACCESS

Edited by:
Tianjie Zhao,
Aerospace Information Research Institute (CAS), China

Reviewed by:
Yao Xiaoliang,
Xi'an University of Technology, China
Jiazuo Zhou,
Institute of Rock and Soil Mechanics (CAS), China

***Correspondence:**
Qingbai Wu
qbwu@lzb.ac.cn

Specialty section:
This article was submitted to Cryospheric Sciences, a section of the journal Frontiers in Earth Science

Received: *02 December 2021*
Accepted: *18 January 2022*
Published: *10 February 2022*

Citation:
Fu Z, Wu Q, Zhang W, He H and Wang L (2022) Water Migration and Segregated Ice Formation in Frozen Ground: Current Advances and Future Perspectives. Front. Earth Sci. 10:826961. doi: 10.3389/feart.2022.826961

A characteristic of frozen ground is a tendency to form banded sequences of particle-free ice lenses separated by layers of ice-infiltrated soil, which produce frost heave. In permafrost, the deformation of the ground surface caused by segregated ice harms engineering facilities and has considerable influences on regional hydrology, ecology, and climate changes. For predicting the impacts of permafrost degradation under global warming and segregated ice transformation on engineering and environmental, establishing appropriate mathematical models to describe water migration and ice behavior in frozen soil is necessary. This requires an essential understanding of water migration and segregated ice formation in frozen ground. This article reviewed mechanisms of water migration and ice formation in frozen soils and their model construction and introduced the effects of segregated ice on the permafrost environment included landforms, regional hydrological patterns, and ecosystems. Currently, the soil water potential has been widely accepted to characterize the energy state of liquid water, to further study the direction and water flux of water moisture migration. Models aimed to describe the dynamics of ice formation have successfully predicted the macroscopic processes of segregated ice, such as the rigid ice model and segregation potential model, which has been widely used and further developed. However, some difficulties to describe their theoretical basis of microscope physics still need further study. Besides, how to describe the ice lens in the landscape models is another interesting challenge that helps to understand the interaction between soil ice segregation and the permafrost environment. In the final of this review, some concerns overlooked by current research have been summarized which should be the central focus in future study.

Keywords: ice lens, permafrost, environment effects, frost heave model, permafrost modelling, review

INTRODUCTION

Frozen ground, defined as soil or rock containing ice that remains at or below 0°C, is widely distributed globally (Qin, 2016). About 50.5% of the long-term average maximum extent of frozen ground in the northern hemisphere undergoes seasonal freezing and thawing, and about 13–18% of the area in the northern hemisphere is occupied by permafrost (Zhang et al., 2003; Gruber, 2012). Permafrost is soil or rock that remains at or below 0°C for at least two consecutive years (Subcommittee, 1988; Qin, 2016). The topsoil that overlays permafrost and undergoes seasonal freezing and thawing is known as the active layer. Changes in permafrost temperature and the active layer thickness (ALT) have significant environmental and socioeconomic implications from the local to global scales. At the local scale, soil freezing and thawing directly affect the physical properties of water and heat transfer in the active layer, eventually altering the heat and water exchange between the land surface and the atmosphere (Frey and McClelland, 2009; Vonk et al., 2019). At the global scale, permafrost thaw impacts are attributed to their influences on biogeochemical processes and greenhouse gas emissions. The total carbon stored in the permafrost regions is estimated to be twice that in the atmosphere (Schuur et al., 2015). The vast amount of carbon stored in permafrost is likely to be released into the atmosphere under a warming climate, exacerbating climate change due to positive greenhouse gas feedbacks.

How permafrost thaws in response to climatic warming and its associated impacts on ecological and hydrological aspects have gained global attention in the scientific community (Shur and Jorgenson, 2007; Koven et al., 2011; Schuur et al., 2015; Streletskiy et al., 2015). Several permafrost monitoring networks, such as the Global Terrestrial Network for Permafrost (GTN-P) (https://gtnp.arcticportal.org/about-the-gtnp), Circumpolar Active Layer Monitoring (CALM) (https://ipa.arcticportal.org/products/gtn-p/calm), and Permafrost and Climate in Europe (PACE) (https://doi.org/10.1002/ppp.377), have been established to record changes in permafrost temperature and ALT regionally and globally (Fagan and Nelson, 2017; Streletskiy et al., 2017; Etzelmuller et al., 2020; Tregubov et al., 2020). In addition to extensive field monitoring, process-based modeling is a complementary approach to understanding water and heat transfer processes and mechanisms in the biogeochemical cycle in permafrost regions. In this regard, land surface models (LSMs), soil-vegetation-atmosphere transfer (SVAT) models, and hydrological or frozen soil water-heat models have been used to simulate permafrost hydrothermal conditions (Flerchinger and Saxton, 1989; Cherkauer and Lettenmaier, 1999; Gouttevin et al., 2012; Swenson et al., 2012; Che et al., 2014; Yi et al., 2014; Wang et al., 2017).

There are various forms of ground ice in permafrost with different sizes, structures, and formation patterns at spatial and temporal scales. The former Soviet Union scholar Ershov et al. (2015) first divided permafrost ground ice into two main types according to the formation causes: intrasedimental ice and buried ice (Ershov et al., 2015). Mackay (1972) further provided a more detailed classification of intrasedimental ice based upon the water source immediately prior to freezing and the principle of water migration. **Figure 1** shows the various types of ground ice exhibit significant differences in thickness and duration of formation and existence. Segregated ice formed by water migration ranges in thickness from hairline width to more than 10 m (Subcommittee, 1988; Mackay and Dallimore, 1992), and it plays a critical role in changing soil structure, affecting the hydrothermal properties of frozen ground (Van Huissteden, 2020). Seasonal segregated ice lens formation and thaw cause frost heaves and thawing settlement. In permafrost, repeated-segregation ice near the permafrost table significantly affects the topographic features and soil hydrologic conditions. Segregated ice formation and water migration cause mass and energy transfer within the active layers to be extremely complex (Xu et al., 2010). In addition, the barrier effect and water migration caused by ice formation alter soil hydrothermal properties, microstructure, and ventilation conditions (He et al., 2020; He et al., 2021). These processes influence the mass and energy exchange between the land surface and the atmosphere, leading to the redistribution of soil carbon and nutrients and impacting vegetation dynamics (Walker et al., 2004). To reveal the physical mechanisms of mass and energy transfer in frozen soil and the environmental impacts of frozen soils, representing the mechanisms that explicitly describe these processes is one of the main challenges in state-of-the-art LSMs.

Frost heave models based on the frozen fringe theory (Miller, 1972) have been used to simulate ice formation (Konrad and Morgenstern, 1980; Sheng et al., 1995; Michalowski and Zhu, 2006; Ji et al., 2019; Zhou and Wei, 2020). These models have detailed descriptions to simulate the ice segregation process in soil freezing. However, it is difficult to apply frost heave model in fieldwork because the empirical work has principally been conducted in highly controlled laboratory conditions (Smith et al., 1985). At the landscape scale, LSMs that involve processes such as hydrogeology, biochemistry, and vegetation dynamics focus more on frozen soil parameterization schemes rather than a specific mechanism in the freeze-thaw processes, such as the segregated ice formed by water migration and freezing front movement (Oleson et al., 2010; Che et al., 2014; Sun, 2015; Andresen et al., 2019; Li et al., 2020). The lack of detailed representation of water migration and ice formation in models probably increases uncertainty in the simulation of soil water content and temperature conditions (Pitman et al., 1999), leading to deviations in the assessment of the ecological and hydrological effects of permafrost at the landscape scale. (Xue et al., 1996; Koren et al., 1999; Liang et al., 2003; Oleson et al., 2013).

The overall framework and linkage between different sections are shown in **Figure 2**. This review discusses the theories of water migration and ice formation and their current modeling methods. Their impacts on the land surface processes (such as the landform, hydrological patterns, and biogeochemical processes) in permafrost regions are involved. Based on the discussion of the water migration and segregated ice formation and their model construction, this review puts forward some reference opinions on developing present theories and permafrost modeling in the future. The summary review will help facilitate studies accounting for the interaction between permafrost, ecosystems, and climate systems.

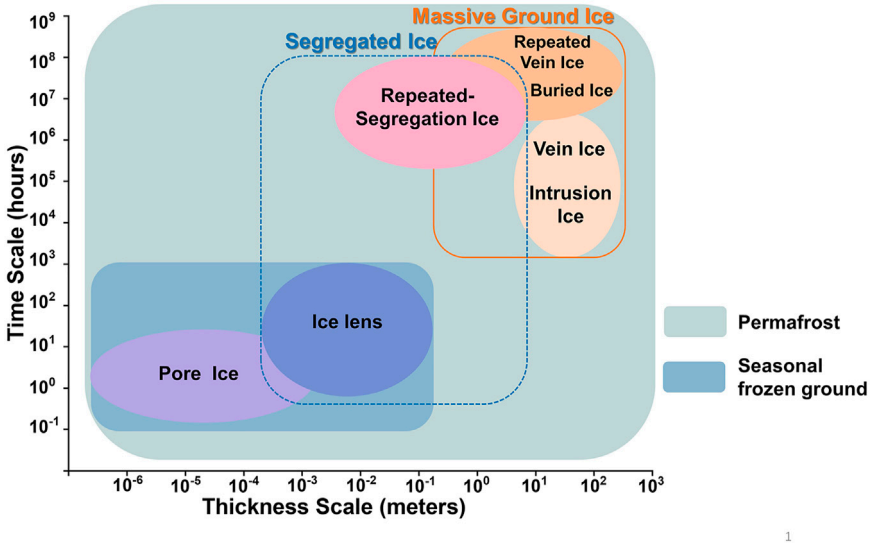

FIGURE 1 | The types of ice in frozen soil range from the pore size to the massive ground ice size at the spatial scale, and their formation ranges from sub-daily to centennial at the temporal scale. The study focuses on the segregated ice and water migration with medium and minor scales (blue dotted line), which exist in permafrost and seasonally frozen ground.

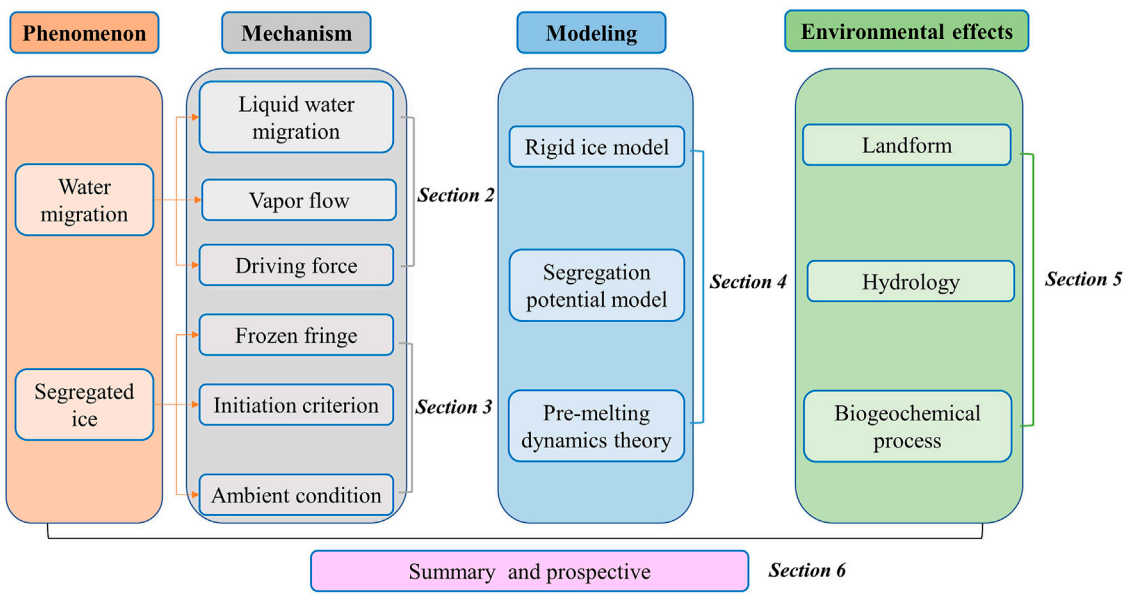

FIGURE 2 | A diagram illustrating the overall framework and linkages of different sections in this article.

WATER MIGRATION DURING THE SOIL FREEZING-THAWING PROCESS

Unfrozen Water Migration

When the temperature drops to the freezing point, where water and ice are in equilibrium with equal free energy, the water is transformed into ice. For pure water under normal conditions, the freezing point equals 0°C, while the freezing point has a depression in soil due to soil salinity, the capillary effect, and adsorption of soil particles (Anderson and Tice, 1972; Banin and Anderson, 1974; Scherer, 1999). Many studies have shown that liquid water exists in the soil pore in equilibrium with ice at temperatures considerably below 0°C (Burt and Williams, 1976; Horiguchi and Miller, 1983;

Smith, 1985; Zhang et al., 2020). This water is known as unfrozen water. Burt and Williams (1976) first measured hydraulic conductivity in freezing soils and demonstrated that the hydraulic conductivity decreased with temperature decreases but did not fall to zero, even at relatively low temperatures.

In general, the water-energy state and movement direction in soil mainly determined by the soil matric potential, which is created by the capillary and adsorption forces of the soil matrix (Or et al., 2002). The matric potential is usually related to soil properties. However, regardless of the soil type, the unfrozen water alongside the ice lens has a matric potential proportional to the temperature depression below 0°C, described by the Clausius-Clapeyron equation (Edlefsen and Anderson, 1943; Williams and Smith, 1989). This equation shows that the potential decreases by approximately 1.2 MPa per °C below 0°C. This potential is significant and creates suction that makes unfrozen water migrate to zones of lower temperature and then accumulate there, leading to the growth of ice lenses (Ferguson et al., 1964; Biermans et al., 1978). The development of ice lenses, called segregated ice, causes considerable volumetric expansion, which is the primary reason for soil frost heave (Hoekstra and Miller, 1963; Kanevskiy et al., 2013). (Taber, 1929; Taber, 1930) was the earliest to deduce that frost heave is caused by liquid migration that supplies growing ice lenses through a series of experiments. This is the first basic theoretical explanation of frost heave, and is typically referred to as the capillary theory (Smith et al., 1985). The growth rate of segregated ice depends on the freezing speed (Station et al., 1915; Bouyoucos, 1920; Watanabe et al., 1997). Besides, when frozen soil thaws unidirectionally, water also migrates from thawed regions to the thawing front, decreasing the water content through dehydration (Cheng, 1982).

Thick segregated ice is one of the main components of ground ice near the permafrost table (Williams, 1968; French, 2017). In permafrost regions, more than 50% of the volumetric ice content of massive ground ice is located near the bottom of the active layer or permafrost table (Mackay, 1972; Hughes, 1974). Mackay (1972) called this kind of ground ice "aggradational ice" and attributed it to the syngenetic growth of permafrost (with the continuous deposition of surface sediments, the upper limit of permafrost rises with the rise of the ground). Cheng (1982) considered that the downward migration of unfrozen water content is always greater than the upward migration in the active layer during a freeze-thaw cycle, accounting for moisture accumulation at the permafrost table. He proposed that accumulation of ice at the permafrost table might occur under all conditions and thus form a thick ground ice layer, namely repeated ice-segregation (Cheng, 1983). This mechanism was verified by Burn and Michel (1988) and Yang et al. (2017) using an isotope technology.

Vapor Flow in Frozen Soil

Unfrozen water migration in frozen soil is more likely to occur in soil with fine particles and high moisture content than dry coarse-grained soil (Burt and Williams, 1976; Fisher et al., 2020). Therefore, in cold regions, replacing the foundation soil of roadbeds or airport runways with dry coarse-grained soil is considered an effective engineering measure to prevent frost heaves (Vinson et al., 1996). However, frost heaves can also occur in high-speed railway embankments and airport runways padded with unsaturated coarse-grained soils (Zhang et al., 2016; Teng et al., 2020). It has been confirmed that gaseous water (vapor) migrates from the warm and humectant side of the soil layer to the cold and dry layer below the closed/impermeable ground surface in coarse-grained soil and then condenses into ice, causing frost heaving (Guthrie et al., 2006; Niu et al., 2017; Yuzhi et al., 2020). This phenomenon is called the "pot effect" or "canopy effect" (Bai et al., 2018). The water vapor migration rate is controlled by the pressure gradient and soil diffusion rate related to the relative humidity (Philip and Vries, 1957). In general, soil with an initial moisture content of less than 30% is more prone to showing the "pot effect" (Bai et al., 2018).

Some results showed that more water comes out of the soil in winter than can be reconciled with the theory for vapor flux (Farouki, 1981; Currie, 1983; Smith and Burn, 1987). Smith and Burn (1987) pointed out that unfrozen water migration is still the dominant mode of transport in contrast with vapor flow by comparing field observations and calculation values. Even so, vapor migration in frozen still has potentially considerable impacts on engineering facilities and the environment. Numerical simulation results indicate that if vapor migration is not considered in unsaturated coarse-grained soils, the predicted value of frost heaving is underestimated by 60% compared to the measured value (Teng et al., 2020). In sandy soils, although the larger soil pores reduce capillarity, it is very conductive to vapor migration (Yu et al., 2018). Intense evaporation occurs on the surface of sandy soil, leading to soil water loss. Without replenishment, the continuous loss of surface soil moisture can cause land desertification, especially in regions with lower groundwater tables (Zhanrong and Shuangping, 2002; Cui and Shao, 2005; Wang et al., 2006b).

Driving Forces of Water Migration

The capillary theory indicates that water migrates toward the freezing front along with the pores among soil particles because of the primary mover of capillary force during freezing. Based on the capillary theory (Everett, 1961), illustrated frost heaving and estimated the amount of frost heaving quantitatively. However, the theoretical value calculated by capillary theory is always smaller than the experimental value, and there is no plausible mechanism within the capillary theory for explaining the initiation of new lenses (Miller, 1972; Peppin and Style, 2013).

With the development of the theory, the hypothesis of film water migration was proposed to make up for these deficiencies (Beskow and Fil, 1935). The film theory suggested that the water film on soil particle surfaces shows asymmetry under temperature gradients, causing a thinner film at the end with low temperature and a thicker film at the opposite end, resulting in the unfrozen imbalance in the water-ice-soil particle system. Suppose the soil particles have identical radii but different water film thicknesses. In that case, the film water will migrate from the place with a thicker film (with more extensive water molecular activity) to the place with a thinner film (with lower water molecular activity) to reach a new thermodynamic equilibrium under the water potential gradients (**Figure 3**). There is a 1/3 power function

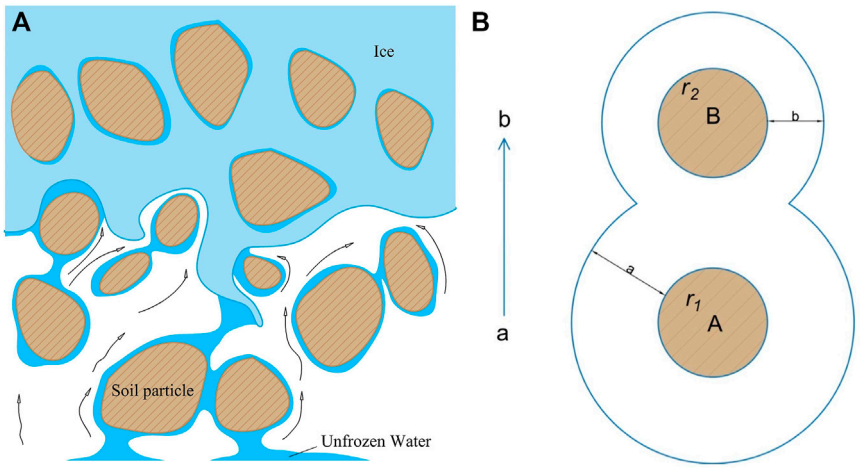

FIGURE 3 | A schematic diagram of film water migration: **(A)** the direction of film water migration; **(B)** the principle of film water migration around soil particles (i.e., A and B are soil particles with equal radius, a and b are water film thickness (a > b), and particle B is closer to the freezing front).

relationship between water film thickness and temperature (Dash, 1989):

$$d = \left(\frac{-A}{6\pi\rho_s L}\right)\left(\frac{T_0 - T}{T_0}\right)^{-1/3}, \quad (1)$$

where d is the film thickness, T is the temperature, A is the Hamker constant, ρ_s is the density of soil particles, L is the latent heat of ice, and T_0 is the freezing temperature of soil water. The film theory that relates unfrozen water migration to temperature gradients has been confirmed in subsequent studies and once substituted the capillary theory as the mainstream theory (Hoekstra, 1966; Hoekstra, 1969; Takagi, 1980; Wilen and Dash, 1995).

In 1963, the International Union of Soil Sciences (IUSS) clarified the definition of soil water potential, pointing out that water migration can be caused by any component (such as pressure, temperature, matric, osmotic, or gravity) of soil water potential (Shao et al., 2006). However, the water potential gradient is difficult to determine in frozen soil because the surficial films are too small. The temperature gradient is the only driving gradient that could be determined directly. Using a thermodynamic approach, A linear relation between temperature below 0°C and soil water potential is derived from the generalized Clausius Clapeyron equation (GCCE) (Gilpin, 1982; Spaans and Baker, 1996; Hansson et al., 2004). GCCE indicates that the temperature specifically controls the difference in potential between solid and liquid phases, and if ice pressure rises, water potential rises too. Therefore, a linear relation is only considered reliable under static conditions (Takashi et al., 1982). However, the freezing and thawing of an open system is more likely to be a non-equilibrium thermodynamic process in many cases (Bronfenbrener, 2013). Wood (1990) suggested a pressure difference between the ice and aqueous phases throughout the freeze-thaw cycle and ice deformation consecutively, making it difficult to approach equilibrium. Li et al. (2001) pointed out that GCCE must satisfy the assumption that temperature and pressure do not change with time. The depression of pore water pressure under open-system freezing is approximately half of that under closed-system freezing while considering the dynamic flow of soil freezing (Miyata and Akagawa, 1997). There are inconsistencies between experiments results and the calculation of GCCE (McGaw et al., 1983; Zhang et al., 2014b). Style and Peppin (2012) suggested that using the GCCE to determine the water pressure at the ice-lens front and applying it to Darcy's law will overestimate the ice growth rate. Ma et al. (2015) discussed the applicability of GCCE and proposed a static and a dynamic model, respectively. The dynamic GCCE model may be closer to the actual freezing process. Thus, it can better describe nonlinear variations in pore water pressure and address inconsistency between calculated values and experiments.

In addition to the above theories, various hypotheses of water migration driving force have been proposed, such as crystallization force, suction force, barometric vacuole, and ice pressure gradient (Xu et al., 2010). These hypotheses explain the mechanism of moisture migration in frozen soil from the perspectives of thermodynamics, mechanics, and physical chemistry. However, each view has its limitations (**Table 1**), representing the driving force under specific conditions (Bouyoucos, 1920; Taber, 1930; Korkina, 1965; Hoekstra, 1969; Gilpin, 1980). There is now a consensus that the water migration in frozen soil is due to multiple factors (such as thermodynamic, mechanics, and physicochemical) that need comprehensive analysis from various perspectives.

ICE SEGREGATION IN FROZEN SOIL

The Structure of Frozen Fringe

In the early stage of research on frozen soil, the capillary theory (primary frost heave) was used to illustrate the formation

TABLE 1 | Hypotheses on the driving force of water migration in frozen soil.

Hypotheses	References	Driving force	Mechanism	Deficiency
Capillary theory	Штукенберг, В. И. (1885)	Capillary force	The capillary force between soil particles drives water migration from the unfrozen zone to the freezing front	The theoretical value is lower than the experimental value. It cannot explain the formation of the first ice lens
Film theory	Beskow and Fil (1935)	Pressure difference	The ice lenses are connected with the water supply via the water film at the ice surface, the film is a path for water migration	The rate of water migration is underestimated
Suction theory	Ershov et al. (2015))	Vacuum suction force	The imbalance of ice crystal growth causes vacuums, and then the water in the unfrozen area is pumped into the crack, forming ice	The theory can only be applied to saturated soil, and the essence of water migration was not studied
Crystallization theory	Taber (1929)	Cohesion of water	The cohesion among water molecules is lower than that between water molecules and ice crystals, driving the water to migrate towards ice crystals' growth	This view can be subsumed into the suction theory
Electro-osmotic theory	Korkina (1965)	Freezing potential	The voltages caused by the rejection of soil ions, cause unfrozen water migration	The magnitude of the electro-osmotic effect cannot be evaluated

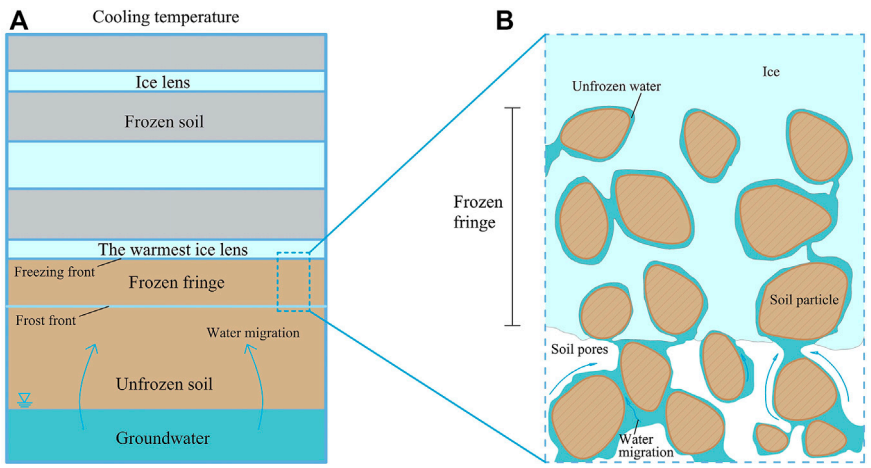

FIGURE 4 | A schematic diagram (not to scale) of frozen fringe: **(A)** shows the relative position of the frozen, frozen fringe, and unfrozen zones within freezing soil and, **(B)** is the magnified views of the frozen fringe zone.

mechanism of segregated ice (Taber, 1930; Gold, 1957; Everett, 1961; Haynes, 1965). Primary heave occurs when there is no frost penetration into the soil, leading to needle ice and for some of the very large lenses of massive ice (Miller, 1972; Goulet, 1995). However, the primary frost heave theory still did not answer the questions: 1) mechanisms to explain the initiation of new ice lenses; and 2) the frost heaving force estimated by the theory does not match the experimental data (Sheppard et al., 1978; Jansson and Halldin, 1979; Guymon et al., 1980). Peppin and Style (2013) considered that the flow rate toward the ice lens tends to be overestimated due to the Clapeyron equation breaking down outside equilibrium under the assumption of local equilibrium at the ice-lens-soil boundary.

Miller (1972) proposed the concept of frozen fringe (secondary frost heave). The frozen fringe is defined as the partially frozen zone between the ice lens and the warmest soil with pore ice, i.e., the soil volume in which the water pressure declines due to coexisting with ice (**Figure 4**) (Gilpin, 1982; Konrad, 1999; Miller, 1972; ONeill and Miller, 1985). Therefore, any internal and external factors that can change soil unfrozen water content will influence the thickness of the frozen fringe, such as soil texture, soil salinity, and the external load (Radd and Oertle, 1973; Loch and Miller, 1975; Konrad and Morgenstern, 1981; Akagawa, 1988; Ma et al., 2015). Some reports have stated that the frozen fringe is non-existent in saturated soil with a particle size larger than 0.1 mm (Liu et al., 2005). However, if the soil water has high salinity, there may well be the coexistence of ice and water below 0°C (Chamberlain, 1983). The ice lens growth rate at the frozen fringe depends on the freezing velocity (Watanabe et al., 1997). During fast freezing, the freezing front moves so rapidly that water cannot migrate towards the freezing front immediately, and the water freezes *in situ* without forming a frozen fringe

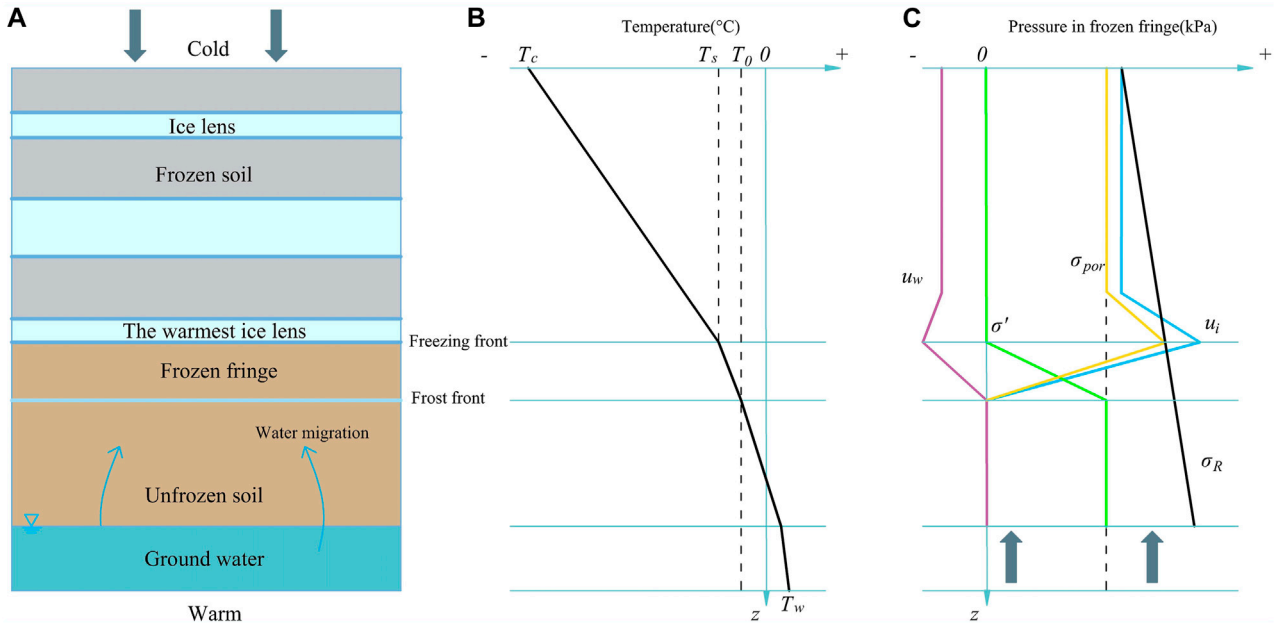

FIGURE 5 | The temperature and pressure of the frozen fringe (based on a static model of the frozen fringe by Ma et al. (2015): **(A)** the location of the ice lens and frozen fringe; **(B)** temperature in the frozen fringe. T_C and T_W are the upper and lower boundary temperatures, respectively; T_S is the segregated temperature; and T_0 is the soil freezing point; **(C)** pressure in the frozen fringe.

(Xu and Deng, 1991). Overall, the internal structure of the frozen fringe is complex, and various physical parameters change significantly in different freezing stages, making it challenging to accurately determine different parameters (Akagawa et al., 2006; Akagawa and Nishisato, 2009).

Initiation Criteria of Ice Lenses

The conditions of moisture, temperature, and stress conditions in the frozen fringe can determine when and where ice lens initiation occurs (Xu et al., 2010). In the frozen fringe, although the permeability decreases rapidly with the formation of porous ice during the freezing process, moisture still migrates to the frozen zone continuously under the pressure gradient caused by the depression of pore water pressure (Peppin and Style, 2013). However, the permeability in the frozen fringe is so poor that moisture accumulates, forming ice lenses at the back of the freezing front (**Figure 4A**) (Rempel, 2007). Ice lenses undergo sustained grow with enough water supply. The location of new ice lenses is related to the hydraulic conductivity of the currently frozen fringe. The growth or stagnation of the ice lenses depends on the temperature at the warmest end of the ice lens, i.e., the segregation temperature (**Figure 4B**) (Konrad and Morgenstern, 1980). Akagawa (1988) found that the segregation temperature was around −0.8°C through experiments. Based on a simple method to determine the segregation temperature and the ice lens location, Xu et al. (2010) found that segregated ice was most likely to form in soil with structural connections. The temperature gradient and water migration caused uneven soil shrinkage, resulting in the appearance of cracks in the frozen fringe (Arenson et al., 2007). In addition to stress and temperature criteria, there are also some other possible criteria for the formation of ice lens. Style et al. (2011) claimed that a new ice lens occurs at a location where supercooling reaches maximum. Zhou and Li (2012) modelled ice lens formation with the concept of separating void ratio, a critical void ratio that enables pore ice to connect into an ice lens.

Figure 5B and **Figure 5C** show the temperature and pressure profiles around the frozen fringe. When discussing the ice lens initiation criteria, typically only the stress conditions are considered to facilitate practical calculation and application (Ma et al., 2015). The stress conditions include pore pressure σ_{por} (Sheng et al., 1995), pore water pressure u_w (Hazirbaba et al., 2011), ice pressure u_i, and overburden σ_R (Nixon, 1991) (**Figure 5C**). ONeill and Miller, 1985 pointed out that a new ice lens forms when the ice pressure in the frozen fringe is greater than or equal to the external load at the cold end of the frozen fringe. Gilpin (1980) proposed critical segregation pressure, in which ice pressure is regarded as the destructive force of soil structures that determines the ice lens formation. An increasing number of studies have shown that the formation of new ice lenses and the halt in the growth of old ice lenses may not occur at the same time, which can be determined using mechanical and thermophysical methods, respectively (Konrad and Duquennoi, 1993; Zhang et al., 2014a). A previous study showed that the stress conditions of ice lens initiation should include two stresses: the driving force of soil fracturing as well as ice lens formation and the constraining force preventing soil fracturing (Ma et al., 2015). Ice lens initiation can only occur when the pore pressure is greater

than or equal to the restraining force, and the effective stress (σ' in **Figure 5C**) equals zero (Ma et al., 2015).

Environment for the Development of Segregated Ice

The natural formation of massive segregated ice is mainly affected by soil properties. Fine-grained soils generally promote segregated ice formation due to their high unfrozen water content (Van Huissteden, 2020). However, Burt and Williams (1976) showed that although clays have the highest unfrozen water content, their low permeability leads to a lower hydraulic conductivity than silts below 0°C. For this reason, silts have a high frost susceptibility compared to clay and are easy to occur the segregated ice (Burt and Williams, 1976; Chamberlain, 1981). The change in soil structures due to frost cracking is another essential mechanism for ground ice formation (Azmatch et al., 2008). During the freezing process, vertical cracks may occur in the frozen fringe and unfrozen areas, leading to appropriate soil local stress conditions for segregated ice growth. Segregated ice may also occur in rocks by accelerating cracking and physical weathering, especially in stratums prone to fission, such as shale or fine-grained porous rocks (Murton and Lautridou, 2003; French and Shur, 2010). Higher soil water content is critical factor for the growth of segregated ice in some permafrost regions. The results of Calmels and Allard (2008) showed that ice content could exceed 50% after frost heaving in wet peat. Segregated ice formation brings about water migration and accumulation in soil with enough groundwater supply recharge. Without sufficient water, segregated ice ceases to grow, and the soil finally becomes consolidated and contracted due to dehydration under freeze-thaw cycles (Van Huissteden, 2020).

LABORATORY STUDIES AND SIMULATIONS OF SEGREGATED ICE

Mathematical models of the soil ice formation process have attracted much attention in the past decades (Harlan, 1973; Jame and Norum, 1980; Hansson et al., 2004; Lai et al., 2014; Liu et al., 2019). These studies help elucidate the mechanism of frost heaving and provide practical measures for frost heave prediction and prevention for engineering. The review does not try to comprehensively discuss all aspects related to soil frost heave, such as the distinction of primary, secondary, and tertiary heave (Miller, 1978; Mackay et al., 1979; Horiguchi, 1980; Smith et al., 1985). Instead, we focus on the processes involved in segregated ice formation, which mostly describes the warmest or first ice lens ice based on the frozen fringe. They can be broadly divided into three types: rigid ice models (ONeill and Miller, 1985; Sheng et al., 1995; Zhou et al., 2018), models based on segregation potential (Gilpin, 1980; Koren et al., 1999; Ji et al., 2019), and pre-melting dynamic models (Wettlaufer et al., 1996; Rempel et al., 2004; Michalowski and Zhu, 2006; Zhou and Wei, 2020). These models differ in practical applications due to different theoretical assumptions and bases.

Rigid Ice Model and Separated Ice Model

The rigid ice model was first proposed by Miller (1972), who considered that ice lens and pore ice in the frozen fringe is a rigid ensemble that moves at a uniform velocity. The pore ice in the frozen fringe is attached to the growing lens above and moves relative to the surrounding soil particles by melting and refreezing as necessary. ONeill and Miller (1985) developed it into a complete model, aiming to directly predict the characteristics of ice lenses and the rate of frost heave as a function of environmental conditions and sediment constitutive behavior. In the model, the relationship between ice content I (%) and water pore pressure P_w (Pa), and temperature T (°C) was connected by the soil-water characteristic curve and integral form of the Clapeyron equation:

$$I = I\left(AP_w + BT\right), \tag{2}$$

where A and B are known constants. In addition, the movement of the ice lens is considered in basic transport equations:

$$\left(\rho_i - \rho_w\right)\frac{\partial \theta_i}{\partial t} - \frac{\partial}{\partial x}\left[\frac{K_h}{g}\left(\frac{\partial P_w}{\partial x} - \rho_w g\right) - \rho_i V_I \theta_i\right] = 0 \tag{3}$$

$$\sum \rho_n c_n \theta_n \frac{\partial T}{\partial t} - \frac{\partial}{\partial x}\left(\lambda \frac{\partial T}{\partial x}\right) - \rho_i L\left(\frac{\partial \theta_i}{\partial t} + V_I \frac{\partial \theta_i}{\partial x}\right) = 0, \tag{4}$$

where ρ_i and ρ_w are ice and water density (kg m^{-3}), respectively; n represents different soil components; c_n is the thermal conductivity of different components (J m^{-1} s^{-1} K^{-1}); θ_n is the volume fraction of the nth component including soil solids (%); V_I is the segregation rate of ice (m s^{-1}); g is gravitational acceleration (m s^{-2}); K_h is the hydraulic conductivity (m s^{-1}), and the function of unfrozen water content in frozen fringe and can be regarded as the saturated hydraulic conductivity in the unfrozen zone; and λ is the thermal conductivity of the soil skeleton (J m^{-1} s^{-1} K^{-1}), which is related to the content of soil components. The segregation rate V_I can be obtained from the conservation of mass in the frozen fringe as

$$V_I = -K_h\left(\frac{\partial P_w}{\partial x} - \rho_w g\right)\frac{1}{\rho_w g\left(1 - \theta_i\right)}. \tag{5}$$

Soil particles lose contact and new ice lenses form when the effective stress of pores in the frozen fringe is greater than or equal to the total load at the end of the frozen fringe:

$$\sigma_n = \chi P_w + \left(1 - \chi\right)P_i \;\geq\; P_0, \tag{6}$$

where σ_n is the effective stress (Pa), and $\chi = \left(\theta_u/\rho\right)^{1.5}$ is the stress-partition parameter (Pa) (Miller, 1978), where θ_u is the unfrozen water content (%) and ρ is the soil density.

The rigid ice model can describe frost-heave behavior by keeping track of only two essential parameters of the ice content in the frozen fringe: 1) spatial variations in the volume fraction of the pore space that is occupied by ice; and 2) spatial variations in the effective permeability caused by these

changes in ice saturation (Rempel, 2010). Both parameters can be obtained from independent laboratory studies (Watanabe and Flury, 2008; Watanabe and Wake, 2009). However, there are still considerable workloads to put it into practical application (Ming and Li, 2016). Many researchers have devoted attention to simplifying the model (Black, 1985; Ishizaki and Nishio, 1988; Sheng et al., 1995). Fowler and Krantz (1994) reduced the computational amount of the rigid-ice model by using asymptotic analysis to reformulate the model and greatly improve its practical implementation. Sheng et al. (1995) modified the governing equation and interruption stress expression, establishing an operable simplified model (PCheave). This model can solve variables such as soil frost heave rate, freeze-thaw front movement speed, and ice volume content, which is helpful for frost heave monitoring in the field (Zhang et al., 2014a).

Segregation Potential Model

The segregation potential model is a semi-empirical model describing the growth of a single ice lens (Konrad and Morgenstern, 1980; Konrad and Morgenstern, 1982b). The basic assumption is that for any identical soil, while the one-dimensional freeze is steady-state, the ratio of the velocity of water migration at the bottom of the last ice lens and the soil temperature gradient below ice lens is a constant, namely, segregation potential SP :

$$V = SP \cdot \Delta T, \tag{7}$$

where V is the velocity of water migration and ΔT is temperature gradient (K cm^{-1}), and the segregated ice content can be calculated by (Konrad et al., 1995):

$$H = 1.09 \int_0^t SP \Delta T dt. \tag{8}$$

The SP, in effect, is a conductivity driven by temperature, and depends on external pressure, suction at the frost front, and rate of cooling of the frozen fringe (Konrad and Morgenstern, 1980; Konrad and Morgenstern, 1982a). All of these parameters may be obtained directly from laboratory frost heave tests at the macroscopic scale. Konrad (2005) reported values of SP ranging 160 to 410 (mm^2/°C·d) for saturated sand–silt–clay mixtures, 52 to 325 (mm^2/°C·d) for till samples, and 84 to 329 (mm^2/°C·d) for fine quarry materials. Water migration and segregated ice can be directly predicted as long as SP has been measured by experiments. (Nixon, 1982; Fukuda et al., 1988; Saarelainen, 1992; Tiedje and Guo, 2012). Konrad and Morgenstern (1984) predicted the frost heave caused by a frozen pipe buried in an unfrozen region using the segregation potential model. The simulation was in good agreement with long-term field observation results. However, Nixon (1987) and Ishizaki and Nishio (1988) pointed out that the model could not describe the ice lens growth under unstable thermal conditions. The model cannot predict the dewatering at the initial stage of freezing. Furthermore, the model did not involve the parameters related to basic soil properties (Li et al., 2000). Based on the segregation potential model and the water activity criteria, Ji et al. (2019) proposed a quasi-static model for ice lens growth to describe the ice lens growth under slowly changing segregation temperature.

Pre-Melting Dynamics Theory

The rigid-ice model and the segregated potential model give a successful prediction of the macroscopic processes of segregated ice. At the microscale, the force-balance condition of the initiation of new lenses still lacks a firm theoretical basis. Römkens and Miller (1973) observed the migration of particles in freezing soil and attributed it to the osmotic transport of water in the film surrounding the particles. The authors explained the force between ice and soil particles based on two models: 1) electrical double-layer effects and the viscous flow of water, and 2) a brine pocket enclosing the particle and diffusion phenomena. Wettlaufer et al. (1996), Wettlaufer et al. (1997) found that due to the thermal molecular repulsion between the porous medium and ice, there is interfacial melting between the ice lens and the matrix. This melting forms a thin liquid water film on the surface of the substrate called pre-melting film (Lu et al., 2017). The net force between the ice and sediment particles can be explained quantitatively as a result of the intermolecular forces that act between them and produce the intervening pre-melting films (Williams, 1995). The intermolecular force changes the thickness of the film between the soil particles and surrounding ice, and increases with the decreasing distance and increasing temperature between soil particles and ice (Rempel et al., 2001). In the presence of pre-melting film, the total surface energy of the soil particle-water and liquid water-ice interface is lower than that of the soil particle-ice surface (Zhou and Meschke, 2013).

Rempel et al. (2004) concluded that the thermal molecular repulsion of both the cold and warm ends of soil particles is imbalanced. Owing to the difference in water film thickness, the force of the cold end is greater than that of the warm end. This force will drive soil particles away from the ice lens, causing ice to melt on the warmer side and water to refreeze on the colder side through thermal regelation. Rempel et al. (2004) developed a model based on mechanical equilibrium and conservation to describe the formation and evolution of ice lenses. Based on the micro thermodynamic theory of ice soil particle interaction, different forms of macro frost heaving processes can be described, including the growth of single ice lens or needle ice, the successive growth of multiple lenses, and the situation with only pore ice (Rempel et al., 2004; Rempel, 2007). It should be noted that the pre-melting film is still affected by thermal molecular forces while the frozen fringe disappears because the warm side coincides with the freezing front. Therefore, the frozen fringe is not always considered in the pre-melting film model (Lu et al., 2017). The derivation and development of pre-melting film originated from the micro-physical mechanism, discussing the essence of soil water and heat change during the freeze-thaw process, opening up a new direction for the macroscopic ice formation process model (Rempel et al., 2004; Zhou and Wei, 2020).

In the 1990s, Fremond and Mikkola (1991) proposed a thermodynamic model based on the law of energy

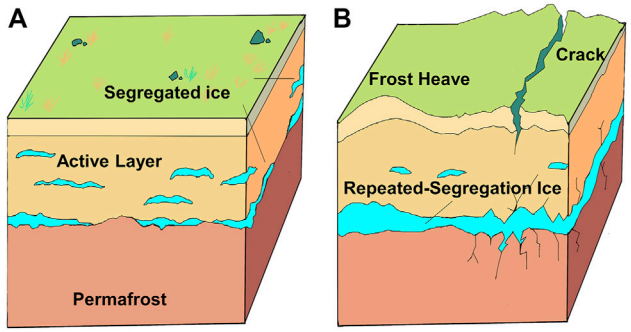

FIGURE 6 | A schematic diagram of landforms in permafrost regions. **(A)** Segregated ice forms in the active layer at first, and the ice lens at the permafrost table is preserved after a freeze-thaw cycle. **(B)** Under a cooling climate, the permafrost table is raised, and the accumulation of segregated ice forms massive repeated-segregation ice, causing frost heave and frost crack.

conservation and entropy increase balance. This model was derived from a series of thermodynamic equations based on the basic axioms. The model can describe the suction caused by pore water freezing and moisture and heat transfer (Ran et al., 2019). However, the application of this model has not been extensive due to its large number of parameters, which are too difficult to obtain in experiments. The model still needs to be further improved and developed in the future.

ENVIRONMENT EFFECTS CAUSED BY THE SEGREGATED ICE FORMATION

Segregated ice is a vital factor affecting the permafrost environment. It is widespread in the active layer from the permafrost table to the ground surface (**Figure 6A**), where there are acute water and heat transports among soil, vegetation, and the atmosphere. These energy exchange processes are significantly affected by segregated ice formation, growing, and melting via changes in the soil hydrothermal properties and soil structures (Wu et al., 2003). Thus, segregated ice formation shapes the unique frozen land morphology, changing the regional topography and hydrological processes, and causes soil and vegetation reorganization in the cold region ecosystems, affecting the carbon and nitrogen cycle and other biogeochemical processes.

Permafrost Landforms

The ice in permafrost has an important role in the formation of topography, or at least, in the origin of minor relief in permafrost regions. Segregated ice development causes frost heave and modifies topography (**Figure 6B**). Sometimes segregated ice development causes polygonal cracks because of the uneven distribution of ice in the soil mass (Walker et al., 2004). Segregated ice is also an essential factor in frost mounds formation (Van Huissteden, 2020). Hummocks are widely distributed in arctic and subarctic permafrost regions (Washburn, 1980), and are caused by the long-term seasonal freeze-thaw of ice lenses at the top and bottom of the active layer (Mackay, 1980). When permafrost degrades, the inhomogeneous melting of segregated ice causes the ground surface to collapse unevenly (Streletskiy et al., 2015; French, 2017). The hollows caused by the subsidence of the ground surface easily collect precipitation, runoff, and meltwater, forming ponds or lakes, changing the surface heat balance (Boike et al., 2015).

Regional Hydrological Processes

Segregated ice affects the hydrological process mainly by changing the hydrological properties and micro-topography by reducing soil permeability (Woo, 2012; Walvoord and Kurylyk, 2016). Massive segregated ice near the permafrost table causes a sharp decrease in permeability of this area. The zone with massive segregated ice can be regarded as a regional aquifer or impermeable layer. The impermeable layer obstructs or weakens the hydraulic connection between groundwater and active layer water, runoff, and even atmospheric precipitation on a seasonal scale (Zhao et al., 2019). In addition, the formation and melting processes of segregated ice accompanied by water migration significantly affect the spatiotemporal characteristics of the hydrological conditions of the active layer (Woo, 2012; Walvoord and Kurylyk, 2016). During warm seasons, the moisture content of the active layer increases due to the influence of rainfall, snowmelt water and excessive ice melting of the ice-rich permafrost table. Before percolating into the deep soil, most of this melted water, is discharged into rivers or lakes through surface runoff or subsurface lateral flow. The runoff variation is related to slope, ALT, and saturation, as well as the supply due to the seasonal melt of segregated ice (Van Huissteden, 2020). During periods of alternating warmth and cold, snow meltwater permeates through the surrounding soil. However, because the soil temperature is still below 0°C, a portion of the meltwater will refreeze, reducing the permeability of the ground surface. Meltwater generates runoff easily, forming ponds (Woo, 2012). In the cold season, there is bidirectional freezing in the active layer, and water migrates toward the freezing front, dehydrating the soil in the middle unfrozen layer (Woo, 2012). Soil fractures due to frost heaves, increasing the infiltration of precipitation and meltwater downward in the warm season (Ostroumov et al., 2001).

Ecosystem and Biogeochemical Processes

Segregated ice affects the growth dynamics of plants indirectly in cold regions by changing soil microstructure, soil ventilation, and thermal conductivity. Meanwhile, the water migration affects the nutrient and water distribution of the active layer, transforming the succession of the whole cold region ecosystem (Wang et al., 2006a). For example, during the development of frost mound, frost heave causes the central location to move upward year by year with the growth of segregated ice. In this process, the organic matter and nutrients at the bottom of active layer are pushed to the center of frost mound, and then transported and accumulated to the surrounding edge by leaching and soil movement (Peterson and Krantz, 2003). It will result in sparse vegetation in the center over time and luxuriant vegetation in the edge of frost mound,

respectively, forming the unique honeycomb vegetation characteristics in permafrost regions (Walker et al., 2004). In the Qinghai Tibet Plateau, thawing segregated ice near the permafrost table weakened its role as an impermeable layer, which lowers water table and dries surface soil (Niu et al., 2011), thus decreasing the water available to plants and the productivity of the ecosystem (Wang et al., 2006a; Yi et al., 2014).

Large amounts of soil organic carbon (SOC) and soil organic nitrogen (SON) are stored in the active layer and underlying permafrost (Tarnocai et al., 2009; Koch et al., 2013; Zubrzycki et al., 2014; Ping et al., 2015). These organic matters easily develop into dissolved organic carbon (DOC) and dissolved organic or inorganic nitrogen (DON, and DIN, respectively) while the segregated ice melts (Wickland et al., 2018). Moreover, various soluble ions migrate to the freeze-thaw front with water migration, increasing their concentration near the ice lens (Ostroumov et al., 2001). Studies have shown that the DOC concentration in the soil solution ranges from 2 to 30 mg C L^{-1} (White, 2020), while that in the segregated ice meltwater is as high as 4–128 mg C L^{-1} (Ewing et al., 2015). Other types of dissolved organic matter (such as root exudates) produced by vegetation may accumulate due to the restriction of subsurface drainage by segregated ice (Michaelson and Ping, 2003). This organic matter is then transported to rivers through runoff (Prokushkin et al., 2009; Ma et al., 2019), strongly affecting oxidation-reduction, decomposition, and other biogeochemical processes.

Ice lenses in frozen soil also affect the below-ground gas transport process. When the soil changes between the freezing and thawing state, the SOC stored in permafrost will be decomposed by soil microbes, generating carbon dioxide (CO_2), methane (CH_4), nitrous oxide (N_2O), or other greenhouse gases (Yang et al., 2014; Zona et al., 2016). Owing to the ice lens barrier, the frozen soil delays the emission of N_2O and CO_2 in winter (Van Bochove et al., 2001; Song et al., 2012). The large autumn burst of CH_4 from the tundra in high latitudes may be related to the freezing and thawing process of permafrost in the Arctic (Mastepanov et al., 2008; Zona et al., 2016; Byun et al., 2017). Because gas solubility is significantly lower in ice than in liquid water, the formation of segregated ice at the freezing front during the bidirectional freezing process in autumn may lead to the efflux of methane previously dissolved in soil water (Byun et al., 2017). However, segregated ice blocks the pores and hinders the gas discharge, leading to the retention of CH_4. Subsequently, frost heaving due to the continuous formation of segregated ice destroys the mechanical structure of soil and causes ground cracking, providing a channel for gas to escape, thus producing a CH_4 peak (Mastepanov et al., 2013). Under a cold climate, the seasonal segregated ice and the trapped CH_4 in the active layer may be permanently incorporated into near-surface or even deeper permafrost (Byun et al., 2017). The reverse is also possible upon climate warming. Higher soil temperature will promote the activity of soil organisms and thus aggravate the decomposition of SOC to release more carbon dioxide (Natali et al., 2015).

SUMMARY AND FUTURE PERSPECTIVES

Since Taber realized that frost heaving mainly comes from liquid water migration that supplies growing ice lenses, people have put forward to various theoretical models to improve the understanding of their mechanism. Now the processes of ice lenses have been explained by mathematical models that successfully verified from the macroscopic features. In permafrost regions, water migration and segregated ice shapes spectacular permafrost topographic features, changes regional hydrological patterns, even makes their carbon cycle differ from that of other soils. Under a warming climate, researchers have much renewed interest in how the processes of water migration and ice formation play roles in the interaction between frozen ground and the environment. This article reviewed the mechanism of water migration and segregated ice formation and different models developed to account for their physical processes, as well as an overview of their impact on the permafrost environment. Given the aspects that current research regarding water migration and ice formation has overlooked, we suggest the following perspectives should be the central focus in future research.

(1) It is the basis for understanding the mechanism of ice segregation to explicitly know the driving forces of unfrozen water migration. Since the theory of unfrozen water film was brought up, the concept of soil water potential has been widely accepted to characterize the energy state of liquid water, to further study the direction and water flux during water moisture migration. Current methods are hard to directly measure the soil water potential in frozen soil, so researchers rely on the Clapeyron equation based on phase equilibrium to convert the temperature gradient to water potential (Loch, 1978; Gilpin, 1980; Drotz et al., 2009; Thomas et al., 2009). However, one of the primary assumptions invoked when employing the Clapeyron equation and its modified versions is that the pore water pressure is measured relative to the pressure in the ice phase, which is often implicitly assumed to be atmospheric (Kurylyk and Watanabe, 2013). In fact, soil increases its strength as temperature declines and as ice progressively fills the pores in the freezing process. This means the ice pressure must rise for a growing ice lens and the potential gradient will no longer be linearly related to the temperature gradient (Wood, 1990). If we can only measure the temperature gradient, it is difficult to fully interpret the reason why the growth rate of ice lenses decreases with temperature. Therefore, the applicability of the Clapeyron equation in frozen soil still needs to be further verified by accurately measuring the pore water pressure and ice pressure in the laboratory, which depends on the progress of measurement technologies. Another concern is the calculation and determination of unfrozen water content, which is also important for the study of water migration. At present, a commonly used method to calculate unfrozen water content

in frozen soil is the empirical formula or relate soil frozen characteristic curve (SFCC) and the soil water characteristic curve (SWCC) by the Clausius-Clapeyron equation (Spaans and Baker, 1996; Kurylyk and Watanabe, 2013; Fu et al., 2021). The latter is inappropriate to apply this equation at disequilibrium, such as during rapid early-stage freezing. The accuracy of the empirical formula largely depends on the calibration dataset size and characteristics. However, because of the possibility of ice be melted by the temperature or moisture probes, it is difficult to conduct long-term monitoring of the energy state of unfrozen water or unfrozen water and ice content in frozen ground under field conditions (He et al., 2018). Many new theories and methods emerged to partition water and ice in partially frozen soil to estimate unfrozen water content and ice content (Gang and Si, 2011; Kojima et al., 2016; Kojima et al., 2020). New theories and methods are in their infancy and have limitations at present. Still, they potentially could greatly improve the measurement techniques and our understanding of unfrozen water migration and ice formation.

2) The measurement of ice content is essential for studying the water migration in frozen soil and is very important for understanding the mechanism of frost heave or thaw settlement. In laboratory experiments, the ice content is usually estimated by subtracting the unfrozen water content from the total water content. The latter could be directly measured by mature methods, such as the neutron moisture meter method (NMM) (Sun et al., 2021) and gamma-ray attenuation method (Zhou et al., 2014) for the total water content, TDR (time-domain reflectometer) method, FDR (frequency-domain reflectometer) method, and NMR (Nuclear Magnetic Resonance) method for unfrozen water content (Feng et al., 2021). However, there is still no suitable method to monitor the ice content, water migration, and their spatial variation under field conditions. One of the critical problems is that we cannot monitor the change of ice content during freezing and thawing without damaging the soil structure. Although some improved methods have been verified in the field (Cheng et al., 2013; Kojima et al., 2020; Wang et al., 2021), there is still no commercial sensor available. Another way is to estimate the ice content by geophysical technology or remote sensing methods, such as ground-penetrating radar (GPR) (Daniels et al., 1995; Lamoureux et al., 2018). However, the GPR method prefers to resolve wedge ice, massive ice, and ice-rich sediments rather than the individual ice lenses with small volume, and it needs to be combined with other means to improve the accuracy of detection (Fortier and Savard, 2010; Sokolov et al., 2020). Satellite remote sensing provides another method to continuously monitor the surface water condition of frozen soil in space via data assimilation (Mwangi et al., 2020; Szczykulska et al., 2021). Cosmic-ray neutron probes (CRNP) allows continuous monitoring of soil ice content at the field scale averaged over several hectares in shallow soil profiles (Mwangi et al., 2020). However, it is still unable to reasonably estimate the ice content of deep soil layer due to soil heterogeneities (Stevanato et al., 2019). With the ever-expanding use of geophysical methods for permafrost and ground ice studies, new inversion means or improved methods should be verified by boreholes or test pits to estimate the spatiotemporal variation and distribution. This will be a new challenge for engineering geologists and shallow geophysicists.

(3) Models aimed to describe the dynamics of ice formation have given a successful prediction of the macroscopic processes of segregated ice, such as the rigid ice model, which has been widely used and further developed. However, the pre-hypothesis of the rigid ice model used to predict the heave rate and the initiation of new lenses still lack a firm theoretical basis at the microscope physics. This means it will produce uncertainty when applying the model in different physical environments by modifying the model parameters. The rigid-ice model assumes that lenses initiate within ice that is connected through the frozen fringe to the active lens. However, experiments showed that there are variety of ice growth forms in addition to lenses (Peppin et al., 2006; Rempel, 2011), and their initiation mechanisms should also be considered. Premelting theory began with surface interface physics provides a new sight in understanding the microphysical interactions that occur between the soil particles, the ice and the liquid (Rempel et al., 2004; Rempel, 2007). The net ice-particle force within the fringe can be calculated by applying the concept of thermodynamic buoyancy (Rempel, 2010). However, as it still employed a few simplifying assumptions in constructing theoretical model, the premelting model needs further development. Engineering applications of the ice formation models is another critical problem. Many works verified the model simulations through laboratory measurements (Williams and Smith, 1989), Unfortunately, relatively little field research has been conducted on frost heave. The empirical work has principally been conducted under highly controlled laboratory conditions, making it difficult to apply theoretical models in field conditions. These difficulties include but are not limited to the following: a) the complex form and various parameters of the model make it difficult for it to be popularized in actual application, b) most models are based on saturated soils, and they are not well suited to application in unsaturated permafrost and c) the considerable diversities of soil particle characteristics in different soils cause it is hard to find a uniform method to evaluate the parameters regard to frost susceptibility, such as the parameterization scheme of soil thermal conductivity and hydraulic conductivity (Gelfan, 2006; He et al., 2020). In the future, simplifying existing models or developing new ice formation models will be an exciting challenge that will facilitate field application. Additionally, combined with more observational data, developing the comprehensive and systematic scheme of permafrost soil thermal and hydraulic conductivity will also help improve the description of soil thermal properties in models.

(4) The development and decline of segregated ice at the permafrost table is an important feature in the change of permafrost, which exerts a strong influence on the development of landforms, hydrology and biochemical processes (Van Huissteden, 2020). Sustained climate warming is accelerating the degradation of permafrost and the thawing of ice lenses near the permafrost table. Under this condition, landscape models were developed to predict the influences of permafrost degradation on hydrological, ecological, and climatic effects (Flerchinger and Saxton, 1989; Cherkauer and Lettenmaier, 1999; Gouttevin et al., 2012; Yang et al., 2018a; Yang et al., 2018b). However, there were significant deviations of simulations when the models applied to permafrost, especially the unfrozen soil moisture during the freezing and thawing process (Swenson et al., 2012; Xiao et al., 2013; Chadburn et al., 2015; Yang et al., 2018a; Luo et al., 2018). One possible reason is the inadequate consideration of the water migration and segregated ice in models. Most landscape models that we have checked simplify, even ignore the process of water migration and ice lenses formation in constructing the model (Dai et al., 2003; Liang et al., 2003; Chen et al., 2007; Swenson et al., 2012; Zheng et al., 2017). Of course, it is necessary and understandable because the factors that control segregated ice formation operate at a sub-mm scale, and are primarily affected by soil properties. This makes incorporating segregated ice behavior into models operating with 1- or 10-km grid cells difficult due to soil spatial heterogeneity. However, when discussing the long-term effects of the permafrost changes, the development and thawing of ice lenses is still an inseparable feature. Some researchers have added excess ground ice to the model for simulating thermal karst caused by permafrost degradation in recent years, but they are not concerned with the long-term process of excess ice formation (Lee et al., 2014; Cai et al., 2020). In the future, we may be able to find methods to connect segregated ice models with landscape models to achieve the modeling of ice lenses that through the hundreds or even ten thousand years of evolvement. This will be a challenging and interesting work that will help us to understand the interaction between soil ice segregation and the permafrost environment, and improve the accuracy of landscape models in permafrost regions.

AUTHOR CONTRIBUTIONS

QW contributed to the conception of the study, supervision and funding acquisition; ZF: contributed to literature synthesis and wrote the manuscript; WZ, HH, and LW helped perform the analysis with constructive discussions.

FUNDING

This work was supported by the Key Program for Frontier Sciences of the Chinese Academy of Sciences (grant numbers QYZDJ-SSW-DQC011), the National Natural Science Foundation of China (grant numbers 41690144), the funding by the Swedish Nation Space Agency 209/19 and Swedish Research Council VR 2020-05338, and the National Natural Science Foundation of China (grant numbers 41877015).

REFERENCES

Akagawa, S. (1988). Experimental Study of Frozen Fringe Characteristics. *Cold Regions Sci. Technology* 15 (3), 209–223. doi:10.1016/0165-232X(88)90068-7

Akagawa, S., and Nishisato, K. (2009). Tensile Strength of Frozen Soil in the Temperature Range of the Frozen Fringe. *Cold Regions Sci. Technology* 57 (1), 13–22. doi:10.1016/j.coldregions.2009.01.002

Akagawa, S., Satoh, M., Kanie, S., and Mikami, T. (2006). Effect of Tensile Strength on Ice Lens Initiation Temperature. *Curr. Practices Cold Regions Eng.*, 1–12. doi:10.1061/40836(210)43

Anderson, D. M., and Tice, A. R. (1972). Predicting Unfrozen Water Contents in Frozen Soils from Surface Area Measurements. *Highw. Res. Rec.* 393, 12–18. doi:10.1016/0022-4898(73)90017-7

Andresen, C. G., Lawrence, D. M., Wilson, C. J., McGuire, A. D., Koven, C., Schaefer, K., et al. (2019). Soil Moisture and Hydrology Projections of the Permafrost Region: A Model Intercomparison. *Cryosphere Discuss.*, 1–20. doi:10.5194/tc-2019-144

Arenson, L. U., Sego, D. C., and Take, W. A. (2007). "Measurement of Ice Lens Growth and Soil Consolidation during Frost Penetration Using Particle Image Velocimetry (PIV)," in 60th Canadian Geotechnical Conference (Ottawa, ON, 2046–2053.

Azmatch, T. F., Arenson, L. U., Sego, D. C., and Biggar, K. W. (2008). "Measuring Ice Lens Growth and Development of Soil Strains during Frost Penetration Using Particle Image Velocimetery (GeoPIV)," in Proceedings of the Ninth International Conference on Permafrost, 89–94.

Bai, R., Lai, Y., Zhang, M., and Gao, J. (2018). Water-vapor-heat Behavior in a Freezing Unsaturated Coarse-Grained Soil with a Closed Top. *Cold Regions Sci. Technology* 155, 120–126. doi:10.1016/j.coldregions.2018.08.007

Banin, A., and Anderson, D. M. (1974). Effects of Salt Concentration Changes during Freezing on the Unfrozen Water Content of Porous Materials. *Water Resour. Res.* 10 (1), 124–128. doi:10.1029/wr010i001p00124

Beskow, D. G., and Fil, B. (1935). Soil Freezing and Frost Heaving with Special Application to Roads and Railroads. *Soil Sci.* 65 (4), 355. doi:10.1097/00010694-194804000-00

Biermans, M. B. G. M., Dijkema, K. M., and De Vries, D. A. (1976). Water Movement in Porous media towards an Ice Front. *Nature* 264 (1-2), 166–167. doi:10.1038/264166a0

Black, P. B. (1985). *The Rigidice Model of Frost Heave and its Input Functions (Frozen Soil, Unfrozen Water Content, Regelation)*. Cornell University.

Boike, J., Georgi, C., Kirilin, G., Muster, S., Abramova, K., Fedorova, I., et al. (2015). Thermal Processes of Thermokarst Lakes in the Continuous Permafrost Zone of Northern Siberia - Observations and Modeling (Lena River Delta, Siberia). *Biogeosciences* 12 (20), 5941–5965. doi:10.5194/bg-12-5941-2015

Bouyoucos, G. (1920). Degree of Temperature to Which Soils Can Be Cooled without Freezing. *Mon. Wea. Rev.* 48 (12), 718. doi:10.1038/scientificamerican04011910.1175/1520-0493(1920)48<718a:dottws>2.0.co;2

Bronfenbrener, L. (2013). Non-equilibrium Crystallization in Freezing Porous media: Numerical Solution. *Cold Regions Sci. Technology* 85 (JAN), 137–149. doi:10.1016/j.coldregions.2012.09.002

Burn, C. R., and Michel, F. A. (1988). Evidence for Recent Temperature-Induced Water Migration into Permafrost from the Tritium Content of Ground Ice Near Mayo, Yukon Territory, Canada. *Can. J. Earth Sci.* 25 (6), 909–915. doi:10.1139/e88-087

Burt, T. P., and Williams, P. J. (1976). Hydraulic Conductivity in Frozen Soils. *Earth Surf. Process.* 1 (4), 349–360. doi:10.1002/esp.3290010404

Byun, E., Yang, J.-W., Kim, Y., and Ahn, J. (2017). Trapped Greenhouse Gases in the Permafrost Active Layer: Preliminary Results for Methane Peaks in Vertical

Profiles of Frozen Alaskan Soil Cores. *Permafrost Periglac. Process.* 28 (2), 477–484. doi:10.1002/ppp.1935

Cai, L., Lee, H., Westermann, S., and Aas, K. S. (2020). Projecting Circum-Arctic Excess Ground Ice Melt with a Sub-grid Representation in the Community Land Model. *Cryosphere Discuss.*, 1–28. doi:10.5194/tc-2019-230

Calmels, F., and Allard, M. (2008). Segregated Ice Structures in Various Heaved Permafrost Landforms through CT Scan. *Earth Surf. Process. Landforms* 33 (2), 209–225. doi:10.1002/esp.1538

Chadburn, S., Burke, E., Essery, R., Boike, J., Langer, M., Heikenfeld, M., et al. (2015). An Improved Representation of Physical Permafrost Dynamics in the JULES Land-Surface Model. *Geosci. Model. Dev.* 8 (5), 1493–1508. doi:10.5194/gmd-8-1493-2015

Chamberlain, E. (1983). "Frost Heave of saline Soils," in Proceedings 4th International Conference on Permafrost, Fairbanks, Alaska, 121–126.

Chamberlain, E. J. (1981). *Frost Susceptibility of Soil, Review of index Tests*. Hanover, NH: Cold Regions Research and Engineering Lab.

Che, M., Chen, B., Chen, J., and Wang, Y. (2014). *Parameterization of Deciduous Vegetation Phenology for the Dynamic Land Model (DLM)*. San Francisco: Agu Fall Meeting.

Chen, B., Chen, J. M., and Ju, W. (2007). Remote Sensing-Based Ecosystem-Atmosphere Simulation Scheme (EASS)-Model Formulation and Test with Multiple-Year Data. *Ecol. Model.* 209 (2), 277–300. doi:10.1016/j.ecolmodel.2007.06.032

Cheng, G. (1982). Effect of Uni-Direction Accumulation of Unfrozen Water in Seasonally Frozen and Thawed Ground. *Chin. Sci. Bull.* (23), 42–45.

Cheng, Q., Sun, Y., Qin, Y., Xue, X., Cai, X., Sheng, W., et al. (2013). *In Situ* measuring Soil Ice Content with a Combined Use of Dielectric Tube Sensor and Neutron Moisture Meter in a Common Access Tube. *Agric. For. Meteorology* 171-172, 249–255. doi:10.1016/j.agrformet.2012.12.004

Cherkauer, K. A., and Lettenmaier, D. P. (1999). Hydrologic Effects of Frozen Soils in the Upper Mississippi River basin. *J. Geophys. Res.* 104 (D16), 19599–19610. doi:10.1029/1999jd900337

Cui, Y., and Shao, J. (2005). The Role of Ground Water in Arid/Semiarid Ecosystems, Northwest China. *Ground Water* 43 (4), 471–477. doi:10.1111/j.1745-6584.2005.0063.x

Currie, J. A. (1983). Gas Diffusion through Soil Crumbs: the Effects of Wetting and Swelling. *J. Soil Sci.* 34 (2), 217–232. doi:10.1111/j.1365-2389.1983.tb01029.x

Dai, Y., Zeng, X., Dickinson, R. E., Baker, I., Bonan, G. B., Bosilovich, M. G., et al. (2003). The Common Land Model. *Bull. Am. Meteorol. Soc.* 84 (8), 1013–1024. doi:10.1175/BAMS-84-8-1013

Daniels, J. J., Roberts, R., and Vendl, M. (1995). Ground Penetrating Radar for the Detection of Liquid Contaminants. *J. Appl. Geophys.* 33 (1), 195–207. doi:10.1016/0926-9851(95)90041-1

Dash, J. G. (1989). Thermomolecular Pressure in Surface Melting: Motivation for Frost Heave. *Science* 246 (4937), 1591–1593. doi:10.1126/science.246.4937.1591

Drotz, S. H., Tilston, E. L., Sparrman, T., Schleucher, J., Nilsson, M., and Öquist, M. G. (2009). Contributions of Matric and Osmotic Potentials to the Unfrozen Water Content of Frozen Soils. *Geoderma* 148 (3-4), 392–398. doi:10.1016/j.geoderma.2008.11.007

Edlefsen, N. E., and Anderson, A. B. C. (1943). Thermodynamics of Soil Moisture. *Hilg* 15 (2), 31–298. doi:10.3733/hilg.v15n02p031

Ershov, E. D., Zhestkova, T. N., Kuchukov, E. Z., Malinovskii, D. V., Chuvilin, E. M., Komarov, I. A., et al. (2015). *Principles of Geocryology. Lithogenetic Geocryology*, 2. Lanzhou, China: Lanzhou University Press.

Etzelmüller, B., Guglielmin, M., Hauck, C., Hilbich, C., Hoelzle, M., Isaksen, K., et al. (2020). Twenty Years of European Mountain Permafrost Dynamics-The PACE Legacy. *Environ. Res. Lett.* 15, 104070. doi:10.1088/1748-9326/abae9d

Everett, D. H. (1961). The Thermodynamics of Frost Damage to Porous Solids. *Trans. Faraday Soc.* 57, 1541. doi:10.1039/tf9615701541

Everett, K. R. (1989). Glossary of Permafrost and Related Ground-Ice Terms. *Arctic Alpine Res.* 21, 213. doi:10.2307/1551636

Ewing, S. A., O'Donnell, J. A., Aiken, G. R., Butler, K., Butman, D., Windham-Myers, L., et al. (2015). Long-term Anoxia and Release of Ancient, Labile Carbon upon Thaw of Pleistocene Permafrost. *Geophys. Res. Lett.* 42 (2410), 10,730–10,738. doi:10.1002/2015gl066296

Fagan, J. D., and Nelson, F. E. (2017). Spatial Sampling Design in the Circumpolar Active Layer Monitoring Programme. *Permafrost Periglac. Process.* 28 (1), 42–51. doi:10.1002/ppp.1904

Farouki, O. T. (1981). *Thermal Properties of Soils*. Hanover, NH: Cold Regions Research and Engineering Lab.

Feng, S., Zhang, H., Lv, J., Dyck, M., Wu, Q., and He, H. (2021). A Scientometric Review of Research Status on Unfrozen Soil Water. *Water* 13 (5), 708. doi:10.3390/w13050708

Ferguson, H., Brown, P. L., and Dickey, D. D. (1964). Water Movement and Loss under Frozen Soil Conditions. *Soil Sci. Soc. America J.* 28 (5), 700–703. doi:10.2136/sssaj1964.03615995002800050034x

Fisher, D. A., Lacelle, D., and Pollard, W. (2020). A Model of Unfrozen Water Content and its Transport in Icy Permafrost Soils: Effects on Ground Ice Content and Permafrost Stability. *Permafrost and Periglac Process* 31 (1), 184–199. doi:10.1002/ppp.2031

Fortier, R., and Savard, C. (2010). "Engineering Geophysical Investigation of Permafrost Conditions underneath Airfield Embankments in Northern Quebec (Canada)," in Geo-2010. Confer. Proceed. Calgary, 1307–1316. Availableat: https://pubs.aina.ucalgary.ca//cpc/CPC6-1307.pdf.

Fowler, A. C., and Krantz, W. B. (1994). A Generalized Secondary Frost Heave Model. *SIAM J. Appl. Math.* 54 (6), 1650–1675. doi:10.1137/s0036139993252554

Fremond, M., and Mikkola, M. (1991). "Thermomechanical Modelling of Freezing Soil," in International symposium on ground freezing, 17–24.

French, H. M. (2017). *The Periglacial Environment*. John Wiley & Sons.

French, H., and Shur, Y. (2010). The Principles of Cryostratigraphy. *Earth-Science Rev.* 101 (3-4), 190–206. doi:10.1016/j.earscirev.2010.04.002

Frey, K. E., and McClelland, J. W. (2009). Impacts of Permafrost Degradation on Arctic River Biogeochemistry. *Hydrol. Process.* 23 (1), 169–182. doi:10.1002/hyp.7196

Fu, Z., Wu, Q., Miles, D., and He, H. (2021). A New Model to Describe Soil Freezing and Thawing Characteristic Curve. *J. Glaciology Geocryology* 43 (02), 437–452. doi:10.7522/j.issn.1000-0240.2020.0090

Fukuda, m., Ogawa, s., and Kamei, t. (1988). Prediction of Field Frost Heave Using the Segregation Potential Theory. *Doboku Gakkai Ronbunshu* 1988 (400), 253–259. doi:10.2208/jscej.1988.400_253

Gelfan, A. (2006). *Physically-based Model of Heat and Water Transfer in Frozen Soil and its Parameterization by Basic Soil Data*, 303. Wallingford, UK: IAHS publication, 293.

Gilpin, R. (1982). "A Frost Heave Interface Condition for Use in Numerical Modelling," in Proc. 4th Canadian Permafrost Conference, Calgary, Canada, 459–465.

Gilpin, R. R. (1980). A Model for the Prediction of Ice Lensing and Frost Heave in Soils. *Water Resour. Res.* 16 (5), 918–930. doi:10.1029/WR016i005p00918

G. N. Flerchinger, G. N., and K. E. Saxton, K. E. (1989). Simultaneous Heat and Water Model of a Freezing Snow-Residue-Soil System I. Theory and Development. *Trans. ASAE* 32 (2), 0565–0571. doi:10.13031/2013.3104110.13031/2013.31040

Gold, L. W. (1957). A Possible Force Mechanism Associated with the Freezing of Water in Porous Materials. *High. Res. Board Bull.* 168, 65–72.

Goulet, F. (1995). Frost Heaving of forest Tree Seedlings: a Review. *New For.* 9 (1), 67–94. doi:10.1007/bf00028927

Gouttevin, I., Krinner, G., Ciais, P., Polcher, J., and Legout, C. (2012). Multi-scale Validation of a New Soil Freezing Scheme for a Land-Surface Model with Physically-Based Hydrology. *The Cryosphere* 6 (2), 407–430. doi:10.5194/tc-6-407-2012

Gruber, S. (2012). Derivation and Analysis of a High-Resolution Estimate of Global Permafrost Zonation. *The Cryosphere* 6 (1), 221–233. doi:10.5194/tc-6-221-2012

Guodong, C. (1983). The Mechanism of Repeated-Segregation for the Formation of Thick Layered Ground Ice. *Cold Regions Sci. Technology* 8 (1), 57–66. doi:10.1016/0165-232X(83)90017-4

Guthrie, W. S., Hermansson, A., and Woffinden, K. H. (2006). "Saturation of Granular Base Material Due to Water Vapor Flow during Freezing: Laboratory Experimentation and Numerical Modeling," in 13th International Conference on Cold Regions Engineering. doi:10.1061/40836(210)66

Guymon, G., Hromadka Ii, T., and Berg, R. (1980). A One Dimensional Frost Heave Model Based upon Simulation of Simultaneous Heat and Water Flux. *Cold Regions Sci. Technology* 3 (2-3), 253–262. doi:10.1016/0165-232X(80)90032-4

Hansson, K., Simunek, J., Mizoguchi, M., Lundin, L.-C., and Van Genuchten, M. T. (2004). Water Flow and Heat Transport in Frozen Soil: Numerical Solution and Freeze-Thaw Applications. *Vadose Zone J.* 3 (2), 693–704. doi:10.2136/vzj2004.069310.2113/3.2.693

Harlan, R. L. (1973). Analysis of Coupled Heat-Fluid Transport in Partially Frozen Soil. *Water Resour. Res.* 9 (5), 1314–1323. doi:10.1029/WR009i005p01314

Haynes, J. M. (1965). *Capillary Properties of Some Model Pore Systems*. Bristol, England: University of Bristol.

Hazirbaba, K., Zhang, Y., and Leroy Hulsey, J. (2011). Evaluation of Temperature and Freeze-Thaw Effects on Excess Pore Pressure Generation of fine-grained Soils. *Soil Dyn. Earthquake Eng.* 31 (3), 372–384. doi:10.1016/j.soildyn.2010.09.006

He, H., Dyck, M. F., Horton, R., Ren, T., Bristow, K. L., Lv, J., et al. (2018). Development and Application of the Heat Pulse Method for Soil Physical Measurements. *Rev. Geophys.* 56 (4), 567–620. doi:10.1029/2017RG000584

He, H., Flerchinger, G. N., Kojima, Y., Dyck, M., and Lv, J. (2021). A Review and Evaluation of 39 thermal Conductivity Models for Frozen Soils. *Geoderma* 382, 114694. doi:10.1016/j.geoderma.2020.114694

He, H., He, D., Jin, J., Smits, K. M., Dyck, M., Wu, Q., et al. (2020). Room for Improvement: A Review and Evaluation of 24 Soil thermal Conductivity Parameterization Schemes Commonly Used in Land-Surface, Hydrological, and Soil-Vegetation-Atmosphere Transfer Models. *Earth-Science Rev.* 211, 103419. doi:10.1016/j.earscirev.2020.103419

Hoekstra, P., and Miller, R. (1963). *Movement of Water in a Film between Glass and Ice*. Cornell University.

Hoekstra, P. (1966). Moisture Movement in Soils under Temperature Gradients with the Cold-Side Temperature below Freezing. *Water Resour. Res.* 2 (2), 241–250. doi:10.1029/WR002i002p00241

Hoekstra, P. (1969). Water Movement and Freezing Pressures. *Soil Sci. Soc. America J.* 33 (4), 512–518. doi:10.2136/sssaj1969.03615995003300040011x

Horiguchi, K. (1980). Experimental Studies with Frozen Soil in an Ice Sandwich Permeameter. *Cold Regions Sci. Technology* 3 (2-3), 177–183. doi:10.1016/0165-232X(80)90023-3

Horiguchi, K., and Miller, R. D. (1983). *Hydraulic Conductivity Functions of Frozen Materials*. Washington, DC: National Academy Press.

Hughes, O. L. (1974). Geology and Permafrost in Relation to Hydrology and Geophysics. *PERMAFROST HYDROLOGY*. doi:10.2307/1551636

Ishizaki, T., and Nishio, N. (1988). "Experimental Study of Frost Heaving of a Saturated Soil," in Proceedings: 5th International Symposium on Ground Freezing, Nottingham, UK, 65–72.

Jame, Y.-W., and Norum, D. I. (1980). Heat and Mass Transfer in a Freezing Unsaturated Porous Medium. *Water Resour. Res.* 16 (4), 811–819. doi:10.1029/WR016i004p00811

Jansson, P.-E., and Halldin, S. (1979). Model for Annual Water and Energy Flow in a Layered Soil. *Dev. Agric. Manag. For. Ecol.* 9, 145–163. doi:10.1016/B978-0-444-41844-9.50017-2

Ji, Y., Zhou, G., Zhou, Y., and Vandeginste, V. (2019). Frost Heave in Freezing Soils: A Quasi-Static Model for Ice Lens Growth. *Cold Regions Sci. Technology* 158, 10–17. doi:10.1016/j.coldregions.2018.11.003

Kanevskiy, M., Shur, Y., Jorgenson, M. T., Ping, C.-L., Michaelson, G. J., Fortier, D., et al. (2013). Ground Ice in the Upper Permafrost of the Beaufort Sea Coast of Alaska. *Cold Regions Sci. Technology* 85 (JAN), 56–70. doi:10.1016/j.coldregions.2012.08.002

Koch, J. C., Runkel, R. L., Striegl, R., and McKnight, D. M. (2013). Hydrologic Controls on the Transport and Cycling of Carbon and Nitrogen in a Boreal Catchment Underlain by Continuous Permafrost. *J. Geophys. Res. Biogeosci.* 118 (2), 698–712. doi:10.1002/jgrg.20058

Kojima, Y., Heitman, J. L., Flerchinger, G. N., Ren, T., and Horton, R. (2016). Sensible Heat Balance Estimates of Transient Soil Ice Contents. *Vadose zone j.* 15 (5), 1–11. doi:10.2136/vzj2015.10.0134

Kojima, Y., Nakano, Y., Kato, C., Noborio, K., Kamiya, K., and Horton, R. (2020). A New Thermo-Time Domain Reflectometry Approach to Quantify Soil Ice Content at Temperatures Near the Freezing point. *Cold Regions Sci. Technology* 174, 103060. doi:10.1016/j.coldregions.2020.103060

Konrad, J.-M., and Duquennoi, C. (1993). A Model for Water Transport and Ice Lensing in Freezing Soils. *Water Resour. Res.* 29 (19), 3109–3124. doi:10.1029/93WR00773

Konrad, J.-M. (2005). Estimation of the Segregation Potential of fine-grained Soils Using the Frost Heave Response of Two Reference Soils. *Can. Geotech. J.* 42 (1), 38–50. doi:10.1139/t04-080

Konrad, J.-M. (1999). Frost Susceptibility Related to Soil index Properties. *Can. Geotech. J.* 36 (3), 403–417. doi:10.1139/cgj-36-3-40310.1139/t99-008

Konrad, J.-M., and Morgenstern, N. R. (1980). A Mechanistic Theory of Ice Lens Formation in fine-grained Soils. *Can. Geotech. J.* 17 (4), 473–486. doi:10.1139/t80-056

Konrad, J.-M., and Morgenstern, N. R. (1982a). Effects of Applied Pressure on Freezing Soils. *Can. Geotech. J.* 19 (4), 494–505. doi:10.1139/t82-053

Konrad, J.-M., and Morgenstern, N. R. (1984). Frost Heave Prediction of Chilled Pipelines Buried in Unfrozen Soils. *Can. Geotech. J.* 21 (1), 100–115. doi:10.1139/t84-008

Konrad, J.-M., and Morgenstern, N. R. (1982b). Prediction of Frost Heave in the Laboratory during Transient Freezing. *Can. Geotech. J.* 19 (3), 250–259. doi:10.1139/t82-032

Konrad, J.-M., and Morgenstern, N. R. (1981). The Segregation Potential of a Freezing Soil. *Can. Geotech. J.* 18 (4), 482–491. doi:10.1139/t81-059

Konrad, J.-M., Roy, M., Rochelle, P. L., Leroueil, S., and Bergeron, G. (1995). Field Observations of Frost Action in Intact and Weathered Champlain Sea clay. *Can. Geotech. J.* 32 (4), 689–700. doi:10.1139/t95-068

Koren, V., Schaake, J., Mitchell, K., Duan, Q.-Y., Chen, F., and Baker, J. M. (1999). A Parameterization of Snowpack and Frozen Ground Intended for NCEP Weather and Climate Models. *J. Geophys. Res.* 104 (D16), 19569–19585. doi:10.1029/1999JD900232

Korkina, R. (1965). Electrical Potentials in Freezing Solutions and Their Effect on Migration, Protsessy Tepla I Massoobmena Y Merzlykh Gornykh Porodakh. *Cold Regions Res. Eng. Lab. Draft Translation* 490, 56–65.

Koven, C. D., Ringeval, B., Friedlingstein, P., Ciais, P., Cadule, P., Khvorostyanov, D., et al. (2011). Permafrost Carbon-Climate Feedbacks Accelerate Global Warming. *Proc. Natl. Acad. Sci.* 108 (36), 14769–14774. doi:10.1073/pnas.1103910108

Kurylyk, B. L., and Watanabe, K. (2013). The Mathematical Representation of Freezing and Thawing Processes in Variably-Saturated, Non-deformable Soils. *Adv. Water Resour.* 60 (oct), 160–177. doi:10.1016/j.advwatres.2013.07.016

Lai, Y., Pei, W., Zhang, M., and Zhou, J. (2014). Study on Theory Model of hydro-thermal-mechanical Interaction Process in Saturated Freezing Silty Soil. *Int. J. Heat Mass Transfer* 78, 805–819. doi:10.1016/j.ijheatmasstransfer.2014.07.035

Lamoureux, S. F., McFadden, S. I., Bevan, G., Rudy, A., Paquette, M., and Fortier, D. (2018). *Localized Ground Ice Subsidence and Soil Water Dynamics as Indicators of Near-Surface Ice Content in the High Arctic*. Washington, DC: AGU Fall Meeting Abstracts, C54A–C05.

Lee, H., Swenson, S. C., Slater, A. G., and Lawrence, D. M. (2014). Effects of Excess Ground Ice on Projections of Permafrost in a Warming Climate. *Environ. Res. Lett.* 9 (12), 124006. doi:10.1088/1748-9326/9/12/124006

Li, N., Cheng, G., Xu, X., and Zhu, Y. (2001). The advance and Review on Frozen Soil Mechanics. *Adv. Mech.* 031 (1), 95–102.

Li, P., Xu, X., and Cheng, F. (2000). State and Progress of Research on the Frozen Finge and Frost Heave Prediction Models. *J. Glaciology Geocryology* V22 (1), 90–85.

Li, X., Wu, T., Wu, X., Zhu, X., Hu, G., Li, R., et al. (2020). Assessing the Simulated Soil thermal Regime from Noah-MPLSM v1.1 for Near-Surface Permafrost Modeling on the Qinghai-Tibet Plateau. *Geosci. Model. Dev. Discuss.* 2020, 1–29. doi:10.5194/gmd-2020-142

Liang, X., Xie, Z., and Huang, M. (2003). A New Parameterization for Surface and Groundwater Interactions and its Impact on Water Budgets with the Variable Infiltration Capacity (VIC) Land Surface Model. *J. Geophys. Res.* 108 (D16). doi:10.1029/2002JD003090

Liu, G., and Si, B. C. (2011). Single- and Dual-Probe Heat Pulse Probe for Determining Thermal Properties of Dry Soils. *Soil Sci. Soc. America J.* 75, 787–794. doi:10.2136/sssaj2010.0241

Liu, J., Tong, C., and Fang, J. (2005). *Introduction to Geotechnical Engineering in Cold Region*. Beijing, China: China Railway Publishing House.

Liu, Q., Wang, Z., Li, Z., and Wang, Y. (2019). Transversely Isotropic Frost Heave Modeling with Heat-Moisture-Deformation Coupling. *Acta Geotech.* 15, 1273–1287. doi:10.1007/s11440-019-00774-1

Loch, J. P. G., and Miller, R. D. (1975). Tests of the Concept of Secondary Frost Heaving. *Soil Sci. Soc. America J.* 39 (6), 1036–1041. doi:10.2136/sssaj1975.03615995003900060012x

Loch, J. P. G. (1978). Thermodynamic Equilibrium between Ice and Water in Porous media. *Soil Sci.* 126 (2), 77–80. doi:10.1097/00010694-197808000-00002

Lu, J., Zhang, M., Zhang, X., and Pei, W. (2017). Review of the Coupled Hydrothermo-Mechanical Interaction of Frozen Soil. *J. Glaciology Geocryology* 39 (1), 102–111.

Luo, S., Chen, B., Lyu, S., Fang, X., Wang, J., Meng, X., et al. (2018). An Improvement of Soil Temperature Simulations on the Tibetan Plateau. *Sci. Cold Arid Regions* 10 (1), 80–94. doi:10.3724/SP.J.1226.2018.00080

Ma, Q., Jin, H., Yu, C., and Bense, V. F. (2019). Dissolved Organic Carbon in Permafrost Regions: A Review. *Sci. China Earth Sci.* 62 (2), 349–364. doi:10.1007/s11430-018-9309-6

Ma, W., Zhang, L., and Yang, C. (2015). Discussion of the Applicability of the Generalized Clausius-Clapeyron Equation and the Frozen Fringe Process. *Earth-Science Rev.* 142, 47–59. doi:10.1016/j.earscirev.2015.01.003

Mackay, J., Ostrick, J., Lewis, C., and MacKay, D. (1979). *Frost Heave at Ground Temperatures below 0 °C, Inuvik, Northwest Territories*. Ottawa, Canada: Geological Survey of Canada Paper, 403–406.

Mackay, J. R., and Dallimore, S. R. (1992). Massive Ice of the Tuktoyaktuk Area, Western Arctic Coast, Canada. *Can. J. Earth Sci.* 29 (6), 1235–1249. doi:10.1139/e92-099

Mackay, J. R. (1980). The Origin of Hummocks, Western Arctic Coast, Canada. *Can. J. Earth Sci.* 17 (8), 996–1006. doi:10.1139/e80-100

Mackay, J. R. (1972). The World of Underground Ice. *Ann. Assoc. Am. Geogr.* 62 (1), 1–22. doi:10.1111/j.1467-8306.1972.tb00839.x

Mastepanov, M., Sigsgaard, C., Dlugokencky, E. J., Houweling, S., Ström, L., Tamstorf, M. P., et al. (2008). Large Tundra Methane Burst during Onset of Freezing. *Nature* 456 (7222), 628–630. doi:10.1038/nature07464

Mastepanov, M., Sigsgaard, C., Tagesson, T., Ström, L., Tamstorf, M. P., Lund, M., et al. (2013). Revisiting Factors Controlling Methane Emissions from High-Arctic Tundra. *Biogeosciences* 10 (7), 5139–5158. doi:10.5194/bg-10-5139-2013

McGaw, R., Berg, R., and Ingersoll, J. (1983). An Investigation of Transient Processes in an Advancing Zone of Freezing. *Proc. 4th Int. Conf. Permafrost*, 821–825.

Michaelson, G. J., and Ping, C. (2003). Soil Organic Carbon and CO2 respiration at Subzero Temperature in Soils of Arctic Alaska. *J. Geophys. Res.* 108 (D2), ALT 5-1-ALT 5–10. doi:10.1029/2001JD000920

Michalowski, R. L., and Zhu, M. (2006). Frost Heave Modelling Using Porosity Rate Function. *Int. J. Numer. Anal. Meth. Geomech.* 30 (8), 703–722. doi:10.1002/nag.497

Miller, R. D. (1972). Freezing and Heaving of Saturated and Unsaturated Soils. *Highw. Res. Rec.* 393 (1), 1–11. doi:10.1021/ba-1972-0110.ap001

Miller, R. D. (1978). "Frost Heaving in Non-colloidal Siols," in Proceedings of the Third International Conference on Permafrost, Edmonton, Canada, 708–713.

Ming, F., and Li, D.-q. (2016). A Model of Migration Potential for Moisture Migration during Soil Freezing. *Cold Regions Sci. Technology* 124 (Apr), 87–94. doi:10.1016/j.coldregions.2015.12.015

Miyata, Y., and Akagawa, S. (1997). An Experimental Study of Dynamic Solid-Liquid Phase Equilibrium in the Pores of a Porous Medium. *Trans. Jpn. Soc. Mech. Eng. B* 63 (611), 2421–2429. doi:10.1299/jsmeb.41.590

Murton, J. B., and Lautridou, J.-P. (2003). Recent Advances in the Understanding of Quaternary Periglacial Features of the English Channel Coastlands. *J. Quat. Sci.* 18 (3-4), 301–307. doi:10.1002/jqs.748

Mwangi, S., Zeng, Y., Montzka, C., Yu, L., and Su, Z. (2020). Assimilation of Cosmic-Ray Neutron Counts for the Estimation of Soil Ice Content on the Eastern Tibetan Plateau. *J. Geophys. Res. Atmos.* 125 (3), e2019JD031529. doi:10.1029/2019JD031529

Natali, S. M., Schuur, E. A. G., Mauritz, M., Schade, J. D., Celis, G., Crummer, K. G., et al. (2015). Permafrost Thaw and Soil Moisture Driving CO2 and CH4 Release from upland Tundra. *J. Geophys. Res. Biogeosci.* 120 (3), 525–537. doi:10.1002/2014JG002872

Niu, F., Li, A., Luo, J., Lin, Z., Yin, G., Liu, M., et al. (2017). Soil Moisture, Ground Temperatures, and Deformation of a High-Speed Railway Embankment in Northeast China. *Cold Regions Sci. Technology* 133 (133), 7–14. doi:10.1016/j.coldregions.2016.10.007

Niu, L., Ye, B., Li, J., and Sheng, Y. (2011). Effect of Permafrost Degradation on Hydrological Processes in Typical Basins with Various Permafrost Coverage in Western China. *Sci. China Earth Sci.* 54 (4), 615–624. doi:10.1007/s11430-010-4073-1

Nixon, J. F. (1991). Discrete Ice Lens Theory for Frost Heave in Soils. *Can. Geotech. J.* 28 (6), 843–859. doi:10.1139/t91-102

Nixon, J. F. (1982). Field Frost Heave Predictions Using the Segregation Potential Concept. *Can. Geotech. J.* 19 (4), 526–529. doi:10.1139/t82-059

Nixon, J. F. (1987). Thermally Induced Heave beneath Chilled Pipelines in Frozen Ground. *Can. Geotech. J.* 24 (2), 260–266. doi:10.1139/t87-031

O'Neill, K., and Miller, R. D. (1985). Exploration of a Rigid Ice Model of Frost Heave. *Water Resour. Res.* 21 (3), 281–296. doi:10.1029/WR021i003p00281

Oleson, K., Lawrence, D., Bonan, G., Drewniak, B., Huang, M., Koven, C., et al. (2013). *Technical Description of Version 4.5 of the Community Land Model (CLM), NCAR Technical Note: NCAR/TN-503+ STR*. Boulder, CO: National Center for Atmospheric Research. doi:10.5065/D6RR1W7M

Oleson, K. W., Lawrence, D. M., Gordon, B., Flanner, M. G., Kluzek, E., Peter, J., et al. (2010). *Technical Description of Version 4.0 of the Community Land Model (CLM)*. doi:10.1029/2010GL042430

Ostroumov, V., Hoover, R., Ostroumova, N., Van Vliet-Lanoë, B., Siegert, C., and Sorokovikov, V. (2001). Redistribution of Soluble Components during Ice Segregation in Freezing Ground. *Cold Regions Sci. Technology* 32 (2), 175–182. doi:10.1016/S0165-232X(01)00031-3

Peppin, S. S. L., Elliott, J. A. W., and Worster, M. G. (2006). Solidification of Colloidal Suspensions. *J. Fluid Mech.* 554, 147–166. doi:10.1017/S0022112006009268

Peppin, S. S. L., and Style, R. W. (2013). The Physics of Frost Heave and Ice-Lens Growth. *Vadose Zone J.* 12 (1), vzj20120049–0049. doi:10.2136/vzj2012.0049

Peterson, R. A., and Krantz, W. B. (2003). A Mechanism for Differential Frost Heave and its Implications for Patterned-Ground Formation. *J. Glaciol.* 49 (164), 69–80. doi:10.3189/172756503781830854

Philip, J. R., and De Vries, D. A. (1957). Moisture Movement in Porous Materials under Temperature Gradients. *Trans. AGU* 38 (2), 222–232. doi:10.1029/TR038i002p00222

Ping, C. L., Jastrow, J. D., Jorgenson, M. T., Michaelson, G. J., and Shur, Y. L. (2015). Permafrost Soils and Carbon Cycling. *SOIL* 1 (1), 147–171. doi:10.5194/soil-1-147-2015

Pitman, A. J., Slater, A. G., Desborough, C. E., and Zhao, M. (1999). Uncertainty in the Simulation of Runoff Due to the Parameterization of Frozen Soil Moisture Using the Global Soil Wetness Project Methodology. *J. Geophys. Res.* 104 (D14), 16879–16888. doi:10.1029/1999JD900261

Prokushkin, A. S., Kawahigashi, M., and Tokareva, I. V. (2009). *Global Warming and Dissolved Organic Carbon Release from Permafrost Soils, Permafrost Soils*. Berlin, Heidelberg: Springer, 237–250. doi:10.1007/978-3-540-69371-0_16

Qin, D. (2016). *Glossary of Cryospheric Science*. Beijing, China: China Meteorological Press.

Radd, F., and Oertle, D. (1973). *Experimental Pressure Studies of Frost Heave Mechanisms and the Growth-Fusion Behavior of Ice* in Proceeding of the Second International Conference on Permafrost, Washington DC Yakutsk, USSR (North American Contribution, publication National Academy of Science), 377–384.

Ran, H., Fan, J., and Huang, Q. (2019). Review of the Coupling of Water and Heat in the Freeze-Thaw Process and its Model of Frozen Soil. *Pratacultural Sci.* 036 (004), 991–999.

Rempel, A. W. (2007). Formation of Ice Lenses and Frost Heave. *J. Geophys. Res.* 112 (F2). doi:10.1029/2006jf000525

Rempel, A. W. (2010). Frost Heave. *J. Glaciol.* 56 (200), 1122–1128. doi:10.3189/002214311796406149

Rempel, A. W. (2011). Microscopic and Environmental Controls on the Spacing and Thickness of Segregated Ice Lenses. *Quat. Res.* 75 (2), 316–324. doi:10.1016/j.yqres.2010.07.005

Rempel, A. W., Wettlaufer, J. S., and Worster, M. G. (2001). Interfacial Premelting and the Thermomolecular Force: Thermodynamic Buoyancy. *Phys. Rev. Lett.* 87 (8), 088501. doi:10.1103/PhysRevLett.87.088501

Rempel, A. W., Wettlaufer, J. S., and Worster, M. G. (2004). Premelting Dynamics in a Continuum Model of Frost Heave. *J. Fluid Mech.* 498, 227–244. doi:10.1017/S0022112003006761

Römkens, M. J. M., and Miller, R. D. (1973). Migration of mineral Particles in Ice with a Temperature Gradient. *J. Colloid Interf. Sci.* 42 (1), 103–111. doi:10.1016/0021-9797(73)90012-X

Saarelainen, S. (1992). *Modelling Frost Heaving and Frost Penetration in Soils at Some Observation Sites in Finland: The SSR Model*. Espoo, Finland: Tampere University of Technology TUT, 120.

Scherer, G. W. (1999). Crystallization in Pores. *Cement Concrete Res.* 29 (8), 1347–1358. doi:10.1016/S0008-8846(99)00002-2

Schuur, E. A. G., McGuire, A. D., Schädel, C., Grosse, G., Harden, J. W., Hayes, D. J., et al. (2015). Climate Change and the Permafrost Carbon Feedback. *Nature* 520 (7546), 171–179. doi:10.1038/nature14338

Shao, M., Wang, Q., and Huang, M. (2006). *Soil Physics*. Beijing, China: Higher Education Press.

Sheng, D., Axelsson, K., and Knutsson, S. (1995). Frost Heave Due to Ice Lens Formation in Freezing Soils. *Hydrol. Res.* 26 (2), 125–146. doi:10.2166/nh.1995.000910.2166/nh.1995.0008

Sheppard, M. I., Mi, S., and Bd, K. (1978). Development and Testing of a Computer Model for Heat and Mass Flow in Freezing Soils, In: proceedings of the 3rd International Conference on Permafrost, Edmonton, Alberta (Edmonton: National research council of Canada) 1, 75–81.

Shur, Y. L., and Jorgenson, M. T. (2007). Patterns of Permafrost Formation and Degradation in Relation to Climate and Ecosystems. *Permafrost Periglac. Process.* 18 (1), 7–19. doi:10.1002/ppp.582

Smith, M., Church, M., and Slaymaker, O. (1985). "Models of Soil Freezing," in *Field and Theory: Lectures in Geocryology*. Editors M. Church and O. Slaymaker (Vancouver, British Columbia: University of British Columbia Press Vancouver).

Smith, M. W., and Burn, C. R. (1987). Outward Flux of Vapour from Frozen Soils at Mayo, Yukon, Canada: Results and Interpretation. *Cold Regions Sci. Technology* 13 (2), 143–152. doi:10.1016/0165-232x(87)90052-8

Smith, M. W. (1985). Observations of Soil Freezing and Frost Heave at Inuvik, Northwest Territories, Canada. *Can. J. Earth Sci.* 22 (2), 283–290. doi:10.1139/e85-024

Sokolov, K., Fedorova, L., and Fedorov, M. (2020). Prospecting and Evaluation of Underground Massive Ice by Ground-Penetrating Radar. *Geosciences* 10 (7), 274. doi:10.3390/geosciences10070274

Song, C., Xu, X., Sun, X., Tian, H., Sun, L., Miao, Y., et al. (2012). Large Methane Emission upon spring Thaw from Natural Wetlands in the Northern Permafrost Region. *Environ. Res. Lett.* 7 (3), 034009. doi:10.1088/1748-9326/7/3/034009

Spaans, E. J. A., and Baker, J. M. (1996). The Soil Freezing Characteristic: Its Measurement and Similarity to the Soil Moisture Characteristic. *Soil Sci. Soc. America J.* 60 (1), 13–19. doi:10.2136/sssaj1996.03615995006000010005x

Station, M. S. U. A. E., McCool, M., and Bouyoucos, G. (1915). *Freezing Point Method as a New Means of Measuring the Concentration of the Soil Solution Directly in the Soil*.

Stevanato, L., Baroni, G., Cohen, Y., Fontana, C. L., Gatto, S., Lunardon, M., et al. (2019). A Novel Cosmic-ray Neutron Sensor for Soil Moisture Estimation over Large Areas. *Agriculture* 9 (9), 202. doi:10.3390/agriculture9090202

Streletskiy, D., Anisimov, O., and Vasiliev, A. (2015). *Permafrost Degradation. Snow & Ice Related Hazards Risks & Disasters*, 303–344. doi:10.1016/B978-0-12-394849-6.00010-X

Streletskiy, D., Biskaborn, B. K., Smith, S., Noetzli, J., Viera, G., and Schoeneich, P. (2017). *Strategy and Implementation Plan 2016-2020 for the Global Terrestrial Network for Permafrost (GTN-P)*. Washington DC: The George Washington University.

Style, R. W., Peppin, S. S. L., Cocks, A. C. F., and Wettlaufer, J. S. (2011). Ice-lens Formation and Geometrical Supercooling in Soils and Other Colloidal Materials. *Phys. Rev. E* 84 (4), 041402. doi:10.1103/PhysRevE.84.041402

Style, R. W., and Peppin, S. S. L. (2012). The Kinetics of Ice-Lens Growth in Porous media. *J. Fluid Mech.* 692, 482–498. doi:10.1017/jfm.2011.545

Sun, L. (2015). *Development of the Distributed Hydrological Model Coupled Snow and Frozen Soil*. Beijing: Chinese Academy of Sciences, 14.

Sun, M., Shi, B., Zhang, C., Liu, J., Guo, J., Zheng, X., et al. (2021). Quantifying the Spatio-Temporal Variability of Total Water Content in Seasonally Frozen Soil Using Actively Heated Fiber Bragg Grating Sensing. *J. Hydrol.*, 127386. doi:10.1016/j.jhydrol.2021.127386

Swenson, S. C., Lawrence, D. M., and Lee, H. (2012). Improved Simulation of the Terrestrial Hydrological Cycle in Permafrost Regions by the Community Land Model. *J. Adv. Model. Earth Syst.* 4 (3), a–n. doi:10.1029/2012ms000165

Szczykulska, M., Boorman, D., Blake, J., and Evans, J. G. (2021). Technical Note: A Revised Incoming Neutron Intensity Correction Factor for Soil Moisture Monitoring Using Cosmic-ray Neutron Sensors. *Hydrol. Earth Syst. Sci. Discuss.*, 1–11. doi:10.5194/hess-2021-564

Taber, S. (1929). Frost Heaving. *J. Geology.* 37 (5), 428–461. doi:10.1086/623637

Taber, S. (1930). The Mechanics of Frost Heaving. *J. Geology.* 38 (4), 303–317. doi:10.1086/623720

Takagi, S. (1980). The Adsorption Force Theory of Frost Heaving. *Cold Regions Sci. Technology* 3 (1), 57–81. doi:10.1016/0165-232X(80)90007-5

Takashi, T., Ohrai, T., Yamamoto, H., and Okamoto, J. (1982). Upper Limit of Heaving Pressure Derived by Pore-Water Pressure Measurements of Partially Frozen Soil. *Dev. Geotechnical Eng.* 18, 245–257. doi:10.1016/0013-7952(81)90064-8

Tarnocai, C., Canadell, J. G., Schuur, E. A. G., Kuhry, P., Mazhitova, G., and Zimov, S. (2009). Soil Organic Carbon Pools in the Northern Circumpolar Permafrost Region. *Glob. Biogeochem. Cycles* 23 (2), a–n. doi:10.1029/2008GB003327

Teng, J., Liu, J., Zhang, S., and Sheng, D. (2020). Modelling Frost Heave in Unsaturated Coarse-Grained Soils. *Acta Geotech.* 15 (1), 3307–3320. doi:10.1007/s11440-020-00956-2

Thomas, H. R., Cleall, P., Li, Y.-C., Harris, C., and Kern-Luetschg, M. (2009). Modelling of Cryogenic Processes in Permafrost and Seasonally Frozen Soils. *Géotechnique* 59 (3), 173–184. doi:10.1680/geot.2009.59.3.173

Tiedje, E., and Guo, P. (2012). Frost Heave Modeling Using a Modified Segregation Potential Approach. *Cold Regions Eng.* 2012, 686–696. doi:10.1061/9780784412473.068

Tregubov, O., Uyaganskii, K., and Nuteveket, M. (2020). Monitoring of Permafrost and Climate Conditions of the Anadyr lowland. *Geogr. Nat. Resour.* (2), 143–152. doi:10.21782/GiPR0206-1619-2020-2(143-152

Van Bochove, E., Thériault, G., Rochette, P., Jones, H. G., and Pomeroy, J. W. (2001). Thick Ice Layers in Snow and Frozen Soil Affecting Gas Emissions from Agricultural Soils during winter. *J. Geophys. Res.* 106 (D19), 23061–23071. doi:10.1029/2000JD000044

Van Huissteden, J. (2020). *The Role of Ground Ice, Thawing Permafrost: Permafrost Carbon in a Warming Arctic*. Cham: Springer International Publishing, 107–177. doi:10.1007/978-3-030-31379-1_3

Vinson, T. S., Rooney, J. W., and Haas, W. H. (1996). *Roads and Airfields in Cold Regions : A State of the Practice Report*. American Society of Civil Engineers.

Vonk, J. E., Tank, S. E., and Walvoord, M. A. (2019). Integrating Hydrology and Biogeochemistry across Frozen Landscapes. *Nat. Commun.* 10 (1), 1–4. doi:10.1038/s41467-019-13361-5

Walker, D. A., Epstein, H. E., Gould, W. A., Kelley, A. M., Kade, A. N., Knudson, J. A., et al. (2004). Frost-boil Ecosystems: Complex Interactions between Landforms, Soils, Vegetation and Climate. *Permafrost Periglac. Process.* 15 (2), 171–188. doi:10.1002/ppp.487

Walvoord, M. A., and Kurylyk, B. L. (2016). Hydrologic Impacts of Thawing Permafrost-A Review. *Vadose Zone J.* 15 (6), vzj2016010010–2001. doi:10.2136/vzj2016.01.0010

Wang, G., Li, Y., Wu, Q., and Wang, Y. (2006a). Impacts of Permafrost Changes on alpine Ecosystem in Qinghai-Tibet Plateau. *Sci. China Ser. D* 49 (011), 1156–1169. doi:10.1007/s11430-006-1156-0

Wang, L., Zhou, J., Qi, J., Sun, L., Yang, K., Tian, L., et al. (2017). Development of a Land Surface Model with Coupled Snow and Frozen Soil Physics. *Water Resour. Res.* 53 (6), 5085–5103. doi:10.1002/2017WR020451

Wang, M., Li, X., and Xu, X. (2021). An Implicit Heat-Pulse-Probe Method for Measuring the Soil Ice Content. *Appl. Therm. Eng.* 196, 117186. doi:10.1016/j.applthermaleng.2021.117186

Wang, z., Liang, X., Wang, D., Wang, J., and Wang, L. (2006b). Experiment Research on Soil Dew of in the Windy beach Area of Ordos Ground Water 28(006), 28–31.

Washburn, A. L. (1980). *Geocryology: A Survey of Periglacial Processes and Environments*. Wiley. doi:10.1111/j.1745-7939.1981.tb0094

Watanabe, K., and Flury, M. (2008). Capillary Bundle Model of Hydraulic Conductivity for Frozen Soil. *Water Resour. Res.* 44 (12). doi:10.1029/2008WR007012

Watanabe, K., Mizoguchi, M., Ishizaki, T., Fukuda, M., and Knutsson, S. (1997). Experimental Study on Microstructure Near Freezing Front during Soil Freezing. *Transactions-Japanese Soc. Irrigation Drainage Reclamation Eng.* 191, 53–58.

Watanabe, K., and Wake, T. (2009). Measurement of Unfrozen Water Content and Relative Permittivity of Frozen Unsaturated Soil Using NMR and TDR. *Cold Regions Sci. Technology* 59 (1), 34–41. doi:10.1016/j.coldregions.2009.05.011

Wettlaufer, J. S., Worster, M. G., Wilen, L. A., and Dash, J. G. (1996). A Theory of Premelting Dynamics for All Power Law Forces. *Phys. Rev. Lett.* 76 (19), 3602–3605. doi:10.1103/PhysRevLett.76.3602

Wettlaufer, J. S., Worster, M. G., and Wilen, L. A. (1997). Premelting Dynamics: Geometry and Interactions. *J. Phys. Chem. B* 101 (32), 6137–6141. doi:10.1021/jp9632201

White, W. M. (2020). *Geochemistry*. John Wiley & Sons.

Wickland, K. P., Waldrop, M. P., Aiken, G. R., Koch, J. C., Jorgenson, M. T., and Striegl, R. G. (2018). Dissolved Organic Carbon and Nitrogen Release from Boreal Holocene Permafrost and Seasonally Frozen Soils of Alaska. *Environ. Res. Lett.* 13 (6), 065011. doi:10.1088/1748-9326/aac4ad

Wilen, L. A., and Dash, J. G. (1995). Frost Heave Dynamics at a Single crystal Interface. *Phys. Rev. Lett.* 74 (25), 5076–5079. doi:10.1103/PhysRevLett.74.5076

Williams, P. J. (1968). Ice Distribution in Permafrost Profiles. *Can. J. Earth Sci.* 5 (6), 1381–1386. doi:10.1139/e68-136

Williams, P. J. (1995). Permafrost and Climate Change: Geotechnical Implications. *Phil. Trans. R. Soc. Lond. A.* 352 (1699), 347–358. doi:10.1098/rsta.1995.0075

Williams, P. J., and Smith, M. W. (1989). *The Frozen Earth: Fundamentals of Geocryology*. Cambridge: Cambridge University Press. doi:10.2307/1551597

Woo, M.-k. (2012). *Active Layer Dynamics. Permafrost Hydrology*. Springer Science & Business Media, 163–227. doi:10.1007/978-3-642-23462-010.1007/978-3-642-23462-0_5

Wood, J. A. (1990). The Role of Irreversible Thermodynamics and Rheology in the Regelation-Flow Phenomenon. *Cold regions Sci. Technol.* 18 (2), 133–145. doi:10.1016/0165-232X(90)90003-F

Wraith, J., Or, D., and Warrick, A. (2001). Soil Water Content and Water Potential Relationships. *Soil Phys. companion* 1, 49–84. doi:10.1201/9781420041651.ch3

Wu, Q., Sheng, Y., and Shi, B. (2003). Relationship between Frozen Soil Together with its Water-Heat Process and Ecological Environment in the Tibetan Plateau. *J. Glaciology Geocryology* 25 (3), 250–255.

Wu, Y. Y. Q., Jiang, G., Zhang, P., and Zhang, P. (2017). Stable Isotopic Stratification and Growth Patterns of Ground Ice in Permafrost on the Qinghai-Tibet Plateau, China. *Permafrost Periglac. Process.* 28 (1), 119–129. doi:10.1002/ppp.1892

Xiao, Y., Zhao, L., Dai, Y., Li, R., Pang, Q., and Yao, J. (2013). Representing Permafrost Properties in CoLM for the Qinghai-Xizang (Tibetan) Plateau. *Cold Regions Sci. Technology* 87, 68–77. doi:10.1016/j.coldregions.2012.12.004

Xu, X., and Deng, Y. (1991). *Experimental Study on Water Migration in Frozen Soil*. Beijing: Science Press.

Xu, X., Wang, J., and Zhang, L. (2010). *Frozen Soil Physics*. Beijing: Science Press.

Xue, Y., Zeng, F. J., and Schlosser, C. A. (1996). SSiB and its Sensitivity to Soil Properties—A Case Study Using HAPEX-Mobilhy Data. *Glob. Planet. Change* 13 (1-4), 0–194. doi:10.1016/0921-8181(95)00045-3

Yang, J., Zhou, W., Liu, J., and Hu, X. (2014). Dynamics of Greenhouse Gas Formation in Relation to Freeze/thaw Soil Depth in a Flooded Peat Marsh of Northeast China. *Soil Biol. Biochem.* 75, 202–210. doi:10.1016/j.soilbio.2014.04.006

Yang, K., Wang, C., and Li, S. (2018a). Improved Simulation of Frozen-Thawing Process in Land Surface Model (CLM4.5). *J. Geophys. Res. Atmos.* 123 (2313), 13,238–13,258. doi:10.1029/2017JD028260

Yang, Q., Dan, L., Wu, J., Jiang, R., Dan, J., Li, W., et al. (2018b). The Improved Freeze-Thaw Process of a Climate-Vegetation Model: Calibration and Validation Tests in the Source Region of the Yellow River. *J. Geophys. Res. Atmos.* 123, 13,346–13,367. doi:10.1029/2017JD028050

Yi, S., Wang, X., Qin, Y., Xiang, B., and Ding, Y. (2014). Responses of alpine Grassland on Qinghai-Tibetan Plateau to Climate Warming and Permafrost Degradation: a Modeling Perspective. *Environ. Res. Lett.* 9 (7), 074014. doi:10.1088/1748-9326/9/7/074014

Yu, L., Zeng, Y., Wen, J., and Su, Z. (2018). Liquid-Vapor-Air Flow in the Frozen Soil. *J. Geophys. Res. Atmos.* 123 (14), 7393–7415. doi:10.1029/2018JD028502

Zhang, L., Ma, W., Yang, C., and Dong, S. (2014a). A Review and prospect of the Thermodyamics of Soils Subjected to Freezing and Thawing. *J. Glaciology Geocryology* 35 (6), 1505–1518. doi:10.7522/j.issn.1000-0240.2013.0167

Zhang, L., Ma, W., Yang, C., and Yuan, C. (2014b). Investigation of the Pore Water Pressures of Coarse-Grained sandy Soil during Open-System Step-Freezing and Thawing Tests. *Eng. Geology.* 181, 233–248. doi:10.1016/j.enggeo.2014.07.020

Zhang, M., Zhang, X., Lai, Y., Lu, J., and Wang, C. (2020). Variations of the Temperatures and Volumetric Unfrozen Water Contents of fine-grained Soils during a Freezing-Thawing Process. *Acta Geotech.* 15 (3), 595–601. doi:10.1007/s11440-018-0720-z

Zhang, S., Teng, J., He, Z., Liu, Y., Liang, S., Yao, Y., et al. (2016). Canopy Effect Caused by Vapour Transfer in Covered Freezing Soils. *Géotechnique* 66 (11), 927–940. doi:10.1680/jgeot.16.P.016

Zhang, T., Barry, R., Knowles, K., Ling, F., and Armstrong, R. (2003). "Distribution of Seasonally and Perennially Frozen Ground in the Northern Hemisphere," in Proceedings of the 8th International Conference on Permafrost, Switzerland (Boca Raton, Florida: AA Balkema Publishers Zürich), 1289–1294.

Zhang, Y., Wen, A., Zhao, W., Liang, X., Li, P., and Černý, R. (2020). Influence of Compaction Level on the Water-Heat-Vapor Characteristics of Unsaturated Coarse-Grained Fillings Exposed to Freezing and Thawing. *Adv. Civil Eng.* 2020 (1), 1–10. doi:10.1155/2020/4536301

Zhanrong, G., and Shuangping, H. (2002). Experimental Study on the Condensation Water in Arid Area, Northwestern China. *Adv. Water Sci.* 13 (5), 623–628. doi:10.1002/aic.10277

Zhao, L., Hu, G., Zou, D.-f., and Wu, X. (2019). Permafrost Changes and its Effects on Hydrological Processes on Qinghai-Tibet Plateau. *China Acad. J. Electron. Publishing House* 34 (11). doi:10.16418/j.issn.1000-3045.2019.11.006

Zheng, D., Van der Velde, R., Su, Z., Wen, J., Wang, X., and Yang, K. (2017). Evaluation of Noah Frozen Soil Parameterization for Application to a Tibetan Meadow Ecosystem. *J. hydrometeorology* 18 (6), 1749–1763. doi:10.1175/jhm-d-16-0199.1

Zhou, G.-q., Zhou, Y., Hu, K., Wang, Y.-j., and Shang, X.-y. (2018). Separate-ice Frost Heave Model for One-Dimensional Soil Freezing Process. *Acta Geotech.* 13 (1), 207–217. doi:10.1007/s11440-017-0579-4

Zhou, J., and Li, D. (2012). Numerical Analysis of Coupled Water, Heat and Stress in Saturated Freezing Soil. *Cold Regions Sci. Technology* 72, 43–49. doi:10.1016/j.coldregions.2011.11.006

Zhou, J., and Wei, C. (2020). Ice Lens Induced Interfacial Hydraulic Resistance in Frost Heave. *Cold Regions Sci. Technology* 171, 102964. doi:10.1016/j.coldregions.2019.102964

Zhou, M. M., and Meschke, G. (2013). A Three-phase Thermo-Hydro-Mechanical Finite Element Model for Freezing Soils. *Int. J. Numer. Anal. Meth. Geomech.* 37 (18), 3173–3193. doi:10.1002/nag.2184

Zhou, X., Zhou, J., Kinzelbach, W., and Stauffer, F. (2014). Simultaneous Measurement of Unfrozen Water Content and Ice Content in Frozen Soil Using Gamma ray Attenuation and TDR. *Water Resour. Res.* 50 (12), 9630–9655. doi:10.1002/2014WR015640

Zona, D., Gioli, B., Commane, R., Lindaas, J., Wofsy, S. C., Miller, C. E., et al. (2016). Cold Season Emissions Dominate the Arctic Tundra Methane Budget. *Proc. Natl. Acad. Sci. USA* 113 (1), 40–45. doi:10.1073/pnas.1516017113

Zubrzycki, S., Kutzbach, L., and Pfeiffer, E.-M. (2014). Permafrost-affected Soils and Their Carbon Pools with a Focus on the Russian Arctic. *Solid Earth* 5 (2), 595–609. doi:10.5194/se-5-595-2014

Conflict of Interest: The authors declare that the research was conducted in the absence of any commercial or financial relationships that could be construed as a potential conflict of interest.

Publisher's Note: All claims expressed in this article are solely those of the authors and do not necessarily represent those of their affiliated organizations, or those of the publisher, the editors and the reviewers. Any product that may be evaluated in this article, or claim that may be made by its manufacturer, is not guaranteed or endorsed by the publisher.

frontiers in Environmental Science

ORIGINAL RESEARCH
published: 21 February 2022
doi: 10.3389/fenvs.2022.836085

Evidence of Warming From Long-Term Records of Climate and Permafrost in the Hinterland of the Qinghai–Tibet Plateau

Fujun Zhou[1,2†], Miaomiao Yao[1,3†], Xingwen Fan[1,3], Guoan Yin[1], Xianglian Meng[2] and Zhanju Lin[1]**

[1]State Key Laboratory of Frozen Soil Engineering, Northwest Institute of Eco-Environment and Resources, Chinese Academy of Sciences (CAS), Lanzhou, China, [2]China Railway First Survey and Design Institute Group Co., Ltd., Xi'an, China, [3]School of Engineering Science, University of Chinese Academy of Sciences, Beijing, China

The Qinghai–Tibet Plateau (QTP) is characterized by its extreme climate and dominated by periglacial processes. Permafrost conditions vary greatly, and the recent changes on the QTP are not well known in the hinterland. Here, we examine the changes in climate and permafrost temperatures in several different regions. Climate data were obtained from three weather stations from 1957 to 2019. Annual mean air temperature (T_a) has gradually increased at .031°C/yr–.039°C/yr. Climate warming has been more rapid in the past two decades, particularly during the cold season (November to February). Precipitation has also been slowly increasing during the instrumental record. However, there is pronounced heterogeneity in the seasonal distribution of precipitation, with very little falling between October and April. Ground temperatures and active-layer thickness (ALT) have been investigated over ~20 years at five sites representative of the hinterland of the QTP. These sites are located along the Qinghai–Tibet Highway, which crosses the permafrost zone and traverses the mountainous area and basin areas. Annual mean ground temperatures within the active layer (T_{al} ~ 1 m depth) indicate recent ground warming at all sites, at rates near .05°C/yr. The ALT at five sites has been increasing steadily by 2–9 cm/yr, with an average of 4.6 cm/yr. The temperature near the permafrost table (T_{ps}) has been increasing at .01°C/yr and .06°C/yr, with an average of .03°C/yr. Permafrost temperatures at 15 m depth (T_g) have been increasing by about .01°C/yr–.02°C/yr. The southern boundary (AD site) of the permafrost has warmed the least among the five locations. In high mountainous areas where permafrost temperatures are low (e.g., KLS site), the annual mean T_g has increased by nearly .02°C/yr. The rate of permafrost warming at a basin site (BLH), with relatively high ground temperatures, was approximately .01°C/yr. The GIPL2.0 model simulation results indicate that the annual mean permafrost temperature at 1 m depth at these sites will increase by .6°C–1.8°C in the next 100 years (to 2100) and that ALT will increase by ~40–100 cm. We also discuss the impacts of permafrost changes on the environment and infrastructure on the QTP. This study provides useful information to understand observed and anticipated permafrost changes in this region, under different shared socioeconomic pathways, which will allow engineers to develop adaptation measures.

Keywords: climate change, permafrost warming, active-layer thickness, ground temperature, Qinghai–Tibet Plateau

OPEN ACCESS

Edited by:
Xiaodong Wu,
Chinese Academy of Sciences (CAS), China

Reviewed by:
Hao Zheng,
Hokkaido University, Japan
Lin Chen,
University of California, Riverside, United States

***Correspondence:**
Xingwen Fan
fanxingwen18@mails.ucas.ac.cn
Zhanju Lin
zhanjulin@lzb.ac.cn

†These authors share first authorship

Specialty section:
This article was submitted to Atmosphere and Climate, a section of the journal Frontiers in Environmental Science

Received: *15 December 2021*
Accepted: *24 January 2022*
Published: *21 February 2022*

Citation:
Zhou F, Yao M, Fan X, Yin G, Meng X and Lin Z (2022) Evidence of Warming From Long-Term Records of Climate and Permafrost in the Hinterland of the Qinghai–Tibet Plateau. Front. Environ. Sci. 10:836085. doi: 10.3389/fenvs.2022.836085

INTRODUCTION

Permafrost is ground that remains at or below 0°C for at least 2 years and is primarily a consequence of climate (Henry and Smith, 2001; Smith and Riseborough, 2002). Permafrost constitutes a critical component of the global cryosphere and underlies approximately 24% of the land surface of the Northern Hemisphere (Anisimov and Nelson, 1996). Permafrost terrain comprises a seasonally thawed active layer underlain by perennially frozen ground. Permafrost is particularly sensitive to climate change due to the presence of ground ice (Haeberli and Hohmann, 2008; Chen et al., 2021). Climate warming increases the active-layer thickness and ground temperature (Wolfe et al., 2000; Smith and Burgess, 2004). Consequently, permafrost thaw may cause disequilibrium in terrestrial hydrologic cycles (Serreze et al., 2000; Hinzman et al., 2005; Walsh et al., 2005; White et al., 2007; Fedorov and Konstantinov, 2008), significant landscape and ecosystem changes (Lewkowicz, 1992; Osterkamp et al., 2000; Jorgenson et al., 2001; Pullman and Shur, 2007; Luo et al., 2019), and damage to infrastructure (U.S. Arctic Research Commission Permafrost Task Force, 2003). Changes in permafrost conditions associated with climate warming have also resulted in widespread thermokarst development (Lin

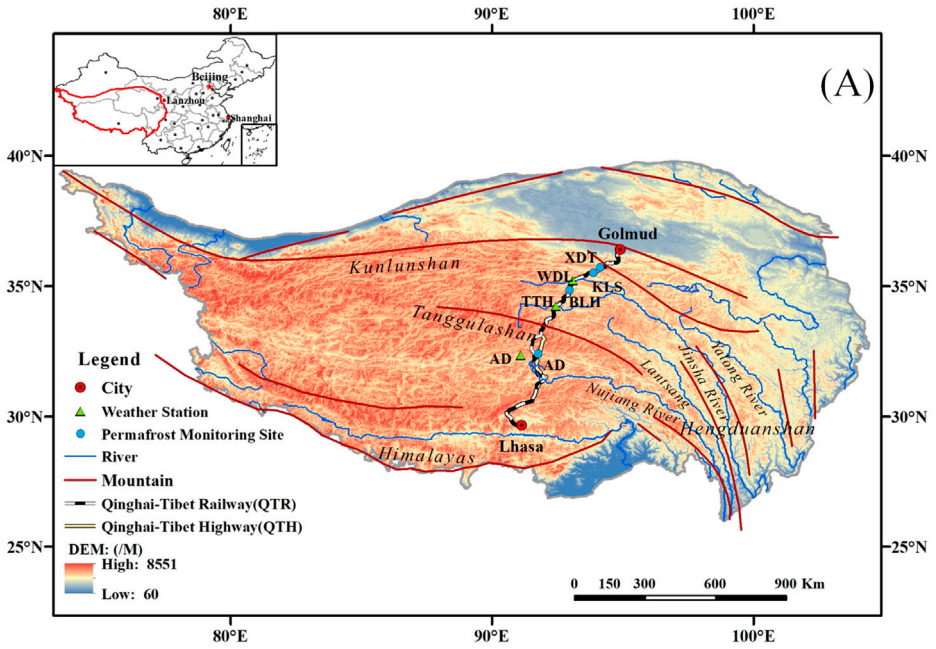

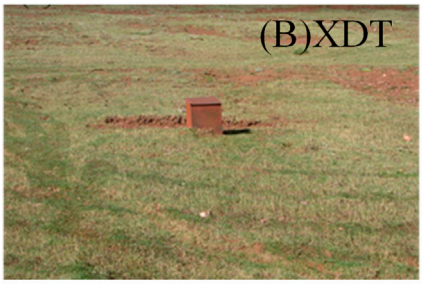

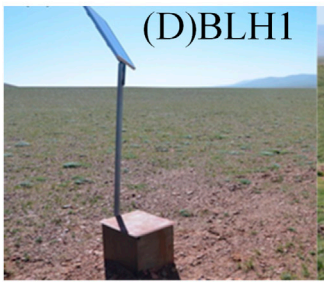

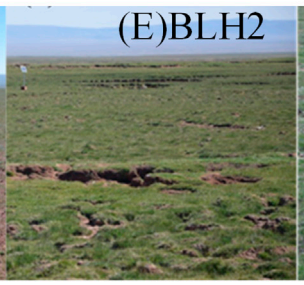

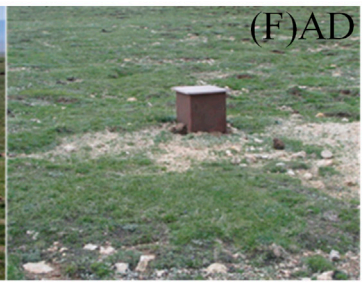

FIGURE 1 | Locations of the five permafrost monitoring sites and three weather stations along the highway **(A)** and the topography conditions at the five permafrost monitoring sites along the highway **(B–F)**.

et al., 2010; Niu et al., 2011; Luo et al., 2015), thaw slump (Niu et al., 2014b; 2016), and increased rates of solifluction. During the 20th century, permafrost warming was documented in the mountains of Eurasia (Harris et al., 2003; Isaksen et al., 2007), Northern Canada (Mackay, 1975; Kwong and Gan, 1994; Burn and Zhang, 2009), and Alaska, USA (Lachenbruch and Marshall, 1986; Osterkamp, 2007; Osterkamp and Romanovsky, 2015).

The Qinghai–Tibet Plateau (QTP) (**Figure 1**) is the largest body of permafrost at high elevation and low latitudes on the earth (Wang and French, 1994; Qiu and Cheng, 1995; Zhou et al., 2000). In the 1950s, the Qinghai–Tibet Highway was built across the plateau to Lhasa, and between 2001 and 2006, a single-track railway (Qinghai–Tibet Railway) was also built up to and over the QTP to Lhasa (Zhang et al., 2008). The total length from Golmud to Lhasa is about 1,120 km; ~630 km are underlain by permafrost, with around 550 km in continuous permafrost and 80 km in discontinuous permafrost. The plateau is characterized by high elevation, periglacial processes, and a cold and arid continental climate (Li et al., 1996; Jin et al., 2008).

With recent climate warming and steadily increasing human activities (Jin et al., 2008; Lin et al., 2011), the permafrost along the highway and railway has been warming rapidly (Wang, 1993; Wang et al., 2000; Wu and Zhang, 2008; Luo et al., 2019). Mean annual ground temperature (MAGT) in seasonally frozen soil and sporadic permafrost has increased by .3°C–.5°C and by .1°C–.3°C in continuous permafrost from the 1970s to 1990s (Wang et al., 2000; Cheng and Wu, 2007). The permafrost distribution has retreated .5–1.0 km at the northern boundary and 1–2 km at the southern boundary from 1975 to 1995 (Niu et al., 2008). Wu and Zhang (2008; 2010) also reported permafrost warming along the Qinghai–Tibetan Highway from 1996 to 2006. The results showed that mean annual permafrost temperatures at 6.0 m depth have increased by .12°C–.67°C and the maximum active-layer thickness (ALT) with an average increasing rate of ~7.5 cm/yr over the same period. However, long-term climate and permafrost changes in recent decades are unclear. In addition, owing to the vast area and complex terrain conditions on the QTP, the climate and permafrost changes have great spatial heterogeneities under the influence of high mountains, plains, valleys, etc.

Therefore, we analyzed the long-term climate and permafrost temperatures in different terrain regions on the QTP. Based on the records of meteorological and ground temperature, the objectives of this study are to (I) define the climatic changes in the past ~60 years in the hinterland of the QTP; (II) examine permafrost changes in the past 20 years at five typical sites; (III) estimate the potential change in permafrost temperature in the next 100 years, and (IV) discuss the possible negative influences of permafrost warming on the environment and engineering in this area.

NATURAL ENVIRONMENTS ON THE QTP

Periglacial Geomorphology

The topography in the hinterland of the QTP is generally complex. Over 90% of the railway underlain by permafrost is above 4,500 m a.s.l. Three major east–west mountain ranges (Kunlunshan, Fenghuoshan, and Tanggula) and three major rivers (Chumaerhe, Tuotuohe, and Tongtianhe) cross the region, dividing it into five general geomorphological units: high mountain areas, foothills or moderately high mountainous areas, upland plateaus, valleys, and basins. Periglacial landforms are widely distributed due to the severe climatic conditions. Near the base of many higher-elevation slopes, strong frost action causes downslope mass movements and creeping gelifluction. Many retrogressive thaw slumps were found on the slopes of lower mountains and hills, and the recorded maximum retrogression rate was 4.5 m/yr in 2000–2002 (Niu et al., 2005; Niu et al., 2012). At upland plains and basins between 4,500–4,700 m elevation, e.g., the Beiluhe Basin and Tuotuohe Basin, there are thousands of thermokarst lakes covering approximately 2–3% of the land surface, and about 1/3 of thermokarst lakes on the high plateau have dried up (Niu et al., 2014a). Climate warming and increasing permafrost temperatures have coincided with an increase in frequency and magnitude of thermokarst in permafrost regions (Luo et al., 2015). Near river valleys and on gentle piedmont slopes, ice domes and frozen mounds are common periglacial landforms in winter.

Vegetation and Soil

Most plants in the permafrost regions are herbaceous perennials less than .15 m tall. Alpine grassland covers about 50% of the land surface, and alpine meadow comprises about 20%. *Stipa purpurea, Carex moorcroftii,* and *Littledalea racemose* are the dominant species in alpine grassland, while *Kobresia pygmaea* and *Kobresia littledalea* are dominant in alpine meadows (Li et al., 1996; Wang et al., 2016; Chen et al., 2020). Alpine grassland is distributed in dry environments on mountains, hills, and upland plains at higher elevation, and the vegetation cover is generally less than 30%. Alpine meadows with >50% of vegetation coverage are found in valleys or basins with higher soil moisture content (Wang et al., 2004; Jin et al., 2008).

The climate here is cold and dry. The surface soil is loose, so there is little resistance to erosion by runoff or aeolian processes. Freeze–thaw cycles also facilitate erosion. Consequently, soil erosion and desertification are common in the hinterland of the QTP. A soil sample test from the Beiluhe Basin shows that the ground surface is typically covered by gravel or sandy silt. Most of the near-surface soil were sand dominated (>60%), with only ~40% silt and clay combined. The soil organic matter (SOM) content is very low (Liu et al., 2014).

Permafrost Conditions

The permafrost in the hinterland of the plateau has a relatively warm temperature and is characterized by high ground ice content. Permafrost with >20% volumetric ice content underlies about 221 km of the region (~40% of the total length), while the portion with MAGT > −1.0°C is 227 km in length. Warm and ice-rich permafrost underlies 124 km of the line (~25%) (Niu et al., 2008). The mean annual ground temperature (MAGT) in most high plains or valleys is

TABLE 1 | Locations of permafrost monitoring sites and weather stations and their surface conditions in the study region [P-t: permafrost thickness (m)].

Sites		E (°)	N (°)	Elev. (m)	Data period	P-t (m)	MAGT (°C)[a]	Topography description	Surface vegetation
Permafrost monitoring sites	XDT	94.09	35.72	4503	2004–2015	<20	0 to −.5	Permafrost northern boundary, valley, island, or sporadic discontinuous permafrost area	Alpine semidesert, grasslands, arid, sparse vegetation, 40%–60% vegetation coverage
	KLS	94.06	35.65	4728	2008–2020	60–120	<−3.0	Middle-to-high mountainous area, continuous permafrost area with low temperature	Sparse alpine grasslands, meadow becoming grasslands, 20%–30% vegetation coverage
	BLH1	92.95	34.85	4634	2001–2013	<60	−.5 to −1.0	Basin area, continuous permafrost area with high temperature and sparsely vegetated ground	Alpine grasslands, semidesert, arid, sparse vegetation, <20% vegetation coverage
	BLH2	92.92	34.82	4650	2007–2020	—	—	Basin area, continuous permafrost area with high temperature and surface coved by the well-vegetated alpine meadow	Alpine swamp meadow, vegetation well developed in places with poor drainage, ~80% vegetation coverage
	AD	91.75	32.40	4801	2003–2015	<40	.5 to −.5	Permafrost southern boundary, valley, degraded melting area, or discontinuous permafrost zone	(Paludified) alpine meadows, alpine grasslands, drying and shrinking wetlands, plant successions, 60%–70% vegetation coverage
Weather stations	WDL	93.08	35.22	4612	1957–2019	—	—	Wudaoliang town, hill slope foot	Transitional area between alpine meadow and sparsely vegetated ground
	TTH	92.43	34.22	4533	1957–2019	—	—	Tuotuohe town, Tuotuohe River bank	Alpine grasslands, semidesert, arid, sparse vegetation
	AD	91.10	32.35	4800	1966–2019	—	—	Anduo county, valley	Alpine swamp meadow

[a]*MAGT, mean annual ground temperature.*

reported as above −1.5°C, and the permafrost thickness is less than 70 m (Wu and Zhang, 2010). In hills and mountains at higher elevations, the MAGT is less than −1.5°C and permafrost thickness exceeds 130 m (Zhou et al., 2000). The active layer thickness in most areas is between 1.5 and 3 m, with a maximum of ~5.0 m below or near the roadbed (Wu and Zhang, 2010). The warm permafrost on the QTP commonly includes 2–3 m thickness massive ground ice below the active layer to depths of 5 m (Lin et al., 2015).

METHODS AND DATA ACQUISITION

Climate Record

Three weather stations (WDL, TTH, and AD) record the climatic conditions along the QTP (**Figure 1**). WDL and TTH weather stations have been operating since October 1956, and the AD station has been operating since November 1965. All weather data are managed by the China Meteorological Data Sharing Service System and available to users for downloading (*http://cdc.cma.gov.cn/home.do*). The data were provided as monthly averages. Data in May 1958 at the TTH station was missed, and the gap was filled by using linear regression.

Permafrost Monitoring

For this study, we selected five typical sites at four locations (**Table 1**; **Figure 1A**) with ~20 boreholes in undisturbed ground at least 20 m from the road. From the north to the south, the XDT site is near the northern boundary of permafrost, which is the discontinuous permafrost island with a relatively high ground temperature (**Figure 1B**). The KLS site on the south slope of the Kunlun Mountains represents the middle-to-high mountainous area with low permafrost temperature (<−3°C) (**Figure 1C**). The BLH1 and BLH2 sites are in the basin with high permafrost temperature (>−1.5°C). The difference between them is that BLH1 drilled early in a sparse vegetation cover ground, and BLH2 is in a alpine meadow area with good vegetation (**Figures 1D,E**). Both KLS and BLH sites lie in the continuous permafrost zone. The AD site is located near the southern boundary of permafrost, where the degraded melting area or discontinuous permafrost zone is present (**Figure 1F**).

Boreholes at each site were drilled to monitor the ground thermal regime from the surface to a depth of 15 m. Thermistor cables with sensors were cased in a steel tube (D = 3–5 cm) and installed in each borehole. The tube was sealed at the bottom and top to prevent moisture from entering and reduce air convection. The boreholes were filled with dry sand to provide conductive contact between the tubes and the ground. The depth interval of the sensors was .5 m in the upper 5 m of the ground, 1 m between 5 and 10 m, and 2 m below 10 m. The cables were assembled at the State Key Laboratory of Frozen Soil Engineering, Chinese Academy of Sciences (CAS). The measurement accuracy of the sensors, calibrated in the laboratory, was estimated at ±.05°C. Several cables were replaced in 2015 because the sensors were damaged during the long work. The data were recorded on a CR3000 logger (Campbell Scientific, Edmonton, AB, Canada) powered by solar-charged batteries. Temperatures were recorded every 4 h, and instrument malfunction caused some data loss (<10%) during the study period. The treatment was by linear regression estimation completion. Mean annual values were calculated for each sensor to determine soil temperature, active layer thickness, freezing degree days, etc.

The ground temperature record from the borehole profile was divided into three critical layers. The first was characterized by the temperature within the active layer. Here, the temperatures from the upper sensors (~1 m depth) at five sites were used to examine thermal conditions within the active layer (T_{al}). The second critical layer was described by the ground temperature at near the permafrost surface or bottom of the active layer (T_{ps}). This temperature is important in characterizing the thermal state of permafrost, and the depth was generally around 2–2.5 m in this study. The third layer was called the depth of zero annual amplitude, and the temperature at this depth represents the annual mean permafrost temperature (T_g). We generally consider the ground temperature at ~15 m as T_g on the QTP because the annual thermal cycle generally penetrates to a depth of 15–20 m. Although the larger perturbation in surface temperature may penetrate much deeper, it takes much longer periodicity to do so (such as a hundred-year scale or longer). Therefore, the variations in annual mean T_g provide a record of the recent permafrost temperatures.

In mountain permafrost regions, the geothermal profiles are generally in a transient state, continually adjusting to changes in the upper boundary temperature that propagate downward into the ground (Beltrami and Harris, 2001; Harris et al., 2009). Therefore, the interpretation of measured temperature profiles should be undertaken carefully, with particular attention being paid to the strong effects of complex surface geometry and rugged alpine topography (Gruber et al., 2010).

The active layer is the layer of ground above the permafrost that freezes and thaws each year. The base of the active layer is at the maximum depth of penetration of the 0°C isotherm (Burn, 1998). In this study, the maximum ALT during each thaw season was estimated by linear interpolation of the daily ground temperatures records obtained in each borehole (Lin et al., 2015).

Estimating Possible Permafrost Warming

We used the Geophysical Institute Permafrost Laboratory (GIPL2.0) transient numerical model to assess the possible permafrost temperature (T, °C) change over time (t, s) and depth (z, m) in the next 100 years (Marchenko et al., 2008; Jafarov et al., 2012). The core of the GIPL2.0 model is based on the one-dimensional heat conduction equation (Sergueev et al., 2003):

$$\left(C(T,z)+L\frac{\partial\theta_w}{\partial_T}\right)-\frac{\partial}{\partial z}\left(k(z,t)\frac{\partial T}{\partial z}\right)=0, \quad (1)$$

where $k(z, t)$ (W m^{-1} K^{-1}) denotes the soil thermal conductivity, $C(T, z)$ (J m^{-3} K^{-1}) is the volumetric heat capacity, and θ_w (%) represents the volumetric water content. L is the volumetric latent heat of freeze/thaw (334 M J m^{-3}). In this study, the frozen and thawed C and k are assigned to each soil layer based on the field measurements (Xu et al., 2010). The θ_w is simulated by empirical experiments and has the following form:

$$\theta_w = n(z)\begin{cases}1, & T > 0\,℃\\ a|T|^{-b}, & T \le 0\,℃\end{cases}, \quad (2)$$

where a and b are empirical constants for specific soil (Xu et al., 2010) and $n(z)$ is the soil water content. θ_w changes with depth and depends on the soil type and ground temperature.

The solution domain of the model in each site was a one-dimensional soil profile from 0–100 m depth containing 139 computational grid nodes. The node spacing increased from .001 m at the ground surface to 10 m at the bottom of the simulation. The model input parameters were the mean monthly air temperature, thermal properties of the soil column, and water content for each site. Snow was not considered in the simulations because there is negligible snow cover along the highway in winter (Lin et al., 2015). Ground thermal properties, including thermal conductivity and volumetric water content, were assigned to each soil layer according to the observed borehole stratigraphy. The volumetric water content was considered a constant.

The ground surface temperature (T_s) was used as the upper boundary condition in the simulations, determined using the air temperatures (T_a) and surface n-factors (Lin et al., 2019; Yin et al., 2021). Monthly air temperatures for each site over the period 1979–2018 were obtained from three weather station records. Concerning the future air temperature series for the model projections, we used the latest two Shared Socioeconomic Pathways (SSP) (O'Neill et al., 2016): 2–4.5 (hereafter SSP245, representing the midrange of future pathways) and 5–8.5 (hereafter SSP245, high end) from the global climate model (GCM) EC-Earth3-Veg (Zhu and Yang, 2020). Monthly GCM air temperatures from 2015 to 2100 were first downscaled to the site location based on the monthly atmospheric lapse rates (ALR, .5°C/100 m; Guo and Wang, 2016; Zhang et al., 2018). The monthly air temperatures were then modified according to the linear regressions between measured monthly temperatures during 2015 and 2018 and the downscaled data for each corresponding location. Finally, we obtained the monthly ground surface temperature series based on the n-factors for the modeling runs. The geothermal gradient (g, ~.14°C m^{-1}) was set as the lower boundary condition (Wu et al., 2000).

Simulations were initialized from the observed ground temperature profiles. The observed ground temperature data were separated into two stages: the first period (2001–2005) was for model calibration, and the second (2005–2018) was for model verification. The model was calibrated and verified using annual borehole temperatures measured at different depths. The simulated values reasonably reproduced the measured values (R^2 > .85). For most of the boreholes, the difference between simulated and measured ground temperature was <.5°C.

RESULTS

Climatic Regime

The plateau has a continental climate, characterized by a long cold season and short warm season. The mean monthly air temperatures were above 0°C from June to September at three weather stations in most years over the last 60 years. Over 90% of

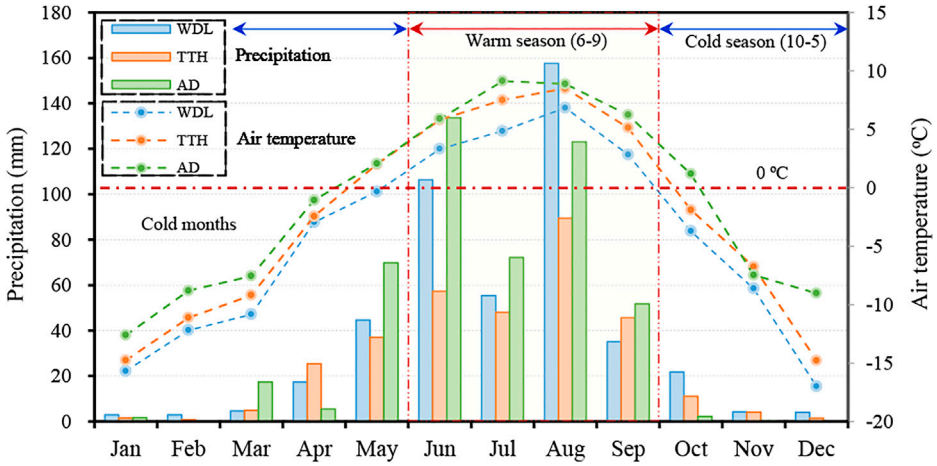

FIGURE 2 | Monthly mean air temperature and precipitation for WDL, TTH, and AD weather stations in 2019. The mean annual temperatures at WDL (1957–2019), TTH (1957–2019), and AD (1966–2019) were –5.1°C, –3.8°C, and –2.4°C, respectively, and mean annual precipitation totals were 299, 293, and 445 mm in the same period (China Meteorological Data Sharing Service System, http://cdc.cma.gov.cn/home.do).

the annual precipitation arrives between May and September, so the hinterland of the QTP is cold and dry in the winter (**Figure 2**).

In 1957–2019, the air temperature at WDL was on average 1.3°C lower than at the TTH station (WDL–TTH). The average differences in monthly mean temperature were lower between November and January (below 1.0°C) than in other months (over 1.0°C). Between 1966 and 2019, the air temperatures at WDL were on average 2.7°C lower than at the AD station (WDL–AD), despite the higher elevation of AD. There were large temperature differences (close to 2–3°C) between the sites in all months of the year (**Table 2**). Air temperatures at the AD station were higher (~1.4°C) than at the TTH station, so the air temperatures gradually increase along the QTP from the north to the south.

The monthly mean air temperatures at three stations are highly correlated:

$$T_{wdl} = 0.91T_{tth} - 1.71 \quad (r^2 = 0.98,\ n = 756,\ p < 0.01), \quad (3)$$

$$T_{wdl} = 0.98T_{ad} - 2.91 \quad (r^2 = 0.89,\ n = 648,\ p < 0.01), \quad (4)$$

where T_{wdl}, T_{tth}, and T_{ad} are the monthly mean air temperatures at WDL, TTH, and AD stations, respectively; n is the total number of months in the study period.

The precipitation regime varies along the QTP. Annually, the AD (445 mm) receives more precipitation than both TTH (293 mm) and WDL (299 mm) stations. Precipitation is generally related to the air temperature. On average, only 5–8% of the annual precipitation at three stations falls as snow between October and April, and the most rain falls between May and September (**Figure 2**).

Long-Term Climate Changes

Precipitation along the QTP has fluctuated and generally increased over the record. Annual precipitation at WDL and TTH stations is correlated for 63 years (r^2 = .59, p < .01). In 1957, the annual precipitation at WDL (302 mm) and TTH (309 mm) was similar, but in 2019, the values were greater (457 and 327 mm, respectively). The average rate of precipitation increase was ~2.0 mm/yr at the WDL station and 1.1 mm/yr at TTH. Annual precipitation at WDL and AD was less strongly correlated over the 54-year record overlap (r^2 = .26, p < .01). The annual precipitation at AD in 1966 was 354 mm, and in 2019, it was 468 mm, a total increase of ~ 100 mm at an average rate of ~1.3 mm/yr (**Figure 3**).

The climate along the railway has been steadily warming over the past 60 years. Annual mean temperatures at WDL and TTH stations were highly correlated for the 63 years of common record between 1957 and 2019 (r^2 = .87, p < .01). In 1957, the annual mean air temperatures at WDL and TTH stations were −6.6°C and −5.1°C, respectively, but rose to −4.5°C and −2.7°C after 63 years. The increase in annual mean air temperature at WDL and TTH between 1957 and 2019 was ~2°C, with an average rate of ~32°C/yr. Annual mean air temperatures at WDL and AD stations were also well correlated over 54 years from 1966 to 2019 (r^2 = .88, p < .01). The annual mean air temperatures at the AD station in 1966 and 2019 were −3.0 and −1.2°C, respectively, a total increase of ~1.8°C with an average rate of ~0.038°C/yr. The warming rates at WDL and TTH near the northern end of the permafrost were lower than those at AD further south (**Figure 4**).

The results of linear regression analysis indicate that the air temperature warming rate in the coldest month was significantly more rapid than that in the warmest month and mean annual value at the three stations. The warming rate along the highway in the warmest month steadily remained at .022°C/yr–.025°C/yr. However, the increase rate in the coldest month closed to .03°C/yr–.04°C/yr, even up to .058°C/yr at the AD station (**Figure 4**).

Climate change rates may change across time periods, which are mainly influenced by the intensity of human activity. Therefore, we have divided the past 60 years into three stages (e.g., before 1979, 1980–1999, and 2000–2019) to estimate decadal-scale patterns in climate change. Mean monthly, mean annual, cold season, and warm season air temperatures from three stations during three periods of the record are presented in **Table 3**. We evaluate the

periodic warming of the air temperature by the increment of the latter stage subtracting the previous stage (**Figure 5**). It is very obvious that the second stage (S2, 1980–1999) increased less than 1°C than the first stage (S1, before 1979) (**Figure 5A**) and even did not show a significant increase in some months (e.g., April). By contrast, the increase in air temperature was very surprising in the last 20 years (S3, 2000–2019) than the previous 20 years (S2, 1980–1999), and the air temperature warming rate in most months was over 1°C, even up to 2–3°C in November–January (**Figure 5B**). These data indicate that climate warming has been more rapid in the recent 20 years.

The precipitation change of three stages was similar to the air temperature (**Figure 5**). Except for the AD station, the precipitation from stage 1 (before 1980) to stage 2 (1980–1999) did not increase significantly; on the contrary, a dry warm season was seen in July–August (**Figure 5C**). By comparison, the precipitation moderately increased from stage 2 (1980–1999) to stage 3 (2000–2019) and increased by ~10 mm in May–September (**Figure 5D**). There was still little precipitation between October and April over the period of record. Overall, the warm and wet summers actually occurred only in the last 10–20 years. Although the plateau has been warming in winter, the dry situation remains unchanged.

Variations in Maximum Active Layer Thickness

The maximum ALT has been consistently increasing at almost all sites and boreholes during the past 20 years (**Figure 6**; **Table 4**). In general, the active layer near the boundary of the permafrost (XDL and AD sites) was thicker than that in the continuous permafrost zone (e.g., BLH and KLS sites). The ALT varied between 4.2–5.5 m at the AD site in 2002–2015 owing to the warm air temperature and more rainfall. The increase of maximum ALT at the AD site was ~9 cm/yr, showing the strong permafrost degradation near the southern limit of the permafrost. The increase rate of maximum ALT at the XDT site was ~2 cm/yr near the northern limit of the permafrost, which is the minimum value among five sites. At the moderately high or alpine areas with the thinnest active layer, such as the KLS site, the increase rate of the maximum active layer was ~4 cm/yr. In the Beiluhe Basin, the boreholes were drilled more at the natural surface. Although the maximum ALT at both sites of BLH1 and BLH2 differed approximately by 20–30 cm, the increase rate of 3–4 cm/yr was basically similar during the past nearly 20 years (**Figure 6**; **Table 4**).

Overall, for all ~20 boreholes at the five sites, the mean increase rate of maximum ALT was 4.6 cm/yr, the median value was 4.2 cm/yr, and the maximum and minimum values were 9.1 and 1.8 cm/yr, respectively.

Long-Term Ground Temperature Dynamics

Annual mean ground temperatures at 1 m depth (T_{al}) at five sites over the last nearly 20 years are shown in **Figure 7A**; **Table 4**. Although the temperatures fluctuated, the increased pattern can still be noticed. The annual mean T_{al} at the BLH1 site did not show an increase over 2002–2013, and a relatively

TABLE 2 | Mean monthly, mean annual (MAAT), cold season (CS), and warm season (WS) air temperature (°C) at WDL and TTH stations over January 1957 to December 2019 and the AD station over January 1966 to December 2019.

Sites		January	February	March	April	May	June	July	August	September	October	November	December	MAAT	CS[a]	WS[a]
Weather stations	WDL	−16.5	−14.2	−10.1	−5.0	−.5	3.0	5.9	5.5	1.7	−4.8	−11.6	−15.1	−5.1	−9.7	4.0
	TTH	−15.9	−13.1	−8.5	−3.5	1.2	5.2	7.9	7.5	3.8	−3.5	−11.3	−15.1	−3.8	−8.7	6.1
	AD	−14.1	−11.2	−6.9	−2.3	2.3	6.4	8.1	7.6	4.7	−1.9	−8.9	−12.9	−2.4	−7.0	6.7
TD between sites[a]	WDL–TTH	−.6	−1.1	−1.6	−1.5	−1.7	−2.2	−2.0	−2.0	−2.1	−1.3	−.3	.0	−1.3	−1.0	−2.1
	WDL–AD	−2.4	−3.0	−3.2	−2.7	−2.8	−3.4	−2.2	−2.1	−3.0	−2.9	−2.7	−2.2	−2.7	−2.7	−2.7

[a]*CS, cold season (October–May); WS, warm season (June–September); TD, temperature difference.*

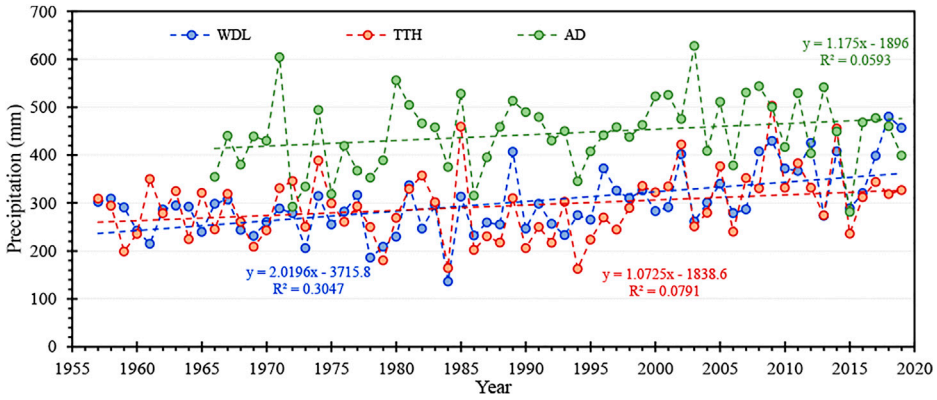

FIGURE 3 | Long-term records in annual total precipitation at WDL and TTH (1957–2019) and AD (1966–2019) weather stations.

constant temperature of ~−.6°C was maintained for more than 10 years. However, the BLH2 site showed a continuous and rapid warming pattern, and the increase rate exceeds .08°C/yr. At the northern and southern limit of the permafrost, the annual mean T_{al} has been gradually increasing at a moderate rate of .03–.05°C/yr. Although the ground at KLS is the coldest, the increase rate of annual mean T_{al} (~.06°C/yr) also reached twice the climate warming rate. The annual mean T_{al} has been increased at four sites among the total five sites, showing an incontestable changing pattern within the active layer. The data series of both sites (BLH1 and BLH2) at the Beiluhe Basin have the longest period of record (19 years) and so may more reliably represent climatic warming rather than interannual temperature fluctuations. The variation in annual mean T_{al} did not faithfully follow the pattern of air temperature changes because it may be influenced by changes in local surface conditions and soil moisture content at the sites.

Annual mean T_{ps} during the past nearly 20 years at five sites is shown in **Figure 7B**; **Table 4**, and the patterns of continued increase were still significant at almost all sites. The warming rates of the annual mean T_{ps} at the northern (XDT site) and southern (AD site) limit of the permafrost were approximately .02°C/yr. At moderately high or alpine areas with the coldest permafrost (KLS site), the warming rate was ~.05°C/yr. At the Beiluhe Basin (BLH1 and two sites), the change of annual mean T_{ps} was similar to the pattern of the T_{al}. The result of monitoring was that annual mean T_{ps} at the BLH1 site basically remained constant and a rapid increase rate of ~.06°C/yr was seen at the BLH2 site. For all five sites and 19 boreholes in the center of the QTP, the mean increase rate of annual mean T_{ps} was .03°C/yr, the median was .02°C/yr, and the maximum was ~.06°C/yr.

Unlike the fluctuant variations of T_{al} and T_{ps}, the annual mean T_g has been steadily increasing at the five sites (**Figure 7C**; **Table 4**). At the northern (XDT) and southern (AD) limit of the permafrost, the increase rates in annual mean T_g were approximately .01°C/yr–.02°C/yr, and it was a little greater at XDT than at the AD site. In moderately high or alpine areas of the Kunlun Mountains, the annual mean T_g warming was about .02°C/yr, which was the most rapid warming rate among the five sites. At Beiluhe Basin, the warming rate of annual mean T_g at both sites was ~.01°C/yr. For all five sites, the mean increase rate of annual mean T_g was .012°C/yr, the median was .011°C/yr, and the maximum and minimum values were .016°C/yr and .004°C/yr, respectively.

Annual Mean Geothermal Profiles

The profiles clearly show increasing annual mean ground temperatures over time at all sites, although the temperature profiles are highly disturbed by topography on the QTP (**Figure 8**). However, the profiles exhibit significantly different characteristics between the sites. At the XDT site near the northern limit of the permafrost, the near-surface ground temperatures changed little, but warming of about .2°C/yr occurred from 2–14 m depth over 10 years (**Figure 8A**). Here, the permafrost degradation showed an upward pattern and the temperature gradient below 2 m was close to zero. In contrast, at the AD site near the southern limit of the permafrost, the warming was in the upper 5 m, while almost no change was registered deeper into the ground (**Figure 8E**). This difference is probably due to the lower air temperatures, lower precipitation, and thicker permafrost near the northern limit than at the southern limit. At the KLS site in moderately high or alpine areas, the increase of ground temperature was also more significant in shallower than deeper layers (**Figure 8B**). Approximately 1–2°C total warming happened mainly within the active layer (above 2.5 m depth), and the warming rate was close to .15°C/yr. The thermal profiles from the KLS site suggest a general common effect, that is, a warming of the upper permafrost surface.

At the BLH1 site in Beiluhe Basin, the near-surface ground temperatures were lower than at depth, indicating thermal equilibrium with surface conditions (**Figure 8C**). The mean warming rate was ~.02°C/yr from the ground surface to a depth of 15 m. However, the profile shows a reversed thermal offset near the ground surface (~1 m depth) so that the mean annual surface temperature is lower than annual mean ground temperatures at both the permafrost surface and between 10–15 m depth. By comparison, the profile at the BLH2 site did not show the reversed thermal offset over 10 years (**Figure 8D**), and it may be related to the well-vegetated alpine

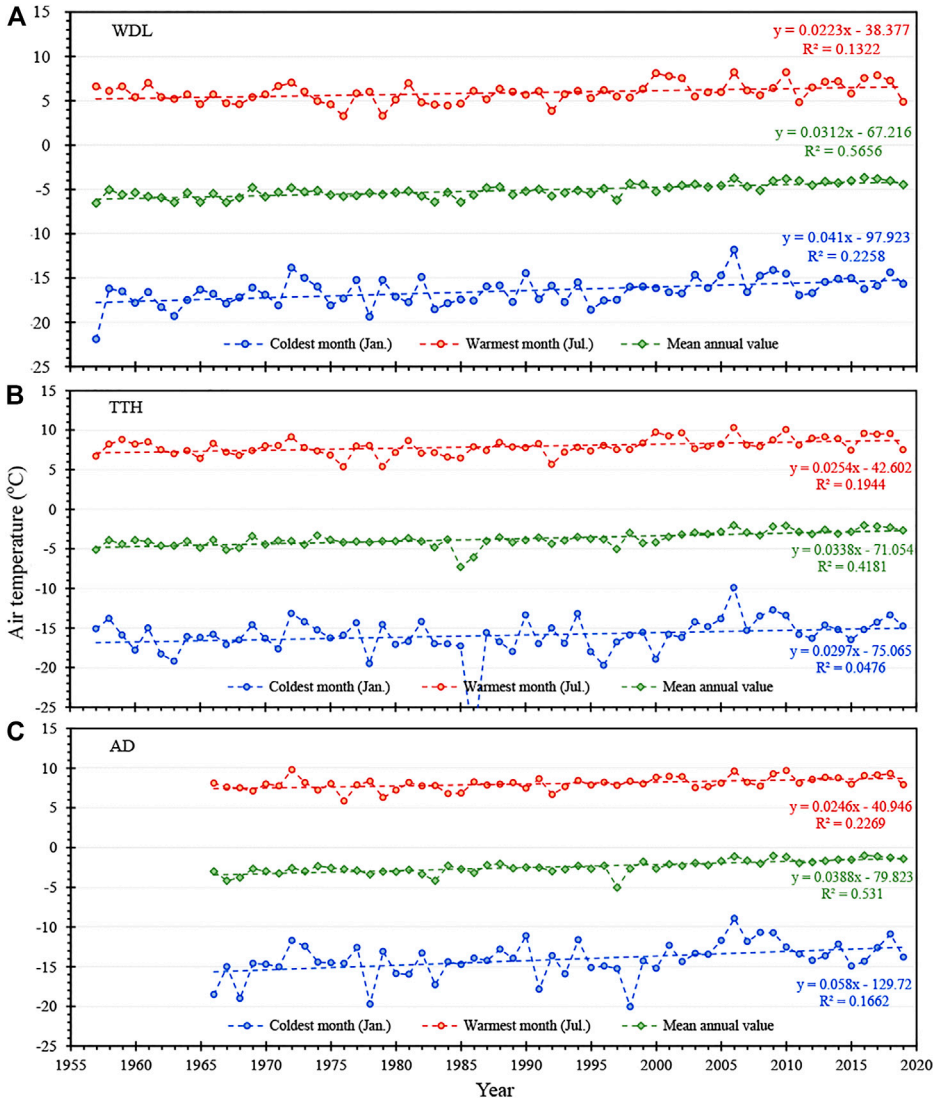

FIGURE 4 | Long-term records in annual mean, coldest month (January), and warmest month (July) air temperatures at three weather stations. **(A)** and **(B)** WDL and TTH (1957–2019), and **(C)** AD (1966–2019).

meadow and wet soil environment. The profile at BLH2 also implies a process of a heat absorption state because the obvious feature is that the ground temperature descends with the depth and a negative thermal gradient above the depth of zero annual amplitude. Although the profiles at BLH sites were different, the gradual increase of ground temperature (~.02°C/yr) was similar over 10–20 years.

Simulation of Permafrost Response to Climate Change in Future

The potential response of the permafrost to climate change in the hinterland of the QTP in the future has been simulated using the GIPL2.0 model. The simulated maximum ALT, the mean annual T_{al}, and the mean annual T_g under the SSP5-8.5 situation were first compared to measured mean data from boreholes at each site of the four sites, and the results are exhibited in **Figure 9**. There is close correspondence between the measured and simulated values from 2001 to 2020. Unfortunately, the maximum ALT is slightly underestimated when the active layer thickness is large, as in the AD site (**Figure 9A**). In contrast, the simulated ground temperature was very close to the measured values, with the RMSE < 1, and R^2 > .9 for all sites (**Figures 9B,C**).

We also simulated the possible changes in maximum ALT and annual mean temperature for depths of 1 m (T_{al}) and 15 m (T_g) to 2100 years (**Figure 10**). The simulation shows that, at the XDT site with island discontinuous permafrost, the max ALT will increase by over 1 m (3–4 m, **Figure 10A**), while the mean annual temperature at 1 m depth was greater in 2100 than in 2020 by ~1.7°C (−.8°C–.9°C, **Figure 10B**). The increase in annual mean T_g appears to be slower than in the previous 20 years, with a rising of ~.5°C (−.7°C to −.2°C, **Figure 10C**). At the KLS site with a

TABLE 3 | Mean monthly, mean annual (MAAT), cold season (CS), and warm season (WS) air temperatures (°C) for three periods at WDL, TTH, and AD weather stations.

Periods	*N*	January	February	March	April	May	June	July	August	September	October	November	December	MAAT	CS	WS
WDL station																
1957–1979	23	−17.1	−15.1	−10.7	−5.1	−.8	2.6	5.5	5.1	1.3	−5.2	−12.4	−15.8	−5.6	−10.3	3.6
1980–1999	20	−16.9	−14.6	−10.0	−5.7	−.5	3.1	5.5	5.2	1.4	−4.9	−11.7	−15.3	−5.4	−10.0	3.8
2000–2019	20	-−15.4	−12.8	−9.5	−4.3	−.2	3.6	6.7	6.3	2.5	−4.1	−10.6	−14.1	−4.3	−8.9	4.8
TTH station																
1957–1979	23	−16.0	−13.7	−9.1	−3.7	.7	4.7	7.5	7.0	3.4	−4.2	−12.0	−15.4	−4.2	−9.2	5.7
1980–1999	20	−17.0	−13.6	−8.5	−4.0	1.4	5.3	7.5	7.3	3.6	−4.0	−12.2	−16.4	−4.2	−9.3	5.9
2000–2019	20	−14.7	−11.8	−7.8	−2.8	1.7	5.8	8.8	8.3	4.6	−2.3	−9.6	−13.6	−2.8	−7.6	6.9
AD station																
1966–1979	14	−15.0	−11.7	−7.4	−2.4	2.0	5.9	7.7	7.1	4.2	−2.6	−9.7	−14.3	−3.0	−7.6	6.2
1980–1999	20	−14.8	−11.9	−6.9	−2.8	2.3	6.4	7.8	7.4	4.4	−2.1	−9.6	−13.6	−2.8	−7.4	6.5
2000–2019	20	−12.8	−10.1	−6.4	−1.8	2.4	6.8	8.6	8.3	5.3	−1.1	−7.6	−11.3	−1.6	−6.1	7.2

MAAT, mean annual temperature; CS, cold season (October–May); WS, warm season (June–September).

continuous and cold permafrost area, the max ALT will increase by about 60 cm, with ~.6°C increase in annual mean T_{al} and ~.4°C increase in annual mean T_g. Meanwhile, at the BLH site with a continuous and warm permafrost area, the max ALT will possibly increase by about 50 cm, with ~1.8°C increase in annual mean T_{al} and ~.2°C increase in annual mean T_g. However, for the AD site of the permafrost south boundary, this is a lower estimate for the change in maximum ALT because the variations in soil moisture clearly have a significant impact on the temperature in the permafrost at a warm and wet region. Even so, the simulated results indicate that the max ALT will increase by about 40 cm, with ~1.5°C increase in annual mean T_{al} and ~.2°C increase in annual mean T_g.

DISCUSSION

Climate Change in the Hinterland

The climate of the QTP is characterized by low mean annual temperatures (<0°C), large daily temperature variability, and low seasonal temperature variability. Climate warming on the plateau was more rapid than the global average (IPCC, 2013). There is little interannual variation in annual mean air temperatures, making the QTP a good region to assess climate change. It has experienced significant warming since the 1950s (Zhao et al., 2004), with temperatures increasing at an average rate of .021°C/yr–.025°C/yr. Air temperatures from 1970 to 2019 show rapid warming, and the most dramatic warming occurred in the 1990s (Gao et al., 2015). The warming trend accelerated after 1997 (.025°C/yr), compared to the warming rate during 1980–1997 (.021°C/yr) (Duan and Xiao, 2015; Bibi et al., 2018). The warming trend of the minimum temperature (.041°C/yr) was about twice as high as that of the rate of maximum temperature (.018°C/yr) (You et al., 2016). The QTP has experienced a slight increase in precipitation since the 1960s (Bibi et al., 2018). Summer precipitation at the QTP increases with altitude (1,000–4,500 m) at a rate of .83% decade^{-1}km^{-1} (Li et al., 2017; Zhang et al., 2017).

Air temperatures at the three stations were highly correlated throughout the year, with coefficients of determination (r^2) above .9 for all months. The increasing trend of precipitation along the highway is 1.1–2.0 mm/yr, with the highest being 2 mm/yr at WDL. The trend is consistent with the increasing trend of rainfall at higher altitudes (Li et al., 2017; Zhang et al., 2017), which also shows the warming and humidification process at the QTP (Yao et al., 2018). The increase in air temperature has been concentrated mainly in the cold season, and the warming rate was above .05°C/yr in November–January. The result is consistent with other studies on the QTP (Zhao et al., 2004) and in Yukon Territory, Canada (Burn and Zhang, 2009). Measured and simulated results both indicate the climate has been warming rapidly in the hinterland of the QTP, which is also consistent with the climate change in the QTP and globally.

Permafrost Change in the Hinterland

The permafrost warming is primarily because of a disruption of the thermal equilibrium of the permafrost. This is usually the result of an

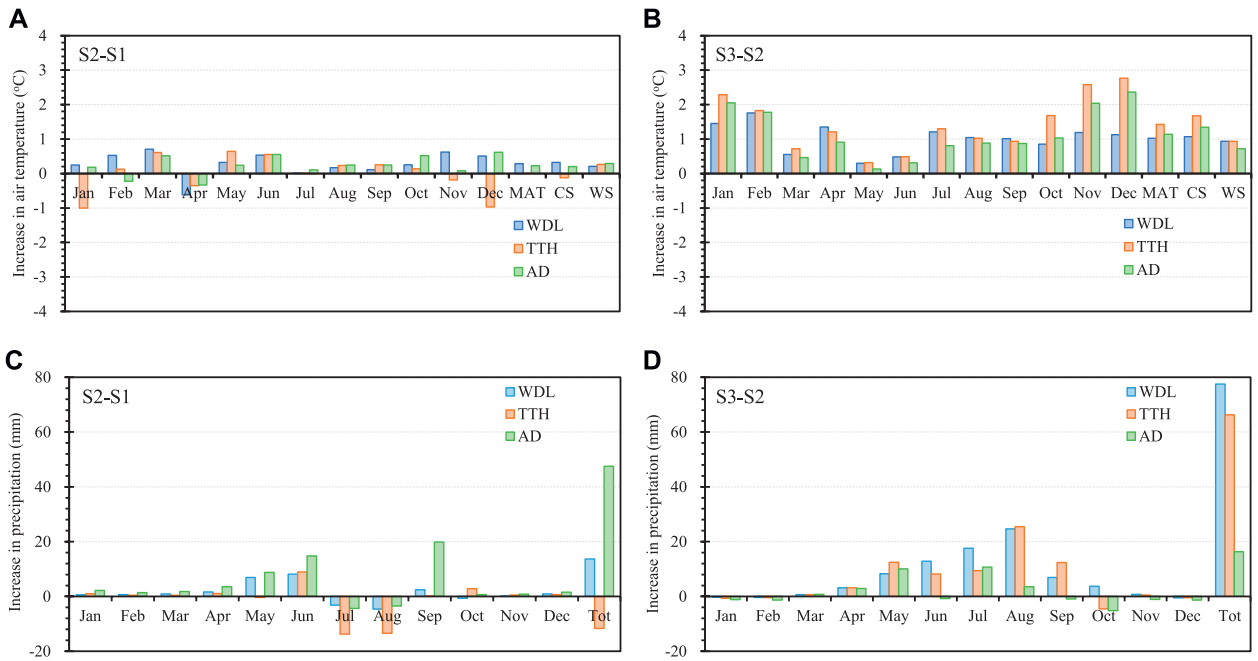

FIGURE 5 | Periodic changes in mean monthly, mean annual (MAT), cold season (CS), and warm season (WS) air temperature at the three weather stations. **(A)** Temperature changes from stage 1 (S1, before 1979) to stage 2 (S2, 1980–1999) and **(B)** from stage 2 (S2, 1980–1999) to stage 3 (S3, 2000–2019). Periodic changes in mean monthly and total precipitation (Tot) at the three weather stations. **(C)** Precipitation changes from stage 1 (S1, before 1979) to stage 2 (S2, 1980–1999) and **(D)** from stage 2 (S2, 1980–1999) to stage 3 (S3, 2000–2019).

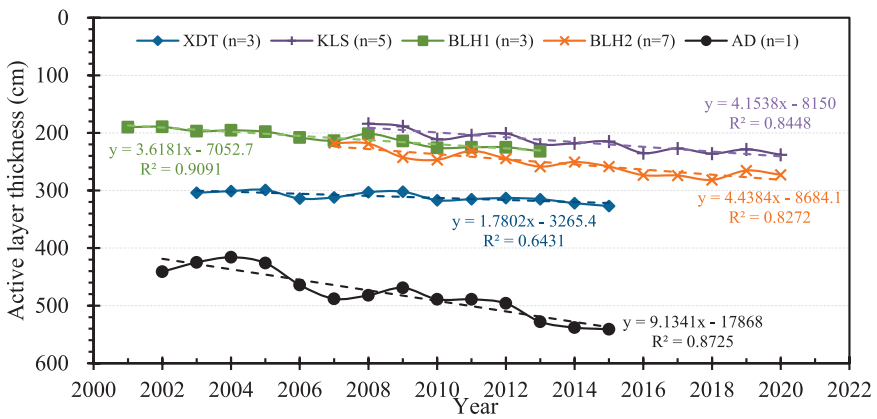

FIGURE 6 | Recent variations in active layer thickness (ALT) at four sites for nearly 20 years. The data are an average value of several boreholes (n) at each site.

increase in active-layer depth and ground temperature. Cheng et al. (2019) found an average warming rate of .048°C/yr at the base of the active layer and .002°C/yr–.031°C/yr at a depth of 10 m based on borehole observation studies along the highway from 2004 to 2018. In all five sites and 19 boreholes in the central QTP, the average annual mean T_{ps} growth rate was .003°C/yr, with a maximum of about .006°C/yr. The near-surface ground temperature fluctuated significantly because of the strong influence from the air temperature, precipitation, and surface conditions, and the changed trend in decadal scale was not significant. Therefore, our results show a small bias.

Hu et al. (2019) found that the ALT increased by 1.95 cm/yr. The changes in the active layer showed spatial heterogeneity, and the steady increases in maximum ALT have coincided with climatic changes. Although the boreholes at each site were at similar elevation and had similar permafrost conditions, the ALT changes varied, likely due to site-specific variation in microtopography, the presence of rock grids, and moisture

TABLE 4 | Maximum active layer depths recorded for nearly 20 years at the five sites in the permafrost areas of the hinterland QTP.

Sites		2001	2002	2003	2004	2005	2006	2007	2008	2009	2010	2011	2012	2013	2014	2015	2016	2017	2018	2019	2020
XDT	ALT (cm)	—	—	304	301	299	314	312	303	302	317	315	313	315	322	327	—	—	—	—	—
	T_{al} (°C)	—	—	—	−1.04	−1.26	−.75	−1.20	−1.92	−1.31	−1.23	−1.07	−1.35	−.99	−.68	−.74	—	—	—	—	—
	T_{ps} (°C)	—	—	—	−.71	−.75	−.65	−.63	−.70	−.59	−.55	−.67	−.62	−.55	−.52	−.47	—	—	—	—	—
	T_g (°C)	—	—	—	−.68	−.67	−.63	−.60	−.60	−.60	−.58	−.56	−.55	−.54	−.52	−.5	—	—	—	—	—
KLS	ALT (cm)	—	—	—	—	—	—	—	184	189	211	204	201	220	218	215	235	227	236	229	238
	T_{al} (°C)	—	—	—	—	—	—	—	−2.83	−2.87	−2.58	−2.68	−3.16	−2.36	−2.23	−2.33	−2.07	−2.14	−2.20	−2.45	−2.22
	T_{ps} (°C)	—	—	—	—	—	—	—	−3.12	−2.99	−2.91	−2.98	−3.06	−2.70	−2.47	−2.57	−2.61	−2.36	−2.39	−2.56	−2.64
	T_g (°C)	—	—	—	—	—	—	—	−3.32	−3.30	−3.29	−3.28	−3.26	−3.25	−3.25	−3.23	−3.21	−3.19	−3.16	−3.16	−3.12
BLH1	ALT (cm)	190	190	197	196	198	208	214	202	214	226	225	225	232	—	—	—	—	—	—	—
	T_{al} (°C)	—	−.53	−.62	−.69	−.77	−.51	−.83	−1.02	−.67	−.56	−.72	−.69	−.59	—	—	—	—	—	—	—
	T_{ps} (°C)	—	−.61	−.61	−.73	−.80	−.58	−.78	−.95	−.75	−.67	−.73	−.74	−.63	—	—	—	—	—	—	—
	T_g (°C)	—	−.69	−.67	−.65	−.64	−.61	−.58	−.58	−.58	−.58	−.57	−.56	−.54	—	—	—	—	—	—	—
BLH2	ALT (cm)	—	—	—	—	—	—	218	219	243	247	231	244	259	250	258	273	274	282	265	273
	T_{al} (°C)	—	—	—	—	—	—	−.83	−.82	−.18	−.10	.17	.20	.15	−.01	.30	.47	.53	.51	.12	.45
	T_{ps} (°C)	—	—	—	—	—	—	−.94	−.95	−.53	−.34	−.30	−.28	−.24	−.35	−.18	−.10	.03	.03	−.31	−.14
	T_g (°C)	—	—	—	—	—	—	−1.02	−1.00	−.88	−.95	−.90	−.92	−.92	−.90	−.91	−.90	−.88	−.85	−.84	−.82
AD	ALT (cm)	—	441	425	416	426	464	488	482	469	489	489	496	528	538	541	—	—	—	—	—
	T_{al} (°C)	—	—	−.32	−.03	.04	.31	.36	−.03	.15	.32	.08	.29	.52	.47	.53	—	—	—	—	—
	T_{ps} (°C)	—	—	−.06	−.08	−.08	−.04	−.01	.00	−.01	.01	.01	.03	.08	.21	.16	—	—	—	—	—
	T_g (°C)	—	—	−.10	−.11	−.12	−.10	−.07	−.08	−.09	−.08	−.08	−.08	−.08	−.08	−.05	—	—	—	—	—

content. Also, along the railroad line, the ALT increased by nearly 1 m on average since 1980 (Zhao et al., 2004). The fastest increase in active layer thickness was observed at the southern boundary of the permafrost, and the result was documented by Wu and Zhang (2010).

The observed permafrost warming at each site is linked to recent climate change. The results of statistics indicate that the permafrost warming was also significantly correlated with the local factors, e.g., elevation, ice content, or vegetation coverage. The change of annual mean T_g is negatively correlated with the temperature of the permafrost itself, indicating that the permafrost is warming more rapidly in regions with colder permafrost (KLS site) than warmer permafrost regions (BLH site). The significant correlation between the annual mean T_g change and ice content indicates that ground temperature increases are more rapid in regions with less ground ice. The positive correlation between annual mean T_g increase and elevation indicates that warming is greater at sites with higher elevation. Finally, vegetation cover was negatively correlated with the annual mean T_g change, and the more the vegetation is, the less the warming due to buffering effect.

Influences of Permafrost Warming on the Environment and Engineering

Considering the driving factors of permafrost warming on the QTP, in general, the causes are classified as natural and human-induced factors (**Figure 11**). The natural factors on the QTP include mainly the increasing annual mean air temperature and precipitation, the rising water of rivers or lakes caused by glacial meltwater, coverage reduction caused by vegetation degradation, surface erosion, and earthquake disturbance. Undoubtedly, the most important causes of permafrost warming are associated with long-term changes of climate (Shur and Osterkamp, 2007). The increase of air temperature and precipitation plays a direct and major role, and it was also confirmed by the climate records of 60 years on the QTP. The effect of natural factors on the permafrost warming is usually a large-scale, long-term, and slow process. The water increase of rivers or lakes supplied by glacial meltwater is gradually becoming another dominant natural factor affecting permafrost warming (Luo et al., 2015; Xie et al., 2020).

The human factors mainly include cuts or destruction by construction projects (e.g., Qinghai–Tibet Railway, highway, oil products pipeline, and fiber-optic cables), disturbance of vehicle movement on road, town or village hot island effect, increasing tourists, CO_2 emission, and overgrazing. In contrast, the anthropogenic perturbations are characterized by the short-term, quick, and regional scale. It can also be demonstrated by an example of construction of the Qinghai–Tibet Highway in the 1970s. The cut in both sides of the road led to the rapidly developing thermokarst processes, vegetation degradation, and significant permafrost warms (Niu et al., 2014b; 2016).

The result of the permafrost warming is rapid permafrost degradation. In continuous permafrost areas, such as the KLS and

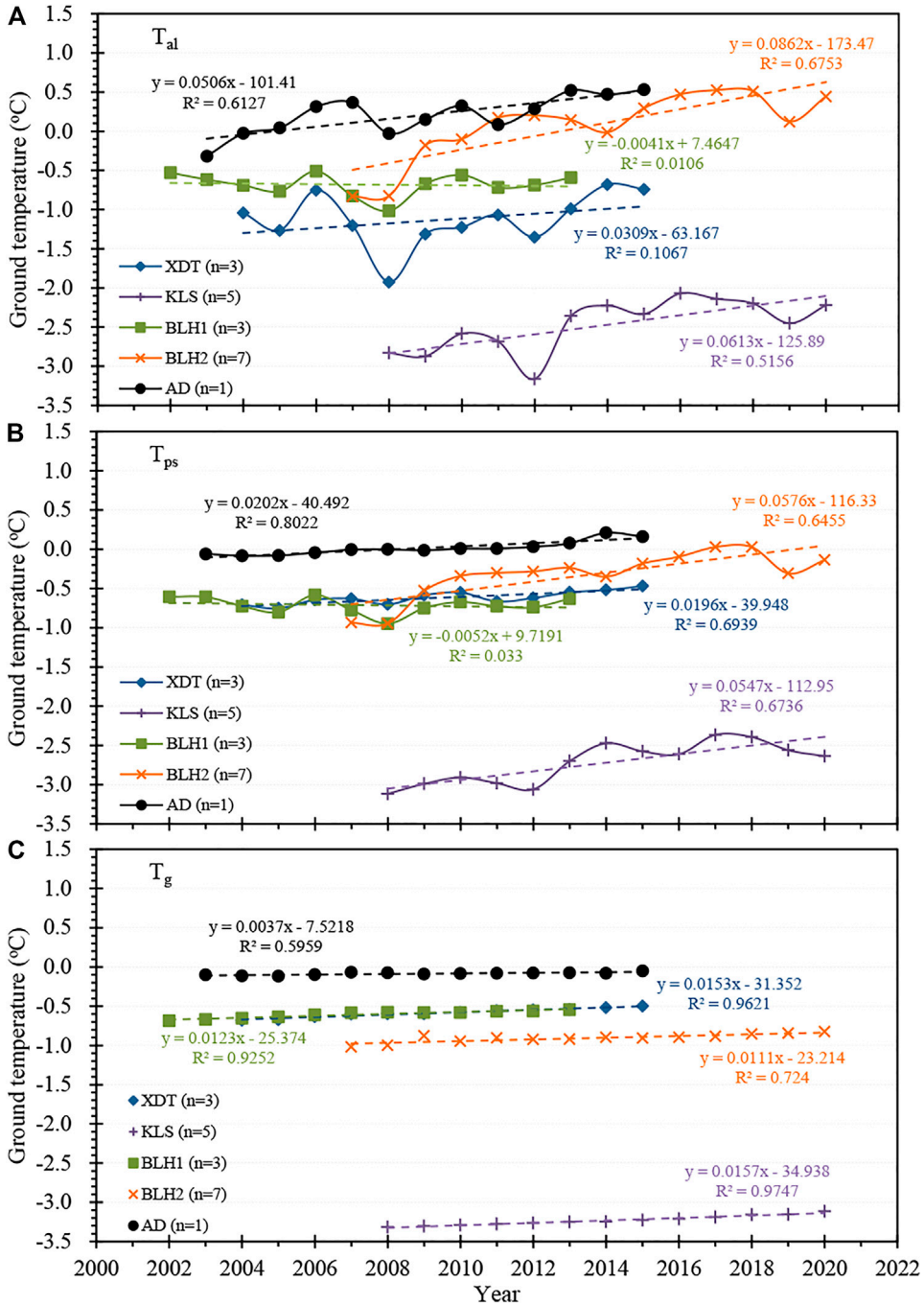

FIGURE 7 | Recent variations in annual mean T_{al} **(A)**, T_{ps} **(B)**, and T_g **(C)** at the five sites for nearly 20 years. The data are an average value of several boreholes (n) at each site.

BLH sites in this study, the permafrost degradation has mainly four modes, e.g., downward, upward, lateral, and composite (Jin et al., 2021). The prominent features indicate mainly the increase of ALT and the rising of annual mean ground temperature, while in discontinuous, sporadic, or island permafrost areas, such as the XDT and AD sites located at the permafrost boundary, the permafrost degradation is mainly in the lateral mode with the characteristics of permafrost continuity decrease and shrinking permafrost area (**Figure 11**).

Permafrost degradation often causes thermal inequilibrium and disequilibrium in hydrologic cycles within the active layer, the seepage of suprapermafrost water, the thaw of ground ice, the

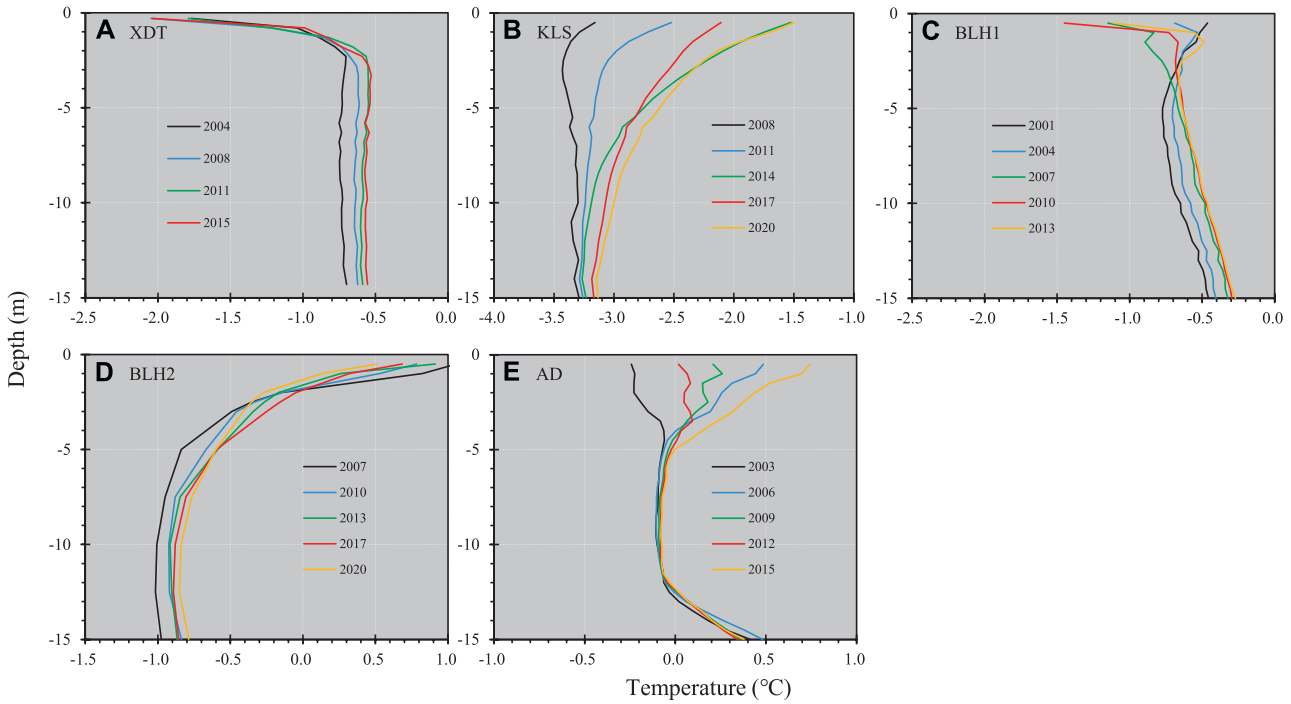

FIGURE 8 | Ground temperature profiles at the five sites. **(A)** XDT, the northern limit of the permafrost, **(B)** KLS, the moderately high or alpine areas, **(C,D)** BLH1-2, the Beiluhe Basin, and **(E)** AD, the southern limit of the permafrost.

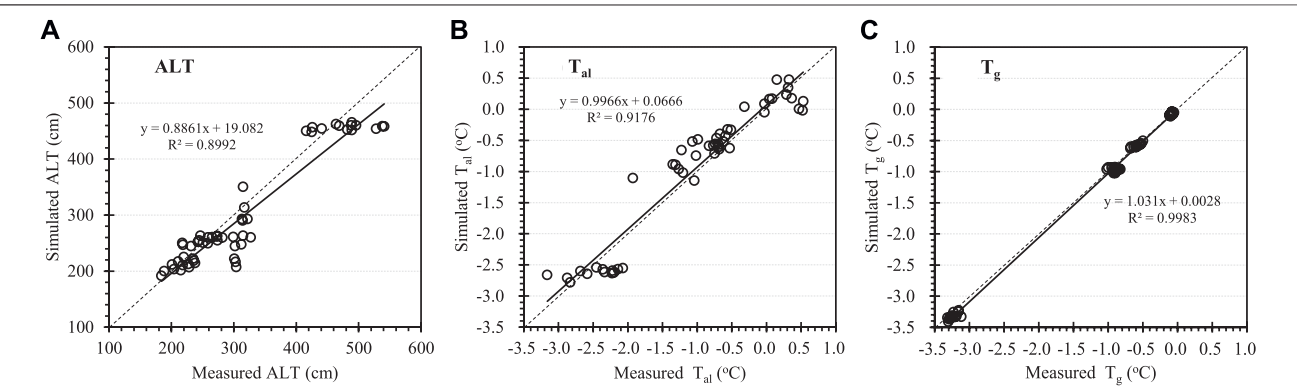

FIGURE 9 | Comparison between the measured and simulated values in one of borehole at the four sites. **(A)** Relationship of the measured and simulated ALT, **(B)** annual mean T_{al}, and **(C)** annual mean T_g.

increase of unfrozen water content in the permafrost layer, and the decrease of bearing capacity (French 2018; Jin et al., 2021). These changes usually result in serious damage to the infrastructure stability and environment in permafrost areas. For the existing engineering, the ground subsidence or compaction caused by permafrost warming will decrease the subgrade stability and increase the frequency of subgrade secondary disease, leading to requirement of expensive maintenance. Meanwhile, the difficulty of line design and planning will increase for new projects.

The impact of permafrost degradation on the environment also involves many aspects. The melting of ground ice caused by permafrost warming often induces a series of thermokarst activities, such as thermokarst lake, thaw slump, and thaw pit (Lin et al., 2010; Niu et al., 2012). The thermokarst process may release chemical solute previously preserved in the permafrost, resulting in higher ionic concentration and pH value of soil in a degenerative area (Lantz et al., 2009). Under the influence of thermokarst processes, the ground temperature status, vegetation structure, and biological community in the adjacent area will be

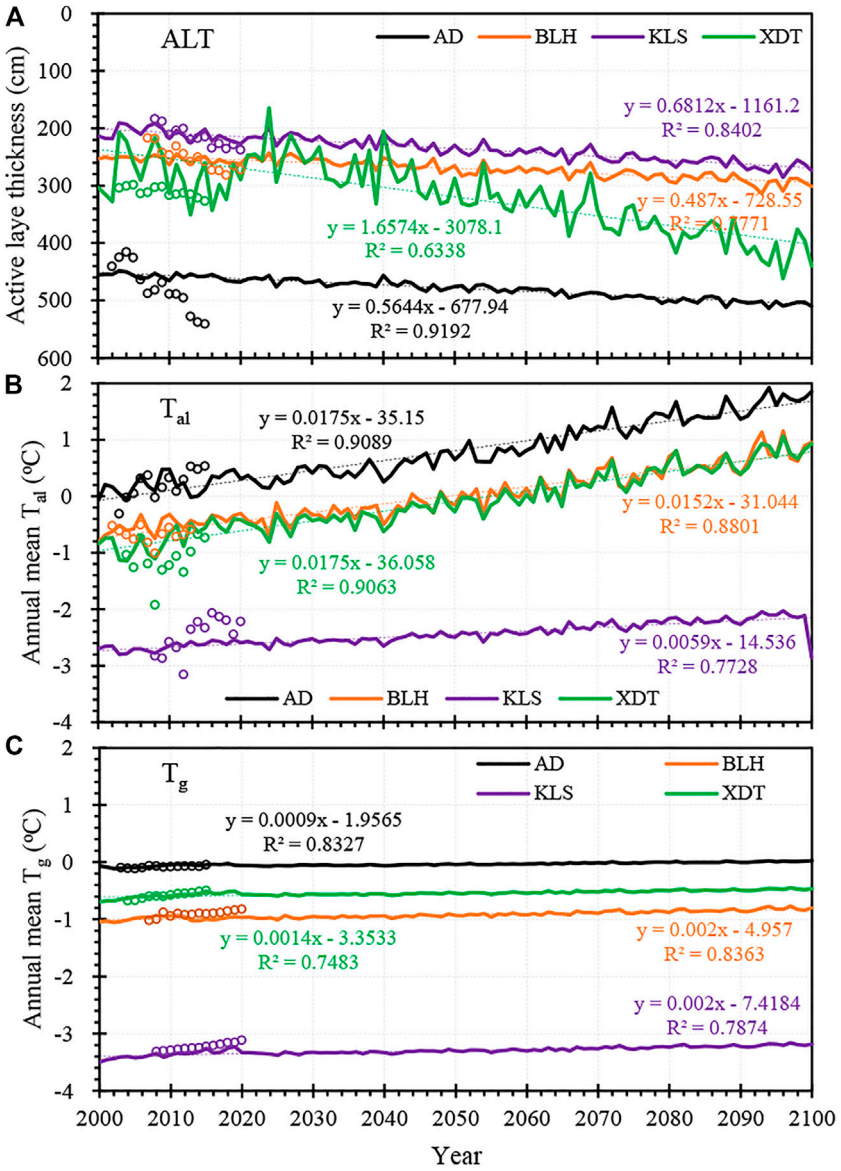

FIGURE 10 | Simulated possible changes of ALT **(A)**, annual mean T_{al} **(B)**, and T_g **(C)** at the four sites over the next 100 years under the SSP585 climate change situation. Circles represent the measured values before 2020.

changed (Mesquita et al., 2010). Moreover, the occurrence of thermokarst will also lead to the release of carbon from the near-surface into the atmosphere, which will then affect the regional carbon cycle process and climate change (Woods et al., 2011).

CONCLUSION

1) A 60-year meteorological record from three weather stations in the hinterland of the Qinghai–Tibet Plateau indicates that the climate is becoming warmer and wetter. The air temperature warming rate of ~.03°C/yr–.04°C/yr is two times the mean global value during the same period. Warming has been most pronounced during winter in the last two decades.

2) Ground temperature measurements were recorded over nearly 20 years at ~20 boreholes at five sites. The top of the permafrost has warmed at ~.03°C/yr, and active layer thickness has increased on average by 4 cm/a. Ground temperature profiles indicate rapid permafrost degradation.

3) Numerical simulations indicate that permafrost temperatures will increase by ~1.7°C in the next 100 years under the SSP5-8.5 climate change scenario. The model indicates that ALT will increase by 1 m.

4) The results of this study indicate the necessity of i) strengthening the monitoring of permafrost change and hazards

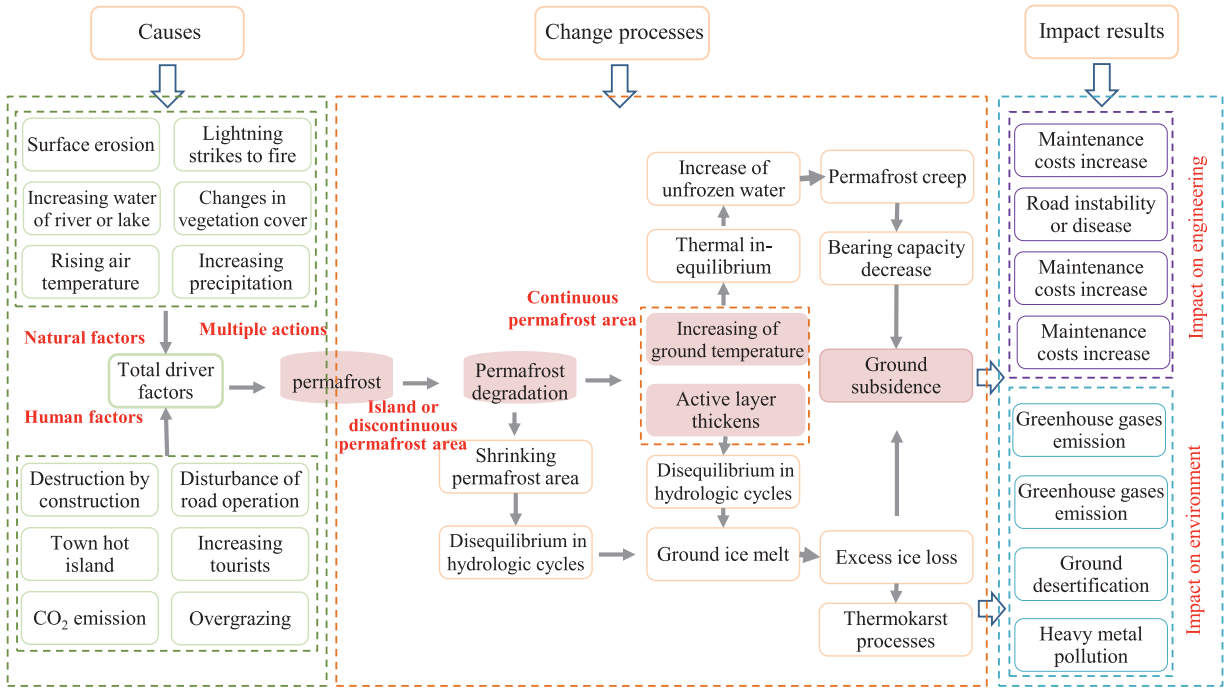

FIGURE 11 | The driving factors that caused permafrost warming and degradation and its impacts on the engineering and environment in a high-altitude permafrost area, the QTP.

associated with thawing and ii) carrying out studies for adapting to permafrost changes along this critical transportation corridor.

DATA AVAILABILITY STATEMENT

The raw data supporting the conclusion of this article will be made available by the authors, without undue reservation.

AUTHOR CONTRIBUTIONS

FZ: writing—original draft, formal analysis. MY: data curation, writing. GY: conceptualization, methodology, software. XF: conceptualization, methodology, validation, writing—review and editing. ZL: writing—review and editing, resources, supervision, project administration, funding acquisition. XM: project administration, funding acquisition.

FUNDING

This work was supported by the National Key Research and Development of China (no. 2017YFA0603101) and the Second Tibetan Plateau Scientific Expedition and Research (STEP) program (grant no. 2019QZKK0905).

ACKNOWLEDGMENTS

We would like to thank the editor and two anonymous reviewers who provided insightful suggestions and Brendan O'Neill for his constructive comments.

REFERENCES

Anisimov, O. A., and Nelson, F. E. (1996). Permafrost Distribution in the Northern Hemisphere under Scenarios of Climatic Change. *Glob. Planet. Change* 14, 59–72. doi:10.1016/09218181(96)00002-1

Beltrami, H., and Harris, R. N. (2001). Foreword: Inference of Climate Change from Geothermal Data. *Glob. Planet. Change* 29, 149–152. doi:10.1016/S0921-8181(01)00085-6

Bibi, S., Wang, L., Li, X., Zhou, J., Chen, D., and Yao, T. (2018). Climatic and Associated Cryospheric, Biospheric, and Hydrological Changes on the Tibetan Plateau: a Review. *Int. J. Climatol* 38 (1), e1–e17. doi:10.1002/joc.5411

Burn, C. R. (1998). The Response (1958-1997) of Permafrost and Near-Surface Ground Temperatures to forest Fire, Takhini River valley, Southern Yukon Territory. *Can. J. Earth Sci.* 35, 184–199. doi:10.1139/e97-105

Burn, C. R., and Zhang, Y. (2009). Permafrost and Climate Change at Herschel Island (Qikiqtaruq), Yukon Territory, Canada. *J. Geophys. Res.* 114, F02001. doi:10.1029/2008JF001087

Chen, L., Voss, C. I., Fortier, D., and Mckenzie, J. M. (2021). Surface Energy Balance of sub-Arctic Roads with Varying Snow Regimes and Properties in Permafrost Regions. *Permafrost and Periglac Process* 32 (4), 681–701. doi:10.1002/ppp.2129

Chen, L., Yu, W., Han, F., Lu, Y., and Zhang, T. (2020). Effects of Desertification on Permafrost Environment in Qinghai-Tibetan Plateau. *J. Environ. Manage.* 262, 110302. doi:10.1016/j.jenvman.2020.110302

Cheng, G. D., Zhao, L., Li, R., Wu, X. D., Sheng, Y., Hu, G. J., et al. (2019). Characteristic, Changes and Impacts of Permafrost on Qinghai-Tibet Plateau. *Chin. Sci. Bull.* 64 (27), 2783. doi:10.1360/TB-2019-0191

Cheng, G., and Wu, T. (2007). Responses of Permafrost to Climate Change and Their Environmental Significance, Qinghai-Tibet Plateau. *J. Geophys. Res.* 112, F02S03. doi:10.1029/2006JF000631

Duan, A., and Xiao, Z. (2015). Does the Climate Warming Hiatus Exist over the Tibetan Plateau. *Sci. Rep.* 5, 13711. doi:10.1038/srep13711

Fedorov, A. N., and Konstantinov, P. Y. (2008). *Recent Changes in Ground Temperature and the Effect on Permafrost Landscapes in Central Yakutia.* 9th Int. Conf. Permafrost. Editors L. K. Douglas and K. M. Hinkel (Alaska, USA: Fairbanks), 433.

French, H. M. (2018). *The Periglacial Environment.* Fourth Edition. Hoboken, NJ: John Wiley & Sons, Inc..

Gao, Y., Li, X., Ruby Leung, L., Chen, D., and Xu, J. (2015). Aridity Changes in the Tibetan Plateau in a Warming Climate. *Environ. Res. Lett.* 10 (3), 034013. doi:10.1088/1748-9326/10/3/034013

Gruber, S., King, L., Kohl, T., Herz, T., Haeberli, W., and Hoelzle, M. (2004). Interpretation of Geothermal Profiles Perturbed by Topography: the Alpine Permafrost Boreholes at Stockhorn Plateau, Switzerland. *Permafrost Periglac. Process.* 15, 349–357. doi:10.1002/ppp.503

Guo, D., and Wang, H. (2016). CMIP5 Permafrost Degradation Projection:A Comparison Among Different Regions. *J. Geophys. Res. Atmos.* 121 (9), 4499–4517. doi:10.1002/2015JD024108

Guoqing, Q., and Guodong, C. (1995). Permafrost in China: Past and Present. *Permafrost Periglac. Process.* 6, 3–14. doi:10.1002/ppp.3430060103

Haeberli, W., and Hohmann, R. (2008). "Climate, Glaciers and Permafrost in the Swiss Alps 2050: Scenarios, Consequences and Recommendations," in *9th Int. Conf. Permafrost*. Editors L. K. Douglas and K. M. Hinkel (Alaska, USA: Fairbanks), 607. June 29–July 3

Harris, C., Arenson, L. U., Christiansen, H. H., Etzelmüller, B., Frauenfelder, R., Gruber, S., et al. (2009). Permafrost and Climate in Europe: Monitoring and Modelling thermal, Geomorphological and Geotechnical Responses. *Earth-Science Rev.* 92, 117–171. doi:10.1016/j.earscirev.2008.12.002

Harris, C., Mühll, D. V., Isaksen, K., Haeberli, W., Sollid, J. L., King, L., et al. (2003). Warming Permafrost in European Mountains. *Glob. Planet. Change* 39 (3-4), 215–225. doi:10.1016/j.gloplacha.2003.04.001

Henry, K., and Smith, M. (2001). A Model-Based Map of Ground Temperatures for the Permafrost Regions of canada. *Permafrost Periglac. Process.* 12 (4), 389–398. doi:10.1002/ppp.399

Hinzman, L. D., Bettez, N. D., Bolton, W. R., Chapin, F. S., Dyurgerov, M. B., Fastie, C. L., et al. (2005). Evidence and Implications of Recent Climate Change in Northern Alaska and Other Arctic Regions. *Climatic Change* 72 (3), 251–298. doi:10.1007/s10584-005-5352-2

Hu, G., Zhao, L., Li, R., Wu, X., Wu, T., Xie, C., et al. (2019). Variations in Soil Temperature from 1980 to 2015 in Permafrost Regions on the Qinghai-Tibetan Plateau Based on Observed and Reanalysis Products. *Geoderma* 337, 893–905. doi:10.1016/j.geoderma.2018.10.044

IPCC (2013). *Fifth Assessment ReportThe Intergovernmental Panel on Climate Change*. Cambidge, United Kingdom and New York, NY: Cambridge University Press.

Isaksen, K., Sollid, J. L., Holmlund, P., and Harris, C. (2007). Recent Warming of Mountain Permafrost in Svalbard and Scandinavia. *J. Geophys. Res.* 112, F02S04. doi:10.1029/2006JF00052210.1029/2006jf000522

Jafarov, E. E., Marchenko, S. S., and Romanovsky, V. E. (2012). Numerical Modeling of Permafrost Dynamics in Alaska Using a High Spatial Resolution Dataset. *The Cryosphere* 6, 613–624. doi:10.5194/tc-6-613-2012

Jin, H.-J., Wu, Q.-B., and Romanovsky, V. E. (2021). Degrading Permafrost and its Impacts. *Adv. Clim. Change Res.* 12, 1–5. doi:10.1016/j.accre.2021.01.007

Jin, H.-j., Yu, Q.-h., Wang, S.-l., and Lü, L.-z. (2008). Changes in Permafrost Environments along the Qinghai-Tibet Engineering Corridor Induced by Anthropogenic Activities and Climate Warming. *Cold Regions Sci. Techn.* 53, 317–333. doi:10.1016/j.coldregions.2007.07.005

Jorgenson, M. T., Racine, C. H., Walters, J. C., and Osterkamp, T. E. (2001). Permafrost Degradation and Ecological Changes Associated with a Warming Climate in Central Alaska. *Clim. Change* 48 (4), 551–579. doi:10.1023/A:1005667424292

Kwong, Y. T. J., and Gan, T. Y. (1994). Northward Migration of Permafrost along the Mackenzie Highway and Climatic Warming. *Climatic Change* 26, 399–419. doi:10.1007/BF01094404

Lachenbruch, A. H., and Marshall, B. V. (1986). Changing Climate: Geothermal Evidence from Permafrost in the Alaskan Arctic. *Science* 234, 689–696. doi:10.1126/science.234.4777.689

Lantz, T. C., Kokelj, S. V., Gergel, S. E., and Henry, G. H. R. (2009). Relative Impacts of Disturbance and Temperature: Persistent Changes in Microenvironment and Vegetation in Retrogressive Thaw Slumps. *Glob. Change Bio* 15 (7), 1664–1675. doi:10.1111/j.1365-2486.2009.01917.x

Lewkowicz, A. G. (1992). "Factors Influencing the Distribution and Initiation of Active-Layer Detachment Slides on Ellesmere Island, Arctic Canada," in *Periglacial Geomorphology*. Editors J. C. Dixon and A. D. Abrahams (Hoboken, N. J: John Wiley), 223–250.

Li, B. Y., Gu, G. A., and Li, S. D. (1996). *The Series of the Comprehensive Scientific Expedition to the Hoh Xil Region-Physical Environment of Hoh Xil Region*. QinghaiBeijing, China: Science Press. (in Chinese).

Li, X., Wang, L., Guo, X., and Chen, D. (2017). Does Summer Precipitation Trend over and Around the Tibetan Plateau Depend on Elevation. *Int. J. Climatol* 37, 1278–1284. doi:10.1002/joc.4978

Lin, Z., Burn, C. R., Niu, F., Luo, J., Liu, M., and Yin, G. (2015). The thermal Regime, Including a Reversed thermal Offset, of Arid Permafrost Sites with Variations in Vegetation Cover Density, Wudaoliang Basin, Qinghai-Tibet Plateau. *Permafrost Periglac. Process.* 26, 142–159. doi:10.1002/ppp.1840

Lin, Z., Gao, Z., Niu, F., Luo, J., Yin, G., Liu, M., et al. (2019). High Spatial Density Ground thermal Measurements in a Warming Permafrost Region, Beiluhe Basin, Qinghai-Tibet Plateau. *Geomorphology* 340, 1–14. doi:10.1016/j.geomorph.2019.04.032

Lin, Z., Niu, F., Liu, H., and Lu, J. (2011). Disturbance-related Thawing of a Ditch and its Influence on Roadbeds on Permafrost. *Cold Regions Sci. Techn.* 66, 105–114. doi:10.1016/j.coldregions.2011.01.006

Lin, Z., Niu, F., Xu, Z., Xu, J., and Wang, P. (2010). Thermal Regime of a Thermokarst lake and its Influence on Permafrost, Beiluhe Basin, Qinghai-Tibet Plateau. *Permafrost Periglac. Process.* 21, 315–324. doi:10.1002/ppp.692

Liu, W., Chen, S., Zhao, Q., Sun, Z., Ren, J., and Qin, D. (2014). Variation and Control of Soil Organic Carbon and Other Nutrients in Permafrost Regions on central Qinghai-Tibetan Plateau. *Environ. Res. Lett.* 9, 114013. doi:10.1088/1748-9326/9/11/114013

Luo, J., Niu, F., Lin, Z., Liu, M., and Yin, G. (2015). Thermokarst lake Changes between 1969 and 2010 in the Beilu River Basin, Qinghai-Tibet Plateau, China. *Sci. Bull.* 60 (5), 556–564. doi:10.1007/s11434-015-0730-2

Luo, J., Yin, G., Niu, F., Lin, Z., and Liu, M. (2019). High Spatial Resolution Modeling of Climate Change Impacts on Permafrost Thermal Conditions for the Beiluhe Basin, Qinghai-Tibet Plateau. *Remote Sensing* 11, 1294. doi:10.3390/rs11111294

Mackay, J. R. (1975). *The Stability of Permafrost and Recent Climatic Change in the Mackenzie Valley, N.W.T. Pap. 75–1, Part B, Pp. 173– 176*. Ottawa, Ont: Geol. Surv. of Can.

Marchenko, S., Romanovsky, V., and Tipenko, G. (2008). *Numerical Modeling of Spatial Permafrost Dynamics in Alaska,* 9th Int. Conf. Permafrost. Editors L. K. Douglas and K. M. Hinkel (Alaska, USA: Fairbanks). June 29–July 3.

Mesquita, P. S., Wrona, F. J., and Prowse, T. D. (2010). Effects of Retrogressive Permafrost Thaw Slumping on Sediment Chemistry and Submerged Macrophytes in Arctic Tundra Lakes. *Freshw. Biol.* 55 (11), 2347–2358. doi:10.1111/j.1365-2427.2010.02450.x

Niu, F., Cheng, G., Ni, W., and Jin, D. (2005). Engineering-related Slope Failure in Permafrost Regions of the Qinghai-Tibet Plateau. *Cold Regions Sci. Techn.* 42, 215–225. doi:10.1016/j.coldregions.2005.02.002

Niu, F. J., Xu, J., Lin, Z. J., and Wang, P. (2008). "Engineering-induced Environmental Hazards in Permafrost Regions of Qinghai–Tibet Plateau," in *9th Int. Conf. Permafrost*. Editors L. K. Douglas and K. M. Hinkel (Alaska, USA: Fairbanks). June 29–July 3.

Niu, F., Lin, Z., Liu, H., and Lu, J. (2011). Characteristics of Thermokarst Lakes and Their Influence on Permafrost in Qinghai-Tibet Plateau. *Geomorphology* 132, 222–233. doi:10.1016/j.geomorph.2011.05.011

Niu, F., Luo, J., Lin, Z., Fang, J., and Liu, M. (2016). Thaw-induced Slope Failures and Stability Analyses in Permafrost Regions of the Qinghai-Tibet Plateau, China. *Landslides* 13 (1), 55–65. doi:10.1007/s10346-014-0545-2

Niu, F., Luo, J., Lin, Z., Liu, M., and Yin, G. (2014a). Morphological Characteristics of Thermokarst Lakes along the Qinghai-Tibet Engineering Corridor. *Arctic, Antarctic, Alpine Res.* 46, 963–974. doi:10.1657/1938-4246-46.4.963

Niu, F., Luo, J., Lin, Z., Liu, M., and Yin, G. (2014b). Thaw-induced Slope Failures and Susceptibility Mapping in Permafrost Regions of the Qinghai-Tibet Engineering Corridor, China. *Nat. Hazards* 74 (3), 1667–1682. doi:10.1007/s11069-014-1267-4

Niu, F., Luo, J., Lin, Z., Ma, W., and Lu, J. (2012). Development and thermal Regime of a Thaw Slump in the Qinghai-Tibet Plateau. *Cold Regions Sci. Techn.* 83-84, 131–138. doi:10.1016/j.coldregions.2012.07.007

O'Neill, B. C., Tebaldi, C., van Vuuren, D. P., Eyring, V., Friedlingstein, P., Hurtt, G., et al. (2016). The Scenario Model Intercomparison Project (ScenarioMIP) for CMIP6. *Geosci. Model. Dev.* 9 (9), 3461–3482. doi:10.5194/gmd-9-3461-2016

Osterkamp, T. E. (2007). Characteristics of the Recent Warming of Permafrost in Alaska. *J. Geophys. Res.* 112, F02S02. doi:10.1029/2006JF000578

Osterkamp, T. E., and Romanovsky, V. E. (2015). Evidence for Warming and Thawing of Discontinuous Permafrost in Alaska. *Permafrost Periglacial Proc.* 10, 172–374. doi:10.1002/(SICI)1099-1530(199901/03)10:13.0.CO

Osterkamp, T. E., Viereck, L., Shur, Y., Jorgenson, M. T., Racine, C., Doyle, A., et al. (2000). Observations of Thermokarst and its Impact on Boreal Forests in Alaska, U.S.A. *Arctic, Antarctic, Alpine Res.* 32 (3), 303–315. doi:10.2307/155252910.1080/15230430.2000.12003368

Pullman, E. R., Torre Jorgenson, M., and Shur, Y. (2007). Thaw Settlement in Soils of the Arctic Coastal Plain, Alaska. *Arctic, Antarctic, Alpine Res.* 39 (3), 468–476. doi:10.2307/2018171810.1657/1523-0430(05-045)[pullman]2.0.co;2

Sergueev, D., Tipenko, G., Romanovsky, V., and Oomanovskii, N. (2003). "Mountain Permafrost Thickness Evolution under Influence of Long-Term Climate Fluctuations (Results of Numerical Simulation)," in Proceedings of the 8th International Conference on Permafrost, July 21-25, 2003, Zurich, Switzerland. Editors M. Phillips, S. M. Springman, and L. U. Arenson (Lisse: A. A. Balkema Publishers), 1017–1021.

Serreze, M. C., Walsh, J. E., Chapin III, F. S., Osterkamp, T., Dyurgerov, M., Romanovsky, V., et al. (2000). Observational Evidence of Recent Change in the Northern High-Latitude Environment. *Clim. Change* 46 (1), 159–207. doi:10.1023/A:1005504031923

Shur, Y., and Osterkamp, T. E. (2007). *Thermokarst*. Fairbanks, Alaska: Institute of Northern EngineeringUniversity of Alaska, 50. Report INE06.11.

Smith, M. W., and Riseborough, D. W. (2002). Climate and the Limits of Permafrost: A Zonal Analysis. *Permafrost Periglac. Process.* 13, 1–15. doi:10.1002/ppp.410

Smith, S. L., and Burgess, M. M. (2004). *Sensitivity of Permafrost to Climate Warming in Canada Bull. 579.* Ottawa, Ont: Geol. Surv. of Can. doi:10.4095/216137

U.S. Arctic Research Commission Permafrost Task Force (2003). *Climate Change, Permafrost, and Impacts on Civil Infrastructure*. Special Report 01-03. Arlington, Virginia: U.S. Arctic Research Commission.

Walsh, J., Anisimov, O., Hagen, J. O. M., Jakobsson, T., and Oerlemans, J. (2005). "Cryosphere and Hydrology," in *Arctic Climate Impact Assessment* (New York: Cambridge Univ. Press), 183.

Wang, B., and French, H. M. (1994). Climate Controls and High-Altitude Permafrost, Qinghai-Xizang (Tibet) Plateau, China. *Permafrost Periglac. Process.* 5, 87–100. doi:10.1002/ppp.3430050203

Wang, G. X., Yao, J. Z., Guo, Z. G., and Cheng, G. D. (2004). Changes of Permafrost Eco-Environments under the Influences of Human Activities, and Their Significance for the Construction of the Qinghai–Tibet Railway. *Chin. Sci. Bull.* 49, 1556–1564. (in Chinese). doi:10.1007/bf03184309

Wang, J., Zhong, M., Wu, R., Dong, Q., Wang, K., and Shao, X. (2016). Response of Plant Functional Traits to Grazing for Three Dominant Species in alpine Steppe Habitat of the Qinghai-Tibet Plateau, China. *Ecol. Res.* 31 (4), 515–524. doi:10.1007/s11284-016-1360-0

Wang, S. L., Jin, H. J., Li, S. X., and Zhao, L. (2000). Permafrost Degradation on the Qinghai-Tibet Plateau and its Environmental Impacts. *Permafrost Periglacial Proc.* 11, 43–53. doi:10.1002/(SICI)1099-1530(200001/03)11:13.0.CO;2-H

Wang, S. L. (1993). Recent Change of Permafrost along Qinghai-Xizang Highway. *Arid Land Geogr.* 16, 1–7. (in Chinese).

White, D., Hinzman, L., Alessa, L., Cassano, J., Chambers, M., Falkner, K., et al. (2007). The Arctic Freshwater System: Changes and Impacts. *J. Geophys. Res.* 112 (G4), a–n. doi:10.1029/2006JG000353

Wolfe, S. A., Kotler, E., and Nixon, F. M. (2000). *Recent Warming Impacts in the Mackenzie delta, Northwest Territories, and Northern Yukon Territory Coastal Areas*. Ottawa, Ont: Geol. Surv. of Can.

Woods, G. C., Simpson, M. J., Pautler, B. G., Lamoureux, S. F., Lafrenière, M. J., and Simpson, A. J. (2011). Evidence for the Enhanced Lability of Dissolved Organic Matter Following Permafrost Slope Disturbance in the Canadian High Arctic. *Geochimica et Cosmochimica Acta* 75, 7226–7241. doi:10.1016/j.gca.2011.08.013

Wu, Q. B., Li, X., and Li, W. J. (2000).The Prediction of Permafrost Change along the Qinghai-Tibet Highway, China. *Permafrost Periglacial Proc.* 4, 371–376. doi:10.1002/1099-1530(200012)11:4<371:AID-PPP354>3.0

Wu, Q., and Zhang, T. (2010). Changes in Active Layer Thickness over the Qinghai-Tibetan Plateau from 1995 to 2007. *J. Geophys. Res.* 115, D09107. doi:10.1029/2009JD01297

Wu, Q., and Zhang, T. (2008). Recent Permafrost Warming on the Qinghai-Tibetan Plateau. *J. Geophys. Res.* 113, D13108. doi:10.1029/2007JD009539

Xie, C. W., Zhang, Y. X., Liu, W. H., Wu, J. C., Yang, G. Q., Wang, W., et al. (2020). Environmental Changes Caused by the Outburst of Zonag Lake and the Possible Outburst Mode of Yanhu Lake in the Hoh Xil Region. *J. Glaciology Geocryology* 42 (4), 1344–1352. doi:10.7522/j.issn.1000-0240.2019.0051

Xu, X. Z., Wang, J. C., and Zhang, L. X. (2010). *Physics of Permafrost*. Beijing: Chinese Science Press.

Yao, T., Xue, Y., Chen, D., Chen, F., Thompson, L., Cui, P., et al. (2019). Recent Third Pole's Rapid Warming Accompanies Cryospheric Melt and Water Cycle Intensification and Interactions between Monsoon and Environment: Multidisciplinary Approach with Observations, Modeling, and Analysis. *B. Am. Meteorol. Soc.* 100, 423–444. doi:10.1175/BAMS-D-17-0057.1

Yin, G.-A., Niu, F.-J., Lin, Z.-J., Luo, J., and Liu, M.-H. (2021). Data-driven Spatiotemporal Projections of Shallow Permafrost Based on CMIP6 across the Qinghai–Tibet Plateau at 1 Km2 Scale. *Adv. Clim. Change Res.* 12, 814–827. doi:10.1016/j.accre.2021.08.009

You, Q., Min, J., Jiao, Y., Sillanpää, M., and Kang, S. (2016). Observed Trend of Diurnal Temperature Range in the Tibetan Plateau in Recent Decades. *Int. J. Climatol.* 36, 2633–2643. doi:10.1002/joc.4517

Zhang, C., Tang, Q., and Chen, D. (2017). Recent Changes in the Moisture Source of Precipitation over the Tibetan Plateau. *J. Clim.* 30, 1807–1819. doi:10.1175/JCLI-D-15-0842.1

Zhang, H., Zhang, F., Zhang, G., Che, T., and Yan, W. (2018). How Accurately Can the Air Temperature Lapse Rate over the Tibetan Plateau Be Estimated from MODIS LSTs. *J. Geophys. Res. Atmos.* 123, 3943–3960. doi:10.1002/2017JD028243

Zhang, T., Baker, T. H. W., Cheng, G.-D., and Wu, Q. (2008). The Qinghai-Tibet Railroad: A Milestone Project and its Environmental Impact. *Cold Regions Sci. Techn.* 53, 229–240. doi:10.1016/j.coldregions.2008.06.003

Zhao, L., Ping, C.-L., Yang, D., Cheng, G., Ding, Y., and Liu, S. (2004). Changes of Climate and Seasonally Frozen Ground over the Past 30 Years in Qinghai-Xizang (Tibetan) Plateau, China. *Glob. Planet. Change* 43, 19–31. doi:10.1016/j.gloplacha.2004.02.003

Zhou, Y. W., Cheng, G. D., and Qiu, G. Q. (2000). *Permafrost in China*. Beijing: Science. Press, 403–404pp. (in Chinese).

Zhu, Y.-Y., and Yang, S. (2020). Evaluation of CMIP6 for Historical Temperature and Precipitation over the Tibetan Plateau and its Comparison with CMIP5. *Adv. Clim. Change Res.* 11 (3), 239–251. doi:10.1016/j.accre.2020.08.001

Conflict of Interest: FZ and XM were employed by the company China Railway First Survey and Design Institute Group Co., Ltd.

The remaining authors declare that the research was conducted in the absence of any commercial or financial relationships that could be construed as a potential conflict of interest.

frontiers | Frontiers in Environmental Science

REVIEW
published: 12 April 2022
doi: 10.3389/fenvs.2022.874635

Assessing Sources and Distribution of Heavy Metals in Environmental Media of the Tibetan Plateau: A Critical Review

Wenjuan Wang[1], *Xiaowen Ji*[2], *Evgeny Abakumov*[1]*, *Vyacheslav Polyakov*[1,3], *Gensheng Li*[4] *and Dong Wang*[5,6]

[1]Department of Applied Ecology, Saint Petersburg State University, Saint Petersburg, Russia, [2]School of Environment and Sustainability, University of Saskatchewan, Saskatoon, SK, Canada, [3]Arctic and Antarctic Research Institute, Saint-Petersburg, Russia, [4]School of Public Policy and Management, China University of Mining and Technology, Xuzhou, China, [5]Cryosphere Research Station on the Qinghai-Tibet Plateau, State Key Laboratory of Cryospheric Science, Northwest Institute of Eco-Environment and Resources, Chinese Academy of Sciences, Lanzhou, China, [6]College of Resources and Environment, University of Chinese Academy of Sciences, Beijing, China

With a unique multi-sphere environmental system, the Tibetan Plateau (TP) plays an essential role in the ecological sheltering function for China and other parts of Asia. However, black carbon, persistent organic pollutants, and heavy metals (HMs) have been increased dramatically since the 1950s, reflecting rising emissions in Asia. In this context, the sources and distribution of HMs were summarized in the environment media of the TP. The results showed that 1) HMs in the TP may be generated from geogenic/pedogenic associations (Cu, Cr, Ni, As, and Co) and anthropogenic activities of local or long-distance atmospheric transmission (Cd, Pb, Zn, and Hg). 2) The atmospheric transport emission sources of HMs are mainly from the surrounding heavily-polluted regions by the Indian and East Asian monsoons and the southern branch of westerly winds. 3) Soil, water, snow, glacier, sediment, and vegetation act as vital sinks of atmospheric deposits of HMs; 4) Significant bioaccumulation of arsenic (As), lead (Pb), and methylmercury (MeHg) have been found in terrestrial and aquatic biota chains in the TP; 5) The enhancement of anthropogenic activities, climate change, glacial retreat and permafrost degradation had potential impacts on the behaviors and fates of HMs in the TP. Therefore, the ecological risk of HMs is of particular concern, and feasible and effective environmental safety strategies are required to reduce the adverse effects of inorganic pollutants in the TP. Our review will provide a reference for researchers to further study regional HMs pollution around the TP.

Keywords: heavy metals, Tibetan plateau, inorganic pollution, cryosphere, climate change

OPEN ACCESS

Edited by:
Wenxin Zhang,
Lund University, Sweden

Reviewed by:
Maierdang Keyimu,
Xinjiang Institute of Ecology and Geography (CAS), China
Xiao-San Luo,
Nanjing University of Information Science & Technology, China

****Correspondence:***
Evgeny Abakumov
e_abakumov@mail.ru

Specialty section:
This article was submitted to Atmosphere and Climate, a section of the journal Frontiers in Environmental Science

Received: *12 February 2022*
Accepted: *22 March 2022*
Published: *12 April 2022*

Citation:
Wang W, Ji X, Abakumov E, Polyakov V, Li G and Wang D (2022) Assessing Sources and Distribution of Heavy Metals in Environmental Media of the Tibetan Plateau: A Critical Review. Front. Environ. Sci. 10:874635. doi: 10.3389/fenvs.2022.874635

1 INTRODUCTION

The Tibetan Plateau (TP) is commonly known as the "Third Pole," the "World Roof," and the "Asia Water Tower" (Yao et al., 2012; Kang et al., 2019a; Chen et al., 2020). The whole plateau region has few industrial activities, and residents mainly live on grazing sheep and yaks, so the TP is considered one of the most remote and primitive places in the world (Sheng et al., 2012; Kang et al., 2016a; Kang

et al., 2016b). However, many studies had shown that the rapid industrializations of South Asia, Southeastern Asia, and East Asia had released heavy metals (HMs) into the atmosphere of the TP in the past few decades (Cong et al., 2007, 2010a, 2014; Kang et al., 2016a; Zhang et al., 2016a). The Himalayas are the highest mountains in the world, which may serve as a natural wall to atmospheric contamination in the southern border area of the TP. However, the high valleys of the Himalayas could act as a channel to transport atmospheric pollutants to the TP (Bonasoni et al., 2010; Wang et al., 2016). Additionally, the contaminants are transported by the Indian and East Asian monsoons in summer and westerlies in winter, affecting remote plateau areas (Yang R. et al., 2014; Sun et al., 2021).

HMs are used to define metals and metalloids associated with potential toxicity and possible pollution (Duffus, 2002; Hodson, 2004). The HMs may release into different environmental media by various ways (Dhaliwal et al., 2020). In addition, HMs are significant anthropogenic contaminants that can be transported for long distances (Ji et al., 2020). Numerous studies have shown that HMs seriously pollute the local environment and transport pollutants to polar and high-altitude regions far away from cities through long-distance transportation (Tripathee et al., 2014; Dong et al., 2015; Jiao et al., 2021). At present, HMs have been found in the Antarctic and Arctic (Planchon et al., 2002; McConnell and Edwards, 2008; Hong et al., 2012; Singh et al., 2013; Abakumov et al., 2017; Casey et al., 2017; Ji et al., 2019; Ji et al., 2021; Alekseev and Abakumov, 2020; Alekseev and Abakumov, 2021). Large HMs have been transported to the Arctic and Antarctic through long-distance atmospheric circulation and deposition (Wilkie and La Farge, 2011).

Similar to the polar regions, the environmental pollution in the TP has been aroused great concern (Qiu, 2014; Wang et al., 2016, Wang X. et al., 2019; Wu et al., 2016; Kang et al., 2019a). HMs have been detected in the air, soil, water, snow, and biota (Wu et al., 2016; Li et al., 2018; Wu et al., 2018; Wu et al., 2019; Li et al., 2020a; Li et al., 2020b; Li M. et al., 2020). Moreover, with climate change, the contaminants released from the degradation of the cryosphere (glaciers, permafrost, ice, and snow) are essential sources of HMs around the TP, which will greatly increase the pollutant accumulation and may have a significant impact on the TP environment.

However, previous studies about HMs in the TP are various and scattered, making it difficult to get a comprehensive understanding of the HMs in the TP. Thus, it is of great significance to study the sources and distribution of HMs around the TP, as well as the regional amplification of HMs and their potential impact in the future. In view of this matter, the objectives of this review are to: 1) summarize current studies concerning the pollution status of HMs in the TP, 2) assess the concentrations, sources, and spatial distribution of HMs in the environmental media of the TP, 3) discuss the effect anthropogenic activities and climate change on the fate of HMs in the TP, and 4) identify research gaps and propose future study needs. This review will be of benefit to quantitatively evaluate the environmental quality of the TP and provide a reference for investigating environmental pollution of the Third Pole.

2 MATERIALS AND METHODS

2.1 Review Strategy

We systematically utilized the electronic databases. For instance, Web of Science, Science Direct, Google Scholar, using the following search terms: Tibetan Plateau & heavy metals & pollution. Moreover, search terms, such as Tibet, Himalayas, the third pole, contamination, pollutants, metals, trace metals, trace elements, risk elements, irons, lead, mercury, were applied to find more publications. Scientific journals, official reports, conference proceedings, and news reports were searched in Chinese and English on the Internet. The abovementioned publications included sources, distribution of HMs in various environmental media, the impact of climate change and anthropogenic activities on HMs in the TP according to 140 articles.

2.2 Data Analysis

Principal component analysis (PCA) and cluster analysis were carried out to reveal sources of HMs. All collected data sets passed KMO and Barrett test (KMO: 0.819, Barrett significance: 0.000). The factors were rotated by the maximum variance method, indicating no correlation between the extracted dimensions. The cluster analysis was carried out according to the square Euclidean distance using the intergroup connection method.

3 RESULTS

3.1 Sources of Heavy Metals

PCA and cluster analysis were carried out to indicate similarities and familiar sources among HMs. Due to the lack of data for Hg in soil and Co in air, statistics only for Cu, Cr, Ni, As, Cd, Pb, and Zn were carried in various environmental media (air, soil, water, precipitation, ice, sediment, biota) (**Figure 1**). The loading plot of PCA for sources of HMs was divided into two components. The PCA1 was characterized by Cu, Cr, Ni, and As association, which contributed to the total dispersion (61.90%). Cd, Pb, and Zn association were typical for PCA2, which describes 17.6%. In addition, the cluster analysis was consistent with PCA, implying that Cu, Cr, Ni, and As may be generated from similar sources, and Cd, Pb, and Zn were enriched by another category. The specific possible sources will be further analyzed in the distribution of each environmental media.

3.2 Heavy Metals in Air

3.2.1 Outdoor Air

The gaseous contaminants around the TP are shown in **Supplementary Table S1**. Previous researchers studied HMs in atmospheric aerosols, total suspended particulate (TSP), PM_{10} and $PM_{2.5}$. Zhang et al. (2012) assessed the chemical composition of aerosols in the southeastern TP and pointed out that As with a higher enrichment factor may be generated from geogenic/pedogenic associations, and Pb, Cu, and Zn were mainly derived from

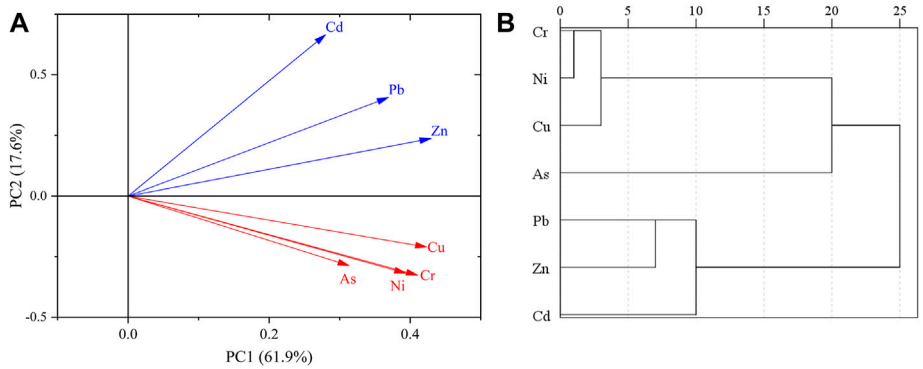

FIGURE 1 | Principal component analysis **(A)** and cluster analysis **(B)** for sources of HMs. Loadings larger than 0.50 are displayed in the principal component analysis.

traffic-related emissions. Huang et al. (2016) collected 80 daily samples of TSP in Lhasa city of Tibet, and the particulate-bound Hg average concentration in the atmosphere was 224 pg m^{-3}, which was far higher than in the Waliguan Mountain (19.4 ± 18.1 pg m^{-3}) and Gongga Mountain (30.7 ± 32.1 pg m^{-3}) (Fu et al., 2008; 2011), indicating that Hg had been accumulated in the atmospheric environment of Lhasa city. The results of PCA of HMs in PM_{10} showed that dust, traffic emissions and waste incineration were the main sources of HMs in Lhasa city (Cong et al., 2011). Yang et al. (2009) noted that the concentrations of HMs in PM_{10} and $PM_{2.5}$ were lower in summer and autumn, which is because HMs were transported to the TP by long-distance atmospheric aerosols caused by sandstorms in Central Asia and contaminants in South Asia during the pre-monsoon (high HMs concentrations in spring) and monsoon seasons (low HMs concentrations in summer) (Cong et al., 2010b; Kang et al., 2016a).

3.2.2 Indoor Air

In the TP, residents burned yak dung, which had a significant impact on the atmosphere, especially in tents (Chen et al., 2015). Li et al. (2012) compared the concentrations of HMs inside and outside tents and revealed the indoor air of the tent was seriously polluted caused by the burning yak dung in residential areas near Nam Co. At the same time, the enrichment factors of the most hazardous elements in indoor and outdoor air were similar, indicating the pollutants released from local tents might affect the outdoor air quality. Kang et al. (2009) reported the indoor air quality of nomadic tents in Nam Co, and pointed out that the average concentrations per day in TSP of Cd (3.16 ng m^{-3}), As (35.00 ng m^{-3}), and Pb (81.39 ng m^{-3}) increased during cooking or heating, which was much higher than MAC from the indoor air quality guidelines (WHO, 2000), indicating that burning yak dung in tents has an impact on the health of Tibetan herdsmen.

Therefore, the aerosol pollutants of the TP are derived from outside and inside (Chen et al., 2015), which were mainly affected by atmospheric transport. Moreover, the burning of local yak dung, fireworks, garbage incineration, traffic, and religious ceremonies cause the increase of HMs concentrations in the air around the TP.

3.3 Heavy Metals in Soil

3.3.1 Soil

Soil plays a critical role in the environment and serves as a sink of various pollutants. The soil samples in **Figure 2** and **Supplementary Table S2** are polluted with varying degrees in the TP. The concentrations of Ni, Pb, Zn, and Co in the topsoil (0–20 cm) of the TP were slightly higher than the upper continental crust (UCC) (Taylor and Mclennan, 1985), and the background values of As and Cr in Tibetan soil were 13.13 and 2.19 times higher than those in the UCC, respectively (MEPC, 1990). In addition, the concentrations of HMs (Pb, Cd, Zn, Cu, Cr, As, Ni, Cd, and Hg) were higher than the background value in the topsoil of Tibet. The concentration of HMs were slightly higher in the northeast, central (Qinghai-Tibet Railway), and southern TP. Besides, the concentrations of HMs in the eastern TP was higher than that of the western TP.

Comparing pH, soil types, altitude, and organic carbon, low temperature may also affect the accumulation of HMs in soils. Zhang H. et al. (2015) pointed out the pH of the soil near the Qinghai-Tibet Roadway was higher than 7.52, which reduced the leaching of toxic metals. In addition, Wang et al. (2015) found Cu, Pb, and Zn were concentrated in the alpine frost desert soil, aeolian sandy soil, and peat soil. Bing et al. (2014) and Luo et al. (2015) noted Pb concentrations in different soil horizons was O (Organic surface layer) > A (Surface soil) > C (Substratum). In addition, soil samplings were conducted in 12 plots in the Shule River Basin of northeast TP, and THg concentration showed a downward trend with altitude (Sun et al., 2017). However, the concentrations of HMs at high altitudes showed increasing trends caused by the ubiquity of extremely low temperatures (Salim et al., 2020). Therefore, high altitudes are more prone to high deposition rates of HMs, which seems to be firmly retained in the soil.

In addition, the effect of transportation on HMs in the soil is a research hotspot in the TP (Zhang et al., 2012; Zhang et al., 2013a; Zhang et al., 2013b; Zhang Y. et al., 2015; Wang et al., 2017). The investigation of HMs in the TP was initially based on the analysis of HMs concentration along the Qinghai-Tibet Railway and Roadway. For example, Zn, Cd, and Pb concentrations in the soil at four depths (5, 10, 20, and 30 cm) of the embankment of

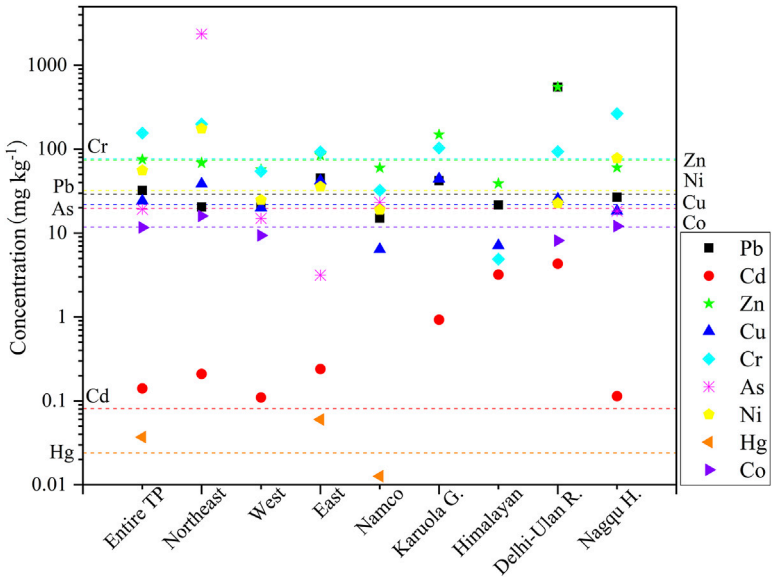

FIGURE 2 | HMs concentrations in the topsoil samples (0–20 cm) over the TP (Li et al., 2009; Wang et al., 2009; Sheng et al., 2012; Zhang et al., 2013b; Xie et al., 2014; Zhang H. et al., 2015; Zhang et al., 2019; Li et al., 2020a; Salim et al., 2020). Notes: The dotted line is HMs background value of soil in Tibet (MEPC, 1990).

the Qinghai-Tibet Railway from Delhi to Ulan were more than seven times higher than those in the continental crust (Zhang et al., 2012). The enrichment factor of Cd was higher than that of other elements (Zhang et al., 2012; Zhang Y. et al., 2015). Among them, HMs concentrations in roadside soil and grass increased with the increase of traffic flow (Wang et al., 2013), while the concentration of HMs in roadside soil decreased with the increase of distance from the roadside (Zhang H. et al., 2015). Besides, other factors (including terrain, road surface material, and land cover) had significant effects on HMs concentrations (Wang et al., 2017).

In addition, Wang et al. (2020) surveyed the concentrations of HMs in urban soil of four cities and pointed out that the local urban domestic waste, industry, transportation and other anthropogenic activities contributed 51.83% to the HMs pollution. Besides, the researchers investigated soils in agricultural and pastoral areas, industrial areas, mining areas, salt-lake areas and urban areas in the northeastern TP and found that industrial and mining areas are with the most serious environmental and health risks (Li et al., 2018, 2020a, 2020b; Wu et al., 2018). Therefore, traffic, urban garbage, industry and mining are the anthropogenic sources of local HMs pollution in the soil of the QTP.

3.3.2 Permafrost

The permafrost range of TP is about 1.06×10^6 km^2, which is the largest permafrost region in middle and low latitudes (Jin et al., 2000; Zou et al., 2017; Huang et al., 2020a). The degradation of permafrost (active layer and frozen ground) increases the risk of HMs release (Hg, As, and Cd) to the TP (Yu et al., 2019; Ci et al., 2020; Mu et al., 2020; Zhang S. et al., 2021) (**Table 1**). For instance, Zhang S. et al. (2021) detected low levels of most HMs except Cd relative to UCC and pointed out that the high concentration of Cd in the Eboling permafrost was caused by anthropogenic activities. Mu et al. (2020) proposed 21.7 Gg of Hg was stored in the permafrost surface layer (0–3 m), indicating that the total Hg mass in the active layer (top 30 cm) of the TP decreased by 17.6%–30.9% on the thermokarst surface.

Thawed Hg was mobile and may be released into the atmosphere as gas or exported to the downstream ecosystems as dissolved liquid in permafrost regions (Ci et al., 2016; Sun et al., 2017; Ci et al., 2018; Gu et al., 2020). So, the continuous degradation of permafrost can lead to the migration and release of Hg stored in permafrost regions, which is an essential source of Hg emission in the environment (Ci et al., 2016; Sun et al., 2017; Ci et al., 2018; Ci et al., 2020). However, relatively few studies have been conducted on the concentration and mass of HMs in the permafrost, except for Hg. Therefore, further attention should be paid to the mass of various HMs in permafrost, especially the secondary emissions of HMs.

3.4 Heavy Metals in Water

3.4.1 Surface Water

As the Water Tower of Asia, the TP supplies drinking water for about one-sixth of the global population (Immerzeel et al., 2010; Keyimu et al., 2021b). Most of the rivers around the TP were not polluted (**Figure 3**; **Supplementary Figure S1**). However, it should be noted that As concentrations in the Indus and the Yarlung Tsangpo rivers were 13.70 and 10.50 μg L^{-1}. Hg were 1.46–4.99 and 1.70 μg L^{-1} in the Yarlung Tsangpo and Yangtze rivers (Qu et al., 2019), which are higher than the Chinese National Standard for drinking water (MAC of As and Hg are 10 and 1 μg L^{-1}) (MOH and SAC, 2006) and the World Health Organization (MAC of As and Hg are 10 and 6 μg L^{-1}) (WHO, 2011).

TABLE 1 | Summary of previous studies on permafrost samples in the TP.

Date	Location	Altitude (m a.s.l)	Measured elements	Concentrations	References
2012	Eboling Mountain	3,615	Fe, Mn, Zn, Ni, Cr, Cu, As, Co, Mo, Cd, Hg	0.01 (Cd)-11,569 ± 58(Fe)	Zhang S. et al. (2021)
2009–2013	TP		Hg	3.35–21.65 Gg (0–3 cm)	Mu et al. (2020)
2013	TP		Hg	63 ± 47 ng g^{-1}	Huang et al. (2020a)
2014	Source of the Yellow River	4,100–5,441	As	4.3–77.1 μg L^{-1}	Yu et al. (2019)
2014–2015	Beiluhe region	4,700	Hg	3–12 ng g^{-1}	Ci et al. (2018)
2010	Shule River Basin	2,519–4,216	Hg	9.5 ± 2.6–17.6 ± 5.6 ng g^{-1}	Sun et al. (2017)
2014	Beiluhe region	4,700–4,800	Hg	13.11 ± 0.51–12.83 ± 0.81 μg kg^{-1}	Ci et al. (2016)

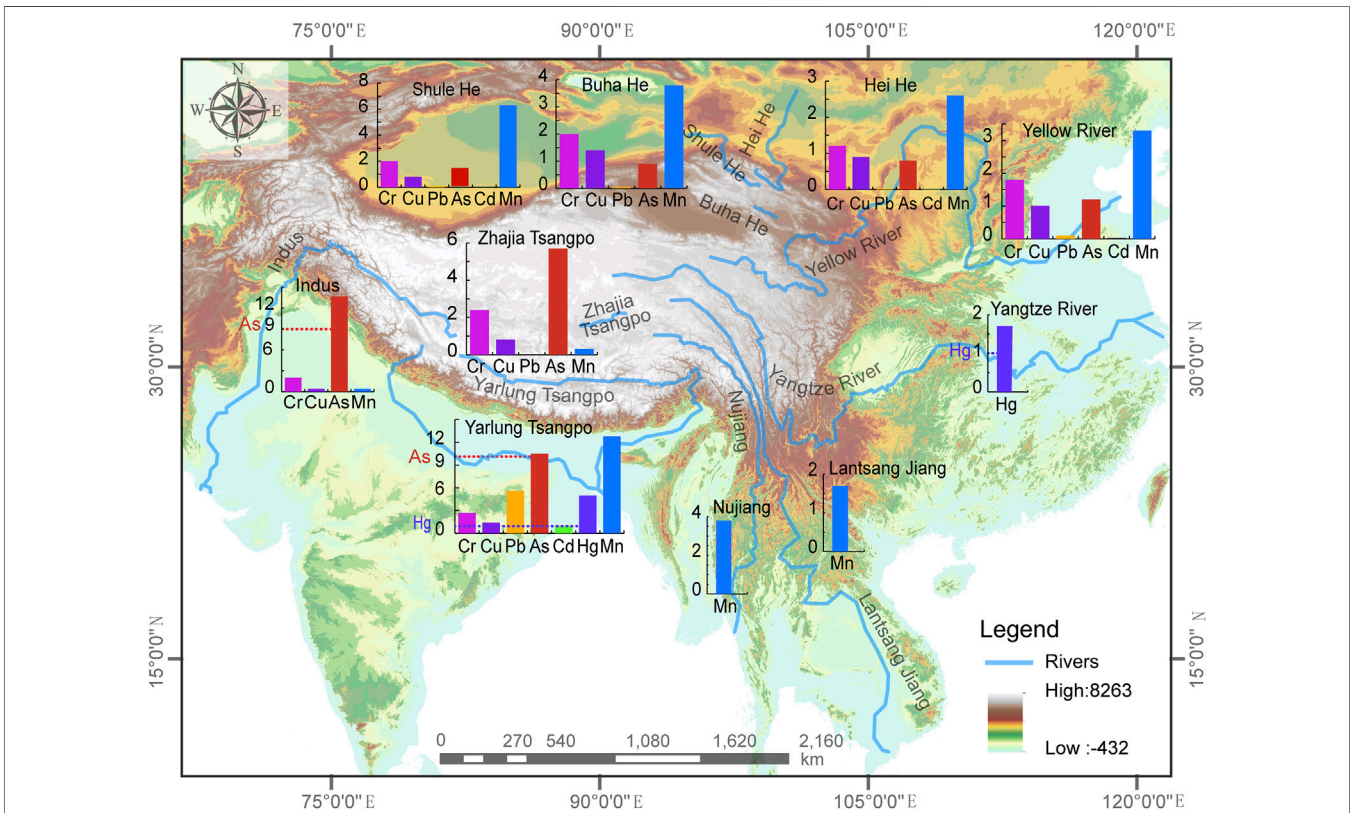

FIGURE 3 | Spatial distribution of main rivers and HMs concentrations (μg L^{-1}) in the TP (Qu et al., 2019). Notes: The dotted line is the maximum allowable concentration of HMs in the drinking water, element dates are from Chinese national standards for drinking water quality (MOH and SAC, 2006). If HMs concentrations don't exceed the maximum allowable concentration, no dotted lines are added.

Furthermore, both natural and anthropogenic sources impact the chemical elements in the water ecosystem of the TP. For instance, geological movements, climate change, and land use-coverage change (LUCC) appear to have significant effects on the chemical composition of rivers (Huang et al., 2009); Zhang Y. et al., 2015 collected 43 surface water samples from the Indus River, Ganges Basins, and Yarlung Tsangpo (Brahmaputra) in 2012, the enrichment factor of As was 30 in the Himalayas, indicating that the river water was seriously affected by anthropogenic activities. Further, Lin et al. (2021) analyzed the chemical composition of water in Lake Bangong Co, and the results of PCA showed that As, Cu, and Cr were mainly from natural resources, while Cd may be caused by anthropogenic activities. Moreover, the dissolved As (Nickson et al., 1998; Zhang J. W et al., 2021) and Hg (Sun et al., 2016) decreased significantly in the downstream of the river due to the adsorption and dilution process of metal elements, indicating that the upstream was affected by anthropogenic activities. Therefore, the surface water of the TP was not polluted except As and Hg.

3.4.2 Groundwater

The TP has active geological activities caused by the interaction of the Eurasian Plate and Indian Ocean plate (Hodges, 2000), which caused high geothermal flows and hydrothermal systems (Guo et al., 2019). Many hot springs on the TP contain high As concentrations, which are harmful to human health (Guo et al., 2019). Furthermore, Zhang J.-W. et al. (2021) observed extremely high concentrations of dissolved As (1,130–9,760 μg L^{-1}) in the hot springs in the upstream of the

Yarlung Zangbo River. Therefore, As dissolves into groundwater from rocks and sediments through the coupling of biogeochemical and hydrological processes (Nickson et al., 1998; Fendorf et al., 2010; Wang Y. et al., 2019).

3.5 Heavy Metals in Precipitation

3.5.1 Rain

The accumulation of HMs in alpine and high-altitude regions is related to the precipitation process (Liu et al., 2016; Huang et al., 2012c; Huang et al., 2015). HMs concentration in rainfall around the TP showed that Nancuo Lake and Mount Everest had lower HMs concentrations, and South Asia and urban areas (Lhasa, Kathmandu, and Jomsom) had higher HMs concentration than rural areas (Dhunche) (**Supplementary Figure S2**) (Cong et al., 2010b; Huang et al., 2013; Tripathee et al., 2014; Tripathee et al., 2020; Dong et al., 2015; Guo et al., 2015). Specifically, Cong et al. (2010b) collected 79 precipitation samples at the Nam Co and found the concentrations of Cr, Zn, Co, Ni, Cd, Cu, and Pb in the wetland soil were higher than those of the Tibetan soil, indicating that the Nam Co may be affected by anthropogenic activities. In addition, Cong et al. (2015) analyzed the HMs concentrations of 42 rain samples from Mount Everest (Himalayas), and Cd was the most affected metal by anthropogenic activities. Further, Tripathee et al. (2014), Tripathee et al. (2019), Tripathee et al. (2020) measured the HMs concentrations in Kathmandu and Jomsom of the Nepal Himalayan region and revealed the concentrations of Hg were 0.019 and 0.022 $\mu g\,L^{-1}$ in Kathmandu and Jomsom, which were similar to Lhasa (0.025 $\mu g\,L^{-1}$) (Huang et al., 2013). Moreover, Cong et al. (2015) inferred that the high concentrations of HMs might be the deposition of HMs (aerosols) exposed to the atmosphere for a long time after the precipitation. Therefore, HMs concentrations in rainfall of the TP have apparent seasonal variation, which is high in the pre-monsoon period (spring) and low in the monsoon period (summer), reflecting the outbreak of brown clouds in South Asia and the influence of rainfall removal factors in the rainy season.

3.5.2 Snow

Snow events remove pollutants from the air to accumulate and agglomerate into the snow (Wang et al., 2016). Numerous studies (Kang et al., 2007; Lee et al., 2008; Huang et al., 2012a; Huang et al., 2012b; Huang et al., 2013; Dong et al., 2015; Li Y. et al., 2020; Jiao et al., 2021) analyzed HMs concentrations in glacier snow samples from multiple locations in the TP (**Figure 4**; **Supplementary Figure S3**). Glacial snow samples were low concentrations of HMs (Jiao et al., 2021). HMs concentrations ranged from 0.006 $\mu g\,L^{-1}$ (Hg) to 25.680 $\mu g\,L^{-1}$ (Cr) (**Figure 6**). In addition, concentrations of HMs in snow in the central and southern TP were significantly higher than that in the northern TP, and that in the central TP was higher than that in the eastern TP. Dong et al. (2015) proposed HMs concentrations decreased gradually from the Himalayan region to the Tanggula Basin and Laohugou Basin, indicating that the migration of HMs from South Asia has a significant impact on the central TP. Li et al. (2020) considered dust is the primary source of major HMs in glacial snow. In addition, Jiao et al. (2021) investigated atmospheric deposition and HMs contamination in the glacial snow of the eastern TP and pointed out that two transportation channels of air pollutants: one was from east to west so that HMs concentrations in remote glaciers such as Hailuogou and Dagu far away from the urban areas were much lower, and another was from south to north in the eastern TP. Similarly, the spatial distribution condition of HMs concentrations in the snow was associated with the atmospheric circulation patterns.

3.6 Heavy Metals in Ice Cores and Sediments

3.6.1 Ice Cores

Ice cores drilled from glaciers provided an excellent record of long-term changes in chemical composition, which could be used to estimate the historical accumulation rate of HMs in the TP (Kang et al., 2016b; Kang et al., 2019a; Kang et al., 2019b). Thus, the aforementioned studies reported the historical trends of HMs concentrations in ice cores (**Figure 5**; **Supplementary Table S3**). Huo et al. (1999) measured the Pb concentration in the ice core of the Dasuopu Glacier of the TP from 1946 to 1996 and indicated that Pb concentration showed an increasing trend. Hong et al. (2009) collected the upper ice core in the East Rongbuk Glacier of the Qomolangma Mountain, which clearly showed the migration and deposition of As, Sb, Mo, and Sn in the atmosphere prevailing in the high-altitude range of the central Himalayas. Kang et al. (2016b) collected an ice core sample for the sequence of atmospheric Hg deposition in the Himalayas; The deposition rate of Hg was relatively low (1500s~the early 1800s), increasing during the Industrial Revolution (1860s–1840s), then increasing sharply after the World War II. Therefore, the effects of natural and anthropogenic activities on HMs were found in the ice core of the TP, suggesting that HMs were transmitted to the interior of the TP through the atmosphere.

3.6.2 Sediments

The previous studies have shown HMs concentrations in sediments of different rivers and lakes in the TP (**Supplementary Table S4**): HMs concentrations were lower than low effect range (Long et al., 1995; Ramesh et al., 2000; Dalai et al., 2004; Bing et al., 2016). Thus, chemical concentration had no adverse effects on biota. For instance, Ramesh et al. (2000) pointed out that the physical weathering process seemed to be a chief controlling factor for distributing rare earth elements and HMs in the sediments of the Himalayan rivers. Additionally, they found Ni, Cd, Cu, Cr, and As concentrations of the sediments exceed the low effect range, indicating that HMs may pose a potential biological threat. In the sediments of the Yarlung Tsangpo River and the Mekong River Delta, As had high concentrations owing to weathering of the bedrock (Li et al., 2011). In addition, recent work in the Koshi River Basin of the Himalayas showed that Ni, Cu, Cd, and Pb had low pollution, which derived from both natural and anthropogenic sources caused by atmospheric migration and traffic emissions (Li et al., 2020).

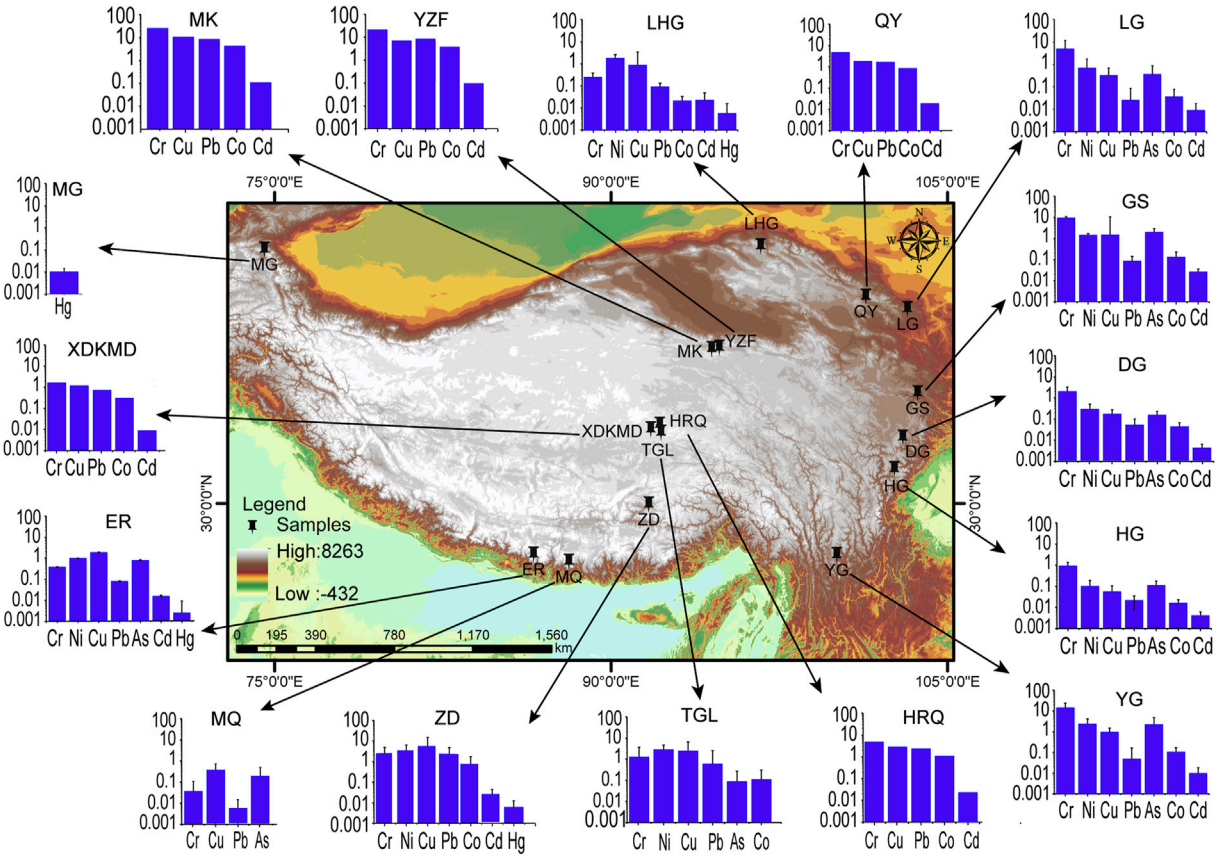

FIGURE 4 | Spatial distribution of snow samples and HMs concentrations (μg L^{-1}) around the TP (Kang et al., 2007; Lee et al., 2008; Liu et al., 2011; Huang et al., 2014; Dong et al., 2015; Li Y. et al., 2020; Jiao et al., 2021). Notes: 1) LG, Lenglongling Glacier; DG, Dagu Glacier; HG, Hailuogou Glacier; GS, Gannan Snow; YG, Yulong Snow-mountain Glacier; QY, Qiyi Glacier; MK, Meikuang Glacier; YZF, Yuzhufeng Glacier; HRQ, Hariqin Glacier; XDKMD, Xiaodongkemadi Glacier; LHG, Laohugou Glacier; TGL, Tanggula Glacier; ZD, Zhadang Glacier; ER, East Rongbuk Glacier; MQ, Mt. Qomolangma. 2) Error bars are added if there is a standard deviation, and no error bars are added if there is no standard deviation.

In addition, sediments have been studied to explore the historical process and spatial distribution in the TP (**Figure 5**). Huang et al. (2020b) analyzed Hg concentration of the sediment at Gaoqiao Lake of the Himalayas and found that the increased Hg accumulation was due to the aggravation of cross-border pollution in South Asia (Kang et al., 2016b). Bing et al. (2016) studied the changes of Pb, Cd, and Zn concentrations in sediments from Gao Haizi Lake, an alpine lake in the eastern TP, and indicated that Zn and Cd fluxes were relatively constant until the 1980s, raised sharply from the 1980s to the 1990s and then maintained stable. However, the Pb flux increased significantly in the 1950s and increased sharply in the 1980s, and peaked in the 1990s and then decreased gradually. Huang et al. (2020b) proposed that the downward trend of Pb accumulation in sediments was due to the Pb decrease in gasoline and the decrease of anthropogenic Pb emissions caused by the phasing out of Pb gasoline (Singh and Singh, 2006). Therefore, the various trends of HMs in the sediment cores reflected the different sources, transport pathways, and geochemical circulation of HMs around the TP.

3.7 Heavy Metals in Biota

3.7.1 Terrestrial Biota

More attention to pollutants in organisms has been paid due to biomagnification and bioconcentration (Wu et al., 2016). Thus, several researchers have studied HMs concentrations of the terrestrial biota (**Supplementary Table S5**). For instance, mosses and lichens have been widely used for biomonitoring of trace metals in the atmosphere (Shao et al., 2016; Fabri et al., 2018). Bing et al. (2014) analyzed the Pb of moss and revealed that its concentration ranged from 20.0 to 62.1 mg kg^{-1} in the Hailuogou Glacier Foreland, eastern TP, suggesting that the contribution of the anthropogenic Pb to the mosses was 41.6%–65.9%. Shao et al. (2017) collected moss and lichen, and THg concentration was 13.1–273.0 and 20.2–345.9 ng g^{-1}, respectively. Moreover, Shao et al. (2017), Shao et al. (2015) pointed out that the concentration of HMs in mosses increased with the elevation, and the spatial distribution of most HMs decreased from west to east and from south to north in the TP.

In addition, HMs concentrations varied with species and organs of vegetations (Nabulo et al., 2006; Zhang et al.,

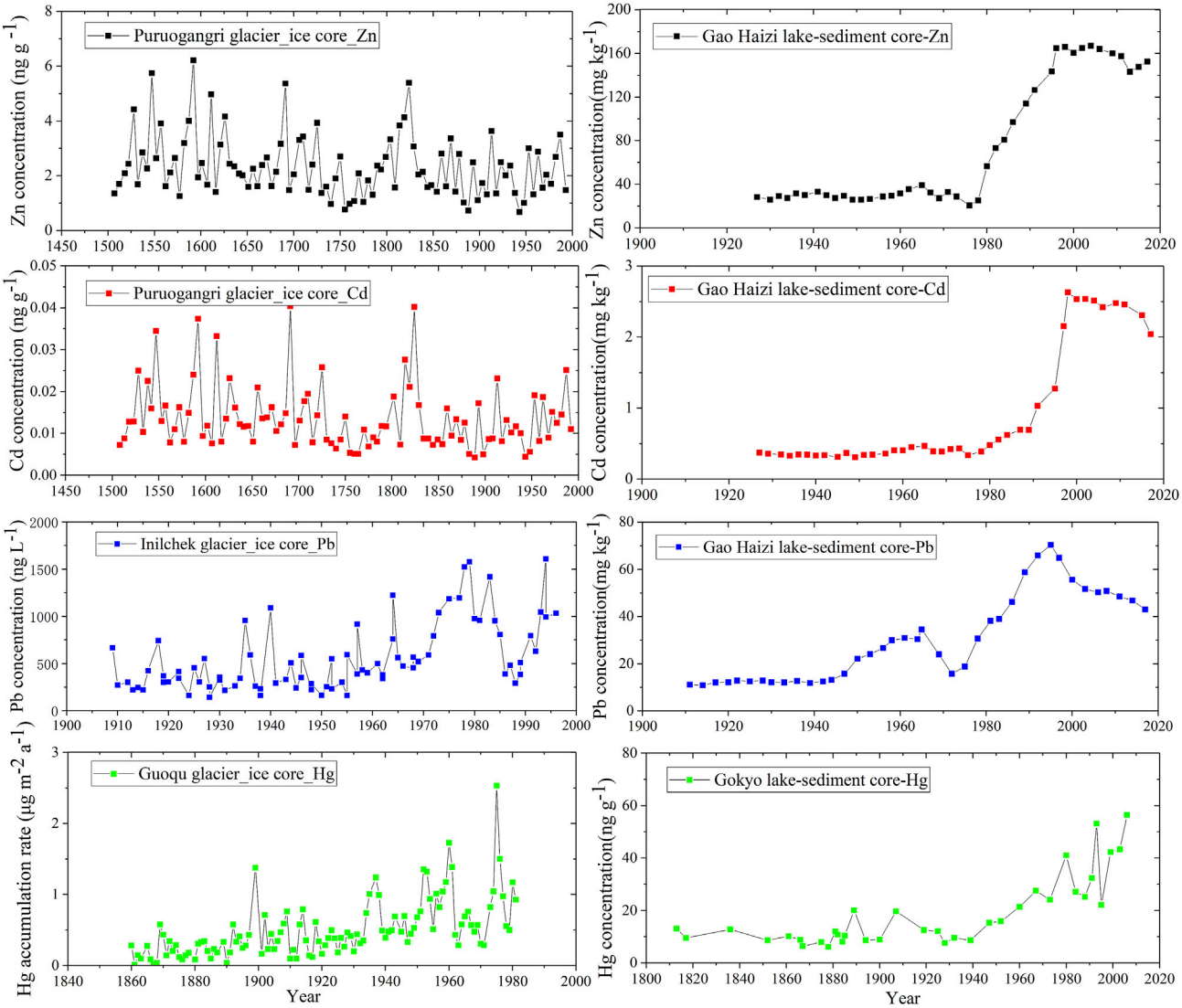

FIGURE 5 | Historical trends of HMs concentrations or accumulation rate in ice core and sediment core from different glaciers and lakes (Bing et al., 2016; Grigholm et al., 2016; Kang, et al., 2016b; Beaudon et al., 2017; Huang, et al., 2020b).

2016b). Jia et al. (2021) measured and analyzed Pb and Cd concentrations in needles and twigs of fir and spruce collected from 26 sites in the eastern TP, indicating concentrations of Pb and Cd in twigs were higher than those in needles. Furthermore, most HMs are still at the root (Eid et al., 2012; Bonanno, 2013), fine roots were able to adsorb Pb in the soil humus horizon (Luo et al., 2015; Jia et al., 2021). In addition, leaves absorbed and accumulated HMs particles directly from the atmosphere (Grigholm et al., 2016). Cd, Mn, Fe, and Zn fell to the surface of leaves and return to the soil through the litter. Sun et al. (2020) measured the gaseous Hg fluxes of alpine meadows in the central TP during the whole vegetation period, suggesting that the alpine steppe hindered the emission of Hg and provided a sink for total gaseous Hg. Therefore, vegetation provides a sink for HMs accumulation.

3.7.2 Aquatic Biota

HMs concentrations in fish were still of great significance for understanding its impact on aquatic ecosystems in the TP (Xiong et al., 2020). As, methylmercury (MeHg), and Pb were observed in wild fish in many lakes and rivers of the TP (**Figure 6**; **Supplementary Table S6**). As and Pb concentrations of wild fish far exceeded the MAC (0.1 and 0.5 mg kg^{-1}) of Chinese Food Health Standard (MOH and SAC, 2017), and Pb concentrations of all lakes and rivers were similar. Hg is easily converted to MeHg, a neurotoxin that bioaccumulate in humans and wildlife (Gilmour et al., 1992; Sun et al., 2021). The average concentration of MeHg in most Tibetan fish was less than the MAC, but the recent survey of wild fish in Niyang River and Lhasa River found that the dry weights of MeHg concentrations were 276–1,158 ng g^{-1}, 281–1,331 ng g^{-1}, exceeding MAC (Shao et al., 2015). Overall, high MeHg concentration in wild fish

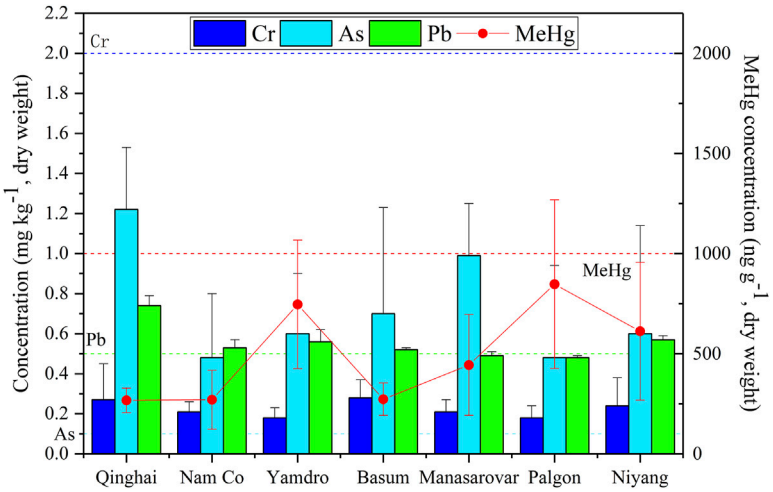

FIGURE 6 | Distribution of different lakes and rivers about HMs concentrations of wild fishes in the TP (Yang et al., 2007; Yang et al., 2011; Yang K. et al., 2014; Shao et al., 2015). Notes: The dotted line is the maximum allowable concentration of HMs in the wild fishes, element data are from Chinese food health criterion (MOH and SAC, 2017).

might be related to low temperature, poor nutrition in the water environment, and slow growth of fish (Zhang Q. et al., 2014; Shao et al., 2015). Therefore, attention should be paid to the high concentrations of As, MeHg and Pb in wild fish in the TP.

4 DISCUSSION

4.1 Sources of Heavy Metals

The results of PCA and cluster analysis indicated that Cu, Cr, Ni, and As may be generated from similar sources, and Cd, Pb, and Zn are enriched by another category. Sheng et al. (2012) pointed out that weathering products of the basic bedrocks might be the chief origins of most HMs in Tibetan soils. For instance, As-enriched rocks, such as shales, are widely distributed in the QTP (Li et al., 2011). Besides, previous studies pointed out that Tibetan soils developed from ultramafic rocks are usually enriched in Ni, Co, and others (Yin and Harrison, 2003). In addition, researchers revealed transportation (Zhang H et al., 2015; Wang et al., 2017), mining and smelting (Bing et al., 2016; Zhang et al., 2019) are the primary anthropogenic sources of elevated Cd, Pb, Zn, and Hg in the TP. Meanwhile, previous reports have demonstrated that Hg accumulation in soils is determined by the formation of organic complex and dissolution processes after precipitation (Huang et al., 2012c; Tripathee et al., 2019; Tripathee et al., 2020), so atmospheric transport and deposition may be the sources of Hg deposited in topsoil. Therefore, HMs may be derived from geogenic/pedogenic associations (Cu, Cr, Ni, As, and Co) and anthropogenic emissions (Cd, Pb, Zn, and Hg) of local or long-distance atmospheric transmission.

4.2 Atmospheric Transport of Heavy Metals

Although the Himalayas in the southern TP hinder atmospheric transport, the transport of pollutants cannot be completely blocked (Wang et al., 2016). For instance, mountain peak-valley wind patterns might promote the trans-Himalayan transportation of contamination (Cong et al., 2015; Lüthi et al., 2015). Additionally, the atmospheric circulation pattern is dominated by the Indian summer monsoons from May to September and the westerlies from October to April in the TP (**Figure 7**). Atmospheric circulation patterns affect remote plateau regions. For instance, Cong et al. (2007) pointed out that South Asia may be the source region of HMs contaminants in TSP of Nam Co. In addition, Zhang N. et al. (2014) evaluated HMs in TSP and $PM_{2.5}$ samples of Qinghai Lake and proposed that Pb and Zn were affected by the wind migration in eastern China. Therefore, the Indian and East Asian monsoons during the monsoon period and southern branch of westerly winds may have a significant impact on the long-distance cross-border migration of HMs in southwestern China, South Asia, and Southeast Asia.

4.3 Local Anthropogenic Heavy Metals Sources

In recent decades, the social economy of the TP has been accelerated, especially the remarkable growth of the transportation industry. Transportation brings many benefits, but it is one of the most essential sources of HMs around the TP (Zhang Y. et al., 2015; Liu et al., 2019). In addition, biomass combustion (yak dung) is a local source of HMs for the TP. The yak dung combustion releases aerosols rich in HMs into the atmosphere (Chen et al., 2015; Ye et al., 2020). Besides, urban living garbage (Wang et al., 2020) and religious rituals (Duo et al., 2015; Cui et al., 2018) may be the main sources of anthropogenic HMs in the TP. Therefore, anthropogenic activities are one of the criminal sources of HMs around the TP.

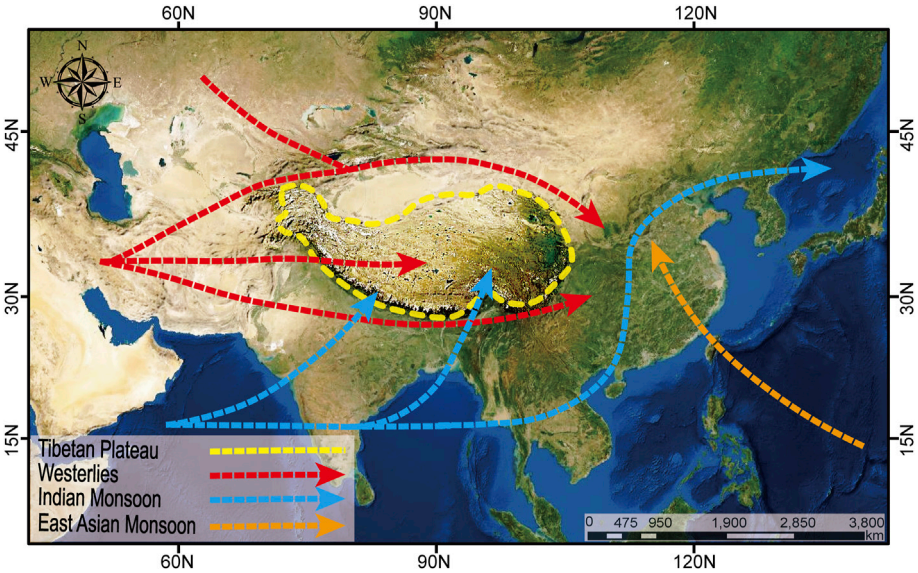

FIGURE 7 | The monsoons of TP (Yang K. et al., 2014).

4.4 Impact of Climate Change on Heavy Metals Emissions

The TP is a vital cryosphere in the middle and low altitude regions (Qiu, 2008; Yao et al., 2012), which has experienced tremendous climate change (Kang et al., 2010; You et al., 2016; Keyimu et al., 2021a). Since 1960, the average temperature has increased by 0.36°C per decade (Wang et al., 2008). In addition, 82% of plateau glaciers have degraded over the past half-century (Qiu, 2008), snow cover has decreased by 5.7%, and 10% of permafrost has degraded from 1997 to 2012 in the TP (Qiu, 2012; Qiu, 2014). Therefore, changes in the cryosphere around the TP affect the geophysical, biological and geochemical interactions of environmental pollutants.

The cryosphere is a temporary repository of pollutants (Kang et al., 2019a). However, with global change, pollutants stored in the cryosphere would be released into the different environmental media (Potapowicz et al., 2019; Zhu et al., 2020). Zhu et al. (2020) analyzed the historical trend of contaminants in lake sediments of the southern TP and concluded that the rate of contaminants released by glacial meltwater is 40%–61%, corresponding to the warmer climate. In addition, permafrost contains more extensive chemical storage, and its degradation accelerated the emission of HMs (Yu et al., 2019; Ci et al., 2020; Mu et al., 2020; Zhang S. et al., 2021). Therefore, climate change causes the cryosphere to melt, releasing HMs, which may increase the accumulation of pollutants and affect the global environment in the future.

4.5 Limitations and Outlooks

The following limitations are put forward to study HMs around the TP: 1) Similar to the Arctic and Antarctica, the TP is also a core region for studying climate change and pollution. For instance, anthropogenic activities cause long-distance transport of pollutants to sink in glaciers and permafrost range; climate warming may promote the secondary release of pollutants from glaciers and permafrost to the atmosphere, discharge with meltwater, and other processes. 2) In terms of pollution source analysis, many studies are carried out by the occurrence frequency of reverse air mass trajectories. Despite providing a potential source, its identification accuracy needs to be improved, especially in the quantitative assessment of transmission flux. Experiments using multiple means such as particle lidar, satellite remote sensing, and isotope tracer methods are needed to combine ground monitoring data with big data models to quantify sources and characteristics of pollutants in TP. 3) In the lakes and rivers of the TP, wild fish with high concentrations of As, Hg, and Pb were found. However, so far, no data have been reported on HMs in the terrestrial food chain, and the impact of HMs on other organisms and humans is still lacking in the TP. 4) Soil, water, snow, glacier, sediment, and biota are essential sinks of atmospheric HMs. However, the specific relationship between HMs in different environmental media is still unclear.

In the future, the following points should be focused on: 1) It is necessary to study the accumulation, distribution, and transformation of HMs and other pollutants in glacial and permafrost degradation regions around the TP. 2) Using particle lidar, satellite remote sensing, isotope tracing, and other means to conduct experiments, and combining ground monitoring data with big data models to quantify the sources and characteristics of pollutants in the TP. 3) The relationship between bioaccumulation of HMs and human health needs to be further studied in the TP. 4) Conducting a coordinated sampling and measurement of various environmental media samples to quantify the pollution status of the TP comprehensively.

5 CONCLUSION

The inorganic pollution in different environmental media was summarized around the TP. The results showed that 1) HMs

in the TP may be generated from geogenic/pedogenic associations (Cu, Cr, Ni, As, and Co) and anthropogenic activities of local or long-distance atmospheric transmission (Cd, Pb, Zn, and Hg). 2) The atmospheric transport emission sources of HMs are mainly from the surrounding heavily-polluted regions by the Indian and East Asian monsoons during the monsoon period and southern branch of westerly winds. 3) Soil, water, glacier, and vegetation are critical reservoirs of HMs. 4) Significant bioaccumulation of As, Pb, and MeHg has been found in terrestrial and aquatic biota chains. 5) The enhancement of anthropogenic activities, climate change, glacial retreat and permafrost degradation had potential effects on the behaviors, fates, and distribution of HMs around the TP. Therefore, we hope that the ecological risks of the TP should be of increasing concern and systematically studied, calling for effective ecological safety strategies to reduce the adverse effects of environmental pollutants in the TP.

AUTHOR CONTRIBUTIONS

WW conducted data curation and wrote the original draft; XJ and EA contributed to conceptualization; EA acquired funding; VP and DW assisted with formal analysis; GL helped with software and contributed to visualization; and WW, XJ, EA, VP, GL, and DW reviewed and edited the manuscript. All authors have read and agreed to the published version of the manuscript.

FUNDING

This research was supported by the China Scholarship Council (201907010003) and Russian Foundation for Basic Research (19-05-50107).

ACKNOWLEDGMENTS

We thank Dr. Shurong Zhou and Dr. Yao Xiao who provided the opportunity to investigate the Tibetan Plateau.

SUPPLEMENTARY MATERIAL

The Supplementary Material for this article can be found online at: https://www.frontiersin.org/articles/10.3389/fenvs.2022.874635/full#supplementary-material

REFERENCES

Abakumov, E., Shamilishviliy, G., and Yurtaev, A. (2017). Soil Polychemical Contamination on Beliy Island as Key Background and Reference Plot for Yamal Region. *Polish Polar Res.* 38, 313–332. doi:10.1515/popore-2017-0020

Alekseev, I., and Abakumov, E. (2021). Content of Trace Elements in Soils of Eastern Antarctica: Variability Across Landscapes. *Arch. Environ. Contam. Toxicol.* 80, 368–388. doi:10.1007/s00244-021-00808-4

Alekseev, I., and Abakumov, E. (2020). The Content and Distribution of Trace Elements and Polycyclic Aromatic Hydrocarbons in Soils of Maritime Antarctica. *Environ. Monit. Assess.* 192. doi:10.1007/s10661-020-08618-2

Beaudon, E., Gabrielli, P., Sierra-Hernández, M. R., Wegner, A., and Thompson, L. G. (2017). Central Tibetan Plateau Atmospheric Trace Metals Contamination: A 500-Year Record from the Puruogangri Ice Core. *Sci. Total Environ.* 601–602, 1349–1363. doi:10.1016/j.scitotenv.2017.05.195

Bing, H., Wu, Y., Zhou, J., Li, R., and Wang, J. (2016). Historical Trends of Anthropogenic Metals in Eastern Tibetan Plateau as Reconstructed from alpine lake Sediments over the Last century. *Chemosphere* 148, 211–219. doi:10.1016/j.chemosphere.2016.01.042

Bing, H., Wu, Y., Zhou, J., Ming, L., Sun, S., and Li, X. (2014). Atmospheric Deposition of lead in Remote High Mountain of Eastern Tibetan Plateau, China. *Atmos. Environ.* 99, 425–435. doi:10.1016/j.atmosenv.2014.10.014

Bonanno, G. (2013). Comparative Performance of Trace Element Bioaccumulation and Biomonitoring in the Plant Species Typha Domingensis, Phragmites Australis and Arundo donax. *Ecotoxicol. Environ. Saf.* 97, 124–130. doi:10.1016/j.ecoenv.2013.07.017

Bonasoni, P., Laj, P., Marinoni, A., Sprenger, M., Angelini, F., Arduini, J., et al. (2010). Atmospheric Brown Clouds in the Himalayas: First Two Years of Continuous Observations at the Nepal Climate Observatory-Pyramid (5079 m). *Atmos. Chem. Phys.* 10, 7515–7531. doi:10.5194/acp-10-7515-2010

Casey, K. A., Kaspari, S. D., Skiles, S. M., Kreutz, K., and Handley, M. J. (2017). The Spectral and Chemical Measurement of Pollutants on Snow Near South Pole, Antarctica. *J. Geophys. Res. Atmos.* 122, 6592–6610. doi:10.1002/2016JD026418

Chen, P., Kang, S., Bai, J., Sillanpää, M., and Li, C. (2015). Yak Dung Combustion Aerosols in the Tibetan Plateau: Chemical Characteristics and Influence on the Local Atmospheric Environment. *Atmos. Res.* 156, 58–66. doi:10.1016/j.atmosres.2015.01.001

Chen, P., Zhang, J., Liu, J., Cao, X., Hou, J., Zhu, L., et al. (2020). Climate Change, Vegetation History, and Landscape Responses on the Tibetan Plateau During the Holocene: A Comprehensive Review. *Quat. Sci. Rev.* 243, 106444. doi:10.1016/J.QUASCIREV.2020.106444

Ci, Z., Peng, F., Xue, X., and Zhang, X. (2016). Air-Surface Exchange of Gaseous Mercury over Permafrost Soil: An Investigation at a High-Altitude (4700 m a.s.l.) and Remote Site in the central Qinghai-Tibet Plateau. *Atmos. Chem. Phys. Discuss.* 16 14741–14754. doi:10.5194/acp-2016-515

Ci, Z., Peng, F., Xue, X., and Zhang, X. (2020). Permafrost Thaw Dominates Mercury Emission in Tibetan Thermokarst Ponds. *Environ. Sci. Technol.* 54, 5456–5466. doi:10.1021/acs.est.9b06712

Ci, Z., Peng, F., Xue, X., and Zhang, X. (2018). Temperature Sensitivity of Gaseous Elemental Mercury in the Active Layer of the Qinghai-Tibet Plateau Permafrost. *Environ. Pollut.* 238, 508–515. doi:10.1016/j.envpol.2018.02.085

Cong, Z., Kang, S., Dong, S., Liu, X., and Qin, D. (2010a). Elemental and Individual Particle Analysis of Atmospheric Aerosols from High Himalayas. *Environ. Monit. Assess.* 160, 323–335. doi:10.1007/s10661-008-0698-3

Cong, Z., Kang, S., Kawamura, K., Liu, B., Wan, X., Wang, Z., et al. (2014). Carbonaceous Aerosols on the South Edge of the Tibetan Plateau: Concentrations, Seasonality and Sources. *Atmos. Chem. Phys.* 15, 1573–1584. doi:10.5194/acp-15-1573-2015

Cong, Z., Kang, S., Liu, X., and Wang, G. (2007). Elemental Composition of Aerosol in the Nam Co Region, Tibetan Plateau, during Summer Monsoon Season. *Atmos. Environ.* 41, 1180–1187. doi:10.1016/j.atmosenv.2006.09.046

Cong, Z., Kang, S., Luo, C., Li, Q., Huang, J., Gao, S., et al. (2011). Trace Elements and Lead Isotopic Composition of PM10 in Lhasa, Tibet. *Atmos. Environ.* 45, 6210–6215. doi:10.1016/j.atmosenv.2011.07.060

Cong, Z., Kang, S., Zhang, Y., Gao, S., Wang, Z., Liu, B., et al. (2015). New Insights Into Trace Element Wet Deposition in the Himalayas: Amounts, Seasonal Patterns, and Implications. *Environ. Sci. Pollut. Res.* 22, 2735–2744. doi:10.1007/s11356-014-3496-1

Cong, Z., Kang, S., Zhang, Y., and Li, X. (2010b). Atmospheric Wet Deposition of Trace Elements to Central Tibetan Plateau. *Appl. Geochem.* 25, 1415–1421. doi:10.1016/j.apgeochem.2010.06.011

Cui, Y. Y., Liu, S., Bai, Z., Bian, J., Li, D., Fan, K., et al. (2018). Religious Burning as a Potential Major Source of Atmospheric fine Aerosols in Summertime Lhasa on the Tibetan Plateau. *Atmos. Environ.* 181, 186–191. doi:10.1016/j.atmosenv.2018.03.025

Dalai, T. K., Rengarajan, R., and Patel, P. P. (2004). Sediment Geochemistry of the Yamuna River System in the Himalaya: Implications to Weathering and Transport. *Geochem. J.* 38, 441–453. doi:10.2343/geochemj.38.441

Dhaliwal, S. S., Singh, J., Taneja, P. K., and Mandal, A. (2020). Remediation Techniques for Removal of Heavy Metals from the Soil Contaminated through Different Sources: A Review. *Environ. Sci. Pollut. Res.* 27, 1319–1333. doi:10.1007/s11356-019-06967-1

Dong, Z., Kang, S., Qin, X., Li, X., Qin, D., and Ren, J. (2015). New Insights into Trace Elements Deposition in the Snow Packs at Remote alpine Glaciers in the Northern Tibetan Plateau, China. *Sci. Total Environ.* 529, 101–113. doi:10.1016/j.scitotenv.2015.05.065

Duffus, J. H. (2002). "Heavy Metals" a Meaningless Term? (IUPAC Technical Report). *Pure Appl. Chem.* 74, 793–807. doi:10.1351/pac200274050793

Duo, B., Zhang, Y., Kong, L., Fu, H., Hu, Y., Chen, J., et al. (2015). Individual Particle Analysis of Aerosols Collected at Lhasa City in the Tibetan Plateau. *J. Environ. Sci.* 29, 165–177. doi:10.1016/j.jes.2014.07.032

Eid, E. M., Shaltout, K. H., El-Sheikh, M. A., and Asaeda, T. (2012). Seasonal Courses of Nutrients and Heavy Metals in Water, Sediment and above- and Below-Ground Typha Domingensis Biomass in Lake Burullus (Egypt): Perspectives for Phytoremediation. *Flora Morphol. Distribut. Funct. Ecol. Plants* 207, 783–794. doi:10.1016/j.flora.2012.09.003

Fabri-Jr, R., Krause, M., Dalfior, B. M., Salles, R. C., de Freitas, A. C., da Silva, H. E., et al. (2018). Trace Elements in Soil, Lichens, and Mosses from Fildes Peninsula, Antarctica: Spatial Distribution and Possible Origins. *Environ. Earth Sci.* 77. doi:10.1007/s12665-018-7298-5

Fendorf, S., Michael, H. A., and Van Geen, A. (2010). Spatial and Temporal Variations of Groundwater Arsenic in South and Southeast Asia. *Science* 328, 1123–1127. doi:10.1126/science.1172974

Fu, X., Feng, X., Zhu, W., Zheng, W., Wang, S., and Lu, J. Y. (2008). Total Particulate and Reactive Gaseous Mercury in Ambient Air on the Eastern Slope of the Mt. Gongga Area, China. *Appl. Geochem.* 23, 408–418. doi:10.1016/j.apgeochem.2007.12.018

Fu, X., Feng, X., and Liang, P. (2011). Temporal Trend and Sources of Speciated Atmospheric Mercury at Waliguan GAW station, Northwestern China. *Atmos. Chem. Phys. Discuss.* 11, 30053–30089. doi:10.5194/acpd-11-30053-2011

Gilmour, C. C., Henry, E. A., and Mitchell, R. (1992). Sulfate Stimulation of Mercury Methylation in Freshwater Sediments. *Environ. Sci. Technol.* 26, 2281–2287. doi:10.1021/es00035a029

Grigholm, B., Mayewski, P. A., Aizen, V., Kreutz, K., Wake, C. P., Aizen, E., et al. (2016). Mid-twentieth century Increases in Anthropogenic Pb, Cd and Cu in central Asia Set in Hemispheric Perspective Using Tien Shan Ice Core. *Atmos. Environ.* 131, 17–28. doi:10.1016/j.atmosenv.2016.01.030

Gu, J., Pang, Q., Ding, J., Yin, R., Yang, Y., and Zhang, Y. (2020). The Driving Factors of Mercury Storage in the Tibetan Grassland Soils Underlain by Permafrost. *Environ. Pollut.* 265, 115079. doi:10.1016/j.envpol.2020.115079

Guo, J., Kang, S., Huang, J., Zhang, Q., Tripathee, L., and Sillanpää, M. (2015). Seasonal Variations of Trace Elements in Precipitation at the Largest City in Tibet, Lhasa. *Atmos. Res.* 153, 87–97. doi:10.1016/j.atmosres.2014.07.030

Guo, Q., Planer-Friedrich, B., Liu, M., Yan, K., and Wu, G. (2019). Magmatic Fluid Input Explaining the Geochemical Anomaly of Very High Arsenic in Some Southern Tibetan Geothermal Waters. *Chem. Geol.* 513, 32–43. doi:10.1016/j.chemgeo.2019.03.008

Hodges, K. V. (2000). Tectonics of the Himalaya and Southern Tibet from Two Perspectives. *Geol. Soc. Am. Bull.*, 112. 3242–3350. doi:10.1130/0016-7606(2000)112<324:tothas>2.0.co;2

Hodson, M. E. (2004). Heavy Metals-Geochemical Bogey Men? *Environ. Pollut.* 129, 341–343. doi:10.1016/j.envpol.2003.11.003

Hong, S., Lee, K., Hou, S., Hur, S. D., Ren, J., Burn, L. J., et al. (2009). An 800-year Record of Atmospheric as, Mo, Sn, and Sb in central Asia in High-Altitude Ice Cores from Mt. Qomolangma (Everest), Himalayas. *Environ. Sci. Technol.* 43, 8060–8065. doi:10.1021/es901685u

Hong, S., Soyol-Erdene, T.-O., Hwang, H. J., Hong, S. B., Hur, S. D., and Motoyama, H. (2012). Evidence of Global-Scale as, Mo, Sb, and Tl Atmospheric Pollution in the Antarctic Snow. *Environ. Sci. Technol.* 46, 11550–11557. doi:10.1021/es303086c

Huang, J., Kang, S., Guo, J., Sillanpää, M., Zhang, Q., Qin, X., et al. (2014). Mercury Distribution and Variation on a High-Elevation Mountain Glacier on the Northern Boundary of the Tibetan Plateau. *Atmos. Environ.* 96, 27–36. doi:10.1016/j.atmosenv.2014.07.023

Huang, J., Kang, S., Guo, J., Zhang, Q., Cong, Z., Sillanpää, M., et al. (2016). Atmospheric Particulate Mercury in Lhasa City, Tibetan Plateau. *Atmos. Environ.* 142, 433–441. doi:10.1016/j.atmosenv.2016.08.021

Huang, J., Kang, S., Guo, J., Zhang, Q., Xu, J., Jenkins, M. G., et al. (2012a). Seasonal Variations, Speciation and Possible Sources of Mercury in the Snowpack of Zhadang Glacier, Mt. Nyainqêntanglha, Southern Tibetan Plateau. *Sci. Total Environ.* 429, 223–230. doi:10.1016/j.scitotenv.2012.04.045

Huang, J., Kang, S., Wang, S., Wang, L., Zhang, Q., Guo, J., et al. (2013). Wet Deposition of Mercury at Lhasa, the Capital City of Tibet. *Sci. Total Environ.* 447, 123–132. doi:10.1016/j.scitotenv.2013.01.003

Huang, J., Kang, S., Yin, R., Guo, J., Lepak, R., Mika, S., et al. (2020a). Mercury Isotopes in Frozen Soils Reveal Transboundary Atmospheric Mercury Deposition over the Himalayas and Tibetan Plateau. *Environ. Pollut.* 256, 113432. doi:10.1016/j.envpol.2019.113432

Huang, J., Kang, S., Yin, R., Lin, M., Guo, J., Ram, K., et al. (2020b). Decoupling Natural and Anthropogenic Mercury and Lead Transport from South Asia to the Himalayas. *Environ. Sci. Technol.* 54, 5429–5436. doi:10.1021/acs.est.0c00429

Huang, J., Kang, S., Zhang, Q., Guo, J., Sillanpää, M., Wang, Y., et al. (2015). Characterizations of Wet Mercury Deposition on a Remote High-Elevation Site in the southeastern Tibetan Plateau. *Environ. Pollut.* 206, 518–526. doi:10.1016/j.envpol.2015.07.024

Huang, J., Kang, S., Zhang, Q., Jenkins, M. G., Guo, J., Zhang, G., et al. (2012b). Spatial Distribution and Magnification Processes of Mercury in Snow from High-Elevation Glaciers in the Tibetan Plateau. *Atmos. Environ.* 46, 140–146. doi:10.1016/j.atmosenv.2011.10.008

Huang, J., Kang, S., Zhang, Q., Yan, H., Guo, J., Jenkins, M. G., et al. (2012c). Wet Deposition of Mercury at a Remote Site in the Tibetan Plateau: Concentrations, Speciation, and Fluxes. *Atmos. Environ.* 62, 540–550. doi:10.1016/j.atmosenv.2012.09.003

Huang, X., Sillanpää, M., Gjessing, E. T., and Vogt, R. D. (2009). Water Quality in the Tibetan Plateau: Major Ions and Trace Elements in the Headwaters of Four Major Asian Rivers. *Sci. Total Environ.* 407, 6242–6254. doi:10.1016/j.scitotenv.2009.09.001

Huo, W., Yao, T., and Li, Y. (1999). Increasing Atmospheric Pollution Revealed by Pb Record of a 7 000-m Ice Core. *Chin.Sci.Bull.* 44, 1309–1312. doi:10.1007/bf02885851

Immerzeel, W. W., Van Beek, L. P. H., and Bierkens, M. F. P. (2010). Climate Change Will Affect the Asian Water Towers. *Science* 328, 1382–1385. doi:10.1126/science.1183188

Ji, X., Abakumov, E., Chigray, S., Saparova, S., Polyakov, V., Wang, W., et al. (2021). Response of Carbon and Microbial Properties to Risk Elements Pollution in Arctic Soils. *J. Hazard. Mater.* 408, 124430. doi:10.1016/j.jhazmat.2020.124430

Ji, X., Abakumov, E., Tomashunas, V., Polyakov, V., and Kouzov, S. (2020). Geochemical Pollution of Trace Metals in Permafrost-Affected Soil in the Russian Arctic Marginal Environment. *Environ. Geochem. Health* 42, 4407–4429. doi:10.1007/s10653-020-00587-2

Ji, X., Abakumov, E., and Xie, X. (2019). Atmosphere-Ocean Exchange of Heavy Metals and Polycyclic Aromatic Hydrocarbons in the Russian Arctic Ocean. *Atmos. Chem. Phys.* 19, 13789–13807. doi:10.5194/acp-19-13789-2019

Jia, L., Luo, J., Peng, P., Li, W., Yang, D., Shi, W., et al. (2021). Distribution Trends of Cadmium and lead in Timberline Coniferous Forests in the Eastern Tibetan Plateau. *Appl. Sci.* 11, 753–810. doi:10.3390/app11020753

Jiao, X., Dong, Z., Kang, S., Li, Y., Jiang, C., and Rostami, M. (2021). New Insights into Heavy Metal Elements Deposition in the Snowpacks of Mountain Glaciers in the Eastern Tibetan Plateau. *Ecotoxicol. Environ. Saf.* 207, 111228. doi:10.1016/j.ecoenv.2020.111228

Jin, H., Li, S., Cheng, G., Shaoling, W., and Li, X. (2000). Permafrost and Climatic Change in China. *Glob. Planet. Change* 26, 387–404. doi:10.1016/S0921-8181(00)00051-5

Kang, S., Chen, P., Li, C., Liu, B., and Cong, Z. (2016a). Atmospheric Aerosol Elements over the Inland Tibetan Plateau: Concentration, Seasonality, and Transport. *Aerosol Air Qual. Res.* 16, 789–800. doi:10.4209/aaqr.2015.05.0307

Kang, S., Huang, J., Wang, F., Zhang, Q., Zhang, Y., Li, C., et al. (2016b). Atmospheric Mercury Depositional Chronology Reconstructed from Lake Sediments and Ice Core in the Himalayas and Tibetan Plateau. *Environ. Sci. Technol.* 50, 2859–2869. doi:10.1021/acs.est.5b04172

Kang, S., Li, C., Wang, F., Zhang, Q., and Cong, Z. (2009). Total Suspended Particulate Matter and Toxic Elements Indoors during Cooking with Yak Dung. *Atmos. Environ.* 43, 4243–4246. doi:10.1016/j.atmosenv.2009.06.015

Kang, S., Xu, Y., You, Q., Flügel, W.-A., Pepin, N., and Yao, T. (2010). Review of Climate and Cryospheric Change in the Tibetan Plateau. *Environ. Res. Lett.* 5, 015101. doi:10.1088/1748-9326/5/1/015101

Kang, S., Zhang, Q., Kaspari, S., Qin, D., Cong, Z., Ren, J., et al. (2007). Spatial and Seasonal Variations of Elemental Composition in Mt. Everest (Qomolangma) Snow/firn. *Atmos. Environ.* 41, 7208–7218. doi:10.1016/j.atmosenv.2007.05.024

Kang, S., Zhang, Q., Qian, Y., Ji, Z., Li, C., Cong, Z., et al. (2019a). Linking Atmospheric Pollution to Cryospheric Change in the Third Pole Region: Current Progress and Future Prospects. *Natl. Sci. Rev.* 6, 796–809. doi:10.1093/nsr/nwz031

Keyimu, M., Li, Z., Fu, B., Liu, G., Zeng, F., Chen, W., et al. (2021a). A 406-Year Non-Growing-Season Precipitation Rreconstruction in the Southeastern Tibetan Plateau. *Clim. Past* 17, 2381–2392. doi:10.5194/CP-17-2381-2021

Keyimu, M., Li, Z., Liu, G., Fu, B., Fan, Z., Wang, X., et al. (2021b). Tree-Ring Based Minimum Temperature Reconstruction on the Southeastern Tibetan Plateau. *Quat. Sci. Rev.* 251, 106712. doi:10.1016/J.QUASCIREV.2020.106712

Kang, S., Zhang, Y., Zhang, Q., Wang, X., Dong, Z., Li, C., et al. (2020b). "Chemical Components and Distributions in Glaciers of the Third Pole," in *Water Quality in the Third Pole: The Roles of Climate Change and Human Activities* (Elsevier), 71–134. doi:10.1016/B978-0-12-816489-1.00003-7

Lee, K., Hur, S. D., Hou, S., Hong, S., Qin, X., Ren, J., et al. (2008). Atmospheric Pollution for Trace Elements in the Remote High-Altitude Atmosphere in central Asia as Recorded in Snow from Mt. Qomolangma (Everest) of the Himalayas. *Sci. Total Environ.* 404, 171–181. doi:10.1016/j.scitotenv.2008.06.022

Li, C., Kang, S., Chen, P., Zhang, Q., and Fang, G. C. (2012). Characterizations of Particle-Bound Trace Metals and Polycyclic Aromatic Hydrocarbons (PAHs) within Tibetan Tents of South Tibetan Plateau, China. *Environ. Sci. Pollut. Res.* 19, 1620–1628. doi:10.1007/s11356-011-0678-y

Li, C., Kang, S., and Zhang, Q. (2009). Elemental Composition of Tibetan Plateau Top Soils and its Effect on Evaluating Atmospheric Pollution Transport. *Environ. Pollut.* 157, 2261–2265. doi:10.1016/j.envpol.2009.03.035

Li, C., Kang, S., Zhang, Q., Gao, S., and Sharma, C. M. (2011). Heavy Metals in Sediments of the Yarlung Tsangbo and its Connection with the Arsenic Problem in the Ganges-Brahmaputra Basin. *Environ. Geochem. Health* 33, 23–32. doi:10.1007/s10653-010-9311-0

Li, L., Wu, J., Lu, J., Min, X., Xu, J., and Yang, L. (2018). Distribution, Pollution, Bioaccumulation, and Ecological Risks of Trace Elements in Soils of the Northeastern Qinghai-Tibet Plateau. *Ecotoxicol. Environ. Saf.* 166, 345–353. doi:10.1016/j.ecoenv.2018.09.110

Li, L., Wu, J., Lu, J., and Xu, J. (2020a). Speciation, Risks and Isotope-Based Source Apportionment of Trace Elements in Soils of the Northeastern Qinghai-Tibet Plateau. *Geochem. Explor. Environ. Anal.* 20, 315–322. doi:10.1144/geochem2019-042

Li, L., Wu, J., Lu, J., and Xu, J. (2020b). Trace Elements in Gobi Soils of the Northeastern Qinghai-Tibet Plateau. *Chem. Ecol.* 36, 967–981. doi:10.1080/02757540.2020.1817403

Li, M., Zhang, Q., Sun, X., Karki, K., Zeng, C., Pandey, A., et al. (2020). Heavy Metals in Surface Sediments in the Trans-himalayan Koshi River Catchment: Distribution, Source Identification and Pollution Assessment. *Chemosphere* 244, 125410. doi:10.1016/j.chemosphere.2019.125410

Li, Y., Huang, J., Li, Z., and Zheng, K. (2020). Atmospheric Pollution Revealed by Trace Elements in Recent Snow from the central to the Northern Tibetan Plateau. *Environ. Pollut.* 263, 114459. doi:10.1016/j.envpol.2020.114459

Lin, L., Dong, L., Wang, Z., Li, C., Liu, M., Li, Q., et al. (2021). Hydrochemical Composition, Distribution, and Sources of Typical Organic Pollutants and Metals in Lake Bangong Co, Tibet. *Environ. Sci. Pollut. Res.* 28, 9877–9888. doi:10.1007/s11356-020-11449-w

Liu, H.-w., ShaojuanYu, J.-j. B., Yu, B., Liang, Y., Duo, B., Fu, J.-j., et al. (2019). Mercury Isotopic Compositions of Mosses, Conifer Needles, and Surface Soils: Implications for Mercury Distribution and Sources in Shergyla Mountain, Tibetan Plateau. *Ecotoxicol. Environ. Saf.* 172, 225–231. doi:10.1016/j.ecoenv.2019.01.082

Liu, Y.-R., He, Z.-Y., Yang, Z.-M., Sun, G.-X., and He, J.-Z. (2016). Variability of Heavy Metal Content in Soils of Typical Tibetan Grasslands. *RSC Adv.* 6, 105398–105405. doi:10.1039/c6ra23868h

Liu, Y., Hou, S., Hong, S., Hur, S.-D., Lee, K., and Wang, Y. (2011). Atmospheric Pollution Indicated by Trace Elements in Snow from the Northern Slope of Cho Oyu Range, Himalayas. *Environ. Earth Sci.* 63, 311–320. doi:10.1007/s12665-010-0714-0

Long, E. R., Macdonald, D. D., Smith, S. L., and Calder, F. D. (1995). Incidence of Adverse Biological Effects within Ranges of Chemical Concentrations in marine and Estuarine Sediments. *Environ. Manage.* 19, 81–97. doi:10.1007/BF02472006

Luo, J., Tang, R., Sun, S., Yang, D., She, J., and Yang, P. (2015). Lead Distribution and Possible Sources along Vertical Zone Spectrum of Typical Ecosystems in the Gongga Mountain, Eastern Tibetan Plateau. *Atmos. Environ.* 115, 132–140. doi:10.1016/j.atmosenv.2015.05.022

Lüthi, Z. L., Škerlak, B., Kim, S.-W., Lauer, A., Mues, A., Rupakheti, M., et al. (2015). Atmospheric Brown Clouds Reach the Tibetan Plateau by Crossing the Himalayas. *Atmos. Chem. Phys.* 15, 6007–6021. doi:10.5194/acp-15-6007-2015

McConnell, J. R., and Edwards, R. (2008). Coal Burning Leaves Toxic Heavy Metal Legacy in the Arctic. *Proc. Natl. Acad. Sci. U.S.A.* 105, 12140–12144. doi:10.1073/pnas.0803564105

MEPC (1990). *Background Values of Soil Elements in China. Minist. Environ. Prot. People's Republic China*. China Environ. Sci. Press, 329–493.

MOH&SAC (2006). *Ministry of Health of the People's Republic of China & Standardization Administration of People's Republic China*. Available at: http://www.moh.gov.cn/publicfiles/business/cmsresources/zwgkzt/wsbz/new/20070628143525.

MOH&SAC (2017). *Ministry of Health of the People's Republic of China & Standardization Administration of People's Republic China. GB 2762-2017 Stand.*

Mu, C., Schuster, P. F., Abbott, B. W., Kang, S., Guo, J., Sun, S., et al. (2020). Permafrost Degradation Enhances the Risk of Mercury Release on Qinghai-Tibetan Plateau. *Sci. Total Environ.* 708, 135127. doi:10.1016/j.scitotenv.2019.135127

Nabulo, G., Oryem-Origa, H., and Diamond, M. (2006). Assessment of Lead, Cadmium, and Zinc Contamination of Roadside Soils, Surface Films, and Vegetables in Kampala City, Uganda. *Environ. Res.* 101, 42–52. doi:10.1016/j.envres.2005.12.016

Nickson, R., McArthur, J., Burgess, W., Ahmed, K. M., Ravenscroft, P., and Rahmanñ, M. (1998). Arsenic Poisoning of Bangladesh Groundwater. *Nature* 395, 338. doi:10.1038/26387

Planchon, F. A. M., Boutron, C. F., Barbante, C., Cozzi, G., Gaspari, V., Wolff, E. W., et al. (2002). Changes in Heavy Metals in Antarctic Snow from Coats Land Since the Mid-19th to the Late-20th Century. *Earth Planet. Sci. Lett.* 200, 207–222. doi:10.1016/S0012-821X(02)00612-X

Potapowicz, J., Szumińska, D., Szopińska, M., and Polkowska, Ż. (2019). The Influence of Global Climate Change on the Environmental Fate of Anthropogenic Pollution Released from the Permafrost. *Sci. Total Environ.* 651, 1534–1548. doi:10.1016/j.scitotenv.2018.09.168

Qiu, J. (2008). China: The Third Pole. *Nature* 454, 393–396. doi:10.1038/454393a

Qiu, J. (2014). Double Threat for Tibet. *Nature* 512, 240–241. doi:10.1038/512240a

Qiu, J. (2012). Thawing Permafrost Reduces River Runoff. *Nature*. doi:10.1038/nature.2012.9749

Qu, B., Zhang, Y., Kang, S., and Sillanpää, M. (2019). Water Quality in the Tibetan Plateau: Major Ions and Trace Elements in Rivers of the "Water Tower of Asia". *Sci. Total Environ.* 649, 571–581. doi:10.1016/j.scitotenv.2018.08.316

Ramesh, R., Ramanathan, A., Ramesh, S., Purvaja, R., and Subramanian, V. (2000). Distribution of Rare Earth Elements and Heavy Metals in the Surficial Sediments of the Himalayan River System. *Geochem. J.* 34, 295–319. doi:10.2343/geochemj.34.295

Salim, Z., Khan, M. U., and Malik, R. N. (2020). Concentration, Distribution and Association of Heavy Metals in Multi-Matrix Samples of Himalayan Foothill Along Elevation Gradients. *Environ. Earth Sci.* 79. doi:10.1007/s12665-020-09218-6

Shao, J.-j., Liu, C.-b., Zhang, Q.-h., Fu, J.-j., Yang, R.-q., Shi, J.-b., et al. (2017). Characterization and Speciation of Mercury in Mosses and Lichens from the High-Altitude Tibetan Plateau. *Environ. Geochem. Health* 39, 475–482. doi:10.1007/s10653-016-9828-y

Shao, J.-j., Shi, J.-b., Duo, B., Liu, C.-b., Gao, Y., Fu, J.-j., et al. (2016). Trace Metal Profiles in Mosses and Lichens from the High-Altitude Tibetan Plateau. *RSC Adv.* 6, 541–546. doi:10.1039/c5ra21920e

Shao, J., Shi, J., Duo, B., Liu, C., Gao, Y., Fu, J., et al. (2016). Mercury in Alpine Fish from Four Rivers in the Tibetan Plateau. *J. Environ. Sci.* 39, 22–28. doi:10.1016/j.jes.2015.09.009

Sheng, J., Wang, X., Gong, P., Tian, L., and Yao, T. (2012). Heavy Metals of the Tibetan Top Soils. *Environ. Sci. Pollut. Res.* 19, 3362–3370. doi:10.1007/s11356-012-0857-5

Singh, A. K., and Singh, M. (2006). Lead Decline in the Indian Environment Resulting from the Petrol-Lead Phase-Out Programme. *Sci. Total Environ.* 368, 686–694. doi:10.1016/j.scitotenv.2006.04.013

Singh, S. M., Sharma, J., Gawas-Sakhalkar, P., Upadhyay, A. K., Naik, S., Pedneker, S. M., et al. (2013). Atmospheric Deposition Studies of Heavy Metals in Arctic by Comparative Analysis of Lichens and Cryoconite. *Environ. Monit. Assess.* 185, 1367–1376. doi:10.1007/s10661-012-2638-5

Sun, R., Sun, G., Kwon, S. Y., Feng, X., Kang, S., Zhang, Q., et al. (2021). Mercury Biogeochemistry over the Tibetan Plateau: An Overview. *Crit. Rev. Environ. Sci. Tech.* 51, 577–602. doi:10.1080/10643389.2020.1733894

Sun, S., Kang, S., Huang, J., Chen, S., Zhang, Q., Guo, J., et al. (2017). Distribution and Variation of Mercury in Frozen Soils of a High-Altitude Permafrost Region on the Northeastern Margin of the Tibetan Plateau. *Environ. Sci. Pollut. Res.* 24, 15078–15088. doi:10.1007/s11356-017-9088-0

Sun, S., Kang, S., Huang, J., Li, C., Guo, J., Zhang, Q., et al. (2016). Distribution and Transportation of Mercury from Glacier to lake in the Qiangyong Glacier Basin, Southern Tibetan Plateau, China. *J. Environ. Sci.* 44, 213–223. doi:10.1016/j.jes.2015.09.017

Sun, S., Ma, M., He, X., Obrist, D., Zhang, Q., Yin, X., et al. (2020). Vegetation Mediated Mercury Flux and Atmospheric Mercury in the Alpine Permafrost Region of the Central Tibetan Plateau. *Environ. Sci. Technol.* 54, 6043–6052. doi:10.1021/acs.est.9b06636

Taylor, S. R., and Mclennan, S. M. (1985). *The continental Crust: Its Composition and Evolution*. Unite states.

Tripathee, L., Guo, J., Kang, S., Paudyal, R., Huang, J., Sharma, C. M., et al. (2019). Spatial and Temporal Distribution of Total Mercury in Atmospheric Wet Precipitation at Four Sites from the Nepal-Himalayas. *Sci. Total Environ.* 655, 1207–1217. doi:10.1016/j.scitotenv.2018.11.338

Tripathee, L., Guo, J., Kang, S., Paudyal, R., Sharma, C. M., Huang, J., et al. (2020). Measurement of Mercury, Other Trace Elements and Major Ions in Wet Deposition at Jomsom: The Semi-arid Mountain valley of the Central Himalaya. *Atmos. Res.* 234, 104691. doi:10.1016/j.atmosres.2019.104691

Tripathee, L., Kang, S., Huang, J., Sharma, C. M., Sillanpää, M., Guo, J., et al. (2014). Concentrations of Trace Elements in Wet Deposition over the central Himalayas, Nepal. *Atmos. Environ.* 95, 231–238. doi:10.1016/j.atmosenv.2014.06.043

Wang, B., Bao, Q., Hoskins, B., Wu, G., and Liu, Y. (2008). Tibetan Plateau Warming and Precipitation Changes in East Asia. *Geophys. Res. Lett.* 35, 14702. doi:10.1029/2008GL034330

Wang, G., Yan, X., Zhang, F., Zeng, C., and Gao, D. (2013). Traffic-related Trace Element Accumulation in Roadside Soils and Wild Grasses in the Qinghai-Tibet Plateau, China. *Ijerph* 11, 456–472. doi:10.3390/ijerph110100456

Wang, G., Zeng, C., Zhang, F., Zhang, Y., Scott, C. A., and Yan, X. (2017). Traffic-Related Trace Elements in Soils along Six Highway Segments on the Tibetan Plateau: Influence Factors and Spatial Variation. *Sci. Total Environ.* 581–582, 811–821. doi:10.1016/j.scitotenv.2017.01.018

Wang, P., Cao, J., Han, Y., Jin, Z., Wu, F., and Zhang, F. (2015). Elemental Distribution in the Topsoil of the Lake Qinghai Catchment, NE Tibetan Plateau, and the Implications for Weathering in Semi-arid Areas. *J. Geochem. Explor.* 152, 1–9. doi:10.1016/j.gexplo.2014.12.008

Wang, X., Cheng, G., Zhong, X., and Li, M.-H. (2009). Trace Elements in Sub-Alpine forest Soils on the Eastern Edge of the Tibetan Plateau, China. *Environ. Geol.* 58, 635–643. doi:10.1007/s00254-008-1538-z

Wang, X., Dan, Z., Cui, X., Zhang, R., Zhou, S., Wenga, T., et al. (2020). Contamination, Ecological and Health Risks of Trace Elements in Soil of Landfill and Geothermal Sites in Tibet. *Sci. Total Environ.* 715, 136639. doi:10.1016/j.scitotenv.2020.136639

Wang, X., Gong, P., Wang, C., Ren, J., and Yao, T. (2016). A Review of Current Knowledge and Future Prospects Regarding Persistent Organic Pollutants Over the Tibetan Plateau. *Sci. Total Environ.* 573, 139–154. doi:10.1016/j.scitotenv.2016.08.107

Wang, X., Wang, C., Zhu, T., Gong, P., Fu, J., and Cong, Z. (2019). Persistent Organic Pollutants in the Polar Regions and the Tibetan Plateau: A Review of Current Knowledge and Future Prospects. *Environ. Pollut.* 248, 191–208. doi:10.1016/j.envpol.2019.01.093

Wang, Y., Pi, K., Fendorf, S., Deng, Y., and Xie, X. (2019). Sedimentogenesis and Hydrobiogeochemistry of High Arsenic Late Pleistocene-Holocene Aquifer Systems. *Earth-Science Rev.* 189, 79–98. doi:10.1016/j.earscirev.2017.10.007

WHO (2000). *Air Quality Guidelines for Europe, Seconded. World Heal.* European series: Organ regional publications, 125–154.

WHO (2011). Guidelines for Drinking-Water Quality. Available at: http://www.ho.int/water_sanitation_health/dwq/gdwq3rev/en/.

Wilkie, D., and La Farge, C. (2011). Bryophytes as Heavy Metal Biomonitors in the Canadian High Arctic. *Arct. Antarct. Alp. Res.* 43, 289–300. doi:10.1657/1938-4246-43.2.289

Wu, J., Duan, D., Lu, J., Luo, Y., Wen, X., Guo, X., et al. (2016). Inorganic Pollution Around the Qinghai-Tibet Plateau: An Overview of the Current Observations. *Sci. Total Environ.* 550, 628–636. doi:10.1016/j.scitotenv.2016.01.136

Wu, J., Lu, J., Li, L., Min, X., and Luo, Y. (2018). Pollution, Ecological-Health Risks, and Sources of Heavy Metals in Soil of the Northeastern Qinghai-Tibet Plateau. *Chemosphere* 201, 234–242. doi:10.1016/j.chemosphere.2018.02.122

Wu, J., Lu, J., Li, L., Min, X., Zhang, Z., and Luo, Y. (2019). Distribution, Pollution, and Ecological Risks of Rare Earth Elements in Soil of the Northeastern Qinghai-Tibet Plateau. *Hum. Ecol. Risk Assess. Int. J.* 25, 1816–1831. doi:10.1080/10807039.2018.1475215

Xie, H., Li, J., Zhang, C., Tian, Z., Liu, X., Tang, C., et al. (2014). Assessment of Heavy Metal Contents in Surface Soil in the Lhasa-Shigatse-Nam Co Area of the Tibetan Plateau, China. *Bull. Environ. Contam. Toxicol.* 93, 192–198. doi:10.1007/s00128-014-1288-4

Xiong, X., Zhang, K., Chen, Y., Qu, C., and Wu, C. (2020). Arsenic in Water, Sediment, and Fish of Lakes from the Central Tibetan Plateau. *J. Geochem. Explor.* 210, 106454. doi:10.1016/j.gexplo.2019.106454

Yang, K., Wu, H., Qin, J., Lin, C., Tang, W., and Chen, Y. (2014). Recent Climate Changes over the Tibetan Plateau and Their Impacts on Energy and Water Cycle: A Review. *Glob. Planet. Change* 112, 79–91. doi:10.1016/j.gloplacha.2013.12.001

Yang, R., Jing, C., Zhang, Q., Wang, Z., Wang, Y., Li, Y., et al. (2011). Polybrominated Diphenyl Ethers (PBDEs) and Mercury in Fish from Lakes of the Tibetan Plateau. *Chemosphere* 83, 862–867. doi:10.1016/j.chemosphere.2011.02.060

Yang, R., Yao, T., Xu, B., Jiang, G., and Xin, X. (2007). Accumulation Features of Organochlorine Pesticides and Heavy Metals in Fish from High mountain lakes and Lhasa River in the Tibetan Plateau. *Environ. Int.* 33, 151–156. doi:10.1016/j.envint.2006.08.008

Yang, R., Zhang, S., and Wang, Z. (2014). Bioaccumulation and Regional Distribution of Trace Metals in Fish of the Tibetan Plateau. *Environ. Geochem. Health* 36, 183–191. doi:10.1007/s10653-013-9538-7

Yao, T., Thompson, L. G., Mosbrugger, V., Zhang, F., Ma, Y., Luo, T., et al. (2012). Third Pole Environment (TPE). *Environ. Dev.* 3, 52–64. doi:10.1016/j.envdev.2012.04.002

Ye, W., Saikawa, E., Avramov, A., Cho, S.-H., and Chartier, R. (2020). Household Air Pollution and Personal Exposure from Burning Firewood and Yak Dung in

Summer in the Eastern Tibetan Plateau. *Environ. Pollut.* 263, 114531. doi:10.1016/j.envpol.2020.114531

Yin, A., and Harrison, T. M. (2003). Geologic Evolution of the Himalayan-Tibetan Orogen. *Annu. Rev. Earth Planet. Sci.* 28, 211–280. doi:10.1146/annurev.earth.28.1.211

Yongjie, Y., Yuesi, W., Tianxue, W., Wei, L., Ya'nan, Z., and Liang, L. (2009). Elemental Composition of PM2.5 and PM10 at Mount Gongga in China during 2006. *Atmos. Res.* 93, 801–810. doi:10.1016/j.atmosres.2009.03.014

You, Q., Min, J., and Kang, S. (2016). Rapid Warming in the Tibetan Plateau from Observations and CMIP5 Models in Recent Decades. *Int. J. Climatol.* 36, 2660–2670. doi:10.1002/joc.4520

Yu, C., Sun, Y., Zhong, X., Yu, Z., Li, X., Yi, P., et al. (2019). Arsenic in Permafrost-Affected Rivers and Lakes of Tibetan Plateau, China. *Environ. Pollut. Bioavailab.* 31, 226–232. doi:10.1080/26395940.2019.1624198

Zhang, H., Fu, X., Lin, C.-J., Shang, L., Zhang, Y., Feng, X., et al. (2016a). Monsoon-Facilitated Characteristics and Transport of Atmospheric Mercury at a High-Altitude Background Site in Southwestern China. *Atmos. Chem. Phys.* 16, 13131–13148. doi:10.5194/acp-16-13131-2016

Zhang, H., Wang, Z., Zhang, Y., Ding, M., and Li, L. (2015). Identification of Traffic-Related Metals and the Effects of Different Environments on Their Enrichment in Roadside Soils along the Qinghai-Tibet Highway. *Sci. Total Environ.* 521–522, 160–172. doi:10.1016/j.scitotenv.2015.03.054

Zhang, H., Wang, Z., Zhang, Y., and Hu, Z. (2012). The Effects of the Qinghai-Tibet Railway on Heavy Metals Enrichment in Soils. *Sci. Total Environ.* 439, 240–248. doi:10.1016/j.scitotenv.2012.09.027

Zhang, H., Yin, R.-s., Feng, X.-b., Sommar, J., Anderson, C. W. N., Sapkota, A., et al. (2013a). Atmospheric Mercury Inputs in Montane Soils Increase with Elevation: Evidence from Mercury Isotope Signatures. *Sci. Rep.* 3. doi:10.1038/srep03322

Zhang, H., Zhang, Y., Wang, Z., and Ding, M. (2013b). Heavy Metal Enrichment in the Soil Along the Delhi-Ulan Section of the Qinghai-Tibet Railway in China. *Environ. Monit. Assess.* 185, 5435–5447. doi:10.1007/s10661-012-2957-6

Zhang, H., Zhang, Y., Wang, Z., Ding, M., Jiang, Y., and Xie, Z. (2016b). Traffic-related Metal(loid) Status and Uptake by Dominant Plants Growing Naturally in Roadside Soils in the Tibetan Plateau, China. *Sci. Total Environ.* 573, 915–923. doi:10.1016/j.scitotenv.2016.08.128

Zhang, J.-W., Yan, Y.-N., Zhao, Z.-Q., Li, X.-D., Guo, J.-Y., Ding, H., et al. (2021). Spatial and Seasonal Variations of Dissolved Arsenic in the Yarlung Tsangpo River, Southern Tibetan Plateau. *Sci. Total Environ.* 760, 143416. doi:10.1016/j.scitotenv.2020.143416

Zhang, N., Cao, J., Ho, K., and He, Y. (2012). Chemical Characterization of Aerosol Collected at Mt. Yulong in Wintertime on the southeastern Tibetan Plateau. *Atmos. Res.* 107, 76–85. doi:10.1016/j.atmosres.2011.12.012

Zhang, N., Cao, J., Liu, S., Zhao, Z., Xu, H., and Xiao, S. (2014). Chemical Composition and Sources of PM2.5 and TSP Collected at Qinghai Lake During Summertime. *Atmos. Res.* 138, 213–222. doi:10.1016/j.atmosres.2013.11.016

Zhang, Q., Pan, K., Kang, S., Zhu, A., and Wang, W.-X. (2014). Mercury in Wild Fish from High-Altitude Aquatic Ecosystems in the Tibetan Plateau. *Environ. Sci. Technol.* 48, 5220–5228. doi:10.1021/es404275v

Zhang, S., Yang, G., Hou, S., Zhang, T., Li, Z., and Du, W. (2021). Analysis of Heavy Metal-Related Indices in the Eboling Permafrost on the Tibetan Plateau. *Catena* 196, 104907. doi:10.1016/j.catena.2020.104907

Zhang, Y., Sillanpää, M., Li, C., Guo, J., Qu, B., and Kang, S. (2015). River Water Quality Across the Himalayan Regions: Elemental Concentrations in Headwaters of Yarlung Tsangbo, Indus and Ganges River. *Environ. Earth Sci.* 73, 4151–4163. doi:10.1007/s12665-014-3702-y

Zhang, Z., Zheng, D., Xue, Z., Wu, H., and Jiang, M. (2019). Identification of Anthropogenic Contributions to Heavy Metals in Wetland Soils of the Karuola Glacier in the Qinghai-Tibetan Plateau. *Ecol. Indic.* 98, 678–685. doi:10.1016/j.ecolind.2018.11.052

Zhu, T., Wang, X., Lin, H., Ren, J., Wang, C., and Gong, P. (2020). Accumulation of Pollutants in Proglacial Lake Sediments: Impacts of Glacial Meltwater and Anthropogenic Activities. *Environ. Sci. Technol.* 54, 7901–7910. doi:10.1021/acs.est.0c01849

Zou, D., Zhao, L., Sheng, Y., Chen, J., Hu, G., Wu, T., et al. (2017). A New Map of Permafrost Distribution on the Tibetan Plateau. *Cryosphere* 11, 2527–2542. doi:10.5194/tc-11-2527-2017

Conflict of Interest: The authors declare that the research was conducted in the absence of any commercial or financial relationships that could be construed as a potential conflict of interest.

Publisher's Note: All claims expressed in this article are solely those of the authors and do not necessarily represent those of their affiliated organizations, or those of the publisher, the editors and the reviewers. Any product that may be evaluated in this article, or claim that may be made by its manufacturer, is not guaranteed or endorsed by the publisher.

frontiers | Frontiers in Environmental Science

ORIGINAL RESEARCH
published: 11 May 2022
doi: 10.3389/fenvs.2022.875450

Spatiotemporal Variations in the Air Freezing and Thawing Index Over the Mongolian Plateau From 1901 to 2019

Xin Ma[1,2], Tonghua Wu[1,2], Xiaofan Zhu[1], Peiqing Lou[1,2], Dong Wang[1,2], Saruulzaya Adiya[3], Dashtseren Avirmed[3], Battogtokh Dorjgotov[3], Jie Chen[1], Chengpeng Shang[1,2], Amin Wen[1,2], Yune La[1,2], Xianhua Wei[1,2] and Ren Li[1]*

[1]Cryosphere Research Station on the Qinghai-Tibet Plateau, State Key Laboratory of Cryospheric Science, Northwest Institute of Eco-Environment and Resources, Chinese Academy of Sciences, Lanzhou, China, [2]University of Chinese Academy of Sciences, Beijing, China, [3]Institute of Geography and Geoecology, Mongolian Academy of Sciences, Ulaanbaatar, Mongolia

The Mongolian Plateau is located in the permafrost transitional zone between high-altitudinal and high-latitudinal permafrost regions in the Northern Hemisphere. Current knowledge of the thermal state and changes in the permafrost on the Mongolian Plateau is limited. This study adopted an improved calculation method of the Mongolian Plateau air freezing and thawing index using the monthly air temperature reanalysis dataset from the Climate Research Unit (CRU). The spatial and temporal variation characteristics from 1901 to 2019 were further assessed by the Mann–Kendall (M–K) test and spatial interpolation methods. The results indicate that the spatial distributions of the freezing and thawing index show clear latitudinal zonality. Over the study period, the air freezing index decreased by 4.1°C·d/yr, and the air thawing index increased by 2.3°C·d/yr. The change point in the air thawing index appeared in 1995 ($p < 0.05$) based on the M–K method, in contrast to the so-called hiatus in global warming. Our results reveal rapid warming on the Mongolian Plateau, especially in the permafrost region, and are useful for studying permafrost changes on the Mongolian Plateau.

Keywords: freezing and thawing index, permafrost, CRU, Mongolian plateau, change-point

OPEN ACCESS

Edited by:
Zoe Courville, Cold Regions Research and Engineering Laboratory, United States

Reviewed by:
Rudiger Gens, University of Alaska Fairbanks, United States
Hotaek Park, Japan Agency for Marine-Earth Science and Technology (JAMSTEC), Japan

***Correspondence:**
Tonghua Wu
thuawu@lzb.ac.cn

Specialty section:
This article was submitted to Interdisciplinary Climate Studies, a section of the journal Frontiers in Environmental Science

Received: *14 February 2022*
Accepted: *21 April 2022*
Published: *11 May 2022*

Citation:
Ma X, Wu T, Zhu X, Lou P, Wang D, Adiya S, Avirmed D, Dorjgotov B, Chen J, Shang C, Wen A, La Y, Wei X and Li R (2022) Spatiotemporal Variations in the Air Freezing and Thawing Index Over the Mongolian Plateau From 1901 to 2019. Front. Environ. Sci. 10:875450. doi: 10.3389/fenvs.2022.875450

INTRODUCTION

Currently, the global climate is warming rapidly, especially in high-latitude and high-altitude regions (Juřička et al., 2020). As an essential component of the cryosphere, permafrost is experiencing significant warming and thawing trends due to climate warming (Vaughan et al., 2014), which are mainly reflected in increasing ground temperature, a thicker active layer, earlier active layer melting time, and later freezing time (Cheng and Wu., 2007; Biskaborn et al., 2019; Cheng et al., 2019; Qi et al., 2021). Permafrost degradation triggers a series of ecological and environmental effects, such as the decomposition of soil organic carbon stored in permafrost and the release of carbon-based greenhouse gases, which can further increase the atmospheric CO_2 concentration and accelerate climate warming through positive feedback processes (Knoblauch et al., 2018; Zhang et al., 2020; Adiya et al., 2021). Along with permafrost degradation, extreme drought events show gradually increasing trends, and such events can cause local pasture and forest fires (Ni et al., 2019; Holloway et al., 2020; Li et al., 2020). Permafrost warming causes the melting of ground ice, leading to ground subsidence and related disaster events, such as thermokarst settlement and thaw slumps. These disasters pose a great threat to the local ecological environment, infrastructure, and property safety

(Sharkhuu, 2003; Dagvadorj et al., 2009; Yao et al., 2013; Hao et al., 2020; Sjoberg et al., 2020). In addition, permafrost degradation also causes significant impacts on local hydrological processes (Qin et al., 2014; Colombo et al., 2018), vegetation, and ecosystems (Qian, 2013; Guo et al., 2018; Peng et al., 2020a). Therefore, the analysis of long-term permafrost dynamics and the associated influential factors can improve the accuracy of risk assessment and early warning predictions of the effects caused by permafrost degradation.

The variation in air and ground temperatures affects the stability and distribution of permafrost and is therefore important for quantifying the permafrost variation over long time periods (Frauenfeld et al., 2007). Permafrost thermal conditions are usually monitored by borehole data or analyzed by experience and a semiempirical method. The input parameters are numerous and difficult to acquire (Gao et al., 2022). The environmental conditions in regions with the frozen ground are harsh. The distribution of existing boreholes is sparse, and thus, the input parameters for the models are always limited. In contrast, the frost number model requires fewer parameters and constructs more straightforward, and the freezing and thawing index have been widely used in permafrost environment studies (Lv et al., 2008; Wu et al., 2011; Harris et al., 2014; Ran et al., 2015). The freezing and thawing index can be divided into two categories. The first includes the surface freezing and thawing index, which reflect the accumulation of ground surface temperatures below or above 0°C during the freezing or thawing period, respectively. The other includes the air freezing and thawing index, which are specifically based on air temperature. However, the study of the continuous freezing and thawing index at the regional scale is constrained by short time series and the uneven spatial distribution of measured ground surface temperature data. These shortcomings are partly because permafrost is mainly distributed in remote cold regions with complex topography (Wu et al., 2011).

The freezing and thawing index are widely used to reflect climate change and to represent permafrost distribution (Chen et al., 2021; Hu et al., 2021). For example, in the Qinghai-Tibet Plateau and its surroundings, the freezing and thawing index show significant feedback with climate warming, the increase in ground surface temperature accelerates permafrost degradation and affects the ecology, hydrology, and environment of permafrost regions (Jiang et al., 2008; Cao et al., 2015; Jiang et al., 2015; Wu et al., 2018; Liu and Luo, 2019). Although the meteorological station data are of high quality, the sparse and uneven distribution of stations means that observational data are rare and short in length. The application of the variations in large-scale and long-term series is limited. In contrast, reanalysis data have notable advantages, such as long-term series and global scale records, in climate studies. For example, Qin et al. (2021) used five different reanalysis databases (ERA, MERRA2, GLDAS, CFS, and CMFD) to compare and analyze the changes in the freezing and thawing index on the Qinghai-Tibet Plateau from 1981 to 2017. The results showed that the MERRA2 reanalysis data have better applicability on the Qinghai-Tibet Plateau than the other reanalysis databases. As an effective indicator, the air freezing index can reflect the current permafrost status in the central and northeastern regions of the Qinghai-Tibet Plateau. Shi et al. (2019) calculated the spatial and temporal variations in the air freezing and thawing index in the circumpolar region from 1901 to 2019 based on Climate Research Unit (CRU) and National Centers for Environmental Prediction (NCEP) reanalysis data and estimated the change in the area of permafrost. That study showed that overall, the freezing index decreased significantly after 1988 and that the thawing index increased since 2015. In summary, from previous studies, to calculate the freezing and thawing index, the daily temperature is used in regions where meteorological stations are uniform and abundant, and the reanalysis of monthly temperature is an optional dataset for the areas without observation data.

The Mongolian Plateau is located in the transitional zone between high-altitudinal and high-latitudinal permafrost regions in the Northern Hemisphere (Zorigt et al., 2020). Most areas in this region lie on the southern boundary of the continuous permafrost zone and feature unstable thermal conditions. The permafrost in this region is sensitive to climate change (Sharkhuu et al., 2008; Heggem et al., 2006; Munkhjargal et al., 2020). Therefore, this area provides a good opportunity to investigate permafrost degradation influenced by air temperature change (Kynicky et al., 2009; Munkhjargal et al., 2020; Wu et al., 2011). Previous studies have mainly been conducted at a local scale (Wu et al., 2011; Munkhjargal et al., 2020; Dashtseren et al., 2021; Ran et al., 2021) or over a short time period. Temperature data from borehole monitoring are sparse, and the existing studies have mainly focused on the regions with field observations. Therefore, our current knowledge is insufficient to understand the spatial and temporal changes in the permafrost environment at the regional scale.

Compared with the field observational data, the CRU reanalysis data have the advantages of long-term series and comprehensive spatial coverage (Simmons et al., 2004; Zhao and Fu, 2006; Harris et al., 2014). The CRU reanalysis data are based on the integration of multiple meteorological datasets and produce a dataset with complete spatial coverage. This study selected the CRU monthly air temperature dataset with a 0.5 × 0.5 spatial resolution. We checked the quality with meteorological station data and calculated the air freezing and thawing index, and analyzed the variations between spatial and temporal on the Mongolian Plateau from 1901 to 2019.

STUDY AREA AND DATA

Climate of the Mongolian Plateau

The Mongolian Plateau is located in the interior of Asia. It covers approximately 2.72×10^6 km^2, including Mongolia, southern Russia, the northern part of the Inner Mongolia Autonomous Region in China, and parts of the Xinjiang Uygur Autonomous Region (Li et al., 2020) (**Figure 1**). The elevation of the Mongolian Plateau gradually decreases from northwest to southeast, with an average elevation of 1,580 m above sea level (a.s.l.). The western and northwestern regions are mainly mountainous with elevations between 2000 and 4,000 m; the central and eastern regions are mainly plains and hills, with elevations of approximately 800–1,500 m; and the southern and

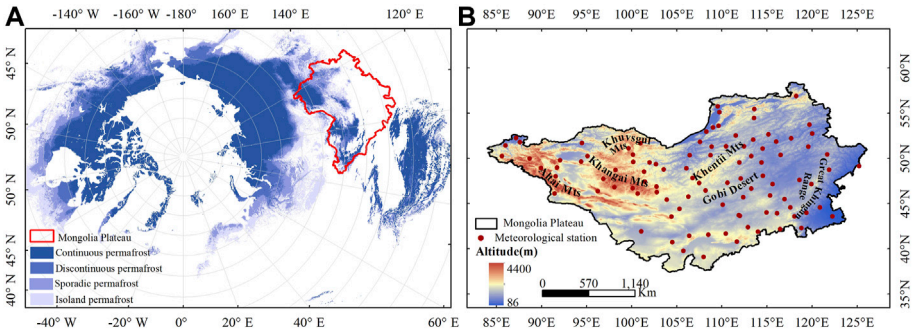

FIGURE 1 | The location of the Mongolian Plateau in the permafrost region of the Northern Hemisphere **(A)** and the distribution of meteorological stations **(B)**. The permafrost distribution data in the Northern Hemisphere **(A)** are derived from Obu et al. (2019) via the data source https://apgc.awi.de/dataset/pex.

southeastern regions are the Gobi Desert, with elevations of approximately 1,000 m (Chen et al., 2020).

The Mongolian Plateau is located in the center of the Asian high-pressure system, which is one of the origins of cold waves in the winter monsoon climate zone (Chen et al., 2020). The climate type is dominated by arid and semiarid climate characteristics with large intra-annual variability in temperature and precipitation (Zhou et al., 2012). Due to the influence of water vapor from the Arctic Ocean to the north and the Pacific Ocean to the east, precipitation on the Mongolian Plateau decreases spatially from southeast to northwest. The mean annual precipitation is approximately 267 mm, and the Selenge River basin in the north can reach an annual precipitation of 500 mm. The southwestern region has an annual precipitation of only approximately 100 mm (Wang et al., 2008). In addition, evapotranspiration in Mongolia showed a gradual increasing trend from 2001 to 2015. The maximum evapotranspiration values were found in the continuous and discontinuous permafrost regions (Yu, 2017).

The permafrost distribution data in the Northern Hemisphere (**Figure 1A**) are derived from Obu et al. (2019) *via* the data source https://apgc.awi.de/dataset/pex.

Reanalysis and Observation Data

The monthly reanalysis data of air temperature were used to analyze the spatiotemporal variations in the freezing and thawing index on the Mongolian Plateau. These data were obtained from the CRU time-series Version 4.05 (CRU TS v4.05) datasets (https://crudata.uea.ac.uk/cru/data/hrg/), and the time series is from 1901 to 2019 with a spatial resolution of 0.5 × 0.5. The CRU dataset combines centennial-scale climate change grid data covering the global scale. The dataset is integrated from several well-known datasets through interpolation and other methods, which are widely used as credible proxy data after comparison (Wen et al., 2006; Chen et al., 2021). In addition, the CRU dataset is continuous in space and time and can reflect long-term trends (Shi et al., 2019). The observational records in most of the meteorological sites are from the post-1980s period, thus limiting the study of early climate and freezing and thawing index changes. The long time series provided by these data can effectively support the research in this study.

The applicability of the CRU data on the Mongolian Plateau was examined and evaluated using observations from 106 meteorological stations in the study area obtained from the National Oceanic and Atmospheric Administration (NOAA https://www.climate.gov/maps-data). Since the time series recorded at the selected meteorological stations were not consistent, we selected temperature data from January 1975 to December 2019 for the quality check of the CRU data.

METHODS

Quality Check of the CRU Reanalysis Dataset

For the accuracy assessment of the CRU reanalysis dataset, four indicators, namely, the mean deviation error (MBE), correlation coefficient (R), normalized standard error (NSSE), and root mean square error (RMSE) are used in this study and are calculated as follows (Qin et al., 2021):

$$MBE = \frac{\sum_{n=1}^{M}(CRUn - OBn)}{M} \quad (1)$$

$$RMSE = \sqrt{\frac{\sum_{n=1}^{M}(CRUn - OBn)^2}{M}} \quad (2)$$

$$NSSE = \sqrt{\frac{\sum_{n=1}^{M}(CRUn - OBn)^2}{\sum_{n=1}^{M}(OBn)^2}} \quad (3)$$

$$RMSE = \frac{\sum_{n=1}^{M}(CRUn - \overline{CRU})(OBn - \overline{OB})}{\sqrt{\sum_{n=1}^{M}(CRUn - \overline{CRU})^2}\sqrt{\sum_{n=1}^{M}(OBn - \overline{OB})^2}} \quad (4)$$

Where M is the total number of samples and $CRUn$ and OBn (n = 1, 2, 3, M) represent the monthly air temperature corresponding to the CRU and meteorological stations. $\overline{CRU}$ and $\overline{OB}$ represent the monthly mean values corresponding to the years of the CRU and meteorological stations, respectively.

Calculation of the Freezing and Thawing Index

The air freezing (thawing) index is the cumulative sum of the air temperatures corresponding to the number of days when the

mean air temperature is equal to or below (above) 0°C during the freezing (thawing) period (**Eqn. 5**). The freezing period is usually defined as July 1 of each year to June 30 of the following year, while the thawing period is defined as January 1 to December 31 of each year (Wu et al., 2011; Luo et al., 2014; Shi et al., 2019).

$$\begin{aligned} TDD &= \int_{t0}^{t1} |Ti|dt, Ti < 0°C \\ FDD &= \int_{t2}^{t3} Tjdt, Tj > 0°C \end{aligned} \tag{5}$$

$$\begin{aligned} TDD &= \sum_{i=1}^{MT} Tj, Tj > 0°C \\ FDD &= \sum_{i=1}^{MF} |Ti|, Ti < 0°C \end{aligned} \tag{6}$$

Where Ti and Tj refer to the freezing and thawing periods when the air temperature is greater than 0°C and less than 0°C, respectively. $t0$ and $t1$ represent the beginning and end times of the freezing period, and $t2$ and $t3$ represent the beginning and end times of the thawing period, respectively. **Eqn. 5** can be simplified to **Eqn. 6**.

However, the acquisition of daily air temperatures on the Mongolian Plateau during 1901–2019 is limited by many factors, and thus the CRU TS V4.05 monthly dataset was used to determine the freezing and thawing index in this study, so the equation can be further written as **Eqn. 7** (Shi et al., 2019).

$$\begin{aligned} TDD &= \sum_{j=1}^{MT} \overline{Tj} \cdot Dj, \overline{Tj} > 0°C \\ FDD &= \sum_{i=1}^{MF} \overline{Ti} \cdot Di, \overline{Ti} < 0°C \end{aligned} \tag{7}$$

Where $\overline{Ti}$ and $\overline{Tj}$ represent the monthly mean values of the freezing and thawing periods, respectively. Di and Dj represent the number of days in the months corresponding to the freezing and thawing periods, respectively.

M–K Test Method

The M–K method (Mann, 1945; Kendall, 1948) is a nonparametric statistical test that has been widely used in trend analysis of time series (You et al., 2010; Wu et al., 2011). In addition, the algorithm can obtain the year in which the trend changes when the value of intersection points is within the confidence intervals (Shi et al., 2019). In the M–K trend analysis, the statistic S of the test is calculated based on the relationship between the time series n and the corresponding continuous values xj and xi, and is defined as follows:

$$S = \sum_{i=1}^{n-1} \sum_{j=i+1}^{n} \mathrm{sgn}(xj - xi)$$

$$\mathrm{sgn}(xj - xi) = \begin{cases} 1, & xj - xi > 0 \\ 0, & xj - xi = 0 \\ -1, & xj - xi < 0 \end{cases} \tag{8}$$

When sample number n > 10, the standard normal system variables are given by **Eqn. 9**, and the variance in the sample, $Var(S)$ is calculated by **Eqn. 10**:

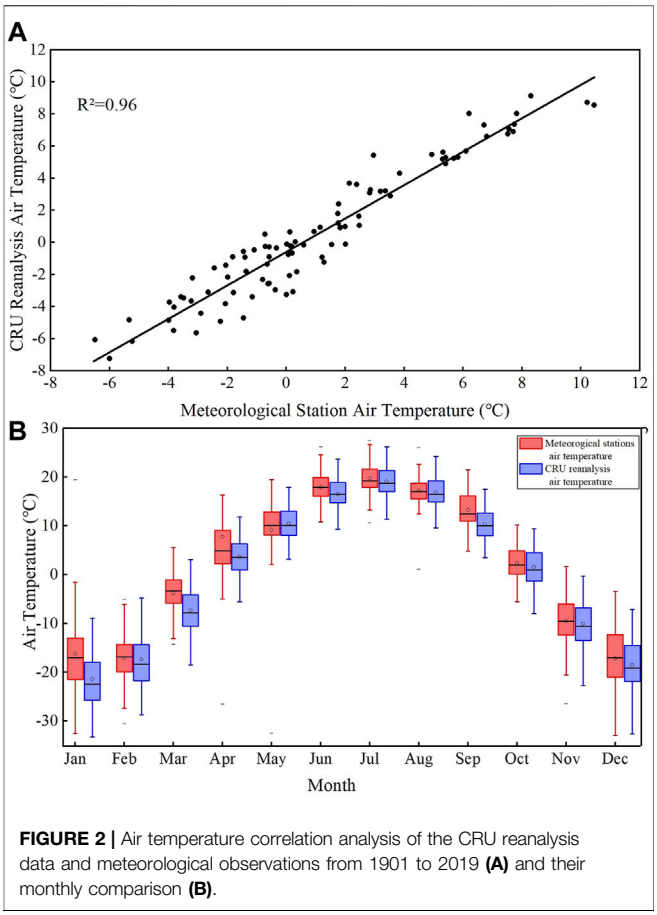

FIGURE 2 | Air temperature correlation analysis of the CRU reanalysis data and meteorological observations from 1901 to 2019 **(A)** and their monthly comparison **(B)**.

$$Z = \begin{cases} \dfrac{S-1}{\sqrt{Var(S)}} & S > 0 \\ 0 & S = 0 \\ \dfrac{S+1}{\sqrt{Var(S)}} & S < 0 \end{cases} \tag{9}$$

$$Var(S) = \frac{n(n-1)(2n+5)}{18} \tag{10}$$

In the bilateral trend test, the trend of the time series data can be judged by the statistic Z at a given confidence level: it is considered an upward trend when Z >0 and a downward trend when Z <0. The magnitude of the Z value is used to determine whether the trend is significant.

In the M–K mutation test, the statistic is defined under the assumption that the time series are independent as follows:

$$\begin{aligned} Sk &= \sum_{i=1}^{k} Ri \quad (k = 2, 3, ..., n) \\ UFk &= \frac{Sk - E(Sk)}{\sqrt{Var(Sk)}} \; (k = 1, 2, ..., n) \\ UBk &= -UFk \quad k = n, n-1, ..., 1 \end{aligned} \tag{11}$$

Where Ri denotes the cumulative number of samples in which $xi > xj$ $(1 \le j \le i)$. When $k = 1$, $UF1 = 0$, and $UB1 = 0$, $E(Sk)$ and

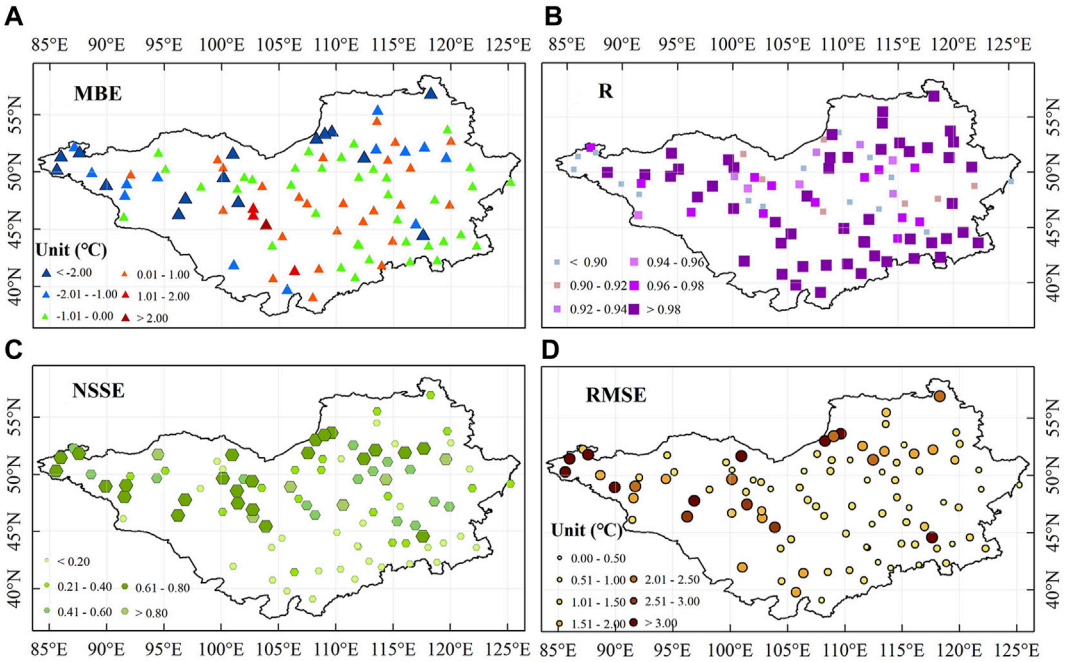

FIGURE 3 | Spatial distribution of four error indicators, including MBE **(A)**, R **(B)**, NSSE **(C)**, and RMSE **(D)**.

$Var(Sk)$ represent the mean and variance, respectively, which can be calculated as follows:

$$E(Sk) = n(n+1)/4$$
$$Var(Sk) = n(n-1)(2n+5)/72 \quad (12)$$

If the two curves UFk and UBk intersect between the critical lines, the change year is considered to correspond to the intersection point.

RESULTS

Reliability Assessment of CRU Air Temperature

Figure 2 shows the annual and monthly fitting results of the meteorological station data and CRU reanalysis data from 1901 to 2019. According to the relevant impacts of different months (**Figure 2B**), the CRU reanalysis data, compared with meteorological observation data, underestimate the actual air temperature on the Mongolian Plateau, especially in winter (December–February) and spring (March–May). In contrast, the results for both summer and autumn are similar, except for a slight underestimation in July and September. The annual fitting result from 1901 to 2019 (**Figure 2A**) shows a significant positive correlation, with a Pearson's correlation coefficient of 0.96 and an explained variance of 0.92, indicating that the CRU dataset is credible for studying air temperature correlation on the Mongolian Plateau.

The indicators for evaluating the applicability of monthly CRU reanalysis data on the Mongolian Plateau were spatially visualized *via* ArcMap spatial analysis (**Figure 3**). The monthly CRU data underestimated the air temperature for 70% of stations, with the mean MBE value being −0.77 and the variation ranging between −7.38 and 2.47. The variation in MBE on the Mongolian Plateau was mostly concentrated between −1 and 0°C. The spatial distribution of the correlation between the CRU data and the meteorological observations at site locations is greater than 0.95 for most sites, with a range of 0.90–0.99. The mean value of NSSE is 0.68, and the value is less than 0.6 for approximately 68% of the sites. The range of RMSE was 0.13–6.78°C, with a mean value of 0.80°C, and approximately 82% of the sites had RMSE values less than 2°C. Based on the statistical results and spatial variations in the four evaluation indices, the R values are high, and the MBE, RMSE, and NSSE values are low. In terms of spatial distribution, most stations show a positive relationship, but a few stations are in the western and northern border areas. Therefore, the CRU reanalysis dataset has good applicability to the Mongolian Plateau region and can be used as a proxy for a long time series for the Mongolian Plateau region.

Spatiotemporal Variations in the Freezing Index

Based on the multivariate statistical relationship (**Eqn. 8**) between the grid data of the mean freezing index calculated from 1901 to 2019 and the longitude, latitude, and elevation of the corresponding points, it can be seen that the spatial distribution of the freezing index on the Mongolian Plateau is influenced by latitude and altitude. As shown in **Figure 4**, the spatial distribution of the freezing index on the Mongolian Plateau exhibits a significant latitudinal gradient. It increases with latitude, with an average value ranging from 1,200 to 3,600°C·d. On the Mongolian Plateau, the highest freezing index value occurs in northern regions, with a value of nearly 5,600°C·d,

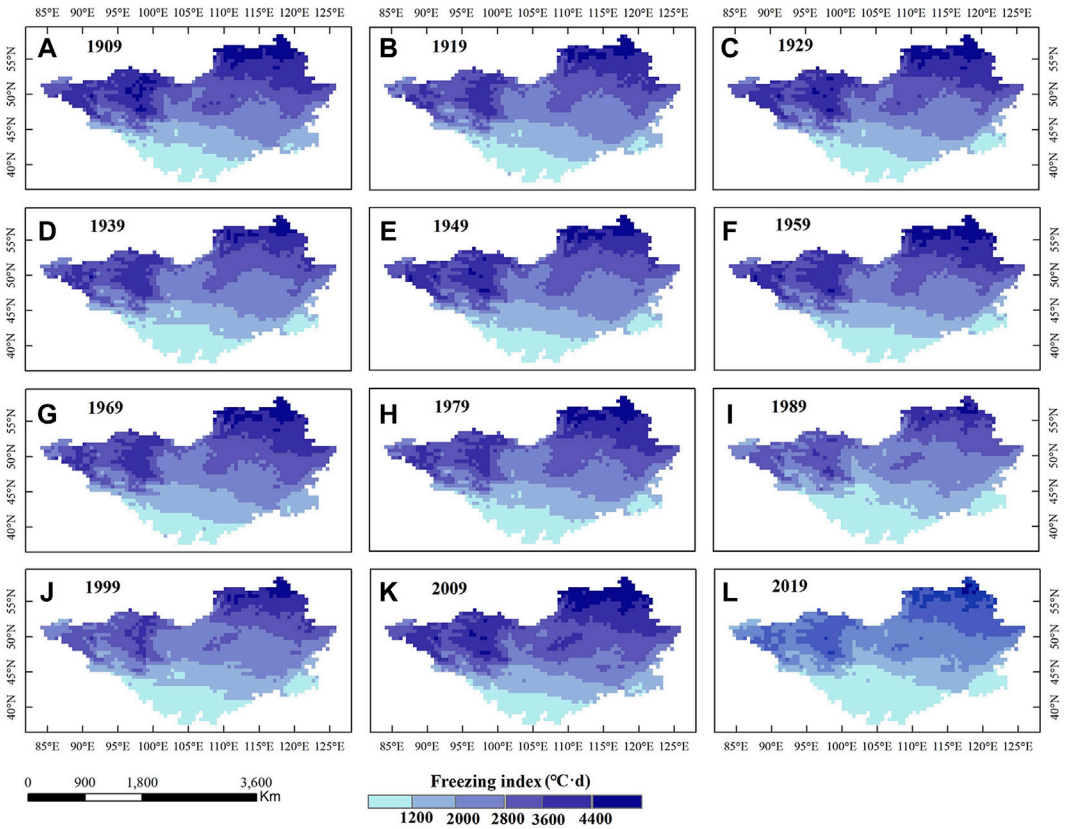

FIGURE 4 | Decadal spatial changes in the air freezing index on the Mongolian Plateau from 1901 to 2019. Labels like **(A–L)** represent the spatial variation of the air freezing index for each decade from 1901 to 2019.

whereas in the southern Gobi Altai and surrounding regions, the values are less than 600°C·d. The spatial distribution of the freezing index also shows altitude differences, and the index decreases faster in high-elevation regions, such as the northeast and northwest on the Mongolian Plateau, than in low-elevation regions.

$$FDD = 0.18lon + 0.94lat + 0.49ele - 0.31\,(R^2 = 0.93) \quad (13)$$

The overall freezing index of the Mongolian Plateau from 1901 to 2019 shows a downward trend of 4.10°C·d/yr. According to long-term changes (**Figure 5A**), the freezing index shows a decreasing trend and changes at different rates. Various characteristics of the freezing index are shown in **Figure 5C**. A decreasing trend appeared in 1902–1903, and a brief increasing trend appears in 1905–1924 and 1929–1930. A decreasing trend with a slow rate of 0.08°C·d/yr was observed from 1930 to 2019.

Spatiotemporal Variations in the Thawing Index

According to the spatial interpolation map of the thawing index (**Figure 6**) and multivariate relationship (**Eqn. 9**), we found that latitude is the main factor and that the thawing index increases gradually with decreasing latitude on the Mongolian Plateau. The thawing index in the northern region varies from 450 to 2,658°C·d, with a mean value of 1,596°C·d, while in the southern region, it varies from 2,000 to 4,000°C·d, with a mean value of 3,216°C·d. High values occur in the Gobi Altai region and the northern part of the Inner Mongolia Autonomous Region of China. During the study period, the region with high values exceeding 3,500°C·d gradually expanded to the south and east. The lowest values appeared in the northern part of the Khuvsgul Mountains, Khangai Mountains, and Khentii Mountains in Mongolia, the Greater Khingan Range in China, and the southern part of Russia. The thawing index varies greatly in the western part. In the northern part of the Inner Mongolia Autonomous Region, the high value region gradually expanded to the east over time. The lowest value gradually increased with time, and the thawing index showed an increasing trend, with significant increases in the Khangai and Khentii Mountain regions located in central Mongolia.

$$TDD = -0.10lon - 0.89lat - 0.76ele + 1.20\,(R^2 = 0.89) \quad (14)$$

The change in the thawing index on the Mongolian Plateau from 1901 to 2019 is opposite that of the freezing index, with an overall upward trend and a positive slope of 2.25°C·d/yr. According to the M–K mutation test (**Figure 5D**), the thawing index began to increase abruptly after 1995 (based on the 0.05 and 0.10 significance levels) (**Figure 5B**). The increasing trend from

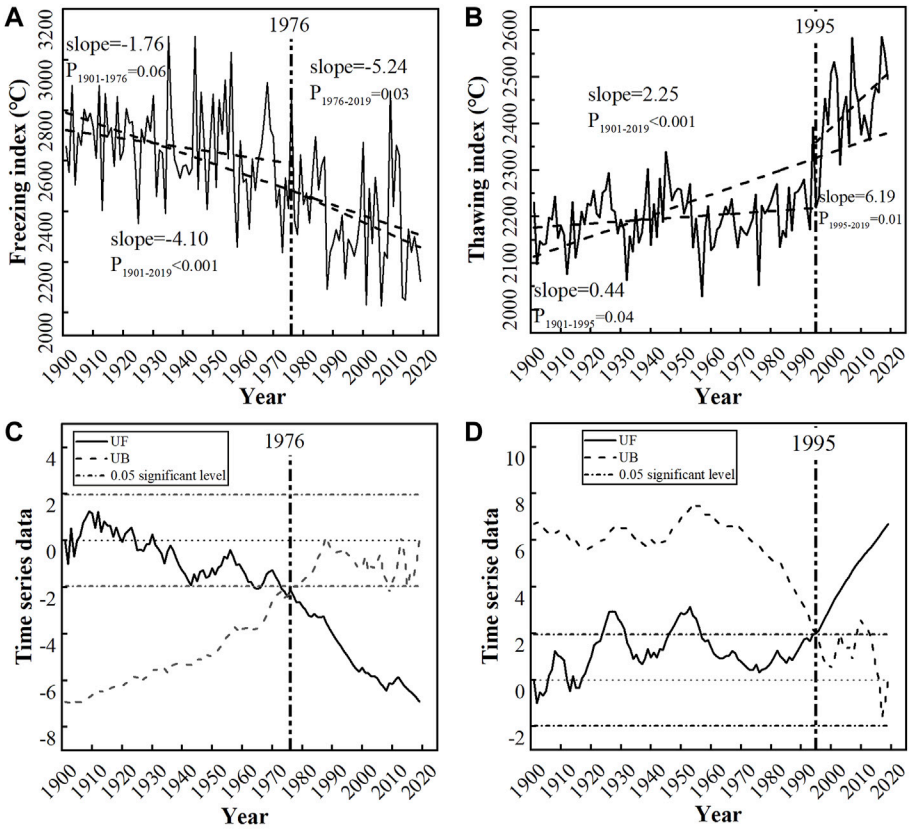

FIGURE 5 | Interannual variation in the freezing **(A)** and thawing **(B)** index and the change point of the freezing **(C)** and thawing **(D)** index from 1901 to 2019 on the Mongolian Plateau.

1901 to 1995 had a flat slope of 0.44°C·d/yr, whereas the increasing trend from 1995 to 2019 had a significantly steeper slope of 6.19°C·d/yr.

DISCUSSION

Freezing and Thawing Index Variation

The permafrost on the Mongolian Plateau is mainly distributed in the northern regions, especially in the northern alpine regions (**Figure 1A**). Sen's slope can reflect the interannual variation in the freezing and thawing index. The slope change in the air freezing index (**Figure 7**) shows that the largest freezing index occurs in the northern alpine regions, and the permafrost temperature increases rapidly in the Khuvsgul and Khangai Mountain regions (Kynicky et al., 2009; Zhao et al., 2010; Ishikawa et al., 2018; Munkhjargal et al., 2020; Dashtseren et al., 2021).

The climate determines the air thawing index, and most regions on the Mongolian Plateau exhibit trends consistent with global warming (Munkhjargal et al., 2020; Peng et al., 2020b). Although the change rates of regions listed in **Table 1** are based on different time periods and data sources, the thawing index values of the regions show increasing trends (Wu et al., 2011; Luo et al., 2014; Wang et al., 2019; Liao et al., 2021). The influence of latitude on the thawing index in this region is smaller than that in the Arctic Circle, which has simple topographic conditions and is more sensitive to climate warming (Johannessen et al., 2016) than the Mongolian Plateau (Shi et al., 2019). The influence of latitude of the thawing index on the Mongolian Plateau is greater than that on the Qinghai-Tibetan Plateau, which has high elevations and complex topographic conditions (Shi et al., 2019).

The spatial variation in the thawing index of the Mongolian Plateau is also affected by both latitude and altitude (Dashtseren et al., 2021), and the change in the thawing index in the low-latitude region is greater than that in the high-latitude region (**Figure 8**). The factors that may cause variations in the freezing and thawing index are elevation and solar radiation. Air temperature and solar radiation both gradually decrease with increasing elevation. In addition, the content of water vapor in the atmosphere may also be an influencing factor. For example, in the low-latitude regions with low water vapor content and weak solar radiation, the freezing index changes only slightly. The air freezing and thawing index changes reflect climate warming, which may accelerate permafrost degradation (Dashtseren et al., 2021).

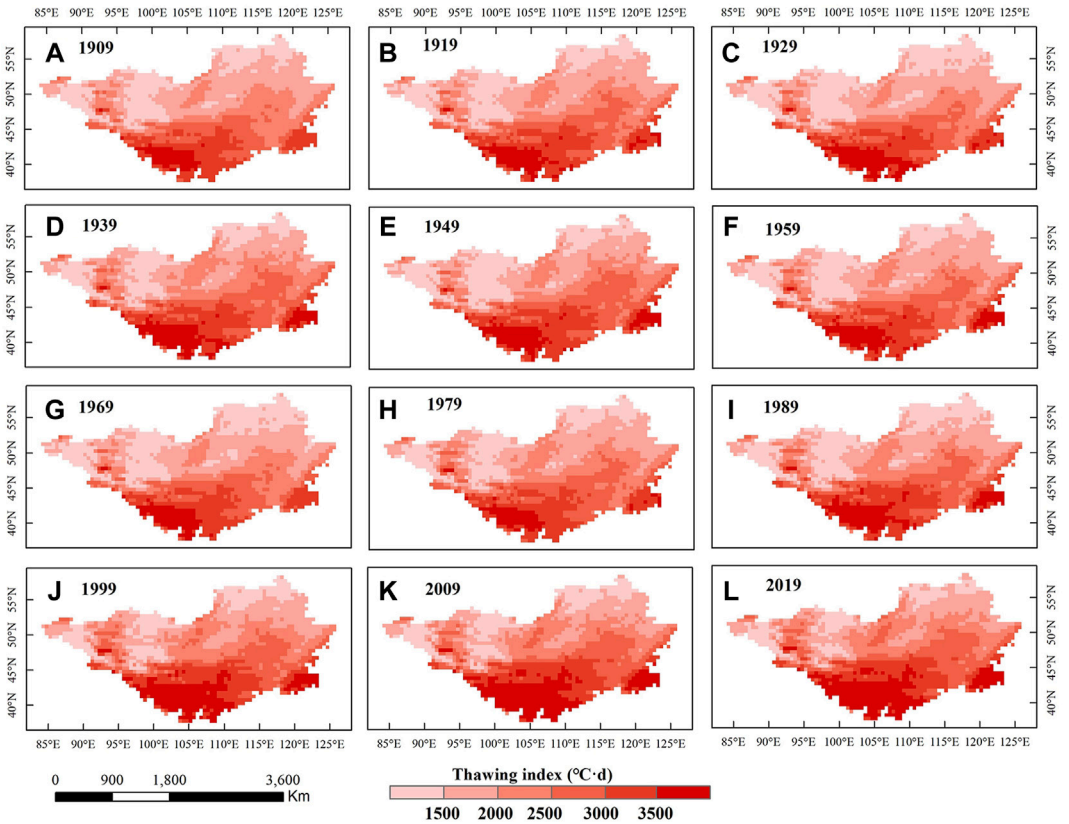

FIGURE 6 | Decadal spatial changes in the air thawing index on the Mongolian Plateau from 1901 to 2019. Labels like **(A–L)** represent the spatial variation of the air thawing index for each decade from 1901 to 2019.

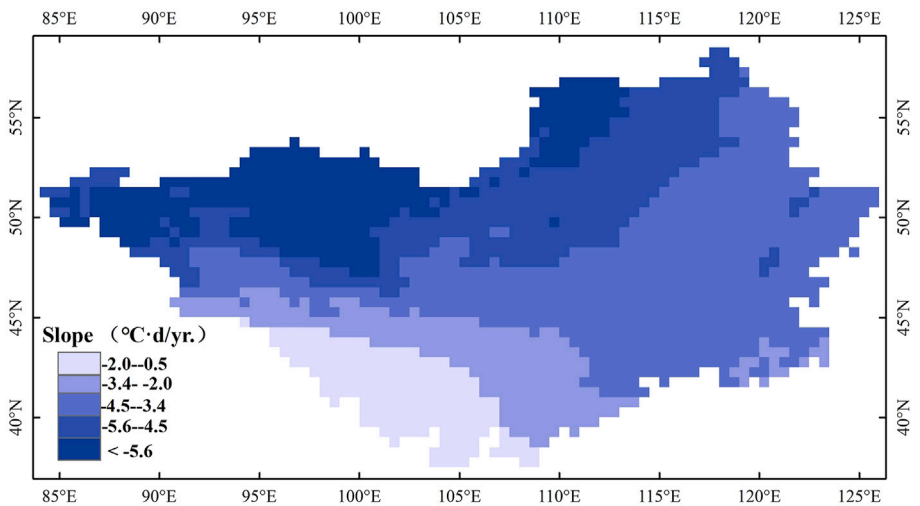

FIGURE 7 | Sen's slope of the freezing index over the Mongolian Plateau from 1901 to 2019.

Uncertainty Analysis

Climate change studies usually require long time series of meteorological data, but the low number and scattered nature of the meteorological stations and boreholes on the Mongolian Plateau make research difficult. Thus, we selected the CRU reanalysis dataset as the data source for analyzing the air freezing and thawing index.

TABLE 1 | Result comparison of thawing index variation in different regions.

Region	Thawing index	Dataset	Time series	Change rate	Literature
Qinghai-Tibet Plateau (QTP)	STI	ERA-Interim	1980–2013	3.75°C·d/yr	Qin et al. (2016)
	ATI	MEERA-2	1981–2017	4.20°C·d/yr	Qin et al. (2021)
	ATI	Observation data	1980–2013	9.3°C·d/yr	Wu et al. (2018)
	ATI	CRUNCEP	1901–2015	0.98°C·d/yr	Shi et al. (2019)
Northern Hemisphere	ATI	CRU, CIMP5	1950–2005	1.14°C·d/yr	Peng et al. (2019)
		Observation data	1980–2018	6.4°C·d/yr	Hu et al. (2021)
Circum-Arctic	ATI	CRUNCEP	1901–1989	0.90°C·d/yr	Shi et al. (2019)
			1989–2015	7.19°C·d/yr	
Mongolian Plateau	ATI	CRU reanalysis	1901–1994	0.44°C·d/yr	This study
			1995–2019	6.19°C·d/yr	
			1901–2019	2.55°C·d/yr	

[a]*STI: surface thawing index. ATI: air thawing index.*

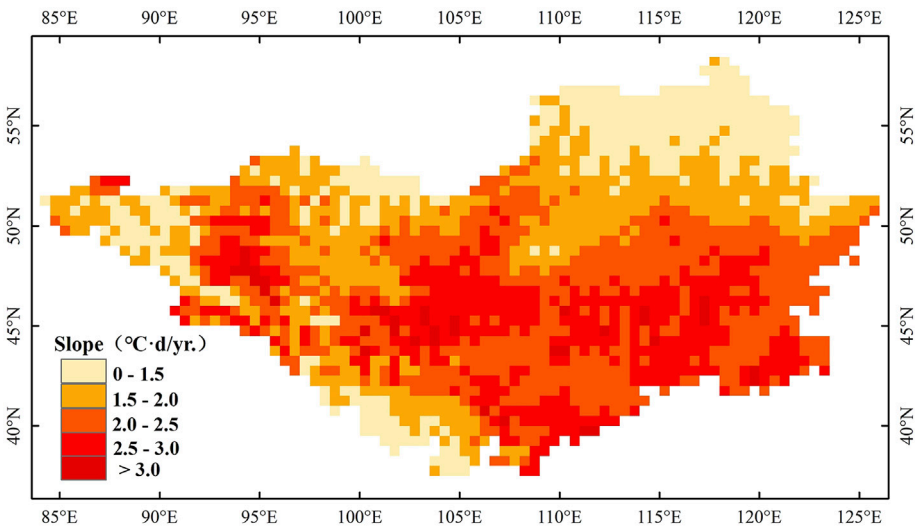

FIGURE 8 | Sen's slope of the thawing index on the Mongolian Plateau from 1901 to 2019.

However, we found that compared to the observed data, the CRU reanalysis data underestimate the air temperature. This may be caused by the fact that, first, the elevation of a grid cell in the CRU reanalysis is higher than that of the meteorological station. This may result in a difference because of the lapse rate of air temperature (Wang et al., 2018; Shi et al., 2019). Generally, the air temperature decreases with elevation at a rate of 0.65°C/100 m, but there will be differences among regions (Frauenfled et al., 2007; Wang et al., 2018). Second, the CRU reanalysis data are produced by integrating data from meteorological stations worldwide. The original uncertainty is present in the new reanalysis dataset (Harris et al., 2014). Third, the CRU reanalysis dataset still has shortcomings at a spatial resolution of 0.5 × 0.5, as each grid corresponds to actual spatial coverage of approximately 3,000 km^2 (Frauenfled et al., 2007; Chen et al., 2021), and the spatial representativeness is low. We checked the CRU quality based on a single station, and the deviations were inevitable.

There are also uncertainties in calculating the air freezing and thawing index (Frauenfeld et al., 2007; Chen et al., 2021). Since the CRU reanalysis data based on calculations in this paper provide monthly mean temperature data, the modification of the calculation formula will further increase the uncertainty of the freezing and thawing index results. Moreover, we use temperature data from January 1975 to December 2019 to perform a quality check of the CRU data using a dependence test due to a lack of comparable data, and thus the CRU reanalysis has uncertainty. The underestimation by the reanalysis data undoubtedly affects the air freezing and thawing index results. The air freezing and thawing index are very important for assessing the permafrost status on the Mongolian Plateau (Wu et al., 2011; Dashtseren et al., 2021; Gao et al., 2022). Therefore, improving data accuracy and reducing the uncertainty of the analysis results are of great importance for studying climate change and the permafrost environment (Frauenfled et al., 2007; Harris et al., 2014; Ran et al., 2015).

CONCLUSION

Based on CRU reanalysis data, we analyze the spatiotemporal variation in the air freezing and thawing index on the Mongolian Plateau from 1901 to 2019. We assess the reliability of CRU air

temperatures with data from 106 meteorological stations on the Mongolian Plateau. The correlation coefficient is 0.96, and the RMSE is approximately 0.80°C. The variation magnitudes of the freezing and thawing index on the Mongolian Plateau from 1901 to 2019 show a reversal in tendencies, and the long-term trends vary from −1.76 to −5.24°C·d/yr and from 0.44 to 6.19°C·d/yr, respectively. Notably, the thawing index experienced rapid increases after 1995. The spatial distributions of the freezing and thawing index are mainly affected by latitude and altitude. With increasing latitude, the freezing index increases from 600°C·d to 5,600°C·d, and the thawing index decreases from 4,500°C·d to 1,000°C·d. The northern alpine regions where permafrost exists show greater changes than the southern desert regions. Future studies are required to improve the spatial and temporal resolution of the air temperature data and their effects on the permafrost environment.

DATA AVAILABILITY STATEMENT

The original contributions presented in the study are included in the article/Supplementary Material, further inquiries can be directed to the corresponding author.

AUTHOR CONTRIBUTIONS

XM: Conceptualization, Methodology, Software, Investigation, Writing—original draft. TW: Conceptualization, Validation, Formal analysis, Visualization, Writing—review and editing. XZ, PL, DW, SA, DA, BD, JC, CS, AW, YL, XW, and RL: Writing—review and editing.

FUNDING

This research was funded by the National Natural Science Foundation of China (41961144021 and 3201101546), the National Key Research and Development Program of China (2020YFA0608501), and the West Light Foundation of Chinese Academy of Sciences.

ACKNOWLEDGMENTS

We would like to thank the Climatic Research Unit at the University of East Anglia, which provided the CRU dataset.

REFERENCES

Adiya, S., Dalantai, S., Wu, T., Wu, X., Yamkhin, J., Bao, Y., et al. (2021). Spatial and Temporal Change Patterns of Near-Surface CO2 and CH4 Concentrations in Different Permafrost Regions on the Mongolian Plateau from 2010 to 2017. *Sci. Total Environ.* 800, 149433. doi:10.1016/j.scitotenv.2021.149433

Biskaborn, B. K., Smith, S. L., Noetzli, J., Matthes, H., Vieira, G., Streletskiy, D. A., et al. (2019). Permafrost Is Warming at a Global Scale. *Nat. Commun.* 10 (1), 264–311. doi:10.1038/s41467-018-08240-4

Cao, B., Zhang, T., Peng, X., Zheng, L., Mu, C., and Wang, Q. (2015). Spatial Variability of Freezing-Thawing Index over the Heihe River Basin. *Adv. Earth Sci.* 30 (3), 357–366. doi:10.11867/j.issn.1001-8166.2015.03.0357

Chen, F., Luo, D., Liu, L., Jin, H., and Li, C. (2021). Variations of Air Freezing/thawing Index during 1901—2018 in the Three-River Source Region. *J. Glaciol. Geocryol.* 43 (2), 417–426. doi:10.7522/j.issn.1000-0240.2021.0015

Chen, J., Huang, W., Zhang, Q., and Feng, S. (2020). Origin of the Spatial Consistency of Summer Precipitation Variability between the Mongolian Plateau and the Mid-latitude East Asian Summer Monsoon Region. *Sci. China Earth Sci.* 63, 1199–1208. doi:10.1007/s11430-019-9593-2

Chen, R. H., Tabatabaeenejad, A., and Moghaddam, M. (2019). Retrieval of Permafrost Active Layer Properties Using Time-Series P-Band Radar Observations. *IEEE Trans. Geosci. Remote Sens.* 57 (8), 6037–6054. doi:10.1109/tgrs.2019.2903935

Cheng, G., and Wu, T. (2007). Responses of Permafrost to Climate Change and Their Environmental Significance, Qinghai-Tibet Plateau. *J. Geophys. Res.* 112, F02S03. doi:10.1029/2006JF000631

Cheng, G., Zhao, L., Li, R., Wu, X., Sheng, Y., Hu, G., et al. (2019). Characteristic, Changes and Impacts of Permafrost on Qinghai-Tibet Plateau. *Chin. Sci. Bull.* 64, 2783–2795. doi:10.1360/TB-2019-0191

Colombo, N., Salerno, F., Gruber, S., Freppaz, M., Williams, M., Fratianni, S., et al. (2018). Review: Impacts of Permafrost Degradation on Inorganic Chemistry of Surface Fresh Water. *Glob. Planet. change* 162, 69–83. doi:10.1016/j.gloplacha.2017.11.017

Dagvadorj, D., Natsagdorj, L., Dorjpurev, J., and Namkhainyam, B. (2009). *Assessment Report on Climate Change, Mongolia*. Mongolia, Ulaanbaatar, Mongolia: Published by Ministry of Environment, Nature and Tourism.

Dashtseren, A., Temuujin, K., Westermann, S., Batbold, A., Amarbayasgalan, Y., and Battogtokh, D. (2021). Spatial and Temporal Variations of Freezing and Thawing Indices from 1960 to 2020 in Mongolia. *Front. Earth Sci.* 9, 713498. doi:10.3389/feart.2021.713498

Frauenfeld, O. W., Zhang, T., and Mccreight, J. L. (2007). Northern Hemisphere Freezing/thawing Index Variations over the Twentieth Century. *Int. J. Climatol.* 27 (1), 47–63. doi:10.1002/joc.1372

Gao, H., Sa, C., Meng, F., Luo, M., Wang, M., Zhang, H., et al. (2022). Temporal and Spatial Characteristics of Permafrost on Mongolian Plateau from 2003 to 2019. *J. Arid Land Resour. Environ.* 26 (03), 99–106. doi:10.13448/j.cnki.jalre.2022.070

Guo, W., Liu, H., Anenkhonov, O. A., Shangguan, H., Sandanov, D. V., Korolyuk, A. Y., et al. (2018). Vegetation Can Strongly Regulate Permafrost Degradation at its Southern Edge through Changing Surface Freeze-Thaw Processes. *Agric. For. Meteorology* 252, 10–17. doi:10.1016/j.agrformet.2018.01.010

Hao, J., Wu, T., Li, R., Wu, X., Xie, C., Zhu, X., et al. (2020). A Case Study on Earthflow in Yushu, Qinghai Province on the Northeastern Tibetan Plateau: Landslide Features and Cause Analysis. *J. Glaciol. Geocryol.* 42 (2), 447–456. doi:10.7522/j.issn.1000-0240.2020.0022

Harris, I., Jones, P. D., Osborn, T. J., and Lister, D. H. (2014). Updated High-Resolution Grids of Monthly Climatic Observations - the CRU TS3.10 Dataset. *Int. J. Climatol.* 34 (3), 623–642. doi:10.1002/joc.3711

Heggem, E. S. F., Etzelmüller, B., Anarmaa, S., Sharkhuu, N., Goulden, C. E., and Nandinsetseg, B. (2006). Spatial Distribution of Ground Surface Temperatures and Active Layer Depths in the Hövsgöl Area, Northern Mongolia. *Permafr. Periglac. Process.* 17 (4), 357–369. doi:10.1002/ppp.568

Holloway, J. E., Lewkowicz, A. G., Douglas, T. A., Li, X., Turetsky, M. R., Baltzer, J. L., et al. (2020). Impact of Wildfire on Permafrost Landscapes: A Review of Recent Advances and Future Prospects. *Permafr. Periglac Process* 31 (3), 371–382. doi:10.1002/ppp.2048

Hu, G., Zhao, L., Wu, T., Wu, X., Park, H., Fedorov, A., et al. (2021). Spatiotemporal Variations and Regional Differences in Air Temperature in the Permafrost Regions in the Northern Hemisphere during 1980-2018. *Sci. Total Environ.* 791, 148358. doi:10.1016/j.scitotenv.2021.148358

Ishikawa, M., Jamvaljav, Y., Dashtseren, A., Sharkhuu, N., Davaa, G., Iijima, Y., et al. (2018). Thermal States, Responsiveness and Degradation of Marginal Permafrost in Mongolia. *Permafr. Periglac Process* 29 (4), 271–282. doi:10.1002/ppp.1990

Jiang, F.-q., Jilili, A.-w., Wang, S.-p., Hu, R.-j., and Li, X.-l. (2015). Annual Thawing and Freezing Indices Changes in the China Tianshan Mountains. *Reg. Environ. Change* 15 (2), 227–240. doi:10.1007/s10113-014-0610-3

Jiang, F., Hu, R., and Li, Z. (2008). Variations and Trends of the Freezing and Thawing Index along the Qinghai-Xizang Railway for 1966-2004. *J. Geogr. Sci.* 18 (1), 3–16. doi:10.1007/s11442-008-0003-y

Johannessen, O. M., Kuzmina, S. I., Bobylev, L. P., and Miles, M. W. (2016). Surface Air Temperature Variability and Trends in the Arctic: New Amplification Assessment and Regionalisation. *Tellus A Dyn. Meteorology Oceanogr.* 68 (1), 28234. doi:10.3402/tellusa.v68.28234

Juřička, D., Novotná, J., Houška, J., Pařílková, J., Hladký, J., Pecina, V., et al. (2020). Large-scale Permafrost Degradation as a Primary Factor in Larix Sibirica Forest Dieback in the Khentii Massif, Northern Mongolia. *J. For. Res.* 31 (1), 197–208. doi:10.1007/s11676-018-0866-4

Kendall, M. G. (1948). *Rank Correlation Methods*. Griffin: APAPsycNet.

Knoblauch, C., Beer, C., Liebner, S., Grigoriev, M. N., and Pfeiffer, E.-M. (2018). Methane Production as Key to the Greenhouse Gas Budget of Thawing Permafrost. *Nat. Clim. Change* 8 (4), 309–312. doi:10.1038/s41558-018-0095-z

Kynický, J., Brtnický, M., Vavříček, D., Bartošová, R., and Majigsuren, U. (2009). *Permafrost and Climatic Change in Mongolia*. Stara Lesna: Sustainable Development and Bioclimate 1.vyd.

Li, C., Sa, C., Liu, G., Wang, M., Meng, F., and Bao, Y. (2020). Spatiotemporal Changes of Snow Cover and its Response to Climate Changes in the Mongolian Plateau from 2000 to 2017. *Chin. J. Grassl.* 42 (02), 95–104. doi:10.16742/j.zgcdxb.20190300

Liao, Y., Li, Y., Fan, J., Galoie, M., and Motamedi, A. (2021). Spatiotemporal Variations of Freezing and Thawing Indices during the Past Four Decades in Tibet. *Front. Ecol. Evol.* 675 750961. doi:10.3389/fevo.2021.750961

Liu, L., and Luo, D. (2019). Spatial and Temporal Characteristics of Air/ground Freezing and Thawing Index in the Middle and Lower Reaches of the Yar ▪lung Zangbo River during 1977 -2017. *J. Glaciol. Geocryol.* 41 (4), 1–11. doi:10.7522/j.issn.1000-0240.2019.0048

Lü, J. J., Li, X. Z., Hu, Y. M., Wang, X. W., and Sun, J. (2008). Application of Frost Number Model in Northeast China Pepmafrost Regionalization. *Ying Yong Sheng Tai Xue Bao* 19 (10), 2271–2276. doi:10.13287/j.1001-9332.2008.0373

Luo, D., Jin, H., Jin, R., Yang, X., and Lü, L. (2014). Spatiotemporal Variations of Climate Warming in Northern Northeast China as Indicated by Freezing and Thawing Indices. *Quat. Int.* 349, 187–195. doi:10.1016/j.quaint.2014.06.064

Mann, H. B. (1945). Nonparametric Tests against Trend. *Econometrica* 13, 245–259. doi:10.2307/1907187

Munkhjargal, M., Yadamsuren, G., Yamkhin, J., and Menzel, L. (2020). Ground Surface Temperature Variability and Permafrost Distribution over Mountainous Terrain in Northern Mongolia. *Arct. Antarct. Alp. Res.* 52 (1), 13–26. doi:10.1080/15230430.2019.1704347

Ni, J., Wu, T., Zhao, L., Li, R., and Xie, C. (2019). Carbon Cycle in Arctic Permafrost Regions: Progress and Prospect. *J. Glaciol. Geocryol.* 41 (4), 845–857. doi:10.7522/j.issn.1000-0240.2019.0402

Obu, J., Westermann, S., Bartsch, A., Berdnikov, N., Christiansen, H. H., Dashtseren, A., et al. (2019). Northern Hemisphere Permafrost Map Based on TTOP Modelling for 2000-2016 at 1 Km2 Scale. *Earth-Science Rev.* 193, 299–316. doi:10.1016/j.earscirev.2019.04.023

Peng, X., Zhang, T., Frauenfeld, O. W., Du, R., Wei, Q., and Liang, B. (2020b). Soil Freeze Depth Variability across Eurasia during 1850–2100. *Clim. Change* 158 (3), 531–549. doi:10.1007/s10584-019-02586-4

Peng, X., Zhang, T., Frauenfeld, O. W., Wang, S., Qiao, L., Du, R., et al. (2020a). Northern Hemisphere Greening in Association with Warming Permafrost. *J. Geophys. Res. Biogeosciences* 125 (1), e2019JG005086. doi:10.1029/2019jg005086

Peng, X., Zhang, T., Liu, Y., and Luo, J. (2019). Past and Projected Freezing/thawing Indices in the Northern Hemisphere. *J. Appl. Meteorology Climatol.* 58 (3), 495–510. doi:10.1175/jamc-d-18-0266.1

Qi, Y., Li, S., Ran, Y., Wang, H., Wu, J., Lian, X., et al. (2021). Mapping Frozen Ground in the Qilian Mountains in 2004-2019 Using Google Earth Engine Cloud Computing. *Remote Sens.* 13 (1), 149. doi:10.3390/rs13010149

Qian, L. (2013). A Review of Studies on Permafrost Changes under Global Warming Background. *Jilin Meteorol.* 2013 (1), 25–28.

Qin, D., Zhou, B., and Xiao, C. (2014). Progress in Studies of Cryospheric Changes and Their Impacts on Climate of China. *J. Meteorol. Res.* 28 (5), 732–746. doi:10.1007/s13351-014-4029-z

Qin, Y., Wu, T., Li, R., Yu, W., Wang, T., Zhu, X., et al. (2016). Using ERA-Interim Reanalysis Dataset to Assess the Changes of Ground Surface Freezing and Thawing Condition on the Qinghai-Tibet Plateau. *Environ. Earth Sci.* 75 (9), 826. doi:10.1007/s12665-016-5633-2

Qin, Y., Wu, T., Zhang, P., Liu, W., Xue, S., and Guo, Z. (2021). Spatiotemporal Freeze-Thaw Variations over the Qinghai-Tibet Plateau 1981-2017 from Reanalysis. *Int. J. Climatol.* 41 (2), 1438–1454. doi:10.1002/joc.6849

Ran, Y., Li, X., Cheng, G., Nan, Z., Che, J., Sheng, Y., et al. (2021). Mapping the Permafrost Stability on the Tibetan Plateau for 2005-2015. *Sci. China Earth Sci.* 64, 62–79. doi:10.1007/s11430-020-9685-3

Ran, Y., Li, X., Jin, R., and Guo, J. (2015). Remote Sensing of the Mean Annual Surface Temperature and Surface Frost Number for Mapping Permafrost in China. *Arct. Antarct. Alp. Res.* 47 (2), 255–265. doi:10.1657/AAAR00C-13-306

Sharkhuu, N. (2003). "Recent Changes in the Permafrost of Mongolia," in Permafrost: Proceedings of the 8th International Conference on Permafrost, Zurich, Switzerland, July 21–25, 2003 (Ulaanbaatar, Mongolia: Institute of Geography, MAS), Vol. 2, 1029–1034.

Sharkhuu, N., Anarmaa, S., Romanovsky, V. E., Yoshikawa, K., Nelson, F. E., and Shiklomanov, N. I. (2008). "Thermal State of Permafrost in Mongolia," in Proceedings of the 9th International Conference on Permafrost, Fairbanks, AK, June 29–July 3, 2008, Vol. 2, 1633–1638.

Shi, Y., Niu, F., Lin, Z., and Luo, J. (2019). Freezing/thawing Index Variations over the Circum-Arctic from 1901 to 2015 and the Permafrost Extent. *Sci. Total Environ.* 660, 1294–1305. doi:10.1016/j.scitotenv.2019.01.121

Simmons, A. J., Jones, P. D., da Costa Bechtold, V., Beljaars, A. C. M., Kållberg, P. W., Saarinen, S., et al. (2004). Comparison of Trends and Low-Frequency Variability in CRU, ERA-40, and NCEP/NCAR Analyses of Surface Air Temperature. *J. Geophys. Res.* 109 (D24). doi:10.1029/2004JD005306

Sjöberg, Y., Siewert, M. B., Rudy, A. C., Paquette, M., Bouchard, F., Malenfant-Lepage, J., et al. (2020). Hot Trends and Impact in Permafrost Science. *Permafr. Periglac. Process.* 31 (4), 461–471. doi:10.1002/ppp.2047

Vaughan, D. G., Comiso, J. C., Allison, I., Carrasco, J., Kaser, G., Kwok, R., et al. (2014). "Observations: Cryosphere," in *Climate Change 2013: The Physical Science Basis. Contribution of Working Group I to the Fifth Assessment Report of the Intergovernmental Panel on Climate Change* (Cambridge, United Kingdom and New York, NY: Cambridge University Press).

Wang, L., Zhen, L., Liu, X., Ochirbat, B., and Wang, Q. (2008). Comparative Studies on Climate Changes and Influencing Factors in Central Mongolian Plateau Region. *Geogr. Res.* 27 (1), 171–180. doi:10.11821/yj2008010019

Wang, R., Zhu, Q., and Ma, H. (2019). Changes in Freezing and Thawing Indices over the Source Region of the Yellow River from 1980 to 2014. *J. For. Res.* 30 (1), 257–268. doi:10.1007/s11676-017-0589-y

Wang, Y., Wang, L., Li, X., and Chen, D. (2018). Temporal and Spatial Changes in Estimated Near-Surface Air Temperature Lapse Rates on Tibetan Plateau. *Int. J. Climatol.* 38 (7), 2907–2921. doi:10.1002/joc.5471

Wen, X., Wang, S., Zhu, J., and David, V. (2006). An Overview of China Climate Change over the 20th Century Using UK UEA/CRU High Resolution Grid Data. *Chin. Jo urnal Atmo sphe ric Sci.* 30 (5), 894–904. doi:10.3878/j.issn.1006-9895.2006.05.18

Wu, T., Qin, Y., Wu, X., Li, R., Zou, D., and Xie, C. (2018). Spatiotemporal Changes of Freezing/thawing Indices and Their Response to Recent Climate Change on the Qinghai–Tibet Plateau from 1980 to 2013. *Theor. Appl. Climatol.* 132 (3), 1187–1199. doi:10.1007/s00704-017-2157-y

Wu, T., Wang, Q., Zhao, L., Batkhishig, O., and Watanabe, M. (2011). Observed Trends in Surface Freezing/thawing Index over the Period 1987-2005 in Mongolia. *Cold Regions Sci. Technol.* 69 (1), 105–111. doi:10.1016/j.coldregions.2011.07.003

Yao, T., Qin, D., Shen, Y., Zhao, L., Wang, N., Lu, A., et al. (2013). Cryospheric Changes and Their Impacts on Regional Water Cycle and Ecological Conditions in the Qinghai-Tibetan Plateau. *Chin. J. Nat.* 35 (3), 179–186. doi:10.3969/j.issn.0253-9608.2013.03.004

You, Q., Kang, S., Pepin, N., Flügel, W.-A., Sanchez-Lorenzo, A., Yan, Y., et al. (2010). Climate Warming and Associated Changes in Atmospheric Circulation in the Eastern and Central Tibetan Plateau from a Homogenized Dataset. *Glob. Planet. Change* 72 (1-2), 11–24. doi:10.1016/j.gloplacha.2010.04.003

Yu, W. J. (2017). *Spatiotemporal Variations of Evapotranspiration Based on Multi-Sources Data in Mongolia*. Lanzhou: Northwest Institute of Eco-Environment and Resources, Chinese Academy of Sciences.

Zhang, F., Mu, M., Fan, C., Jia, L., Mu, C., Zhao, L., et al. (2020). Studies of Permafrost Carbon Cycle in the Third Polar and Arctic Regions. *J. Glaciol. Geocryol.* 42 (1), 170–181. doi:10.7522/jissn.1000-0240.2020.0005

Zhao, L., Wu, Q., Marchenko, S. S., and Sharkhuu, N. (2010). Thermal State of Permafrost and Active Layer in Central Asia during the International Polar Year. *Permafr. Periglac. Process.* 21 (2), 198–207. doi:10.1002/ppp.688

Zhao, T., and Fu, C. (2006). Comparison of Products from ERA-40, NCEP-2, and CRU with Station Data for Summer Precipitation over China. *Adv. Atmos. Sci.* 23 (4), 593–604. doi:10.1007/s00376-006-0593-1

Zhou, X., Shi, H., Wang, X., and Meng, F. (2012). Study on the Temporal and Spatial Dynamic Changes of Land Use and Driving Forces Analysis of Mongolia Plateau in Recent 30 Years. *Acta Agric. Zhejianggensis* 24 (6), 1102–1110.

Zorigt, M., Myagmar, K., Orkhonselenge, A., van Beek, E., Kwadijk, J., Tsogtbayar, J., et al. (2020). Modeling Permafrost Distribution over the River Basins of Mongolia Using Remote Sensing and Analytical Approaches. *Environ. Earth Sci.* 79 (12), 1–11. doi:10.1007/s12665-020-09055-7

Conflict of Interest: The authors declare that the research was conducted in the absence of any commercial or financial relationships that could be construed as a potential conflict of interest.

frontiers | Frontiers in Environmental Science

ORIGINAL RESEARCH
published: 26 May 2022
doi: 10.3389/fenvs.2022.888937

Observed Changes in Extreme Temperature and Precipitation Indices on the Qinghai-Tibet Plateau, 1960–2016

Xiangwen Gong[1,2,3,4], *Xuyang Wang*[1,2,5]*, *Yuqiang Li*[1,2,5], *Lei Ma*[3,4], *Manyi Li*[3,4] and *Hongtao Si*[3,4]

[1]Northwest Institute of Eco-Environment and Resources, Chinese Academy of Sciences, Lanzhou, China, [2]School of Resources and Environment, University of Chinese Academy of Sciences, Beijing, China, [3]Observation and Research Station of Ecological Restoration for Chongqing Typical Mining Areas, Ministry of Natural Resources, Chongqing Institute of Geology and Mineral Resources, Chongqing, China, [4]Wansheng Mining Area Ecological Environment Protection and Restoration of Chongqing Observation and Research Station, Chongqing Institute of Geology and Mineral Resources, Chongqing, China, [5]Naiman Desertification Research Station, Northwest Institute of Eco-Environment and Resources, Chinese Academy of Sciences, Tongliao, China

OPEN ACCESS

Edited by:
Cuicui Mu,
Lanzhou University, China

Reviewed by:
Oluwafemi E. Adeyeri,
City University of Hong Kong, Hong Kong SAR, China
Ping Wang,
Institute of Geographic Sciences and Natural Resources Research (CAS), China

***Correspondence:**
Xuyang Wang
xuyangwang@lzb.ac.cn

Specialty section:
This article was submitted to Atmosphere and Climate, a section of the journal Frontiers in Environmental Science

Received: 03 March 2022
Accepted: 29 April 2022
Published: 26 May 2022

Citation:
Gong X, Wang X, Li Y, Ma L, Li M and Si H (2022) Observed Changes in Extreme Temperature and Precipitation Indices on the Qinghai-Tibet Plateau, 1960–2016. Front. Environ. Sci. 10:888937. doi: 10.3389/fenvs.2022.888937

The Qinghai-Tibet Plateau (QTP), also known as the Earth's "third pole," is sensitive to climate change due to its extensive areas at high elevation, which are presently dominated by snow and ice. Based on daily observations from 1960 to 2016 at 94 meteorological stations, we quantified and compared changes in climate extremes on China's QTP using 16 extreme temperature indices and 11 extreme precipitation indices, which calculated using colder (1961–1990) and warmer (1988–2016) base periods, respectively. The study showed that when a warmer base period is used, the trend magnitude of the cold temperature indices is amplified, while the trend magnitude of the warm temperature indices and the percentile-based precipitation indices are diminished. The regionally averaged temperature index trends were consistent with global warming, namely warmth indices such as the number of warm days, warm nights, summer days, and tropical nights all showed significant increases. However, the cold indices, such as the number of cool days, cool nights, ice days, and frost days, decreased significantly. The number of frost days and ice days decreased the fastest (3.9 and 2.9 days/decade, respectively), while the length of the growing season increased the fastest (2.9 days/decade). The warming trend strengthened with increasing latitude, and the occurrences of daytime extreme temperature events increased with increasing longitude. In addition, cold temperature events increased in frequency and intensity at high elevations, while warm temperature events decreased. We also found that average monthly maximum 1-day precipitation and maximum consecutive 5-day precipitation increased by 0.1 and 0.3 mm per decade, respectively. Extreme precipitation occurrences were more common in places with low latitudes and high longitudes. The strengthening Subtropical High Area (SHA) and Subtropical High Intensity (SHI), Westward movement of Subtropical High Western Ridge Point (SHW) have contributed to the changes in climate extremes on the Qinghai-Tibet Plateau. The study's findings will provide a more comprehensive reference for predicting

the occurrence of extreme events and improving the region's disaster prevention capability.

Keywords: climate extreme indices, precipitation, temperature, atmospheric circulation, qinghai-tibet plateau

1 INTRODUCTION

Global warming has become an indisputable fact. The sixth assessment report released by the Intergovernmental Panel on Climate Change (IPCC) stated that the global average surface air temperature observed from 2010 to 2019 increased by 1.06°C (with a range from 0.88 to 1.21°C) compared to the period from 1850 to 1900 (Eyring et al., 2021). It is generally believed that changes in the frequency or intensity of extreme weather and climate events would have greater impacts on both human society and natural systems than changes in the mean climate variables (Patz et al., 2005; McMichael et al., 2006; Thornton et al., 2014). According to the IPCC (2022), human-induced climate change, including more frequent and intense extreme events, has caused widespread adverse impacts and related losses and damages to nature and people, beyond natural climate variability. The rise in weather and climate extremes has led to some irreversible impacts as natural and human systems are pushed beyond their ability to adapt.

To improve this understanding, increasing attention has focused on the changes of temperature and precipitation extremes around the world. On a global scale, it has been confirmed that changes in climatic extremes impacted a considerable amount of the global geographical area during the second half of the 20th century (Frich et al., 2002). As a result of the warming, during the 20th century, there were widespread dramatic shifts in temperature extremes, especially for indices derived from the daily minimum temperature. Simultaneously, extreme precipitation changes revealed a widespread and considerable rise, but they were less geographically consistent than temperature increases (Alexander et al., 2006). In addition, changes in temperature extremes differed between paired urban and non-urban sites at a global scale, changes in extreme precipitation indices for matched urban and non-urban stations indicated no substantial distinction (Mishra et al., 2015).

Various regional research on temperature and precipitation extreme indices have been carried out in various areas, including the Central and South America (Aguilar et al., 2005; Haylock et al., 2006; Skansi et al., 2013), Europe (Klein Tank and Können, 2003), Asia-Pacific region (Griffiths et al., 2005), the Arabian Peninsula (Alsarmi and Washington, 2014), Africa (New et al., 2006; Dike et al., 2020), Central and South Asia (Klein Tank et al., 2006), and Georgia (Keggenhoff et al., 2014). These findings provide strong evidence that global warming is the primary factor causing significant changes in temperature and precipitation extremes, and the changes showed large regional variability because the magnitude and characteristics of climate change vary across geographically diverse regions. Extreme precipitation indices, such as the intensity and frequency of extreme precipitation events or the number of days with extreme precipitation and heavy precipitation events, have increased significantly in recent decades in the United States (Karl et al., 1995; Karl et al., 1996; Griffiths and Bradley 2007; Pryor et al., 2009), central India (Goswami et al., 2006), Japan (Iwashima and Yamamoto, 1993), southern Africa (Mason et al., 1999), and Bulgaria (Bocheva et al., 2009). However, extreme precipitation events have decreased in Germany (Tromel and Schonwiese, 2007), Poland (Lupikasza, 2009), and the Iberian Peninsula (Rodrigo, 2009). Thus, regional differences in temperature and precipitation extremes have been observed, implying an urgent need to improve regional studies of spatial and temporal trends in extreme climate events based on field observations.

In China, various regional studies on severe temperature and precipitation indices have been undertaken, and the results showed that global warming was generating major changes in temperature and precipitation extremes. These results generally showed that extreme cold indices, such as the number of frost days, cold days, and cold nights, have decreased in frequency and intensity, while warmth indices, such as the number of summer days, warm days, and warm nights, have increased, with varying magnitudes across China's diverse regions (Li et al., 2011; Zhen and Li, 2014; Guan et al., 2015; Zhong et al., 2017). In northeastern, northwestern, and central China, the numbers of extreme precipitation events have declined, but have increased in northern, southwestern, and southern China (Lu et al., 2014; Li et al., 2015; Sun et al., 2016). All these variables showed regional disparities in change, demonstrating the need and practicality of researching the response to catastrophic climate events from a regional viewpoint (You et al., 2011). Unfortunately, the IPCC Assessment Report (Houghton et al., 2001) stated that China is a data-poor region, making it difficult to describe global precipitation trends from 1976 to 1999. As a result, providing more regional analysis for climate extremes and covering a longer period is becoming increasingly important.

The Qinghai-Tibet Plateau (QTP) is a giant Chinese geomorphological unit, and lies at the highest elevation of any plateau in the world. It has a unique natural environment and high spatial differentiation. The tectonic uplift of the plateau has profoundly affected the evolution of its natural environment and of adjacent areas, and climate change on the plateau is closely related to global environmental changes (Zheng, 1999). Therefore, the QTP is a "global climatic change's driver and amplifier" (Pan and Li, 1996) and "the best natural laboratory for unified research on global change and Earth system science" (Bi, 1997). In recent years, a series of studies have been carried out on the QTP, focusing on the climate dynamic characteristics. For example, Liu and Chen (2000) examined station surface air temperature records and discovered that the majority of the QTP has warmed

statistically since the mid-1950s. Wang et al. (2008) found that surface air temperature on the QTP increased by about 1.8°C during 1960–2007, or 0.36°C per decade. Li and Chi (2014) evaluated the thermal comfort and its changes in the QTP over the last 50 years using the physiological equivalent temperature, and revealed that annual cumulative number of thermally favorable days has been increasing, and that of cold stress has been reducing. Zhang et al. (2016) reported that showed QTP shows warm wet climate change dominated by temperature and humidity increase during 1971–2010. Wang et al. (2017) found that annual temperature on the QTP increased at a 0.42°C decade^{-1} rate from 1979 to 2012, with a 0.48°C decade^{-1} increase in the winter. Warming has clearly occurred over the QTP in recent decades, and the rate of warming on the QTP exceeds the averages for the Northern Hemisphere and the same latitudinal zone (Liu and Chen, 2000).

In comparison, extreme climate events on the QTP have not been widely studied, especially in terms of the regional variation of temperature and precipitation extremes and its change mechanism across the entire study area. A few extreme temperature studies have been conducted on the QTP, for example, You et al. (2008) reported that during 1961–2005 in the eastern and central QTP, the regional occurrence of extreme warm days and nights has increased by 1.26 and 2.54 days decade^{-1}, and cold days and nights decreased by −0.85 and −2.38 days decade^{-1}, respectively. Cuo et al. (2013) found that during 1957–2009 the mean minimum and maximum temperatures in the northern part of the QTP increased by 0.04 and 0.03°C year^{-1}, respectively. Wang et al. (2013) confirmed that during 1973–2011 most warm-related indices of temperature extremes increase while cold-related indices show opposite trends over the western QTP. Ding et al. (2018) investigated the spatiotemporal distributions of 10 temperature extremes over the major river basins on the QTP from 1963 to 2015, and discovered that the warming rates of annual temperature extremes do not appear to be strongly influenced by elevation on the QTP. These studies concentrated on the QTP's sub-regions, but because of the different time periods and datasets used, it is difficult to infer regional variations in temperature extremes from these studies. Furthermore, research on the temporal and spatial dynamics of precipitation extremes in this region is lacking.

The World Meteorological Organization Commission for Climatology's Expert Team on Climate Change Detection, Monitoring, and Indicators, as well as the Climate Variability and Predictability project, have developed a set of indices (Peterson et al., 2001) that serve as a common guideline for regional climate analysis. The aim of this study is to use field-measured values of these indices to gain a better knowledge of recent changes in climate severe event variability, severity, frequency, and duration across the entire QTP. To do so, we analyzed temperature and precipitation extreme indices based on data from numerous meteorological stations in the region. We hypothesized that both temperature and precipitation extreme indices on the plateau would show significant long-term trends, and that these trends would exhibit spatial variation related to variations in the plateau's geographic characteristics, and the temporal variations are mainly associated with atmospheric circulation patterns.

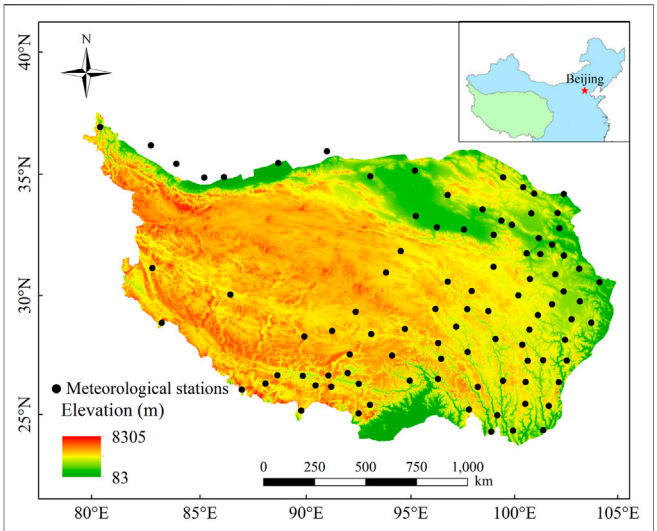

FIGURE 1 | Study area and the distribution of meteorological stations. A total of 89 meteorological stations were located within the Qinghai-Tibet Plateau, and 5 stations were in areas surrounding the plateau.

2 DATA AND METHODS

2.1 Study Area

We defined the boundary of the QTP based on the system for defining China's physical and geographical regions (Zheng, 1996). The plateau is situated in southwestern China (**Figure 1**), where it covers an area of 2,603,431 km^2. The elevation is generally greater than 4,000 m. The plateau is surrounded by high and extensive mountain ranges interlaced with valleys and basins. The northwest is generally cold and dry, while the southeast is warm and wet. Across the entire QTP, the annual average temperature ranging from −5.6 to 17.6°C across the region, and the temperature difference between day and night ranges from 14 to 17°C. The precipitation distribution is uneven, with annual precipitation averaging more than 2000 mm in the southeast and approximately 17.6 mm in the northwest (Zhang et al., 2017). The annual average wind speed is generally greater than 3.0 m s^{-1} in the northwest, with more than 50 gale days (i.e., a wind speed ≥17 m s^{-1}) annually (Li et al., 2001).

2.2 Data and Quality Control

We collected quality-controlled meteorological data from 94 meteorological stations over the QTP, including daily maximum and minimum temperatures, as well as daily precipitation (**Figure 1**). The National Climate Center of the China Meteorological Administration (http://data.cma.cn) provided the data from 1960 to 2016 (the most recent

TABLE 1 | List of the temperature and precipitation indices used in this study, which were defined by the Expert Team on Climate Change Detection and Indices (http://etccdi.pacificclimate.org/list_27_indices.shtml).

Index	Description	Definition	Unit
FD	Frost days	Annual count for days when the minimum temperature (TN) < 0°C	Days
SU	Summer days	Annual count for days when the maximum temperature (TX) > 25°C	Days
ID	Ice days	Annual count for days when TX < 0°C	Days
TR	Tropical nights	Annual count for days when TN > 20°C	Days
TXx	Maximum TX	Monthly maximum value of TX	°C
TNx	Maximum TN	Monthly maximum value of TN	°C
TXn	Min TX	Monthly minimum value of TX	°C
TNn	Min TN	Monthly minimum value of TN	°C
TN10p	Cool nights	Percentage of days when TN < 10th percentile	%
TX10p	Cool days	Percentage of days when TX < 10th percentile	%
TN90p	Warm nights	Percentage of days when TN > 90th percentile	%
TX90p	Warm days	Percentage of days when TX > 90th percentile	%
WSDI	Warm spell duration indicator	Annual count of the number of periods with at least 6 consecutive days when TX > 90th percentile	Days
CSDI	Cold spell duration indicator	Annual count of the number of periods with at least 6 consecutive days when TN < 10th percentile	Days
GSL	Growing season length	Annual count between first span after 1 January of at least 6 days with daily mean temperature (TM) > 5°C and first span after 1 July of 6 days with TM < 5°C	Days
DTR	Diurnal temperature range	Monthly mean difference between TX and TN	°C
RX1day	Maximum 1-day precipitation amount	Monthly maximum 1-day precipitation	mm
Rx5day	Maximum 5-day precipitation amount	Monthly maximum consecutive 5-day precipitation	mm
SDII	Simple daily intensity index	Annual total precipitation divided by the number of wet days (defined as daily precipitation (PRCP)≥1.0 mm) in the year	mm/day
R10mm	Number of heavy precipitation days	Annual count of days when PRCP ≥ 10 mm	Days
R20mm	Number of very heavy precipitation days	Annual count of days when PRCP ≥ 20 mm	Days
R50mm	Number of days above 50 mm	Annual count of days when PRCP ≥ 50 mm	Days
CDD	Consecutive dry days	Maximum number of consecutive days with daily rainfall < 1 mm	Days
CWD	Consecutive wet days	Maximum number of consecutive days with daily rainfall ≥ 1 mm	Days
R95PTOT	Very wet days	Annual total PRCP for days when daily rainfall > 95th percentile	mm
R99pTOT	Extremely wet days	Annual total PRCP for days when daily rainfall > 99th percentile	mm
PRCPTOT	Annual total wet-day precipitation	Annual total PRCP in wet days (daily rainfall ≥ 1 mm)	mm

data available) was obtained. Due to strict quality control, it includes: 1) Climatic limit value or allowable value check, 2) station extreme value check, 3) internal consistency check between timing value, daily average and daily extreme value, 4) time consistency check, 5) space Consistency check, 6) manual verification and correction, the quality and integrity of the data set are greatly improved. To further ensure data quality, 1) we replaced all missing values with an internal format recognized by the R statistical software (i.e., NA, for not available), and 2) replaced all unreasonable values with NA. Unreasonable values include 1) a daily rainfall that was less than 0 mm and 2) a daily minimum temperature that was higher than the daily maximum temperature. We also found outliers in daily maximum and minimum temperatures, which we characterized as daily values that were outside of a range specified as n times the standard deviation (STD) of that day's value. In this study, we defined that threshold as the mean plus or minus 5 STD based on the criteria used in previous studies (Rusticucci and Barrucand, 2004; Haylock et al., 2008; Croitoru and Piticar, 2013).

Non-climatic effects such as weather station relocation, land use changes, instrument adjustments, and observational hours can all have an impact on observed climate data (Peterson et al., 1998; Aguilar et al., 2003). These effects cause inhomogeneity, resulting in a shift in the mean of a time series, which can lead to first order autoregressive errors. To detect and adjust first-order autoregressive errors produced by shifts, we utilized version 4 of the RHtests program created by Wang and Feng at the Climate Research Branch of the Meteorological Service of Canada (http://etccdi.pacificclimate.org/software.shtml). The penalized maximum t test (Wang et al., 2007) and the penalized maximal *F* test (Wang, 2008b) were used in the RHtests package, which are incorporated in a recursive testing algorithm that adjusts empirically for an autocorrelation with a lag of –1 (if any) in the time series (Wang, 2008a). The default parameters in RHtests packages were used to detect and adjust for a whole data series in each station at the 0.05 significance level. RHtests packages can detect possible single or multiple change-points in a time series, and confirmed step changes can be adjusted (Wang et al., 2013). Once a possible change has been identified, the metadata (including documented station relocation and instrument update) should be checked to identify any potentially valid explanations. Notably, a homogenous time series that is well correlated with the base series may be used as a reference series. When a homogenous reference series is not available, the RHtestsV4 package can detect changepoints. However, the results are less reliable and require further investigation. Data homogenization should not be performed automatically without the use of a reference series

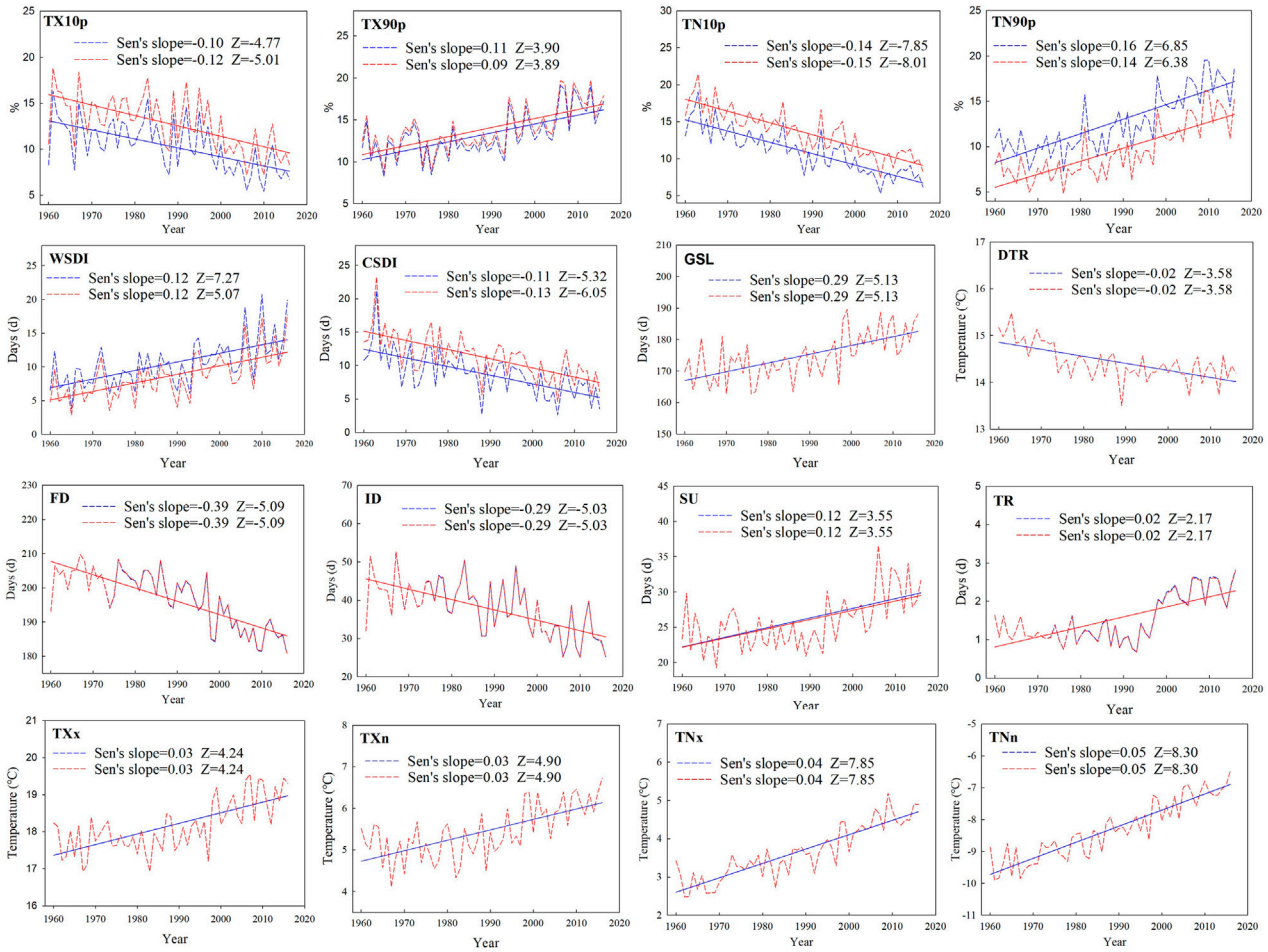

FIGURE 2 | Regionally averaged time series for the extreme temperature indices on the Qinghai-Tibet Plateau from 1960 to 2016. The indices are defined in **Table 1**. The red and blue dashed lines represent the different base periods of which the percentiles were derived, 1988–2016 (warmer) and 1961–1990 (colder) respectively. Solid red and blue lines denote the linear trends for both base periods.

(i.e., without intensive manual analysis of the statistical test results). Furthermore, because the time series being tested may have a zero trend or a linear trend over the entire period of record. The problem of uneven distribution of false alarm rate and detection power is also greatly alleviated by using empirical penalty functions. As a result, RHtestsV4 (and RHtestsV3 and RHtestsV2) outperforms RHtestsV0.95, which did not account for autocorrelation and did not address the problem of uneven distribution of false alarm rate and detection power (Wang et al., 2007; Wang, 2008b).

2.3 Index Calculations

The climatic extreme indices were computed using the RClimDex program created by Xuebin Zhang and Feng Yang of the Canadian Meteorological Service (Zhang and Yang, 2004). To investigate the problematic impact of using a different base period (colder 1961–1990 vs. warmer 1988–2016) on the extreme temperature and precipitation indices, as well as the corresponding trend magnitude. The current study's extreme indices (16 temperature and 11 precipitation indices; **Table 1**) were calculated using two different base periods for comparison. The first base period was the 1961–1990 standard normal period (WMO, 2017). The second base period lasted from 1988 to 2016. The first base period represents a relatively cold period, whereas the second base period represents a significantly warmer period (Yosef et al., 2021). In recent years, these indices have been widely applied to assess variations in temperature and precipitation extremes for different regions of the world (Croitoru et al., 2016; Filahi et al., 2016; Sun et al., 2016; Supari et al., 2017; Gbode et al., 2019). **Table 1** provides a brief description of each index. Based on how the temperature indices are computed, they can be further grouped into four categories (Croitoru and Piticar, 2013; Wang et al., 2018). The absolute indices are defined based on a fixed threshold for the recorded temperature, and comprise the number of summer days (SU), frost days (FD), ice days (ID), and tropical nights (TR). The percentile-based threshold indices comprise the number of cool nights (TN10p), cool days (TX10p), warm nights (TN90p), warm days (TX90p), warm and cold spell durations (WSDI and CSDI), which were identified using percentile-based thresholds (with values of 10 and 90% for the

TABLE 2 | The correlation matrix (Spearman's correlation coefficient) for the relationships among the extreme-temperature indices in the Qinghai-Tibet Plateau from 1960 to 2016. Note: ** represents significance at $p < 0.01$. All other values are not significant. Index names are defined in **Table 1**.

Indices	FD	SU	ID	TR	TX10p	TX90p	TN10p	TN90p	TXx	TXn	TNx	TNn	GSL	WSDI	CSDI	DTR
FD	1															
SU	−0.56**	1														
ID	0.71**	−0.46**	1													
TR	−0.63**	0.64**	−0.53**	1												
TX10p	0.66**	−0.46**	0.97**	−0.55**	1											
TX90p	−0.63**	0.93**	−0.52**	0.65**	−0.53**	1										
TN10p	0.79**	−0.47**	0.84**	−0.57**	0.83**	−0.59**	1									
TN90p	−0.83**	0.64**	−0.64**	0.66**	−0.60**	0.74**	−0.77**	1								
TXx	−0.80**	0.64**	−0.85**	0.57**	−0.85**	0.71**	−0.79**	0.73**	1							
TXn	−0.77**	0.67**	−0.83**	0.59**	−0.79**	0.67**	−0.76**	0.69**	0.83**	1						
TNx	−0.90**	0.59**	−0.75**	0.61**	−0.72**	0.70**	−0.89**	0.86**	0.86**	0.74**	1					
TNn	−0.89**	0.55**	−0.79**	0.59**	−0.75**	0.64**	−0.93**	0.87**	0.81**	0.80**	0.93**	1				
GSL	−0.85**	0.63**	−0.57**	0.45**	−0.51**	0.66**	−0.62**	0.69**	0.77**	0.70**	0.78**	0.73**	1			
WSDI	−0.47**	0.82**	−0.40**	0.52**	−0.40**	0.84**	−0.50**	0.65**	0.60**	0.52**	0.62**	0.58**	0.58**	1		
CSDI	0.60**	−0.44**	0.72**	−0.46**	0.76**	−0.54**	0.83**	−0.56**	−0.71**	−0.62**	−0.71**	−0.71**	−0.49**	−0.49**	1	
DTR	0.42**	−0.02	0.06	−0.22	0.04	−0.12	0.49**	−.50**	−0.10	−0.02	−0.50**	−0.50**	−0.24	−0.16	0.31*	1

lower and upper bounds, respectively). The extremal indices comprise indices computed based on the absolute values observed in the area without taking any thresholds into account: the monthly maximum value of the daily maximum temperature (TXx), monthly maximum value of daily minimum temperature (TNx), monthly minimum value of the daily maximum temperature (TXn), and monthly minimum value of daily minimum temperature (TNn). The last category extremes include the growing season length (GSL) and diurnal temperature range (DTR). The precipitation indices are divided into 2 percentile, 3 thresholds, 2 durations, 2 extremal values, and 2 additional indices, with 1 dry index and 10 wet indices (Powell and Keim, 2015).

2.4 Atmospheric Circulation Patterns

The monthly Arctic Oscillation (AO), North Atlantic Oscillation (NAO), Southern Oscillation Index (SOI), and Pacific Decadal Oscillation (PDO) data from 1960 to 2016 were available from the National Oceanic and Atmospheric Administration (http://www.esrl.noaa.gov/psd/data/climateindices/list/). In addition, the monthly West Pacific Subtropical High Index (WPSHI), including the Subtropical High Area (SHA) index, Subtropical High Intensity (SHI) index, Subtropical High Ridge Line (SHR) index, and Subtropical High Western Ridge Point (SHW) index, which obtained from the Climate Diagnostics and Prediction Division, National Climate Center, China Meteorological Administration (http://cmdp.ncc-cma.net/Monitoring/). SHW and SHR indicate the location and direction of Western Ridge Point and Ridge Line. When the Western Ridge Point is located further east, the SHW will increase; and when the Subtropical High Ridge Line is located further north, the SHR will increase.

2.5 Analytical Methods

Time series data is often influenced by previous observations. When data is not random and influenced by autocorrelation, modified Mann-Kendall (MMK) tests may be used for trend detction studies. Hamed and Rao (1998) have proposed a variance correction approach to address the issue of serial correlation in trend analysis. Data are initially detrended and the effective sample size is calculated using the ranks of significant serial correlation coefficients which are then used to correct the inflated (or deflated) variance of the test statistic. Therefore, the MMK test was performed to analyze the time series trends for the climate indices at each meteorological station in this study, and the magnitude of the trends was calculated using the Sen's slope estimator (Sen, 1968). A trend is considered significant if it is statistically significant at the 5% level. This trend analysis was conducted using Hamed and Rao Modified MK Test in python package "pyMannKendall" (Hussain and Mahmud, 2019). To characterize the spatial pattern of trends in the climatic indices, we utilized the data visualization in version 10.3 of the ArcMap software (http://www.esri.com). We employed Spearman's correlation coefficient to find significant relationships among the extremal variables. Partial correlation coefficient was used to detect significant relationships between extreme climate

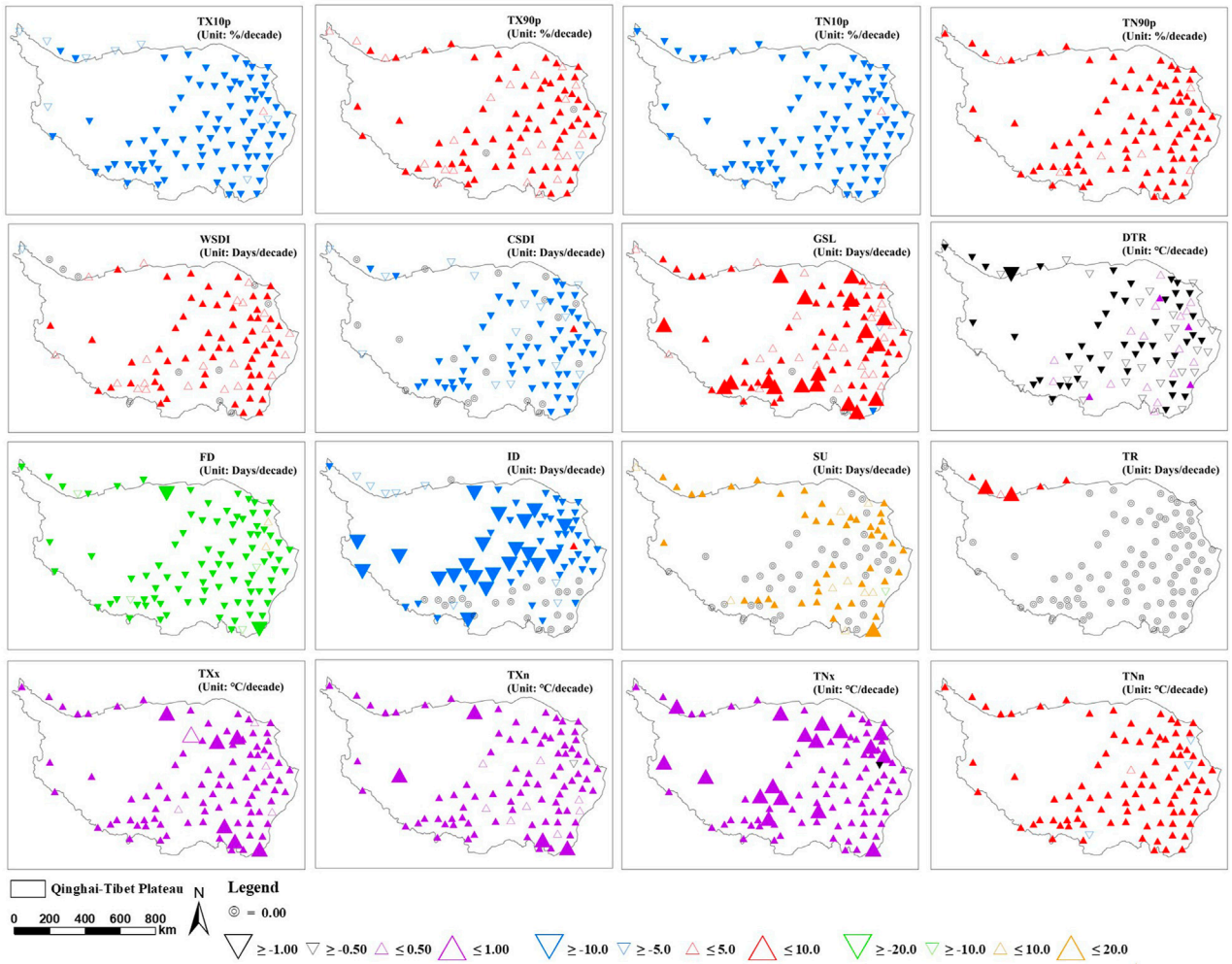

FIGURE 3 | Spatial pattern of the trends for temperature indices from the 94 meteorological stations in the Qinghai-Tibet Plateau from 1960 to 2016 (base period from 1961–1990). **Table 1** shows the definitions of the indices. The spatial distribution of the indices trends was represented using upward facing triangles for positive and downward facing triangles for negative trends. Different sizes of triangles indicate different magnitudes of trends. Filled triangles represent statistically significant at 95% level, i.e., $p < 0.05$. Double circles denote no trend. Notes: Black (−1.00 ≤ Slope <0.00), Blue (−10.0 ≤ Slope <0.00), Green (−20.0 ≤ Slope <0.00); Purple (0.00 < Slope ≤1.00), Red (0.00 < Slope ≤10.00), Orange (0.00 < Slope ≤20.00, PRCPTOT >20.0).

events and geographic attributes (latitude, longitude, and elevation). Furthermore, regional averages for each index were computed to summarize the long-term changes observed in QTP (1960–2016). The regional averaged temperature and perception indices were calculated by taking the unweighted mean of the indices at each station.

3 RESULTS AND DISCUSSION

3.1 Trends in Extreme Temperature Events

3.1.1 Temporal Trends for Temperature Extremes

On the QTP, the regionally averaged annual occurrence of cold indices, including the numbers of cool days (TX10p), cool nights (TN10p), ice days (ID), and frost days (FD) decreased significantly ($p < 0.001$), at rates of 1.0, 1.5, 2.7, and 3.9 days per decade, respectively (**Figure 2**), with the trend was strongest for TN10p ($Z = -7.39$). In contrast, the numbers of warm days (TX90p), warm nights (TN90p), summer days (SU), and tropical nights (TR) grew significantly ($p < 0.001$) at rates of 1.1, 1.6, 1.4, and 0.3 days per decade, respectively. The most significant increase ($Z = 6.64$) was seen in TN90p. **Figure 2** shows the changes in the regionally averaged annual occurrence of temperature extremes when they are derived from the two base periods, 1961–1990 (colder) versus 1988–2016 (warmer). We found significant differences in the percentile-based threshold indices (including TN10p, TX10p, TN90p, TX90p, WSDI, and CSDI) calculated using two base periods, but no differences in the other temperature extremes. Specially, the indices defined by a threshold less than 10th percentile (TX10p, TN10p, CSDI) were larger when a warmer base

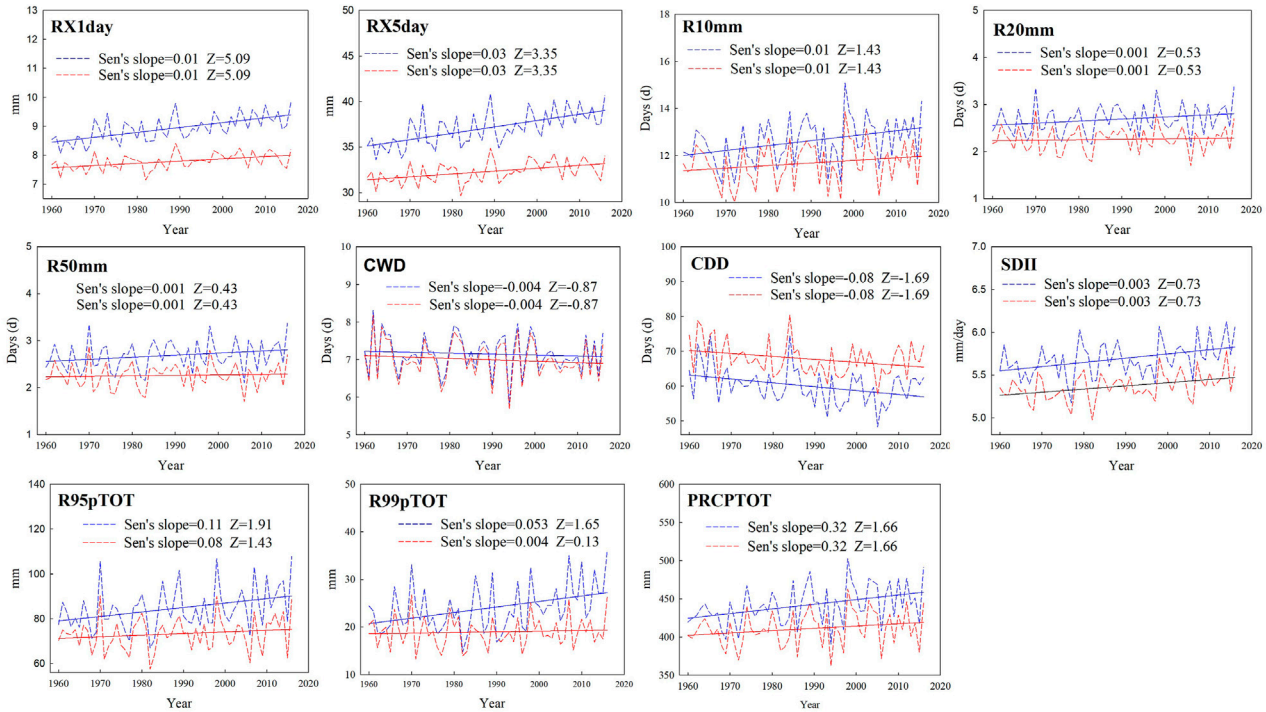

FIGURE 4 | Regionally averaged series for the extreme precipitation indices on the Qinghai-Tibet Plateau from 1960 to 2016. **Table 1** shows the definitions of the indices. The red and blue dashed lines represent the different base periods of which the percentiles were derived, 1988–2016 (warmer) and 1961–1990 (colder) respectively. Solid red and blue lines denote the linear trends for both base periods.

period (1988–2016) was used rather than a colder base period (1961–1990), whereas the 90th percentile indices were the opposite. Furthermore, it was found that the trend magnitude of the cold indices (TX10p, TN10p, CSDI) is amplified while the trend magnitude of the warm indices (TX90p, TN90p) is diminished when a warmer base period is used. For example, the regional averaged trend for CSDI was 1.3 days per decade versus 1.1 days per decade when warmer (1988–2016) and colder (1961–1990) base periods were used, respectively. The change rate of the TX90p was 0.9% per decade versus 1.1% per decade based on warmer (1988–2016) and colder (1961–1990) periods. Klein Tank et al. (2009) stated that when estimating the changes in the indices over time, the choice of another normal period (e.g., 1971–2000) has only a minor impact on the results. This claim is consistent with the findings of Yosef et al. (2019), who found that percentiles from the base periods 1961–1990 and 1971–2000 have a similar impact on trend magnitude of order. This assertion, however, does not hold in a rapidly changing (non-stationary climate) world with a clear and continuing warming trend. Our results showed that the choice of base period has a significant effect on the magnitude of the slope, namely when a warmer base period is used, the trend magnitude of the 10th percentile-based indices is amplified, while the trend magnitude of the 90th percentile-based indices is reduced. This mainly attributed to the presence of continuous global warming, deriving percentiles from a distribution shifted to the right results in higher thresholds that must be met. As a result, when the 10th percentile was derived from a recent warmer (e.g., 1988–2017) base period, the threshold (absolute) values were higher than when the 10th percentile was derived from a colder (1961–1990) base period, resulting in a stronger (steeper) trend magnitude. This was contrast to when the 10th percentiles were calculated using the 1961–1990 base period. In the last two decades, exceeding the thresholds derived from that distribution has become quite rare. As a result, the slope was more gentle in this case. The 90th percentile, which was derived from a warmer base period, showed the opposite trend. In this case, the threshold values were higher than in the cooler past, reducing the frequency with which these high thresholds were exceeded in the past and now (Yosef et al., 2021).

From 1960 to 2016, the cold temperature indices in the QTP generally exhibited significant decreasing trends, whereas the warm temperature indices showed significant growing trends. Similar findings have been seen in Europe (Klein Tank and Können, 2003), Central and South America (Aguilar et al., 2005), and Africa (New et al., 2006; Gbode et al., 2019). The cold extremes (FD and ID) showed stronger trends (larger slope and *Z* values) than the warm extremities (SU and TR), suggesting unequal changes in the lower and upper tail extremities resulting in temperature variation, which was inconsistent with studies in Europe (Klein Tank and Können, 2003; Moberg et al., 2006) and Middle East countries (Zhang et al., 2005), but this finding was in agreement with earlier studies in the Yellow River Basin (Wang et al., 2012), the Loess Plateau (Sun et al., 2016), and northern

China (Wang et al., 2018), demonstrating that warming since 1960 was caused by decreases of the cold extremes rather than increases of the warm extremes. The warmest day (TXx), warmest night (TNx), coldest day (TXn), and coldest night (TNn) extremal indices all indicated substantial warming trends, at rates of 0.30, 0.40, 0.30, and 0.50°C per decade ($p < 0.001$), and the trend was strongest for TNn ($Z = 8.30$). Trends in the night-time indices (TN10p, TN90p, TNx, and TNn) were stronger (larger Z scores) than those of their corresponding daytime indices (TX10p, TX90p, TXx and TXn), demonstrating that nocturnal warming contributed more to the overall warming process than daylight warming (Manton et al., 2001; Peterson et al., 2002; Griffiths et al., 2005; Klein Tank et al., 2006; Revadekar et al., 2013; Yan et al., 2014). In addition, for the variability extremes, both the average the diurnal temperature range (DTR) and the cold spell duration (CSDI) demonstrated clear downward patterns. However, the growing season length (GSL) and warm spell duration (WSDI) increased significantly. The change rate of GSL in the QTP was lower than the average value for the Yarlung Tsangpo River Basin (4.33 days/decade; Liu et al., 2019) and Loess Plateau (3.16 days/decade; Sun et al., 2016), but larger than those in northwestern China (2.74 days/decade; Song et al., 2015), the Yangtze River Basin (0.23 days/decade; Wang et al., 2014), and the Yunnan-Guizhou Plateau (0.12 days/decade; Li et al., 2012a).

The main factors influencing extreme temperatures were thought to be anthropogenic forcing and climatic natural variability (Hegerl et al., 2004). According to Kiktev et al. (2003), increasing greenhouse gas emissions played a significant role in the climate model's simulation of extreme weather. By analyzing the trends of extremes in different underlying surfaces, Zhou and Ren (2011) discovered that urbanization had an impact on a series of extreme temperature indices in north China. Urbanization accelerated the downward trend in cold index series (frost days, cool nights, and cool days) and the upward trend in warm indices related to minimum temperature (summer days and warm nights). The causes of warming in temperature extremes in QTP, on the other hand, should be investigated further.

3.1.2 Spatial Trends for Temperature Extremes

To gain a better understanding of the spatial variation for temperature extremes, we mapped the spatial patterns of the annual trends based on the Sen's slopes at each 94

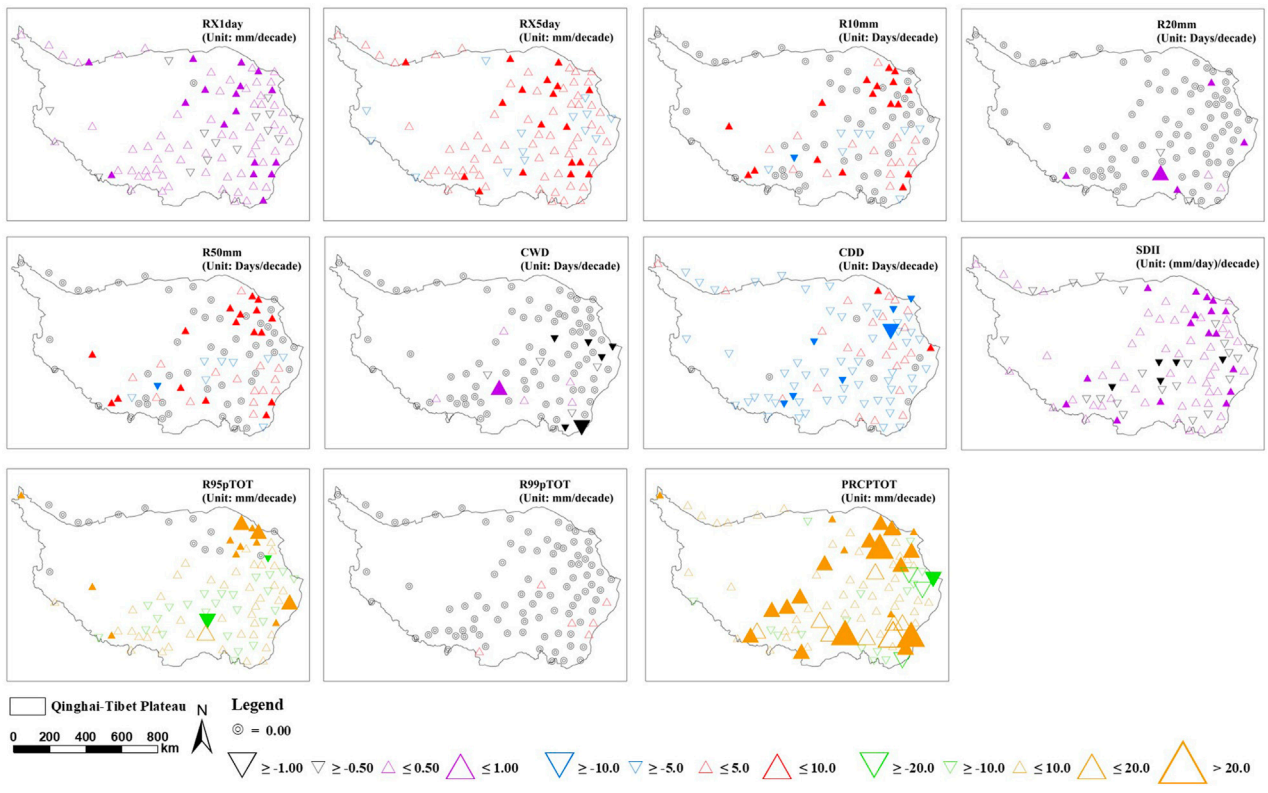

FIGURE 5 | Spatial pattern of the trends for precipitation indices from the 94 meteorological stations in the Qinghai-Tibet Plateau from 1960 to 2016 (base period from 1961–1990). **Table 1** shows the definitions of the indices. The spatial distribution of the indices trends was represented using upward facing triangles for positive and downward facing triangles for negative trends. Different sizes of triangles indicate different magnitudes of trends. Filled triangles represent statistically significant at 95% level, i.e., $p < 0.05$. Double circles denote no trend. Black (−1.00 ≤ Slope <0.00), Blue (−10.0 ≤ Slope <0.00), Green (−20.0 ≤ Slope <0.00); Purple (0.00 < Slope ≤1.00), Red (0.00 < Slope ≤10.00), Orange (0.00 < Slope ≤20.00, PRCPTOT >20.0).

meteorological stations throughout and around the QTP (**Figure 3**). These trends are significant at a 95% confidence level (i.e., $p \leq 0.05$). During the period from 1961 to 2016, no change in TR (93.62%) within the QTP was found (Sen's slope = 0), and only 5 stations on the northern edge showed a significant increasing trend. The cold indices (FD, TN10p, TX10p, ID, CSDI) showed significant ($p < 0.05$) decreasing trends in the QTP, and the corresponding significantly decreased stations accounted for 93.62, 92.55, 90.43, 67.02, and 63.83%. However, the overall warming indices (TN90p, TX90p, WSDI, SU) showed significant increase trends in the whole study area, and the proportion of stations with significant increase were 92.55, 72.34, 67.02, and 56.38%. Similarly, the extremal indices (TNx, TNn, TXx, TXn) showed significant increase trends in most areas of the study area, and the proportions of stations with significant increase were 100, 95.74, 94.68, and 90.43%. In addition, the proportion of stations with significantly increased GSL and DTR accounted for 70.21 and 52.13%, respectively.

3.1.3 Correlations Among the Temperature Indices

The relationships among the extreme-temperature indices are illustrated in the correlation matrix (**Table 2**), there were significant correlations in numerous different temperature indices. For the absolute indices (FD, ID, SU, TR) and relative indices (TX10p, TX90p, TN10p, TN90p), significant positive correlations were discovered between the warmth and cold indices. Each warmth index, on the other hand, was negatively associated with each cold index. This is in line with the previous findings, which revealed that cold indices were trending downwards while warmth indices were trending upwards. Furthermore, significant negative correlations were found between the cold absolute indices (FD and ID) and the extremal indices (TXx, TXn, TNx, and TNn), but significant positive correlations were found between the warmth absolute indices (SU and TR) and the extremal indices (TXx, TXn, TNx, and TNn). GSL and WSDI had a large negative relationship with FD and ID, but a significant positive relationship with SU and TR, which was consistent with previous studies (Lin et al., 2017; Wang et al., 2018).

3.2 Trends for Extreme Precipitation Events

3.2.1 Temporal Trends for Precipitation Extremes

As shown in **Figure 4**, the extreme precipitation indices calculated using the warmer base period (1988–2016) were all lower than those computed using the colder base period (1961–1990), except for the CDD. For most extreme precipitation indices, using a different base period (colder or warmer) changed the intercept without influencing the slope. However, our analyses showed that percentile-based precipitation indices (e.g., days with daily rainfall >95th and 99th percentile) are particularly susceptible to the problematic use of different base periods. The regional averaged trend for R99pTOT increased by 0.5 days per decade versus 0.04 days per decade when colder (1961–1990) and warmer (1988–2016) base periods were used, respectively, indicating that the trend magnitude of the percentile-based precipitation indices (R95pTOT and R99pTOT) is diminished when a warmer base period is used.

The regionally averaged monthly maximum 1-day precipitation (RX1day) and maximum consecutive 5-day precipitation (RX5day) increased significantly, at rates of 0.1 and 0.3 mm per decade, respectively. RX1day had the strongest trend during the study period ($Z = 5.09$), but PRCPTOT had the steepest slope (3.2 mm/decade). The rate of change for RX5day (0.3 mm/decade) was higher than that in the Yunnan-Guizhou plateau (0.03 mm/decade; Li et al., 2012a), northeastern China (0.13 mm/decade; Song et al., 2015), but lower than those in northwestern China (0.85 mm/decade), for China as a whole (1.90 mm/decade; You et al., 2011), and at a global scale (0.55 mm/decade; Alexander et al., 2006). In addition, the rate of rise in annual total precipitation (PRCPTOT) in this study (3.2 mm/decade) was higher than those in northeastern China (1.65 mm/decade; Song et al., 2015), China's Loess Plateau (1.50 mm/decade; Sun et al., 2016), and China's Yangtze River (1.90 mm/decade; Wang et al., 2014), but lower than in the Guinea coast of Nigeria (8.03 mm/decade; Gbode et al., 2019), Romania (4.14 mm/decade; Croitoru et al., 2016), Georgia (7.9 mm/decade; Keggenhoff et al., 2014), and on a global scale (10.59 mm/decade; Alexander et al., 2006). Notably, PRCPTOT showed a negative trend in Indonesia (−4.30 mm/decade; Supari et al., 2017), contrary to our research trend.

3.2.2 Spatial Trends for Precipitation Extremes

In most regions of the QTP from 1960 to 2016, the extreme precipitation indices exhibited increasing trends, as seen in **Figure 5**. The significant increasing trend ($p < 0.05$) of extreme precipitation index (R10mm, R50mm, RX5day, RX1day, R95pTOT) was mainly distributed in the northeast of QTP, and the stations accounted for 20.21, 20.21, 19.15, 18.09 and 15.96%, respectively. PRCPTOT showed a significant increasing trend ($p < 0.05$), accounting for 23.4% of the total sites, mainly distributed in the northeast and southwest of the QTP. In contrast, CDD decreased in most areas, especially in the high-elevation area of the central west, while CWD decreased significantly ($p < 0.05$) in the eastern part of the QTP, accounting for 10.64% of the total stations. At the same time, the extreme precipitation index (R99pTOT, R20mm, CWD, R10mm, R50mm) of more than 50% stations remained unchanged (Sen's slope = 0), with a proportion of 93.62, 90.43, 81.91, 56.38 and 56.38%, respectively.

3.2.3 Correlations Among the Precipitation Indices

As shown in **Table 3**, we discovered strong positive relationships between the annual total precipitation (PRCPTOT, daily precipitation >1 mm) and all the other extreme precipitation indices except R50 mm (not significant) and the consecutive dry days (CDD, $r = -0.24$). The Spearman's correlation coefficients were greater than 0.50 for the relationships between the PRCPTOT and several of the extreme precipitation indices:

TABLE 3 | The correlation matrix (Spearman's correlation coefficient) for the relationships among the extreme- precipitation indices in the Qinghai-Tibet Plateau from 1960 to 2016. Index names are defined in **Table 1**.

Indices	RX1day	RX5day	SDII	R10mm	R20mm	R50mm	CDD	CWD	R95pTOT	R99pTOT	PRCPTOT
RX1day	1										
RX5day	0.98**	1									
SDII	0.51**	0.49**	1								
R10mm	0.53**	0.53**	0.68**	1							
R20mm	0.48**	0.48**	0.61**	0.71**	1						
R50mm	0.50**	0.52**	0.46**	0.1	0.35**	1					
CDD	−0.24	−0.25	0.20	−0.08	−0.02	−0.02	1				
CWD	−0.16	−0.15	0.08	0.33*	0.19	−0.10	−0.06	1			
R95pTOT	0.66**	0.66**	0.71**	0.76**	0.84**	0.48**	−0.05	0.17	1		
R99pTOT	0.54**	0.55**	0.46**	0.32*	0.47**	0.57**	0.04	−0.08	0.65**	1	
PRCPTOT	0.59**	0.58**	0.55**	0.93**	0.68**	0.15	−0.24	0.40**	0.72**	0.30*	1

*Note: ** and * represent significance at* $p < 0.01$ *and* $p < 0.05$*, respectively. All other values are not significant.*

TABLE 4 | Partial correlation coefficient between the temperature extremes from 1960 to 2016 and the latitude, longitude, and elevation of the measurement sites in the Qinghai-Tibet Plateau. Index names are defined in **Table 1**.

Indices	Latitude	Longitude	Elevation
FD	0.89**	0.13	0.94**
SU	−0.28**	−0.62**	−0.87**
ID	0.81**	−0.10	0.77**
TR	0.10	−0.65**	−0.63**
TXx	−0.72**	−0.13	−0.92**
TXn	−0.83**	−0.44**	−0.89**
TNx	−0.86**	−0.42**	−0.95**
TNn	−0.91**	−0.38**	−0.94**
TX10p	−0.20	0.30**	−0.15
TX90p	−0.23*	0.63**	−0.19
TN10p	0.12	0.06	0.23*
TN90p	−0.35**	−0.02	−0.19
WSDI	0.20	−0.38**	0.25*
CSDI	0.33**	−0.33**	−0.53**
DTR	0.38**	0.00	0.21*
GSL	−0.41**	−0.17	−0.65**

*Note: ** and * represent significance at* $p < 0.01$ *and* $p < 0.05$*, respectively. All other values are not significant.*

TABLE 5 | Partial correlation coefficient between precipitation extremes from 1960 to 2016 and the latitude, longitude, and elevation of the measurement sites in the Qinghai-Tibet Plateau. Index names are defined in **Table 1**.

Indices	Latitude	Longitude	Elevation
RX1day	−0.73**	0.75**	−0.28**
RX5day	−0.74**	0.75**	−0.27**
SDII	−0.73**	0.67**	−0.16
R10mm	−0.73**	0.68**	−0.37**
R20mm	−0.70**	0.49**	−0.52**
R50mm	−0.65**	0.42**	−0.57**
CDD	0.46**	−0.70**	−0.11
CWD	−0.74**	0.64**	0.19
R95pTOT	−0.71**	0.71**	−0.26*
R99pTOT	−0.71**	0.73**	−0.23*
PRCPTOT	−0.71**	0.71**	−0.21*

*Note: ** represents significance at* $p < 0.01$*. All other values are not significant.*

the monthly maximum 1-day precipitation (RX1day), maximum consecutive 5-day precipitation (RX5day), heavy precipitation (R10mm), very heavy precipitation (R20mm), simple daily intensity index (SDII), and annual precipitation on very wet days (R95pTOT). Most of the extreme precipitation indices had substantial positive associations, although there were negative correlations between consecutive dry days (CDD) and the precipitation indices. This confirmed our previous research results for China as a whole (Wang et al., 2020).

3.3 Relationships Between Extreme Temperature Events and Geographic Factors

The temperature extremes showed a lot of variety across space. We looked at the relationships between extreme temperature events and the latitude, longitude, and elevation of each meteorological station to figure out what was causing the varied trends in different regions (**Table 4**). The sun incidence angle is affected by latitude, and the distribution of energy across the Earth's surface is influenced as a result. In general, Higher latitude places get less heat due to a lower sun incidence angle, resulting in colder temperatures. In contrast, lower latitudes have greater temperatures because more solar energy is intercepted. Warming trends are particularly visible in the northern hemisphere at high latitudes (Serreze et al., 2000). In the present study, the absolute indices (FD, ID, SU, TR) showed a substantial positive relationship with latitude, whereas the extremal indices for the warmest day (TXn, TNn) revealed negative correlations with latitude, showing that the magnitude of daily extreme temperature incidents would diminish with increasing latitude. The relative warmth indices (TX10p and TN10p) showed positive correlations with latitude, although the correlation was only significant for TX10p, whereas the relative cold indices (TX90p and TN90p) both showed significant negative correlations. This suggests that as latitude increased, the warming trend grew more pronounced, which is consistent with prior study in the Yangtze River Basin (Guan et al., 2015) and the Chinese Hengduan Mountains (Li et al., 2012a; Li et al., 2012b). Furthermore, two of the variability extremes (CSDI and

TABLE 6 | Correlations (Pearson's *r)* between temperature extremes and atmospheric circulation patterns.

Indices	SHA	SHI	SHR	SHW	AO	NAO	PDO	SOI
TX10p	–0.546**	–0.518**	0.080	0.581**	0.112	0.148	–0.107	–0.027
TX90p	0.554**	0.542**	0.062	–0.544**	0.115	–0.063	–0.072	0.043
TN10p	–0.626**	–0.587**	0.038	0.693**	–0.167	–0.052	–0.211	0.035
TN90p	0.672**	0.653**	0.008	–0.683**	0.021	–0.178	0.024	0.098
FD	–0.664**	–0.656**	–0.008	0.651**	–0.033	0.134	–0.020	–0.217
SU	0.504**	0.500**	0.134	–0.478**	0.081	–0.066	–0.106	0.079
ID	–0.619**	–0.598**	0.078	0.643**	0.076	0.120	–0.177	0.019
TR	0.550**	0.558**	–0.008	–0.516**	0.000	–0.220	–0.094	0.175
TXx	0.591**	0.577**	0.116	–0.601**	0.003	–0.065	0.041	0.090
TXn	0.607**	0.605**	0.036	–0.570**	–0.020	–0.187	–0.002	0.138
TNx	0.590**	0.577**	0.067	–0.589**	0.234	–0.003	0.120	0.096
TNn	0.416**	0.390**	–0.133	–0.463**	–0.125	–0.045	0.107	–0.059
GSL	0.575**	0.568**	0.099	–0.570**	0.101	0.008	–0.025	0.156
WSDI	0.592**	0.604**	0.053	–0.560**	0.032	–0.067	0.111	–0.014
DTR	–0.021	0.001	0.136	0.084	0.180	–0.020	–0.035	0.116
CSDI	–0.516**	–0.482**	0.004	0.608**	–0.093	–0.077	–0.221	0.087

DTR) showed significant positive correlations with latitude, whereas GSL was not significantly correlated with latitude.

Longitude influences regional climate change through impacting water and energy transfer between coastal regions (including southwestern areas such as the Indian Ocean and northern areas such as the Arctic Ocean) and China's inland areas (Zhong et al., 2017). In current study, two of the absolute indices (SU and TR) and two of the variability extremes (WSDI and CSDI) showed significant negative correlations with longitude, whereas two of the relative warmth indices (TX10p and TX90p) were significantly positively correlated with longitude, indicating that the occurrence of daytime extreme temperature events would become more common as longitude increased.

Elevation influences regional climate change by determining the vertical distribution of energy and water. In current study, only one of the cold indices (FD) showed a significant ($p < 0.01$) positive correlation with elevation, whereas both warmth indices (SU and TR) showed significant negative correlations with elevation ($p < 0.05$). This meant that cold temperature episodes became more frequent and intense at higher elevations, whereas warm temperature events became less frequent and intense. The indices for the warmest day (TXx), warmest night (TNx), coldest day (TXn), and coldest night (TNn) all had significant negative associations with elevation ($p < 0.05$), indicating that the frequency of daily extreme temperature events would decrease as elevation was increased. In addition, the warm spell duration (WSDI) increased significantly with increasing elevation, whereas the cold spell duration (CSDI) and growing season length (GSL) both decreased with increasing elevation.

3.4 Relationships Between Extreme Precipitation Events and Geographic Factors

We also looked at the links between extreme precipitation events and latitude, longitude, and elevation (**Table 5**). There were strong negative associations between latitude and all the precipitation metrics, with the exception of a substantial positive association for the number of dry days in a row (CDD). This suggests that extreme precipitation events were more common at low latitudes, probably owing mainly to the greater precipitation due to the proximity of low-latitude areas to moist coastal areas in eastern China and orographic effects created by the southern mountains. Longitude showed the opposite effect on extreme precipitation events, with strong positive correlations between all precipitation indices and longitude, except for CDD (with a significant negative correlation) and R50mm showing a nonsignificant correlation (**Table 5**). It is possible that this is because locations with a greater longitude are closer to the coast, where the moisture supply is much greater than in dry regions farther to the west. This also confirmed our previous research results across China (Wang et al., 2020). We found no significant correlations between the precipitation indexes and elevation, possibly because of the negative interaction between elevation and proximity to moisture sources.

3.5 Relationships Between Temperature Extremes and Atmospheric Circulation Patterns

As an important component of East Asian monsoon, the West Pacific Subtropical High (WPSH) has a significant impact on temperature and precipitation in China (Zhao and Wang, 2017). Zhong et al. (2017) found that the Northern Hemisphere Subtropical High area and intensity indices showed positive correlations with the warm indices and extreme indices, while showed the reverse relationship with the cold indices. Sun et al. (2016) also found that the SHI strongly influences warm/cold extremes and contributes significantly to climate changes in the Loess Plateau. **Table 6** shows the correlations between temperature extremes and atmospheric circulation patterns. The warming trends in the temperature extremes on the QTP were closely related with the WPSHI, which represents a large-scale anticyclonic circulation identified as one of the dominant components of the East Asian summer monsoon climate system, accounting for roughly one-quarter of the Northern Hemisphere surface in summer (Huang et al., 2014). The Subtropical High Intensity (SHI) and Subtropical High Area (SHA) showed significant positive correlations with warmth indices

TABLE 7 | Correlations (Pearson's *r*) between precipitation extremes and atmospheric circulation patterns.

Indices	SHA	SHI	SHR	SHW	AO	NAO	PDO	SOI
RX1day	0.534**	0.517**	0.131	–0.565**	0.153	–0.013	0.065	0.218
RX5day	0.532**	0.513**	0.107	–0.561**	0.163	0.001	0.081	0.220
SDII	0.524**	0.531**	0.088	–0.455**	–0.093	–0.116	0.090	0.248
R10mm	0.431**	0.445**	0.172	–0.395**	–0.045	–0.124	0.054	0.256
R20mm	0.339*	0.358**	0.132	–0.300*	–0.104	–0.102	0.086	0.183
R50mm	0.327*	0.315*	–0.006	–0.321*	–0.018	–0.121	0.144	0.029
CDD	–0.280*	–0.216	0.150	0.362**	–0.281*	–0.064	–0.199	0.066
CWD	0.010	0.026	–0.005	0.001	–0.212	–0.092	0.042	0.117
R95pTOT	0.416**	0.440**	0.190	–0.349**	–0.023	–0.088	0.034	0.283*
R99pTOT	0.422**	0.454**	0.133	–0.345**	–0.083	–0.153	0.022	0.255
PRCPTOT	0.408**	0.419**	0.148	–0.397**	–0.039	–0.195	0.021	0.317*

(TX90p, TN90p, SU, TR, WSDI), extremal indices (TXx, TXn, TNx, TNn) and the growing season length, whereas SHI and SHA showed significant negative correlations with cold indices (TX10p, TN10p, FD, ID, CSDI). The correlations between the Subtropical High Western Ridge Point (SHW) and temperature extremes showed the opposite responses. When the SHW moves northward, the cold events were likely to increase significantly, whereas the warming events were likely to decrease significantly on the Qinghai-Tibet Plateau. Furthermore, the WPSH is linked to the warming trend by extending the length of the growing season. These findings suggest that the WPSH has a strong influence on warm/cold extremes and contributes significantly to QTP climate change.

The Arctic Oscillation (AO) is a major controlling factor in Northern Hemisphere climate variability, as well as the strength of the East Asian winter monsoon and the Siberian higher-pressure system (You et al., 2013). In this study, the AO was shown to be less sensitive to changes in climate extremes on the QTP. Similar findings were discovered on China's Loess Plateau (Sun et al., 2016). One possible explanation for this correlation is a decrease in the intensity of the Asian winter monsoon.

3.6 Relationships Between Precipitation Extremes and Atmospheric Circulation Patterns

As shown in **Table 7**, SHI and SHA had positive correlations with all the extreme precipitation indices, except for the reverse relationship with CDD, indicating that the frequency and intensity of extreme precipitation events increased with increasing intensity and area of the West Pacific Subtropical High. On the contrary, SHW had negative correlations with all the extreme precipitation indices, except for positive correlations with CWD and CDD. This indicates that when the SHW moves westward, extreme precipitation events are likely to increase significantly, whereas the extreme precipitation events would decrease if SHW moves eastward.

4 CONCLUSION

In this study, we quantified and compared changes in climate extremes on China's QTP from 1960 to 2016 using 16 extreme temperature indices and 11 extreme precipitation indices, which calculated using colder (1961–1990) and warmer (1988–2016) base periods, respectively. When a warmer base period is used, the trend magnitude of the cold temperature indices is amplified while the trend magnitude of the warm temperature indices and the percentile-based precipitation indices are diminished. As a result, using a recent warmer base period may lead to the incorrect conclusion, misrepresenting the actual changes to global climate.

The temperature indices' regionally averaged trends were consistent with the consequences of global warming. During the study period, the warmth indices, which included the numbers of warm days, warm nights, summer days, and tropical nights, showed considerably increasing trends. In contrast, the cold indices, such as the numbers of cool days, cool nights, ice days, and frost days, declined dramatically. Furthermore, within the same time period, the extreme daily indices, such as the warmest day, warmest night, coldest day, and coldest night, all showed substantial upward trends. The relative warmth indices tended to show positive correlations with latitude, whereas the relative cold indices tended to show negative correlations, suggesting that the warming trend became more pronounced as latitude increased. The relative daytime indices were significantly positively correlated with longitude, indicating that the occurrences of daytime extreme temperature events would increase with increasing longitude. In addition, at high elevations, the frequency and intensity of cold temperature occurrences increased, while warm temperature events showed the opposite tendency. The total annual precipitation and extreme precipitation events showed increasing trends from 1960 to 2016, except for the numbers of consecutive dry and wet days. Furthermore, the extreme precipitation events were more frequent at lower latitudes and higher longitudes, but there was no relationship with elevation. These results confirmed our hypotheses that monitoring of temperatures and precipitation on the QTP would show trends consistent with global warming, and would reveal significant spatial variation in these trends. The West Pacific Subtropical High Index (WPSHI), such as the Subtropical High Area (SHA), Subtropical High Intensity (SHI), and Subtropical High Western Ridge Point (SHW) strongly influence temperature and precipitation extremes. The strengthening SHA and SHI, Westward movement of SHW have contributed to the changes in climate extremes on the Qinghai-Tibet Plateau.

Despite the large number of monitoring stations, coverage of the study area was not optimal, particularly for the large gap in coverage in the northwestern plateau. Adding stations in this region or finding

ways to use satellite data to monitor these remote areas would mitigate this problem. Furthermore, due to the atmospheric circulation change is an important mechanism effecting the heat and moisture transportation in this region, The current study mainly focuses on the impact mechanism of atmospheric circulation patterns on extreme climate change. Other factors, such as cloud amount, surface coverage, human-induced urbanization may also impact the climate extremes. Therefore, more detailed studies are still needed to understand the internal regime of change in extreme climate events on the QTP.

DATA AVAILABILITY STATEMENT

The raw data supporting the conclusion of this article will be made available by the authors, without undue reservation.

AUTHOR CONTRIBUTIONS

The corresponding author presented the overall idea for this manuscript XW, XG, and YL planned and designed the experiments, data processing, analysis and interpretation, as well as authoring the manuscript. LM, ML, and HS contributed resources to the project.

FUNDING

This research was supported by the Second Tibetan Plateau Scientific Expedition and Research (STEP) program (Grant No. 2019QZKK0305), and the National Natural Science Foundation of China (grant Nos. 32001214, 41807525 and 31971466).

REFERENCES

Aguilar, E., Auer, I., Brunet, M., Peterson, T. C., and Wieringa, J. (2003). *Guidelines on Climate Metadata and Homogenization*. WMO/TD No. 1186. Geneva, Switzerland: World Meteorological Organization.

Aguilar, E., Peterson, T. C., Obando, P. R., Frutos, R., Retana, J. A., Solera, M., et al. (2005). Changes in Precipitation and Temperature Extremes in Central America and Northern South America, 1961-2003. *J. Geophys. Res.* 110, D23107. doi:10.1029/2005JD006119

Alexander, L. V., Zhang, X., Peterson, T. C., Caesar, J., Gleason, B., Klein Tank, A. M. G., et al. (2006). Global Observed Changes in Daily Climate Extremes of Temperature and Precipitation. *J. Geophys. Res.* 111, D05109. doi:10.1029/2005JD006290

Alsarmi, S. H., and Washington, R. (2014). Changes in Climate Extremes in the Arabian Peninsula: Analysis of Daily Data. *Int. J. Climatol.* 34 (5), 1329–1345. doi:10.1002/joc.3772

Bi, S. (1997). A Best Laboratory of the Universal Research for the Earth's Global Change and Earth System Science—The Qinghai-Tibet Plateau. *Syst. Eng. Theory Pract.* 17 (5), 72–77. (In Chinese).

Bocheva, L., Marinova, T., Simeonov, P., and Gospodinov, I. (2009). Variability and Trends of Extreme Precipitation Events Over Bulgaria (1961-2005). *Atmos. Res.* 93, 490–497. doi:10.1016/j.atmosres.2008.10.025

Croitoru, A.-E., Piticar, A., and Burada, D. C. (2016). Changes in Precipitation Extremes in Romania. *Quat. Int.* 415, 325–335. doi:10.1016/j.quaint.2015.07.028

Croitoru, A.-E., and Piticar, A. (2013). Changes in Daily Extreme Temperatures in the Extra-Carpathians Regions of Romania. *Int. J. Climatol.* 33, 1987–2001. doi:10.1002/joc.3567

Cuo, L., Zhang, Y., Wang, Q., Zhang, L., Zhou, B., Hao, Z., et al. (2013). Climate Change on the Northern Tibetan Plateau during 1957-2009: Spatial Patterns and Possible Mechanisms. *J. Clim.* 26 (1), 85–109. doi:10.1175/JCLI-D-11-00738.1

Dike, V. N., Lin, Z.-H., and Ibe, C. C. (2020). Intensification of Summer Rainfall Extremes over Nigeria during Recent Decades. *Atmosphere* 11 (10), 1084. doi:10.3390/atmos11101084

Ding, J., Cuo, L., Zhang, Y., and Zhu, F. (2018). Monthly and Annual Temperature Extremes and Their Changes on the Tibetan Plateau and its Surroundings during 1963-2015. *Sci. Rep.* 8 (1), 11860. doi:10.1038/s41598-018-30320-0

Eyring, V., Gillett, N. P., Achuta Rao, K. M., Barimalala, R., Barreiro Parrillo, M., Bellouin, N., et al. (2021). "Human Influence on the Climate System," in *Climate Change 2021: The Physical Science Basis. Contribution of Working Group I to the Sixth Assessment Report of the Intergovernmental Panel on Climate Change* (Cambridge and New York: Cambridge University Press). In Press.

Filahi, S., Tanarhte, M., Mouhir, L., El Morhit, M., and Tramblay, Y. (2016). Trends in Indices of Daily Temperature and Precipitations Extremes in Morocco. *Theor. Appl. Climatol.* 124, 959–972. doi:10.1007/s00704-015-1472-4

Frich, P., Alexander, L., Della-Marta, P., Gleason, B., Haylock, M., Klein Tank, A., et al. (2002). Observed Coherent Changes in Climatic Extremes during the Second Half of the Twentieth Century. *Clim. Res.* 19, 193–212. doi:10.3354/cr019193

Gbode, I. E., Adeyeri, O. E., Menang, K. P., Intsiful, J. D. K., Ajayi, V. O., Omotosho, J. A., et al. (2019). Observed Changes in Climate Extremes in Nigeria. *Meteorol. Appl.* 26 (4), 642–654. doi:10.1002/met.1791

Goswami, B. N., Venugopal, V., Sengupta, D., Madhusoodanan, M. S., and Xavier, P. K. (2006). Increasing Trend of Extreme Rain Events Over India in a Warming Environment. *Science* 314, 1442–1445. doi:10.1126/science.1132027

Griffiths, G. M., Chambers, L. E., Haylock, M. R., Manton, M. J., Nicholls, N., Baek, H.-J., et al. (2005). Change in Mean Temperature as a Predictor of Extreme Temperature Change in the Asia-Pacific Region. *Int. J. Climatol.* 25, 1301–1330. doi:10.1002/joc.1194

Griffiths, M. L., and Bradley, R. S. (2007). Variations of Twentieth-Century Temperature and Precipitation Extreme Indicators in the Northeast United States. *J. Clim.* 20, 5401–5417. doi:10.1103/PhysRevB.71.22411910.1175/2007jcli1594.1

Guan, Y., Zhang, X., Zheng, F., and Wang, B. (2015). Trends and Variability of Daily Temperature Extremes during 1960-2012 in the Yangtze River Basin, China. *Glob. Planet. Change* 124, 79–94. doi:10.1016/j.gloplacha.2014.11.008

Hamed, K. H., and Ramachandra Rao, A. (1998). A Modified Mann-Kendall Trend Test for Autocorrelated Data. *J. Hydrology* 204, 182–196. doi:10.1016/S0022-1694(97)00125-X

Haylock, M. R., Hofstra, N., Klein Tank, A. M. G., Klok, E. J., Jones, P. D., and New, M. (2008). A European Daily High-Resolution Gridded Data Set of Surface Temperature and Precipitation for 1950-2006. *J. Geophys. Res.* 113, D20119. doi:10.1029/2008JD010201

Haylock, M. R., Peterson, T. C., Alves, L. M., Ambrizzi, T., Anunciação, Y. M. T., Baez, J., et al. (2006). Trends in Total and Extreme South American Rainfall in 1960-2000 and Links with Sea Surface Temperature. *J. Clim.* 19, 1490–1512. doi:10.1175/JCLI3695.1

Hegerl, G. C., Zwiers, F. W., Stott, P. A., and Kharin, V. V. (2004). Detectability of Anthropogenic Changes in Annual Temperature and Precipitation Extremes. *J. Clim.* 17 (19), 3683–3700. doi:10.1175/1520-0442(2004)017<3683:doacia>2.0.co;2

Houghton, J. T., Ding, Y., Griggs, D. J., Noguer, M., Linden, P. J., Dai, X., et al. (2001). "Observed Climate Variability and Change," in *Climate Change 2001: The Science of Climate Change* (Cambridge, UK: Cambridge University Press), 156–159. doi:10.1038/ngeo301

Huang, Y., Wang, H., Fan, K., and Gao, Y. (2014). The Western Pacific Subtropical High after the 1970s: Westward or Eastward Shift? *Clim. Dyn.* 44 (7-8), 2035–2047. doi:10.1007/s00382-014-2194-5

Hussain, M., and Mahmud, I. (2019). pyMannKendall: A Python Package for Non Parametric Mann Kendall Family of Trend Tests. *J. Open Source Softw.* 4 (39), 1556. doi:10.21105/joss.01556

IPCC (2022). "Climate Change 2022: Impacts, Adaptation, and Vulnerability," in *Contribution of Working Group II to the Sixth Assessment Report of the*

Intergovernmental Panel on Climate Change. Editors H-O Pörtner, DC Roberts, M Tignor, ES Poloczanska, K Mintenbeck, A Alegría, et al. (Cambridge and New York: Cambridge University Press).

Iwashima, T., and Yamamoto, R. (1993). A Statistical Analysis of the Extreme Event: Long-Term Trend of Heavy Daily Precipitation. *J. Meteorol. Soc. Jpn.* 71 (5), 637–640. doi:10.2151/jmsj1965.71.5_637

Karl, T. R., Knight, R. W., Easterling, D. R., and Quayle, R. G. (1996). Indices of Climate Change for the United States. *Bull. Amer. Meteor. Soc.* 77 (2), 279–292. doi:10.1175/1520-0477(1996)077<0279:ioccft>2.0.co;2

Karl, T. R., Knight, R. W., and Plummer, N. (1995). Trends in High-Frequency Climate Variability in the Twentieth Century. *Nature* 377, 217–220. doi:10.1038/377217a0

Keggenhoff, I., Elizbarashvili, M., Amiri-Farahani, A., and King, L. (2014). Trends in Daily Temperature and Precipitation Extremes over Georgia, 1971–2010. *Weather Clim. Extrem.* 4, 75–85. doi:10.1016/j.wace.2014.05.001

Kiktev, D., Sexton, D. M. H., Alexander, L., and Folland, C. K. (2003). Comparison of Modeled and Observed Trends in Indices of Daily Climate Extremes. *J. Clim.* 16 (22), 3560–3571. doi:10.1175/1520-0442(2003)016<3560:comaot>2.0.co;2

Klein Tank, A. M. G., and Können, G. P. (2003). Trends in Indices of Daily Temperature and Precipitation Extremes in Europe, 1946-99. *J. Clim.* 16, 3665–3680. doi:10.1175/1520-0442(2003)016<3665:tiiodt>2.0.co;2

Klein Tank, A. M. G., Peterson, T. C., Quadir, D. A., Dorji, S., Zou, X., Tang, H., et al. (2006). Changes in Daily Temperature and Precipitation Extremes in Central and South Asia. *J. Geophys. Res.* 111, D16105. doi:10.1029/2005JD006316

Klein Tank, A. M. G., Zwiers, F. W., and Zhang, X. (2009). *Guidelines on Analysis of Extremes in a Changing Climate in Support of Informed Decisions for Adaptation*. Geneva, Switzerland: Climate data and monitoring, WCDMP-No. 72, WMO-TD No.1500.

Li, R., and Chi, X. (2014). Thermal Comfort and Tourism Climate Changes in the Qinghai-Tibet Plateau in the Last 50 Years. *Theor. Appl. Climatol.* 117 (3-4), 613–624. doi:10.1007/s00704-013-1027-5

Li, S., Dong, Y. X., and Dong, G. R. (2001). *Sandy Desertification Problem and Sustainable Development in Qinghai-Tibet Plateau*. Beijing: China Tibetology Publishing House. (in Chinese).

Li, Y.-G., He, D., Hu, J.-M., and Cao, J. (2015). Variability of Extreme Precipitation over Yunnan Province, China 1960-2012. *Int. J. Climatol.* 35, 245–258. doi:10.1002/joc.3977

Li, Z., He, Y., Wang, C., Wang, X., Xin, H., Zhang, W., et al. (2011). Spatial and Temporal Trends of Temperature and Precipitation during 1960-2008 at the Hengduan Mountains, China. *Quat. Int.* 236, 127–142. doi:10.1016/j.quaint.2010.05.017

Li, Z., He, Y., Wang, P., Theakstone, W. H., An, W., Wang, X., et al. (2012a). Changes of Daily Climate Extremes in Southwestern China during 1961-2008. *Glob. Planet. Change* 80-81, 255–272. doi:10.1016/j.gloplacha.2011.06.008

Li, Z., Zheng, F.-L., Liu, W.-Z., and Jiang, D.-J. (2012b). Spatially Downscaling GCMs Outputs to Project Changes in Extreme Precipitation and Temperature Events on the Loess Plateau of China during the 21st Century. *Glob. Planet. Change* 82-83, 65–73. doi:10.1016/j.gloplacha.2011.11.008

Lin, P., He, Z., Du, J., Chen, L., Zhu, X., and Li, J. (2017). Recent Changes in Daily Climate Extremes in an Arid Mountain Region, a Case Study in Northwestern China's Qilian Mountains. *Sci. Rep.* 7 (1), 2245. doi:10.1038/s41598-017-02345-4

Liu, C., Li, Y., Ji, X., Luo, X., and Zhu, M. (2019). Observed Changes in Temperature and Precipitation Extremes over the Yarlung Tsangpo River Basin during 1970-2017. *Atmosphere* 10, 815. doi:10.3390/atmos10120815

Liu, X., and Chen, B. (2000). Climatic Warming in the Tibetan Plateau during Recent Decades. *Int. J. Climatol.* 20 (14), 1729–1742. doi:10.1002/1097-0088(20001130)20:14<1729::aid-joc556>3.0.co;2-y

Lu, H., Chen, S., Guo, Y., He, Y., Xu, S., Lu, H., et al. (2014). Spatio-temporal Variation Characteristics of Extremely Heavy Precipitation Frequency over South China in the Last 50 Years. *J. Trop. Meteorol.* 20, 279–288. doi:10.16555/j.1006-8775.2014.03.010

Lupikasza, E. (2009). Spatial and Temporal Variability of Extreme Precipitation in Poland in the Period 1951-2006. *Int. J. Climatol.* 30, 991–1007. doi:10.1002/joc.1950

Manton, M. J., Della-Marta, P. M., Haylock, M. R., Hennessy, K. J., Nicholls, N., Chambers, L. E., et al. (2001). Trends in Extreme Daily Rainfall and Temperature in Southeast Asia and the South Pacific: 1961-1998. *Int. J. Climatol.* 21, 269–284. doi:10.1002/joc.610

Mason, S. J., Waylen, P. R., Mimmack, G. M., Rajaratnam, B., and Harrison, J. M. (1999). Changes in Extreme Rainfall Events in South Africa. *Clim. Change* 41 (2), 249–257. doi:10.1023/A:1005450924499

McMichael, A. J., Woodruff, R. E., and Hales, S. (2006). Climate Change and Human Health: Present and Future Risks. *Lancet* 367, 859–869. doi:10.1016/S0140-6736(06)68079-3

Mishra, V., Ganguly, A. R., Nijssen, B., and Lettenmaier, D. P. (2015). Changes in Observed Climate Extremes in Global Urban Areas. *Environ. Res. Lett.* 10 (2), 024005. doi:10.1088/1748-9326/10/2/024005

Moberg, A., Jones, P. D., Lister, D., Walther, A., Brunet, M., Jacobeit, J., et al. (2006). Indices for Daily Temperature and Precipitation Extremes in Europe Analyzed for the Period 1901-2000. *J. Geophys. Res.* 111, D22106. doi:10.1029/2006JD007103

New, M., Hewitson, B., Stephenson, D. B., Tsiga, A., Kruger, A., Manhique, A., et al. (2006). Evidence of Trends in Daily Climate Extremes Over Southern and West Africa. *J. Geophys. Res.* 111, 3007–3021. doi:10.1029/2005JD006289

Pan, B., and Li, J. (1996). Qinghai-Tibetan Plateau: a Driver and Amplifier of the Global Climatic Change. *J. Lanzhou Univ. (Nat. Sci.)* 32 (1), 108–115. (In Chinese). doi:10.13885/j.issn.0455-2059.1996.01.024

Patz, J. A., Campbell-Lendrum, D., Holloway, T., and Foley, J. A. (2005). Impact of Regional Climate Change on Human Health. *Nature* 438, 310–317. doi:10.1038/nature04188

Peterson, T. C., Easterling, D. R., Karl, T. R., Groisman, P., Nicholls, N., Plummer, N., et al. (1998). Homogeneity Adjustments Ofin Situ Atmospheric Climate Data: a Review. *Int. J. Climatol.* 18, 1493–1517. doi:10.1002/(sici)1097-0088(19981115)18:13<1493::aid-joc329>3.0.co;2-t

Peterson, T. C., Folland, C., and Gruza, G. (2001). *Report on the Activities of the Working Group on Climate Change Detection and Related Rapporteurs 1998–2001*. Report WCDMP-47, WMO-TD 1071. Geneva, Switzerland: World Meteorological Organization.

Peterson, T. C., Taylor, M. A., Demeritte, R., Duncombe, D. L., Burton, S., Thompson, F., et al. (2002). Recent Changes in Climate Extremes in the Caribbean Region. *J. Geophys. Res.* 107, 4601. doi:10.1029/2002JD002251

Powell, E. J., and Keim, B. D. (2015). Trends in Daily Temperature and Precipitation Extremes for the Southeastern United States: 1948-2012. *J. Clim.* 28, 1592–1612. doi:10.1175/JCLI-D-14-00410.1

Pryor, S. C., Howe, J. A., and Kunkel, K. E. (2009). How Spatially Coherent and Statistically Robust Are Temporal Changes in Extreme Precipitation in the Contiguous USA? *Int. J. Climatol.* 29, 31–45. doi:10.1002/joc.1696

Revadekar, J. V., Hameed, S., Collins, D., Manton, M., Sheikh, M., Borgaonkar, H. P., et al. (2013). Impact of Altitude and Latitude on Changes in Temperature Extremes Over South Asia during 1971-2000. *Int. J. Climatol.* 33, 199–209. doi:10.1002/joc.3418

Rodrigo, F. S. (2009). Changes in the Probability of Extreme Daily Precipitation Observed from 1951 to 2002 in the Iberian Peninsula. *Int. J. Climatol.* 30, 1512–1525. doi:10.1002/joc.1987

Rusticucci, M., and Barrucand, M. (2004). Observed Trends and Changes in Temperature Extremes Over Argentina. *J. Clim.* 17, 4099–4107. doi:10.1175/1520-0442(2004)017<4099:otacit>2.0.co;2

Sen, P. K. (1968). Estimates of the Regression Coefficient Based on Kendall's Tau. *J. Am. Stat. Assoc.* 63 (324), 1379–1389. doi:10.1080/01621459.1968.10480934

Serreze, M. C., Walsh, J. E., Chapin III, F. S., Osterkamp, T., Dyurgerov, M., Romanovsky, V., et al. (2000). Observational Evidence of Recent Change in the Northern High-Latitude Environment. *Clim. Change* 46, 159–207. doi:10.1023/A:1005504031923

Skansi, M. D. L. M., Brunet, M., Sigró, J., Aguilar, E., Arevalo Groening, J. A., Bentancur, O. J., et al. (2013). Warming and Wetting Signals Emerging from Analysis of Changes in Climate Extreme Indices over South America. *Glob. Planet. Change* 100, 295–307. doi:10.1016/j.gloplacha.2012.11.004

Song, X., Song, S., Sun, W., Mu, X., Wang, S., Li, J., et al. (2015). Recent Changes in Extreme Precipitation and Drought Over the Songhua River Basin, China, during 1960-2013. *Atmos. Res.* 157, 137–152. doi:10.1016/j.atmosres.2015.01.022

Sun, W., Mu, X., Song, X., Wu, D., Cheng, A., and Qiu, B. (2016). Changes in Extreme Temperature and Precipitation Events in the Loess Plateau (China) during 1960-2013 under Global Warming. *Atmos. Res.* 168, 33–48. doi:10.1016/j.atmosres.2015.09.001

Supari, S., Tangang, F., Juneng, L., and Aldrian, E. (2017). Observed Changes in Extreme Temperature and Precipitation over Indonesia. *Int. J. Climatol.* 37, 1979–1997. doi:10.1002/joc.4829

Thornton, P. K., Ericksen, P. J., Herrero, M., and Challinor, A. J. (2014). Climate Variability and Vulnerability to Climate Change: A Review. *Glob. Change Biol.* 20, 3313–3328. doi:10.1111/gcb.12581

Trömel, S., and Schönwiese, C.-D. (2007). Probability Change of Extreme Precipitation Observed from 1901 to 2000 in Germany. *Theor. Appl. Climatol.* 87 (1-4), 29–39. doi:10.1007/s00704-005-0230-4

Wang, B., Bao, Q., Hoskins, B., Wu, G., and Liu, Y. (2008). Tibetan Plateau Warming and Precipitation Changes in East Asia. *Geophys. Res. Lett.* 35 (14), 63–72. doi:10.1029/2008GL034330

Wang, Q., Zhang, M., Wang, S., Ma, Q., and Sun, M. (2014). Changes in Temperature Extremes in the Yangtze River Basin, 1962-2011. *J. Geogr. Sci.* 24 (1), 59–75. doi:10.1007/s11442-014-1073-7

Wang, S., Zhang, M., Wang, B., Sun, M., and Li, X. (2013). Recent Changes in Daily Extremes of Temperature and Precipitation Over the Western Tibetan Plateau, 1973-2011. *Quat. Int.* 313-314 (6), 110–117. doi:10.1016/j.quaint.2013.03.037

Wang, W., Shao, Q., Yang, T., Peng, S., Yu, Z., Taylor, J., et al. (2012). Changes in Daily Temperature and Precipitation Extremes in the Yellow River Basin, China. *Stoch. Environ. Res. Risk Assess.* 27 (2), 401–421. doi:10.1007/s00477-012-0615-8

Wang, X. L. (2008a). Accounting for Autocorrelation in Detecting Mean Shifts in Climate Data Series Using the Penalized Maximal T or F Test. *J. Appl. Meteorol. Clim.* 47, 2423–2444. doi:10.1175/2008JAMC1741.1

Wang, X., Li, Y., Chen, Y., Lian, J., Luo, Y., Niu, Y., et al. (2018). Temporal and Spatial Variation of Extreme Temperatures in an Agro-Pastoral Ecotone of Northern China from 1960 to 2016. *Sci. Rep.* 8, 8787. doi:10.1038/s41598-018-27066-0

Wang, X., Li, Y., Wang, M., Li, Y., Gong, X., Chen, Y., et al. (2020). Changes in Daily Extreme Temperature and Precipitation Events in Mainland China from 1960 to 2016 under Global Warming. *Int. J. Climatol.* 41, 1465–1483. doi:10.1002/joc.6865

Wang, X. L. (2008b). Penalized Maximal F Test for Detecting Undocumented Mean Shift without Trend Change. *J. Atmos. Ocean. Tech.* 25, 368–384. doi:10.1175/2007JTECHA982.1

Wang, X. L., Wen, Q. H., and Wu, Y. (2007). Penalized Maximal T Test for Detecting Undocumented Mean Change in Climate Data Series. *J. Appl. Meteorol. Clim.* 46, 916–931. doi:10.1175/JAM2504.1

Wang, X., Pang, G., Yang, M., and Zhao, G. (2017). Evaluation of Climate on the Tibetan Plateau Using Era-Interim Reanalysis and Gridded Observations during the Period 1979-2012. *Quat. Int.* 444, 76–86. doi:10.1016/j.quaint.2016.12.041

World Meteorological Organization (2017). *WMO Guidelines on the Calculation of Climate Normal*. Geneva, Switzerland: WMO-No. 1203.

Yan, H. M., Chen, W. N., Yang, F. X., Liu, J. Y., and Ji, Y. Z. (2014). The Spatial and Temporal Analysis of Extreme Climatic Events in Inner Mongolia during the Past 50 Years. *Geogr. Res.* 33, 14–22. doi:10.11821/dlyj201401002

Yosef, Y., Aguilar, E., and Alpert, P. (2019). Changes in Extreme Temperature and Precipitation Indices: Using an Innovative Daily Homogenized Database in Israel. *Int. J. Climatol.* 39, 5022–5045. doi:10.1002/joc.6125

Yosef, Y., Aguilar, E., and Alpert, P. (2021). Is it Possible to Fit Extreme Climate Change Indices Together Seamlessly in the Era of Accelerated Warming? *Intern. J. Climatol.* 41 (Suppl. 1), E952–E963. doi:10.1002/joc.6740

You, Q., Kang, S., Aguilar, E., Pepin, N., Flügel, W.-A., Yan, Y., et al. (2011). Changes in Daily Climate Extremes in China and Their Connection to the Large Scale Atmospheric Circulation during 1961-2003. *Clim. Dyn.* 36 (11-12), 2399–2417. doi:10.1007/s00382-009-0735-0

You, Q., Kang, S., Aguilar, E., and Yan, Y. (2008). Changes in Daily Climate Extremes in the Eastern and Central Tibetan Plateau during 1961-2005. *J. Geophys. Res.* 113 (D7), 1639–1647. doi:10.1029/2007jd009389

You, Q., Ren, G., Fraedrich, K., Kang, S., Ren, Y., and Wang, P. (2013). Winter Temperature Extremes in China and Their Possible Causes. *Int. J. Climatol.* 33 (6), 1444–1455. doi:10.1002/joc.3525

Zhang, C.-L., Li, Q., Shen, Y.-P., Zhou, N., Wang, X.-S., Li, J., et al. (2017). Monitoring of Aeolian Desertification on the Qinghai-Tibet Plateau from the 1970s to 2015 Using Landsat Images. *Sci. Total Environ.* 619-620, 1648–1659. doi:10.1016/j.scitotenv.2017.10.137

Zhang, X., Aguilar, E., Sensoy, S., Melkonyan, H., Tagiyeva, U., Ahmed, N., et al. (2005). Trends in Middle East Climate Extreme Indices from 1950 to 2003. *J. Geophys. Res.* 110, D22104. doi:10.1029/2005JD006181

Zhang, X., and Yang, F. (2004). *RClimDex (1.0) User GuideClimate Research Branch*. Downsview, Ontario, Canada: Environment Canada.

Zhang, Z., Han, W., Wang, J., Cai, Y., Gang, L., Cai, Z., et al. (2016). Characteristics of Climate Change and its Response in the Qinghai-Tibet Plateau during 1971-2010. *J. Landsc. Res.* 8 (6), 41–52. doi:10.16785/j.issn1943-989x.2016.6.011

Zhao, Z., and Wang, Y. (2017). Influence of the West Pacific Subtropical High on Surface Ozone Daily Variability in Summertime Over Eastern China. *Atmos. Environ.* 170, 197–204. doi:10.1016/j.atmosenv.2017.09.024

Zhen, Y., and Li, X. (2014). Recent Trends in Daily Temperature Extremes over Northeastern China (1960-2011). *Quat. Int.* 380-381, 35–48. doi:10.1016/j.quaint.2014.09.010

Zheng, D. (1999). A Study on the Physico-Geographical Regional System of the Tibetan Plateau. *Sci. China (Ser. D)* 26 (4), 336–341. (In Chinese). doi:10.13249/j.cnki.sgs.1999.04.002

Zheng, D. (1996). The System of Physico-Geographical Regions of the Qinghai-Xizang (Tibet). *Plateau. Sci. China (Ser. D)* 39 (4), 410–417. (In Chinese). doi:10.1144/GSL.QJEGH.1996.029.P3.08

Zhong, K., Zheng, F., WuQin, H. C., Qin, C., and Xu, X. (2017). Dynamic Changes in Temperature Extremes and Their Association with Atmospheric Circulation Patterns in the Songhua River Basin, China. *Atmos. Res.* 190, 77–88. doi:10.1016/j.atmosres.2017.02.012

Zhou, Y., and Ren, G. (2011). Change in Extreme Temperature Event Frequency over Mainland China, 1961–2008. *Clim. Res.* 50 (2–3), 125–139. doi:10.3354/cr01053

Conflict of Interest: The authors declare that the research was conducted in the absence of any commercial or financial relationships that could be construed as a potential conflict of interest.

frontiers | Frontiers in Environmental Science

ORIGINAL RESEARCH
published: 31 May 2022
doi: 10.3389/fenvs.2022.892925

Hydrologic Controls on Peat Permafrost and Carbon Processes: New Insights From Past and Future Modeling

Claire C. Treat[1]*, *Miriam C. Jones*[2], *Jay Alder*[3] and *Steve Frolking*[4]

[1]Alfred Wegener Institute Helmholtz Center for Polar and Marine Research, Potsdam, Germany, [2]Florence Bascom Geoscience Center, U.S. Geological Survey, Reston, VA, United States, [3]Geology, Minerals, Energy, and Geophysics Science Center, U.S. Geological Survey, Corvallis, OR, United States, [4]Institute for the Study of Earth, Oceans and Space, University of New Hampshire, Durham, NH, United States

Soil carbon (C) in permafrost peatlands is vulnerable to decomposition with thaw under a warming climate. The amount and form of C loss likely depends on the site hydrology following permafrost thaw, but antecedent conditions during peat accumulation are also likely important. We test the role of differing hydrologic conditions on rates of peat accumulation, permafrost formation, and response to warming at an Arctic tundra fen using a process-based model of peatland dynamics in wet and dry landscape settings that persist from peat initiation in the mid-Holocene through future simulations to 2100 CE and 2300 CE. Climate conditions for both the wet and dry landscape settings are driven by the same downscaled TraCE-21ka transient paleoclimate simulations and CCSM4 RCP8.5 climate drivers. The landscape setting controlled the rates of peat accumulation, permafrost formation and the response to climatic warming and permafrost thaw. The dry landscape scenario had high rates of initial peat accumulation (11.7 ± 3.4 mm decade^{-1}) and rapid permafrost aggradation but similar total C stocks as the wet landscape scenario. The wet landscape scenario was more resilient to 21st century warming temperatures than the dry landscape scenario and showed 60% smaller C losses and 70% more new net peat C additions by 2100 CE. Differences in the modeled responses indicate the largest effect is related to the landscape setting and basin hydrology due to permafrost controls on decomposition, suggesting an important sensitivity to changing runoff patterns. These subtle hydrological effects will be difficult to capture at circumpolar scales but are important for the carbon balance of permafrost peatlands under future climate warming.

Keywords: permafrost, peatlands and wetlands, tundra, peat accumulation, Holocene, ecological modeling

OPEN ACCESS

Edited by:
Xiaodong Wu,
Chinese Academy of Sciences (CAS), China

Reviewed by:
Kuang-Yu Chang,
Berkeley Lab (DOE), United States
Chunjing Qiu,
Laboratoire des Sciences du Climat et de l'Environnement (LSCE), France

***Correspondence:**
Claire C. Treat
Claire.treat@awi.de

Specialty section:
This article was submitted to Atmosphere and Climate, a section of the journal Frontiers in Environmental Science

Received: *09 March 2022*
Accepted: *05 May 2022*
Published: *31 May 2022*

Citation:
Treat CC, Jones MC, Alder J and Frolking S (2022) Hydrologic Controls on Peat Permafrost and Carbon Processes: New Insights From Past and Future Modeling. Front. Environ. Sci. 10:892925. doi: 10.3389/fenvs.2022.892925

1 INTRODUCTION

Soils in the permafrost region store large amounts of soil carbon (C), an estimated 1,015–1,035 Pg C (Hugelius et al., 2014; Mishra et al., 2021). Nearly 20% of this soil C can be found in permafrost peatlands, wetlands with thick organic soils and high organic matter concentration, which store 185 ± 70 Pg C (Hugelius et al., 2020). These peatlands have accumulated thick organic soils over millennia due to higher rates of vegetation productivity than decomposition. The formation and

presence of permafrost in peatlands, or ground that has remained frozen for more than 2 years (Brown et al., 2001, revised 2001), effectively stops decomposition of organic material frozen in the permafrost peat. In some regions, particularly in regions with continuous permafrost, permafrost aggradation and peat accumulation can go hand in hand, limiting decomposition before peat is incorporated into permafrost. These relatively undecomposed peat profiles can indicate syngenetic permafrost formation along with distinct ice structures within the permafrost peat (Kanevskiy et al., 2014), while in more southern sites, epigenetic permafrost formed substantially after peat deposition (Treat and Jones, 2018). The formation of epigenetic permafrost in peatlands is controlled by climate at the time of permafrost formation (Zoltai, 1995), while the spatial distribution of permafrost in peatlands with discontinuous, isolated, and sporadic permafrost is likely related to the hydrology. A case study from Western Canada found that the spatial distribution of permafrost in peatlands was likely controlled by regional hydrologic patterns, including runoff within wetlands and their watersheds (Quinton et al., 2009). Thus, both climate and hydrology are key drivers of the spatial and temporal distribution of permafrost.

Exactly what factors contribute to the differences in peat accumulation rates under permafrost conditions during the Holocene is unclear. In an earlier large synthesis of peat accumulation rates, both the difference in the timing of permafrost aggradation (i.e., epigenetic or syngenetic) and the spatial distribution of permafrost affected the apparent peat accumulation rates (Treat et al., 2016a). In tundra sites within the continuous permafrost zone, apparent peat accumulation rates varied widely after permafrost aggradation (25%–75% quantile range: 14.9–111.0 g C m^{-2} yr^{-1}). In sites with warmer, epigenetic permafrost within the discontinuous permafrost zone, the apparent peat accumulation rates since permafrost aggradation were not as variable as in tundra but were 20%–40% lower than comparable permafrost-free fens and bogs. Some northern peat cores also showed very high rates of peat accumulation in the early to mid-Holocene during their initial phase of peat accumulation (Lavoie and Richard, 2000; Jones and Yu, 2010). These high rates of peat accumulation were hypothesized to be driven by enhanced productivity due to high seasonality and solar insolation during the early Holocene (Jones and Yu, 2010). Given the wide range and high rates of peat accumulation found in tundra sites, we hypothesized that syngenetic permafrost formation could be another mechanism for high rates of peat accumulation due to the limited decomposition that occurs with rapid incorporation into the permafrost, as has been suggested in boreal sites (Jones et al., 2017; Manies et al., 2021). However, the conditions that cause this the rapid incorporation of peat into permafrost are unclear.

The rates and amount of carbon that could potentially be released with permafrost thaw are highly uncertain (Schuur et al., 2015; McGuire et al., 2018). Field studies in thawed permafrost peatlands in Southwestern Alaska show that C losses following permafrost thaw can be large, as much as 30% of old peat C stocks (Jones et al., 2017). However, earlier modeling of permafrost peatlands in Western Canada showed that permafrost peatland C was relatively resilient to 21st century warming, with C losses <5% of the old C in peat (Treat et al., 2021). One hypothesis to explain the difference between the outcomes is related to permafrost history, where sites with syngenetic permafrost have relatively undecomposed organic matter that is vulnerable to decomposition when the peat is thawed whereas sites with epigenetic permafrost have undergone more decomposition and the peat is less vulnerable when it thaws (Treat et al., 2014; Manies et al., 2021).

Given that the spatial distribution of permafrost can be controlled by regional hydrology (Quinton et al., 2009) and that we observed a strong sensitivity of the peat profile at a high Arctic site to the model parameterization representing the regional hydrology in our earlier work (Treat et al., 2021), we also hypothesized that the rapid rates of peat accumulation in permafrost could be driven by the site hydrology and whether the peatland was relatively dry or wet. The objective of this study was to test the effects of hydrology on rates and timing of peat accumulation and vulnerability to permafrost thaw. Specifically, we tested the parameter representing the relative amount of water a peatland retains, the balance between the water inputs from the surrounding watershed and the runoff to downstream areas, which can differ across the landscape due to watershed characteristics and regional hydrology (Woo and Young, 2006). We used a process-based model to simulate peatland development in a permafrost peatland in the Canadian Arctic. Simulations ran from peatland initiation at the site in 6,620 BP to present day and projections for 21st century climate warming. We used two contrasting water table scenarios that were driven by the model parameterization representing the regional hydrology, including the water inputs from the surrounding watershed and the runoff to downstream areas. Note that precipitation in both scenarios was the same. Finally, we compared the resulting differences in peat accumulation, permafrost aggradation, and the response to climatic warming between the two scenarios and as well as to field observations.

2 MATERIALS AND METHODS

2.1 Site Description

Thelon-Kazan Peatland (TKP) was selected as a site for an earlier modeling study using a climatic gradient through Western-Central Canada (Treat et al., 2021). In that study, we discovered divergent peat profiles at TKP depending on the parameterization for the hydrological landscape setting. Here, we are exploring those different patterns to develop a more general hypothesis or possible explanation about peat/permafrost dynamics in contrasting hydrological and landscape settings, rather than trying to recreate the C accumulation dynamics at TKP. TKP is located in the Canadian Arctic, approximately 400 km north of treeline in the continuous permafrost zone (66° 27.07′ N, 104° 50.08′ W), where the mean annual air temperature was −11.3°C and mean annual precipitation was 272 mm (Station Baker Lake A 1980–2010; https://climate.weather.gc.ca/climate_normals/; accessed 12 December 2019). The TKP peatland is a fen with

high-centered polygonal features and an active layer thickness of 30–40 cm, where peat cores were described by Vardy et al. (2005); Vardy et al. (2000). The manually digitized data from TKP were included in an earlier synthesis (Treat et al., 2016a) and used in an earlier modeling effort (Treat et al., 2021). Three cores were taken at TKP using monolith extraction in the surface soil and motor-driven CRREL Permafrost augers at some point prior to 1998; the exact timing of core collection is unknown. Here we focus on core TK1P2 (also called TKP-2). The TK1P2 core was collected from the center of a high-center polygon and accumulated 193 cm of peat since 6,620 cal. BP (basal age: 5820 ± 70 ^{14}C BP; WAT-3066). The peat core (TK1P2) was mainly composed of Cyperaceae with mosses, lichens, and dwarf shrubs in the surface 35 cm (Vardy et al., 2000; Vardy et al., 2005). Data available from the TKP cores includes bulk density, carbon or organic matter content, radiocarbon dates, and plant macrofossil analysis. The data from TKP are available for download (doi: 10.1594/PANGAEA.863697; Treat et al., 2016b); the dataset key (Variable: Auth. Site.CoreID) for TKP is VAR-TKP-01.

2.2 Model Description

We used HPM-Arctic (Treat et al., 2021), which couples a carbon-hydrologic model for peatlands (Frolking et al., 2010) with the Geophysical Institute Permafrost Lab soil thermal model GIPL2 (Marchenko et al., 2008). HPM-Arctic simulates peat formation since initiation to present and into the future, also generating time series of active layer thickness and age of the peat at the bottom of the active layer. HPM-Arctic has been tested and implemented for a transect of peatland sites across western Canada, including TKP (Treat et al., 2021). The model code, parameters, and climate driver data are available from: https://doi.org/10.5281/zenodo.4647666; derivation of parameters and climate drivers is described below.

Briefly, HPM simulates the development of a peat profile over millennia, from initiation, using an annual litter cohort approach with three major plant types (shrubs, herbaceous taxa, and mosses). In HPM-Arctic, the changes in vegetation and NPP are driven primarily by changes in water table depth, following the original HPM formulation (Frolking et al., 2010). Changes in water table can be driven either by external climate forcings (precipitation vs. ET), or by internal peat dynamics, including peat accumulation. NPP temperature sensitivity was modeled as a Q_{10} function, with a Q_{10} value of 1.8, based on an empirical relationship between mean annual air temperatures and above-ground net primary productivity for mosses, vascular plants, and trees that was developed for a transect of peatland sites in boreal Manitoba, Canada (Camill et al., 2001). CO_2 concentration impacts on productivity are not accounted for in HPM.

Each year's annual litter input is aggregated into a litter cohort and tracked as it becomes buried and decomposed through the millennia of the simulation. HPM tracks the fraction of total plant litter inputs (above- and below-ground) remaining in annual peat cohorts through the entire profile. This fraction modifies the initial peat litter quality, so that under the same environmental conditions, peat that has lost half its mass to decomposition will decompose at half the rate of fresh peat (Clymo, 1992; Frolking et al., 2001). Decomposition rates are dynamic and dependent on plant litter types (e.g., species-specific decomposition rates), water table or water content, and soil temperature. HPM simulates the water-filled pore space of the unsaturated peat water filled pore space, based on peat bulk density and distance above the water table. In that zone, there is an optimum WFPS for decomposition, with rates falling for drier and wetter peat. Full anoxia occurs some distance below the simulated water table for several reasons: the actual water table is more dynamic than monthly time step simulations, oxygen and other terminal electron acceptors can be delivered to the peat in groundwater flow (much greater for fen than bog), and precipitation water, and also diffuse into the deeper peat from the underlying subsoil or the atmosphere. HPM simplifies these complex phenomena by specifying an exponential decline in the anoxia multiplier on decomposition from its value at the water table to a minimum value, following the original HPM formulation (Frolking et al., 2010). This decline is parameterized to happen much more abruptly in bog than fen conditions.

When decomposing peat becomes frozen into permafrost, it stops decomposing until permafrost thaw, preserving the quality of the peat at freeze-up, which affects the rate of decomposition at thaw. Active layer thickness, updated annually, is determined by identifying the soil depth immediately above where the temperature remains below 0°C for 2 years continuously, in accordance to the definition of permafrost (Harris et al., 1988). HPM-Arctic uses a simple "old-new" carbon tracking algorithm, whereby after a specified year all moss, sedge, and shrub plant litter gets labeled as "new," so that its accumulation as peat and loss through decomposition can be tracked separately from the older peat derived from plant litter inputs prior to the specified year. The year 2015 C.E. is defined in the model as both present-day and the boundary between new (future) and old (past) carbon inputs.

2.3 Model Optimization and Evaluation

Some site-specific calibrations were done for several model parameters to capture variability (often not quantified) related to individual watershed and site characteristics (**Table 1**). Peat initiation often occurs in a local topographic low, receiving run-on from the surrounding watershed; as the peat accumulates and the peat surface rises, it can shift to a local topographic high point, and shed water (run off) rather than receive it (Charman, 2002). The site-specific model parameters include the accumulating peat height at which this shift from run-on to run-off occurred ($H_{run-on/off}$) along with a constant scaling factor, and the peat height when initial fen-type vegetation transitioned to bog-type vegetation (H_{FBT}). When the peat height exceeds the site-specific H_{FBT}, the peatland transitions from a fen to a bog, which involves a decrease in annual NPP to a varying degree (Rydin and Jeglum, 2006) modeled with a site specific fractional parameter ($F_{NPP\text{-}bog}$). With greater lateral hydrological inflow, and therefore a shorter water residence time in the saturated zone, fen conditions are assigned a longer scale length (persistence of partial anoxia below the water table) to a full anoxia impact on decomposition rate. This is modeled with an anoxia scale length parameter (Frolking et al., 2010), which controls how far/quickly

TABLE 1 | Model parameterization used in HPM-Arctic for the wet and dry landscape scenarios at Thelon-Kazan Peatland (TKP).

Parameter	Description	Wet	Dry
	Time of peat initiation (BP)	6,620	6,620
$H_{run\text{-}on/off}$	Height run-on/off (m)	4.5[a]	0.5
H_{FBT}	Height of fen-bog transition (m)	2.1	2.1
$F_{NPP\text{-}bog}$	NPP multiplier at H_{FBT}	0.48	0.48
$AnoxiaScale\text{-}_{Fen}$	anoxia scale length in fen when height < H_{FBT} (m)	3.0	3.0
$AnoxiaScale\_{Bog}$	anoxia scale length in bog when height > H_{FBT} (m)	1.2	1.2
Max NPP	Maximum annual NPP under ideal conditions (kg m^{-2} y^{-1})	1.1	1.1
RMSE	Root mean square error, model vs. observed age-depth profile (**Figure 2A**)	21	92

**The age of the peat surface was assumed to be the same as the year of sampling and included in the age-depth model.*
[a]A value deeper than the peat height indicates that the peat will continues to receive run-off until the threshold is reached.

reduced electron acceptors are replenished below the water table. This affects peat decomposition rates below the water table. Frozen peat decomposition rates are set to zero (also for seasonal winter frost), while decomposition persists in the seasonally-thawed surface active layer.

Site-specific parameter values were determined from a combination of observations and/or optimization routines (**Table 1**; Treat et al., 2021). The parameter H_{FBT} was determined by trial and error from the final peat height and observations of the height of the fen-to-bog transitions (H_{FBT}) in the site core profile; the model parameter H_{FBT} generally was higher than in the observations. $H_{run\text{-}on/off}$ was determined by trial and error when the difference between the final modeled peat height and observed peat height reached <10 cm, as well as the macrofossil composition compared with the dominant modeled PFTs, which indicated relative water table position over time (e.g., dry or wet). The other three parameters ($F_{NPP\text{-}bog}$, and anoxia scale lengths for fen and bog) were determined from minimizing the root mean squared error between the observed and modeled age-depth profiles, where the age of the peat surface was assumed to be the year of sampling. At TKP, the parameterization used results from earlier model runs at Ennadai Lake, a polygonal permafrost peatland site in NW Territories (c.f. Treat et al., 2021) and generalized parameters for temperate and boreal peatlands (Frolking et al., 2010) due to the limited number of radiocarbon dates (e.g., **Figure 2**), which limited the number of tunable model parameters (under constraint problem). However, the study goal was not to find the closest agreement to a particular peat core at TKP, but to test a hypothesis about how local hydrology (wet/dry) in a permafrost setting can impact peat accumulation rates and carbon loss upon thaw.

For calculating organic matter stocks and C stocks, model output (mass of peat) was multiplied by mean values determined from a synthesis of over 10,000 peat layers spanning the pan-Arctic permafrost region (Treat et al., 2016a). The conversion factor from model peat mass to organic matter (OM) was 0.924 g OM g^{-1} peat. The conversion factor from organic matter to carbon was 0.495 gC g^{-1} OM. While this assumption does introduce some uncertainty into the model results for predictions of future carbon losses, these are likely not the major sources of uncertainty in predicting future C loss as other processes, including changes in landscape hydrology in permafrost regions, are less well known and have larger impacts (Quinton et al., 2010).

2.4 Model Scenarios

The two landscape scenarios at TKP used identical climate drivers, initiation times, vegetation parameters, and most site-specific model parameters (**Table 1**). We created two model scenarios, dry and wet landscape position, by varying a single site-specific model parameter, $H_{run\text{-}on/off}$ (**Table 1**), which is the height of the peat when it begins to shed water, exerting a strong control on the water table level and soil moisture. The dry landscape scenario used $H_{run\text{-}on/off}$ = 0.5 m, which meant that the peat height quickly crossed the threshold to generate runoff, i.e., peat accumulation caused the site to become a local high point in the landscape, and so the peat profile became relatively dry. The wet landscape scenario used $H_{run\text{-}on/off}$ = 4.5 m, a peat height that was not reached during the simulation, ensuring a relatively wet peat profile throughout the simulation. While HPM-Arctic does not simulate a surface energy balance, both scenarios are driven by identical climate forcings and modeled active layer depths are consistent with recent meta-analysis results (Clayton et al., 2021). Secondly, an earlier study showed relatively small differences in net radiation among different tundra sites without standing water, relative to sites with standing water, within the same region (Rouse et al., 2000); mean annual water table in these two landscape scenarios is below the peat surface, meaning that there is no standing water and that the net radiation absorbed by the sites is similar.

2.5 Model Climate Drivers

We utilize the TraCE-21ka transient paleoclimate simulations (Liu et al., 2009: https: //www. earthsystemgrid. org/project/trace. html) to drive HPM-Arctic with monthly temperature and precipitation from 8,000 B.P. to 1990 CE (8 Kyr timeseries). The continuous TraCE-21ka simulations include time-dependent changes in atmospheric greenhouse gases, insolation, and paleogeography as sea level rises from the melting of the large northern hemisphere ice sheets. Monthly temperature and precipitation time series for TKP were extracted from the 3.75° × ~3.75° climate model grid by bilinear interpolation and then bias-corrected using contemporary regional climate data. To obtain timeseries of temperature for input to HPM-Arctic, we computed anomalies of the 8 Kyr time series to the TraCE-21ka 1950–1990 CE mean and applied the anomalies additively to a modern observed gridded data set (CRU TS v3.32; Harris et al., 2014) using the same base period. The

8 kyr precipitation timeseries was derived by applying the ratio of the 8 Kyr precipitation to the 1950–1990 CE mean as a scaler to the CRU data. As with the TraCE-21ka data, the CRU grid (0.5° × 0.5°) was interpolated to our site locations.

To continue the 8 Kyr timeseries into the future, we adopt the CCSM4 RCP8.5 simulation from the Coupled Model Intercomparison Project Phase 5 (CMIP5; Taylor et al., 2012). The RCP8.5 scenario was chosen as an end-member or upper bound to capture the greatest projected changes in temperature. CCSM4 (Gent et al., 2011) is the successor to the CCSM3 model used in the TraCE-21ka simulations, and so was chosen for model consistency. While focusing on one model projection is a limitation, CCSM4 also has an transient climate response (the response to a 1% yr^{-1} doubling of atmospheric CO_2) of 1.8°C, which is the same as the CMIP5 ensemble multi-model mean of 1.8°C (Flato et al., 2013), giving us confidence the projected temperature changes at our sites are not unreasonable relative to the full CMIP5 ensemble. To extract projected time series at the peatland site locations, we use the same process of bilinear interpolation from the CCSM4 grid (0.9° × 1.25°) and applying CRU bias correction using the 1950–1990 CE climatology period. In our analysis and results below, HPM-Arctic is driven by TraCE-21ka output prior to 1990 CE and CCSM4 afterwards. The RCP8.5 simulations span 2005 through 2100 CE. To capture the effects of new equilibrium climate conditions at 2100 on the relatively slow processes of peat accumulation and loss, we extended RCP8.5 from 2100 for an additional 200 years by randomly sampling full years from the final 25 years of the simulation (2076–2100 CE) using the R command "sample" (replace = T). The modeled climate drivers are shown in **Supplementary Figure S1**.

2.6 Statistical Analysis and Data Analysis

All statistical analyses were conducted using R statistical software (Team, 2008). Errors represent standard deviation. In order to compare modeled C losses with observations, we used the peat C stock in 2015 CE, and the results from old/new C tracker in 2100 CE and 2300 CE. Net C loss (or gain) was calculated from the difference in total C stocks in 2015 and 2100 CE or 2300 CE; new C additions and old C losses were calculated relative to the stocks in 2015.

3 RESULTS AND DISCUSSION

3.1 Peat Accumulation, Permafrost Formation From 7000 BP to 0 BP

The model of peat development for TKP under wet and dry landscape settings produced divergent peat water table and active layer depths (**Figure 1**), and vegetation species composition (**Table 2**) despite using the same climatic drivers (**Supplementary Figure S1**). Simulated peat depths between the wet and dry scenarios in the present day show that 1.9 m accumulated in the wet scenario and 2.8 m in the dry scenario (**Figure 1**; **Table 2**). The water table in the wet scenario remained near the surface (mean: 3 ± 2 cm depth) throughout the simulation (**Figure 1A**), while the water table in the dry scenario was deeper (mean: 31 ± 9 cm depth, **Figure 1B**). The timing of peat and permafrost development also differed between the wet and dry scenarios. Modeled active layer depths in the present day were <50 cm in the dry scenario and >80 cm in the wet scenario (**Table 2**). Present-day vegetation differed between the two scenarios, with shrubs having the highest NPP in the dry scenario and herbaceous species (e.g., sedges) having the highest NPP in the wet scenario (**Table 2**).

3.1.1 Wet Landscape Setting Scenario

In the wet landscape scenario, permafrost aggraded in the peat profile after 5900 BP, about 700 years into the simulation (prior to that time, permafrost was present in the underlying mineral soil). Peat deposited after 3100 BP remained in the active layer throughout the simulation (**Supplementary Figure S2**). Modeled, decadal-smoothed rates of peat accumulation for the wet scenario ranged from −8.7–11.5 mm $decade^{-1}$ (**Figure 1C**). The peat accumulation rates differed dramatically before (4.3 ± 3.5 mm $decade^{-1}$) and after (<0 mm $decade^{-1}$) the fen-bog transition at 2150 BP (**Figure 1C**) due to declining vegetation (litter) productivity.

3.1.2 Dry Landscape Setting Scenario

In the dry landscape scenario, the modeled water table dropped well below the surface after the initial period of peat initiation and remained deeper throughout the simulation (**Figure 1B**). Permafrost aggraded in the peat profile approximately 200 years later in the dry scenario than the wet scenario, after 5700 BP. Subsequently, both peat and peat in the permafrost aggraded rapidly, with more than 1 m of peat added in the next 1,150 years (**Figure 1B**). Mean peat accumulation rates were 11.7 ± 3.4 mm per decade during this period (5700 BP–4550 BP), and the residence time of the peat in the active layer was <200 years before being incorporated into the rapidly aggrading permafrost in the peat profile (**Supplementary Figure S2**). During this period of rapid peat and permafrost aggradation, mean NPP in the dry landscape scenario was 54 g Cm^{-2} y^{-1}, while in the wet scenario it was 84 g Cm^{-2} y^{-1}. The more rapid rates of incorporation of peat into the permafrost resulted in relatively little decomposition with, a mean of 52% of the original peat mass remaining in the permafrost peat (**Figure 1**). The active layer remained comparatively shallow throughout (**Figure 1B**). After the modeled fen-bog transition at 4550 BP, the peat accumulation decreased to a mean rate of 1.4 ± 2.1 mm $decade^{-1}$ (**Figure 1D**) and the residence time in the active layer increased.

3.1.3 Age-Depth Differences

Differences in peat depth between the dry and wet landscape scenarios at TKP (**Figures 1A,B**) resulted in age-depth profiles that differed between these two landscape settings (**Figure 2A**). The age-depth profile for the wet scenario was a better fit to the observations at TKP than the dry scenario (**Figure 2A**; RMSE = 21 for wet vs. 92 for dry), as was the organic matter density below 0.5 m depth (**Figure 2B**), suggesting that the wet scenario more accurately reflects the development at TKP. The difference in peat thickness between the two scenarios (1.9 m in the wet scenario vs. 2.8 m in the dry scenario) reflects the significant difference in the

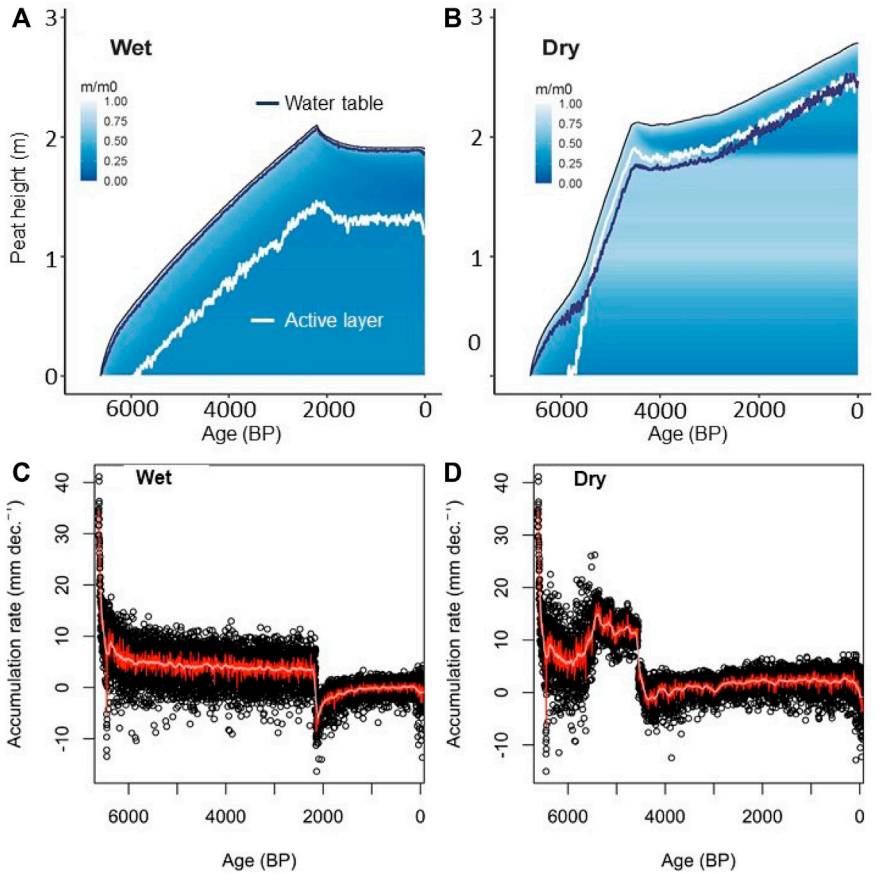

FIGURE 1 | Time series of peat profiles at TKP with two different values of model parameter for the peat height when run-on switches to run-off ($H_{run\text{-}on/off}$): **(A)** $H_{run\text{-}on/off}$ = 4.5 results in a wetter peat profile with a water table (blue line) near the peat surface; **(B)** $H_{run\text{-}on/off}$ = 0.5 results in a drier peat profile and an unsaturated (dry) active layer (white line); m/m0 represents the peat litter cohort mass remaining, high values indicating relatively undecomposed peat; **(C)** Modeled peat accumulation rates for the wet landscape scenario (black circles), as well as smoothed rates using decadal (red) and centennial (gray) filters; **(D)** Modeled peat accumulation rates for the dry landscape scenario (black circles), as well as smoothed rates using decadal (red) and centennial (gray) smoothing. All other parameters and climate drivers were the same between the two simulations.

TABLE 2 | Field observations and model results for present day (2015: means of 2006–2015 CE) and future scenarios, including 2100 (means of 2091–2100 CE) and 2300 (means of 2291–2300 CE) for peat height, peat organic matter (OM) stocks, water table depth, maximum annual active layer thickness, and dominant vegetation types, both by productivity (e.g., mean decadal NPP of surface vegetation) and the dominant type preserved in the peat core record.

Year/ scenario	Landscape Scenario	Peat height (m)	Peat OM (kg OM m^{-2})	Water table depth (m below surf)	Active layer thickness (m)	Dominant vegetation—NPP	Dominant vegetation—Peat
1993/4	Observed	1.93	220	(0.40)	0.40	Shrub	Sedge/Shrub
2015—Wet	Wet	1.90	195	0.03	0.87	Sedge	Moss
2100—Wet	Wet	1.85	190	0.15	0.79	Sedge	Moss
2300—Wet	Wet	1.77	180	0.17	0.81	Shrub	Moss
2015—Dry	Dry	2.77	200	0.33	0.48	Shrub	Moss
2100—Dry	Dry	2.63	190	0.44	0.78	Shrub	Moss
2300—Dry	Dry	2.31	170	0.50	0.66	Shrub	Moss

organic matter densities of the two simulated profiles (**Figures 1**, **2B**). However, neither modeling scenario captures the high density of organic matter observed in the surface 0–0.5 m of the peat core, though the wet scenario does have higher bulk density around 0.5 m than deeper in the profile (**Figure 2B**). The combined effect of the differences in thickness and the difference in organic matter density between the wet and dry scenarios resulted in relatively small differences (3%) in organic matter

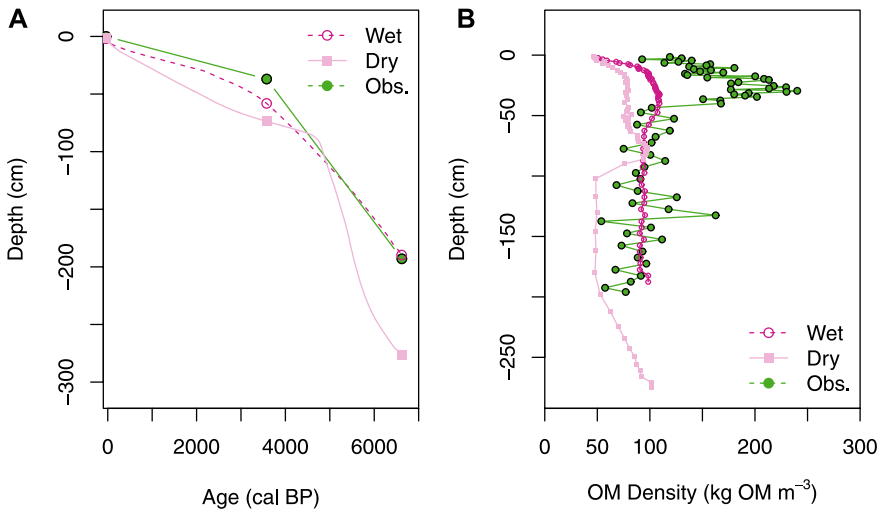

FIGURE 2 | Depth profiles for TKP for modeled scenarios (wet, dry landscapes) and observations (Obs.). **(A)** Modeled age-depth profiles (light pink and dark pink) are continuous with circles corresponding to the ages of the observations, while the green line connecting the observations is a linear interpolation between the three observed points. **(B)** Modeled and observed organic matter density with depth.

stocks (wet: 195 kg OM m^{-2}, dry: 200 kg OM m^{-2}). Therefore, in permafrost peats, the peat height or peat depth should not be used to predict C stocks (**Table 2**). This result points to the challenge of predicting peat carbon or organic matter stocks in permafrost soils using peat depth (Hugelius et al., 2020) as both results from this study (**Table 2**) and that study show little correlation between peat depth and C stock. Similarly, gap-filling carbon density for determination of peatland C stocks in permafrost peatlands (i.e., Nichols and Peteet, 2019) is also problematic (**Figure 2B**; **Table 2**), which is also compounded by the relatively high variability in bulk density found across tundra permafrost peats (coefficient of variation = 130%; Treat et al., 2016a).

3.2 Future Projections of Peat, Permafrost, and C Balance

The RCP 8.5 driven HPM-Arctic simulations at TKP under wet and dry landscape settings for the future resulted in substantially different outcomes at 2100 CE for peat temperatures and permafrost, hydrology, vegetation, and carbon cycle, despite having the same climatic drivers. By 2100 CE, transient warming projected under RCP 8.5 increased mean annual air temperature from −11.3°C to −4.4°C. Despite the strong warming, permafrost remained in the peat profile (**Figure 3**). Warmer temperatures increased evapotranspiration, which combined with gradual thawing of permafrost increased the depths to the perched water table (**Table 2**). The changes in water table shifted the modeled species composition, while the warmer air temperature increased modeled NPP (**Figure 4**). Along with warming temperatures, the changes in water table, active layer thickness, increased decomposition as well as net primary productivity altered the peat profiles and C balance by 2100 (**Figures 5**, **6**).

Under the assumption that 21st century warming stabilized between 2100 and 2300 CE, the peat temperatures at TKP differed little between 2100 and 2300 CE in the two scenarios, and were still cold enough to maintain permafrost (**Figure 3B**). However, active layer thickness decreased by roughly 10 cm between 2100 and 2300 in both scenarios (**Table 2**), as the decrease in peat height (5–30 cm) due to net peat loss (decomposition) exceeded the gradual thawing at the top of the permafrost peat (**Figure 5**). Still, an additional ~10 cm of permafrost peat thawed in both scenarios between 2100 and 2300. Net C losses by 2300 were larger than in 2100 as the increase in NPP and net peat accumulation were smaller than the decomposition of the old carbon (**Figure 6**). These C losses represented a small to moderate fraction of total peat C stocks which is in rough agreement with other high Arctic cold and wet sites (Elberling et al., 2013). Overall, these findings agree with earlier studies that projected larger permafrost C losses at 2300 than 2100, and show that these net losses are dependent on both new C sequestration in the soil and old permafrost C losses (**Figure 6**).

3.2.1 Wet Landscape Setting Scenario

By 2100, warmer soil temperatures resulted in increased peat decomposition as well as thawing of the top permafrost. The peat loss resulted in lower total peat height, which actually decreased the modeled active layer thickness from 0.9 to 0.8 m (**Figure 5**). Changes in the active layer thickness, along with increased evapotranspiration, resulted in a ~12 cm deeper water table (**Table 2**). NPP increased 70% by 2100 relative to 2015, with the shrub share of productivity increasing from <10% to 30% (**Figure 4A**). In both 2015 and 2100, NPP was ~50% larger in the wet than the dry scenario due to productivity of mosses and herbaceous species. Despite a decrease in the total peat height, only a small net loss of peat from the active layer was indicated by the relatively constant value of m/m0 at a particular peat

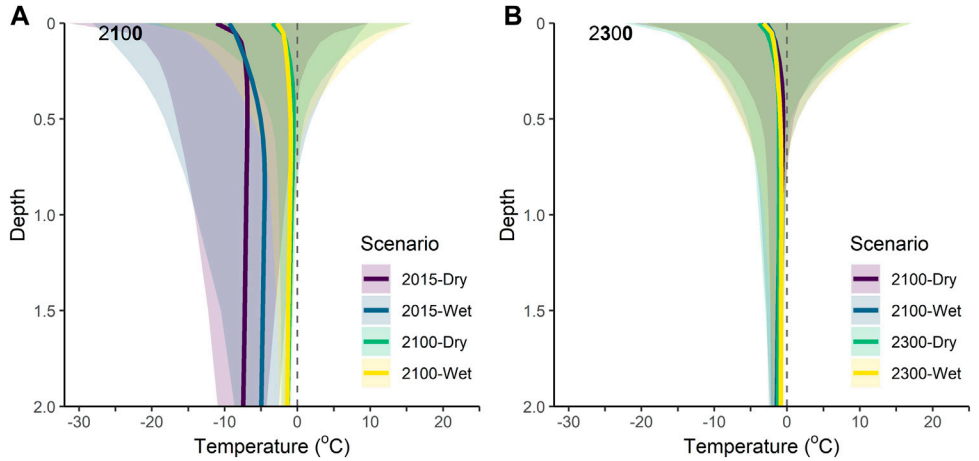

FIGURE 3 | Distribution of modeled peat temperatures at TKP for Dry and Wet Landscape scenarios for time periods: **(A)** 2015 (mean from 2006 to 2015) and 2100 (mean from 2091 to 2100); **(B)** 2100 (mean from 2091 to 2100) and 2300 (mean from 2291 to 2300). Heavy lines represent the mean annual peat temperatures, while the shaded areas represent the temperature range between the mean minimum annual and mean maximum annual temperature over the periods of interest.

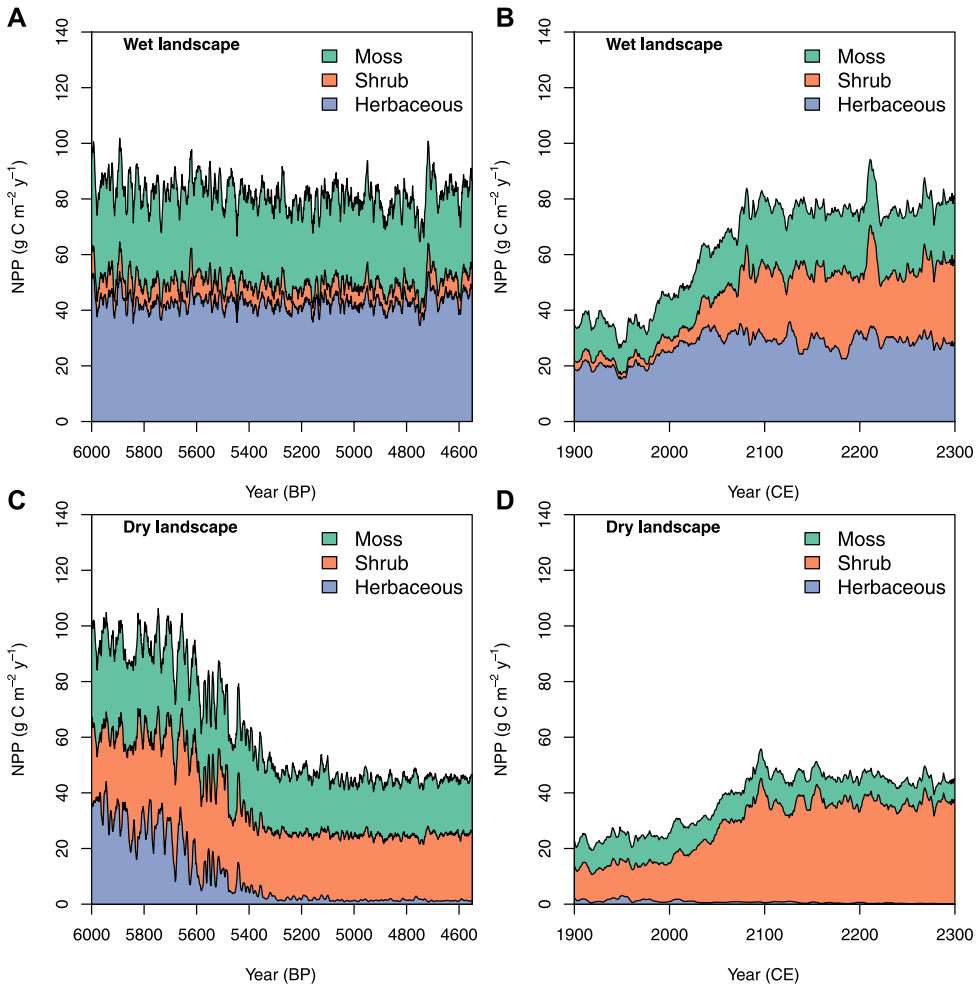

FIGURE 4 | Modeled net primary productivity for moss, shrub, and herb plant functional types in the wet (top) and dry (bottom) landscape scenarios for two time periods: 6,000 BP–4,550 BP (left) and between 1900 and 2300 CE (right). **(A)** Wet landscape scenario, 6000 - 4550 BP; **(B)** Wet landscape scenario, 1900 - 2300 CE; **(C)** Dry landscape scenario, 6000 - 4550 BP; **(D)** Dry landscape scenario, 1900 - 2300 CE.

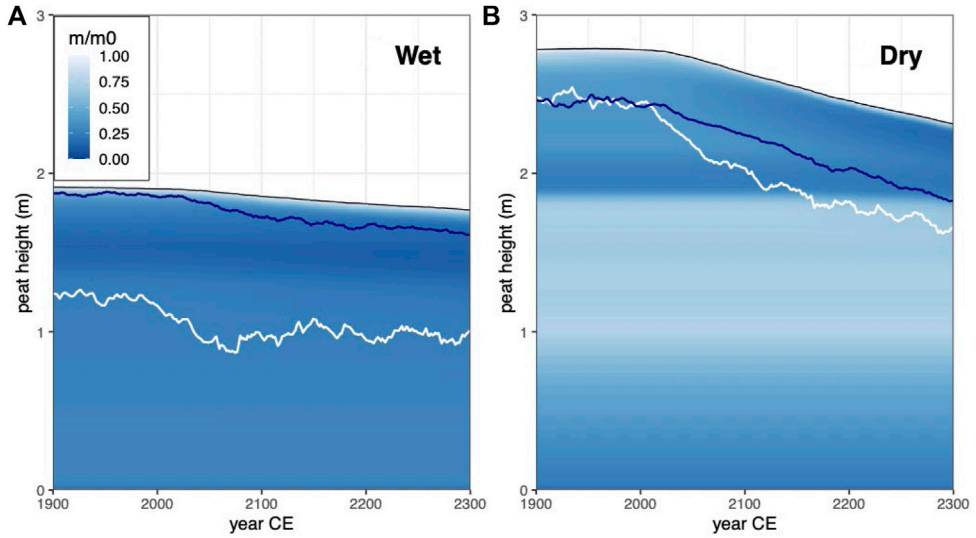

FIGURE 5 | Future projections of peat profiles at TKP under RCP8.5 using two different values of model parameter for the height when run-on switches to run-off ($H_{run\text{-}on/off}$): **(A)** $H_{run\text{-}on/off}$ = 4.5 results in a wetter peat profile with a water table (blue line) near the peat surface; **(B)** $H_{run\text{-}on/off}$ = 0.5 results in a drier peat profile and an unsaturated active layer. All other parameters and climate drivers were the same between the two simulations. The white line represents top of permafrost; m/m0 represents the peat litter cohort mass remaining, high values indicating relatively undecomposed peat.

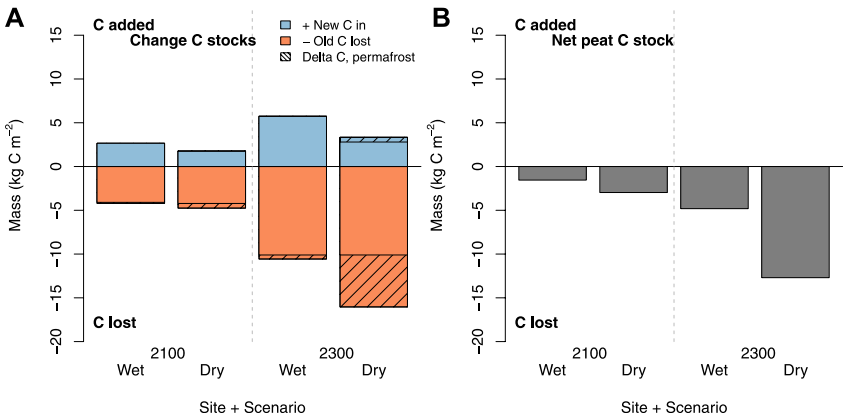

FIGURE 6 | Simplified peat profile diagrams for changes in C stock for the two landscape scenarios (Wet, Dry) in 2100 CE and 2300 CE relative to 2015 CE. **(A)** Changes in C stocks, including new peat C added (blue) and old peat C lost (orange). The amount of new peat added or old peat lost from permafrost is indicated by the black diagonal stripes. New C additions and old carbon losses are defined as peat deposited before 2015 (old) or after 2015 (new). **(B)** Net change in peat C stocks in the two landscape scenarios for the two time periods. All scenarios showed a net peat C loss.

height above the active layer (**Figure 5A**). New peat C accumulations from net primary productivity offset more than 60% of old C loss (defined as peat C accumulated before 2015), resulting in a net C loss in the wet scenario of −1.6 kg Cm^{-2} by 2100 (**Figure 6**).

The relatively stable forcing air temperature between 2100 CE and 2300 CE resulted in no significant change in NPP in the wet scenario. Decomposition of old peat in the active layer continued due to warmer temperatures, resulting in projected net C losses of −5 kg Cm^{-2} by 2300 CE (**Figure 6**). Little C was lost from the permafrost in the wet scenario (<0.4 kg Cm^{-2}). The total old C losses represented a small fraction (5%) of total peat C stocks by 2300 CE.

3.2.2 Dry Landscape Setting Scenario

Between 2015 and 2100, peats below 0.3 m warmed more in the dry than the wet landscape scenario (**Figure 3**). The modeled active layer thickness increased from 0.5 to 0.8 m by 2100 (**Figure 5**) and the water table depth increased by ~12 cm. NPP increased by 80% and was primarily driven by increased NPP in shrubs, while NPP of mosses and herbaceous species declined (**Figure 4B**). Modeled peat loss occurred in the active layer over a longer time period

between 2000 and 2300 (**Figure 5B**), but subsidence was not strong enough to result in an increase in the water table level relative to the surface (**Table 2**; **Figure 5**). 21st century warming and drying related to lower water table resulted in most of the active layer peat further decomposing (darkening of active layer peat in **Figure 5B**). This resulted in a net decrease in peat height of >0.1 m (**Figure 5B**) as the increased decomposition resulted in both net peat loss and an increase in bulk density of the remaining peat in the active layer (2015 mean: 75 kg OM m^{-3}; 2100 mean: 90 kg OM m^{-3}). Despite thawing of more than 40 cm of permafrost peat (**Figure 5B**), only −0.5 kg Cm^{-2} was lost from newly thawed permafrost peat by 2100, representing 15% of net C loss (**Figure 6**). The smaller NPP (**Figure 4B**) along with enhanced decomposition due to warmer, drier conditions (**Figure 5B**), led to smaller net accumulation of new peat, which offset only 35% of the already larger losses of old C (**Figure 6**). The projected net C loss in the dry scenario was −3.0 kg Cm^{-2} by 2100, nearly double the losses in the wet scenario.

The relatively stable forcing air temperature between 2100 CE and 2300 CE resulted in a 20% decrease in NPP in the dry scenario as the water table continued to drop (**Figures 4**, **5**; **Table 2**). Projected net C losses were −13 kg Cm^{-2} by 2300, which represents 15% of the total peat C stock. Strong net losses of old permafrost C (−6 kg Cm^{-2}) represented ~40% of the net C loss by 2300.

3.3 Drivers of Permafrost Formation and Peat C Accumulation

In this modeling study, an important result was that permafrost formation and stability was strongly influenced by the parameter that represents the regional hydrology and the wetland connectivity to the watershed, $H_{run\text{-}on/off}$ (**Figure 1**). Specifically, $H_{run\text{-}on/off}$ represents the height of the peat when the peatland stops receiving run-on from the surrounding landscape and begins to shed water *via* run-off, as occurs in domed bogs (Charman, 2002). While the $H_{run\text{-}on/off}$ parameter was important for maintaining a shallow water table level, for example representing wetlands that are still connected to the surrounding watershed (Woo and Young, 2006), it also controlled rates of peat accumulation through feedbacks between the water table position and the peat thermal properties, which influenced the thickness of the active layer and ultimately decomposition rates. Peat accumulation results from rates of productivity exceeding rates of decomposition. During the period of exceptional high peat accumulation rates between peat initiation in 5700 BP to 4550 BP (**Figure 1D**), NPP in the wet landscape was on average 50% greater than the dry landscape NPP (**Figures 4A,C**), yet **Figure 1D** shows that peat accumulation rates are >2.5 times larger for this dry landscape scenario. Since the differences in peat accumulation that can be attributed to differences in productivity would favor the wet scenario, the observed difference must be due to slower rates of decomposition.

In peatlands, hydrology controls the decomposition rates through two mechanisms: oxygen availability (the standard peat situation of saturation and slow decomposition) and peat thermodynamics. Peat thermodynamics controls soil temperature and therefore, permafrost formation and active layer thickness. Permafrost formation and active layer thickness, in turn, controls decomposition rates, which are very low to negligible in permafrost (Schädel et al., 2016). In the dry landscape scenario during rapid peat accumulation, these effects on thermodynamics (i.e., shallower active layer) are stronger than the effects of substantially higher aerobic decomposition rates occurring in the peat acrotelm.

In this study, vertical peat accumulation was ultimately governed by the residence time of peat in the active layer, or the length of time when peat can be decomposed before it is frozen into the permafrost (**Figure 1**). In these permafrost systems, the active layer depth rather than acrotelm controlled decomposition in dry peats so that decomposition was limited not by the normal (in peatlands) anaerobic conditions but rather temperature limited by permafrost presence. The duration of time for decomposition (e.g., number of years with unfrozen conditions) in the active layer controlled the degree of peat decomposition, which has both a direct effect (loss of mass/material) and an indirect effect (increasing bulk density with increased humification). This effect is illustrated by contrasting patterns of peat accumulation and permafrost formation, with a higher degree of decomposition prior to permafrost preservation (**Figure 1**) and lower carbon loss with subsequent thaw in wetter conditions (**Figure 6**).

The higher degree of decomposition in the wet landscape scenario is related to the shallow water table, which results in a larger thermal mass, enhanced heat transfer to deeper peat and subsequently a deeper active layer (**Figures 1**, **5**). In an analysis of active layer depth and soil water content data from sites across Alaska, Clayton et al. (2021) found that while active layer depth generally increased with increasing active layer soil water content, as water content in the top 12 cm of the soil increased the active layer also increased, and active layers also tended to be deeper as soils became saturated. These exceptions reflect the conditions of the TKP wet scenario. With this deeper active layer, the residence time for a peat cohort within the active layer (transit time from the peat surface to the permafrost surface) was about 1,000 ± 100 years or more (**Supplementary Figure S2**). By then the peat was highly decomposed, had lost most of its original litter mass (mean: ~73% mass loss), and the organic matter density was near the maximum, resulting in less peat thickness per unit mass of peat and a shallower peat profile (**Figure 2B**), and relatively low rates of peat accumulation (overall: 2.9 mm $decade^{-1}$; **Figure 1C**).

In contrast, when the peatland began to shed water earlier in its development, the drier peat, deeper water table, and resultingly shallow active layer led ultimately to deeper peat with lower organic matter density (**Figures 1**, **2**). These results show that higher peat accumulation and preservation can occur with a deep water table and dry peat surface, which are usually

associated with low rates of peat accumulation such as those found in permafrost palsas and bogs (Treat et al., 2016a). Notably, the rapid peat accumulation rates simulated during c.5700–4550 BP were not due to years of very high accumulation (i.e., >2 mm y^{-1} or 20 mm $decade^{-1}$), but rather no years of decomposition that exceeded litter input. In contrast, negative accumulation years were common during other periods during the dry scenario and the entire wet scenario (**Figures 1C,D**). These results illustrate an important role for the decomposition of older peat (roughly 200–800 years in this case) found in the deeper active layer and overall C balance of the peatlands more generally.

Contrasts between wet and dry landscape scenarios (**Figure 1**) present a possible explanation for how rapid rates of peat accumulation could occur as a result of shallow and relatively rapid permafrost formation in dry peat. This rapid permafrost aggradation coupled with a shallow active layer provides an alternative, or additional, explanation to the hypothesis that high rates of peat accumulation are driven primarily by enhanced seasonality attributed to solar insolation in the early Holocene (Lavoie and Richard, 2000; Jones and Yu, 2010). In a core, the rapid peat accumulation in permafrost would appear as well-preserved, relatively undecomposed peat at depth; unfortunately, the profile description from TKP is not detailed enough to determine whether this is observed *in-situ* but this seems unlikely given the relatively good agreement between the TKP core and the wet scenario (**Figure 2**; **Table 1**). Future work could focus on testing this hypothesis.

Other Arctic peat deposits support the hypothesis for rapid peat accumulation under dry permafrost conditions. Peat cores collected in a polar desert (1980–2010 MAAT: −17.1°C; Canadian Climate Normals, Environment Canada, Alert Station) on Northern Ellesmere Island, Canada at southern Piper Pass show extensive (>3 m thick) peat deposits that formed on the edges of steep banks during the mid-Holocene (LaFarge-England et al., 1991). High peat accumulation rates of 12–38 mm $decade^{-1}$ are associated with well-preserved plant macrofossils, indicating the rapid incorporation of peat into permafrost before it decomposes (syngenetic permafrost). The species assemblage indicates periods of dominant xeric moss species followed by soligeneous fen mosses and vascular plant species. These dry, well-drained conditions supported peat formation primarily through snowmelt water inputs, which enabled vegetation and moss growth, and the rapid incorporation of this material into permafrost prior to decomposition, similar to the dry model scenario (**Figures 1B**, **5B**).

3.4 Permafrost C Vulnerability and Resilience in Peatlands

Permafrost C vulnerability and resilience to warming in these simulations was determined by both the water table position (related to the landscape setting and regional hydrology) and the legacy of the peat profiles themselves. In the future scenario in the dry landscape setting, warming soil temperatures (**Figure 3**) released the temperature control on decomposition rates, which were multiplied by aerobic conditions in the peat acrotelm (**Figure 5**). The legacy effect of previous decomposition also affected the vulnerability: the lower degree of decomposition in peat currently residing at the top of the permafrost in the dry landscape setting (**Figure 5**), when combined with a strong increase in peat temperature (**Figure 3**), increases the peat vulnerability to decomposition with permafrost thaw (**Figure 6**). Similar results have been shown in incubations of permafrost peat, where poorly decomposed peat in the permafrost is decomposed at similar rates to peats from the active layer (Treat et al., 2014). The dry conditions also decrease the resilience of these peatlands through lower rates of productivity (**Figure 4**), which are unable to offset losses of peat C (**Figure 6**), ultimately leading to substantially higher predicted net C loss, e.g., higher C vulnerability with permafrost thaw than in the wet landscape scenario (**Figure 6**). Therefore, while soil temperatures also warmed, anaerobic conditions associated with hydrology (**Figure 5**, high WT) and higher NPP (**Figure 4**; driven by less drought stress) led to lower net C losses (**Figure 6**).

Under wetter conditions, more humified peat accumulated more slowly due to a longer residence time in the active layer (**Figure 1**, **Supplementary Figure S2**), but then was more resilient against C loss in future scenarios (**Figure 6**). This was due to increases in vegetation productivity enabled by sufficient moisture (**Figure 4**) and smaller decomposition peat losses (**Figure 5**).

We note that the model simulations presented here have some limitations to assessing permafrost vulnerability: they currently do not include abrupt permafrost thaw, which will likely affect ice-rich permafrost peatlands (Olefeldt et al., 2016) and strongly alter ecosystem function and C exchange (Turetsky et al., 2020). If abrupt thaw results in a water table closer to the surface, this could potentially enhance vegetation productivity similar to the outcome in the wet landscape scenario (e.g., Camill et al., 2001: **Figure 4**) which might offset more of the peat C losses (**Figure 6**). Changes to the regional hydrology in the future due to permafrost thaw have a key role in the future vulnerability but are very difficult to predict (Quinton et al., 2010).

Some field studies in Alaska have shown substantial differences in the observed peat C dynamics after permafrost thaw that could be explained by timing of permafrost aggradation and peat accumulation demonstrated by the modeling scenarios. In Southwestern Alaska, permafrost peatland sites at Innoko and Koyukuk showed evidence of syngenetic permafrost aggradation within the peat (Jones et al., 2017; O'Donnell et al., 2012). At the APEX Bog site in interior Alaska, permafrost aggraded millennia after peat accumulation (e.g., epigenetic permafrost; Manies et al., 2021). Following permafrost thaw, substantially less carbon was lost from the epigenetic permafrost site than the syngenetic sites that accumulated peat and permafrost simultaneously (Jones et al., 2017; Manies et al., 2021). In the modeled scenarios, rapid permafrost accumulation in the dry scenario (e.g., syngenetic formation) showed carbon losses with warming that were nearly twice that of the wet scenario (**Figure 6**),

where the longer residence time in a non-frozen state allowed for greater decomposition and a less labile carbon source upon thaw (**Figure 5**). While the context differs from the modeled scenario presented here both in terms of permafrost history (significantly longer permafrost-free conditions at the epigenetic site in the chronosequence) and permafrost thaw (abrupt thaw instead of active layer deepening), these model results provide a plausible explanation for these differing vulnerabilities of these permafrost peatlands.

3.5 Implications for Modeling Peat and Permafrost Carbon

The main result shown here is that wet and dry landscape settings can result in different peat accumulation histories and peat qualities, even in the same climate setting (**Figure 1**). If the active layer depth is shallow (dry landscape scenario), peat is less degraded before freezing into the permafrost and so is more susceptible to enhanced decomposition upon permafrost thaw. Because the wet scenario experienced greater decomposition prior to making it into the permafrost, less of it decomposes following thaw. Both peat accumulation history and peat quality have implications for peat C loss in future warming scenarios (**Figures 5**, **6**) due to both permafrost thaw and also legacy effects. To simulate this in a model requires permafrost dynamics (common to many models) and peat stratigraphy, i.e., resolving the peat quality (degree of humification or decomposition) down the peat profile into the permafrost. This probably does not necessarily require annual litter cohorts as used in HPM-Arctic, but a single or just a few peat pools would probably not characterize the peat quality accurately enough.

Very few models simulate peat accumulation over millennia in the permafrost zone. This is a complex task for most earth system models as only a few incorporate peatlands into their land surface schemes (Kleinen et al., 2012; Largeron et al., 2018; Qiu et al., 2018; Chaudhary et al., 2020), and millennial length earth system model simulations are computationally costly. Often, the peatlands are initialized using datasets for timing and peatland extent. Here, we show that key parameters for determining carbon vulnerability and feedbacks, such as peat thickness, bulk density, and humification, must be considered and may vary depending on permafrost history. Some of these important uncertainty factors may be quantifiable from the global peat core databases (Loisel et al., 2014; Treat et al., 2016a; Treat et al., 2016b), but this may require details that many researchers may not have included their analyses. A first step would be to determine whether the hypothesis presented here (dry landscape setting, presence of permafrost, and shallow active-layer depth coincident with rapid peat accumulation) can be evaluated with existing peat core data, and if so, to determine whether these conditions can be associated with landscape topography and climate conditions in a way that provides some predictive power for peat initialization.

Furthermore, it is important to keep in mind that future peat vulnerability to climate change is related to several factors: thaw rate, subsequent water table dynamics, and nature of thawing peat (i.e., susceptibility to further decomposition, which may depend on both the inherent tissue lability of the plants comprising the peat and the degree of humification upon freezing into the permafrost. While this study only addresses this final point, we show that decomposition processes (i.e., degree of decomposition and litter quality) are quite important for both peat accumulation rates and post-thaw carbon losses.

Ultimately, the differences in past C accumulation rates and future C losses between these wet and dry landscape setting scenarios were driven by the model parameterization representing the regional hydrology, including the water inputs from the surrounding watershed and the runoff to downstream areas. By demonstrating the differences in peat profiles between the wet and dry scenarios using the same climate drivers, as well as an inter-site comparison between two sites with contrasting hydrology (TKP and southern Piper Pass), these results suggest that permafrost behavior and peat profiles are strongly dependent on landscape characteristics controlling hydrology (Woo and Young, 2006). The regional hydrology and wetland basin characteristics subsequently determined both peat accumulation history and future changes in peat organic matter stocks with permafrost thaw and on-going warming. These findings point to the importance of considering regional hydrology and wetland basin characteristics due to their controls on wetland hydrology, which will likely be a major control on the response of permafrost carbon in peatlands to warming and permafrost thaw. This study highlights the limitations for accurately predicting changes in C balance in response to permafrost thaw without careful hydrologic assessments. This presents a significant challenge for global-scale models and future emphasis would be better placed on improving hydrologic assessments at local to regional scales.

DATA AVAILABILITY STATEMENT

The datasets presented in this study can be found in online repositories. The names of the repository/repositories and accession number(s) can be found below: The observations used for model validation can be accessed (https://doi.org/10.1594/PANGAEA.863697); the dataset key (Variable: Auth.Site.CoreID) for TKP is VAR-TKP-01. The model code, parameters, and climate driver data are available from: https://doi.org/10.5281/zenodo.4647666.

AUTHOR CONTRIBUTIONS

CT and SF designed the study and performed the model experiments. JA provided the climate driver data. CT, MJ, and SF analysed and interpreted the data and wrote the paper with input from all authors.

FUNDING

This study was supported by the United States National Science Foundation (#1802825, CT and SF), ERC-H2020 #851181

FluxWIN (CT), the Helmholtz Impulse Initiative and Networking Fund (CT), the Fulbright Finland and Saastamoinen Foundations (SF), USGS Climate and Land-use Change R&D Program (JA and MJ).

ACKNOWLEDGMENTS

We thank Lesleigh Anderson, Steve Hostetler, and two reviewers for constructive comments on this manuscript. We acknowledge earlier field work and analysis done by SR Vardy and BG Warner at Thelon-Kazan Peatlands, Nunavut, Canada.

SUPPLEMENTARY MATERIAL

The Supplementary Material for this article can be found online at: https://www.frontiersin.org/articles/10.3389/fenvs.2022.892925/full#supplementary-material

REFERENCES

Brown, J., Ferrians, O. J., Jr., Heginbottom, J. A., and Melnikov, E. S. (1998, revised 2001). *Circum-Arctic Map of Permafrost and Ground-Ice Conditions*. Boulder, CO: National Snow and Ice Data Center/World Data Center for Glaciology, Digital Media.

Camill, P., Lynch, J. A., Clark, J. S., Adams, J. B., and Jordan, B. (2001). Changes in Biomass, Aboveground Net Primary Production, and Peat Accumulation Following Permafrost Thaw in the Boreal Peatlands of Manitoba, Canada. *Ecosystems* 4 (5), 461–478. doi:10.1007/s10021-001-0022-3

Charman, D. J. (2002). *Peatlands and Environmental Change*. Chichester, UK: John Wiley & Sons.

Chaudhary, N., Westermann, S., Lamba, S., Shurpali, N., Sannel, A. B. K., Schurgers, G., et al. (2020). Modelling Past and Future Peatland Carbon Dynamics across the pan-Arctic. *Glob. Change Biol.* 26 (7), 4119–4133. doi:10.1111/gcb.15099

Clayton, L. K., Schaefer, K., Battaglia, M. J., Bourgeau-Chavez, L., Chen, J., Chen, R. H., et al. (2021). Active Layer Thickness as a Function of Soil Water Content. *Environ. Res. Lett.* 16 (5), 055028. doi:10.1088/1748-9326/abfa4c

Clymo, R. S. (1992). Models of Peat Growth. *Suo* 43, 127–136.

Elberling, B., Michelsen, A., Schädel, C., Schuur, E. A. G., Christiansen, H. H., Berg, L., et al. (2013). Long-term CO2 Production Following Permafrost Thaw. *Nat. Clim. Change* 3 (10), 890–894. doi:10.1038/nclimate1955

Flato, G. M., Marotzke, J., and Abiodun, B. (2013). "Evaluation of Climate Models," in *Climate Change 2013: The Physical Science Basis. Contribution of Working Group I to the Fifth Assess- Ment Report of the Intergovernmental Panel on Climate Change*. T. F. Stocker, D. Qin, G-K. Plattner, M. Allen, S. Boschung, J. Nauels, et al. (Cambridge, UK: Cambridge University Press), 741–866.

Frolking, S., Roulet, N. T., Tuittila, E., Bubier, J. L., Quillet, A., Talbot, J., et al. (2010). A New Model of Holocene Peatland Net Primary Production, Decomposition, Water Balance, and Peat Accumulation. *Earth Syst. Dynam.* 1 (1), 115–167. doi:10.5194/esd-1-1-2010

Frolking, S., Roulet, N. T., Moore, T. R., Richard, P. J. H., Lavoie, M., and Muller, S. D. (2001). Modeling Northern Peatland Decomposition and Peat Accumulation. *Ecosystems* 4 (5), 479–498. doi:10.1007/s10021-001-0105-1

Gent, P. R., Danabasoglu, G., Donner, L. J., Holland, M. M., Hunke, E. C., Jayne, S. R., et al. (2011). The Community Climate System Model Version 4. *J. Clim.* 24 (19), 4973–4991. doi:10.1175/2011jcli4083.1

Harris, I., Jones, P. D., Osborn, T. J., and Lister, D. H. (2014). Updated High-Resolution Grids of Monthly Climatic Observations - the CRU TS3.10 Dataset. *Int. J. Climatol.* 34 (3), 623–642. doi:10.1002/joc.3711

Harris, S. A., French, H. M., Heginbottom, J. A., Johnston, G. H., Ladanyi, B., Sego, D. C., et al. (1988).*Glossary of Permafrost and Related Ground-Ice Terms*. Technical Memorandum No. 142. Ottawa, CA: National Research Council of Canada, 154.

Hugelius, G., Loisel, J., Chadburn, S., Jackson, R. B., Jones, M., MacDonald, G., et al. (2020). Large Stocks of Peatland Carbon and Nitrogen Are Vulnerable to Permafrost Thaw. *Proc. Natl. Acad. Sci.* 117 (34), 20438–20446. doi:10.1073/pnas.1916387117.201916387

Hugelius, G., Strauss, J., Zubrzycki, S., Harden, J. W., Schuur, E. A. G., Ping, C.-L., et al. (2014). Estimated Stocks of Circumpolar Permafrost Carbon with Quantified Uncertainty Ranges and Identified Data Gaps. *Biogeosciences* 11 (23), 6573–6593. doi:10.5194/bg-11-6573-2014

Jones, M. C., Harden, J., O'Donnell, J., Manies, K., Jorgenson, T., Treat, C., et al. (2017). Rapid Carbon Loss and Slow Recovery Following Permafrost Thaw in Boreal Peatlands. *Glob. Change Biol.* 23 (3), 1109–1127. doi:10.1111/gcb.13403

Jones, M. C., and Yu, Z. (2010). Rapid Deglacial and Early Holocene Expansion of Peatlands in Alaska. *Proc. Natl. Acad. Sci.* 107 (16), 7347–7352. doi:10.1073/pnas.0911387107

Kanevskiy, M., Jorgenson, T., Shur, Y., O'Donnell, J. A., Harden, J. W., Zhuang, Q., et al. (2014). Cryostratigraphy and Permafrost Evolution in the Lacustrine Lowlands of West-Central Alaska. *Permafr. Periglac. Process.* 25 (1), 14–34. doi:10.1002/ppp.1800.n/a-n/a

Kleinen, T., Brovkin, V., and Schuldt, R. J. (2012). A Dynamic Model of Wetland Extent and Peat Accumulation: Results for the Holocene. *Biogeosciences* 9 (1), 235–248. doi:10.5194/bg-9-235-2012

LaFarge-England, C., Vitt, D. H., and England, J. (1991). Holocene Soligenous Fens on a High Arctic Fault Block, Northern Ellesmere Island (82 Degrees N), N.W.T., Canada. *Arct. Alp. Res.* 23 (1), 80–98. doi:10.2307/1551441

Largeron, C., Krinner, G., Ciais, P., and Brutel-Vuilmet, C. (2018). Implementing Northern Peatlands in a Global Land Surface Model: Description and Evaluation in the ORCHIDEE High-Latitude Version Model (ORC-HL-PEAT). *Geosci. Model Dev.* 11 (8), 3279–3297. doi:10.5194/gmd-11-3279-2018

Lavoie, M., and Richard, P. J. (2000). The Role of Climate on the Developmental History of Frontenac Peatland, Southern Quebec. *Can. J. Bot.* 78, 668–684. doi:10.1139/b00-043

Liu, Z., Otto-Bliesner, B. L., He, F., Brady, E. C., Tomas, R., Clark, P. U., et al. (2009). Transient Simulation of Last Deglaciation with a New Mechanism for Bølling-Allerød Warming. *Science* 325 (5938), 310–314. doi:10.1126/science.1171041

Loisel, J., Yu, Z., Beilman, D. W., Camill, P., Alm, J., Amesbury, M. J., et al. (2014). A Database and Synthesis of Northern Peatland Soil Properties and Holocene Carbon and Nitrogen Accumulation. *Holocene* 24 (9), 1028–1042. doi:10.1177/0959683614538073

Manies, K. L., Jones, M. C., Waldrop, M. P., Leewis, M. C., Fuller, C., Cornman, R. S., et al. (2021). Influence of Permafrost Type and Site History on Losses of Permafrost Carbon after Thaw. *J. Geophys. Res. Biogeosciences* 126 (11), e2021JG006396. doi:10.1029/2021jg006396

Marchenko, S., Romanovsky, V., and Tipenko, G. (2008). "Numerical Modeling of Spatial Permafrost Dynamics in Alaska," in Ninth International Conference On Permafrost. *Fairbanks, AK*. Editors D. L. Kane and K. M. Hinkel (Fairbanks, AK, United States: Institute of Northern Engineering, University of Alaska Fairbanks), 1125–1130.

McGuire, A. D., Lawrence, D. M., Koven, C., Clein, J. S., Burke, E., Chen, G., et al. (2018). Dependence of the Evolution of Carbon Dynamics in the Northern Permafrost Region on the Trajectory of Climate Change. *Proc. Natl. Acad. Sci.* 115, 3882–3887. doi:10.1073/pnas.1719903115

Mishra, U., Hugelius, G., Shelef, E., Yang, Y., Strauss, J., Lupachev, A., et al. (2021). Spatial Heterogeneity and Environmental Predictors of Permafrost Region Soil Organic Carbon Stocks. *Sci. Adv.* 7 (9), eaaz5236. doi:10.1126/sciadv.aaz5236

Nichols, J. E., and Peteet, D. M. (2019). Rapid Expansion of Northern Peatlands and Doubled Estimate of Carbon Storage. *Nat. Geosci.* 12 (11), 917–921. doi:10.1038/s41561-019-0454-z

O'Donnell, J. A., Jorgenson, M. T., Harden, J. W., David McGuire, A., Kanevskiy, M. Z., and Wickland, K. P. (2012). The Effects of Permafrost Thaw on Soil Hydrologic, Thermal, and Carbon Dynamics in an Alaskan Peatland. *Ecosystems* 15, 213–229. doi:10.1007/s10021-011-9504-0

Olefeldt, D., Goswami, S., Grosse, G., Hayes, D., Hugelius, G., Kuhry, P., et al. (2016). Circumpolar Distribution and Carbon Storage of Thermokarst Landscapes. *Nat. Commun.* 7, 13043. doi:10.1038/ncomms13043

Qiu, C., Zhu, D., Ciais, P., Guenet, B., Krinner, G., Peng, S., et al. (2018). ORCHIDEE-PEAT (Revision 4596), a Model for Northern Peatland CO_2, Water, and Energy Fluxes on Daily to Annual Scales. *Geosci. Model Dev.* 11 (2), 497–519. doi:10.5194/gmd-11-497-2018

Quinton, W. L., Hayashi, M., and Chasmer, L. E. (2009). Peatland Hydrology of Discontinuous Permafrost in the Northwest Territories: Overview and Synthesis. *Can. Water Resour. J.* 34 (4), 311–328. doi:10.4296/cwrj3404311

Quinton, W. L., Hayashi, M., and Chasmer, L. E. (2010). Permafrost-thaw-induced Land-Cover Change in the Canadian Subarctic: Implications for Water Resources. *Hydrol. Process.* 25, 152–158. doi:10.1002/hyp.7894

Rouse, W. R., Lafleur, P. M., and Griffis, T. J. (2000). Controls on Energy and Carbon Fluxes from Select High-Latitude Terrestrial Surfaces. *Phys. Geogr.* 21 (4), 345–367. doi:10.1080/02723646.2000.10642714

Rydin, H., and Jeglum, J. K. (2006). *Biology of Peatlands*. Oxford, UNITED KINGDOM: Oxford University Press.

Schädel, C., Bader, M. K. F., Schuur, E. A. G., Biasi, C., Bracho, R., Čapek, P., et al. (2016). Potential Carbon Emissions Dominated by Carbon Dioxide from Thawed Permafrost Soils. *Nat. Clim. Change* 6 (10), 950–953. doi:10.1038/nclimate3054

Schuur, E. A. G., McGuire, A. D., Schädel, C., Grosse, G., Harden, J. W., Hayes, D. J., et al. (2015). Climate Change and the Permafrost Carbon Feedback. *Nature* 520 (7546), 171–179. doi:10.1038/nature14338

Taylor, K. E., Stouffer, R. J., and Meehl, G. A. (2012). An Overview of CMIP5 and the Experiment Design. *Bull. Am. Meteorological Soc.* 93 (4), 485–498. doi:10.1175/bams-d-11-00094.1

R Development Core Team (2008). *R: A Language and Environment for Statistical Computing*. Vienna, Austria: R Foundation for Statistical Computing.

Treat, C. C., Jones, M. C., Alder, J., Britta, A., Sannel, K., Camill, P., et al. (2021). Predicted Vulnerability of Carbon in Permafrost Peatlands with Future Climate Change and Permafrost Thaw in Western Canada. *J. Geophys. Res.* 126, e2020JG005872. doi:10.1029/2020jg005872

Treat, C. C., Jones, M. C., Camill, P., Gallego-Sala, A., Garneau, M., Harden, J. W., et al. (2016a). Effects of Permafrost Aggradation on Peat Properties as Determined from a pan-Arctic Synthesis of Plant Macrofossils. *J. Geophys. Res. Biogeosci.* 121 (1), 78–94. doi:10.1002/2015jg003061

Treat, C. C., Jones, M. C., Camill, P., Gallego-Sala, A., Garneau, M., Harden, J. W., et al. (2016b). Data supplement to: Effects of Permafrost Aggradation on Peat Properties as Determined from a pan-Arctic Synthesis of Plant Macrofossils. *J. Geophys. Res. Biogeosciences* 121 (1), 78–94. doi:10.1002/2015JG003061. PANGAEA

Treat, C. C., and Jones, M. C. (2018). Near-surface Permafrost Aggradation in Northern Hemisphere Peatlands Shows Regional and Global Trends during the Past 6000 Years. *Holocene* 28 (6), 998–1010. doi:10.1177/0959683617752858

Treat, C. C., Wollheim, W. M., Varner, R. K., Grandy, A. S., Talbot, J., and Frolking, S. (2014). Temperature and Peat Type Control CO 2 and CH 4 Production in Alaskan Permafrost Peats. *Glob. Change Biol.* 20 (8), 2674–2686. doi:10.1111/gcb.12572

Turetsky, M. R., Abbott, B. W., Jones, M. C., Anthony, K. W., Olefeldt, D., Schuur, E. A. G., et al. (2020). Carbon Release through Abrupt Permafrost Thaw. *Nat. Geosci.* 13 (2), 138–143. doi:10.1038/s41561-019-0526-0

Vardy, S. R., Warner, B. G., Turunen, J., and Aravena, R. (2000). Carbon Accumulation in Permafrost Peatlands in the Northwest Territories and Nunavut, Canada. *Holocene* 10 (2), 273–280. doi:10.1191/095968300671749538

Vardy, S., Warner, B., and Asada, T. (2005). Holocene Environmental Change in Two Polygonal Peatlands, South-Central Nunavut, Canada. *Boreas* 34 (3), 324–334. doi:10.1080/03009480510013033

Woo, M. K., and Young, K. L. (2006). High Arctic Wetlands: Their Occurrence, Hydrological Characteristics and Sustainability. *J. Hydrology* 320 (3-4), 432–450. doi:10.1016/j.jhydrol.2005.07.025

Zoltai, S. C. (1995). Permafrost Distribution in Peatlands of West-Central Canada during the Holocene Warm Period 6000 Years Bp. *Geogr. Physique Quaternaire* 49 (1), 45–54. doi:10.7202/033029ar

Conflict of Interest: The authors declare that the research was conducted in the absence of any commercial or financial relationships that could be construed as a potential conflict of interest.

Publisher's Note: All claims expressed in this article are solely those of the authors and do not necessarily represent those of their affiliated organizations, or those of the publisher, the editors and the reviewers. Any product that may be evaluated in this article, or claim that may be made by its manufacturer, is not guaranteed or endorsed by the publisher.

frontiers | Frontiers in Earth Science

ORIGINAL RESEARCH
published: 26 July 2022
doi: 10.3389/feart.2022.910078

Active Layer and Permafrost Investigations Using Geophysical and Geocryological Methods—A Case Study of the Khanovey Area, Near Vorkuta, in the NE European Russian Arctic

Mara Rossi[1], Michela Dal Cin[1,2], Stefano Picotti[2], Davide Gei[2], Vladislav S. Isaev[3], Andrey V. Pogorelov[3], Eugene I. Gorshkov[3], Dmitrii O. Sergeev[4], Pavel I. Kotov[3], Massimo Giorgi[2] and Mario L. Rainone[1]*

[1]Engineering and Geology Department, Università degli Studi G. D'Annunzio Chieti—Pescara, Chieti, Italy, [2]National Institute of Oceanography and Applied Geophysics—OGS, Trieste, Italy, [3]Faculty of Geology, Lomonosov Moscow State University, Moscow, Russia, [4]Sergeev Institute of Environmental Geoscience, Moscow, Russia

OPEN ACCESS

Edited by:
Xiaodong Wu,
Chinese Academy of Sciences (CAS), China

Reviewed by:
Evgeny Abakumov,
Saint Petersburg State University, Russia
Weibo Liu,
Northwest Institute of Eco-Environment and Resources (CAS), China

***Correspondence:**
Stefano Picotti
spicotti@ogs.it

Specialty section:
This article was submitted to Cryospheric Sciences, a section of the journal Frontiers in Earth Science

Received: 31 March 2022
Accepted: 01 June 2022
Published: 26 July 2022

Citation:
Rossi M, Dal Cin M, Picotti S, Gei D, Isaev VS, Pogorelov AV, Gorshkov EI, Sergeev DO, Kotov PI, Giorgi M and Rainone ML (2022) Active Layer and Permafrost Investigations Using Geophysical and Geocryological Methods—A Case Study of the Khanovey Area, Near Vorkuta, in the NE European Russian Arctic. Front. Earth Sci. 10:910078. doi: 10.3389/feart.2022.910078

Permafrost in the NE European Russian Arctic is suffering from some of the highest degradation rates in the world. The rising mean annual air temperature causes warming permafrost, the increase in the active layer thickness (ALT), and the reduction of the permafrost extent. These phenomena represent a serious risk for infrastructures and human activities. ALT characterization is important to estimate the degree of permafrost degradation. We used a multidisciplinary approach to investigate the ALT distribution in the Khanovey railway station area (close to Vorkuta, Arctic Russia), where thaw subsidence leads to railroad vertical deformations up to 2.5 cm/year. Geocryological surveys, including vegetation analysis and underground temperature measurements, together with the faster and less invasive electrical resistivity tomography (ERT) geophysical method, were used to investigate the frozen/unfrozen ground settings between the railroad and the Vorkuta River. Borehole stratigraphy and landscape microzonation indicated a massive prevalence of clay and silty clay sediments at shallow depths in this area. The complex refractive index method (CRIM) was used to integrate and quantitatively validate the results. The data analysis showed landscape heterogeneity and maximum ALT and permafrost thickness values of about 7 and 50 m, respectively. The active layer was characterized by resistivity values ranging from about 30 to 100 Ωm, whereas the underlying permafrost resistivity exceeded 200 Ωm, up to a maximum of about 10 kΩm. In the active layer, there was a coexistence of frozen and unfrozen unconsolidated sediments, where the ice content estimated using the CRIM ranged from about 0.3 – 0.4 to 0.9. Moreover, the transition zone between the active layer base and the permafrost table, whose resistivity values ranged from 100 to 200 Ωm for this kind of sediments, showed ice contents ranging from 0.9 to 1.0. Taliks were present in some depressions of the study area, characterized by minimum resistivity values lower than 10 Ωm. This thermokarst activity was more active close to the railroad because of the absence of insulating vegetation. This study

contributes to better understanding of the spatial variability of cryological conditions, and the result is helpful in addressing engineering solutions for the stability of the railway.

Keywords: electrical resistivity tomography (ERT), geocryology, permafrost degradation, rock physics, landscape microzonation, active layer, climate change, Arctic tundra

1 INTRODUCTION

Permafrost is defined as ground with a temperature remaining below 0°C for at least two consecutive years (ACGR—Associate Committee on Geotechnical Research, 1988; Isaev et al., 2020). Perennial frozen ground occupies around a quarter of the terrestrial surface in the Northern Hemisphere (Zhang et al., 1999; Gruber, 2012; Wang et al., 2019; Vasiliev et al., 2020) and more than 60% of the Russian territory (Anisimov and Reneva, 2006). The percentage of lateral continuity of permafrost can be classified into continuous (90–100%), discontinuous (50–90%), sporadic (10–50%), and isolated (<10%) (Brown et al., 1997; Brown et al., 2002). This distribution is represented in **Figure 1** for the European Russian Arctic and Northwestern Siberia, a region experiencing some of the highest rates of permafrost degradation (Romanovsky et al., 2010; Streletskiy et al., 2015; Romanovsky et al., 2018; Biskaborn et al., 2019).

The permafrost thermal state is highly sensitive to the changing climatic conditions (ACGR—Associate Committee on Geotechnical Research, 1988; Yershov, 1998; Harris et al., 2017; IPCC et al., 2017). The Arctic amplification, a proven phenomenon for which the Arctic is warming about twice as fast as the rest of the world, is altering the permafrost distribution and leading to its degradation (IPCC et al., 2017; Biskaborn et al., 2019; NOAA/NASA, 2020; NSIDC—National Snow and Ice Data Center, 2020). Several studies in the Eurasian Arctic (e.g., Streletskiy et al., 2015; Buldovicz et al., 2018; Romanovsky et al., 2018; Abramov et al., 2019; Maslakov et al., 2019) have already documented permafrost degradation induced by warming mean annual air temperatures (from 0.05 to 0.07°C yr^{-1} since 1970; Vasiliev et al., 2020). In the Arctic Russia,

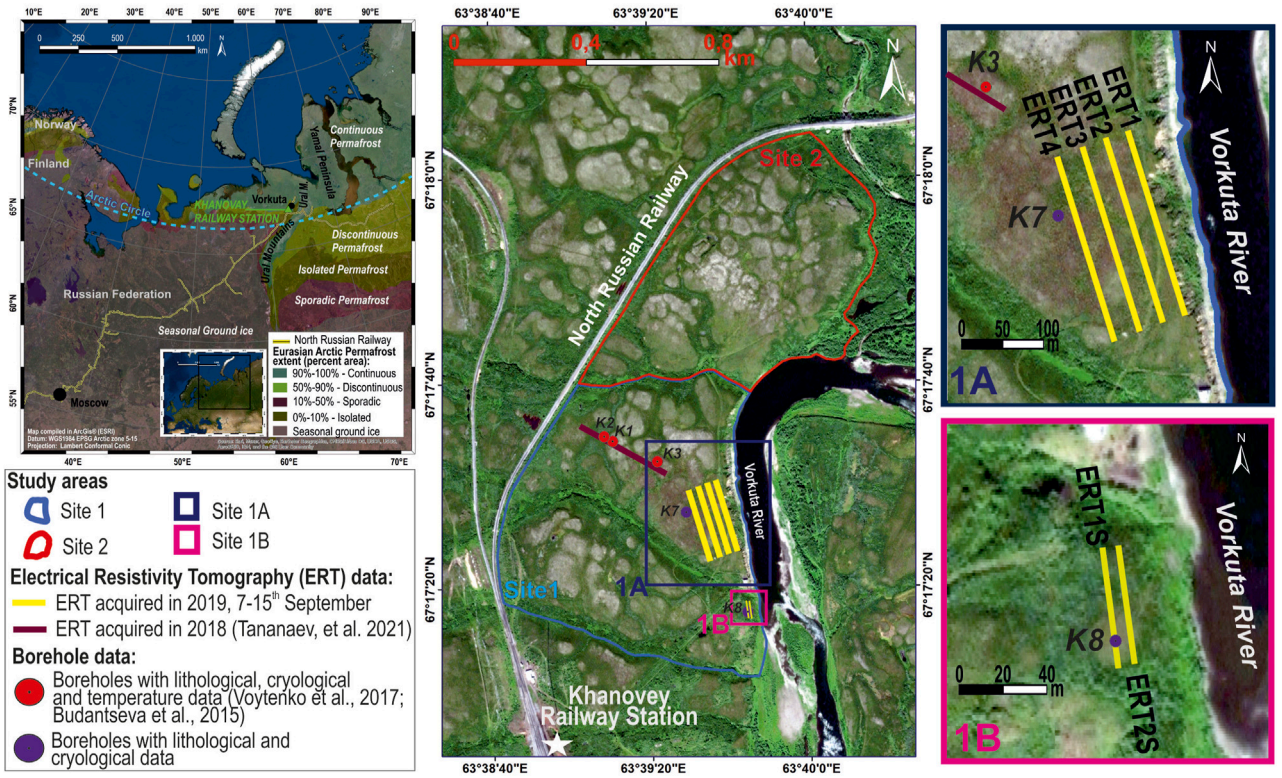

FIGURE 1 | The top left map shows the location of the study area (Khanovey railway station, close to Vorkuta city) in the NE European Russian Arctic, along with the percentage of permafrost lateral continuity in the region (according to the classification of Brown et al., 1997; Brown et al., 2002). The map at the center of the figure shows the survey location area, with the position of boreholes and geophysical data used in this study. The profile positions of the geoelectric surveys performed in 2019 in Site 1A and Site 1B are highlighted in blow-ups on the right. Maps compiled using ArcGis® (Esri) software. Datum: WGS84; projection: UTM 41N. Satellite base image (Gis layer "World Imagery") and permafrost extent (Gis layer "North Hemisphere Permafrost_WFL1") were retrieved in 2019 from the ArcGis online database resources.

FIGURE 2 | Railroad deformation associated with permafrost degradation along the North Russian Railway close to the Khanovey field site at the western foothills of the Ural Mountains.

permafrost is warming relatively slower than the Arctic air and it became about ~1.5°C–2.5°C warmer during the last half-century (Biskaborn et al., 2019; Melnikov et al., 2022). As a consequence, the top layer of permafrost, subject to seasonal thawing and freezing (i.e., the active layer), increases its thickness (i.e., the active layer thickness—ALT), causing a northward retreat of permafrost extent and a widespread reduction in the capacity of soil to carry loads (Yershov, 1998; Osterkamp and Burn, 2003). Over the past 2 decades, ALT has increased at all Russian European Circumpolar-Active Layer-Monitoring (CALM) sites, showing strong positive trends varying from 0.3 to 3.0 cm per year (Kaverin et al., 2021). As the ground thaws and freezes, it contracts and expands, inducing subsidence (thaw settlement), stress on foundations, and surface deformation of infrastructures (Chen et al., 2014). This is due to the modification of the soil mechanical properties by thermokarst processes, leading to decreasing ground bearing effectiveness, which, in turn, produces deformation and collapse of buildings, bridges, roads, etc. (e.g., Hong et al., 2014; You et al., 2017).

These phenomena profoundly affect the natural Arctic environment, as well as most of the socio-economic sectors of northern communities (IPCC et al., 2017; Marohasy, 2017). More than half of the Arctic inhabitants live in Russian territories underlain by permafrost. Population density and socio-economic development levels are highly variable across the Russian Arctic (EEA—European Environment Agency, 2017; Hjort et al., 2022). Ranging from the largest cities (e.g., Vorkuta, Yakutsk, and Norilsk) to sparse and isolated villages, urbanized settlements are of various sizes, which are often related to the availability of basic resources for living and livelihood (Streletskiy and Shiklomanov, 2016; Streletskiy et al., 2019). However, the accessibility of these resources is becoming increasingly problematic. The systematic loss in the continuity of permafrost due to global warming presents serious problems because of the high costs of construction and infrastructure maintenance, limiting access to people and goods supply from and to the Arctic regions (Marohasy, 2017; Allen et al., 2018).

Permafrost degradation leads to serious consequences for ecosystems, hydrological systems, and infrastructure integrity. The most important are the following: greenhouse gases release (Yang et al., 2010; Streletskiy et al., 2015); slowly moving landslides (frozen debris lobes); coastal erosion (Kasprzak et al., 2017; Maslakov et al., 2019; Isaev et al., 2020; Sinitsyn et al., 2020); ground subsidence; and the decrease in bearing capacity (Streletskiy et al., 2015; Voytenko and Sergeev, 2016; Isaev et al., 2020). In particular, it causes damages to infrastructure networks (e.g., Chen et al., 2014), resulting in deformation and subsidence of railway line tracks (e.g., **Figure 2**). The presence of anomalous unfrozen ground zones close to the railroads, related to groundwater circulation and thermokarst processes, changes the thermal state of the ground and plays a huge role to infrastructure damage (e.g., Drozdov et al., 2015; Isaev et al., 2020; Hjort et al., 2022). This phenomenon produces a strong impact on economic costs for infrastructure maintenance (Voytenko et al., 2017; Streletskiy et al., 2019; Melnikov et al., 2022), rising the vulnerability of people and human activity.

Although climatic factors play major roles in explaining permafrost thickness and active layer trends across large regions, vegetation, soil properties (e.g., thermal capacity), and land-use are also influencing factors (Wagner et al., 2018; Vasiliev et al., 2020; Schneider von Deimling et al., 2021). Permafrost warming can be locally amplified as a consequence of construction operations, embankment geometry, snow accumulation on side slopes, or changes in material properties (Zhang et al., 2004; Vasiliev et al., 2020). The warming effects can worsen if inadequate construction methods and procedures are adopted, such as soil compaction, removal of peat, and

destruction of the vegetation cover (Drozdov et al., 2015). Monitoring of the extension and thickness of permafrost and active layer by employing different investigation methodologies is fundamental for designing effective infrastructure consolidation plans and targeted solutions (e.g., Schwamborn et al., 2008; Voytenko and Sergeev, 2016; Gilbert et al., 2019; Tyurin et al., 2019).

A variety of methods commonly used for ALT and permafrost investigations can be found in the literature. Direct methods include mechanical probing, soil temperature monitoring, and visual observations (Hinkel and Nicholas, 1995; Brown et al., 2000). These methods form the basis of the CALM program (https://www2.gwu.edu/~calm/), started in 1991 to study the impacts of climate change on permafrost environments (Brown et al., 2000; Hinkel and Nelson, 2003; Kaverin et al., 2021). Another direct method is the use of the annual thawing index based on surface air temperature data (e.g., Peng et al., 2016). In turn, modeling approaches have been applied to describe ALT variations at different spatial scales (Nelson et al., 1997; Nelson et al., 1999; Hinzman et al., 1998; Oelke et al., 2003; Sazonova and Romanovsky, 2003).

Regional active layer conditions are difficult to be determined from direct ground surveys of permafrost features (e.g., digging, core drilling, and temperature measurements in boreholes) because of the large permafrost extent, high costs, and inconsistent sampling (Duguay et al., 2005). As a consequence, indirect methods for regional ALT estimation are often employed, which provide near-surface indicators of underlying ground conditions. These methods consist in remote sensing observations (e.g., Yi and Kimball, 2020) incorporating different global satellite data (radar, microwave, and infrared) of vegetation cover, ground thermal (air and surface temperatures), and hydrological (snow depth and soil moisture) parameters in order to capture abrupt shifts in landscape properties between predominantly frozen and unfrozen conditions (Kimball et al., 2004; Kim et al., 2011; Park et al., 2016). Repeated observation at representative sites over long periods is essential to evaluate regional patterns and trends related to permafrost degradation.

Geophysical surveys, as ground-penetrating radar (GPR) and electrical resistivity tomography (ERT), have been extensively used to study active layer and permafrost features. However, although the GPR technique performs well only for low clay contents in the subsoil (e.g., Arcone and Delaney, 1982; Palacky, 1988; Delaney et al., 1990; Doolittle et al., 1990; Arcone et al., 1998; Hinkel et al., 2001), the ERT method enables the characterization of both the active layer and the underlying permafrost for almost all soil textures (e.g., Kasprzak, 2015; Seppi et al., 2015; Kasprzak et al., 2017; Léger et al., 2017; Picotti et al., 2017; Francese et al., 2019; Farzamian et al., 2020; Isaev et al., 2020). In addition, electromagnetic induction methods have been successfully used to estimate the thickness of permafrost (e.g., Isaev et al., 2020).

The purpose of this research is to integrate geophysical and geocryological methods for permafrost and ALT investigations in the northwestern European Arctic (Komi Republic). The target zone is the Khanovey railway station area, close to Vorkuta city, located on the west of the Ural Mountains (**Figure 1**). The study area, characterized by Quaternary sediments lying on Permian coal shale bedrock, exhibits a continuous permafrost layer (Tananaev et al., 2021). This region is crossed by the North Russian Railway, which represents the only land connection between Moscow city and the northern Arctic territories. Several studies report that this important railroad infrastructure is suffering from deformation reaching 2.5 cm yr^{-1} due to the thawing of permafrost (e.g., Voytenko and Sergeev, 2016; Vasiliev et al., 2020). At the nearby Talnik CALM site, the average ALT increased steadily in the 1998–2019 period from 76 to 152 cm, showing a site-averaged trend of 4 cm yr^{-1} (Kaverin et al., 2021).

This research encompasses engineering/geocryological surveys (borehole drilling and thermometry), geophysical surveys (geoelectric), landscape microzonation, and digital mapping. These investigation methods provided data with different resolutions, which were combined together to characterize the unfrozen and frozen ground thickness distribution in the Khanovey field site. The complex refractive index method (CRIM) rock-physics theory has also been applied to enhance data integration and to quantitatively validate the geophysical results. This research is useful to address engineering solutions that ensure stability and operational performance to the railway, e.g., railway line diversion or employment of the thermosyphon and insulation cover technologies (e.g., Wagner, 2014; Isaev et al., 2016; Ulyanov, 2021).

2 AREA DESCRIPTION

The investigated area is located in the Bolshezemelskaya tundra, about 60 km west of the foothills of the Ural Mountains. It has an extension of approximately 1 km^2, and it is delimited by the Vorkuta riverbank on the eastern side and by the North Russian Railway on the western side. It was subdivided into two parts: the southern area (Site 1, delimited by the light blue line in the map of **Figure 1**), the main target of this study, and the northern area (Site 2, delimited by the red line in the map of **Figure 1**), where geocryological data were collected in 2019 for future geophysical investigations. In Site 1, the geological, cryological, and geophysical data were collected in 2019 and previous years.

With respect to orography, the territory is an accumulative plain, with an absolute surface at 70–200 m above sea level (a.s.l.) and erosions within the plains, with depths of 20–40 m (Isaev V. S. et al., 2022). In landscape terms, the site is characterized by a peaty-bumpy tundra, which is a system of microdepressions and hollows interspersed by hillocks.

The Khanovey study area is part of the Timan–Pechora sedimentary basin, which belongs to the submerged north-eastern part of the European Platform. More into detail, the site is settled over the tectonic unit of the Pre-Urals Foredeep (Klimenko et al., 2011). The sedimentary sequence of the area consists of Silurian siliceous shale deposits that originate at the initial stage of formation of the young Timan–Pechora platform, lying at a depth of approximately 250 m. These sediments are covered by lower Carboniferous coal, dolomite, and limestone (Vorgashorskaya Formation) emerging at a depth of about 50 m.

Lower Permian sediments are constituted by about 15 m thick alternation of sandstone, siltstone, and mudstone (Artinskian Stage) and by about 4–20 m coal layers (Kungurian Stage). Quaternary sediments are represented by Middle Pleistocene marine and ice-marine deposits (loam and silt of yellow-brown color) and Upper Pleistocene and Holocene alluvial sediments. The total thickness of the Quaternary sediments is 15–30 m, with an average of 20 m (USSR Engineering Geology, 1991; Isaev V. S. et al., 2022). These alluvial and moraine deposits are the basement of the railway embankment throughout the surveyed area (Vasiliev et al., 2020). They lie on the lower frozen Carboniferous coal deposits of the Vorgashorskaya Formation that crop out on the riverbanks of the Vorkuta River (Isaev V. S. et al., 2022).

Regional climate has a Subarctic character: summer is short and cool, and winter is long and cold, lasting over 8 months from October to May. The total period without negative daily temperatures is only 70 days in average per year, and the mean annual daily temperature is −5.6°C (Tananaev et al., 2021). Total annual snow accumulation is increasing. Precipitation is about 430 mm, of which from 50% to 70% fall as snow (Tananaev et al., 2021). In tundra landscape, snow accumulation increased by 1.8 cm yr^{-1} over the period 1998–2018 (Vasiliev et al., 2020).

The thickness of permafrost in this area was estimated to range between 40 and 95 m using the near-field transient electromagnetic sounding method (Isaev et al., 2020). Railway engineering service confirmed these values by means of seismic data analysis and core drilling operations.

The maximum annual ground temperature ranges between −0.5°C and −1.0°C at zero annual amplitude depth (around 12 m, Tananaev et al., 2021). A residual thaw layer is occurring annually between the base of the seasonally freezing layer at 2–3 m depth and the top of the permafrost layer at 4–5 m depth (Tananaev et al., 2021). Important cryogenic processes occur, including thermokarst and fluvial thermal erosion. Frost boils are also common cryogenic features, mostly occurring in a narrow belt surrounding the water track valleys (Tananaev et al., 2021).

Of particular interest is the diffuse presence of thermokarst phenomena. Thermokarst is a permafrost degradation process initially caused by a disruption of the ground thermal equilibrium that increases the ALT (Jorgenson, 2022). The land surface expression of this process is a thermokarst area generally characterized by marshy hollows. The progressive permafrost degradation can evolve in the development of a closed or an open talik, i.e., an anomalous unfrozen ground enclosed in permafrost or open to the surface, respectively. Further melting of ground ice leads to complete degradation, with all permafrost thawed. In this case, the thermokarst process degenerates to the development of a deep (or through) talik, without permafrost either at the top or the bottom (Jorgenson, 2022). The land surface expression of taliks generally consists in shallow thermokarst lakes and rivers, particularly in regions of continuous permafrost. In the case of deep taliks, the presence of thermokarst lakes depends on the type of soil. Often, both the surface water and the pore water in the underneath sediments do not freeze in winter.

The Khanovey site is an example of a permafrost degradation process at a metastable stage, referred to as "climate-driven, ecosystem-protected permafrost" (Vasiliev et al., 2020). Melting of ground ice near the permafrost table produces uneven thaw and thermokarst, affecting infrastructure and engineering constructions. Here, permafrost degradation and the gradual lowering of the permafrost table lead to vertical deformation (up to 2.5 cm yr^{-1}) of the North Russian Railway roadbed (**Figure 2**), a process accelerated by the removal of peat during the construction, with a consequent change of the local thermal regime (Voytenko and Sergeev, 2016; Vasiliev et al., 2020).

3 METHODS AND DATASETS

Data were mostly acquired at the end of the warm season, between 1 and 23 September 2019, during the international educational course "Vorkuta Engineer-Geocryological Field Work" held by Lomonosov Moscow State University–MSU in collaboration with Norwegian University of Science and Technology–NTNU. The late summer period guarantees the collection of data on the maximum annual thickness of the active layer. Several direct and indirect surveys were carried out and integrated together for a detailed ALT mapping.

Geocryological and landscape surveys, in accordance with Russian standards of permafrost investigations, encompassed borehole coring, probing, and digital mapping. These measurements allowed the subdivision of the area into zones as a function of size relief, geomorphological characteristic, slope exposition, vegetation cover, drainage condition, ALT direct estimates, lithology, and cryogenic processes (e.g., thermokarst, frost heaving, frost boil, and solifluction).

Since 2012, several boreholes have been drilled within the study area, which provide useful lithological information. Furthermore, thermometric sensors were installed in 2015, and ground temperatures profiles were reconstructed using records from 2015 to 2018. Information from three boreholes was used in this study to calibrate the geophysical data.

Indirect geophysical investigations were carried out to integrate the geocryological and landscape data. The geoelectric method was used for frozen and unfrozen ground characterization, which included the ice content estimation in the active layer and the ALT mapping. Previous and new geoelectric profiles (**Figure 1**) were combined with ground thermometry and borehole data to get information about the frozen and unfrozen ground distribution between the railway and the Vorkuta River.

Thermometric measurements in boreholes, core lithologies, geophysical surveys, drilling, and probing have been carried out in Site 1. Geophysical surveys consist in geoelectric measurements, as an integration to the previous geoelectric survey (September 2018), to map the distribution of permafrost and of the active layer. New landscape zonation and geophysical investigations were conducted during the September 2019 field work to integrate the satellite images and data of previous surveys (e.g., ground temperature measurements, borehole information, and geoelectric data).

Two areas were selected for the geoelectric acquisitions within Site 1, both near the western Vorkuta riverbank: Site 1A to the north and Site 1B to the south (**Figure 1**). Site 2 was an unexplored area until September 2019, when only a landscape survey was performed.

The combination of all methods employed in this study provided investigations at different resolutions, allowing the characterization of the unfrozen and frozen patterns and thickness distribution from the surface up to tens of meters depth. Furthermore, it is essential to distinguish between different types of taliks in thermokarst areas. Taliks are bodies of unfrozen ground occurring in a permafrost area due to a local anomaly in ground thermal conditions. They can be closed, open, or deep (through), depending on whether the talik is surrounded by permafrost, open at the top, or open both at the top and the bottom. Geophysical methodologies are fundamental for the detection and differentiation of these features and for defining the rock-physical properties of the frozen soil. In this perspective, the CRIM rock-physics theory can be very useful to link the underground resistivity values to the petrophysical properties (porosity, clay, and ice content) and to enhance integration among the results from geophysical and other surveys (core lithologies, thermometric data, and landscape zonation).

3.1 Geocryological Survey and Landscape Microzonation

Satellite images (of year 2019) were interpreted to preliminarily identify the main morphological elements such as the following: water streams, depressions, hilltops with different vegetation, river embankments, river terraces, anthropogenic structures (such as buildings, railroads, and pits), lakes, channels, and gully erosions. Correlations among landscape type, color and tone, texture, shape, and size of areas were applied to perform this analysis (according to Jensen, 2007).

Moreover, a geocryological field survey (Yershov, 1998) encompassed direct sampling and observation at 73 and 14 points within Site 1 and Site 2, respectively. The following types of information were identified and collected:

- relief surface characteristics. Mesorelief > 2 m height above mean topography (a.m.t.), which is about 85 m a.s.l.; microrelief < 2 m height a.m.t., defined as flat or moundy. When moundy, the height of the mounds is reported;
- surface drainage type (swamp, stream, wet, moist, dry, and very dry);
- vegetation type (lichen, moss, shrub, shrubbish, bush, and grass), according to Goryachkin et al. (1994);
- surface soil sediment classification on a texture basis (clay, silty clay, silty sand, sand, gravel, pebble, and cobble), according to the Folk diagram (Folk, 1954);
- cryogenic processes, such as thermokarst phenomena, frost heaving (i.e., upward or downward displacement of the ground surface caused by freezing and thawing of water in soil), and frost boil (i.e., nonsorted circles resulting from deformation and mixing soils caused by frost heave during freeze back of the active layer);
- morphological elements/processes: river terraces, gully erosion, and solifluction (i.e., slow downhill flow of saturated soil).

Direct estimations of ALT were also performed by digging and probing with a 2 m long metallic probe, in accordance with CALM methodology. Shovel excavations (until 1.50 m depth) allowed us to analyze the cryolithology of seasonally thawing/freezing sediments.

The collected morphological (both from preliminary analysis of satellite image and from direct field survey) and geocryological data (field survey), together with classified landscape microzones, were cataloged and digitalized as georeferenced layers using the ArcGIS® (Esri) software to produce the geocryological and landscape microzonation map.

3.2 Boreholes and Temperature Measurements

Between 2012 and 2018, eight boreholes were drilled in the Khanovey area. Five of these boreholes are of particular interest for this study: K1, K2, K3, K7, and K8 (**Figure 1**). K1 and K2 were drilled in 2014 down to depths of 4.85 and 4.80 m, respectively. Borehole K3 was drilled in 2015 down to a depth of 5.80 m. Borehole K7 was executed in 2017 down to a depth of 2.90 m, and K8 was executed in 2018 down to a depth of 4 m. Rotational or rotational-pressure drilling methods were employed. Rotary core drilling was carried out with the help of a motorized drill for a maximum investigation depth of each borehole. Lithological and geocryological information are available for all five boreholes, from the top to the bottom of the holes (Voytenko et al., 2017).

To analyze the thermal conductivity of the shallower soil, ground temperatures were recorded from October 2015 to October 2018 using a thermistor set composed of GeoPrecision Logger Thermistor strings (https://www.thermistor-string.com/) and Hobo Thermistor strings (https://www.onsetcomp.com/products/sensors/s-tmb-m0xx/) installed in boreholes K1, K2, and K3.

3.3 Geophysical Surveys

Thawing permafrost is strongly linked to local scale changes in the rock-physical properties of frozen soil, which can be monitored using geophysical and geocryological methods. The degree of freezing of interstitial water has a negligible effect on density and magnetic permeability, precluding the use of gravimetric and magnetic techniques. It is fortunate that freezing has a marked effect on dielectric permittivity (Thomson et al., 2012), conductivity (Palacky, 1988; Seppi et al., 2015; Picotti et al., 2017; Francese et al., 2019), and seismic wave velocities (Carcione and Seriani, 1998). Hence, geoelectric, electromagnetic, and seismic methods constitute the best approaches to quantify the thawing degree of ice in sediments.

In this work, geophysical investigations were performed by acquiring both geoelectric and GPR profiles. Although the study area posed severe limits to the GPR technique due to the presence

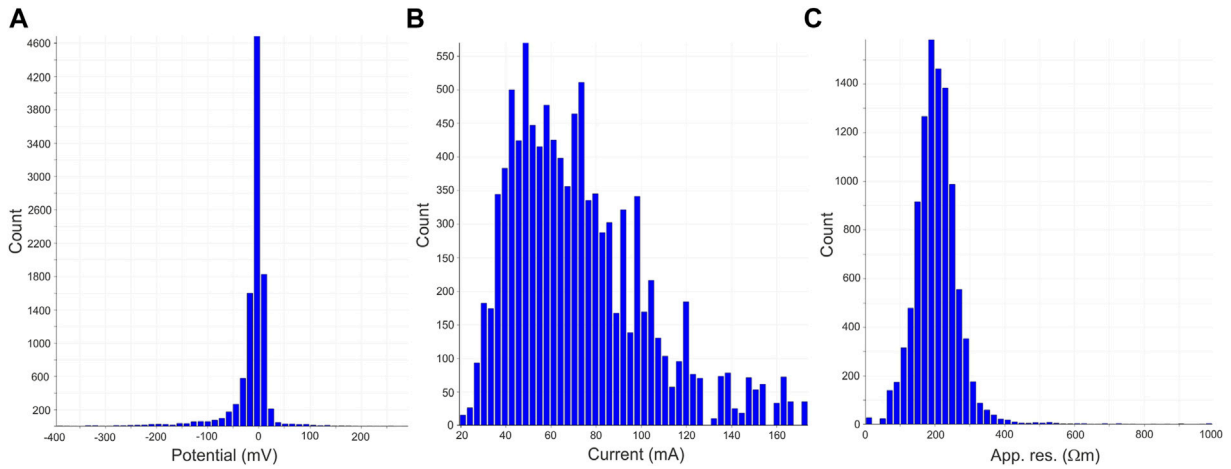

FIGURE 3 | Histograms of **(A)** potentials, **(B)** injected currents, and **(C)** apparent resistivities.

of massive clay contents in the subsoil, the geoelectric method enabled us to characterize both the shallow unfrozen and deep frozen ground, as well as the ALT. The geoelectric method can accurately distinguish between frozen and unfrozen soil based on the spatial variations of resistivity. ERT has been proven to be the most effective technique for monitoring ice content because upon freezing, electrolytic conduction is suppressed, reducing ion mobility and implying a marked increase in the resistivity of the ground (Palacky, 1988; Petrenko and Whitworth, 2002).

3.3.1 Geoelectric Data Acquisition

An IRIS Syscal Pro electrical resistivity meter, an all-in-one multinode resistivity system, was used for geoelectric field acquisition. The combination of both the dipole–dipole and pole–dipole configurations ensures high sensitivity to lateral and vertical resistivity variations, as well as a good signal-to-noise ratio and penetration. A total of six geoelectric profiles were acquired from 7 to 15 September 2019 in Site 1A and Site 1B (**Figure 1**). The interest in these two sites is due to the fact that a wildfire occurred a few decades ago in the former and a new borehole is planned in the latter. Four parallel 240 m long profiles (ERT1, ERT2, ERT3, and ERT4) were recorded in Site 1A using a 5 m electrode spacing. Two parallel 48 m long profiles (ERT1S and ERT2S) were acquired in Site 1B using a 1 m electrode spacing. The lines were oriented in the NW–SE direction in Site 1A and approximately in the N–S direction in Site 1B. In the latter, only the dipole–dipole configuration was used for both lines.

3.3.2 Geoelectric Data Processing and Electrical Resistivity Tomography

The geoelectric data were processed and inverted by adopting ERTLab™—ViewLab3D™ (http://www.geostudiastier.it/) package. Prior to the inversion procedure for the production of the resistivity model (imaging), the dataset was subjected to quality control. Overall, the dataset was of excellent quality, and for this reason, only 1% of the total quadrupoles were removed. Data processing was based on the following criteria (e.g., Seppi et al., 2015; Picotti et al., 2017): elimination of measurements with instrumental standard deviation (obtained through multiple measurement stacks) larger than 10%, removal of the receiver potentials lower (in absolute value) than 0.01 mV, and filtering of negative apparent resistivity values (that have physical meaning only in 3D surveys).

Figure 3 shows the histograms of the statistical distribution of the potentials, currents, and apparent resistivities after filtering. The currents injected at the transmission electrodes had an average value of about 72 mA, and the average apparent resistivity value was around 200 Ωm.

The processed data were then inverted in order to perform imaging and obtain a realistic distribution of subsoil resistivity. The inversion parameters were the following:

- mesh size in the x and z directions equal to half of the electrode spacing: 2.5 m in Site 1A and 0.5 m in Site 1B;
- initial homogeneous resistivity model equal to the average of the apparent resistivity values;
- noise level of 3%, estimated via a statistical analysis of the reciprocal measurements.

Tomographic inversion converged after a maximum of four iterations for all considered datasets.

The ERT was carried out also using another software, the Geotomo Res2dInv (https://www.geotomosoft.com/) package, leading to very similar results. The resulting ERT sections were then interpreted using the Kingdom™ (IHS Markit) and ArcGIS® (Esri) packages to produce the ALT map and integrate together the geocryological and geophysical results.

4 RESULTS

4.1 Landscape Zonation

On the basis of the morphological and geocryological investigations, 12 different types of landscape microzones were

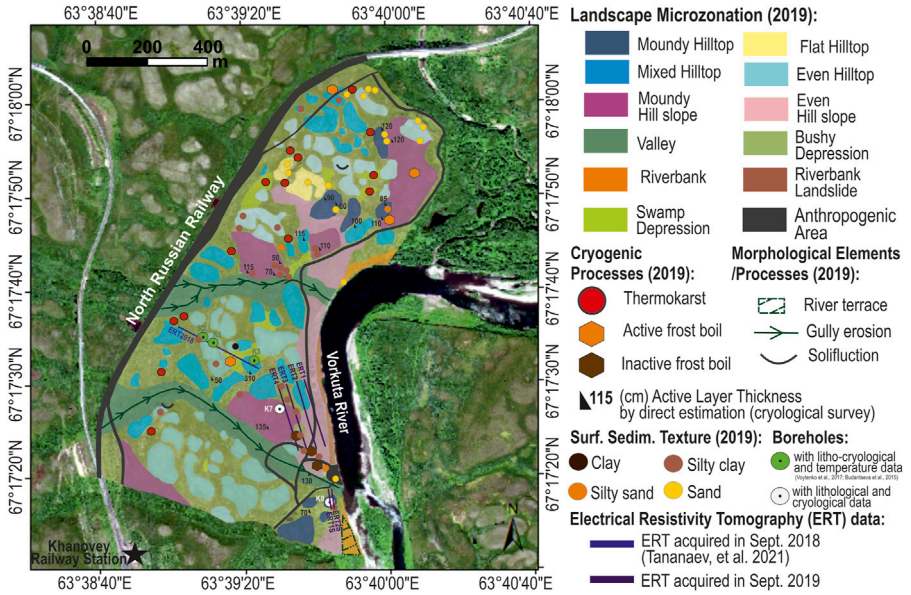

FIGURE 4 | Landscape microzonation map resulting from the morphological analysis and geocryological survey in September 2019 in the Khanovey study area. The position of boreholes and geophysical profiles used in this study are also shown. Silty clay deposits (brown dots) represent the major soil sediment texture type, except for the riverbank and for the northern sector, where abundant sand deposits are present (yellow dots). The active layer thickness values (direct estimations) are indicated by black triangles. Thermokarst phenomena, mainly located close to the railway embankments, is indicated by red dots; solifluction, inactive and active frost boils, gully erosion, and river terrace are also displayed. The surveyed area can be subdivided into 12 different landscapes as indicated in the legend and in **Table 1**. Map compiled using ArcGis® (Esri) software. Datum: WGS84; projection: UTM 41N. Satellite base image (Gis layer "World Imagery") retrieved in 2019 from the ArcGis online database resources.

classified in both Site 1 and Site 2 (**Figure 4**). The 12 classified microzones were the following: moundy hilltop, mixed hilltop, even hilltop, bushy depression, swamp depression (**Figures 5A, B**), even hillslope (**Figure 5C**), flat hilltop (**Figure 5D**), moundy hillslope (**Figure 5E**), riverbank (**Figure 5F**) and riverbank landslide, valley, and anthropogenic area (e.g., **Figures 2**, **5A**).

The peculiar characteristics of each microzone are summarized in **Table 1**, and **Figure 4** displays the geocryological features and the landscape microzonation map performed for the surveyed area (both Site 1 and Site 2).

The land surface is characterized by large polygonal features, with a diameter between about 10 and 150 m. Mesorelief (>2 m height a.m.t.) and microrelief (<2 m height a.m.t.) are typical of the area. The hill landscapes (hilltop and hillslope) are classified on the basis of the shape and slope pattern as follows: flat, moundy, even (uniform hill), and mixed. The term "moundy" refers to a rugged and irregular hill with mounds up to about 20–50 cm a.m.t. high. The main difference between moundy and mixed hill is due to the vegetation pattern and smaller mound height (up to 20 cm a.m.t.) in mixed hill. Depressions are subdivided according to the vegetation type into the following: bushy (characterized by tall shrubs and birches) and swamp/grass depressions (characterized by moss and grass). Flat areas of flood plain and a river terrace are present in the southern eastern sector of Site 1, both covered by grass. The anthropogenic area, usually characterized by sand and gravel, includes railroad, pathways, the base camp set up during the field work, the coal pit, and the pump station.

The study area is covered by unconsolidated fine-grained sediments related to Quaternary glaciomarine deposits. Clay and silty clay sediments are dominant, except for the riverbank and the northern sector of Site 2, where sand and silty sand deposits dominate the moundy, even, and flat hilltops. At the toe of the even hillslope, occasional clasts of pebble to cobble size can be found. Two interpretations can explain this: uprising of the coarse grains due to the frost heave phenomena or fluvial deposit associated with the adjacent valley.

Within the valley landscape (covered by clay and silty clay), gullies erosion with U-shaped profiles are characterized by stream surface drainage and small waterfalls that evidence a recent development. The riverbank landslide consists of sand and gravel. Along the Vorkuta River, riverbanks form an about 45° slope (**Figure 5F**). In the riverbank area, a shallow study section, dug by shovel and less than 2 m deep, reveals that the uppermost sediments are dominated by sandy loam, mainly massive, with occasional clasts of pebble to cobble size and iron precipitations. Striated clasts indicate that the sediment is evidently of glacial origin. A deeper laminated coarse sand unit, with clasts of pebble to cobble size, is present. Grain size rapidly declines away from the riverbank, with sediments becoming finer.

Hilltops with <1° slope (e.g., even hilltop) are associated with phenomena related to seasonal freeze–thaw, which saturates the soil on the surface and induces solifluction movements along the slope. Thermokarst phenomena (**Figures 5A, B**) and frost boils are cryogenic processes associated with permafrost. Frost boils are subdivided into active and inactive (covered by vegetation). In

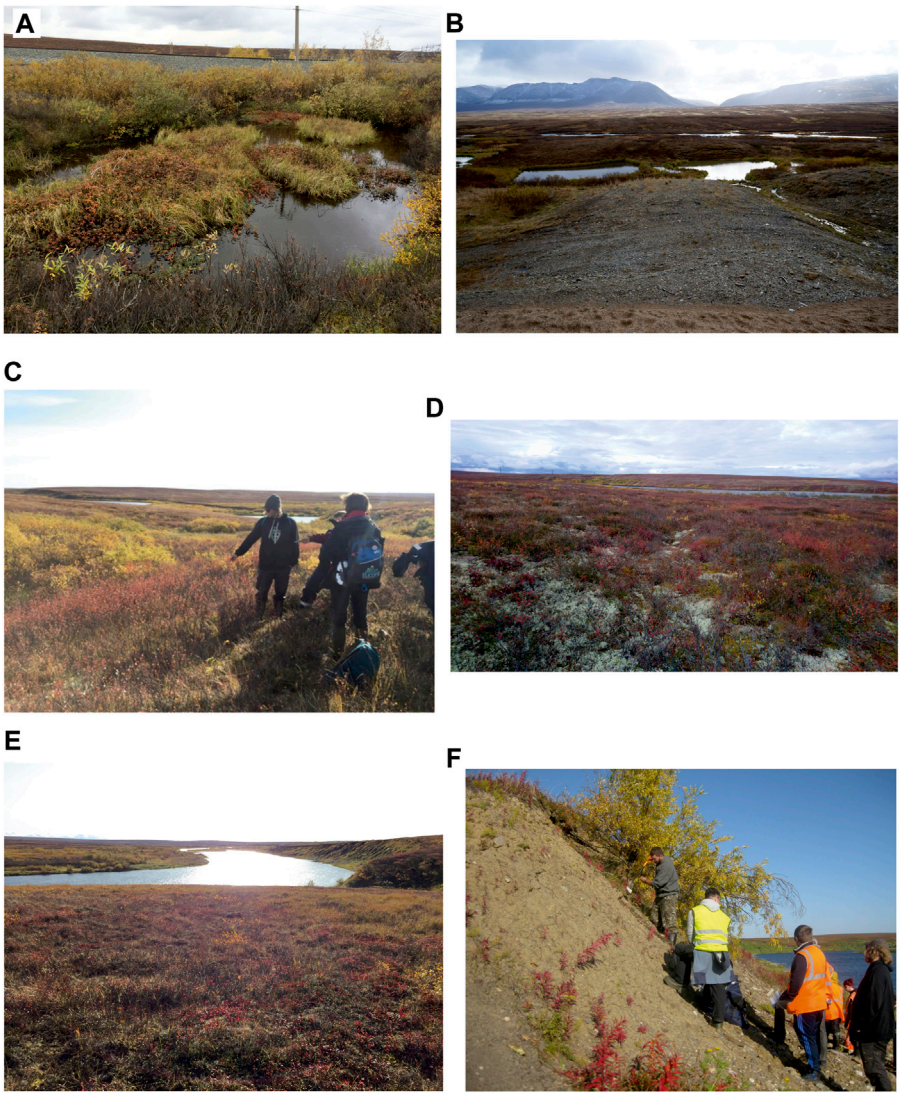

FIGURE 5 | (A) thermokarst phenomena close to the railway. **(B)** thermokarst phenomena, within bushy and swamp depressions, that mark the Arctic landscape at the western foothills of the Ural Mountains. **(C)** even hillslope landscape characterized by small mounds (maximum 20 cm high) covered by lichen (e.g., reindeer lichens, in white) and small shrubs (e.g., *Vaccinium myrtillus* or blueberry) vegetation. **(D)** flat hilltop landscape example, close to the railway, mainly characterized by lichen (e.g., reindeer lichen, in white), small shrub (e.g., *Rhododendron tomentosum* or Labrador tea), and few amount of moss vegetation. **(E)** moundy hillslope landscape with massive mounds about 25–50 cm high covered by lichen, dwarf birch, moss, and grass. Wet intermound depressions are also abundant. **(F)** vorkuta riverbank covered by patches of grass and, in this case, an isolated tree.

the latter, the interrupted frost heaving due to the increase in the thaw layer allows plants to encroach the area. Thermokarst areas usually develop close to the eastern side of the railroad (**Figure 4**) because of the vegetation layer removal during the construction of embankments.

The tundra vegetation of the study area is mainly constituted by lichen, moss, grass, tall and small shrubs, and dwarf and tall birches. There are no forest trees, except a few trees grown in the valley. Moss (e.g., *Myosotis asiatica* and the *Saxifraga* and *Sphagnum* genera) grows in wet areas typically characterizing the swamp depression, moundy hillslope, but is lesser in flat hilltop. Grass (e.g., *Equisetum arvense or Carex*) grows in wet areas too, such as swamp depressions, valley, and moundy hillslopes, and locally in the riverbank. Moreover, grass outlines thermokarst areas, where the depressed land is soaked in water (**Figures 5A, B**). Lichen (e.g., *Cladonia rangiferina*, known also as reindeer lichen) dominates dry surfaces, such as hilltops and the upper part of the even and moundy hillslopes. Small shrubs (e.g., *Rhododendron tomentosum* or Labrador tea, *Salix arctica* or Arctic willow, *Vaccinium myrtillus* or blackberry, *Vaccinium cyanococcus* or blueberry, *Vaccinium vitis-idaea* or lingonberry, *Arctostaphylos uva-ursi* or bearberry, and *Empetrum nigrum* or crowberry) are adapted to live in both dry and wet surface areas, like flat and even hilltops, even hillslope and the valley, whereas tall shrubs are present only within wet environments as troughs of mixed hilltop and bushy

TABLE 1 | Characteristics of the 12 different types of landscape microzones identified in the Khanovey area (Site 1 and Site 2) by the geocryological survey. The main types of surface relief, drainage, vegetation, surface sediment texture classification, and cryogenic processes are reported.

Color legend	Landscape microzone	Relief surface characteristics	Surface drainage type	Vegetation type	Sediment texture of upper units	Cryogenic processes
	Moundy hilltop	Meso: even to small relief Micro: 20–50 cm high mounds	Dry	Lichen on mounds and tall shrub in troughs	Sand or silty sand	Frost heave
	Even hilltop	Meso: even Micro: even	Dry	Lichen, locally small shrub	Clay and silty clay (in Site 1 and southern Site 2); sand and silty sand (northern Site 2)	Frost heave and locally solifluction
	Mixed hilltop	Meso: even to small relief Micro: 0–20 cm high mounds	Dry	Lichen on mounds (microrelief) and tall shrub in troughs	Silty clay	—
	Valley	Meso: U-shaped profile Micro: even to small bumps	Moist to wet with stream	Tall birch, small shrub, grass	Clay or silty clay	Gully erosion
	Bushy depression	Meso: depressed areas in-between hilltops Micro: even to small bumps	Moist to wet	Tall birch and tall shrub	Clay and silty clay (in Site 1 and southern Site 2); sand and silty sand (northern Site 2)	Locally thermokarst and/or frost boil
	Swamp/grass depression	Meso: in-between hilltop Micro: moundy	Moist to wet, swamp	Moss, grass	Clay and silty clay	Frost heave, and locally thermokarst and/or frost boil
	Riverbank landslide	Meso: more than 40 cm high relief Micro: even to small bumps	Very dry	No vegetation or patches of grass	Sand and gravel	—
	Riverbank	Meso: less than 40 cm high relief Micro: small bumps	Dry	No vegetation or patches of grass	Usually coarse (sand, pebble, cobble)	Locally river terraces
	Moundy hillslope	Meso: even Micro: 20–50 cm high mounds	Wet	Upper slope: lichen. Middle-lower slope: moss, grass, dwarf birch	Silty clay	Frost heave and locally frost boil
	Even hillslope	Meso: even Micro: even	Dry	Lichen, small shrub	Silty clay	Locally frost boil at the toe
	Flat hilltop	Meso: flat Micro: flat	Dry	Lichen, small shrub, and few amounts of moss	Sand	—
	Anthropogenic	Irrelevant	Varying	No vegetation or patches of grass	Sand or gravel filling	—

depressions. Tall birches (*Betula glandulosa*) and dwarf birches (*Betula nana*) grow in moist to wet landscapes, with the former in valley and bushy depression and the latter in moundy middle-lower slope.

ALT direct estimations showed an average value of about 1 m, with values ranging from 0.5 to 3.1 m, but these measurements are not reliable because ALT could be larger than that directly estimated, due to the limits of the digging and/or probing methods and/or the possible presence of taliks. The geocryological features and the landscape microzonation map performed for the surveyed area (both Site 1 and Site 2) are displayed in **Figure 4**.

4.2 Ground Thermometry and Coring

Temperature data for at least two consecutive years (2016–2018) are available only for boreholes K1, K2, and K3. The lithological and vertical ground temperature profiles corresponding to these boreholes are shown in **Figures 6A, B**, respectively. **Figure 6B** shows the annual maximum, minimum, and mean temperature curves together with the permafrost table depth (where

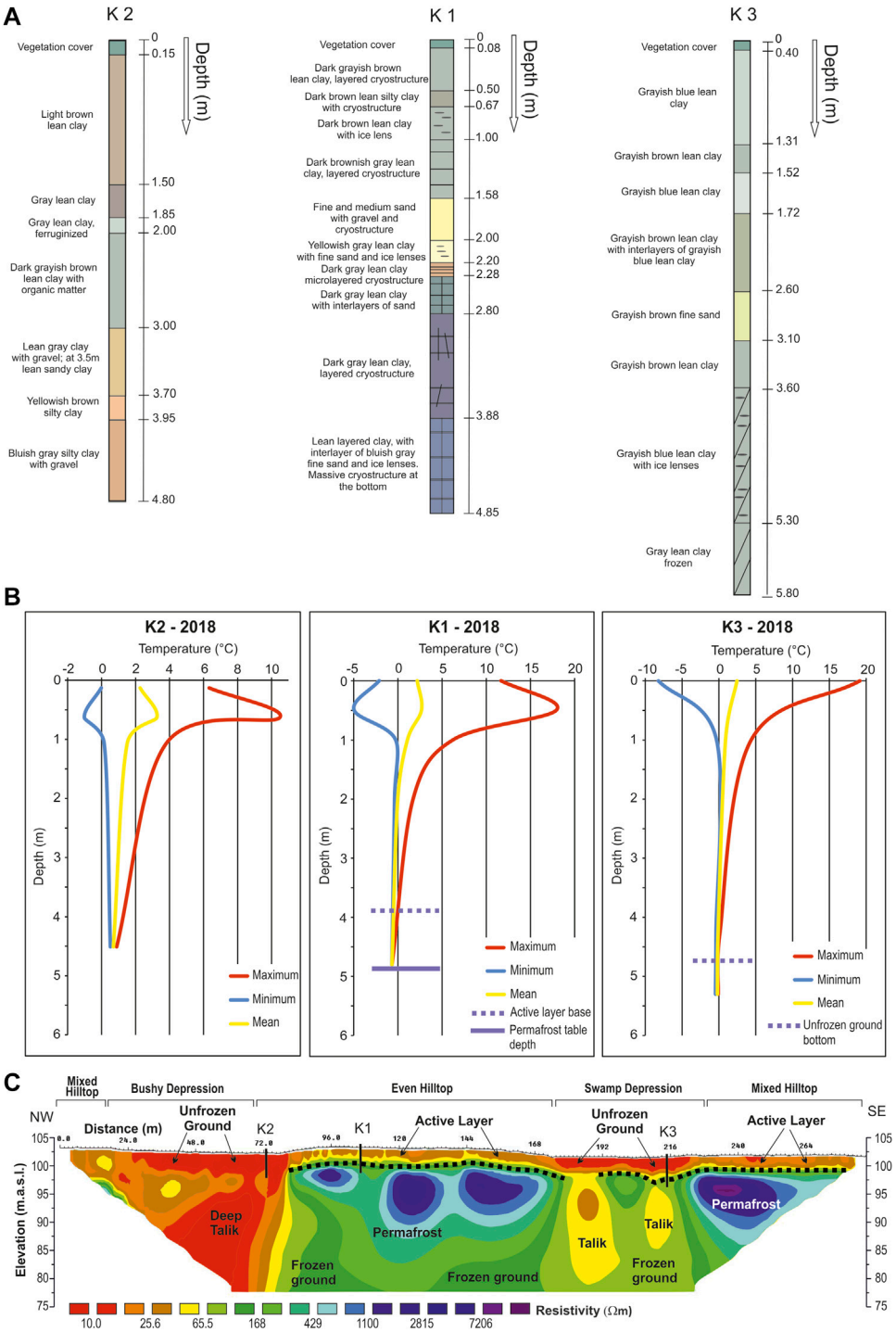

FIGURE 6 | (A) lithological and geocryological core analysis of boreholes K1, K2, and K3 (data from Budantseva et al., 2015; Voytenko et al., 2017). **(B)** maximum, minimum, and mean temperature curves of the year 2018, where the unfrozen ground bottom, the active layer bottom, and the permafrost table depth are indicated. **(C)** interpretation of the ERT2018 resistivity section (modified from Tananaev et al., 2021), crossing boreholes K1, K2, and K3. The interpretation of the active layer and unfrozen ground bottom (black dashed line), marked by the resistivity value of 100 Ωm, is in agreement with the core analysis and with the temperature profiles at K1 and K3. Wide temperature fluctuations occur in the active layer, characterized by low resistivity values (ρ < 100 Ωm). A deep talik is present in the NW sector, explaining the unusual trend in the temperature profile of the K2 borehole. Two taliks enclosed in the frozen ground are present beneath the swamp depression zone, between K1 and K3 (ρ < 80 Ωm), covered by a 3 m thick unfrozen ground layer. One of the two taliks is open to the surface.

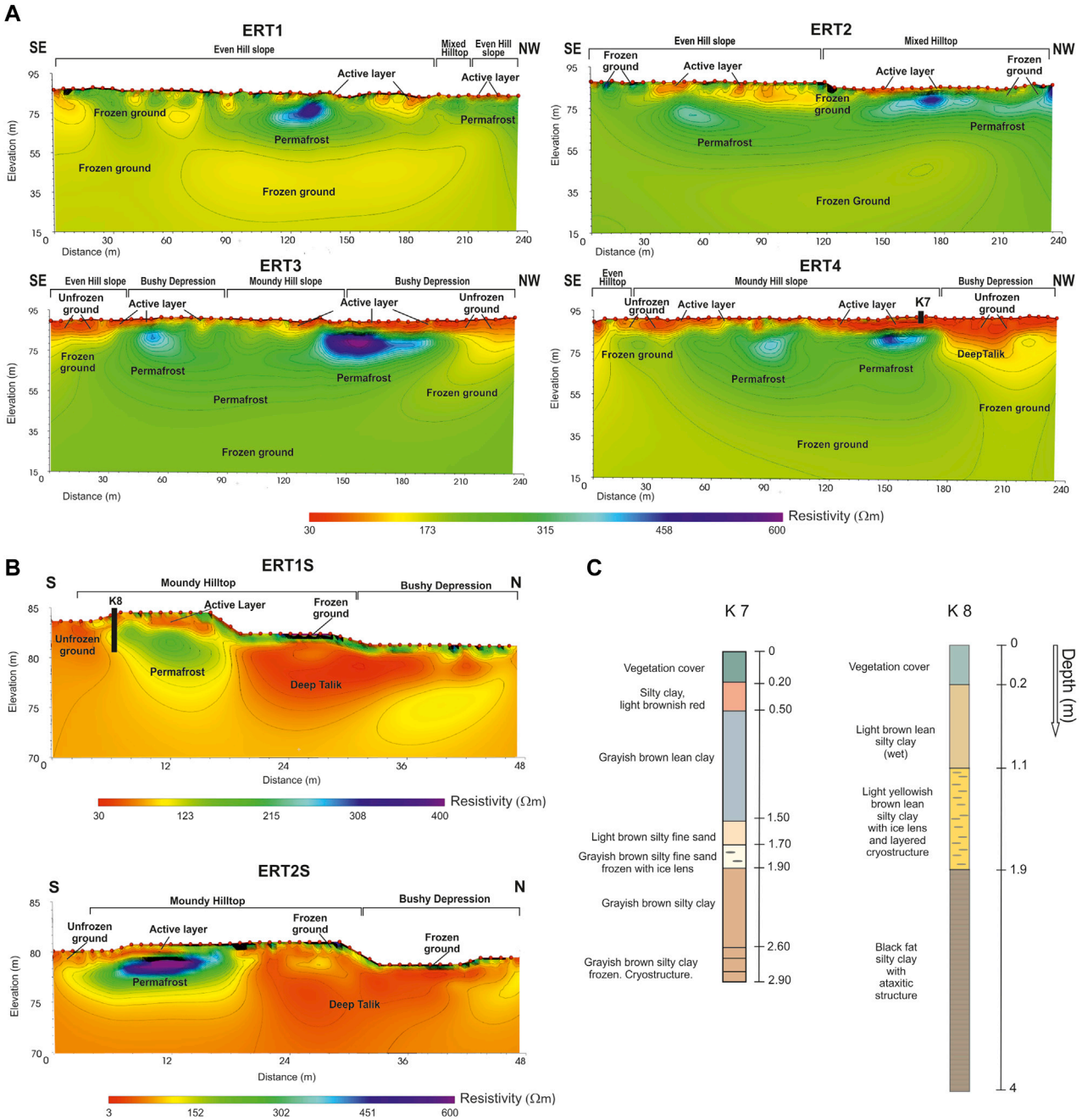

FIGURE 7 | ERT sections in **(A)** Site 1A (ERT1, ERT2, ERT3, and ERT4) and in **(B)** Site 1B (ERT1S and ERT2S). The positions of boreholes K7 and K8 are indicated on the profiles ERT4 and ERT1S, respectively. The interpretation of the ERT profiles is based on the analyzed resistivity-cryological patterns. ERT sections exhibit a continuous permafrost layer with resistivity values in the range $200 < \rho < 600$ Ωm, underlying a low resistivity ($\rho < 100$ Ωm) active layer. Red dots represent the electrodes deployed along the topographic surface. **(C)** K7 and K8 borehole stratigraphy (data from Budantseva et al., 2015; Voytenko et al., 2017). The cryolithology highlights the presence of silty clay frozen bodies with cryogenic structures in both boreholes, in agreement with the ERT results. Hence, the silty clay with an ataxitic structure at about 2 m depth in K8 produces the resistivity decrease observed in the ERT1S and ERT2S profiles.

detectable), which corresponds to the surface where the temperature is always under 0°C. In general, the measurements show that in the active layer, the temperature reaches a maximum value of about 18°C during summer and a minimum value down to less than −5°C during winter. K1 and K3 boreholes show larger temperature fluctuations near the surface, where the thermal heat transfer is more intense. The permafrost table is clearly identified only at the bottom of borehole K1, at about 4.8 m depth (**Figure 6B**), where the temperature is always below 0°C and massive cryogenic structures are present in the lithological profiles.

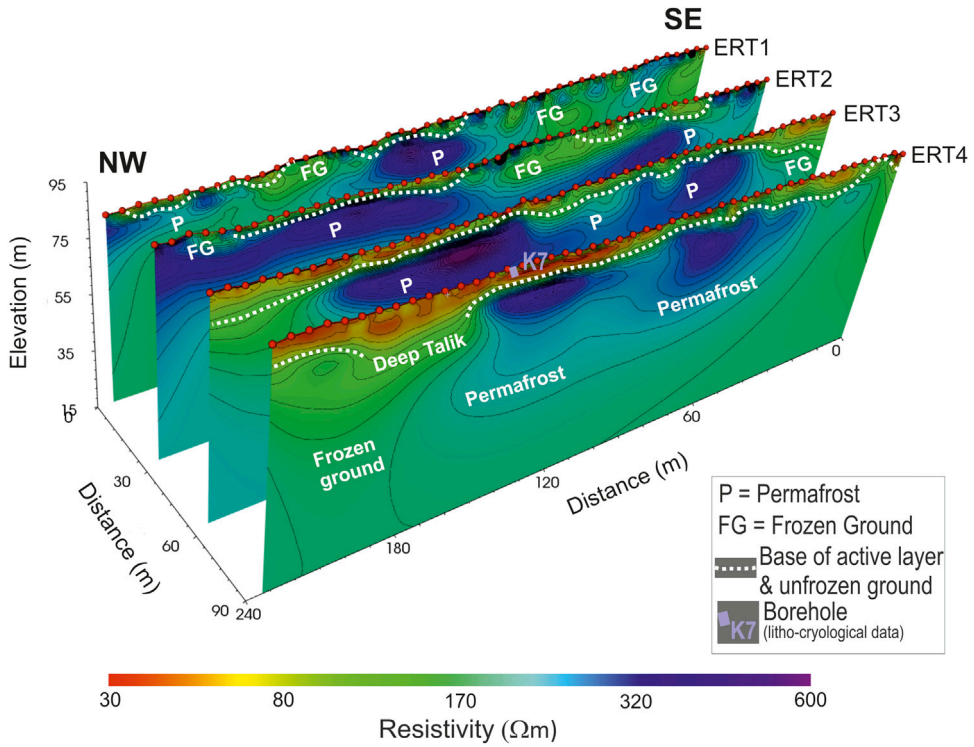

FIGURE 8 | 3D representation of the ERT sections in Site 1A. According to the CRIM analysis and to the resistivity-cryological patterns, the interpretation of the active layer and unfrozen ground bottom (white dashed line) is marked by a resistivity value of 100 Ωm. This interpretation, together with the topographic surface (highlighted by red dots representing electrodes deployed during the acquisition), was used to build the ALT and UGT map shown in **Figure 9**. The talik, permafrost, and frozen and unfrozen ground areas are also highlighted.

The active layer and unfrozen ground bottom are identified in boreholes K1 and K3, at depths of about 3.7 and 4.7 m, respectively, and coincide with the presence of frozen sediments in the lithological profiles and temperatures around 0°C. The bottom of the K3 borehole shows temperatures very close to 0°C, and the permafrost table cannot be clearly identified. On the other hand, borehole K2 exhibits only positive temperatures. Here, the total absence of cryogenic structures (**Figure 6A**) confirms that a deep unfrozen ground (a talik) dominates the area.

Borehole stratigraphy shows that clay and silty clay sediments are dominant, confirming the results of landscape zonation. Core samples often exhibit a layered cryostructure along boreholes K1 and K3.

4.3 Electrical Resistivity Tomography Sections

The ERT profiles in the study sites are interpreted and integrated with the geocryological data, landscape zonation (**Figure 4**), and borehole data. Lithological data are available for boreholes K1, K2, and K3 (**Figure 6A**), located along a previous geoelectric survey (profile ERT2018, **Figure 6C**) acquired in September 2018 (Isaev et al., 2020), and for boreholes K7 and K8 (**Figure 7C**), located on profiles ERT4 (**Figure 7A**) and ERT1S (**Figure 7B**), respectively. The ERT2018 section was obtained using the Geotomo Res2dInv package. The acquisition and processing of the ERT2018 profile are described by Isaev et al. (2020) and Tananaev et al. (2021).

4.3.1 Previous Surveys

The resistivity (ρ) values of the previous geoelectric survey ERT2018 (**Figure 6C**), acquired in September 2018, are compared with the results obtained from the lithological (**Figure 6A**) and thermometric (**Figure 6B**) data at K1, K2, and K3 boreholes. As shown in **Figure 1**, this profile crosses exactly all three considered boreholes.

As evidenced in the previous section, massive cryostructure and frozen sediments are present at the bottom of K1 and K3 boreholes, as a useful indicator of the permafrost table and of the base of the active layer and unfrozen ground. Comparing the borehole data with the resistivity values of ERT2018 section (**Figures 6A–C**), it is possible to correlate the active layer base and the permafrost table to resistivity values of approximately 100 and 200 Ωm, respectively. As explained in detail in the Discussion section, the ranges of resistivity values for frozen and unfrozen ground strongly depend on the type of soil. Because clay and silty clay are the dominant sediment type in the study area, these two resistivity thresholds represent the characteristic resistivity values for the active layer base and the permafrost table in the whole area investigated by the geoelectric surveys (**Figure 1**). Therefore, we based our interpretation of the ERT sections on the following approximate scale of resistivity values: lower than 100 Ωm for the unfrozen ground, active layer, and taliks; ranging between 100 and about 200 Ωm for the frozen ground; and higher than about 200 Ωm for the permafrost. We point out that this resistivity scale is no more

valid for other types of soil, characterized by lower clay contents. A similar scale of resistivity has been adopted in other works for this kind of soils (e.g., Vanhala et al., 2010; Isaev V. et al., 2022).

On the basis of this resistivity scale, we interpreted the base of the unfrozen ground and of the active layer along the ERT2018 section (**Figure 6C**). According to the definition of the active layer, in this interpretation, we indicated as active layer only the parts of the thawed superficial ground underlain by permafrost whereas the other parts were indicated as unfrozen ground. Low-resistivity values are present at shallow depths along the entire profile, in good agreement with the ALT and unfrozen ground thickness (UGT) values in correspondence of boreholes K1 and K3, respectively. The active layer is present in the central and south-eastern parts of the section, it is about 3.5 m thick and exhibits an average resistivity of 40–50 Ωm. The unfrozen ground layer is thicker (about 4.5–5.0 m) and exhibits a lower average resistivity (approximately 20 Ωm) in the south-eastern part of the section, in correspondence of the swamp depression zone. These evidences are in agreement with the temperatures and lithological profile of K3, showing a lower ice content than that of K1.

High-resistivity zones in the ERT section at depths larger than 5 m, with resistivity values up to about 10 kΩm, can be associated with the presence of permafrost. This correlation is in agreement with temperatures below zero and with the presence of massive cryogenic structures at the bottom of the borehole K1. As explained in the Discussion, if clay is predominant also in the deeper parts of the section, the maximum thickness of the permafrost layer should be about 25 m.

As displayed in **Figure 6C**, the profile shows that the borehole K2 is located in correspondence of a wide and deep low-resistivity body (10 Ωm < ρ < 70 Ωm), showing a 1 m deep topographical depression at the surface (bushy depression landscape microzone, **Figure 4**). The unusual temperature trend and the lithological profile of K2 indicate the presence of an extensive anomalous unfrozen ground area. Considering the permafrost thickness in this section, this low-resistivity area can be ascribed to a deep talik. Furthermore, two other taliks are probably present between K1 and K3 (ρ < 80 Ωm), corresponding to a swamp depression zone. One of the two taliks is enclosed in frozen ground, whereas the second shows lower average resistivity values, and it is open to the surface. On the basis of our interpretation, the medium around the two taliks shows resistivity values between 100 and 200 Ωm, typical of frozen ground (see also the Discussion) and, most probably, there is no permafrost below them. Therefore, the area including these two taliks can be considered an early-stage deep talik.

This correlation of different types of data from previous surveys enables a better interpretation of the resistivity-cryological patterns on the four new ERT sections acquired in 2019.

4.3.2 Site 1A

The four geoelectric profiles acquired in Site 1A in September 2019, namely, ERT1, ERT2, ERT3, and ERT4, are NW–SE oriented and 30 m spaced to each other (**Figure 1**). They are located at an average elevation of about 90 m a.s.l. The ground surface topography is characterized by microdepressions of extension ~1 m^2, interspersed with hillocks with an elevation difference of about 1 m. On the basis of the resistivity scale adopted for ERT2018, the resulting profiles show the presence of a continuous high-resistivity permafrost layer (200 Ωm < ρ < 600 Ωm) underneath a thin frozen ground layer (100 Ωm < ρ < 200 Ωm) and a low-resistivity (ρ < 100 Ωm) active layer (**Figures 7A**, **8**). As conducted for the ERT2018 profile (see also the Discussion), we interpreted the four sections by adopting a value of 100 Ωm as the characteristic resistivity value of the active layer and unfrozen ground bottom in this area (**Figure 8**). Also in this case, we indicated as active layer only the parts of the thawed superficial ground underlain by permafrost and as unfrozen ground the other parts. The surveyed area is characterized by an ALT ranging from about 0.5 to 7 m, while the UGT can reach 9 m in some areas.

The southern part of line ERT1 exhibits a superficial resistive body of about 100–300 Ωm, which denotes discontinuous permafrost and frozen ground. Likewise, the high-resistivity feature at the southern edge of the line ERT2 is characterized by resistivity values similar to those of the permafrost layer. This feature, revealing a frozen ground and massive cryostructure, is located on an even hillslope covered by lichens and small shrubs. Moving northward along the profile, a local thicker (about 4–6 m) low-resistivity active layer (30 Ωm < ρ < 100 Ωm) is present. In the central-northern part of the ERT2, corresponding to a mixed hilltop landscape, covered by lichen on mounds and tall shrubs in the troughs, the ALT becomes thinner, varying between about 0.5 and 2 m.

Lines ERT3 and ERT4 are located on a fairly flat peat surface with few small hollows (1–2 m deep). They exhibit an ALT ranging from 1 to 7 m (an average thickness of about 4 m) with resistivity values ranging from 30 to 100 Ωm. The higher ALT values are present in the NW part of the area, in correspondence of a bushy depression covered by tall birches and shrubs. Borehole K7 is located approximately 5 m on the west with respect to the ERT4 profile. A silty clay frozen body with a cryogenic structure is present at the bottom of this borehole, from 2.6 to 2.9 m depth (**Figure 7C**). This borehole is not deep enough to reach the base of the active layer, which is about 7 m deep in this position, as inferred from the interpretation of the ERT4 section. However, this profile evidences a high-resistivity (~100 Ωm) thin lens (~1 m thick) embedded in the active layer, in agreement with the borehole K7 geocryological core analysis. On the basis of the interpretation of the ERT4 profile, the north-west area shows an extensive low-resistivity unfrozen ground, which is about 16 m thick, underlined by a deep frozen ground body where the permafrost table cannot be detected. This area, characterized by a marshland bushy depression landscape, can be associated with the presence of a deep talik.

The interpretation of the ERT profiles (**Figures 7A**, **8**) enabled us to map the extension and thickness of the unfrozen ground and active layer. However, they contain useful information also about permafrost thickness. These sections show a gradual decrease in the ground resistivity with depth. On the basis of our resistivity scale, if the underground lithology does not vary significantly with depth and clay is predominant (as shown by landscape zonation and borehole stratigraphy), the maximum thickness of

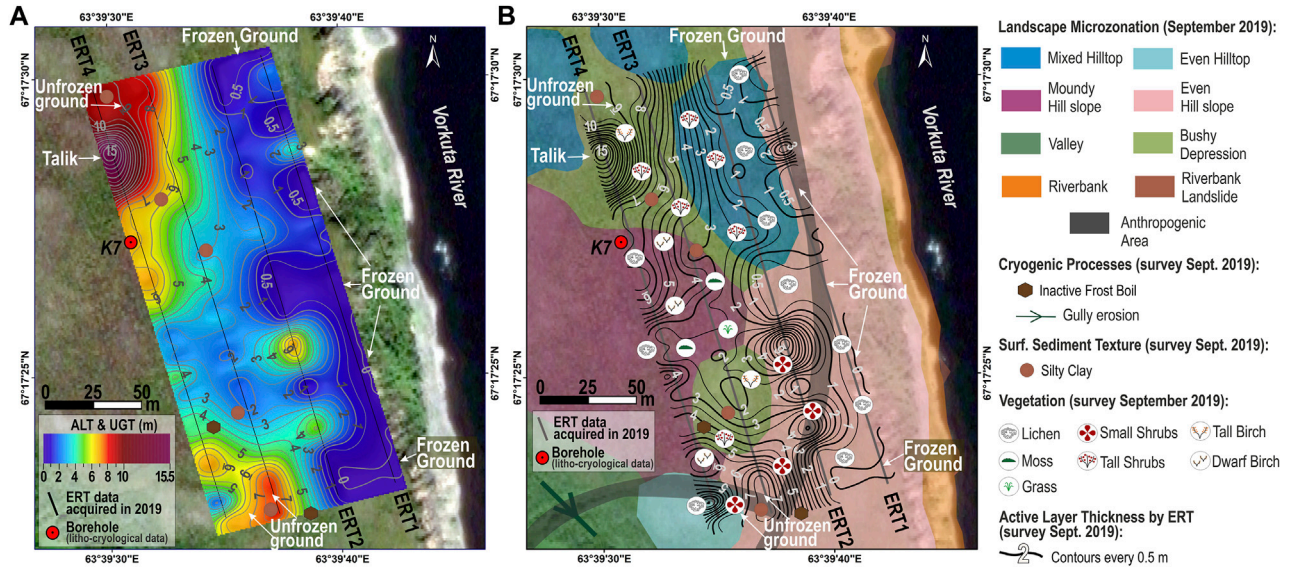

FIGURE 9 | (A) ALT and UGT map (contours every 0.5 m) performed from the interpretation of the ERT1, ERT2, ERT3, and ERT4 profiles acquired in Site 1A, superimposed on the satellite image. The map highlights a gradual decrease in ALT by moving eastward to the Vorkuta River; the ALT ranges from 0 m (dark blue) in the eastern side of the map to about 7 m (red) in the NW part. ALT values greater than 7 m represent unfrozen ground areas not underlined by permafrost or an area occupied by a talik. The talik, located in the north-western side of ERT4, exhibits an unfrozen ground thickness up to about 16 m (highlighted in purple). The position of borehole K7 is indicated (red circle). Surface lithology information collected during the geocryological survey is also shown, evidencing that silty clay deposits (brown dots) represent the major soil texture type. **(B)** ALT isolines (every 0.5 m) superimposed to the landscape microzonation, morphological and cryogenic processes, and vegetation type (2019 field survey). The hilltops are characterized by frozen ground, the hillslopes are characterized by frozen ground to thin/large ALT (1–7 m), and depressions are marked by thick unfrozen ground (7–9 m) or a talik area (9–16 m thick thaw soil in the NW of the map). Local inactive frost boils (dark brown hexagons) are located in correspondence of a 4–5 m ALT, within even hillslope and bushy depression microzone types. The anthropogenic zone (dark gray area) corresponds here to unpaved pathways. Maps compiled using ArcGis® (Esri) software. Datum: WGS84; projection: UTM 41N. Satellite base image (Gis layer "World Imagery") retrieved in 2019 from the ArcGis online database resources.

the permafrost layer should be about 30 m for ERT1, 40 m for ERT2 and ERT4, and 50 m for ERT3 (**Figures 7A**, **8**). These values are quite in agreement with previous investigations (e.g., Isaev et al., 2020), reporting a permafrost thickness larger than 40 m in this area.

However, as explained in detail in the Discussion, note that the deepest parts of the ERT sections are unreliable because the sensitivity of the geoelectric method decreases with depth. For this reason, in this case, the bottom of the permafrost layer cannot be well defined if its thickness exceeds 50 m.

4.3.3 Site 1B

The two geoelectric profiles ERT1S and ERT2S (**Figure 7B**), acquired in September 2019, are parallel to each other and located about 30 m west to the Vorkuta River in Site 1B (**Figure 1**). The landscape is characterized by a 2–2.5 m high (with respect to the average surface elevation of about 81.5 m a.s.l.) moundy hilltop located to the south (with lichens on mounds and tall shrubs in troughs) and a bushy depression covered by tall birches and shrubs located to the north. Rainwater flows south-eastward in the depression and within the valley landscape, draining the surface to the Vorkuta River.

The depression is characterized by low-resistivity (ρ < 100 Ωm, with very low-resistivity values down to about 3 Ωm) sediments covered by a ~0.5 m thick high-resistivity (100 < ρ < 600 Ωm) superficial layer. Despite the low penetration depth of these two short profiles, this low-resistivity body is probably related to a deep talik area. The K8 borehole (**Figure 7C**) is located at the moundy hilltop, right on the ERT1S line. Borehole stratigraphy shows a 1.1 m thick wet shallow layer overlying a 0.8 m thick layer with an internal cryostructure, matching quite well the resistivity distribution. Silty clay sediments are predominant also in this area. Permafrost is present below the southern moundy hilltop area, at about 1.5 m depth, and it consists in a 4 m thick high-resistivity layer (200 < ρ < 600 Ωm). In the southern part of both lines, the 1 m thick low-resistivity thawed soil overlying the permafrost is associated with the active layer. Close to the southern edges of profiles ERT1S and ERT2S, resistivity values lower than 100 Ωm indicate the presence of unfrozen ground both in the upper and deeper parts, suggesting that this area could be ascribed to a deep talik as well.

5 DISCUSSION

In the context of accelerating global warming, construction of foundation infrastructures on permafrost requires appropriate methodologies for subsoil characterization (e.g., soil type and petrophysical and mechanical properties). Although the geoelectric technique has been proven an efficient

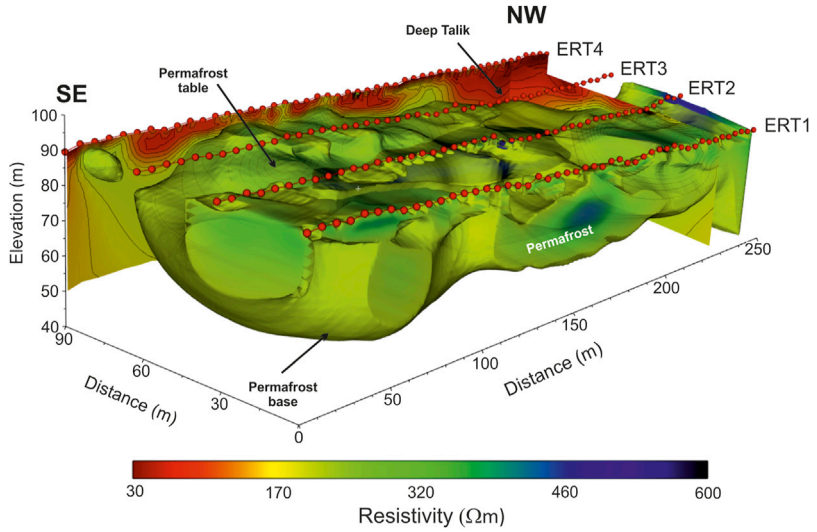

FIGURE 10 | Permafrost volume obtained by a 3D interpolation of the resistivity values higher than 200 Ωm over the four ERT sections of Site 1A. Permafrost thickness substantially reduces and becomes discontinuous upon approaching the riverbank.

methodology for permafrost characterization, it shows some limitations that can be resumed in these two main points:

- ERT surveys alone are not sufficient to infer the petrophysical properties of the investigated subsoil, namely, the ice content S_i, porosity Φ, and clay content C. To this aim, it is necessary to integrate ERT data with other geophysical methodologies, for example, the active seismic or GPR methods (e.g., Böhm et al., 2015). Nevertheless, in the absence of other geophysical complementary data, it is possible to estimate some properties using a suitable rock-physics theory and geocryological data describing the type of soil. In the following subsection, we propose a methodology based on the CRIM to analyze how the ice content, clay content, and porosity influence the resistivity of the investigated soils.
- As previously explained, the deepest parts of the ERT sections are generally unreliable because the sensitivity of the geoelectric method decreases with depth. For this reason, often the bottom of the permafrost layer can hardly be resolved. For a homogeneous subsoil, the maximum depth of investigation z_{max} is defined as the depth at which the normalized sensitivity function, integrated with respect to depth, is equal to 1/2 (Edwards, 1977; Szalai et al., 2009). It follows that $z_{max} \approx L/6$ where L is the total array length. In our case, using both the dipole–dipole and pole–dipole arrays, in Site 1A, we have $z_{max} \approx 70$ m.

The results obtained from the ERT2018 profile (calibrated by thermometric and core lithology data) and from the ERT data acquired in 2019 (calibrated by core lithology data) allowed the characterization of the permafrost, frozen ground, and active layer distribution of the Khanovey area near the Vorkuta River. The isopach map shown in **Figure 9A** has been obtained by interpolating the interpreted ALT and UGT displayed in **Figure 8**. As previously explained, we indicated as active layer only the parts of the thawed superficial ground underlain by permafrost, and as unfrozen ground the other parts. **Figure 9A** highlights a gradual increase in ALT moving westward, from ERT1 to ERT4, where it reaches a maximum value of about 7 m, close to the talik. Then, there is an intermediate unfrozen ground zone of thickness ranging from 7 to 9 m around the talik.

It is possible to correlate those results to geomorphological setting, vegetation, geocryological processes, drainage condition, and landscape zonation, which are strictly related to frozen ground distribution. For instance, the ALT (and UGT) increases in areas such as bushy depressions with tall birches and tall shrubs, whereas hilltops covered by lichens and shrubs are characterized by a shallower permafrost table (**Figures 9A, B**). The ALT isolines, obtained from the four ERT 2019 profiles, are also shown in **Figure 9B**, where they are superimposed to the landscape microzonation and geocryological map. The map evidences that silty clay deposits are the major soil type in Site 1A. Moreover, the hilltops are characterized by frozen ground, the hillslopes are characterized by frozen ground to thin/medium ALT (1–7 m), and depressions are marked by thick unfrozen ground (7–9 m) and a deep talik in the NW area. On the basis of our interpretation, the talik is characterized by a 9–16 m thick thawed soil overlying frozen ground. Local inactive frost boils are located in correspondence of a 4–5 m thick active layer, where the permafrost table depth starts increasing westward. Within even hillslope and bushy depression microzone types, the interrupted frost boil due to the increase in the thawed layer allows plants, such as tall birches and tall shrubs, to encroach the area.

Our results showed that permafrost thickness substantially reduces upon approaching the riverbank. A permafrost volume, obtained by a 3D interpolation of the resistivity values higher than 200 Ωm over the four ERT sections of Site 1A, is displayed in **Figure 10**. This figure clearly shows that the permafrost becomes thinner and discontinuous

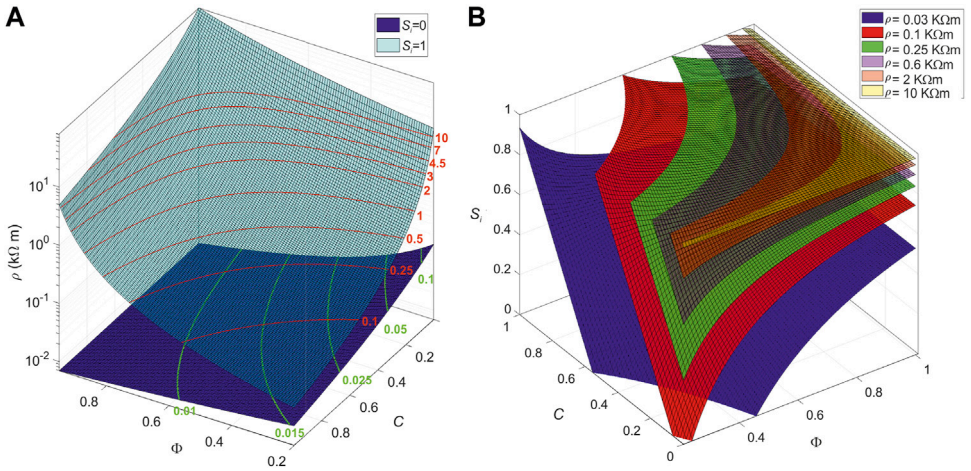

FIGURE 11 | Results of the CRIM petrophysical analysis. **(A)** resistivity of sediments fully saturated by water (S_i = 0, violet surface) and ice (S_i = 1, cyan surface), computed using **Eq. 1**. Red and green isolines connect points of equal resistivity on the two surfaces. Cyan and violet surfaces correspond to permafrost and unfrozen ground, respectively. **(B)** ice saturation S_i computed using **Eq. 2** for different sediment resistivity. Computation performed by adopting the MATLAB™ software package.

TABLE 2 | Typical material electrical properties.

Material	Conductivity (S/m)	References
Sand/silt (quartzites)	$\sigma_q = 10^{-4}$ S/m	Schön (1996)
Clay	σ_c = 0.05 S/m	Schön (1996)
Groundwater	σ_w = 0.15 S/m	Schön (1996)
Ice	$\sigma_i = 10^{-5}$ S/m	Petrenko and Whitworth (2002)

going eastward. At the same time, **Figure 9** shows that the ALT gradually reduces upon approaching the riverbank. This phenomenon is most probably due to the presence of the river. In fact, rivers in permafrost regions can have very significant influence on the thermal state of the nearby permafrost. The thermal impact of warm water and insolation on the riverbank slopes affects the local thermal field and increases the annual temperature of grounds. The difference between the riverbank ground and the internal frozen ground reaches 1°C–2°C for the Vorkuta River zone (Tananaev et al., 2021). The impact area is quite wide, and usually, boreholes are located at least 50 m from the riverbank to avoid this warming effect.

The fact that the anthropogenic zone of Site 1 is an unpaved footpath means that it does not affect the frozen conditions of the ground, in contrast to the effects of the railway track along which abundant thermokarst lakes are detected (**Figures 4**, **5A, B**).

5.1 Complex Refractive Index Method

The CRIM formula for shaly sandstone with negligible permittivity and partially saturated with groundwater and ice can be expressed as

$$\sigma = \left[(1-\Phi)(1-C)\sigma_q^{\gamma} + (1-\Phi)C\sigma_c^{\gamma} + \Phi S_i\sigma_i^{\gamma} + \Phi(1-S_i)\sigma_w^{\gamma}\right]^{1/\gamma}, \quad \gamma = 1/2 \tag{1}$$

(e.g., Schön, 1996; Carcione et al., 2012), where σ_q, σ_c, σ_w, and σ_i are the sand/silt grain (quartz), clay, groundwater, and ice conductivities and σ is the conductivity of the composite medium. Generally, σ_i depends on temperature and ice impurity content, and σ_w depends on water salinity. **Table 2** shows the typical electrical properties of the different soil components. If γ is a free parameter, **Eq. 1** is termed the Lichtnecker–Rother formula. It is based on ray approximation. The travel time in each medium is inversely proportional to the electromagnetic velocity, which, in turn, is inversely proportional to the square root of the complex dielectric constant. At low frequencies, displacement currents can be neglected and the above equation is obtained. For a zero clay content and by neglecting σ_q and σ_i, **Eq. 1** is exactly Archie's law used in Hoversten et al. (2006).

In our case, under realistic assumptions, we can use **Eq. 1** to compute the ice content as a function of the porosity, the clay content, and the measured resistivity:

$$S_i = \frac{(1-\Phi)(1-C)\sigma_q^{\gamma} + (1-\Phi)C\sigma_c^{\gamma} + \Phi\sigma_w^{\gamma} - \sigma^{\gamma}}{\Phi\left(\sigma_w^{\gamma} - \sigma_i^{\gamma}\right)}, \quad \gamma = 1/2 \tag{2}$$

Figure 11A shows the resistivity values corresponding to permafrost and unfrozen ground, computed using **Eq. 1** as a function of porosity Φ and clay content C. The two surfaces represent the resistivity of sediments fully saturated by water (S_i = 0, violet surface) and ice (S_i = 1, cyan surface), respectively. Red and green isolines connect points of equal resistivity on the two surfaces. Moreover, the ice saturation S_i, computed using **Eq. 2** for different sediment resistivity values, is displayed in **Figure 11B**. The computation was performed using the MATLAB™ software package.

We highlight the following points:

1. The bottom of boreholes K1, K3, and K7 is characterized by the presence of a massive cryostructure and silty clay frozen sediments (**Figures 6A**, **7C**). This means that clay is predominant ($C >$ 0.5) and $S_i \approx$ 1. Moreover, the temperature profile evidences that the bottom of the K1 and K3 boreholes corresponds to the permafrost table

and to the unfrozen ground bottom, respectively. The ERT2018 section shows that at the bottom of borehole K1 (**Figure 6C**), there is a sharp transition of the resistivity from about 100 Ωm (frozen soil) to 200 Ωm (massive cryostructure). This evidence is in agreement with the cyan surface of **Figure 11A**, where the 100 Ωm isoline indicates the presence of frozen soil with ice content S_i very close to 1 when $C > 0.53$ and $\Phi < 0.55$. It is interesting to note that the same isoline on the violet surface may indicate the presence of unfrozen ground for very low clay content and porosity. Therefore, because the results of the landscape zonation showed that the characteristics of the shallow sediments are invariable in correspondence of all ERT profiles (**Figure 4**), our assumption to consider the resistivity of about 100 Ωm as a marker of the base of the active layer in this area is thus justified.

2. The transition zone from the base of the active layer ($\rho \approx$ 100 Ωm) and the permafrost table ($\rho \approx$ 200 Ωm) is characterized by very high ice saturations (**Figure 11B**). For example, if we consider a sediment with $\Phi = 0.47$ and $C = 0.58$, the ice content can vary from about 0.85 ($\rho = 100$ Ωm) to 1 ($\rho = 200$ Ωm).
3. The maximum permafrost resistivity in the ERT sections of Sites 1A and 1B is about 600 Ωm, whereas in ERT2018, it reaches values up to about 10 kΩm (**Figures 6C**, **7A, B**). The cyan surface in **Figure 11A** shows that this large difference mainly depends on the sediment clay content. In fact, when $\Phi < 0.5$, a resistivity of 600 Ωm indicates the presence of permafrost with moderate/high clay content ($C > 0.3$), and a resistivity of 10 kΩm indicates frozen sediments with low clay content ($C < 0.1$), mainly composed of silt/sand. Therefore, the sediments corresponding to the permafrost layer in the ERT2018 profile probably have a lower clay content in comparison to those of Sites 1A and 1B.
4. Talik and unfrozen ground areas are characterized by minimum resistivity values of 10 Ωm in ERT2018, 30 Ωm in the ERT sections of Sites 1A, and 3 Ωm in the ERT2S section (**Figures 6C**, **7A, B**). The green isolines in **Figure 11A** indicate that these values strongly depend on the clay content and porosity of unfrozen sediments. A resistivity of 10 Ωm indicates sediments mainly composed of clay with very high porosity ($\Phi \approx 0.5$). This evidence is confirmed by the K2 stratigraphy, which indicates a massive prevalence of clay and silty clay in the talik. A resistivity of 30 Ωm indicates sediments with $\Phi < 0.5$ and $C < 0.7$. Resistivity values lower than 10 Ωm in the depression of Site 1B are probably due to the presence of fluid (water) flow toward the Vorkuta River.
5. Lithological and geocryological core analysis of boreholes K1 and K7 show that in the active layer there is a coexistence of frozen and unfrozen sediments (**Figures 6A**, **7C**). This evidence produces a strong vertical and horizontal variability of resistivity, from about 30 to 100 Ωm. Ice content S_i strongly depends on Φ and C. For example, **Figure 11B** shows that for a sediment with $\rho = 30$ Ωm and $\Phi = 0.4$, S_i can vary from 0.3 ($C = 0.4$) to about 0.7 ($C = 1$). K1 and K7 borehole stratigraphy and landscape microzonation (**Figure 4**; **Table 1**) exhibit a predominance of clay in the active layer. If we consider a sediment with $\Phi = 0.4$ and $C = 0.7$, the ice content can vary from 0.4 ($\rho = 30$ Ωm) to about 0.9 ($\rho = 100$ Ωm). If the clay content is lower, say $C = 0.3$, the ice content can vary from 0.1 ($\rho = 30$ Ωm) to 0.6 ($\rho = 100$ Ωm). Note that for $\Phi < 0.5$, a sediment with low clay content can be partially saturated with ice and groundwater also when $\rho \geq 600$ Ωm. For example, the ice content of sand with $\Phi = 0.4$ can vary from 0.78 ($\rho =$ 600 Ωm) to 0.98 ($\rho = 10$ kΩm).
6. The ERT sections in Site 1A show a gradual decrease in ground resistivity with depth. As explained in the previous section, if the underground lithology does not vary significantly with depth and clay is predominant (as shown by landscape zonation and borehole stratigraphy), permafrost should also be present in the deeper parts of some sections. Instead, if the clay content decreases significantly with depth, we no longer have permafrost at a certain depth. For example, let us consider profile ERT3, which exhibits an average resistivity of about 250 Ωm at 40 m a.s.l. If $\Phi = 0.4$ and $C \geq 0.35$, **Figure 11B** shows that the pore space is fully saturated by ice and the medium is permafrost. If $C < 0.35$, there should be also water in the pore space (e.g., with $C = 0.2$, we have $S_i = 0.8$) and the medium is no more permafrost.

This discussion shows that the results obtained from the lithological and geocryological core analysis, ERT, landscape microzonation, and ground thermometry are in agreement with each other.

6 CONCLUSION

Permafrost retreat and degradation are some of the main concerns related to Arctic amplification. Rising temperatures are leading to a gradual deepening of the permafrost table, causing subsidence and a consequent reduction of the ground capacity to carry loads, which leads to the deformation of infrastructures. Investigation and monitoring of permafrost distribution and degradation dynamics are therefore crucial to assess the stability of engineering infrastructures and prevent possible damages.

In this study, we employed geophysical and geocryological methods to characterize the active layer close to a 1.5 km long segment of the Russian North Railway, in the Arctic area of the Khanovey railway station (Komi Republic, Russia). Landscape microzonation, borehole drilling, ground temperature measurements, and geoelectric surveys were carried out. ERT was adopted to invert the geoelectric data and to image the resistivity distribution of the subsurface between the railway and the Vorkuta River. Landscape mapping was performed by satellite image analysis and by collecting field information on geomorphology, vegetation, drainage, cryostructure and lithology, ALT, and soil temperature.

The analysis and integration of different type of data enabled to assess the thawing condition of permafrost in the study area. The correlation of ground temperature and lithological data from three boreholes with a geoelectric profile enabled a better interpretation of the resistivity-cryological patterns. The CRIM was used to integrate and quantitatively validate the results.

Borehole stratigraphy and landscape microzonation indicate a massive prevalence of clay and silty clay at shallow depths. CRIM suggests that the resistivity value of about 100 Ωm can be considered marker of the active layer bottom for this kind of sediments. On the basis of this assumption, the active layer shows a thickness ranging from 0.5 to 7 m and the average ALT is about 4 m. Moreover, in the active layer, there is a coexistence of frozen and unfrozen unconsolidated sediments showing resistivity values ranging from about 30 to 100 Ωm. Here, the ice content estimated using CRIM ranges between about 0.3–04 to 0.9. The underlying permafrost shows resistivity values higher than 200 Ωm. Very high-resistivity values exceeding 600 Ωm and up to 10 kΩm are typical of frozen sediments with massive cryostructure and clay content lower than 30%.

If the underground lithology does not vary significantly with depth and clay is predominant, the maximum thickness of the permafrost layer in the surveyed area should be about 50 m. This thickness, confirmed by previous investigations in this site, gradually reduces and becomes discontinuous upon approaching the riverbank.

The area is characterized by the presence of diffuse thermokarst processes. Open, closed, and deep taliks with resistivity ranging between about 3 and 70 Ωm are scattered in the study area. Taliks are often located in bushy and swamp depressions with birch, shrub, and grass, generally characterized by warmer unfrozen ground. In general, shrubby hillslopes exhibit higher ALT values, and the opposite situation happens in moundy hills mostly covered by lichens.

Thermokarst phenomena develop mainly along the railroad area as a consequence of the thermal regime variation effect due to different factors, e.g., changes in the natural condition of the soil, vegetation removal during railway construction, and the role of railway embankment as a barrier to surface water run-off. Frost heaving is a consequence of the seasonal freezing and thawing of the ground. Thawing permafrost is dangerous because it can trigger thermokarst processes with the consequent development of taliks, which represent a serious hazard for railway embankment stability.

The multidisciplinary approach used in this study, with methods providing investigations at different and complementary resolutions, can also be applied to the western area of Sites 1 and 2, closer to the railway. There, detailed geocryological information and landscape zonation are now available, and therefore, new geophysical acquisition can be planned in order to further investigate the deeper characteristics of the ground. For example, new surveys can be designed to discriminate whether the mapped superficial swamp depressions and thermokarst lakes are underlain by permafrost or represent a shallower expression of a deep talik. This procedure of integration, after an update of any change of landscape and cryological conditions through time, is essential in such geocryologically heterogeneous and complex environment. Moreover, a repetition of the geophysical survey in the same places through the years would enable us to monitor changing conditions in time-lapse. Periodic geocryological and geophysical surveys are therefore required to monitor the rapid evolution of permafrost conditions and to deal with the extreme landscape variability, instability, and heterogeneity of the field area. In this contest, the obtained results will represent valuable information to address the design of engineering solutions and to ensure the structural stability of infrastructures, such as reinforcing the construction foundations and maintaining the thermal balance of the ground. For example, thermosyphons represent a well-established technology, widely used in various Russian permafrost areas to stabilize infrastructures. Another solution could be the diversion of the railroad where the active layer is thinner and the underlying permafrost is thicker and stable.

DATA AVAILABILITY STATEMENT

The datasets presented in this study can be found in online repositories. The names of the repository/repositories and accession number(s) can be found below: https://disk.yandex.ru/d/WOch52cAOx9SHQ?w=1.

AUTHOR CONTRIBUTIONS

VI conceived this research and, together with AP, EG, DS, and PK, designed and executed the geophysical and geocryological surveys in the Khanovey area. MR participated in the field work, performed large parts of the data processing, and wrote the first draft of the manuscript. MR, MDC, SP, DG, and MG carried out the geophysical data analysis, interpretation, and data integration. MDC and SP contributed to the writing of the manuscript and, together with MLR, supervised the work of MR. All authors contributed to manuscript revision and read and approved the submitted version.

FUNDING

This research was supported by Norwegian Center for International Cooperation in Education through the "Russian-Norwegian research-based education in cold regions engineering" project (RuNoCORE; CPRU-2017/10015).

ACKNOWLEDGMENTS

Special thanks to the Master's students of Lomonosov Moscow State University, Norwegian University of Science and Technology, and Università degli Studi G. D'Annunzio (Italy) for the assistance in the field activity and to the National Institute of Oceanography and Applied Geophysics—OGS (Italy) for the support in geophysical data analysis. We acknowledge IHS Markit, Geostudi Astier s.r.l., Geotomo Inc., and The MathWorks Inc. for the academic licenses of Kingdom™, ERTLab™—ViewLab3D™, Res2dInv™, and MATLAB™ software packages, respectively. We thank the reviewers, whose constructive comments allowed us to improve the manuscript.

REFERENCES

Abramov, A., Davydov, S., Ivashchenko, A., Karelin, D., Kholodov, A., Kraev, G., et al. (2019). Two Decades of Active Layer Thickness Monitoring in Northeastern Asia. *Polar Geogr.* 44, 186–202. doi:10.1080/1088937X.2019.1648581

ACGR - Associate Committee on Geotechnical Research (1988). "Glossary of Permafrost and Related Ground-Ice Terms," in *Permafrost Subcommittee, National Research Council of Canada*. Editors S. A. Harris, H. M. French, J. A. Heginbottom, G. H. Johnston, B. Ladanyi, D. C. Sego, et al.

Allen, M. R., Dube, O. P., Solecki, W., Aragón-Durand, F., Cramer, W., Humphreys, S., et al. (2018). "Framing and Context," in *Global Warming of 1.5°C. An IPCC Special Report on the Impacts of Global Warming of 1.5°C above Pre-industrial Levels and Related Global Greenhouse Gas Emission Pathways, in the Context of Strengthening the Global Response to the Threat of Climate Change, Sustainable Development, and Efforts to Eradicate Poverty [Masson-Delmotte,*. Editors V. P. Zhai and H. O. Pörtner.

Anisimov, O., and Reneva, S. (2006). Permafrost and Changing Climate: The Russian Perspective. *AMBIO A J. Hum. Environ.* 35 (4), 169–175. doi:10.1579/0044-7447(2006)35[169:pacctr]2.0.co;2

Arcone, S. A., and Delaney, A. J. (1982). Dielectric Properties of Thawed Active Layers Overlying Permafrost Using Radar at VHF. *Radio Sci.* 17, 618–626. doi:10.1029/RS017i003p00618

Arcone, S. A., Lawson, D. E., Delaney, A. J., Strasser, J. C., and Strasser, J. D. (1998). Ground-penetratinng Radar Reflection Profiling of Groundwater and Bedrock in an Area of Discontinuous Permafrost. *Geophysics* 63, 1573–1584. doi:10.1190/1.1444454

Biskaborn, B. K., Smith, S. L., Noetzli, J., Matthes, H., Vieira, G., Streletskiy, D. A., et al. (2019). Permafrost Is Warming at a Global Scale. *Nat. Commun.* 10, 264. doi:10.1038/s41467-018-08240-4

Böhm, G., Carcione, J. M., Gei, D., Picotti, S., and Michelini, A. (2015). Cross-Well Seismic and Electromagnetic Tomography for CO_2 Detection and Monitoring in a Saline Aquifer. *J. Petroleum Sci. Eng.* 133, 245–257. doi:10.1016/j.petrol.2015.06.010

Brown, J., Ferrians, O. J, Heginbottom, J. A., and Melnikov, E. S. (1997). *Circum-Arctic Map of Permafrost and Ground-Ice Conditions*. Washington, DC.

Brown, J., Ferrians, O., Heginbottom, J. A., and Melnikov, E. (2002). *Circum-Arctic Map of Permafrost and Ground-Ice Conditions*. Boulder, Colorado USA: Version 2, NSIDC: National Snow and Ice Data Center.

Brown, J., Hinkel, K. M., and Nelson, F. E. (2000). The Circumpolar Active Layer Monitoring (Calm) Program: Research Designs and Initial Results1. *Polar Geogr.* 24 (3), 166–258. doi:10.1080/10889370009377698

Budantseva, N. A., Gorshkov, E. I., Isaev, V. S., Semenkov, I. N., Usov, A. N., ChizhovaVasil'chuk, Ju. N., et al. (2015). Engineering–geological and Geochemical Features of Palsa and Lithalsa Landscapes in the Area of the "Khanovey" Scientific Educational Facility. *Inzh. Geol.* 3, 34–50. Available at: https://www.researchgate.net/publication/280943215_ENGINEERING-GEOLOGICAL_AND_GEOCHEMICAL_FEATURES_OF_PALSA_AND_LITHALSA_LANDSCAPES_IN_THE_AREA_OF_THE_KHANOVEY_SCIENCE_EDUCATION_STATION

Buldovicz, S. N., Khilimonyuk, V. Z., Bychkov, A. Y., Ospennikov, E. N., Vorobyev, S. A., Gunar, A. Y., et al. (2018). Cryovolcanism on the Earth: Origin of a Spectacular Crater in the Yamal Peninsula (Russia). *Sci. Rep.* 8, 13534. doi:10.1038/s41598-018-31858-9

Carcione, J. M., Gei, D., Picotti, S., and Michelini, A. (2012). Cross-Hole Electromagnetic and Seismic Modeling for CO_2 Detection and Monitoring in a Saline Aquifer. *J. Petroleum Sci. Eng.* 100, 162–172. doi:10.1016/j.petrol.2012.03.018

Carcione, J. M., and Seriani, G. (1998). Seismic and Ultrasonic Velocities in Permafrost. *Geophys. Prospect.* 46 (4), 441–454. doi:10.1046/j.1365-2478.1998.1000333.x

Chen, T., Ma, W., Wu, Z.-J., and Mu, Y.-h. (2014). Characteristics of Dynamic Response of the Active Layer Beneath Embankment in Permafrost Regions along the Qinghai-Tibet Railroad. *Cold Regions Sci. Technol.* 98, 1–7. doi:10.1016/j.coldregions.2013.10.004

Delaney, A. J., Arcone, S. A., and Chacho, E. F. (1990). Winter Short-Pulse Studies on the Tanana River, Alaska. *Arctic* 43, 244–250. doi:10.14430/arctic1618

Doolittle, J. A., Hardisky, M. A., and Gross, M. F. (1990). A Ground-Penetrating Radar Study of Active Layer Thicknesses in Areas of Moist Sedge and Wet Sedge Tundra Near Bethel, Alaska, U.S.A. *Arct. Alp. Res.* 22 (2), 175–182. doi:10.1080/00040851.1990.12002779

Drozdov, D., Rumyantseva, Y., Malkova, G., Romanovsky, V., Abramov, A., Konstantinov, P., et al. (2015). "Monitoring of Permafrost in Russia and the International GTN-P Project," in 68th Canadian Geotechnical Conf. GEOQuébec 2015. paper 617.

Duguay, C. R., Green, J., and Derksen, C.English (2005). "Preliminary Assessmentof the Impact of Lakes on Passive Microwave Snow Retrieval Algorithms in the Arc-Tic," in Proceedings of 62nd Eastern Snow Conference (Canada: Waterloo, Ontario), 223–228.

Edwards, L. S. (1977). A Modified Pseudosection for Resistivity and IP. *Geophysics* 42 (5), 1020–1036. doi:10.1190/1.1440762

EEA - European Environment Agency (2017). *The Arctic Environment - European Perspectives on a Changing Arctic*. Luxembourg: Publications Office of the European Union.

Farzamian, M., Vieira, G., Monteiro Santos, F. A., Yaghoobi Tabar, B., Hauck, C., Paz, M. C., et al. (2020). Detailed Detection of Active Layer Freeze-Thaw Dynamics Using Quasi-Continuous Electrical Resistivity Tomography (Deception Island, Antarctica). *Cryosphere* 14, 1105–1120. doi:10.5194/tc-14-1105-2020

Folk, R. L. (1954). The Distinction between Grain Size and Mineral Composition in Sedimentary-Rock Nomenclature. *J. Geol.* 62, 344–359. doi:10.1086/626171

Francese, R. G., Bondesan, A., Giorgi, M., Picotti, S., Carcione, J., Salvatore, M. C., et al. (2019). Geophysical Signature of a World War I Tunnel-like Anomaly in the Forni Glacier (Punta Linke, Italian Alps). *J. Glaciol.* 65, 798–812. doi:10.1017/jog.2019.59

Goryachkin, S. V., Zlotin, R. I., and Tertitsky, G. M. (1994). "Russian-Swedish Expedition," in *Tundra Ecology-94": Diversity of Natural Ecosystems in the Russian Arctic* (A guidebook).

Gruber, S. (2012). Derivation and Analysis of a High-Resolution Estimate of Global Permafrost Zonation. *Cryosphere* 6, 221–233. doi:10.5194/tc-6-221-2012

Gilbert, G., Instanes, A., Instanes, A., Sinitsyn, A., and Aalberg, A. (2019). Characterization of Two Sites for Geotechnical Testing in Permafrost: Longyearbyen, Svalbard. *AIMS Geosci.* 5 (4), 868–885. doi:10.3934/geosci.2019.4.868

Harris, S. A., Brouchkov, A., and Guodong, C. (2017). *Geocryology: Characteristics and Use of Frozen Ground and Permafrost Landforms*. 1st Edition. London: CRC Press, 810. doi:10.4324/9781315166988

Hinkel, K. M., Doolittle, J. A., Bockheim, J. G., Nelson, F. E., Paetzold, R., Kimble, J. M., et al. (2001). Detection of Subsurface Permafrost Features with Ground-Penetrating Radar, Barrow, Alaska. *Permafr. Periglac. Process.* 12, 179–190. doi:10.1002/ppp.369

Hinkel, K. M., and Nicholas, J. R. J. (1995). Active Layer Thaw Rate at a Boreal Forest Site in Central Alaska, U.S.A. *Arct. Alp. Res.* 27 (1), 72–80. doi:10.1080/00040851.1995.1200309810.2307/1552069

Hinkel, K. M., and Nelson, F. E. (2003). Spatial and Temporal Patterns of Active Layer Thickness at Circumpolar Active Layer Monitoring (Calm) Sites in Northern Alaska, 1995–2000. *J. Geophys. Res.* 108 (D2), 8168. doi:10.1029/2001JD000927

Hinzman, L. D., Goering, D. J., and Kane, D. L. (1998). A Distributed Thermal Model for Calculating Soil Temperature Profiles and Depth of Thaw in Permafrost Regions. *J. Geophys. Res.* 103 (D22), 28975–28991. doi:10.1029/98JD01731

Hjort, J., Streletskiy, D., Doré, G., Wu, Q., Bjella, K., and Luoto, M. (2022). Impacts of Permafrost Degradation on Infrastructure. *Nat. Rev. Earth Environ.* 3 (1), 24–38. doi:10.1038/s43017-021-00247-8

Hong, E., Perkins, R., and Trainor, S. (2014). Thaw Settlement Hazard of Permafrost Related to Climate Warming in Alaska. *Arctic* 67 (1), 93–103. doi:10.14430/arctic4368

Hoversten, G. M., Cassassuce, F., Gasperikova, E., Newman, G. A., Chen, J., Rubin, Y., et al. (2006). Direct Reservoir Parameter Estimation Using Joint Inversion of Marine Seismic AVA and CSEM Data. *Geophysics* 71, C1–C13. doi:10.1190/1.2194510

IPCC (2017). "Report of the Intergovernmental Panel on Climate Change Expert Meeting on Mitigation, Sustainability and Climate Stabilization Scenarios," in *IPCC Working Group III Technical Support Unit*. Editors P. R. Shukla, J. Skea,

R. Diemen, E. Huntley, M. Pathak, J. Portugal Pereira, et al. (London, UK: Imperial College London), 44.

Isaev, V. S., Kotov, P. I., and Khilimonjuk, V. Z. (2022). "Manual for Vorkuta Fieldwork Activities,". Editors P. I. Kotov and G. I. Gordeeva (Moscow, Russia: KDU), 200.

Isaev, V., Kioka, A., Kotov, P., Sergeev, D. O., Uvarova, A., Koshurnikov, A., et al. (2022). Multi-parameter Protocol for Geocryological Test Site: A Case Study Applied for the European North of Russia. *Energies* 15 (6), 2076. doi:10.3390/en15062076

Isaev, V., Kotov, P., and Sergeev, D. (2020). "Technogenic Hazards of Russian North Railway," in *Transportation Soil Engineering in Cold Regions. Lecture Notes in Civil Engineering*. Editors A. Petriaev and A. Konon (Singapore: Springer), Vol. 1, 311–320.

Isaev, V. S., Tyurin, A. I., Sergeev, D. O., Gorshkov, E. I., Volkov, N. G., and Stefanov, S. M. (2016). The Day of Science and Innovation: New Methods and Ways of Field Geocryological Researches. *Vestn. Mosk. Univ. Seriâ 4, Geol.* 1, 98–102. doi:10.33623/0579-9406-2016-1-98-102

Jensen, J. R. (2007). *Remote Sensing of the Environment: An Earth Resource Perspective*. Harlow: Brigham Young University. Pearson College Div.

Jorgenson, M. T. (2022). "Thermokarst," in *Treatise on Geomorphology*. Editor J. F. Shroder. Second Edition (Academic Press), 4, 392–414. doi:10.1016/b978-0-12-818234-5.00058-4

Kasprzak, M. (2015). High-resolution Electrical Resistivity Tomography Applied to Patterned Ground, Wedel Jarlsberg Land, South-West Spitsbergen. *Polar Res.* 34, 25678. doi:10.3402/polar.v34.25678

Kasprzak, M., Strzelecki, M. C., Traczyk, A., Kondracka, M., Lim, M., and Migała, K. (2017). On the Potential for a Bottom Active Layer Below Coastal Permafrost: the Impact of Seawater on Permafrost Degradation Imaged by Electrical Resistivity Tomography (Hornsund, SW Spitsbergen). *Geomorphology* 293, 347–359. doi:10.1016/j.geomorph.2016.06.013

Kaverin, D., Malkova, G., Zamolodchikov, D., Shiklomanov, N., Pastukhov, A., Novakovskiy, A., et al. (2021). Long-Term Active Layer Monitoring at CALM Sites in the Russian European North. *Polar Geogr.* 44 (3), 203–216. doi:10.1080/1088937X.2021.1981476

Kim, Y., Kimball, J. S., McDonald, K. C., and Glassy, J. (2011). Developing a Global Data Record of Daily Landscape Freeze/thaw Status Using Satellite Passive Microwave Remote Sensing. *IEEE Trans. Geosci. Remote Sens.* 49 (3), 949–960. doi:10.1109/TGRS.2010.2070515

Kimball, J. S., McDonald, K. C., Running, S. W., and Frolking, S. E. (2004). Satellite Radar Remote Sensing of Seasonal Growing Seasons for Boreal and Subalpine Evergreen Forests. *Remote Sens. Environ.* 90, 243–258. doi:10.1016/j.rse.2004.01.002

Klimenko, S. S., Anischenko, L. A., and Antoshkina, A. I. (2011). Chapter 13 The Timan–Pechora Sedimentary Basin: Palaeozoic Reef Formations and Petroleum Systems. *Geol. Soc.* 35, 223–236. doi:10.1144/M35.13

Léger, E., Dafflon, B., Soom, F., Peterson, J., Ulrich, C., and Hubbard, S. (2017). Quantification of Arctic Soil and Permafrost Properties Using Ground-Penetrating Radar and Electrical Resistivity Tomography Datasets. *IEEE J. Sel. Top. Appl. Earth Obs. Remote Sens.* 10 (10), 4348–4359. doi:10.1109/JSTARS.2017.2694447

Marohasy, J. (2017). *Climate Change: The Facts 2017. With the Contribution of: John Abbot, Sallie Baliunas, Simon Breheny, Paul Driessen, Tony Heller, Craig Idso, Clive James, Bjørn Lomborg, Pat Michaels, John Nicol, Jo Nova, Ian Plimer, Tom Quirk, Peter Ridd, Matt Ridley, Ken Ring, John Roskam, Nicola Scafetta, Willie Soon, Roy Spencer, Jaco Vlok, Anthony Watts*. Redland Bay, Ql: Connor Court Publishing, 380.

Maslakov, A., Shabanova, N., Zamolodchikov, D., Volobuev, V., and Kraev, G. (2019). Permafrost Degradation within Eastern Chukotka CALM Sites in the 21st Century Based on CMIP5 Climate Models. *Geosciences* 9, 232. doi:10.3390/geosciences9050232

Melnikov, V. P., Osipov, V. I., Brouchkov, A. V., Falaleeva, A. A., Badina, S. V., Zheleznyak, M. N., et al. (2022). Climate Warming and Permafrost Thaw in the Russian Arctic: Potential Economic Impacts on Public Infrastructure by 2050. *Nat. Hazards* 112, 231–251. doi:10.1007/s11069-021-05179-6

Nelson, F. E., Shiklomanov, N. I., Mueller, G. R., Hinkel, K. M., Walker, D. A., and Bockheim, J. G. (1997). Estimating Active-Layer Thickness over a Large Region: Kuparuk River Basin, Alaska, U.S.A. *Arct. Alp. Res.* 29 (4), 367–378. doi:10.2307/1551985

Nelson, F. E., Shiklomanov, N. I., and Mueller, G. R. (1999). Variability of Active-Layer Thickness at Multiple Spatial Scales, North-central Alaska, U.S.A. *Arct. Antarct. Alp. Res.* 31 (2), 179–186. doi:10.1080/15230430.1999.12003295

NOAA/NASA (2020). Annual Global Analysis for 2019. Global Report. Available at: https://www.ncdc.noaa.gov/sotc/global/201913.

NSIDC - National Snow and Ice Data Center (2020). Advancing Knowledge of Earth's Frozen Regions. Cryosphere Glossary. Available at: https://nsidc.org/cryosphere/glossary.

Oelke, C., Zhang, T., Serreze, M. C., and Armstrong, R. L. (2003). Regional-scale Modeling of Soil Freeze/thaw over the Arctic Drainage Basin. *J. Geophys. Res.* 108 (D10), 4314. doi:10.1029/2002JD002722

Osterkamp, T. E., and Burn, C. R. (2003). "Permafrost," in *Encyclopedia of Atmospheric Sciences*. Editors J. R. Holton, J. Pyle, and J. A. Curry (Oxford: Academic Press), 1717–1729. doi:10.1016/B0-12-227090-8/00311-0

Palacky, G. J. (1988). "Resistivity Characteristics of Geologic Targets," in *Electromagnetic Methods in Applied Geophysics*. Editor M. N. Nabighian (Tulsa, Oklahoma: Society of Exploration Geophysicists), 53–129.

Park, H., Kim, Y., and Kimball, J. S. (2016). Widespread Permafrost Vulnerability and Soil Active Layer Increases over the High Northern Latitudes Inferred from Satellite Remote Sensing and Process Model Assessments. *Remote Sens. Environ.* 175, 349–358. doi:10.1016/j.rse.2015.12.046

Peng, X., Zhang, T., Cao, B., Wang, Q., Wang, K., Shao, W., et al. (2016). Changes in Freezing-Thawing Index and Soil Freeze Depth over the Heihe River Basin, Western China. *Arct. Antarct. Alp. Res.* 48, 161–176. doi:10.1657/AAAR00C-13-127

Petrenko, V. F., and Whitworth, R. W. (2002). *Physics of Ice*. New York: Oxford University Press, 373.

Picotti, S., Francese, R., Giorgi, M., Pettenati, F., and Carcione, J. M. (2017). Estimation of Glacier Thicknesses and Basal Properties Using the Horizontal-To-Vertical Component Spectral Ratio (HVSR) Technique from Passive Seismic Data. *J. Glaciol.* 63, 229–248. doi:10.1017/jog.2016.135

Romanovsky, V. E., Smith, S. L., Isaksen, K., Shiklomanov, N. I., Streletskiy, D. A., Kholodov, A. L., et al. (2018). Terrestrial Permafrost. In 'State of the Climate in 2017. *Bull. Am. Meteorol. Soc.* 99, 161–165. doi:10.1175/2018BAMSStateoftheClimate.1

Romanovsky, V. E., Drozdov, D. S., Oberman, N. G., Malkova, G. V., Kholodov, A. L., Marchenko, S. S., et al. (2010). Thermal State of Permafrost in Russia. *Permafr. Periglac. Process.* 21, 136–155. doi:10.1002/ppp.683

Sazonova, T. S., and Romanovsky, V. E. (2003). A Model for Regional-Scale Estimation of Temporal and Spatial Variability of Active Layer Thickness and Mean Annual Ground Temperatures. *Permafr. Periglac. Process.* 14, 125–139. doi:10.1002/ppp.449

Schneider von Deimling, T., Lee, H., Ingeman-Nielsen, T., Westermann, S., Romanovsky, V., Lamoureux, S., et al. (2021). Consequences of Permafrost Degradation for Arctic Infrastructure - Bridging the Model Gap between Regional and Engineering Scales. *Cryosphere* 15, 2451–2471. doi:10.5194/tc-15-2451-2021

Schön, J. H. (1996). *Physical Properties of Rocks. Handbook of Geophysical Exploration*. Oxford: Pergamon Press.

Schwamborn, G., Heinzel, J., and Schirrmeister, L. (2008). Internal Characteristics of Ice-Marginal Sediments Deduced from Georadar Profiling and Sediment Properties (Brøgger Peninsula, Svalbard). *Geomorphology* 95, 74–83. doi:10.1016/j.geomorph.2006.07.032

Seppi, R., Zanoner, T., Carton, A., Bondesan, A., Francese, R., Carturan, L., et al. (2015). Current Transition from Glacial to Periglacial Processes in the Dolomites (South-Eastern Alps). *Geomorphology* 228, 71–86. doi:10.1016/j.geomorph.2014.08.025

Sinitsyn, A. O., Guegan, E., Shabanova, N., Kokin, O., and Ogorodov, S. (2020). Fifty Four Years of Coastal Erosion and Hydrometeorological Parameters in the Varandey Region, Barents Sea. *Coast. Eng.* 157, 103610. doi:10.1016/j.coastaleng.2019.103610

Streletskiy, D., Anisimov, O., and Vasiliev, A. (2015). "Chapter 10 - Permafrost Degradation," in *Snow and Ice-Related Hazards, Risks and Disasters*. Editor A. Vasiliev (Elsevier), 303–344. doi:10.1016/B978-0-12-394849-6.00010-X

Streletskiy, D. A., Suter, L. J., Shiklomanov, N. I., Porfiriev, B. N., and Eliseev, D. O. (2019). Assessment of Climate Change Impacts on Buildings, Structures and Infrastructure in the Russian Regions on Permafrost. *Environ. Res. Lett.* 14, 025003. doi:10.1088/1748-9326/aaf5e6

Streletskiy, D., and Shiklomanov, N. (2016). "Russian Arctic Cities through the Prism of Permafrost," in *Sustaining Russia's Arctic Cities: Resource Politics, Migration, and Climate Change*. Editor R. W. Orttung (Berghahn Press), 201–220. doi:10.2307/j.ctvswx6s0.14

Szalai, S., Novák, A., and Szarka, L. (2009). Depth of Investigation and Vertical Resolution of Surface Geoelectric Arrays. *J. Environ. Engg. Geophys.* 14, 15–23. doi:10.2113/JEEG14.1.15

Tananaev, N., Isaev, V., Sergeev, D., Kotov, P., and Komarov, O. (2021). Hydrological Connectivity in a Permafrost Tundra Landscape Near Vorkuta, North-European Arctic Russia. *Hydrology* 8 (3), 106. doi:10.3390/hydrology8030106

Thomson, L. I., Osinski, G. R., and Pollard, W. H. (2012). The Dielectric Permittivity of Terrestrial Ground Ice Formations: Considerations for Planetary Exploration Using Ground-Penetrating Radar. *J. Geophys. Res.* 117, n–a. doi:10.1029/2012JE004053

Tyurin, A. I., Isaev, V. S., Sergeev, D. O., Tumskoi, V. E., Volkov, N. G., Sokolov, I. S., et al. (2019). Improvement of Field Methods for Engineering Geocryological Surveying. *Mosc. Univ. Geol. Bull.* 74, 297–309. doi:10.3103/S014587521903013X

Ulyanov, V. Y. (2021). Ways to Increase the Efficiency of Thermopressiometry. *Visn. Dnipropetr. Nac. Univ. zaliznično Transp. Im. Akad. V. Lazarâna* 2 (92), 84–91. doi:10.15802/stp2021/237279

USSR Engineering Geology(1991). *Platform Regions of the European Part of the USSR*. Book 2. Moscow: Nedra.

Vanhala, H., Lintinen, P., Oberman, N., and Jokinen, J. (2010). "Monitoring Permafrost Degradation with Geophysical Methods," in *Report of Year 2009 Studies by the River Ko-Rotaikha, NW Russia* (Geological survey of Finland Report, Finland).

Vasiliev, A. A., Drozdov, D. S., Gravis, A. G., Malkova, G. V., Nyland, K. E., and Streletskiy, D. A. (2020). Permafrost Degradation in the Western Russian Arctic. *Environ. Res. Lett.* 15, 045001. doi:10.1088/1748-9326/ab6f12

Voytenko, A. S., Grishakina, E. A., Grishakina, E. A., Isayev, V. S., Koshurnikov, A. V., Pogorelov, A. A., et al. (2017). Importance of Permafrost Changes for Infrastructure Exploitation and Environmental Protection (Case Study of Local Investigation in Lower Part of Vorkuta River). *Arctic: Ecol.Econ.* 2 (26), 53–61. doi:10.25283/2223-4594-2017-2-53-61

Voytenko, A. S., and Sergeev, D. O. (2016). "Cumulative Economic Damages in Permafrost Based on an Example of a Linear Infrastructure (Railway Khanovey – Pesets)," in Proceedings of the XI International Conference on Permafrost. Editors F. Günther and A. M. Potsdam.

Wagner, A. M., Lindsey, N. J., Dou, S., Gelvin, A., Saari, S., Williams, C., et al. (2018). Permafrost Degradation and Subsidence Observations during a Controlled Warming Experiment. *Sci. Rep.* 8 (1), 10908. doi:10.1038/s41598-018-29292-y

Wagner, A. M. (2014). *Review of Thermosyphon Applications*. Hanover, New Hampshire: Cold Regions Research and Engineering Laboratory, US Army Engineer Research and Development Center. *ERDC/CRREL TR*-14-1.

Wang, C., Wang, Z., Kong, Y., Zhang, F., Yang, K., and Zhang, T. (2019). Most of the Northern Hemisphere Permafrost Remains under Climate Change. *Sci. Rep.* 9, 3295. doi:10.1038/s41598-019-39942-4

Yang, Z.-p., Ou, Y. H., Xu, X.-l., Zhao, L., Song, M.-h., and Zhou, C.-p. (2010). Effects of Permafrost Degradation on Ecosystems. *Acta Ecol. Sin.* 30 (1), 33–39. doi:10.1016/j.chnaes.2009.12.006

Yershov, E. D. (1998). *General Geocryology. Studies in Polar Research Series. First Published in Russian as Obshchaya Geokriologiya by Nedra, 1990. Xxiii + 580 Pp. Cambridge*. New York, Melbourne: Cambridge University Press.

Yi, Y., and Kimball, J. S. (2020). *ABoVE: Active Layer Thickness from Remote Sensing Permafrost Model, Alaska, 2001-2015*. Oak Ridge, Tennessee, USA: ORNL DAAC.

You, Y., Wang, J., Wu, Q., Yu, Q., Pan, X., Wang, X., et al. (2017). Causes of Pile Foundation Failure in Permafrost Regions: The Case Study of a Dry Bridge of the Qinghai-Tibet Railway. *Eng. Geol.* 230, 95–103. doi:10.1016/j.enggeo.2017.10.004

Zhang, T., Barry, R. G., and Armstrong, R. L. (2004). Application of Satellite Remote Sensing Techniques to Frozen Ground Studies. *Polar Geogr.* 28, 163–196. doi:10.1080/789610186

Zhang, T., Barry, R. G., Knowles, K., Heginbottom, J. A., and Brown, J. (2008). Statistics and Characteristics of Permafrost and Ground-Ice Distribution in the Northern Hemisphere. *Polar Geogr.* 31 (2), 47–68. doi:10.1080/10889370802175895

Conflict of Interest: The authors declare that the research was conducted in the absence of any commercial or financial relationships that could be construed as a potential conflict of interest.

frontiers | Frontiers in Environmental Science

TYPE Original Research
PUBLISHED 17 August 2022
DOI 10.3389/fenvs.2022.909848

OPEN ACCESS

EDITED BY
Alexander Kokhanovsky,
Max Planck Institute for Chemistry, Germany

REVIEWED BY
Qiang Guo,
China Jiliang University, China
Wei Shan,
Northeast Forestry University, China
Zhenzhu Xi,
Central South University, China

*CORRESPONDENCE
Changwei Xie,
xiecw@lzb.ac.cn

SPECIALTY SECTION
This article was submitted to Environmental Informatics and Remote Sensing, a section of the journal Frontiers in Environmental Science

RECEIVED 31 March 2022
ACCEPTED 18 July 2022
PUBLISHED 17 August 2022

CITATION
Yang G, Xie C, Wu T, Wu X, Zhang Y, Wang W and Liu G (2022), Detection of permafrost in shallow bedrock areas with the opposing coils transient electromagnetic method. *Front. Environ. Sci.* 10:909848. doi: 10.3389/fenvs.2022.909848

Detection of permafrost in shallow bedrock areas with the opposing coils transient electromagnetic method

Guiqian Yang[1,2], Changwei Xie[1]*, Tonghua Wu[1], Xiaodong Wu[1], Yuxin Zhang[1,2], Wu Wang[1] and Guangyue Liu[1]

[1]Cryosphere Research Station on the Qinghai-Tibet Plateau, State Key Laboratory of Cryospheric Science, Northwest Institute of Eco-Environment and Resources, Chinese Academy of Sciences, Lanzhou, China, [2]University of Chinese Academy of Sciences, Beijing, China

The transient electromagnetic method (TEM) is a geophysical method for detecting underground geological bodies by following the principle of electromagnetic induction, which has been widely used in permafrost exploration. In the practical applications of the TEM to investigate permafrost, it is found that in certain areas with shallow buried bedrock, the electrical resistivity near the surface cannot be obtained, and both frozen soil and underground bedrock exhibit a high electrical resistivity, so it is difficult to determine the distribution characteristics of the permafrost thickness. Based on this background, by analyzing measured data, it is considered that the reason for this situation is that the noise superposition effect generated by the receiving coil under the action of the primary field forms a shallow detection blind area. This study uses equivalent anti-flux opposing coils to eliminate the abovementioned blind area and realize measurement in the permafrost area of Mahan Mountain in Lanzhou. The results showed that the opposing coils transient electromagnetic method (OCTEM) can clearly detect low-resistivity anomalies near the boundary and permafrost base in the Mahan Mountain area, solve the problem of the shallow detection blind area of the conventional TEM, effectively eliminate the interference caused by the primary field, and greatly improve the horizontal and vertical resolutions.

KEYWORDS

permafrost, shallow bedrock, opposing coils transient electromagnetic method, TEM, exploration

Introduction

Geophysical methods have been widely used in the study of permafrost and cold area engineering in most cold areas worldwide. The transient electromagnetic method (TEM, also known as the time-domain electromagnetic method) is a geophysical method that uses grounded or ungrounded energized coils to launch a pulse field underground and observe the secondary field during the shutdown process of the primary field to detect the target (Nabighian and Macnae, 1991; Telford et al., 1991). Compared to other electrical

measurement methods, such as resistivity sounding and electrical resistivity tomography (ERT), used in frozen soil exploration, the TEM provides many advantages, such as a large detection depth, noncontact and nonintrusive conditions, and less environmental interference (Nabighian, 1984; Szarka, 1988; Hauck and Mühll, 1999a; Danielsen et al., 2003; Christiansen et al., 2006; Barsukov and Fainberg, 2013). The TEM has also been widely used in permafrost exploration (Hoekstra, 1973; Harris, et al., 2001; Hauck, 2001). The basis of TEM application in permafrost detection is that water in permafrost exists in the form of solid ice, and the resistivity of ice is much higher than that of liquid water in non-permafrost areas (Henderson, 1980; King et al., 1987; Harada et al., 2000; Hauck et al., 2001). When other components of rock and soil remain unchanged, this difference in resistivity is enough to cause obvious distinctions in the secondary field to identify permafrost.

However, in permafrost areas with shallow bedrock distributions, because the resistivity value of bedrock components does not significantly differ from that of ice (the resistivity values of most types of rocks are close to or higher than those of ice), instruments must attain a higher accuracy to detect and identify ice containing permafrost. According to actual exploration campaigns (Harada et al., 2000; Harada et al., 2006; Wang et al., 2011a; Liu et al., 2015a; Yang et al., 2019) and this study, it is found that in certain areas with shallow buried bedrock, there are three problems in the detection process *via* the conventional TEM: first, a low resistivity value and no change along the transverse direction are observed within 15 m below the surface; second, there is little difference between the boundaries of permafrost and bedrock; third, there is no obvious deviation between the apparent resistivity at the permafrost base and that of the bedrock layer. Obviously, although the TEM achieves a satisfactory application effect in permafrost exploration (Hauck et al., 2001; Mühll et al., 2001; Mühll et al., 2002), there are still unsolved problems in distribution areas of shallow buried bedrock.

At present, the common receiving method of the TEM entails the use of an induction coil to measure the change rate of the magnetic field. Telford et al. (1991), Ji et al. (2006), Wang et al. (2011b), and Xue et al. (2007) proposed that when the transmitting current is turned off, the receiving coil itself generates an induced electromotive force and superimposes this force on the induced electromotive force generated by the underground eddy current field, resulting in distortion of the early signal of transient electromagnetic measurement and formation of a shallow detection blind area. To eliminate the induced electromotive force of the receiving coil itself, at present, most instruments adopt separation designs of the transceiver (McNeill, 1991), but the effect is not ideal. Smith and Balch (2000) and Walker and Rudd (2009) obtained the underground secondary field by observing the transient response and emission current waveform throughout the entire process and then eliminating the primary field from the measured total field through numerical calculation, but there was a notable difference between theoretical calculation and practical values. Kuzmin and Morrison (2014) proposed the use of a magnetic cancellation coil to reduce the influence of the primary field, which has been widely used in aviation transient electromagnetics. However, this technology requires that the transmitting coil, diamagnetic coil, and receiving coil be coplanar and coaxial, the coil radius difference be large, and these caused the spatial distribution of the shallow underground primary field be complex. As such, Xi et al. (2016a); Xi et al. (2016b) proposed the opposing coils transient electromagnetic method (OCTEM) involving the application of a reverse current to two parallel and vertically coaxial identical coils and indicated that there is a plane with a zero primary field magnetic flux between the two coils. Placing the receiving coil in the zero-magnetic flux plane to receive the secondary field can eliminate the primary field–induced interference to improve the detection accuracy and transverse resolution (Xi et al., 2016a; Xi et al., 2016b).

To solve the abovementioned difficulties of permafrost detection in shallow bedrock areas, the OCTEM is introduced in this study. Detection experiments are performed by using the traditional TEM and OCTEM, and the final detection results are compared and analyzed. The distribution of permafrost in this area is determined by combining the surface characteristics, borehole temperature measurement results, and stratum drilling results, and the thickness of permafrost in this area is determined through geophysical exploration for the first time. At the same time, it is considered that the OCTEM effectively solves the shallow detection blind area problem of the traditional TEM in permafrost exploration, improves the detection accuracy and horizontal resolution, and is suitable for multiyear geophysical exploration and investigation of permafrost in shallow bedrock areas.

Materials and methods

The basic working principle of the TEM is shown in Figure 1 (choosing the central loop device as an example). A pulse current $\boldsymbol{I_1}$ of a certain frequency is applied to the transmitting coil TX arranged at the surface to transmit a primary pulse magnetic field $\boldsymbol{H_1}$ underground. When $\boldsymbol{H_1}$ encounters substances with good underground conductivity, eddy current $\boldsymbol{I_2}$ is generated underground, and $\boldsymbol{I_2}$ produces a changed secondary field $\boldsymbol{H_2}$. $\boldsymbol{H_2}$ induces a current in the receiving coil RX arranged at the surface to generate an induced electromotive force (Figure 1A). After recording these parameters, the distribution characteristics of the secondary field can be obtained through inversion calculation and finally converted into the resistivity property distribution of underground materials to achieve detection. In the use of the conventional TEM, it is believed that the receiving coil only receives information on the secondary field and the

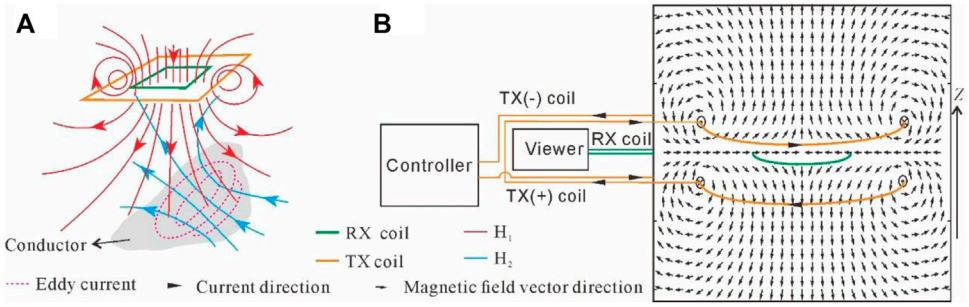

FIGURE 1
Schematic diagram of the TEM working principle. **(A)** Central loop device and the electromagnetic induction process of TEM coils. **(B)** OCTEM device diagram and magnetic field distribution in space after the reverse power supply. The receiving coil indicated by green is located at the zero-flux surface.

primary field during the shutdown period is regarded as zero. In fact, there is still a primary field in the space when the primary field is deactivated, so the receiving coil measures the superposition effect of the primary and secondary fields. This causes challenges in practical detection applications. In view of this situation, to eliminate the interference caused by the primary field, the OCTEM designed two coaxial transmitting coils with an equivalent reverse power supply (Xi et al., 2016a). Because the power supply current $\boldsymbol{I}$ is equal but reverse between these two coils (Figure 1B), their primary field is zero in a plane at the middle between them (Xi et al., 2016a), and only the half-space field generated by the lower part of the TX coil exists underground. When the receiving coil is arranged at the zero-flux surface, only the pure secondary field is received (Figure 1B). Based on this arrangement, the OCTEM is introduced in this study to solve the problem whereby the permafrost in the Mahan Mountain area with shallow bedrock has not been clearly detected by geophysical methods for a long time.

The nano-TEM involving a central loop device, as the conventional TEM adopted in this study, is a shallow detection method that is widely used. This device is a simplification of TEM devices without reducing measurement accuracy (Zonge International Inc., 2015). It is characterized by a high resolution, small volume effect, and suitable coupling with the target detector. The instrument used is the GDP-32II electrical method workstation produced by Zonge Engineering and Research Organization, Inc. (1992). The calculation equations for the apparent resistivity and apparent depth are as follows:

$$\rho_s = \frac{\mu_0}{4\pi}\left(\frac{2\mu_0 NSns}{5}\right)^{2/3} \cdot t^{-\frac{5}{3}}\left[\frac{I}{V(t)}\right]^{2/3} \tag{1}$$

where ρ_s is the apparent resistivity (Ω·m), $\mu_0 = 4\pi \times 10^{-7}$ N/A^2 is the permeability of vacuum, N is the number of transmitting coil turns, S is the single-turn transmitting coil area (m^2), n is the number of receiving coil turns, s is the single-turn receiving coil area (m^2), t is the time (ms), I is the transmitting current (A), and V (t) is the induced electromotive force generated in the receiving coil (μV).

$$h_s = \left[\frac{3M_s q}{16\pi V,(t)S_\tau}\right]^{\frac{1}{4}} - \frac{t}{\mu_{0S_\tau}} \tag{2}$$

where h_s is the apparent depth (m), M_s is the transmitting magnetic moment ($A \cdot m^2$), q is the effective area of the receiving coil (m^2), $V,(t)$ is the induced voltage value observed at time t (μV), and S_τ is the longitudinal conductance (S/m).

The instrument used in this OCTEM study is the HPTEM-18 device produced by Hunan 5D Geophyson Co., Ltd. (http://www.5dgeo.cn/). The calculation equation for the apparent resistivity used to process OCTEM data is as follows:

$$\rho_a = \left(\frac{I \cdot A_R \cdot A_T}{V}\right)^{2/3} \cdot \left(\frac{1}{t}\right)^{5/3} \cdot 6.3219E-3 \tag{3}$$

where I is the transmitting current (A), A_R is the receiving coil area (m^2), A_T is the transmitting coil area (m^2), t is the time (μs), and ρ_a is the apparent resistivity (Ω·m). The algorithm can qualitatively analyze abnormal bodies at a horizontal position along the direction of the survey line.

Overview of permafrost in the study area

Permafrost in Mahan Mountain, Lanzhou, China, is the only preserved permafrost found on the Loess Plateau of China (Xie et al., 2013). It has the characteristics of small distribution area, high temperature, and small thickness (Qiu et al., 1994). Therefore, it is very sensitive to climate change and is known as a living fossil of permafrost research on the Loess Plateau (Xie et al., 2013). The peak of Mahan Mountain is 3,670.3 m above sea

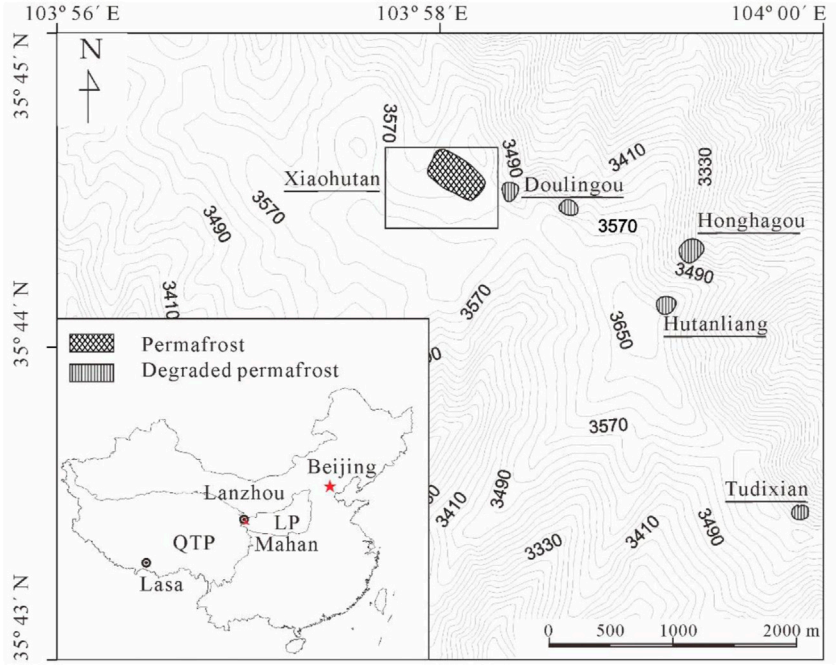

FIGURE 2
Location map of Mahan Mountain and the permafrost distribution. QTP indicates the Qinghai–Tibet Plateau; LP indicates the Loess Plateau.

level, while permafrost is distributed within the range of 3,500–3,650 m above sea level (Figure 2). The annual average temperature is −2.3°C, the annual precipitation is 494 mm (Li, 1986), and the annual average surface temperature is approximate −0.23°C (Xie et al., 2013). In 1985, permafrost was discovered in Mahan Mountain for the first time, namely, a 12-m-thick permafrost layer in the exposed stratum of a shady slope artificial quarry at an altitude of 3,630 m. The thickness of the active layer ranges from 2.5 to 3.0 m, in which water exists in the form of bedrock fissure ice, and the thickness of the pure ice layer reaches up to 5–10 cm (Li, 1986), which is very rare in the high mountains of western China. In 1993, Li and Li (1993) arranged boreholes in Xiaohutan, Doulingou, Honghagou, and Tudixian for drilling investigation. According to survey data, the area of permafrost in Xiaohutan is approximately 0.15 km^2, which is roughly consistent with the distribution of well-developed hummocks on the surface. The permafrost thickness ranges from 5–30 m, the active layer thickness (ALT) is approximately 1.5 m, the ALT in the boundary area is only 1.2 m, and only more than 10 square meters and approximately 3-m-thick permafrost in Honghagou is retained. While there is a notable difference between Doulingou and Tudixian, certain areas contain permafrost, while others do not. They proposed that the distribution of permafrost in this area is very complex. From 2008 to 2009, Xie et al. (2010, 2013) conducted a new survey in the area where Li and Li (1993) had previously arranged boreholes. According to their results, permafrost was found only in Xiaohutan. It was speculated that the permafrost in other areas may have been completely degraded (Xie et al., 2013). According to the distribution of hummocks on the surface, it was considered that the area of permafrost was reduced from 0.15 to 0.13 km^2 (Xie et al., 2013). In recent years, researchers have applied the TEM, ground-penetrating radar (GPR), borehole temperature measurement, model analysis, and other methods to study permafrost in Mahan Mountain (Dong, 2013; Liu et al., 2015b; Yang et al., 2019). It is considered that the permafrost in Mahan Mountain is only distributed in Xiaohutan with a distribution area of approximately 0.11 km^2 and a thickness from 20–30 m, which is considered to occur in a state of rapid degradation.

According to the investigation of Li and Li (1993) and Xie et al. (2010, 2013), the minimum temperature of permafrost in Mahan Mountain reaches −0.2°C at depths from 10 to 16 m, and the upper and lower depths rise at a rate of 0.01°C/m, which is typical of high-temperature permafrost. At present, there are seven temperature measurement boreholes distributed in the study area (Figure 3), which are all distributed in and near Xiaohutan. Among them, boreholes 2, 3, 4, and 5 are located in the distribution range of permafrost, and boreholes 1, 6, and 7 are located in non-permafrost areas. We regularly monitored the ground temperature at different depths *via* a high-precision thermistor with an accuracy of 0.03°C. Figure 4 shows the

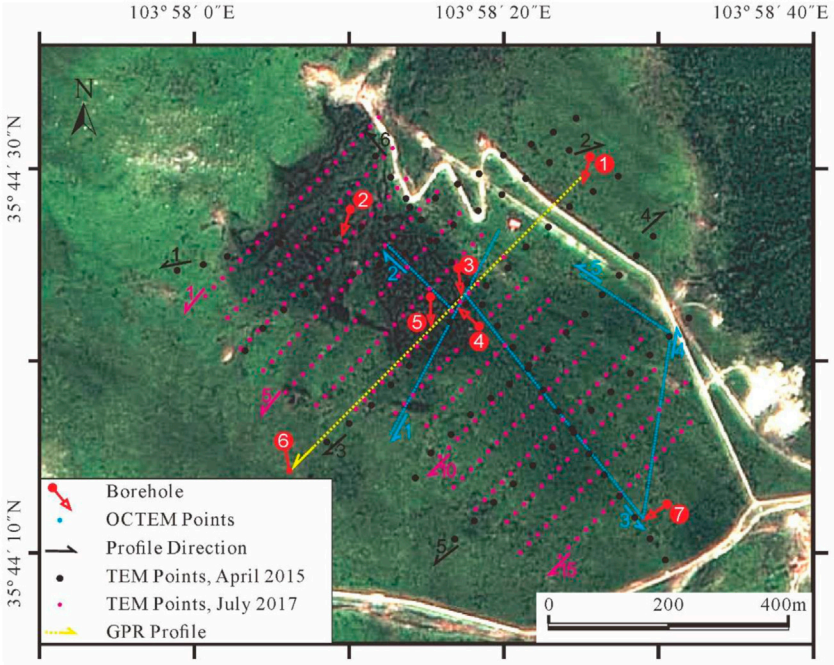

FIGURE 3
Satellite map of the Mahan Mountain permafrost region and geophysical exploration work location.

temperature measurement curves for seven boreholes. According to the ground temperature monitoring results, the temperature of permafrost in the area is generally higher than −0.2°C, the thickness of permafrost generally approaches or exceeds 20 m, and the maximum thickness is approximately 30 m. The temperature measurement results for boreholes 2, 4, and 5 show a slight warming trend. The ground temperature in borehole 2 at the edge of permafrost is close to 0°C, and the ground temperature in borehole 4 at the center of permafrost in Xiaohutan is the lowest. The temperature changes slowly in permafrost and rapidly in bedrock.

The strata in this area mainly include the Presinian Mahan Group. The lithology is mainly composed of various migmatites, followed by gneiss, schist, and marble. The bedrock is generally buried shallowly. According to field outcrop and borehole data, the thickness of the unconsolidated sedimentary layer in Mahan Mountain generally ranges from 0.7 to 1.5 m, and the sedimentary layer gradually thickens with decreasing altitude. However, in the Xiaohutan depression, where developed permafrost, the unconsolidated sedimentary layer thickens from the smallest value of 1.2 m at the edge to the center and can reach 8 m at the thickest location at the center of the depression. The weathering degree of the upper part of the underlying bedrock is high, and permafrost is mainly developed in voids in this broken bedrock. With increasing depth, the weathering degree decreases, and the ice content in permafrost also decreases. Figure 5 shows the stratigraphic characteristics of this typical layer in the Xiaohutan depression for boreholes 3 and 5. Obviously, the difference between the permafrost in Mahan Mountain and that in most areas is the lower part of the permafrost is completely developed in bedrock and the fragmentation degree of bedrock controls the ice content in permafrost.

Obviously, the electrical changes in the strata in this area are mainly determined by the water conditions in the voids of the broken bedrock and the thickness of the loose sedimentary layer. The loose layer in the upper part of the formation contains more water storage structures and more suitable surface water conditions, so the surface obviously exhibits low resistivity. The lower permafrost is mainly distributed in the weathered broken layer of bedrock, so it exhibits a higher resistivity than that of the upper layer. In addition, the development of solid ice can theoretically produce a higher resistivity than that of the surrounding strata at the same depth. At the lower surface and boundary of permafrost, because the horizontal formation components change slightly, only the existing form of water changes. The area of the meltwater distribution differs from that of permafrost with solid ice. The formation is deeper, the bedrock tends to be complete, and the resistivity value tends to remain stable. Based on the abovementioned understanding, in this study, the formation resistivity change caused by other small changes

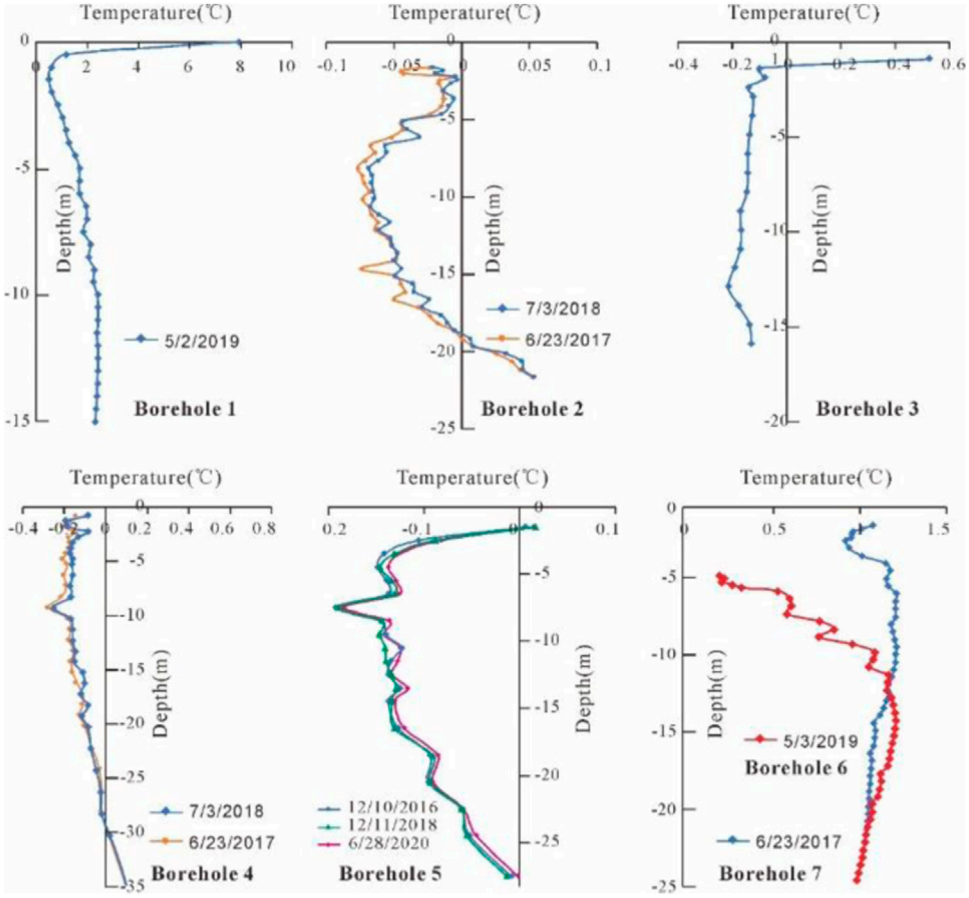

FIGURE 4
Mahan Mountain borehole temperature measurement curve.

is ignored, and it is considered that all resistivity differences are caused by water change.

Data acquisition

Nano-TEM detection at 94 measuring points (black dots in Figure 3) was conducted in Xiaohutan of Mahan Mountain in Lanzhou in April 2015, with a point spacing of 50 m, forming six detection profiles. In July 2017, 12 profiles with 273 measuring points (pink dots in Figure 3) were remeasured with the same detection parameters and 20 m as the point spacing. To ensure more accurate detection results, the total station was used to accurately locate the measurement points. The measurements were repeated three–five times at each point. In June 2018, single-point nano-TEM sounding was conducted in many areas in Mahan Mountain. In July 2020 and September 2020, an HPTEM-18 equivalent anti-magnetic flux transient electromagnetic system based on the OCTEM principle was used twice to complete five detection profiles in the permafrost area of Mahan Mountain, with a total of 294 measurement points (blue dots in Figure 3). The locations of these measurement profiles are also shown in Figure 3, and the spacing between the measurement points is 5 m. Among these profiles, profile 1 passes through the permafrost distribution area, profile 2 is in the permafrost area, half of profile 3 passes through the permafrost distribution area, and profiles 4 and 5 are located in the hummock degradation area at the permafrost boundary. Table 1 lists the actual detection parameters.

Data processing

During nano-TEM data processing, the three measured datasets with the most similar measurement results were selected to participate in the calculation to ensure that the results reduced the random interference as much as possible. STEMNV software was used for two-dimensional fitting with a layered stratum model. The OCTEM uses multiple stacking steps

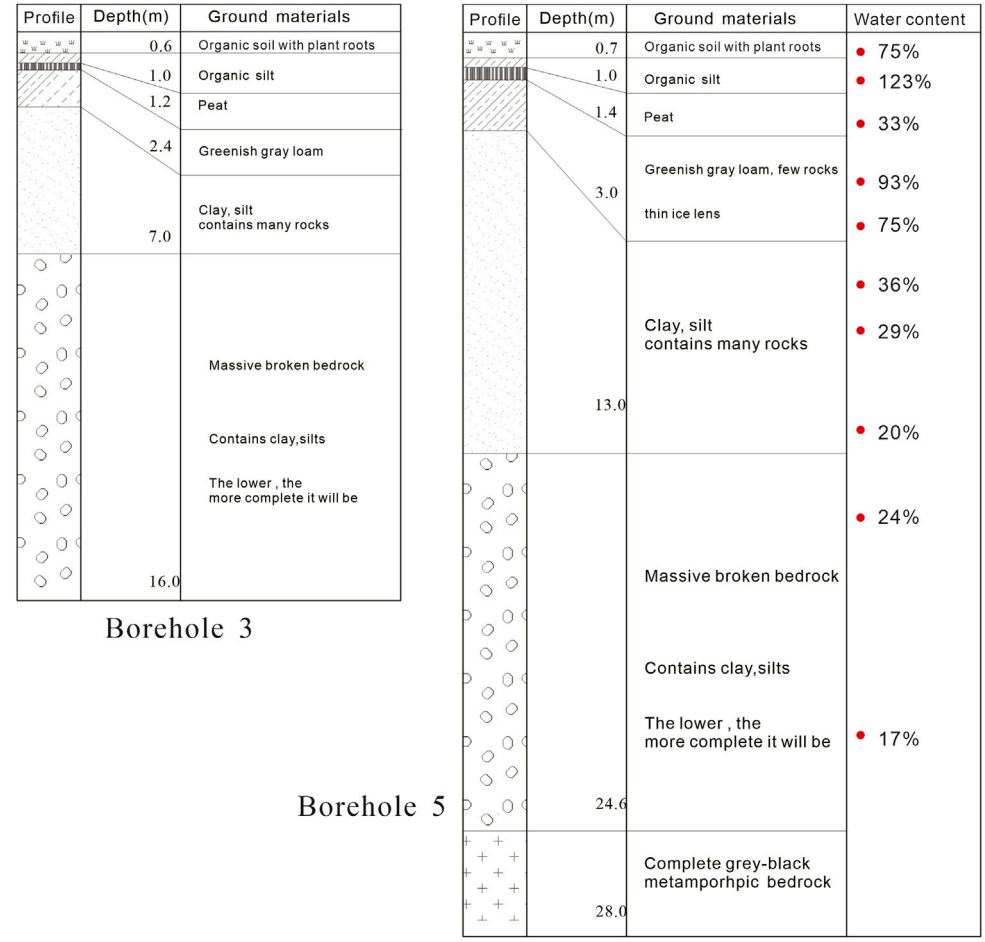

FIGURE 5
Observation map of the strata and water content in boreholes 3 and 5 in Mahan Mountain.

TABLE 1 Detection parameters used in the nano-TEM and OCTEM.

Detection parameter	Nano-TEM	OCTEM
Instrument	GDP-32II	HPTEM-18
Transmission current	1 A	10 A
Frequency	32 Hz	62.5 Hz
Repeat number	3	2
Side length of the TX coil	20 m	1.24 m
Turns of the TX coil	1	10
Side length of the RX coil	5 m	0.5 m
Turns of the RX coil	1	10

(more than 300 times) to improve the signal-to-noise ratio, and HPTEM-18 data processing software was used to process the measured data. In the process of data processing, unreasonable measured data could be corrected and eliminated at any time to ensure the reliability of the data processing results. After the data calculation step, all the data of this study were compiled into profiles in Surfer software (www.goldensoftware.com), and the agreed color scheme was used.

Detection results

Before the discovery of permafrost in Mahan Mountain, scholars conducted resistivity sounding exploration in the peak area of Mahan Mountain to determine whether permafrost had developed and remained. Due to the shallow distribution of bedrock in Mahan Mountain and the high resistivity of bedrock close to frozen soil, the detection results (Figure 6) did not identify the existence of frozen soil (Guo, 1982). When the semipolar distance AB/2 ranges from 1.5–6 m, the apparent resistivity value of the formation increases

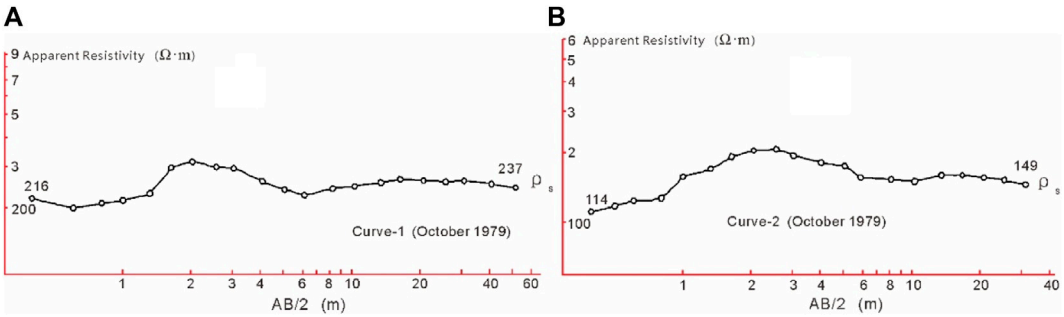

FIGURE 6
Two permafrost DC sounding curves of Mahan Mountain. **(A)** located on the top of the mountain with thin loose layer and higher apparent resistivity value; **(B)** located slightly lower with thick loose layer and lower apparent resistivity value.

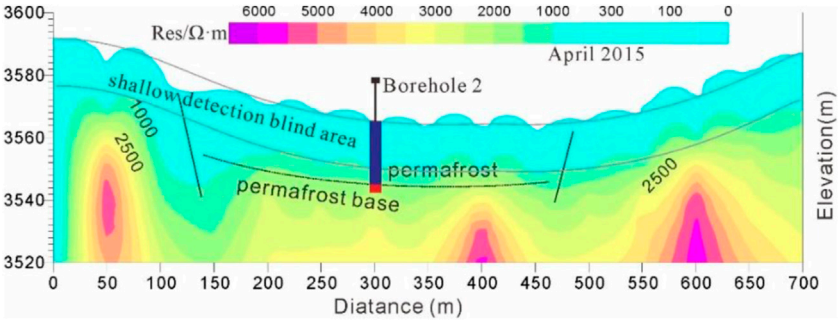

FIGURE 7
Nano-TEM sounding profile 2 of Mahan Mountain, April 2015.

obviously, but the amplitude is small. Now, we know that the determined high-resistivity anomaly is permafrost. Therefore, it is speculated that there is little difference between the resistivity values of permafrost and underlying bedrock in this area. According to Hauck and Muhll (1999b), and Hauck et al. (2003), this occurs because DC detection is affected by the upper stratum, and the greater the detection depth is, the smaller the difference in resistivity will be. However, the difference is that TEM detection involves the induction of the primary field within a specific layer at a certain time, so the formation itself slightly impacts TEM detection, and the TEM can measure more obvious differences in formation resistivity. Figure 6 also shows that the resistivity of Mahan Mountain permafrost reaches as low as 200–300 Ω m. In fact, the resistivities of the weathered bedrock, surface melting layer, and surface freezing layer were also measured, reaching approximately 600, 25, and 80 Ω m, respectively, at −3°C and 4,800 Ω m at −13°C, which is consistent with the results measured under DC conditions (Yang et al., 2019). In this study, the reference resistivity of the surface melting layer was selected as 25 Ω m.

Nano-TEM measurement

The final inversion results show low-resistivity anomalies in the profile; in combination with the satellite image depicted in Figure 3, it can be found that these anomalies are consistent with the distribution of surface wetlands (the dark area in Figure 3 is the Xiaohutan depression, and hummocks are more notably developed in the dark area), and there is no longitudinal change in the profile within 15 m. The measured permafrost depth in the four boreholes located in the permafrost range is no more than 30 m, while the inversion results cannot significantly detect the low-resistivity characteristics of the lower limit of permafrost within 40 m. Choosing profile 2 detected in April 2015 as an example (Figure 7), we can find low-resistivity anomalies at 100 and 500 m, while these two locations signify the boundary of the distribution of hummocks at the surface. If the hummocks on the surface are consistent with the distribution of permafrost, 100 and 500 m represent the boundaries of permafrost. Through comparison of Figures 3 and 7, it can be found that the 100–500 m section in the satellite map is a continuous hummock area and a continuous geological body with medium- and high-resistivity

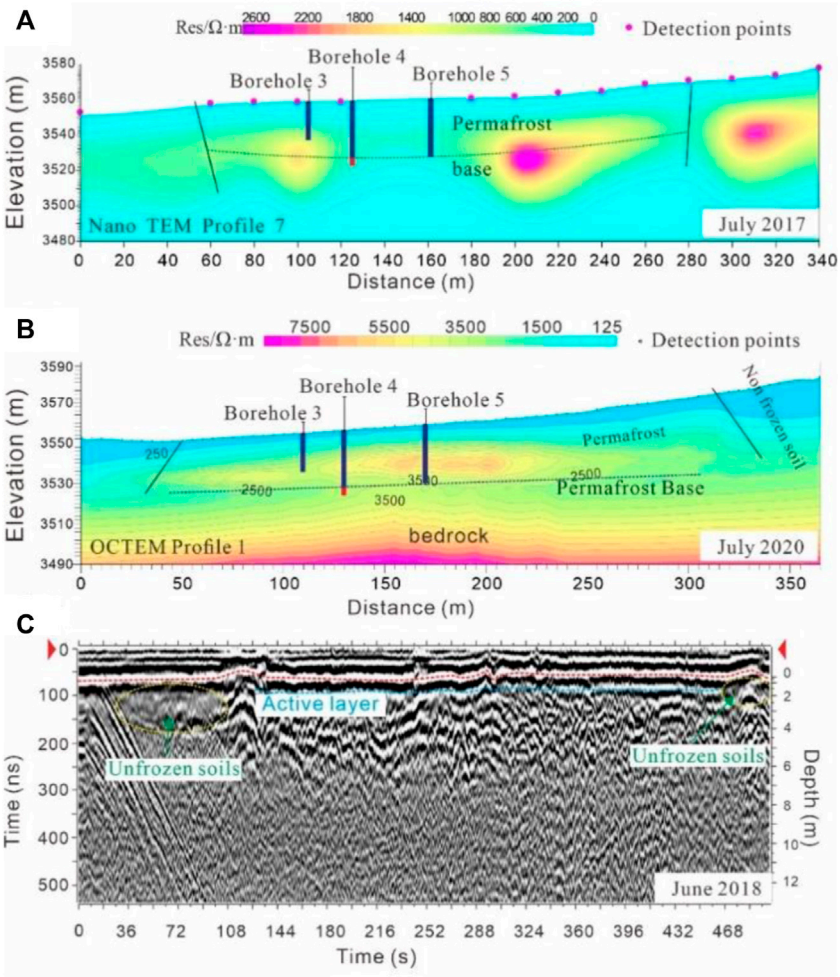

FIGURE 8
Comparison of the nano-TEM, OCTEM, and GPR methods in identifying permafrost in the shallow bedrock area of Mahan Mountain. **(A)** Nano-TEM profile with a 20-m point spacing. **(B)** OCTEM profile with a 5-m point spacing. **(C)** 50-MHz GPR detection profile.

values in the TEM profile, which is consistent with the boundary characteristics of permafrost. Before this study, the distribution range of permafrost in Mahan Mountain was obtained according to drilling results and the development range of surface hummocks, but there are no continuous observation data to prove that this approach is correct. In addition, at a depth of approximately 15 m, there is an obvious shallow detection blind area, which shows low resistivity and is inconsistent with the high resistivity of permafrost. Borehole 2 is approximately 50 m away from the 300-m location (Figure 3). The temperature measurement results show that the temperature reaches 0°C at a depth of approximately 19 m, which suggests that the thickness of permafrost here is approximately 20 m (Figure 4), which is not found from the TEM results.

Does the abovementioned occur because the spacing between the survey points is too large, resulting in the lack of profile continuity? The detection results obtained low-resistivity anomalies along the profile consistent with the boundary distribution of surface wetlands, but anomalies remain that are inconsistent with the continuity characteristics of frozen soil in the possible permafrost distribution area. Choosing profile 7 detected in July 2017 (Figure 8A) as another example, the spacing of the measuring points was 20 m. Through specific analysis of the profile, it can be observed that low-resistivity anomalies are obvious where the measuring points are missing. However, there is still an obvious shallow detection blind area after the spacing of the measuring points is improved, while there is still no change in the identification of the permafrost base. We speculate that anomalies may be caused by fractures in the bedrock and distribution of groundwater. However, in terms of lower limit identification of permafrost, reducing the distance between measurement points still fails to clearly detect the water characteristics at the lower boundary of permafrost. Theoretically, to eliminate this problem in the shallow layer, increasing the number of turns of the measuring coil can suppress random interference and improve the signal-to-noise ratio

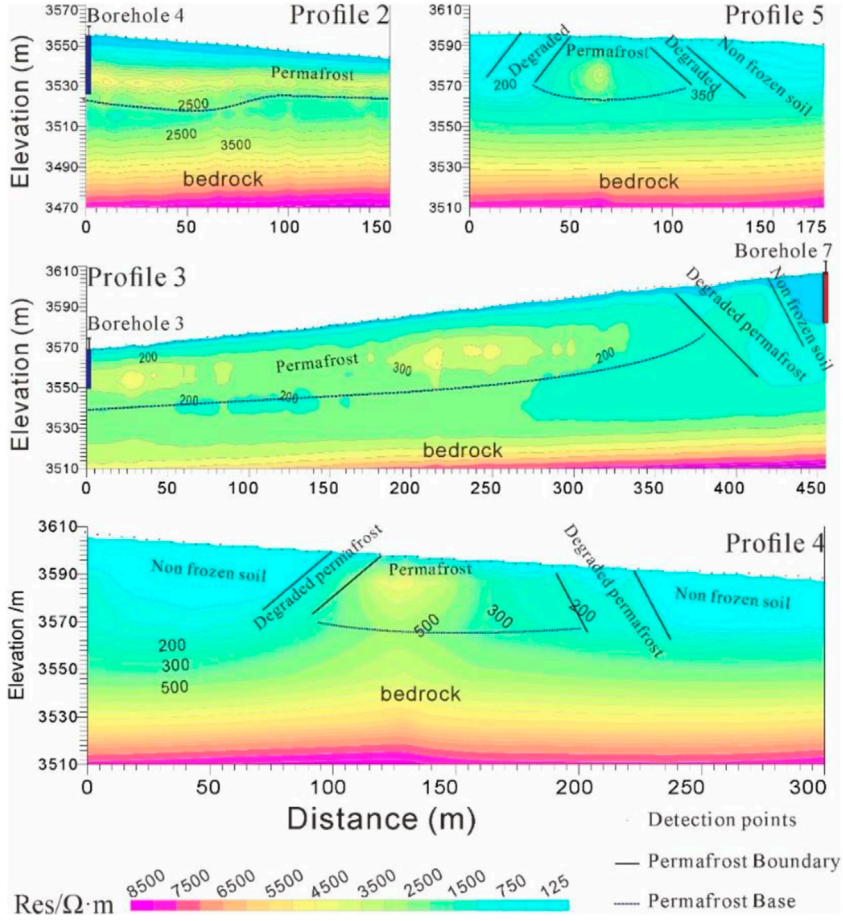

FIGURE 9
OCTEM sounding profiles in Mahan Mountain.

and fidelity. In June 2018, the other test parameters remained unchanged. We measured and compared the number of turns of the transmitting and receiving coils in this area. The results show that increasing the number of turns of the transmitting coil slightly affects the detection results, while reducing the coil size decreases the detection depth.

Through the abovementioned experiments, it can be concluded that the nano-TEM shows an obvious shallow detection blind area in the exploration of permafrost in Mahan Mountain, Lanzhou, although this method achieves a certain identification ability regarding the boundary of permafrost but cannot effectively identify the permafrost base.

Opposing coils transient electromagnetic method measurement

OCTEM exploration profile 1 (Figure 8B) extends from northeast to southwest, with a total of 72 measuring points and a total length of 365 m (Figure 3). The surface enters the Xiaohutan depression with hummock distributions from 45 to 320 m, and hummocks then disappear, which is consistent with the high-resistivity distribution detected by the OCTEM. The hummocks within 100–245 m below the ground surface are well-developed and dark in color. The hummocks on both sides are degraded outward, which is also very obvious in the OCTEM profile. In the OCTEM profile, the resistivity value in this section is significantly higher than that on both sides. Under the condition that the lateral conditions of the formation are similar, the reason for this difference in lateral resistivity is the differential distribution of conductive substances in the formation. It is believed that the distribution difference of the water resistivity is small only when the bedrock remains relatively shallow buried in the permafrost area for many years. The profile shows that there is an obvious low-resistivity distribution layer at depths above 3,526 m above sea level, and the depth of this layer varies between 25 and 30 m, which coincides with the lower limit depth of permafrost obtained *via* borehole and ground

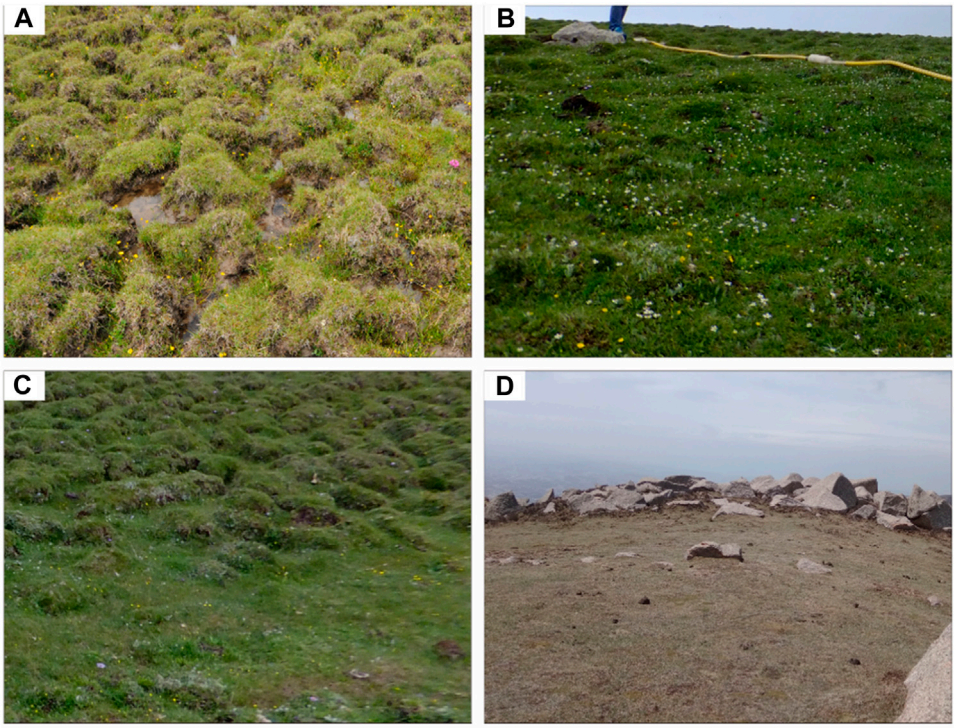

FIGURE 10
Photos of surface vegetation in the Mahan Mountain area. **(A)** In the permafrost region, shot at location a in Figure 11. **(B)** Non-permafrost region, shot at location b in Figure 11. **(C)** Degraded permafrost region, shot at location c in Figure 11. **(D)** Bedrock exposed area, shot at the top of the mountain.

temperature monitoring. Permafrost degradation dissolves solid ice in bedrock voids, and part of the meltwater flows away from the rock voids. At the same time, water is adsorbed by silt, clay, and other particles in the formation or accumulates in unconnected rock pores so that the resistivity at the lower limit and boundary of permafrost is lower than that of permafrost. At an elevation of 3,526 m in the figure, the resistivity is lower than that of the upper and lower strata, which is in line with the low-resistivity characteristics of meltwater at the permafrost boundary. By comparing the nano-TEM (Figure 8A) and GPR results (Figure 8C) at similar locations (Figure 3), it can be found that the OCTEM is the most intuitive and accurate method for identifying permafrost bases and boundaries.

OCTEM profile 2 (shown in Figure 9) is located in the central area of the Xiaohutan depression, with 31 measuring points from southeast to northwest, and the length of the profile is 150 m. The surface contains well-developed hummocks (Figure 10A), and the surface soil is saturated with water. It can be found that there is a high-resistivity layer with a thickness from 25 to 30 m above the bedrock from the beginning to the end. This layer slowly thins from the center of the depression (the starting point of profile 2, near borehole 4) to the edge, but the change range is small. The thickness of the high-resistivity layer at the end is reduced to 20 m. Borehole 4 at the starting point shows that the thickness of permafrost here is approximately 28 m, and the thickness of permafrost at the end is approximately 22 m, which agrees with the temperature measurement results in borehole 2 (the distance between borehole 2 and the end of profile 2 is approximately 65 m).

OCTEM profiles 3, 4, and 5 (Figure 9) show permafrost boundary test results. Profile 3 starts from the central area of the permafrost distribution and passes through the permafrost area along the southeast direction. The hummocks on the surface degenerate from 380 m along profile 3 and disappear at 420 m (Figure 10B shows that the surface hummocks have been completely degraded), which is strictly consistent with the high-resistivity anomaly detected. The high-resistivity anomaly exhibits a clear low-resistivity lower interface, which shows obvious permafrost base characteristics. Profiles 4 and 5 both have sparse hummocks in the middle, and the hummocks on both sides are completely degraded (Figure 10C shows the obvious boundary of the surface meadow). All the high-resistivity layers in the OCTEM profiles are clear, and the location of the high-resistivity anomaly is consistent with the distribution of surface hummocks. Profile 3 has a relatively stable distribution of high resistivity values, with clear low resistivity values at the lower interface, and the depth varies between 23 and

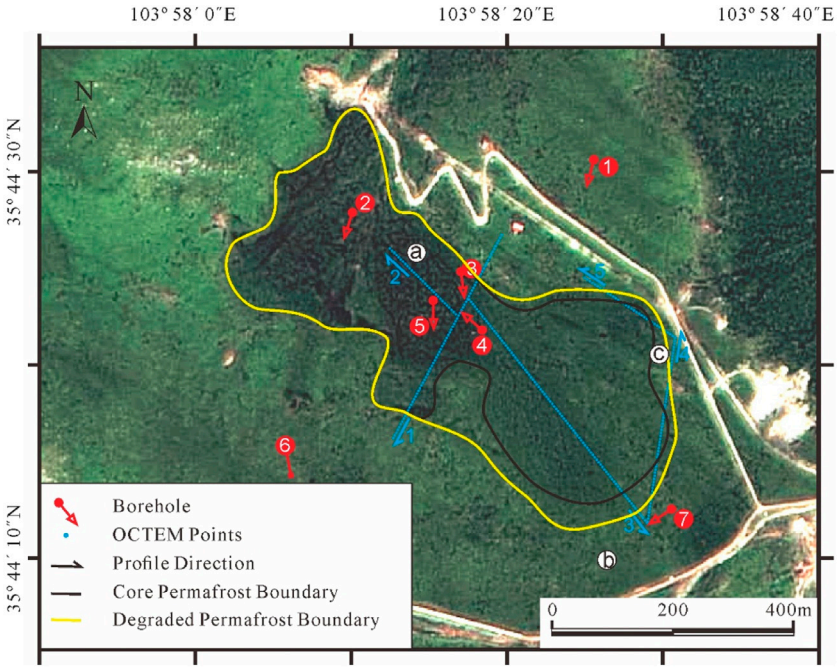

FIGURE 11
Distribution range of permafrost in Mahan Mountain based on geophysical exploration and surface vegetation characteristics.

29 m. From 380 to 420 m, the hummocks are sparsely distributed and seriously degraded and disappear completely at 420 m. The section shows that the resistivity is slightly higher than that in the melting area, and the boundary with the melting area is clear. It is speculated that the permafrost in this section occurs in the degraded state and contains more meltwater than does the non-degraded permafrost. However, because solid ice has not completely melted, the resistivity is higher than that in the melting area. The normal annual temperature measurement result for borehole 7 at the end of the survey line is positive (Figure 4), which is consistent with the detection result. Along the direction of Profile 3, at the top of the mountain about 180 m away from the end of Profile 3, the vegetation is almost completely degraded and massive bedrock is exposed (Figure 10D). Profile 4 (95–200 m) and profile 5 (15–95 m) show continuous high-resistivity anomalies with clear lower interfaces. It should be noted that obvious changes in hummocks appear on the surface at these two locations. The hummocks on the surface are only distributed from 90 to 205 m along profile 4 and are only distributed from 10 to 120 m along profile 5.

Through the aforementioned analysis, in the area measured by the OCTEM in this study, the thickness of permafrost generally varies between 20 and 30 m and has a clear boundary and base characteristics, which directly confirms the corresponding relationship between permafrost and hummock distribution. According to this correspondence, combined with satellite images and actual survey data, we mapped the distribution range of permafrost in Maxian Mountain (closed area of the yellow line in Figure 11). In contrast to previous work, this study identified a region where permafrost occurs in a degraded state but is not yet completely degraded (the area between the brown and yellow lines in Figure 11).

Conclusion

By comparing the application of the nano-TEM and OCTEM, it can be found that there is an obvious detection blind area in the exploration of permafrost in Mahan Mountain with the conventional TEM, and it is difficult to distinguish permafrost vertically developed in bedrock. However, the OCTEM can effectively eliminate the primary field interference, so this method attains a higher detection accuracy and can observe small changes in the formation water content horizontally and vertically to identify the spatial distribution of permafrost. In addition, through this comparative experiment, new insights into the distribution of permafrost in Mahan Mountain are obtained. For the first time, the observation results confirm that the distribution of surface hummocks in this area is consistent with that of permafrost and degraded hummocks indicate permafrost degradation.

Previously, the distribution area of permafrost in Mahan Mountain was considered to be degraded to 0.13 km^2. However, now, the actual distribution area of permafrost has not reached this value, but the boundary area is obviously degrading.

Meltwater has accumulated in the degraded area, showing the distribution characteristics of the core area–degraded area–completely degraded area from the center toward the outside. According to the distribution statistics of hummocks on the surface, at present, the distribution area of the permafrost core area in Mahan Mountain is only 0.11 km^2, with an outer circumference of approximately 0.04 km. The area with a sparse distribution of surface hummocks occurs in a state of rapid degradation, and obvious water characteristics can be detected in the strata.

Although the OCTEM eliminates the primary field interference, solves the problem of shallow detection blind areas, and detects the permafrost distribution in shallow bedrock in the Mahan Mountain area, this does not indicate that this method can effectively detect permafrost in all shallow bedrock areas. The OCTEM is particularly sensitive to water content. The permafrost in the Mahan Mountain area is typical high-temperature permafrost, and there is water accumulation in both the boundary area and permafrost base, so permafrost can be detected and identified. However, many permafrost zones in shallow bedrock areas do not exhibit similar conditions. Therefore, more research is needed on whether the OCTEM can identify low-temperature permafrost in shallow bedrock areas.

Data availability statement

The raw data supporting the conclusion of this article will be made available by the authors, without undue reservation.

Author contributions

TW, XW, and CX contributed to the conception of the study, supervision, and funding acquisition; GY: contributed to literature synthesis and wrote the manuscript; GL, WW, and YZ provide field actual measurement and helped perform the analysis with constructive discussions.

Funding

This work was supported by the Strategic Priority Research Program of Chinese Academy of Sciences (XDA23060703); the National Natural Science Foundation of China (41671068); and the State Key Laboratory of Cryospheric Science (SKLCS-ZZ-2022).

Acknowledgments

We thank Wei Xu from the 149 Team of Gansu Coalfields Geological Bureau for providing instruments and field guidance for this study, and collecting OCTEM data in person, as well as providing guidance for later data processing.

Conflict of interest

The authors declare that the research was conducted in the absence of any commercial or financial relationships that could be construed as a potential conflict of interest.

Publisher's note

References

Barsukov, P. O., and Fainberg, E. B. (2013). Three-dimensional interpretation of TEM soundings. *Izv. Phys. Solid Earth* 49 (4), 517–525. doi:10.1134/S1069351313040022

Christiansen, A. V., Auken, E., and Sørensen, K. (2006). "The transient electromagnetic method," in *Groundwater geophysics* (Berlin, Heidelberg: Springer), 179–225. doi:10.1007/3-540-29387-6

Danielsen, J. E., Auken, E., Jørgensen, F., Søndergaard, V., and Sørensen, K. I. (2003). The application of the transient electromagnetic method in hydrogeophysical surveys. *J. Appl. Geophys.* 53 (4), 181–198. doi:10.1016/j.jappgeo.2003.08.004

Dong, X. C. (2013). Characteristics of surface energy budget components in permafrost region of the Mahan Mountain, Lanzhou. *J. Glaciol. Geocryol.* 35 (2), 320–326. doi:10.7522/j.issn.1000-0240.2013.0038

Guo, D. X. (1982). Preliminary approach to the existence of permafrost in Mahan mountain area, Lanzhou. *J. Glaciol. Geocryol.* 4 (4), 63–66. (in Chinese)

Harada, K., Wada, K., and Fukuda, M. (2000). Permafrost mapping by transient electromagnetic method. *Permafr. Periglac. Process.* 11 (1), 71–84. doi:10.1002/(SICI)1099-1530(200001/03)11:1<71::AID-PPP339>3.0.CO;2-#

Harada, K., Wada, K., Sueyoshi, T., and Fukuda, M. (2006). Resistivity structures in alas areas in Central Yakutia, Siberia, and the interpretation of permafrost history. *Permafr. Periglac. Process.* 17 (2), 105–118. doi:10.1002/ppp.551

Harris, C., Haeberli, W., Mühll, D. V., and King, L. (2001). Permafrost monitoring in the high mountains of europe: The PACE project in its global context. *Permafr. Periglac. Process.* 12 (1), 3–11. doi:10.1002/ppp.377

Hauck, C. (2001). Geophysical methods for detecting permafrost in high mountains. *PhD thesis ETH Zurich* 171, 204.

Hauck, C., Guglielmin, M., Isaksen, K., and Vonder Mühll, D. (2001). Applicability of frequency-domain and time-domain electromagnetic methods for mountain permafrost studies. *Permafr. Periglac. Process.* 12 (1), 39–52. doi:10.1002/ppp.383

Hauck, C., Mühll, D. V., and Maurer, H. (2003). Using DC resistivity tomography to detect and characterize mountain permafrost. *Geophys. Prospect.* 51 (4), 273–284. doi:10.1046/j.1365-2478.2003.00375.x

Hauck, C., and Mühll, D. V. (1999a). Detecting alpine permafrost using electromagnetic methods. *Adv. Cold-Region Therm. Eng. Sci.* 533, 475–482. doi:10.1007/BFb0104205

Hauck, C., and Mühll, D. V. (1999b). "Using DC resistivity tomography to detect and characterise mountain permafrost," in Proceeding of the 61st EAGE Conference and Exhibition, June 1999 (Helsinki, Finland: European Association of Geoscientists and Engineers). doi:10.3997/2214-4609.201407626

Henderson, J. D. (1980). "Permafrost mapping along transportation corridors," in *Proc. Symp. Permafrost geophysics* (Techn. Memorandum), 128, 130–138. (No. 5).

Hoekstra, P. (1973). "Electromagnetic probing of permafrost," in Proceedings of 2nd International Conference on Permafrost (Yakutsk, USSR: North American Contribution), 517–526.

Ji, Y. J., Lin, J., Yu, S. B., Wang, Z., and Wang, J. (2006). A study on solution of transient electromagnetic response during transmitting current turn-off in the ATTEM system. *Chin. J. Geophys.* 49 (6), 1718–1725. doi:10.1002/cjg2.1000

King, L., Fisch, W., Haeberli, W., and Wächter, H. P. (1987). A sensory-integrative approach to the education of the autistic child. *Occup. Ther. Health Care* 23 (2), 77–85. doi:10.1080/J003v04n02_08

Kuzmin, P. V., and Morrison, E. B. (2014). *U.S. Patent No. 8,786,286*. Washington, DC: U.S. Patent and Trademark Office.

Li, S. D. (1986). Permafrost found on maxian mountains near Lanzhou. *J. Glaciol. Geocryol.* 8 (4), 409–410. (in Chinese)

Li, Z. F., and Li, S. D. (1993). Regional features of permafrost in Mahan Mountain and their relationship to the environment. *J. Glaciol. Geocryol.* 15 (001), 83–89. (In Chiese).

Liu, G. Y., Wang, W., Zhao, L., Chen, J., Pang, Q. Q., Wang, Z. W., et al. (2015a). Using transient electromagnetic method to sound permafrost depth in the West Kunlun Mountains. *J. Glaciol. Geocryol.* 37 (1), 38–48. doi:10.7522/j.issn.1000-0240.2015.0004

Liu, W. H., Xie, C. W., Zhao, L., Wu, T. H., Li, R., Wang, W., et al. (2015b). Simulating the active layer depth and analyzing its influence factors in permafrost of the Mahan Mountain, Lanzhou. *J. Glaciol. Geocryol.* 37, 1443–1452. doi:10.7522/j.isnn.1000-0240.2015.0160

McNeill, J. D. (1991). *PROTEM-47 Transient electromagnetic system manual*. www.geonics.com.

Mühll, D. V., Hauck, C., Gubler, H., McDonald, R., and Russill, N. (2001). New geophysical methods of investigating the nature and distribution of mountain permafrost with special reference to radiometry techniques. *Permafr. Periglac. Process.* 12 (1), 27–38. doi:10.1002/ppp382

Mühll, D. V., Hauck, C., and Gubler, H. (2002). Mapping of mountain permafrost using geophysical methods. *Prog. Phys. Geogr. Earth Environ.* 26 (4), 643–660. doi:10.1191/0309133302pp356ra

Nabighian, M. N. (1984). Foreword and introduction. *Geophysics* 49 (7), 849–853. doi:10.1190/1.1441730

Nabighian, M. N., and Macnae, J. C. (1991). Time domain electromagnetic prospecting methods. *Electromagn. Methods Appl. Geophys.* 2, 427–520. doi:10.1190/1.9781560802686

Qiu, G. Q., Liu, J. S., and Liu, H. X. (1994). *Geocryological glossary*. Lanzhou: Gansu Science and Technology Press. (in Chinese).

Smith, R. S., and Balch, S. J. (2000). Robust estimation of the band-limited inductive-limit response from impulse-response TEM measurements taken during the transmitter switch-off and the transmitter off-time: Theory and an example from Voisey's Bay, Labrador, Canada. *Geophysics* 65 (2), 476–481. doi:10.1190/1.1444741

Szarka, L. (1988). Geophysical aspects of man-made electromagnetic noise in the Earth — a review. *Surv. Geophys.* 9, 287–318. doi:10.1007/BF01901627

Telford, W. M., Geldart, L. P., and Sheriff, R. E. (1991). *Applied geophysics*. Cambridge: Cambridge University Press.

Walker, S., and Rudd, J. (2009). Extracting more information from on-time data. *ASEG Ext. Abstr.* 2009 (1), 1–8. doi:10.1071/ASEG2009ab053

Wang, W., Liu, G. Y., Yu, Q. H., and Sheng, Y. (2011a). Geophysical mapping permafrost using TEM. *J. Glaciol. Geocryol.* 33 (1), 156–163. doi:10.1007/s12182-011-0118-0

Wang, T., Yu, Q. H., You, Y. H., Wang, W., and Du, E. J. (2011b). The application of electromagnetic technology to permafrost exploration. *Geophys. Geochem. Explor.* 35 (5), 638–642. doi:10.1002/(SICI)1099-1530(200001/03)11:13.0.CO;2-#

Xi, Z., Long, X., Huang, L., Zhou, S., Song, G., Hou, H., et al. (2016a). Opposing-coils transient electromagnetic method focused near-surface resolution. *Geophysics* 81 (5), E279–E285. doi:10.1190/Geo2014-0564.1

Xi, Z., Long, X., Huang, L., Zhou, S., Gang, S., Hai-Tao, H., et al. (2016b). Opposing coils transient electromagnetic method for shallow subsurface detection. *Chin. J. Geophys.* 59 (9), 551–559. doi:10.1002/cjg2.30006

Xie, C. W., Zhao, L., Wu, J. C., and Qiao, Y. P. (2010). Features and changing tendency of the permafrost in mahan mountain, Lanzhou. *J. Glaciol. Geocryol.* 32 (5), 893–890. doi:10.3724/SP.J.1231.2010.06586

Xie, C., Gough, W. A., Tam, A., Zhao, L., and Wu, T. (2013). Characteristics and persistence of relict high-altitude permafrost on Mahan Mountain, loess plateau, China. *Permafr. Periglac. Process.* 24 (3), 200–209. doi:10.1002/ppp.1776

Xue, G. Q., Li, X., and Di, Q. Y. (2007). The progress of TEM in theory and application. *Prog. Geophys.* 22 (4), 1195–1200. doi:10.1016/S1872-5791(08)60015-9

Yang, G. Q., Xie, C. W., Wang, W., Du, E., Liy, W., Zhang, Y., et al. (2019). Study on TEM sounding permafrost with shallow bedrock. *J. Glaciol. Geocryol.* 41 (5), 1067–1077. doi:10.7522/j.issn.1000-0240.2019.0328

Zonge Engineering and Research Organization, Inc (1992). *Introduction to TEM. Extracted from practical geophysics II: Northwest mining association.*

Zonge International Inc (2015). *NanoTEM® near-surface method*. Available from: http://zonge.com/geophysical-methods/electrical-em/nanotem/ (accessed June 14, 2015).

frontiers | Frontiers in Environmental Science

ORIGINAL RESEARCH
published: 17 August 2022
doi: 10.3389/fenvs.2022.932993

Homogenization in Species Composition and No Change in Aboveground Biomass Across Tibetan Permafrost Regions Over Ten Years

Yan Yang[1], *Kari Klanderud*[2], *Yinghui Yang*[3], *Huaan Jin*[1], *Yaqiong Lu*[1], *Tongzuo Zhang*[4] *and Genxu Wang*[5]*

[1]Key Laboratory of Mountain Surface Processes and Ecological Regulation, Institute of Mountain Hazards and Environment, Chinese Academy of Sciences, Chengdu, China, [2]Faculty of Environmental Sciences and Natural Resource Management, Norwegian University of Life Sciences, Ås, Norway, [3]School of Mathematics, Southwest Jiaotong University, Chengdu, China, [4]Northwest Institute of Plateau Biology, Chinese Academy of Sciences, Xining, China, [5]State Key Laboratory of Hydraulics and Mountain River Engineering, College of Water Resource and Hydropower, Sichuan University, Chengdu, China

The Tibetan Plateau is the most extensive high-elevation grassland on Earth, with the largest expanse of high-elevation permafrost. It is experiencing climate warming that is projected to continue at rates above the global mean, potentially jeopardizing ecosystem functioning. We conducted a broad-scale resampling project in the permafrost region of Tibet to examine if plant production and diversity had changed over time. We recorded vascular plant species occurrences and harvested aboveground biomass at 36 alpine grassland sites in 2008 and 2018. Our results show that aboveground biomass increased for legumes and forbs, but decreased for grasses and sedges, resulting in no overall change in the aboveground biomass during the 10-year period. Our results indicate that functional group abundance may shift from grasses and sedges toward more legumes and forbs, and that species composition is becoming more similar between grassland types, and thus, beta diversity is decreasing in the permafrost region of Tibet.

Keywords: productivity, resampling, climate warming, species richness, the Tibetan Plateau

OPEN ACCESS

Edited by:
Xiaodong Wu,
Chinese Academy of Sciences (CAS), China

Reviewed by:
Dongliang Luo,
Northwest Institute of Eco-Environment and Resources (CAS), China
Zhenfeng Xu,
Sichuan Agricultural University, China

***Correspondence:**
Genxu Wang
wanggx@scu.edu.cn

Specialty section:
This article was submitted to Interdisciplinary Climate Studies, a section of the journal Frontiers in Environmental Science

Received: *30 April 2022*
Accepted: *09 June 2022*
Published: *17 August 2022*

Citation:
Yang Y, Klanderud K, Yang Y, Jin H, Lu Y, Zhang T and Wang G (2022) Homogenization in Species Composition and No Change in Aboveground Biomass Across Tibetan Permafrost Regions Over Ten Years. Front. Environ. Sci. 10:932993. doi: 10.3389/fenvs.2022.932993

INTRODUCTION

Alpine ecosystems are temperature-limited systems and predicted to be sensitive to climate change (Elmendorf et al., 2015). The projected rate of future warming in the alpine region is also faster than that of the global average (Stocker et al., 2014). Thus, understanding how climate warming affects alpine communities is especially important for our ability to predict impacts of future climate change. An increasing number of studies report shifts in vegetation composition, biomass, and diversity in arctic and alpine tundra (Klein et al., 2004; Walker et al., 2006; Elmendorf et al., 2012a; Elmendorf et al., 2012b; Liu et al., 2018; Yang et al., 2018), and these changes will have cascading effects on the structure and function of alpine ecosystems (Yang et al., 2011; Bjorkman et al., 2018; Niittynen et al., 2020; Wu et al., 2021). For example, experimental warming increases primary productivity and decreases species numbers in the arctic and alpine plant communities (Klein et al., 2004; Elmendorf et al., 2012a; Yang et al., 2015), shifts abundances of different functional groups (Ganjurjav et al., 2016; Liu et al., 2018), and lengthens the growing season leading to advancing leaf and reproduction phenology, and delayed withering (Cleland et al., 2007; Dorji et al., 2013; Meng et al., 2016; Prevéy et al., 2018; Lian et al., 2020). Rapid and accelerating increases in species richness over the past

century have been reported in European mountaintops (Steinbauer et al., 2018), and remote sensing shows vegetation change over the same period in alpine ecosystems (Pattison et al., 2015; Zhu et al., 2016; Verbyla and Kurkowski 2019; May et al., 2020), likely as a result of climate warming.

Most resurvey studies have so far been performed in European mountains, and in areas without permafrost, and observations of changes in plant community composition and productivity over time are confined to site-level experiments (Walker et al., 2006; Elmendorf et al., 2012a; Bjorkman et al., 2018; Yang et al., 2018). Interestingly, a synthesis of long-term monitoring studies across multiple alpine and arctic sites found that forb responses to climate warming differed between sites with and without permafrost (Elmendorf et al., 2012b). Thus, there is a need for more knowledge on recent changes in plant community productivity and species richness across larger permafrost regions to understand how changes in such areas may affect carbon cycling and biodiversity under climate change.

Changes in the aboveground net primary productivity (ANPP) is a crucial factor affecting the carbon cycling of terrestrial ecosystems (Oberbauer et al., 2007; Rodriguez et al., 2018), and may influence the carbon feedback between the terrestrial biosphere and the atmosphere (Shen et al., 2015). Over the past decades, many experimental studies have explored how plant community composition and primary productivity respond to climate change (Franklin et al., 2016; Liu et al., 2017; Ma et al., 2017). Regional-scale evidence for changes in plant productivity has mainly come from remote-sensing data (Piao et al., 2006; Pouliot et al., 2009; Gao et al., 2019) and plant community dynamics from plot-based observations with experimental manipulation (Elmendorf et al., 2012b). There are, however, limitations in both remotely sensed data as these do not identify species-level productivity and diversity (Zhang G. et al., 2013), and in experimental manipulations, which do not reflect realistic climate change (Korell et al., 2019). Broad-scale resurvey studies with sufficient replication of sites can detect region-scale changes in plant species richness (Klanderud and Birks 2003; Gottfried et al., 2012; Pauli et al., 2012; Steinbauer et al., 2018), but few works have historic data for biomass (Ding et al., 2017). Observations of changes in plant community composition and productivity over time are confined to site-level experiments (Walker et al., 2006; Elmendorf et al., 2012a; Bjorkman et al., 2018; Yang et al., 2018).

The Tibetan Plateau has the largest expanse of high-elevation permafrost in the world and has unique ecosystems typically characterized by low temperature, low atmospheric pressure, and oxygen concentrations, and are experiencing climate warming that may jeopardize the functioning of the ecosystems (Klein et al., 2014; He et al., 2021). The presence or absence of permafrost determines the structure and nutrient status of the soil and affects plant community structure and production (Yi et al., 2011; Yang et al., 2018). The grasslands in the permafrost region of the Tibetan Plateau support a diverse assemblage of wildlife and pastoralism as a primary livelihood activity (Klein et al., 2014; Rodriguez et al., 2018). A vegetation greening measured by normalized difference vegetation index (NDVI) in the alpine grasslands of the Tibetan Plateau (Xu et al., 2008; Zhong et al., 2010; Peng et al., 2012; Zhang L. et al., 2013; Zhang et al., 2017) suggests increased plant growth over the past decades. Remotely sensed metrics, such as NDVI, is, however, unable to detect finer-scale changes in plant species diversity and biomass of different functional groups, which are important for understanding ecosystem change (Hopping et al., 2018). Thus, to examine recent changes in functional group biomass and species diversity in Tibet, we performed a resampling study of 36 sites surveyed for the first time in 2008. By revisiting the same sites and using methods as similar as possible to the original survey, we repeated the survey in 2018 to examine the following questions: 1) Have plant community diversity and evenness, biomass, cover, and species richness of different functional groups changed during the 10 years? 2) Are there differences in change between grassland types? We tested the hypothesis that climate changes over the past decades increased plant biomass and species richness and diversity in the permafrost region of Tibet, and that graminoids increased more in abundance than forbs, as observed in climate warming experiments in other alpine and arctic regions (Elmendorf et al., 2012a; Yang et al., 2018).

MATERIAL AND METHODS

Study Area

Permafrost on the Tibetan Plateau covers 1.5 million km^2, approximately half the area of the plateau. It accounts for 70.5% of the permafrost area in high Asia and 75% of the permafrost in the Northern Hemisphere mountains (Yang et al., 2010). The mean annual air temperature on the plateau ranges from −3.1 to 4.4°C, and the mean annual precipitation ranges from 103 to 694 mm (Ding et al., 2017). During the past three decades, the plateau has experienced an increase in the mean annual air temperature of 0.5°C per decade and soil temperature of 0.6°C per decade at 10 cm depths. Precipitation and soil moisture also increased over the past three decades (Ding et al., 2017). Observational data from monitoring stations on the plateau indicate that the mean annual permafrost temperature at 6.0 m depth increased by 0.43°C from 1996 to 2006 at an average annual rate of 0.04°C (Wu and Zhang 2008), and increased by 0.1°C from 2006 to 2010 at an average annual rate of 0.02°C (Wu et al., 2012). Alpine grasslands, which consist primarily of alpine meadow and alpine steppe vegetation, cover more than two-thirds of the plateau (Xu et al., 2017). In our 36 resurvey sites, the dominant species in the alpine meadow are cold-tolerant sedges, such as *Kobresia pygmaea*, *K. humilis*, and *K. tibetica*, and in the alpine steppe, common species are the grass *Stipa purpurea* and the sedge *Carex moorcroftii*. Major soil types are cambisols in the meadow and xerosols in the steppe (Lu et al., 2004).

Vegetation Resampling

To detect changes in plant community biomass and species richness across the Tibetan alpine permafrost regions, we compiled a broad-scale repeated-sampling based on the field

campaigns in 2008 and 2018. Both campaigns were conducted during the growing season from 20 July to 20 August. The sampling sites span elevations from 4,300 to 5,130 m, and were set along the Qinghai–Xizang Highway to cover the permafrost area across a 600-km range from the northern boundary of permafrost at Xidatan to the southern boundary at Anduo (Zou et al., 2017). Each of the 36 sites was surveyed in both 2008 and 2018 (**Supplementary Figure S1**). Plant community survey and biomass sampling was performed using the same sampling scheme in both years. Specifically, the sites were established 1 km away from the highway, and consisted of six 1 × 1 m^2quadrats randomly located in a 20 × 20 m^2 plot at each site in 2008. In 2018, we established six new 1 × 1 m^2 quadrats in the same 20 × 20 m^2 plot. We recorded plant species composition and cover in each 1 × 1 m^2 quadrat, and harvested live aboveground biomass of each species at peak biomass in both years. We harvested all individuals of each species in each quadrate, and put each species of each quadrate in separate paper bags. All the samples were oven dried at 70°C and weighted on a semi-analytical balance in the lab.

Climate and Grazing Data

The monthly air temperature and precipitation data for each site between 2008 and 2018 were extracted from the nearest grids in the surface gridded product (ground resolution 0.5°) of the China Meteorological Data Service Center of National Meteorological Information Center, China (http://data.cma.cn/data/cdcdetail/dataCode/SURF_CLI_CHN_TEM_MON_GRID_0.5.html; http://data.cma.cn/data/cdcdetail/dataCode/SURF_CLI_CHN_PRE_MON_GRID_0.5.html). Given the potential grazing effects on vegetation during the resurvey period, data on the numbers of grazing livestock were collected by grassland monitoring stations in Qumalai county and Tanggula area for each year from 2008 to 2018, which covered the majority of the resurveyed sites in this study (**Supplementary Figure S1**).

Statistical Analyses

We calculated the total plant community biomass, number of species, and cover of different functional groups for each plot and year. Diversity, using Shannon's diversity index (H), was calculated as $H = -\sum p_i (\ln [p_i])$, where p_i is the proportion of a particular species cover in plot. Evenness (E) was calculated from diversity (H) and species richness (S) as $E = \log(H)/\ln(S)$.

We obtained change values of paired samples between 2018 and 2008. We transformed the change values into relative change ratios by dividing the mean values over the study period and then we calculated the estimates and 95% confidence intervals of the change ratios for all the response variables. Thus, significant changes in these variables between 2008 and 2018 are shown if the confidence intervals are not crossing the zero line. Change in aboveground biomass, species richness, plant cover, diversity, and evenness over time was analyzed separately using repeated-measures mixed effects models with the year and the interaction between year and grassland type (alpine meadow and alpine steppe) as fixed effects and plot nested in block as random effects.

To examine if species richness changed more in some plant families than others, we tested difference in species numbers for each family between 2008 and 2018 using a *t*-test. To determine the effects of year on species composition of all species, we performed permutational multivariate analyses of variance (PERMANOVA) on the species abundance using Bray–Curtis distance matrices. For testing the effect of years between 2008 and 2018, we defined a restricted permutation design with sampling within plots in different years permuted as time series. Furthermore, to visualize differences in community composition between 2008 and 2018, we performed a nonmetric multidimensional scaling analysis using Bray–Curtis distance matrices, three dimensions (k = 3) to meet the stress criterion of <0.2 (Clarke 1993). All analyses were performed in R version 4.0.0 (R Development Core Team, 2019).

RESULTS

There was a gradual decrease in summer precipitation and increase in summer temperature during the study period from 2008 to 2018 across all sites (**Figures 1A,B**). Although the total aboveground biomass did not change over time (**Table 1**), some functional groups changed depending on the grassland type (**Table 1**; **Figure 2**). Specifically, we found a marginal increase in legume biomass in steppe and forb biomass in both steppe and meadow, and a decreasing tendency in grass and sedge biomass between 2008 and 2018 in both meadow and steppe (**Figure 2**).

Total species richness increased at 22 of the 36 sites between 2008 and 2018, with a mean increase of 2.1 species per site, but this was not statistically significant across the grassland types (**Table 1**; **Figure 3**). Only the number of legume species decreased significantly over time, particularly in the meadows (**Table 1**; **Figure 3**). There was also a tendency toward decreased species richness of grasses and sedges in the meadows, leading to a decrease in total species richness here (**Figure 3**). In the steppe, on the other hand, forbs and total species richness appeared to increase between 2008 and 2018 (**Figure 3**). When testing the changes per plant family, there was a significant increase in species richness for Asteraceae, Scrophulariaceae, Gentianaceae, Umbelliferae, Crassulaceae, Papaeraceae, Ranunculaceae, and Liliaceae species between 2008 and 2018 (**Supplementary Table S1**).

Legume, forb, and total vegetation cover increased over time in both meadow and steppe (**Table 1**; **Figure 4**). Diversity appeared to increase in the steppe (**Figure 5**), whereas evenness increased in both the grassland types (**Table 1**; **Figure 5**).

The NMDS showed that species composition is clearly distinguished between the two grassland types, meadow and steppe, but that species composition is becoming slightly more similar over time (**Figure 6**; **Table 2**).

DISCUSSION

Our resampling of alpine grasslands in the Tibetan Plateau shows that the total community-level primary production and

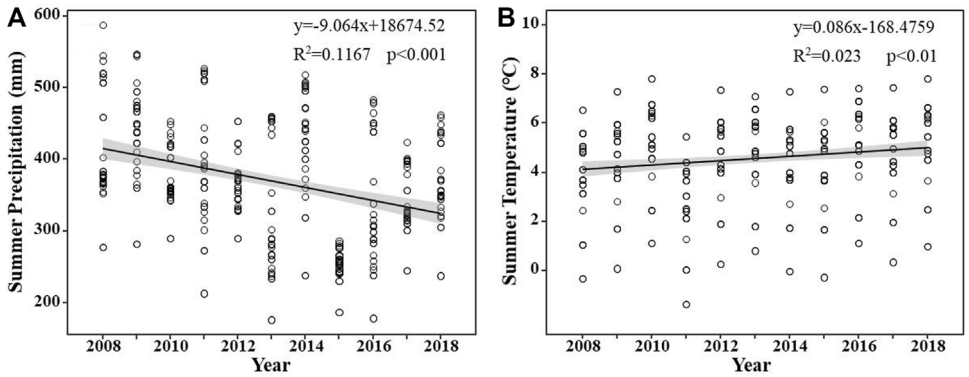

FIGURE 1 | Summer precipitation **(A)** and air temperature **(B)** between 2008 and 2018 in all the sites we surveyed in the permafrost region of the Tibetan Plateau. Solid circle, alpine meadow; blank circle, alpine steppe.

TABLE 1 | Results of the mixed effect model testing for the effects of year (2008 vs. 2018), grassland type (meadow vs. steppe), and the interaction between year and grassland type on aboveground biomass, species richness, and plant cover of all species, grasses, sedges, legumes, and forbs, and diversity and evenness. Asterisks denote significant differences at $p < 0.05$*, $p < 0.01$**, $p < 0.001$***.

Response variable	Year			Grassland type			Year:grassland type		
	df	F	*p*	df	F	*P*	df	F	*P*
Aboveground biomass									
All species	1, 34	1.908	0.176	1, 33	1.035	0.316	1, 34	1.284	0.265
Grasses	1, 34	0.405	0.529	1, 33	12.829	**	1, 34	0.596	0.445
Sedges	1, 34	3.516	0.069	1, 33	14.191	***	1, 34	3.027	0.090
Legumes	1, 34	0.362	0.551	1, 33	9.155	**	1, 34	3.670	0.063
Forbs	1, 34	0.084	0.774	1, 33	8.881	**	1, 34	2.419	0.129
Species richness									
All species	1, 34	1.139	0.293	1, 33	0.000	0.983	1, 34	0.056	0.814
Grasses	1, 34	1.472	0.233	1, 33	8.805	**	1, 34	1.061	0.310
Sedges	1, 34	1.514	0.227	1, 33	7.059	*	1, 34	1.032	0.317
Legumes	1, 34	7.119	*	1, 33	11.972	*	1, 34	0.400	0.531
Forbs	1, 34	0.377	0.543	1, 33	0.487	0.490	1, 34	0.239	0.628
Cover (%)									
Total cover	1, 34	4.720	*	1, 33	24.844	***	1, 34	0.126	0.724
Grasses	1, 34	0.016	0.900	1, 33	9.304	**	1, 34	6.378	*
Sedges	1, 34	4.848	*	1, 33	42.020	***	1, 34	0.789	0.380
Legumes	1, 34	0.095	0.760	1, 33	0.025	0.875	1, 34	0.231	0.634
Forbs	1, 34	13.826	***	1, 33	1.040	0.315	1, 34	0.071	0.791
Diversity	1, 34	3.375	0.074	1, 33	10.096	**	1, 34	0.298	0.588
Evenness	1, 34	8.266	**	1, 33	15.560	***	1, 34	0.253	0.618

total species richness did not change over the 10-year study period (**Table 1**), in contrast to our hypothesis, but vegetation cover and evenness increased. However, the different functional groups showed different tendencies over 10 years, with grasses and sedges tending to decrease, and forbs and legumes increasing in biomass and cover, in contrast to our hypothesis.

The increase of forbs in our study is, interestingly, in line with Elmendorf et al. (2012b), who found that forb abundance increased under climate warming only in sites with permafrost. These results are also in line with the warming experiments in the same mesic meadows, which showed decreased grass and sedge, and increased legume and forb productivity (Yang et al., 2015), likely due to the interspecific competition rather than a direct response to warming. These results may also show compensatory interactions among functional groups (Bai et al., 2004; Connell and Ghedini, 2015; Liu et al., 2017), suggesting that a species increase in abundance is a response to the reduction of another in a fluctuating environment (Naeem and Li 1997). The lack of change in total biomass from 2008 to 2018 in our study is in line with a previous study resampling biomass in the same region (Ding et al., 2017) and in a long-term monitoring experiment in a mesic meadow of northeastern Tibet (Liu et al., 2017; Wang et al., 2020). These results are, however, in contrast to alpine and arctic tundra elsewhere, where increased height of the vegetation canopy in most areas indicate increasing biomass (Elmendorf et al., 2012a; Myers-Smith et al., 2015). One

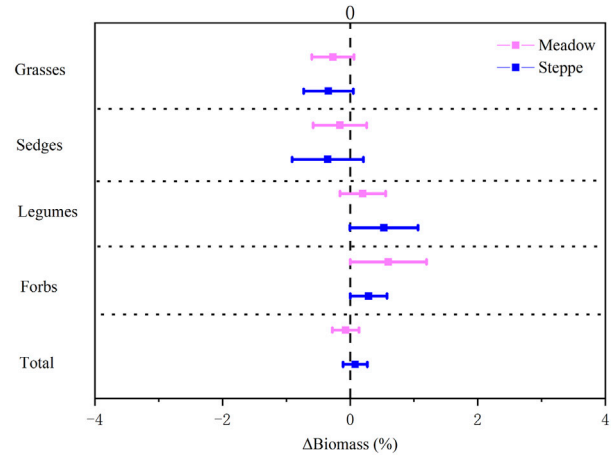

FIGURE 2 | Changes in biomass of grasses, sedges, legumes, forbs, and total biomass in alpine meadow (red) and steppe (blue) from 2008 to 2018 in the permafrost region of the Tibetan Plateau. Relative change rate in aboveground biomass (ΔBiomass %) was calculated as the ratio of the absolute change (in units of g m^{-2}) to the mean biomass over the study period. Data are shown as estimate ±95% confidence intervals (CI). Data greater than zero represent a significant increase in the measured variable, and data lower than zero represent a significant decrease between 2008 and 2018.

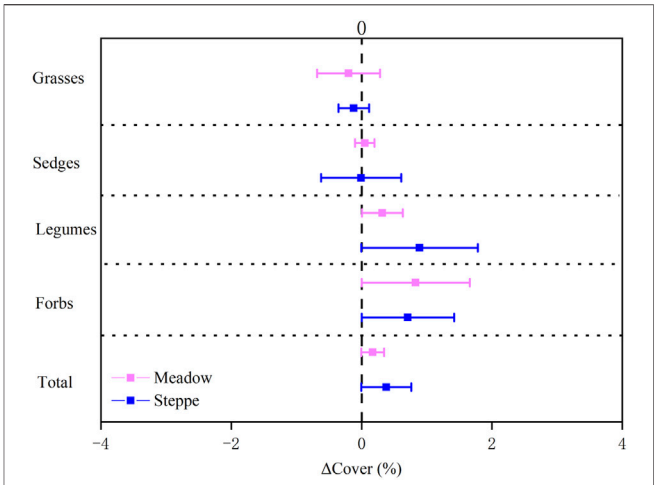

FIGURE 4 | Change in grass, sedge, legume, forb, and total plant cover in alpine meadow (red) and steppe (blue) from 2008 to 2018 in the permafrost region of the Tibetan Plateau. The relative change rate in cover (ΔCover, %) was calculated as the ratio of the absolute change (in units of %) to the mean cover value over the study period. Data were shown as estimate ±95% confidence intervals (CI). Data greater than zero represent a significant increase in the measured variable, and data lower than zero represent a significant decrease between 2008 and 2018.

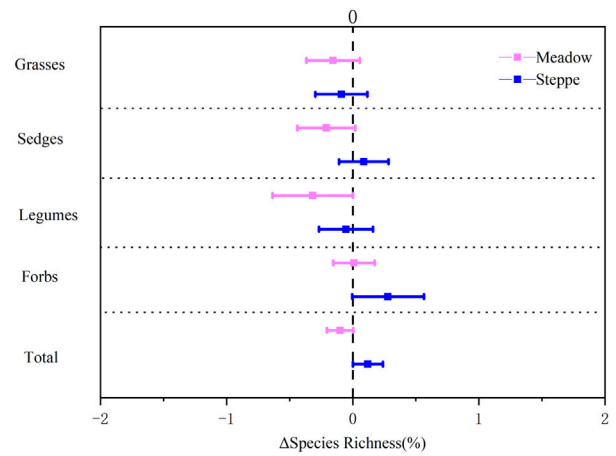

FIGURE 3 | Change in species richness of grasses, sedges, legumes, forbs, and all species in alpine meadow (red) and steppe (blue) from 2008 to 2018 in the permafrost region of the Tibetan Plateau. Relative change rate in the number of species (ΔSpecies Richness) was calculated as the ratio of the absolute change (in units of species m^{-2}) to the mean species richness over the study period. Data are shown as estimate ±95% confidence intervals (CI). Data greater than zero represent a significant increase in the measured variable, and data lower than zero represent a significant decrease between 2008 and 2018.

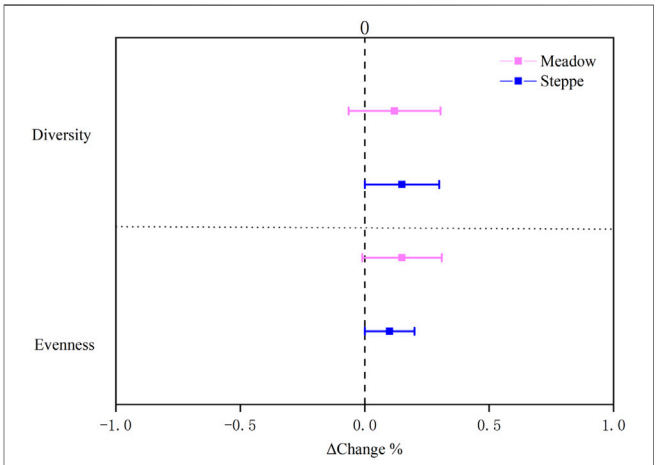

FIGURE 5 | Change in diversity and evenness in alpine meadow (red) and steppe (blue) grasslands from 2008 to 2018 in the permafrost region of the Tibetan Plateau. Relative change rate (ΔChange) was calculated as the ratio of the absolute change to the mean value over the study period. Data were shown as estimate ±95% confidence intervals (CI). Data greater than zero represent a significant increase in measured variable, and lower than zero represent a significant decrease between 2008 and 2018.

important difference between our study area in Tibet and alpine and arctic tundra elsewhere is the more extensive grazing by livestock in the Tibetan Plateau. This grazing pressure has been relatively stable during the last decades (**Supplementary Figure S2**), and may have buffered an increase in biomass due to climate change. The basic characteristic of degraded alpine grasslands is decreased numbers of graminoids (Zhou et al., 2005), as we found in our study (**Figure 3**; **Table 1**). Many of the forb species that increased in cover (**Figure 4**; **Table 1**), such as the *Cremanthodium liheare*, *Saussurea graminea*, *Leontopodium leontopodioides*, *Ajania tenuifolia*, *Pedicularis kansuensis*, and

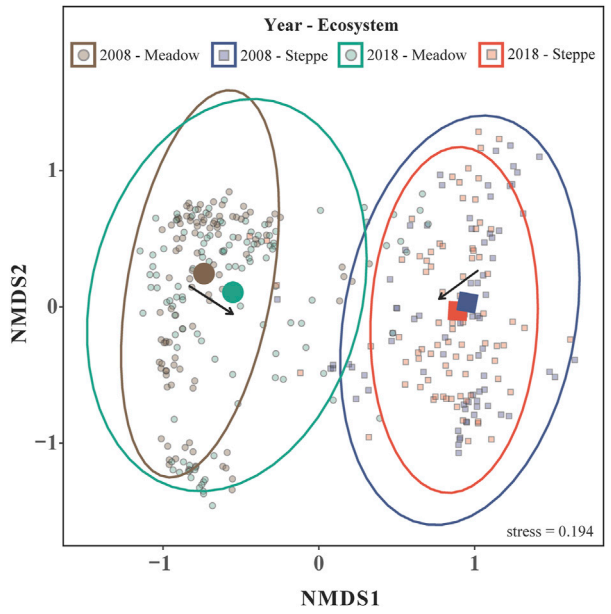

FIGURE 6 | Nonmetric dimensional scaling (NMDS) analysis showing differences in plant species composition between 2008 and 2018 for alpine meadow and steppe communities in the permafrost region of the Tibetan Plateau along the first and second NMDS axes.

TABLE 2 | Results of permutational multivariate analysis of variance (PERMANOVA) using Bray–Curtis distance matrices, testing for the effect of year on community species composition from both 2008 and 2018. Asterisks denote significant differences at $p < 0.01$ (**), $p < 0.001$ (***).

	All species community composition				
	df	SS	R^2	F	p
Year	1	3.852	0.027	10.481	***
Residuals	374	137.459	0.972	—	—
Total	375	141.311	1.000	—	—

Number of permutations: 5,000

Gentiana leucomelaena Maxim., are toxic weeds and not preferred by animals (Zhao 2009; Wang and Kang 2011). Thus, the decrease in grass and sedge biomass observed in our study and others, and the increase in forbs (**Figure 2**), may lead to a decrease in forage quality in the alpine grasslands of Tibet.

Changes in species richness mainly depended on grassland type in our study (**Table 1**). Number of grass, sedge, and legume species showed a decreasing tendency, leading to decreased total species richness in the meadow, which is in line with the results of *in situ* warming experiments reporting decreased species richness in Tibet (Klein et al., 2004; Yang et al., 2018) and in other alpine and arctic regions (Hollister et al., 2005). However, the overall community diversity and evenness increased, and, although not statistically significant, species richness increased in 61% of the sites we resurveyed, most of them in the steppe grasslands. These results are in line with the resurveys of European mountain summits, where the number of species increased during recent decades (Pauli et al., 2012; Steinbauer et al., 2018). The lack of a strong species richness effect may be due to the relatively short period of 10 years in our study. Interestingly, species composition in the two grassland types became more similar during the 10 years (**Figure 6**; **Table 2**). This homogenization is in line with a resampling study from alpine Norway, which also showed homogenization in species composition over time (Odland et al., 2010).

The increase in the total plant cover in our study is in line with increased greening measured as NDVI in the alpine grassland of Tibet (Peng et al., 2012; Zhang et al., 2017). The lack of change in the total biomass production, thus, indicates that NDVI cannot simply be translated into biomass.

Summer precipitation decreased and summer temperature increased in the study area during the study period (**Figure 1**). The observed decreased tendency in grasses and sedges may be due to shallow roots and thus difficulty in acquiring deeper soil water than the more deep-rooted forbs (Klein et al., 2007). Deep soil moisture and temperature have been shown to be the main drivers of legume species richness (Ganjurjav et al., 2016), and the increase in legume biomass in our study over time is in line with site-level experiments, finding that legumes increased in abundance after four years of warming (Peng et al., 2020). Legumes may increase their abundance in sites where soil moisture (Cowles et al., 2016; Ganjurjav et al., 2016) and nitrogen are limited by cryoturbation induced by warming, leading to nitrogen deficiency in the upper soil layer (Chang et al., 2017).

In conclusion, we found that overall biomass and species richness of the alpine grasslands of the permafrost region of Tibet studied here have been relatively stable during the last decade (**Table 1**). This can be due to the relatively short term of the study, but also due to a potential buffering by the grazing livestock. Homogenization in species composition over time indicated decreased beta diversity, and the observed change tendencies in different functional groups may suggest a decrease in forage quality through a shift from grasses and sedges to less preferred legumes and forbs. Given the important contribution of forage quality to local husbandry, these findings are important when formulating management policies for the permafrost region of Tibet.

DATA AVAILABILITY STATEMENT

The original contributions presented in the study are included in the article/**Supplementary Material**. Further inquiries can be directed to the corresponding author.

AUTHOR CONTRIBUTIONS

YaY and GW collected samples and field data. YaY analyzed data, and YaY, YiY, and HJ drew figures. TZ and YL provided data about grazing and climate. YaY, KK, and GW designed or advised

on the experiment and paper writing. YaY and KK led the study and all authors provided edits on the manuscript.

FUNDING

This study was supported by the Strategic Priority Research Program of the Chinese Academy of Sciences (No. XDA20050102 and No. XDA23060601), "Kunlun Talents · Senior Innovation and Entrepreneurship Talents" project of the People's Government of Qinghai Province, and the National Natural Science Foundation of China (41571204, 41861134039, 41701081, and 42061013). Our gratitude extends to the administration bureau of three-River-Rource National Park, the Fenghuoshan Field Station of the Northwest Research Institute Co., Ltd. of the China Railway Engineering Corporation and Beiluhe Observation and Research Station on Frozen Soil Engineering and Environment, Northwest Institute of Eco-Environment and Resources, CAS, for their assistance in the field and the Alpine Ecosystem Observation and Experiment Station of Mt. Gongga, CAS, for their assistance with Laboratory work.

ACKNOWLEDGMENTS

We thank Prof. Lianwen Zhao, Yao Xiao, and Tao Zhang for helping in early data analysis and field work and Tang Chuanchuan, Yang Kai, and Zeng Fang for helping in the laboratory. We appreciate Prof. Guoying Zhou in the Northwest Institute of Plateau Biology, CAS in the initial field work stage.

SUPPLEMENTARY MATERIAL

The Supplementary Material for this article can be found online at: https://www.frontiersin.org/articles/10.3389/fenvs.2022.932993/full#supplementary-material

REFERENCES

Bai, Y. F., Han, X. G., Wu, J. G., Chen, Z. Z., and Li, L. H. (2004). Ecosystem Stability and Compensatory Effects in the Inner Mongolia Grassland. *Nature* 431, 181–184.

Bjorkman, A. D., Myers-Smith, I. H., Elmendorf, S. C., Normand, S., Rüger, N., Beck, P. S. A., et al. (2018). Plant Functional Trait Change across a Warming Tundra Biome. *Nature* 562 (7725), 57–62. doi:10.1038/s41586-018-0563-7

Chang, R. Y., Wang, G. X., Yang, Y. H., and Chen, X. P. (2017). Experimental Warming Increased Soil Nitrogen Sink in the Tibetan Plateau. *J. Geophy. Res. Biogeo.* 122.

Clarke, K. R. (1993). Non-parametric Multivariate Analyses of Changes in Community Structure. *Austral Ecol.* 18, 117–143. doi:10.1111/j.1442-9993.1993.tb00438.x

Cleland, E. E., Chuine, I., Menzel, A., Mooney, H. A., and Schwartz, M. D. (2007). Shifting Plant Phenology in Response to Global Change. *Trends Ecol. Evol.* 22, 357–365.

Connell, S. D., and Ghedini, G. (2015). Resisting Regime-Shifts: The Stabilising Effect of Compensatory Processes. *Trend Ecol. Evol.* 30 (9), 513–515.

Cowles, J. M., Wragg, P. D., Wright, A. J., Powers, J. S., and Tilman, D. (2016). Shifting Grassland Plant Community Structure Drives Positive Interactive Effects of Warming and Diversity on Aboveground Net Primary Productivity. *Glob. Change Biol.* 22, 741–749. doi:10.1111/gcb.13111

Ding, J., Chen, L., Ji, C., Hugelius, G., Li, Y., Liu, L., et al. (2017). Decadal Soil Carbon Accumulation across Tibetan Permafrost Regions. *Nat. Geosci.* 10, 420–424. doi:10.1038/ngeo2945

Dorji, T., Totland, Ø., Moe, S. R., Hopping, K. A., Pan, J. B., and Klein, J. A. (2013). Plant Functional Traits Mediate Reproductive Phenology and Success in Response to Experimental Warming and Snow Addition in Tibet. *Glob. Change Biol.* 19, 459–472.

Elmendorf, S. C., Henry, G. H. R., Hollister, R. D., Björk, R. G., Bjorkman, A. D., Callaghan, T. V., et al. (2012a). Global Assessment of Experimental Climate Warming on Tundra Vegetation: Heterogeneity over Space and Time. *Ecol. Lett.* 15, 164–175. doi:10.1111/j.1461-0248.2011.01716.x

Elmendorf, S. C., Henry, G. H. R., Hollister, R. D., Björk, R. G., Boulanger-Lapointe, N., Cooper, E. J., et al. (2012b). Plot-scale Evidence of Tundra Vegetation Change and Links to Recent Summer Warming. *Nat. Clim. Change* 2, 453–457. doi:10.1038/nclimate1465

Elmendorf, S. C., Henry, G. H. R., Hollister, R. D., Fosaa, A. M., Gould, W. A., Hermanutz, L., et al. (2015). Experiment, Monitoring, and Gradient Methods Used to Infer Climate Change Effects on Plant Communities Yield Consistent Patterns. *Proc. Natl. Acad. Sci. USA.* 112, 448–452.

Franklin, J., Serra-Diaz, J. M., Syphard, A. D., and Regan, H. M. (2016). Global Change and Terrestrial Plant Community Dynamics. *Proc. Natl. Acad. Sci. U.S.A.* 113, 3725–3734. doi:10.1073/pnas.1519911113

Ganjurjav, H., Gao, Q., Gornish, E. S., Schwartz, M. W., Liang, Y., Cao, X., et al. (2016). Differential Response of Alpine Steppe and Alpine Meadow to Climate Warming in the Central Qinghai-Tibetan Plateau. *Agric. For. Meteorology* 223, 233–240. doi:10.1016/j.agrformet.2016.03.017

Gao, M., Piao, S., Chen, A., Yang, H., Liu, Q., Fu, Y. H., et al. (2019). Divergent Changes in the Elevational Gradient of Vegetation Activities over the Last 30 Years. *Nat. Commun.* 10, 2970. doi:10.1038/s41467-019-11035-w

Gottfried, M., Pauli, H., Futschik, A., Akhalkatsi, M., Barančok, P., Benito Alonso, J. L., et al. (2012). Continent-wide Response of Mountain Vegetation to Climate Change. *Nat. Clim. Change* 2 (2), 111–115. doi:10.1038/nclimate1329

He, J.-S., Dong, S., Shang, Z., Sundqvist, M. K., Wu, G., and Yang, Y. (2021). Above-belowground Interactions in Alpine Ecosystems on the Roof of the World. *Plant Soil* 458, 1–6. doi:10.1007/s11104-020-04761-4

Hollister, R. D., Webber, P. J., and Tweedie, C. E. (2005). The Response of Alaskan Arctic Tundra to Experimental Warming: Differences between Short- and Long-Term Responses. *Glob. Change Biol.* 11, 525–536. doi:10.1111/j.1365-2486.2005.00926.x

Hopping, K. A., Yeh, E. T., and Harris, R. B.Gaerrang (2018). Linking People, Pixels, and Pastures: a Multi-Method, Interdisciplinary Investigation of How Rangeland Management Affects Vegetation on the Tibetan Plateau. *Appl. Geogr.* 94, 147–162. doi:10.1016/j.apgeog.2018.03.013

Klanderud, K., and Birks, H. J. B. (2003). Recent Increases in Species Richness and Shifts in Altitudinal Distributions of Norwegian Mountain Plants. *Holocene* 13 (1), 1–6. doi:10.1191/0959683603hl589ft

Klein, J. A., Harte, J., and Zhao, X.-Q. (2004). Experimental Warming Causes Large and Rapid Species Loss, Dampened by Simulated Grazing, on the Tibetan Plateau. *Ecol. Lett.* 7, 1170–1179. doi:10.1111/j.1461-0248.2004.00677.x

Klein, J., Harte, J., and Zhao, X. Q. (2007). Experimental Warming, not Grazing, Decreases Rangeland Quality on the Tibetan Plateau. *Ecol. Appl.* 17 (2), 541–557.

Klein, J. A., Hopping, K. A., Yeh, E. T., Nyima, Y., Boone, R. B., and Galvin, K. A. (2014). Unexpected Climate Impacts on the Tibetan Plateau: Local and Scientific Knowledge in Findings of Delayed Summer. *Glob. Environ. Change* 28, 141–152. doi:10.1016/j.gloenvcha.2014.03.007

Korell, L., Auge, H., Chase, J. M., Harpole, S., and Knight, T. M. (2019). We Need More Realistic Climate Change Experiments for Understanding Ecosystems of the Future. *Glob. Change Biol.* 26, 325–327. doi:10.1111/gcb.14797

Lian, X., Piao, S., Li, L. Z. X., Li, Y., Huntingford, C., Ciais, P., et al. (2020). Summer Soil Drying Exacerbated by Earlier Spring Greening of Northern Vegetation. *Sci. Adv.* 6, eaax0255. doi:10.1126/sciadv.aax0255

Liu, H., Mi, Z., Lin, L., Wang, Y., Zhang, Z., Zhang, F., et al. (2017). Shifting Plant Species Composition in Response to Climate Change Stabilizes Grassland Primary Production. *Proc. Natl. Acad. Sci. U. S. A.* 115 (16), 4051–4056. doi:10.1073/pnas.1700299114

Liu, H. Y., Mi, Z. R., Lin, L., Wang, Y. H., Zhang, Z. H., Zhang, F. W., et al. (2018). Shifting Plant Species Composition in Response to Climate Change Stabilizes Grassland Primary Production. *Proc. Natl. Acad. Sci. USA.* 115 (16), 4051–4058.

Lu, H. Y., Wu, N., Gu, Z., Wang, L., Wu, H., Wang, G., et al. (2004). Distribution of Carbon Isotope Composition of Modern Soils on the Qinghai-Tibetan Plateau. *Biogeochem* 70, 273–297. doi:10.1023/b:biog.0000049343.48087.ac

Ma, Z., Liu, H., Mi, Z., Zhang, Z., Wang, Y., Xu, W., et al. (2017). Climate Warming Reduces the Temporal Stability of Plant Community Biomass Production. *Nat. Commun.* 8, 15378. doi:10.1038/ncomms15378

May, J. L., Hollister, R. D., Betway, K. R., Harris, J. A., Tweedie, C. E., Welker, J. M., et al. (2020). NDVI Changes Show Warming Increases the Length of the Green Season at Tundra Communities in Northern Alaska: A Fine-Scale Analysis. *Front. Plant Sci.* 11, 1174. doi:10.3389/fpls.2020.01174

Meng, F., Cui, S., Wang, S., Duan, J., Jiang, L., Zhang, Z., et al. (2016). Changes in Phenological Sequences of Alpine Communities across a Natural Elevation Gradient. *Agric. For. Meteorology* 224, 11–16. doi:10.1016/j.agrformet.2016.04.013

Myers-Smith, I. H., Elmendorf, S. C., Beck, P. S. A., Wilmking, M., Hallinger, M., Blok, D., et al. (2015). Climate Sensitivity of Shrub Growth across the Tundra Biome. *Nat. Clim. Change* 5, 887–891. doi:10.1038/nclimate2697

Naeem, S., and Li, S. (1997). Biodiversity Enhances Ecosystem Reliability. *Nature* 390, 507–509. doi:10.1038/37348

Niittynen, P., Heikkinen, R. K., and Luoto, M. (2020). Decreasing Snow Cover Alters Functional Composition and Diversity of Arctic Tundra. *Proc. Natl. Acad. Sci. U. S. A.* 117 (35), 21480–21487. doi:10.1073/pnas.2001254117

Oberbauer, S. F., Tweedie, C. E., Welker, J. M., Fahnestock, J. T., Henry, G. H. R., Webber, P. J., et al. (2007). Tundra CO_2 Fluxes in Response to Experimental Warming across Latitudinal and Moisture Gradients. *Ecol. Monogr.* 77, 221–238. doi:10.1890/06-0649

Odland, A., Høitomt, T., and Olsen, S. L. (2010). Increasing Vascular Plant Richness on 13 High Mountain Summits in Southern Norway since the Early 1970s. *Arct. Antarct. Alp. Res.* 42 (4), 458–470. doi:10.1657/1938-4246-42.4.458

Pattison, R. R., Jorgenson, J. C., Raynolds, M. K., and Welker, J. M. (2015). Trends in NDVI and Tundra Community Composition in the Arctic of NE Alaska between 1984 and 2009. *Ecosystems* 18, 707–719. doi:10.1007/s10021-015-9858-9

Pauli, H., Gottfried, M., Dullinger, S., Abdaladze, O., Akhalkatsi, M., Alonso, J. L. B., et al. (2012). Recent Plant Diversity Changes on Europe's Mountain Summits. *Science* 336, 353–355. doi:10.1126/science.1219033

Peng, A., Klanderud, K., Wang, G., Zhang, L., Xiao, Y., and Yang, Y. (2020). Plant Community Responses to Warming Modified by Soil Moisture in the Tibetan Plateau. *Arct. Antarct. Alp. Res.* 52 (1), 60–69. doi:10.1080/15230430.2020.1712875

Peng, J., Liu, Z., Liu, Y., Wu, J., and Han, Y. (2012). Trend Analysis of Vegetation Dynamics in Qinghai-Tibet Plateau Using Hurst Exponent. *Ecol. Indic.* 14, 28–39. doi:10.1016/j.ecolind.2011.08.011

Piao, S., Fang, J., Zhou, L., Ciais, P., and Zhu, B. (2006). Variations in Satellite-Derived Phenology in China's Temperate Vegetation. *Glob. Change Biol.* 12, 672–685. doi:10.1111/j.1365-2486.2006.01123.x

Pouliot, D. A., Rasim, L., and Ian, O. (2009). Trends in Vegetation NDVI From 1km AVHRR Data Over Canada for the Period 1985–2006. *Int. J. Remote Sens.* 30 (1), 149–168.

Prevéy, J. S., Rixen, C., Rüger, N., Høye, T. T., Bjorkman, A. D., Myers-Smith, I. H., et al. (2019). Warming Shortens Flowering Seasons of Tundra Plant Communities. *Nat. Ecol. Evol.* 3, 45–52. doi:10.1038/s41559-018-0745-6

Rodriguez, A. M., Jacobo, E. J., and Golluscio, R. A. (2018). Glyphosate Alters Aboveground Net Primary Production, Soil Organic Carbon, and Nutrients in Pampean Grasslands (Argentina). *Rangel. Ecol. Manag.* 71, 119–125. doi:10.1016/j.rama.2017.07.009

R Development Core Team (2019). *R: A Language and Environment for Statistical Computing*. Vienna, Austria: R foundation for statistical computing.

Shen, M., Piao, S., Jeong, S.-J., Zhou, L., Zeng, Z., Ciais, P., et al. (2015). Evaporative Cooling over the Tibetan Plateau Induced by Vegetation Growth. *Proc. Natl. Acad. Sci. U.S.A.* 112 (30), 9299–9304. doi:10.1073/pnas.1504418112

Steinbauer, M. J., Grytnes, J.-A., Jurasinski, G., Kulonen, A., Lenoir, J., Pauli, H., et al. (2018). Accelerated Increase in Plant Species Richness on Mountain Summits Is Linked to Warming. *Nature* 556, 231–234. doi:10.1038/s41586-018-0005-6

Stocker, T. F., Qin, D., Plattner, G.-K., Tignor, M., Allen, S. K., Boschung, J., et al. (2014). *Climate Change 2013: The Physical Science Basis: Working Group I Contribution to the Fifth Assessment Report of the Intergovernmental Panel on Climate Change*. Cambridge, UK: Cambridge Univ. Press.

Verbyla, D., and Kurkowski, T. A. (2019). NDVI-climate Relationships in High-Latitude Mountains of Alaska and Yukon Territory. *Arct. Antarct. Alp. Res.* 51 (1), 397–411. doi:10.1080/15230430.2019.1650542

Walker, M. D., Wahren, C. H., Hollister, R. D., Henry, G. H. R., Ahlquist, L. E., Alatalo, J. M., et al. (2006). Plant Community Responses to Experimental Warming across the Tundra Biome. *Proc. Natl. Acad. Sci. U.S.A.* 103 (5), 1342–1346. doi:10.1073/pnas.0503198103

Wang, L. Y., and Kang, H. J. (2011). *Grassland Resources and the Dominated Plants Atlas of Sanjiangyuan Region*. Xining, China: Qinghai People's Publishing House.

Wang, H., Liu, H. Y., Cao, G. M., Ma, Z. Y., Li, Y. K., Zhang, F. W., et al. (2020). Alpine Grassland Plants Grow Earlier and Faster but Biomass Remain Unchanged Over 35 Years of Climate Change. *Ecol. Lett.* 23, 701–710.

Wu, M. H., Chen, S. Y., Chen, J. W., Xue, K., Chen, S. L., Wang, X. M., et al. (2021). Reduced Microbial Stability in the Active Layer Is Associated with Carbon Loss under Alpine Permafrost Degradation. *Proc. Natl. Acad. Sci. U. S. A.* 118 (25), e2025321118. doi:10.1073/pnas.2025321118

Wu, Q. B., and Zhang, T. J. (2008). Recent Permafrost Warming on the Qinghai-Tibetan Plateau. *J. Geophys. Res. Atmos.* 113, D13108. doi:10.1029/2007JD009539

Wu, Q., Zhang, T., and Liu, Y. (2012). Thermal State of the Active Layer and Permafrost along the Qinghai-Xizang (Tibet) Railway from 2006 to 2010. *Cryosphere* 6, 607–612. doi:10.5194/tc-6-607-2012

Xu, Y., Knudby, A., Ho, H. C., Shen, Y., and Liu, Y. (2017). Warming over the Tibetan Plateau in the Last 55 Years Based on Area-Weighted Average Temperature. *Reg. Environ. Change* 17, 2339–2347. doi:10.1007/s10113-017-1163-z

Xu, Z. X., Gong, T. L., and Li, J. Y. (2008). Decadal Trend of Climate in the Tibetan Plateau-Regional Temperature and Precipitation. *Hydrol. Process.* 22 (16), 3056–3065. doi:10.1002/hyp.6892

Yang, M., Nelson, F. E., Shiklomanov, N. I., Guo, D., and Wan, G. (2010). Permafrost Degradation and its Environmental Effects on the Tibetan Plateau: a Review of Recent Research. *Earth-Science Rev.* 103, 31–44. doi:10.1016/j.earscirev.2010.07.002

Yang, Y., Hopping, K. A., Wang, G., Chen, J., Peng, A., and Klein, J. A. (2018). Permafrost and Drought Regulate Vulnerability of Tibetan Plateau Grasslands to Warming. *Ecosphere* 9 (5), e02233. doi:10.1002/ecs2.2233

Yang, Y., Luo, Y., and Finzi, A. C. (2011). Carbon and Nitrogen Dynamics during Forest Stand Development: a Global Synthesis. *New Phytol.* 190, 977–989. doi:10.1111/j.1469-8137.2011.03645.x

Yang, Y., Wang, G., Klanderud, K., Wang, J., and Liu, G. (2015). Plant Community Responses to Five Years of Simulated Climate Warming in an Alpine Fen of the Qinghai-Tibetan Plateau. *Plant Ecol. Div.* 2 (8), 211–218. doi:10.1080/17550874.2013.871654

Yi, S. H., Zhou, Z. Y., Ren, S. L., Xu, M., Qin, Y., Chen, S. Y., et al. (2011). Effects of Permafrost Degradation on Alpine Grassland in a Semi-Arid Basin on the Qinghai-Tibetan Plateau. *Environ. Res. Lett.* 6, 045403.

Zhang, G., Zhang, Y., Dong, J., and Xiao, X. (2013). Green-up Dates in the Tibetan Plateau Have Continuously Advanced from 1982 to 2011. *Proc. Natl. Acad. Sci. U.S.A.* 110 (11), 4309–4314. doi:10.1073/pnas.1210423110

Zhang, L., Guo, H., Ji, L., Lei, L., Wang, C., Yan, D., et al. (2013). Vegetation Greenness Trend (2000 to 2009) and the Climate Controls in the Qinghai-Tibetan Plateau. *J. Appl. Remote Sens.* 7, 073572. doi:10.1117/1.jrs.7.073572

Zhang, W., Zhou, T., and Zhang, L. (2017). Wetting and Greening Tibetan Plateau in Early Summer in Recent Decades. *J. Geophys. Res. Atmos.* 122, 5808–5822. doi:10.1002/2017jd026468

Zhao, X. Q. (2009). *Alpine Meadow Ecosystem and Global Change*. Beijing, China: Science Press.

Zhong, L., Ma, Y., Salama, M. S., and Su, Z. (2010). Assessment of Vegetation Dynamics and Their Response to Variations in Precipitation and Temperature in the Tibetan Plateau. *Clim. Change* 103, 519–535. doi:10.1007/s10584-009-9787-8

Zhou, H., Zhao, X., Tang, Y., Gu, S., and Zhou, L. (2005). Alpine Grassland Degradation and its Control in the Source Region of the Yangtze and Yellow Rivers, China. *Grassl. Sci.* 51, 191–203. doi:10.1111/j.1744-697x.2005.00028.x

Zhu, Z. C., Piao, S., Myneni, R. B., Huang, M., Zeng, Z., Canadell, J. G., et al. (2016). Greening of the Earth and its Drivers. *Nat. Clim. Change* 6, 791–795. doi:10.1038/nclimate3004

Zou, D., Zhao, L., Sheng, Y., Chen, J., Hu, G., Wu, T., et al. (2017). A New Map of Permafrost Distribution on the Tibetan Plateau. *Cryosphere* 11, 2527–2542. doi:10.5194/tc-11-2527-2017

Conflict of Interest: The authors declare that the research was conducted in the absence of any commercial or financial relationships that could be construed as a potential conflict of interest.

Publisher's Note: All claims expressed in this article are solely those of the authors and do not necessarily represent those of their affiliated organizations, or those of the publisher, the editors, and the reviewers. Any product that may be evaluated in this article, or claim that may be made by its manufacturer, is not guaranteed or endorsed by the publisher.

frontiers | Frontiers in Environmental Science

TYPE Original Research
PUBLISHED 25 August 2022
DOI 10.3389/fenvs.2022.893478

OPEN ACCESS

EDITED BY
Wenxin Zhang,
Faculty of Science, Lund University, Sweden

REVIEWED BY
Ko Van Huissteden,
VU Amsterdam, Netherlands
Mousong Wu,
Nanjing University, China

*CORRESPONDENCE
Torben Windirsch,
torben.windirsch@awi.de

SPECIALTY SECTION
This article was submitted to Atmosphere and Climate, a section of the journal Frontiers in Environmental Science

RECEIVED 10 March 2022
ACCEPTED 02 August 2022
PUBLISHED 25 August 2022

CITATION
Windirsch T, Grosse G, Ulrich M, Forbes BC, Göckede M, Wolter J, Macias-Fauria M, Olofsson J, Zimov N and Strauss J (2022), Large herbivores on permafrost— a pilot study of grazing impacts on permafrost soil carbon storage in northeastern Siberia. *Front. Environ. Sci.* 10:893478. doi: 10.3389/fenvs.2022.893478

Large herbivores on permafrost—a pilot study of grazing impacts on permafrost soil carbon storage in northeastern Siberia

Torben Windirsch[1,2]*, Guido Grosse[1,2], Mathias Ulrich[3,4], Bruce C. Forbes[5], Mathias Göckede[6], Juliane Wolter[1,7], Marc Macias-Fauria[8], Johan Olofsson[9], Nikita Zimov[10] and Jens Strauss[1]

[1]Alfred Wegener Institute Helmholtz Centre for Polar and Marine Research, Potsdam, Germany, [2]Department for Geosciences, University of Potsdam, Potsdam, Germany, [3]Institute for Geography, University of Leipzig, Leipzig, Germany, [4]German Federal Environment Agency, Dessau, Germany, [5]Arctic Centre, University of Lapland, Rovaniemi, Finland, [6]Department Biogeochemical Signals, Max Planck Institute for Biogeochemistry, Jena, Germany, [7]Institute of Biochemistry and Biology, University of Potsdam, Potsdam, Germany, [8]Biogeosciences Lab, School of Geography and the Environment, University of Oxford, Oxford, England, [9]Department of Ecology and Environmental Science, Umeå University, Umeå, Sweden, [10]Northeast Science Station, Pacific Institute for Geography, Far-Eastern Branch of Russian Academy of Science, Chersky, Russia

The risk of carbon emissions from permafrost is linked to an increase in ground temperature and thus in particular to thermal insulation by vegetation, soil layers and snow cover. Ground insulation can be influenced by the presence of large herbivores browsing for food in both winter and summer. In this study, we examine the potential impact of large herbivore presence on the soil carbon storage in a thermokarst landscape in northeastern Siberia. Our aim in this pilot study is to conduct a first analysis on whether intensive large herbivore grazing may slow or even reverse permafrost thaw by affecting thermal insulation through modifying ground cover properties. As permafrost soil temperatures are important for organic matter decomposition, we hypothesize that herbivory disturbances lead to differences in ground-stored carbon. Therefore, we analyzed five sites with a total of three different herbivore grazing intensities on two landscape forms (drained thermokarst basin, Yedoma upland) in Pleistocene Park near Chersky. We measured maximum thaw depth, total organic carbon content, $\delta^{13}C$ isotopes, carbon-nitrogen ratios, and sediment grain-size composition as well as ice and water content for each site. We found the thaw depth to be shallower and carbon storage to be higher in intensively grazed areas compared to extensively and non-grazed sites in the same thermokarst basin. First data show that intensive grazing leads to a more stable thermal ground regime and thus to increased carbon storage in the thermokarst deposits and active layer. However, the high carbon content found within the upper 20 cm on intensively grazed sites could also indicate higher carbon input rather than reduced decomposition, which requires further studies including investigations of the hydrology and general ground conditions existing prior to grazing introduction. We explain our findings by intensive animal trampling in winter and vegetation changes, which overcompensate summer ground warming. We conclude that grazing

intensity—along with soil substrate and hydrologic conditions—might have a measurable influence on the carbon storage in permafrost soils. Hence the grazing effect should be further investigated for its potential as an actively manageable instrument to reduce net carbon emission from permafrost.

KEYWORDS

organic material inventory, animal husbandry, bio-geo interactions, rewilding, climate change

Introduction

In the context of global climate warming, carbon emissions from Arctic permafrost regions have been identified as a key source of greenhouse gases (GHGs), further accelerating the permafrost carbon-climate feedback and increasing atmospheric warming (Schuur et al., 2015; Turetsky et al., 2019; Bowen et al., 2020). An estimated 1300 gigatons (Gt) of carbon are stored within the upper 3 m of ground in the permafrost region, of which approximately 1,000 Gt are perennially frozen (Hugelius et al., 2014; Mishra et al., 2021). These 1,300 Gt account for approximately 35% of global soil carbon, with 2,050–2,800 Gt globally present in the top 3 m of non-permafrost regions (Schuur et al., 2015; Jackson et al., 2017; Strauss et al., 2021). With further Arctic warming now and in the future, deposits of organic-rich material embedded in permafrost are expected to become widely available for microbial decomposition and increased GHG production with permafrost thaw (Schuur et al., 2008).

In general, there are processes leading to carbon accumulation in permafrost areas, such as deposition of organic-rich sediments (via aeolian or fluvial transport, Huh et al. (1998); Chlachula (2003)), increased *in situ* biomass accumulation (via increased plant growth, Schuur et al. (2008)), cryoturbation (Kaiser et al., 2007), and animal influence via feces. This last one is linked to increased plant growth by providing easily available nutrients (Grellmann 2002); moreover, the disturbance of the surface layer via trampling mixes fresh organic matter (OM) into the ground, providing additional OM input that adds to the previously permafrost-preserved OM.

Vegetation composition and snow conditions together play major roles in mediating Arctic surface, near-surface, and sub-surface temperature regimes by influencing the land surface energy budget, and thus the belowground carbon cycle. Both vegetation and snow can be heavily influenced by the presence of large herbivorous animals. Plant growth itself affects above and below ground carbon storage as plants take up carbon dioxide from the environment, temporarily fixing carbon in their biomass, while plant litter and roots become components of the active layer of soils (the seasonal thaw layer on top of permafrost). Dense vegetation cover may cause relative ground cooling by reducing summer energy exchange by creating wind protection and a stable air layer between the ground's surface and the canopy (Zhang et al., 2013; Mod and Luoto 2016; te Beest et al., 2016). In winter, shrub vegetation effectively traps snow, leading to locally higher snow accumulation (Domine et al., 2016), hence insulation and therefore maintains relatively warm ground temperatures throughout winter (Sannel 2020). In contrast, graminoid vegetation facilitates ground cooling in winter, as it bends beneath accumulating snow, reducing the volume of air trapped beneath the snow (Blok et al., 2010). In summer, graminoid vegetation is also less insulating, leading to stronger ground warming underneath the canopy. However, this summer effect is offset by the vast difference between summer and winter seasonal length in the Arctic. In this way, graminoids contribute to a net cooling effect (Macias-Fauria et al., 2020). However, due to warming climate and an associated extension of the growing season, an increase in the establishment and growth of shrub vegetation has already been observed (Frost et al., 2013) and is projected to increase in the Arctic tundra regions (Zhang et al., 2013).

Previous studies have reported on the effect of herbivore—mainly reindeer—presence on carbon storage in tundra biomes (Olofsson 2006; Falk et al., 2015; Olofsson and Post 2018; Ylänne et al., 2018). Those investigations mainly focused on the above-ground biomass changes and concluded that the effects of grazing-associated vegetation changes from shrubs to graminoid vegetation enhance soil carbon sequestration and might help reduce soil carbon emissions. In contrast to these findings, Monteath et al. (2021) challenge the idea of a rewilding strategy—reintroducing and promoting (semi-) wild animals—against Arctic carbon emissions, stating that cause and consequence in herbivore extinction and Arctic shrubification are unclear. While their macrofossil analysis suggests that extinction was a consequence of habitat loss in a warming climate, leading to shrub expansion and vegetation shifts, a study using ancient DNA analysis found the opposite (Murchie et al., 2021). Modeling studies have tried to quantify the impact of large herbivores on permafrost soil carbon storage (Zimov et al., 2009; Beer et al., 2020). These modeling exercises and predictions have, however, not yet been tested in the field.

Some researchers have proposed to actively exploit these processes and properties in order to preserve permafrost and limit permafrost carbon emissions as a consequence of a warming climate. The establishment of sufficiently large numbers of herbivores as ecosystem engineers could intensify

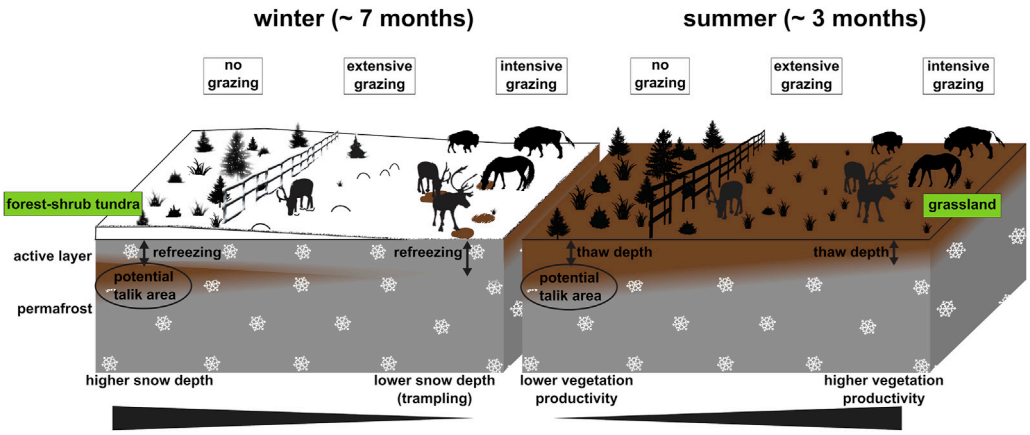

FIGURE 1
Graphical representation of the Pleistocene Park hypothesis (Zimov 2005); Left: during winter time (~60% of the year), a greater number of large animals trample down and/or partly remove the snow cover, facilitating the full refreezing of the active layer; as the active layer refreezes in winter in the graminoid-dominated areas, thawing is reduced compared to non-grazed tundra and forest areas; Right: during summer time (~30% of the year), a greater number of animals enhances a vegetation shift from shrubby towards graminoid-dominated, increasing vegetation productivity but also ground warming by disturbing the heat insulation layer; since the ground under intensive grazing impact is colder and is fully refrozen at the beginning of summer, overall thaw depth is smaller in these areas by the end of summer.

grazing and trampling pressure in today's tundra and forest-tundra landscapes (Olofsson and Post 2018; Beer et al., 2020). During the late Pleistocene, the mammoth steppe was characterized by highly productive grasslands with high grazing pressure by large herbivores. Olofsson et al. (2004) and Zimov (2005) suggested that grazing and trampling in the Arctic reduces shrub abundance. This could help to shift shrubifying tundra ecosystems towards grass and forb dominated ecosystems similar to the mammoth steppe in terms of productivity and thermal insulation properties. Such a vegetation shift is also suggested to cause an albedo increase and hence lower latent and sensible heat fluxes due to overall reduced energy input (te Beest et al., 2016). In winter, dense populations of large herbivores may also affect the insulation effect of snow on the ground by trampling down or removing the dense snow cover in their search for forage, leading to enhanced refreezing of the ground (Figure 1) (Beer et al., 2020).

The Pleistocene Park project, near Chersky in northeastern Siberia, aims to re-establish a megaherbivore-driven system via rewilding of the forest-tundra with greater numbers of modern large and cold-adapted herbivores. These include, among others, musk oxen, Yakutian horses, Kalmyk cattle, bison, and reindeer. With this study focusing on sites in Pleistocene Park, we aim to identify the effects of dense and functionally diverse herbivory pressure on an ice-rich Arctic permafrost landscape. Therefore, we compare belowground carbon and sediment characteristics at five sites in two landscape units with different grazing intensities. We hypothesize that a high large herbivore density and hence intensive grazing and trampling reduces decomposition of preserved OM by reducing ground temperatures. Our work constitutes a pilot study that opens the path for further field-based multi-proxy and multi-disciplinary approaches.

Study area

Our study area, Pleistocene Park, is located in northeastern Siberia in the floodplains of the Kolyma River, approximately 100 km inland from the Arctic Ocean (Figure 2) (Fuchs et al. (2021)). The landscape is characterized by thermokarst lakes, drained thermokarst basins with different depths, and uplands of late-Pleistocene ice- and organic-rich permafrost deposits (i.e., Yedoma; (Schirrmeister et al., 2011; Palmtag et al., 2015).

Climate in this region is characterized by large temperature amplitudes (average of −33°C in January; average of 12°C in July) with a mean annual temperature of -11°C (Göckede et al., 2017). Annual precipitation is 197 mm; March is the driest month (7 mm) and August receives the most precipitation (30 mm). The main seasons for precipitation are summer and autumn (Göckede et al., 2017).

The prevailing deposit types are Yedoma and thermokarst deposits (Veremeeva et al., 2021) with the latter covering approximately 58% of the land area in regions with high Yedoma coverage, and up to 96.4% in regions with low Yedoma deposit occurrence. These deposits are interspersed with marshes, river valleys, and deltas (Veremeeva et al., 2021).

Vegetation within the thermokarst basins generally varies with the local wetness gradient and to some extent with grazing intensity. *Carex appendiculata* tussocks dominate in shallow water around lake margins. In frequently flooded areas, tall

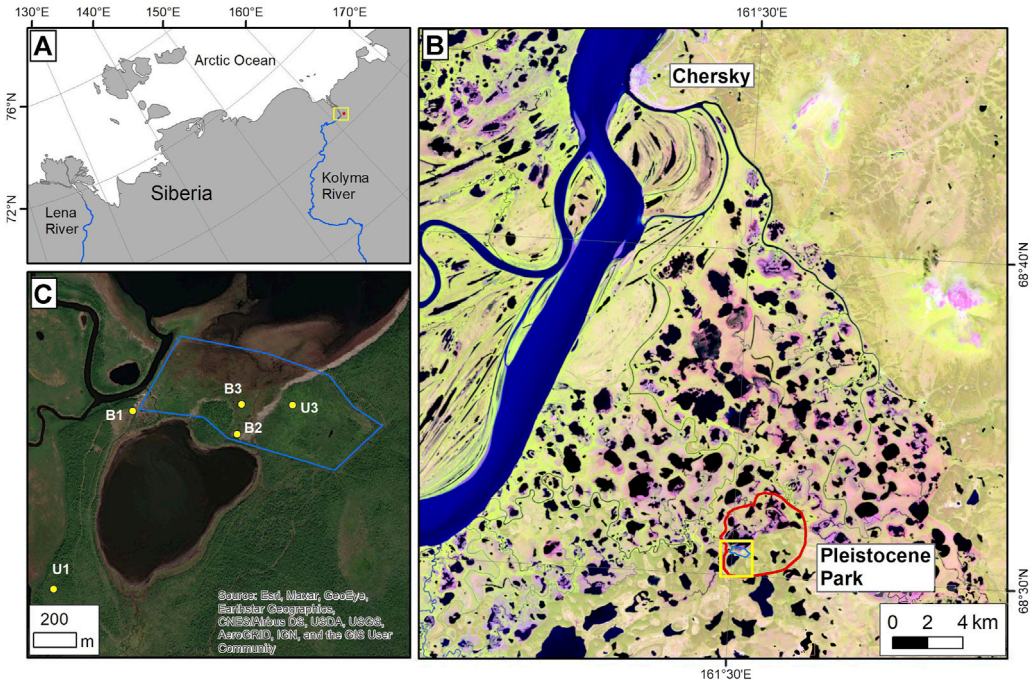

FIGURE 2
Location of the study area in northeastern Siberia marked with a yellow frame **(A)**. In the Landsat-8 satellite image (band combination of shortwave infrared 1 - near infrared - red, 2019-07-04) of panel **(B)** the red line marks the area of Pleistocene Park south of Chersky; the yellow frame indicates the location of the field study sites shown in **(C)**. Panel **(C)** shows a high resolution GeoEye satellite image (2018-07-21; ArcGIS Online base map provided by the Environmental Systems Research Institute, ESRI) with Pleistocene Park fences (blue) and sampling sites labeled as B, indicating drained basin sites, and U, indicating Yedoma upland sites; numbers indicate the grazing intensity of each site, from 1 (no grazing) to 3 (intensive grazing).

grasses (e.g., *Calamagrostis langsdorfii*) grow up to 70 cm high, which is a little higher than in surrounding areas (Corradi et al., 2005). Seasonal flooding typically occurs after snow melt during the spring freshet, temporarily refilling the drained thermokarst basins and covering sampling site B3 (Figure 2). Here, graminoids (mainly *Poaceae*) make up the main vegetation type and show signs of animal grazing (Figure 3, B3). A driftwood belt was present towards the outer basin margins (between B3 and B2 in our study area). The sampling site B2 is located on the elevated reaches of a basin and is characterized by extensively grazed lower-growing graminoid-dominated (*Poaceae*) vegetation with occasional forbs (Figure 3, B2). Towards the edge of the basin, drier ground is covered with dense trees and shrubs (*Larix* spp., *Salix* spp.) up to 2.5 m height, which grow into forests in some places (Figure 2, west of B3 and B2). Sampling site B1 is located on the edge between the basin and the upland and represents a non-grazed surface. It is characterized by grasses (e.g., *Beckmannia syzigachne*, *Hordeum jubatum*), forbs (e.g., *Saxifraga* spp.), *Equisetum* spp., and low-growing shrubs (e.g., *Salix* spp.) (Figure 3, B1). This site was covered in *Larix* forest until deforestation in 2015. A mix of dwarf and taller shrubs (e.g., *Salix* spp.), forbs, and grasses is found on the Yedoma uplands, where sites U3 and U1 are located (Figure 3, U3). Shrubs reach a height of up to 2.5 m. The lower vegetation features diverse forbs, grasses, and *Equisetum* spp. reaching 10–20 cm in height.

The Pleistocene Park project was started in 1996 as a large-scale and long-term ecosystem change experiment (Zimov 2020). For this experiment, a large number of Yakutian horses, Kalmykian cattle, reindeer, bison, and musk oxen as well as moose, sheep, yaks, and European bison—all large and cold-adapted herbivores—were gradually introduced into a 40-ha fenced area, which stretches across tundra and forest-tundra vegetation over a landscape characterized by Yedoma uplands and partially drained thermokarst basins. Today, this 40-ha area is the heartland of a 160 km^2 fenced park that constitutes a unique experimental site for examining rewilding impacts on Arctic ecosystems (Macias-Fauria et al., 2020). The presence of these animals—and some man-made interventions such as removal of trees to build fences on the periphery of the park—has already transformed most of the previous tundra vegetation into grassland, while forest areas are developing towards more open vegetation. However, responses in soil property changes from surface effects, especially below the active layer, are slow, so these deep deposits are most likely not yet influenced by animal activity after a 23-year time period. Long-

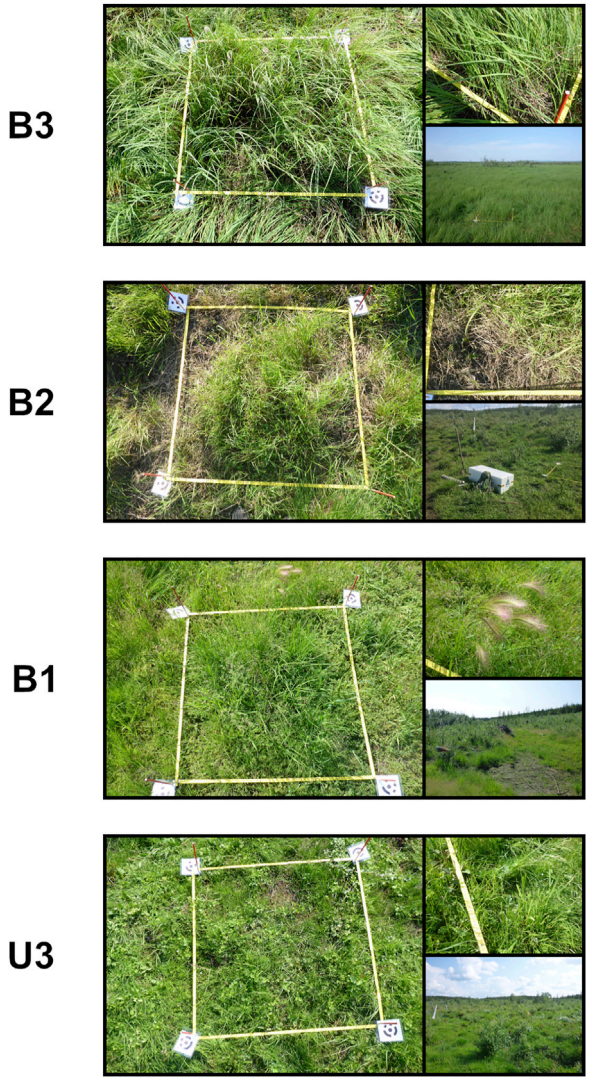

FIGURE 3
Vegetation photos of the study sites sampled in July 2019; each site comprises a 1 by 1 m plot photo (left), a vegetation detail photo (top right) and a landscape photo (bottom right).

term studies on GHG emissions have been conducted in nearby areas of Pleistocene Park. For instance, Göckede et al. (2017); Göckede et al. (2019) investigated the carbon and energy budgets of tundra wetlands and regime shifts related to drainage disturbance on a nearby floodplain of the Kolyma River. They found that an undisturbed wetland, similar to the non-grazed wetlands in the Pleistocene Park area, acted as a moderate annual sink for CO_2, and as a moderate source for CH_4. Both carbon and energy cycles were shown to be highly sensitive to shifts in hydrology. Our sites and therefore results are very similar to their study sites as vegetation, sediment, and climate are the same, based on the close distance of the locations. A recent study by Fischer et al. (2022) found similar results as close as 10 m from our B3 site.

Methods

Field sampling approach

The sampling sites were chosen based on their grazing intensity, which was identified by long-term monitoring of animal preferences for grazing sites and additional observations over several days at the start of the field campaign in July 2019. We applied a space-for-time approach to compare apparently similar sites selected within the same landscape units that ideally only differed by grazing intensity, instead of long-term monitoring of non-grazed sites along with gradual herbivore introduction. For this pilot study with limited field time, we decided to prioritize the number of herbivore treatments and landscape positions investigated over the number of replicates within a given treatment and site in order to allow a preliminary analysis of a larger range of site conditions. We implemented a nomenclature scheme for our study sites that provides information on the landscape type (B for thermokarst basin or U for Yedoma upland) and the grazing intensity (3: intensive grazing; 2: occasional grazing; 1: no grazing). Five sites were selected to cover these different site characteristics. We sampled one soil core per site during our field campaign (Figure 2): B3 was an intensively grazed site in a wet area of a thermokarst basin; B2 was an extensively grazed site within the thermokarst basin, close to the fence of Pleistocene Park; B1 was a non-grazed site within the thermokarst basin, just outside the park's fence; U3 was an intensively grazed site on a Yedoma upland; and U1 was a non-grazed site on a Yedoma upland. "Intensive grazing" and "occasional grazing" are relative terms in this context, with "intensive" referring to a daily presence of feeding animals over several hours throughout each day and "occasional" describing an occasional animal presence with feeding occurring along animal tracks. Location details are provided in Table 1.

In this setup, the area outside the fence was defined as an exclosure with no access for the park's animals. We chose our sampling sites so that the three B sites were located in the same drained thermokarst basin, and the two U sites were located on the same Yedoma upland complex. The goal was to choose sites with similar properties so the animal influence was the main variable and differences between all other characteristics were minimized. Unfortunately, site B1 was experimentally deforested in 2015, prior to our study, which resulted in an unavoidable environmental difference that may have impacted soil composition at this site. The main impact is most likely soil compaction of the active layer due to the use of heavy machines. Also, flooding regime (seasonal or occasional) is different between our sites and might have some effect on the soils. Since animal trampling as well as defecation and browsing always occur where animals graze, in the following we will use the term "grazing" to indicate all animal activity including trampling, defecation, and foraging. Each site is exposed to

TABLE 1 Sampling site locations and characteristics.

Site	Latitude	Longitude	Grazing intensity	Main vegetation type	Flooding regime	Active layer depth (July 2019) [cm bs]	Total core length [cm]	Main sediment material
B1	68.512167°N	161.496278°E	No grazing	Graminoids, forbs and shrubs	Occasional	80	127	Silt, peat layer (85–115 cm bs)
B2	68.511111°N	161.508528°E	Occasional	Graminoids and forbs	Occasional	51	108	Clayish silt
B3	68.512694°N	161.508750°E	Intensive	Graminoids	Seasonal	38	110	Clayish silt
U1	68.504469°N	161.488390°E	No grazing	NA	None	NA	72	Silt
U3	68.512778°N	161.514611°E	Intensive	Graminoid-rich tundra and shrubs	None	53	114	Clayish silt

the same grazing pressure year-round, as there are no separate summer and winter ranges, enabling us to study the net effect of the animals' winter and summer impacts.

Firstly, we prepared a visual description of the surroundings at each sampling site, including the main vegetation type. We identified and sampled the most abundant vegetation species and estimated their coverage based on one by 1 m plots (Figure 3).

Secondly, we removed the active layer using a spade, until we hit permafrost. We measured the thaw depth and sampled the soil profile by using fixed-volume steel cylinders with a volume of 250 cm^3. Due to very wet ground conditions, we were not able to collect cylinder samples at the intensively grazed site B3, where the ground was saturated from the surface to the frozen ground (38 cm). Instead, we cut blocks 8–10 cm high (see also Windirsch et al. (2021) for exact sample dimensions) out of the soil profile using a knife. The organic top layer was sampled separately at all sites.

Thirdly, we used a Snow Ice and Permafrost Research Establishment (SIPRE) permafrost auger with an inner diameter of 7.6 cm in order to sample both the still-frozen parts of the active layer and the underlying permafrost. We reached maximum sampling depths of 110 cm below surface (bs) at B3, 108 cm bs at B2, 127 cm bs at B1, and 114 cm bs at U3 (Supplementary Figures S2, S3). After drilling, soil samples and cores were individually wrapped in sterile plastic bags. All samples were brought in a frozen state to our laboratories for further analysis.

Due to high and dense shrub vegetation and therefore inaccessibility, we were not able to sample the U1 location during our summer field campaign. The Yedoma upland site outside the fence of Pleistocene Park was therefore sampled in the following winter with the SIPRE auger to a depth of 72 cm bs and was completely frozen at the time of extraction.

Laboratory work

In the laboratory the frozen cores were cut into approximately 5 cm samples according to stratigraphy using a band saw. Afterwards, all samples were freeze-dried (Zirbus Sublimator 15) and weighed pre- and post-drying for ice and water content determination (Mettler Toledo KERN FCB 8K0.1, accuracy ±0.1 g). The dry samples were split into subsamples for biogeochemical and sedimentological analysis. In the following, the mean sample depth will be used to describe the position of each sample within the soil column.

The subsamples for biogeochemical analysis were homogenized using a planetary mill (Fritsch Pulverisette 5) and weighed into tin capsules and steel crucibles for measurement. We determined total carbon (TC), total nitrogen (TN), and total organic carbon (TOC) by combustion analysis using a vario EL III and a soliTOC cube (both Elemantar Analysensysteme). Afterwards, the carbon-nitrogen ratio (TOC/TN) was calculated from TOC and TN, giving information about the state of degradation and the source of the OM. TOC/TN ratios could not be calculated for samples with TN or TOC below the detection limit of 0.1 wt%.

OM for radiocarbon dating was taken from the dried original samples. For dating, the Mini Carbon Dating System (MICADAS) at the Alfred Wegener Institute Bremerhaven was used. We calculated the results in calibrated years before present (cal yr BP) using the calibration software Calib 8.2 and applying the IntCal20 calibration curve (Reimer et al., 2020; Stuiver et al., 2021).

We analyzed the ratio of stable carbon isotopes and used it as a proxy for the degree of decomposition of the OM following Diochon and Kellman (2008). Soil $\delta^{13}C$ values differ between material sources and can distinguish between vegetation communities (Malone et al., 2018). Samples for $\delta^{13}C$ analysis were homogenized using a planetary mill, and subsequently treated with hydrochloric acid at 50°C to remove carbonates. Measurements were done using a Delta V Advantage Isotope Ratio mass spectrometer (MS) supplement equipped with a Flash 2000 Organic Elemental Analyzer. Results are given in ‰ compared to the Vienna Pee Dee Belemnite (VPDB) standard (Coplen et al., 2006).

Finally, we determined grain size distribution within samples to check sediment substrate similarity. Therefore, OM was removed from the samples using hydrogen peroxide. Grain size distributions were subsequently measured using a MasterSizer 3000 (Malvern Panalytical).

Data analysis and external data

We determined the annual average number of freezing days (daily mean air temperature below 0°C) over a period of 9 years. For this we used data from 2009 to 2017 measured at the Chersky meteorological station (station RSM00025123). Data were obtained from the National Oceanic and Atmospheric Administration's National Climatic Data Center (NOAA NCDC) database.

In order to check for differences between intensively grazed and non-grazed sites, we combined our TOC data for intensive (B3 and U3) and non-grazed (B1 and U1) sites. We did this for the minimum active layer depth (38 cm at B3) to ensure similar conditions for all sites used. This left us with $n = 11$ samples for intensively grazed, $n = 5$ samples for occasionally grazed, and $n = 10$ samples for non-grazed sites. Since grazing intensities were artificially altered during the last few decades, we expect the most pronounced differences in the seasonally thawed layer, which corresponds to more recent periods. We visualized the distribution of TOC contents in the active layer in boxplots for intensive, occasional, and non-grazed sites of our study to explore possible differences in TOC content in relation to grazing intensity.

To identify correlations between TOC content, water or ice content, and sediment type (via mean grain size), we used principal component analysis (PCA). Data were initially normalized to values between 0 and 1. The PCA was conducted in the R environment using the "stats" package (RCoreTeam 2021).

Results

Vegetation assessment

At site B3 we found *Calamagrostis langsdorfii* as the only species in our one by 1 m plot with a coverage of more than 95%. No other species was found underneath. *C. langsdorfii* reached a height of approximately 30 cm. At B2 *Poaceae* were dominant but could not be identified on a species level due to a lack of blossoms as well as herbivory damages (Figure 3). Therefore, height could also not be recorded accurately. *Poaceae* covered approximately 70% of our plot with small amounts of *Salix* ssp. in between (less than 10% coverage). Close to our plot, *Salix* ssp. and *Larix* ssp. shrubs were present with a height of up to 2.5 m. Contrary to the grazed sites, the predominant species at B1 was *Beckmannia syzigachne* with an approximate coverage of 65% and an approximate height of 25 cm (Figure 3). Underneath, low extents of *Saxifraga* ssp., *Equisetum* ssp. and low-growing *Salix* ssp. were found. After deforestation in 2015, no *Larix* ssp. were present. U3 featured a much lower-growing vegetation (up to 15 cm height), holding approximately 50% of unidentified graminoids which could not be identified due to herbivory damages (Figure 3). In between we found *Rubus* ssp. (15–20%), *Saxifraga* ssp. (less than 5%), *Salix* ssp. (less than 5%), and some individuals of *Vaccinium* ssp. and *Arnica* ssp., which all lacked flowers and could therefore not be identified on species level. Towards the less intensively grazed upland areas, *Salix* ssp. shrubs up to 2.5 m in height grew with increasing density.

Seasonal thaw depth

We found that the seasonal thaw depth (July 2019) decreased with grazing intensity, giving a thaw depth of 38 cm below surface (bs) in B3, 59 cm bs in B2, and 85 cm bs in B1 with a semi-frozen zone between 80 and 85 cm bs. In U3, we measured a thaw depth of 53 cm bs. Since U1 was sampled in winter, we were not able to measure thaw depth at this site.

Carbon parameters (TOC, TOC/TN ratios, and $\delta^{13}C$ ratios)

At B3, TOC generally decreased from top to bottom with the highest value of 25.66 wt% at 20.25 cm bs and the lowest value of 1.18 wt% at 92.5 cm bs (Figure 4). In contrast to this, TOC values for B2 peaked around the frozen-unfrozen interface with values between 4.89 wt% (21.25 cm bs) and 30.10 wt% (64 cm bs); the frozen part contained generally more TOC. The highest TOC values among all sites were found in a peat layer at B1 in the frozen core part, with a peak value of 52.80 wt% (92.5 cm bs). The unfrozen core part contained much less OC with values between 0.79 wt% (35.25 cm bs) and 9.65 wt% (3.75 cm bs).

At the U3 upland site, TOC was higher in the unfrozen core part with values between 3.52 wt% (11.25 cm bs) and 10.73 wt% (49 cm bs). In the frozen core part below, TOC values were rather homogeneous, varying between 1.01 wt% (103.5 cm bs) and 2.65 wt% (58.5 cm bs). In contrast to the previous sites, TOC at U1 was homogeneous throughout the core at values between 1.24 wt% (33 cm bs) and 2.54 wt% (27 cm bs) with a slight increase at the bottom to 4.50 wt% (71 cm bs).

While TOC/TN ratios for B3 (range 12.68–25.96) and B2 (range 14.83–18.48) were similar (Figure 5), values for B1 were

10.3389/fenvs.2022.893478

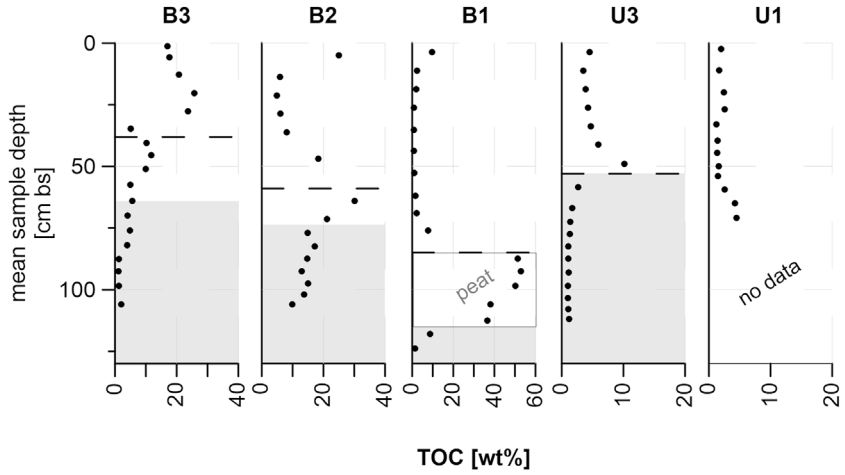

FIGURE 4
Total organic carbon (TOC) values of all study sites; dashed lines mark the seasonal thaw depth measured in July 2019; gray areas are assumed to be permafrost based on cryostratigraphic characteristics; please note the different scales on the x-axes.

higher, in the range of 16.94–24.90. In the upland sites, there was a strong contrast between U3 (11.40–29.19, mean of 17.75) and U1 (28.63 and 29.27) in TOC/TN ratios.

$\delta^{13}C$ values were also similar between the basin sites (B3: −30.63‰ vs. VPDB (uppermost sample) to −26.43‰; B2: −29.60‰ to −28.13‰; B1: −30.17‰ to −27.89‰) (Figure 4). Upland sites showed higher $\delta^{13}C$ values in the range of −28.06‰ to −23.49‰. For full $\delta^{13}C$ values, please see Supplementary Figure S4 or the published data set (Windirsch et al., 2021).

Radiocarbon dates were measured from samples at greater depth than the expected grazing influence. These data are provided in the Supplementary Table S1.

Grainsize distribution and water content

The soil cores were silty overall and had relatively homogeneous grain size distribution (Figure 6) across sites (Supplementary Figures S2, S3). In B3, clay content decreased slowly with depth from 16.69 vol% at 76 cm bs to 7.50 vol% at 106 cm bs, while at the same time sand content increased from 3.46 vol% to 10.68 vol%. Clay content varied throughout B2 with a minimum of 14.16 vol% at 28.75 cm bs and a localized maximum of 22.17 vol% at 13.75 cm bs (Figure 6). Sand content decreased with depth, starting at 12.73 vol% (5 cm bs) and reaching 2.43 vol% at the bottom (106 cm bs). In B1, clay content showed a peak value of 21.96 vol% at 76 cm bs, followed by a peat layer down to 106 cm bs with no grain size data available. Mean clay content for this core was 10.84 vol%. Sand content varied between 5.37 vol% (35.25 cm bs) and 11.31 vol% (43.75 cm bs) with two low values, 2.54 vol% at 52.75 cm bs and 2.22 vol% at 124 cm bs.

U3 showed similar characteristics as B3 with clay content decreasing with depth (highest value 19.76 vol% at 49 cm bs, lowest value 6.34 vol% at 112 cm bs), while simultaneously the sand content increased to a peak value of 11.52 vol% at 103.5 cm bs (Figure 6). Grain size composition for U1 showed no peaks, with clay contents between 8.03 vol% (71 cm bs) and

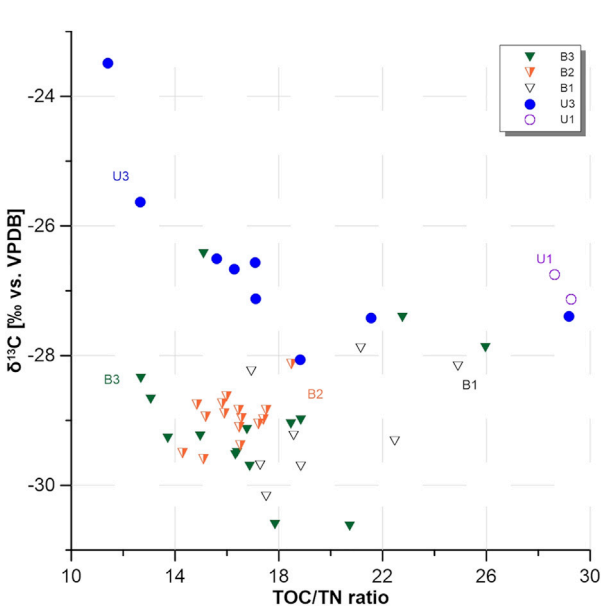

FIGURE 5
Total organic carbon to total nitrogen (TOC/TN) ratios plotted against the stable carbon isotope ($\delta^{13}C$) ratios of all sampling sites.

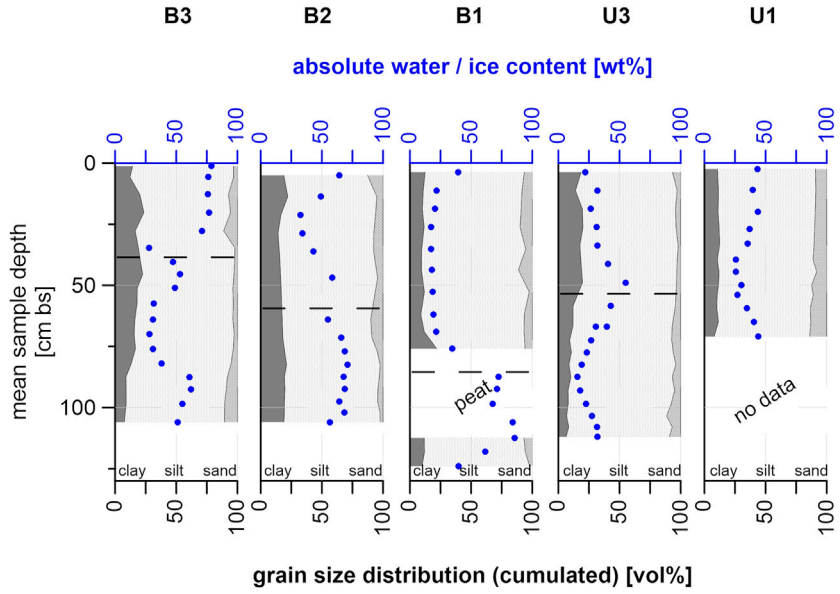

FIGURE 6
Grain size distribution for all sampling sites plotted against depth; absolute water and/or ice content added in blue; dashed lines mark the seasonal thaw depth measured in July 2019.

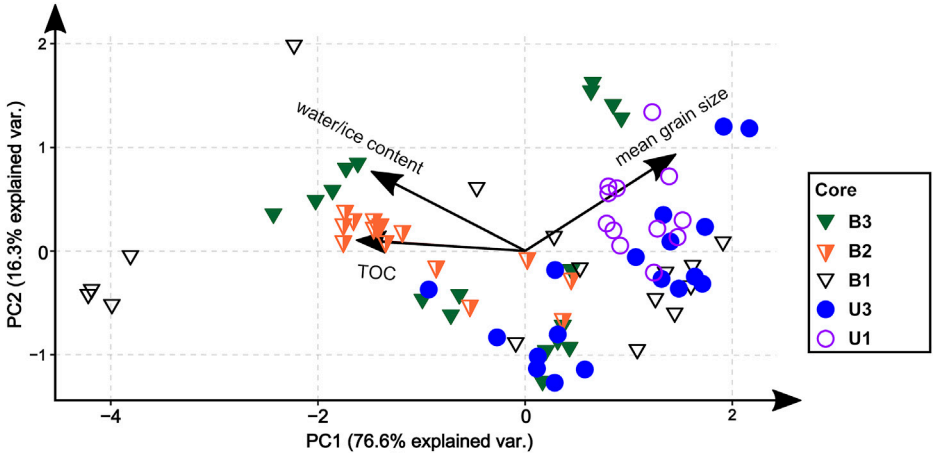

FIGURE 7
Results of the principal component analysis (PCA) for variables total organic carbon (TOC), water/ice content, and mean grain size.

12.60 vol% (33 cm bs) and sand contents between 8.20 vol% (44.5 cm bs) and 14.01 vol% (71 cm bs).

The absolute water and/or ice content showed generally drier conditions in the frozen core of B3, with values fluctuating between 27.67 wt% (34.75 cm bs) and 78.59 wt% (1.25 cm bs). Similar characteristics were present in B2 (34.26 wt% at 28.75 cm bs to 71.10 wt% at 82.5 cm bs). In contrast, B1 showed large differences between the unfrozen upper part (17.19 wt% at 35.25 cm bs, 39.36 wt % at 3.75 cm bs) and the frozen lower part (39.59 wt% at 124 cm bs, 85.74 wt% at 112.5 cm bs).

U3 showed similar water content values at the top (32.00 wt% at 11.25 cm bs) and bottom (31.93 wt% at 112 cm bs) with higher values around the freezing interface (55.01 wt% at 49 cm bs) and lower values above and below that (22.11 wt% at 3.75 cm bs and 15.59 wt% at 87.5 cm bs). Water content in U1 was more stable, ranging between 25.63 wt% (39.5 cm bs) and 43.88 wt%

10.3389/fenvs.2022.893478

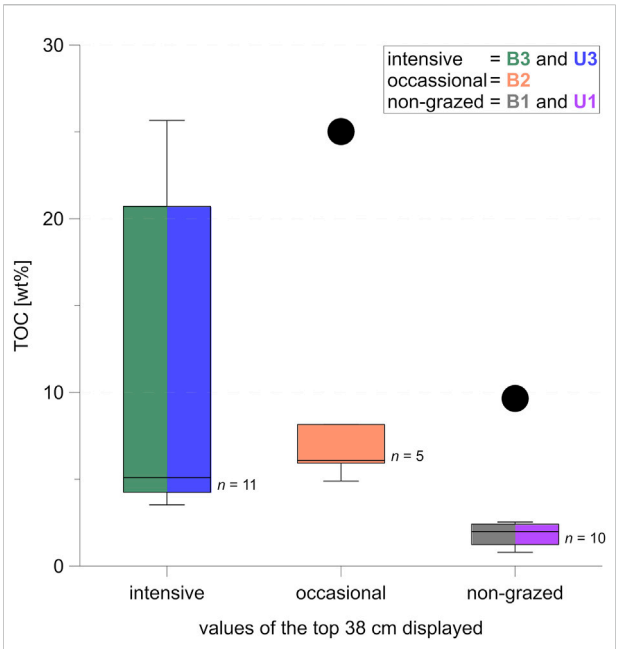

FIGURE 8
Boxplots for total organic carbon (TOC) data of all samples from the uppermost 38 cm of all intensive, occasional, and non-grazed sampling sites; sites B3 and U3 are combined into the "intensive" boxplot, B2 is shown in the "occasional" boxplot, and B1 and U1 are combined into the "non-grazed" boxplot; the median is shown by the horizontal line within each box; box margins show the upper and lower quartile; whiskers mark minimum and maximum values; outliers (indicated by dots) are more than 1.5 box lengths away from box margins; colors indicate which sites are represented in which box.

(71 cm bs) with a similar value at the top (43.24 wt% at 2.5 cm bs).

The stable isotope characteristics of the pore water are shown in Supplementary Figure S5.

Statistics and correlation analysis

The PCA revealed a positive correlation between water/ice content and TOC content (Figure 7). While B3, B2, U3, and U1 tended to form clusters, B1 values were spread across parameters. For full PCA scores, see Supplementary Table S2 as well as Supplementary Figure S1.

In Figure 8 we visualized the range of the TOC values in the minimum active layer (depth 38 cm), grouped by grazing intensity (Figure 8). TOC is clearly higher under intensive grazing compared to non-grazed sites, with no overlap except for outliers. Due to potential dependency of TOC values within the unfrozen part of a core, and due to the small sample sizes, we did not test for statistical significance.

Discussion

Effects of grazing on vegetation structure and permafrost thaw

For our studied cores we found that intensively grazed sites (B3, U3) were covered by generally shorter and sparser vegetation (Figure 3, B3: grassland; Figure 3, U3: shrubby grassland tundra), with taller grazing-resistant individuals in between, compared to occasionally or non-grazed sites (Figure 3, B2: grasses and herbs, and B1: grasses, herbs and low shrubs). This could likely be a result of the reduction in shrub expansion through large herbivore action (Suominen and Olofsson 2000), while the differences in the flooding regime between the sites promoting different vegetation types might also have an impact on this. The grazed sites located in the thermokarst basin (B3 and B2) were still flooded seasonally. The upland sites were generally better drained than the sites within the basin. We aimed to select representative sampling locations, based on overall vegetation and observed animal routes. However, we had limited information on representativeness in terms of soil type and wetness across this landscape. Still, we ensured that our study sites are comparable in terms of soil properties by measuring grain size composition of the soil material (Figure 6). This revealed similar characteristics across sites with slight variations in clay and sand content, and silt contents ranging between 68 and 87 vol%, which shows that our sites are comparable in terms of physical soil properties.

Our results showed that the changes in vegetation height and structure correlated with large herbivore activity. This is in agreement with former studies in similar Arctic settings (Sundqvist et al., 2019; Skarin et al., 2020; Verma et al., 2020). However, the effects of seasonal flooding on vegetation composition and structure (sites B3 and B2) cannot be neglected. These differences in flooding regime marked a disparity between our sampling sites, since flooding at the basin sites B3 and B2 occurred seasonally or infrequently, while there are no records of any flooding for the other sites.

In our study area, shrubs were established on the upland before the introduction of large numbers of animals, and are now retreating, probably due to grazing pressure. While there are now higher shrubs at U3, there is a gradient in density of *Salix* ssp. shrubs towards less intensively grazed areas from individual shrubs to dense, forest-like coverage. At the edges of the drained thermokarst basin, shrubification took place on spots that could only be grazed occasionally (Olofsson et al., 2009) after the water level had retreated; the water retreated as the lake drained, allowing for incremental vegetation establishment. This leaves us with high soil wetness as another explanation for the absence of shrub vegetation (Martin et al., 2017). The clearing of the larch forest at the

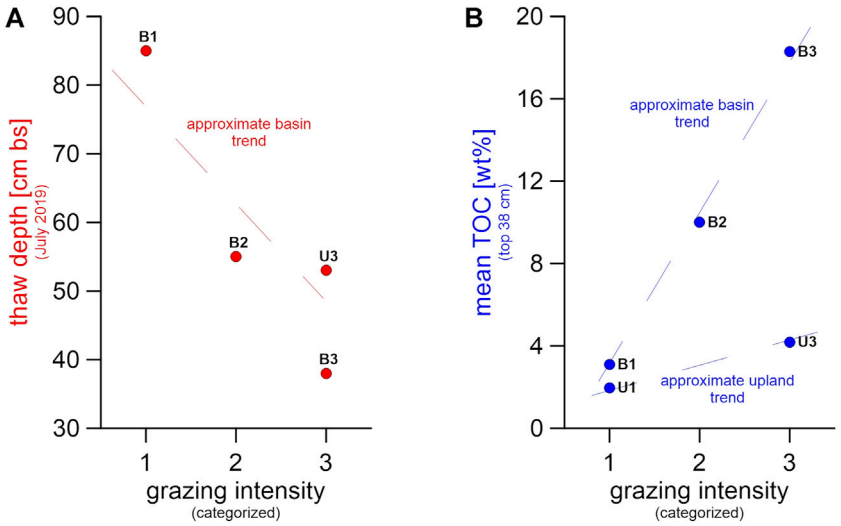

FIGURE 9
Visualization of **(A)** thaw depth and **(B)** mean total organic carbon (TOC) of the uppermost 38 cm for all sampling sites, plotted versus grazing intensities 1 (no grazing) to 3 (intensive grazing); as site U1 was only sampled in winter, we do not have a summer thaw depth measurement for this site.

non-grazed site B1 4 years prior to our study is also a plausible explanation for the limited shrub extent there.

The restricted grazing space within the fenced Pleistocene Park area led to a higher revisitation rate of animals to sites within the fence. This artificially increased grazing pressure led to the different vegetation structures observed inside and outside of the fence. Such shorter graminoid vegetation types are linked to grazing intensity (Forbes 2006). Monteath et al. (2021) found that the extinction of the Pleistocene megafauna was not responsible for causing an increase in shrubification, but rather that shrubification as a consequence of climate change during the early Holocene could have led to the extinction of megafauna as a result of habitat loss. However, modern rewilding approaches are planned and realized with recent herbivores capable of living in today's climate, though species composition might have to be adjusted continuously with warming conditions. Also, the cause and consequence in this setup are still unclear, with opposite findings across studies, depending on the methods applied (Murchie et al., 2021). Numerous studies have found that contemporary herbivores were indeed capable of reducing shrub extent in Arctic environments on a local scale (Olofsson et al., 2009; Köster et al., 2015; Ylänne et al., 2018; Verma et al., 2020; Mekonnen et al., 2021). We found shallow thaw depths at intensively grazed sites and a much thicker active layer at the non-grazed B1 site. Generally, the increase in active layer thickness is associated with warming of the ground, influenced by summer temperatures, flooding, insulation from snow, and vegetation density and composition (Walker et al., 2003; Skarin et al., 2020; Magnússon et al., 2022). Therefore, as was stated by Zimov et al. (2012), the direct influence on these insulating factors could affect the active layer dynamics due to a stronger cooling of the ground in winter (Figure 1). However, to determine any clear trends, repeated annual measurements of the thaw depth are needed.

Data from our basin sites showed that the more intensively grazed area featured smaller seasonal thaw depths in July 2019, compared to the occasionally or non-grazed sites (Figures 4, 9A). Keeping in mind the seasonal flooding at B3 and B2, one would expect greater thaw depths at these sites, since higher soil moisture promotes heat flow, and the relatively warm flood water adds heat to the soil as well (Magnússon et al., 2022). Examining the assumed permafrost table depth based on cryostratigraphic characteristics in the cores, we observed a contrary effect with an active layer depth of 61 cm bs under intensive grazing at B3, 74 cm bs under occasional grazing at B2, and 115 cm bs for the non-grazed B1 site. This supports our original hypothesis of grazing impacts being the main driver behind thaw depth differences, likely via vegetation changes.

At B3, the graminoid vegetation lay flat beneath the snow cover, offering little or no insulation. The snow itself was compacted by animal trampling, which further reduced the insulation properties of the snow cover. On the other hand, the forb undergrowth of the grassland at B2 provided slightly more resistance against the weight of the snow cover. Combined with less intensive trampling and, thus, a less compacted snow cover, the B2 sampling site was characterized by better winter insulation properties compared to B3. The *Salix* shrubs at B1 promoted localized snow trapping and a loose snowpack, both of which have been shown to provide effective insulation

against cold winter air temperatures (Myers-Smith et al., 2011). Trampling was also missing in this non-grazed area. In addition to those surface conditions, the composition of the sediment itself could have contributed to a deeper active layer at site B1. From the grain size distribution data (Figure 6) we saw that material among all studied sites was quite homogeneous (Table 1). Exceptions were the sampling sites B1 and U1, which had a lower proportion of clay and were therefore generally dominated by coarser-grained material. High ice contents in the frozen part of the B1 core support the idea of an insulating effect of the peat layer that prevented the ground from thawing any deeper, but also helped to maintain the thick active layer found here. This assumption implies that the peat layer worked as a heat flux barrier for the permafrost below, stopping summer thaw from the top, but also preventing bottom-up refreezing in winter. This could lead to present or future talik formation above the peat layer.

We were not able to compare thaw depths for the upland sites: the cryostratigraphically determined permafrost table depth of approximately 50 cm bs at U3 was, however, smaller than the active layer depths measured by Abramov et al. (2019) and Shmelev et al. (2021) for the close-by Mt. Rodinka site, located on a Yedoma upland with a mean active layer depth of 80 cm. Also evident in this study (Abramov et al., 2019) were smaller thaw depths, around 40 cm, for thermokarst basin sites featuring shorter vegetation in the Kolyma region, which is similar to our B3 site.

In our study, the reduced active layer thickness observed at the intensively grazed sites could also have originated from active layer compression by animal trampling, which would mean that even with shallower thaw depth the same amount of soil thawed. However, this last point cannot be tested with our data, since we were not able to measure bulk densities due to wet ground conditions and root structures. While such ground compaction is very common in peatlands (Batey 2009), the sandy silt soils that we found are only moderately compressible (Akayuli et al., 2013; Halcomb and Sjostedt 2019), especially as they were frozen throughout a major time of the year, making soil compaction a weak argument for the shallow active layer at intensively grazed sites. The regular flooding of the intensively grazed basin site, which usually leads to an increase in thaw depth (Magnússon et al., 2022), combined with the in fact shallower active layer found in our study when comparing to the non-grazed B1 site, suggests that the cooling effects induced by animal activity could be much larger than previously expected.

Carbon accumulation under grazing impact

We identified several variables that may be responsible for explaining differences in TOC between sites, including herbivory. Besides shorter graminoid vegetation types, other effects were also aligned with cooler temperature and/or less carbon degradation, such as soil moisture, as visualized by our PCA (Figure 7). This coexisting influence of grazing and soil moisture should be tested in other locations. However, the contrast in TOC/TN ratios and $\delta^{13}C$ ratios (Figure 5) of the studied deposits between intensive and non-grazed locations suggested that animal presence is affecting OM decomposition (if we assume a comparable OM source). But based on the differences in vegetation cover, we found that this contrast might also originate from different OM input as well as from different nitrogen input via the presence or absence of animal droppings. Since grazing alters the vegetation cover—assuming that in the absence of large herbivores the vegetation would be more homogeneous throughout the study area—the observed strong differences in TOC/TN and $\delta^{13}C$ ratios have likely resulted from the differences in animal impact on the landscape. Grazing is, therefore, a reasonable explanation for the strong differences between sites, including TOC content.

Mean TOC was six times higher in the top 38 cm of B3 (minimum active layer depth) compared to B1, with intermediate values in B2 (Figures 4, 8). For the upland sites, mean TOC was twice as high under intensive grazing in those core sections lying within minimum active layer depth (38 cm, B3) compared to non-grazed cores. The effect was not visible in lower core parts, perhaps because of the relatively short time span of 23 years since intensified animal introduction into the area (Figure 4). Instead, the TOC pattern in the frozen core parts was opposite to the higher TOC found in the active layer under intensive grazing influence. This suggests different pre-existing site conditions prior to herbivore introduction. The contrasting TOC pattern in the active layer suggests that animal grazing can help increase carbon storage in a relatively short time span (Figure 9B) but grazing needs more time to affect deeper permafrost carbon storage apart from thermal stability, hence reduced thaw depth. Therefore, the TOC differences between sites were not significant when comparing the entire depth of the sampled cores. We explain this as a result of i) the TOC-rich peat layer found in B1 that shifts the TOC median value for non-grazed sites upwards, combined with ii) low TOC values in the frozen part of the intensively grazed sites which offset the high active layer TOC. Since the peat layer was found at 85 cm bs and dated to 4,327 cal yr BP, we expect no connection to herbivory influence in a 23-year timespan, which is why we tested for significance in the active layer.

The significant differences in upper soil TOC between sites of intensive large herbivore presence (B3 and U3) and non-grazed sites (B1 and U1) agreed with the expected effects of grazing (Figure 9B).

All organic carbon found in the upland areas showed higher $\delta^{13}C$ values (Figure 5), which we interpreted as a result of colder, drier, and more compact ground conditions in the Yedoma

deposits and therefore less OM decomposition, as well as differences in plant species, resulting in different $\delta^{13}C$ signals compared to the seasonally flooded and less compact ground of the drained thermokarst basin. Higher TOC/TN ratios in non-grazed sites indicated a different source material, originating from shrubby tundra, in comparison to grassland vegetation in occasionally and intensively grazed sites. However, these vegetation differences might originate from animal grazing impacts.

Above-ground carbon storage is also an important aspect of ecosystem carbon storage. Although we were unable to address above-ground carbon storage in this study, grazing activities of large herbivores have likely had an impact on above-ground biomass storage in vegetation by providing nitrogen fertilization via droppings. Mekonnen et al. (2021) stated that under intensified shrubification, shrubs take up large amounts of nutrients from the soil into the vegetation biomass. It is possible that CO_2 emissions from the soil might also be partially captured by this boosted plant growth and incorporated into plant biomass. However, nutrient availability is much more important for plant growth and hence carbon accumulation. Such nutrients become available when OM is decomposed, but the increased carbon accumulation by plant growth can to some extent offset the carbon losses associated with permafrost-stored OM decomposition (Keuper et al., 2012; Turetsky et al., 2020). While shrub growth increases above-ground biomass, it generally leads to net ecosystem carbon losses via heterotrophic respiration (Phillips and Wurzburger 2019). The formation of grasslands, on the other hand, increases above-ground carbon cycling as well, showing high productivity (Gao et al., 2016). While showing the highest respiration rates, soil carbon accumulation in wet Arctic grasslands is greatest when compared to other Arctic vegetation types (Bradley-Cook and Virginia 2018). This might be linked to the relative ease of grassland litter transfer into the soil, e.g. via animal trampling, as well as deeper root penetration of graminoids, compared to shrubby and sturdier vegetation (Wang et al., 2016). Based on this, we expect an increase in above-ground short-term carbon fixation in the more productive graminoid vegetation at intensively-grazed sites compared to non-grazed tundra sites, but cannot make any quantitative statements on this for our sites due to a lack of data regarding this matter.

We summarize two points from our carbon data:

(1) In the upper part of the soil cores, TOC contents were higher in more intensively grazed sites, with a decrease with less grazing for both thermokarst-affected and Yedoma sites (Figure 9B). As the soil and sediment characteristics of the non-grazed U1 Yedoma site matched findings from other Yedoma studies (Strauss et al., 2012; Jongejans et al., 2018; Windirsch et al., 2020), we consider this as the pre-grazing Holocene state (i.e., not heavily grazed state). This suggests that intensive grazing for 23 years has already increased TOC amounts stored in the active layer by a factor of two (Figure 4). At thermokarst sites, hydrology has an impact on TOC storage as well, which is seen in the strong correlation between TOC content and water content in the PCA (Figure 7). However, a direct comparison to a pre-grazing state for our sites is not possible.

(2) Intensively grazed areas displayed a shallower thaw depth (Figure 9A). This was in line with the hypothesis that connected ground cooling effects with snow removal or snow compaction. These changes in snow properties can result from vegetation shifts towards graminoid communities, which trap less snow, as well as snow compaction by animal trampling. Also, here an active layer depth reduction could have happened in a rather short period of time. While TOC was significantly higher in the active layer in intensively grazed sites, the shallower thaw depths associated with these intensively grazed sites might contribute to stabilizing the underlying permafrost, hence preventing fossil permafrost-stored OM from degradation. However, our study cannot rule out influencing factors other than grazing adding to the trends illustrated in Figure 9.

Even if we cannot quantify the landscape and its carbon storage with no artificially introduced herbivores, we can make some assumptions based on other studies' findings. These assumptions are hypothetical for our study area, but based on previously published studies. In a partially drained thermokarst basin within a Yedoma landscape, relatively warm soil conditions and hence a deep active layer would most likely be found in the drained basin (Windirsch et al., 2020). Normally, the active layer would first become shallower after lake drainage, with less water content leading to reduced heat flux into the soil and making room for cold winter air, and stabilize once tundra vegetation, shrubs, or even small trees re-establish, working as ground insulators in summer (Blok et al., 2010) in the absence of grazing. Over time, peat formation is likely to take place if wetness is still high, increasing carbon concentration and insulation effects on the underlying ground (Jones et al., 2012). In regularly flooded thermokarst basin areas, a graminoid vegetation holding vast extents of *Eriophorum* spp. will likely develop, while dry basin areas will normally feature *Salix* spp. shrubs (Regmi et al., 2012). On the surrounding uplands we expect a generally homogeneous appearance of soil carbon and vegetation, where differences are controlled by local parameters. These controls include differences in cryostratigraphy, substrate, and water availability, among others. On uplands we expect to find tundra vegetation, most likely with increasing shrubification throughout the last decades. Moreover we expect forested areas on those uplands with differing thaw depth between vegetation types and a thick but stable active layer beneath forests (Stuenzi et al., 2021). A deepening active layer is likely to occur

underneath tundra as a result of global climate warming, which also increases shrubification (Wilcox et al., 2019) and therefore snow trapping. While shrubification may shield the ground from further summer thawing, the contrasting seasonal lengths of summer and winter may come into effect, reducing summer thaw but preventing winter refreezing at the same time. These literature-based qualitative scenarios suggest that the grazing impacts observed in our study, especially as regards alterations in vegetation and thaw depth, might represent a major system change; this may also be true for the increase in carbon storage at the intensively grazed U3 upland site. Hence, larger scale grazing could potentially help to keep carbon in the ground and reduce natural carbon emissions from permafrost, although in no case would this be a substitute for decarbonizing the current industrialized society. Due to technical constraints, the efficacy of this landscape management tool should not be overestimated.

Methodological limitations of the pilot study

Due to the spatial and temporal limitations in the data we collected, we cannot unambiguously distinguish between previous conditions at our sites, and the overall herbivory impact on soil TOC. Soil carbon distribution as well as local environmental differences influencing thaw depth might have existed before herbivore introduction; this cannot be accounted for in our study. However, the presence of rather fresh material present in the seasonal thaw layer at sites B3 and U3 (Supplementary Table S1) suggested a link to modern disturbances (Supplementary Table S1), for which animal trampling, bioturbation, or cryoturbation all provide a valid explanation.

Despite results being consistent with the expected effects of grazing on ground temperature proposed by Zimov et al. (2012), the missing core replication of the present study combined with the expected spatial heterogeneity of active layer depths indicated that this interpretation needs further data for validation. Further, more replicated studies, potentially combined with spatially comprehensive modeling exercises, are advised along with monitoring of exclosure sites with gradual herbivore introduction. Also a 23-year time period of herbivore activity is likely too short to affect deeper and permanently frozen deposits but mainly affects the active layer both in terms of chemical properties and thaw depth.

The larch forest clear cut at B1 marked a clear difference between our sampling sites, as stable boreal forest is known to protect permafrost against summer heat (Stuenzi et al., 2021), maintaining a deep but stable active layer. However, we still encountered the greatest seasonal thaw depth here. This greater thaw depth here agreed with the findings of relatively warmer but stable permafrost temperatures below forests in the Arctic and boreal region (Kropp et al., 2020) and was likely a relic of the previous forest-covered state. We found no sign of active layer refreezing. The thaw depth extended down to the peat layer, which started at 85 cm bs; the peat layer might have been functioning as a heat flux insulator both for summer thawing (from the top) and winter refreezing (from the bottom). Also, a detailed assessment of effects of different vegetation compositions typical for pastures in the Arctic on heat fluxes is needed.

Ultimately, more studies and monitoring setups on the impact of large herbivore grazing on permafrost soil carbon storage are needed across the Arctic. Hence, we hesitate to draw universal conclusions on herbivory effects from our data, including the extension of these results to much larger regions.

Conclusion

We found evidence from our permafrost study sites that intensive grazing by large herbivorous animals might have contributed to keeping the soil cool and maintaining—or even slightly increasing—carbon storage in our studied permafrost sites over a 23-year time period. At the same time, annual thaw depth was found to be lower at intensively grazed sites. These changes of ground characteristics are likely a combined result of vegetation changes and snow insulation reduction, probably amplified by additional carbon input due to intense herbivore impacts. Vegetation appears to have changed from shrubby tundra to grasslands under herbivory impact in our study area. Differences in soil moisture seem to play a role at our sites as well, and further research on the hydrological conditions and connections at our sites is needed. To further investigate herbivory effects, it is necessary to sample grazing intensity transects at higher spatial and temporal resolution and replication and to repeat this approach in other permafrost areas as well. Also, more detailed monitoring approaches are needed, such as the setup of exclosure sites that allow for direct comparison of a range of sampled parameters with sites under the influence of different grazing intensities.

We conclude that intensified animal husbandry could locally contribute to stabilizing carbon storage in the active layer at non-forest permafrost sites, and might further preserve carbon stored in permafrost ground by maintaining a frozen state. This management practice may fit into a broader set of tools that could be used to mitigate the consequences of local permafrost thaw in order to buffer climate change impacts. Answering the interesting question of whether such an approach could be scalable to larger regions was not part of our study.

Data availability statement

The datasets presented in this study can be found in online repositories. The datasets presented are deposited with the PANGAEA data repository, accessible using https://doi.org/10.1594/PANGAEA.933446.

Author contributions

TW, GG, MU, and JS designed the study. TW conducted field and laboratory work, prepared the graphics, and led the writing of this manuscript. TW, GG, MU, and JS analyzed and interpreted the laboratory results. GG designed the maps used in this study. BF, MM-F, and JO provided expertise on herbivory and herbivore-environment interactions. JW contributed expertise in vegetation classification and statistics. NZ and MG provided expertise on the area and local environment processes and characteristics as well as on the Pleistocene Park experiment. All authors contributed to compiling and editing the manuscript.

Funding

The field campaign was carried out in the framework of the CACOON (Changing Arctic Carbon Cycle in the Coastal Ocean Near-Shore) project (#03F0806A (German Federal Ministry of Education and Research)) and as part of the PeCHEc (Permafrost Carbon Stabilization by Recreating a Herbivore-Driven Ecosystem) project funded by the Potsdam Graduate School. The authors received additional support from the Geo.X research network (SO_087_GeoX). Additional funding was provided by the CHARTER (Drivers and Feedbacks of Changes in Arctic Terrestrial Biodiversity) project (grant agreement ID 869471). We further acknowledge base funding provided by the Alfred Wegener Institute expedition funds, as well as support by the Open Access Publication Funds of Alfred-Wegener-Institut Helmholtz-Zentrum für Polar- und Meeresforschung.

Acknowledgments

We thank the Field Experiments & Instrumentation team at the Max Planck Institute for Biogeochemistry in Jena as well as Juri Palmtag for helping with the drilling campaign. We further acknowledge Dyke Scheidemann, Jonas Sernau, and Angelique Opitz (Carbon and Nitrogen Lab [CarLa]) as well as Mikaela Weiner and Hanno Meyer (Stable Isotope Lab) from AWI for assistance in the laboratory. We thank Christian Knoblauch (Universität Hamburg) for helping with TOC measurements. We further thank J. Otto Habeck (Universität Hamburg) for his help in designing this study. This study was supported by the Northeast Science Station team in Chersky, Sakha

Conflict of interest

The authors declare that the research was conducted in the absence of any commercial or financial relationships that could be construed as a potential conflict of interest.

Publisher's note

Supplementary material

The Supplementary Material for this article can be found online at: https://www.frontiersin.org/articles/10.3389/fenvs.2022.893478/full#supplementary-material

References

Abramov, A., Davydov, S., Ivashchenko, A., Karelin, D., Kholodov, A., Kraev, G., et al. (2019). Two decades of active layer thickness monitoring in northeastern Asia. *Polar Geogr.* 44, 186–202. doi:10.1080/1088937X.2019.1648581

Akayuli, C., Ofosu, B., Nyako, S. O., and Opuni, K. O. (2013). The influence of observed clay content on shear strength and compressibility of residual sandy soils. *Int. J. Eng. Res. Appl.* 3 (4), 2538–2542.

Batey, T. (2009). Soil compaction and soil management – A review. *Soil Use Manag.* 25 (4), 335–345. doi:10.1111/j.1475-2743.2009.00236.x

Beer, C., Zimov, N., Olofsson, J., Porada, P., and Zimov, S. (2020). Protection of permafrost soils from thawing by increasing herbivore density. *Sci. Rep.* 10 (1), 4170. doi:10.1038/s41598-020-60938-y

Blok, D., Heijmans, M. M. P. D., Schaepman-Strub, G., Kononov, A. V., Maximov, T. C., and Berendse, F. (2010). Shrub expansion may reduce summer permafrost thaw in Siberian tundra. *Glob. Chang. Biol.* 16 (4), 1296–1305. doi:10.1111/j.1365-2486.2009.02110.x

Bowen, J. C., Ward, C. P., Kling, G. W., and Cory, R. M. (2020). Arctic amplification of global warming strengthened by sunlight oxidation of permafrost carbon to CO2. *Geophys. Res. Lett.* 47 (12), e2020GL087085. doi:10.1029/2020GL087085

Bradley-Cook, J. I., and Virginia, R. A. (2018). Landscape variation in soil carbon stocks and respiration in an Arctic tundra ecosystem, west Greenland. *Arct. Antarct. Alp. Res.* 50 (1), S100024. doi:10.1080/15230430.2017.1420283

Chlachula, J. (2003). The Siberian loess record and its significance for reconstruction of Pleistocene climate change in north-central Asia. *Quat. Sci. Rev.* 22 (18), 1879–1906. doi:10.1016/S0277-3791(03)00182-3

Coplen, T. B., Brand, W. A., Gehre, M., Gröning, M., Meijer, H. A. J., Toman, B., et al. (2006). New guidelines for δ13C measurements. *Anal. Chem.* 78 (7), 2439–2441. doi:10.1021/ac052027c

Corradi, C., Kolle, O., Walter, K., Zimov, S. A., and Schulze, E.-D. (2005). Carbon dioxide and methane exchange of a north-east Siberian tussock tundra. *Glob. Chang. Biol.* 11 (11), 1910–1925. doi:10.1111/j.1365-2486.2005.01023.x

Diochon, A., and Kellman, L. (2008). Natural abundance measurements of 13C indicate increased deep soil carbon mineralization after forest disturbance. *Geophys. Res. Lett.* 35, L14402. doi:10.1029/2008GL034795

Domine, F., Barrere, M., and Morin, S. (2016). The growth of shrubs on high arctic tundra at bylot island: Impact on snow physical properties and permafrost thermal regime. *Biogeosciences* 13 (23), 6471–6486. doi:10.5194/bg-13-6471-2016

Falk, J. M., Schmidt, N. M., Christensen, T. R., and Ström, L. (2015). Large herbivore grazing affects the vegetation structure and greenhouse gas balance in a high arctic mire. *Environ. Res. Lett.* 10, 045001. doi:10.1088/1748-9326/10/4/045001

Fischer, W., Thomas, C. K., Zimov, N., and Göckede, M. (2022). Grazing enhances carbon cycling but reduces methane emission during peak growing season in the Siberian Pleistocene Park tundra site. *Biogeosciences* 19 (6), 1611–1633. doi:10.5194/bg-19-1611-2022

Forbes, B. C. (2006). *The challenges of modernity for reindeer management in northermost Europe*, 184. Berlin, Heidelberg: Springer, 11–25.

Frost, G. V., Epstein, H. E., Walker, D. A., Matyshak, G., and Ermokhina, K. (2013). Patterned-ground facilitates shrub expansion in Low Arctic tundra. *Environ. Res. Lett.* 8 (1), 015035. doi:10.1088/1748-9326/8/1/015035

Fuchs, M., Bolshiyanov, D., Grigoriev, M. N., Morgenstern, A., Pestryakova, L., Tsibizov, L., et al. (2021). *Russian-German cooperation: Expeditions to Siberia in 2019*. Bremerhaven: Alfred Wegener Institute for Polar and Marine Research, 749.

Gao, Q., Schwartz, M. W., Zhu, W., Wan, Y., Qin, X., Ma, X., et al. (2016). Changes in global grassland productivity during 1982 to 2011 attributable to climatic factors. *Remote Sens.* 8, 384. doi:10.3390/rs8050384

Göckede, M., Kittler, F., Kwon, M. J., Burjack, I., Heimann, M., Kolle, O., et al. (2017). Shifted energy fluxes, increased Bowen ratios, and reduced thaw depths linked with drainage-induced changes in permafrost ecosystem structure. *Cryosphere* 11 (6), 2975–2996. doi:10.5194/tc-11-2975-2017

Göckede, M., Kwon, M. J., Kittler, F., Heimann, M., Zimov, N., and Zimov, S. (2019). Negative feedback processes following drainage slow down permafrost degradation. *Glob. Change Biol.* 25 (10), 3254–3266. doi:10.1111/gcb.14744

Grellmann, D. (2002). Plant responses to fertilization and exclusion of grazers on an arctic tundra heath. *Oikos* 98 (2), 190–204. doi:10.1034/j.1600-0706.2002.980202.x

Halcomb, S., and Sjostedt, S. (2019). "Surcharge embankment on marine clayey silt case study and lessons learned," in Eighth International Conference on Case Histories in Geotechnical Engineering, Philadelphia, Pennsylvania, March 24–27, 2019, 119–130. Geo-Congress 2019.

Hugelius, G., Strauss, J., Zubrzycki, S., Harden, J. W., Schuur, E. a. G., Ping, C. L., et al. (2014). Estimated stocks of circumpolar permafrost carbon with quantified uncertainty ranges and identified data gaps. *Biogeosciences* 11, 6573–6593. doi:10.5194/bg-11-6573-2014

Huh, Y., Tsoi, M.-Y., Zaitsev, A., and Edmond, J. M. (1998). The fluvial geochemistry of the rivers of eastern Siberia: I. Tributaries of the lena river draining the sedimentary platform of the siberian craton. *Geochimica Cosmochimica Acta* 62 (10), 1657–1676. doi:10.1016/S0016-7037(98)00107-0

Jackson, R. B., Lajtha, K., Crow, S. E., Hugelius, G., Kramer, M. G., and Piñeiro, G. (2017). The ecology of soil carbon: Pools, vulnerabilities, and biotic and abiotic controls. *Annu. Rev. Ecol. Evol. Syst.* 48 (1), 419–445. doi:10.1146/annurev-ecolsys-112414-054234

Jones, M. C., Grosse, G., Jones, B. M., and Walter Anthony, K. (2012). Peat accumulation in drained thermokarst lake basins in continuous, ice-rich permafrost, northern Seward Peninsula, Alaska. *J. Geophys. Res.* 117, G2. doi:10.1029/2011JG001766

Jongejans, L. L., Strauss, J., Lenz, J., Peterse, F., Mangelsdorf, K., Fuchs, M., et al. (2018). Organic matter characteristics in yedoma and thermokarst deposits on Baldwin Peninsula, west Alaska. *Biogeosciences* 15 (20), 6033–6048. doi:10.5194/bg-15-6033-2018

Kaiser, C., Meyer, H., Biasi, C., Rusalimova, O., Barsukov, P., and Richter, A. (2007). Conservation of soil organic matter through cryoturbation in arctic soils in Siberia. *J. Geophys. Res.* 112, G02017. doi:10.1029/2006JG000258

Keuper, F., van Bodegom, P. M., Dorrepaal, E., Weedon, J. T., van Hal, J., van Logtestijn, R. S. P., et al. (2012). A frozen feast: Thawing permafrost increases plant-available nitrogen in subarctic peatlands. *Glob. Chang. Biol.* 18 (6), 1998–2007. doi:10.1111/j.1365-2486.2012.02663.x

Köster, K., Berninger, F., Köster, E., and Pumpanen, J. (2015). Influences of reindeer grazing on above- and belowground biomass and soil carbon dynamics. *Arct. Antarct. Alp. Res.* 47 (3), 495–503. doi:10.1657/AAAR0014-062

Kropp, H., Loranty, M. M., Natali, S. M., Kholodov, A. L., Rocha, A. V., Myers-Smith, I., et al. (2020). Shallow soils are warmer under trees and tall shrubs across Arctic and Boreal ecosystems. *Environ. Res. Lett.* 16 (1), 015001. doi:10.1088/1748-9326/abc994

Macias-Fauria, M., Jepson, P., Zimov, N., and Malhi, Y. (2020). Pleistocene Arctic megafaunal ecological engineering as a natural climate solution? *Phil. Trans. R. Soc. B* 375, 20190122. doi:10.1098/rstb.2019.0122

Magnússon, R. Í., Hamm, A., Karsanaev, S. V., Limpens, J., Kleijn, D., Frampton, A., et al. (2022). Extremely wet summer events enhance permafrost thaw for multiple years in Siberian tundra. *Nat. Commun.* 13 (1), 1556. doi:10.1038/s41467-022-29248-x

Malone, E. T., Abbott, B. W., Klaar, M. J., Kidd, C., Sebilo, M., Milner, A. M., et al. (2018). Decline in ecosystem δ13C and mid-successional nitrogen loss in a two-century postglacial chronosequence. *Ecosystems* 21 (8), 1659–1675. doi:10.1007/s10021-018-0245-1

Martin, A. C., Jeffers, E. S., Petrokofsky, G., Myers-Smith, I., and Macias-Fauria, M. (2017). Shrub growth and expansion in the arctic tundra: An assessment of controlling factors using an evidence-based approach. *Environ. Res. Lett.* 12 (8), 085007. doi:10.1088/1748-9326/aa7989

Mekonnen, Z. A., Riley, W. J., Berner, L. T., Bouskill, N. J., Torn, M. S., Iwahana, G., et al. (2021). Arctic tundra shrubification: A review of mechanisms and impacts on ecosystem carbon balance. *Environ. Res. Lett.* 16 (5), 053001. doi:10.1088/1748-9326/abf28b

Mishra, U., Hugelius, G., Shelef, E., Yang, Y., Strauss, J., Lupachev, A., et al. (2021). Spatial heterogeneity and environmental predictors of permafrost region soil organic carbon stocks. *Sci. Adv.* 7, eaaz5236. doi:10.1126/sciadv.aaz5236

Mod, H. K., and Luoto, M. (2016). Arctic shrubification mediates the impacts of warming climate on changes to tundra vegetation. *Environ. Res. Lett.* 11 (12), 124028. doi:10.1088/1748-9326/11/12/124028

Monteath, A. J., Gaglioti, B. V., Edwards, M. E., and Froese, D. (2021). Late Pleistocene shrub expansion preceded megafauna turnover and extinctions in eastern Beringia. *Proc. Natl. Acad. Sci. U. S. A.* 118 (52), e2107977118. doi:10.1073/pnas.2107977118

Murchie, T. J., Monteath, A. J., Mahony, M. E., Long, G. S., Cocker, S., Sadoway, T., et al. (2021). Collapse of the mammoth-steppe in central Yukon as revealed by ancient environmental DNA. *Nat. Commun.* 12 (1), 7120. doi:10.1038/s41467-021-27439-6

Myers-Smith, I. H., Forbes, B. C., Wilmking, M., Hallinger, M., Lantz, T., Blok, D., et al. (2011). Shrub expansion in tundra ecosystems: Dynamics, impacts and research priorities. *Environ. Res. Lett.* 6 (4), 045509. doi:10.1088/1748-9326/6/4/045509

Olofsson, J., Oksanen, L., Callaghan, T., Hulme, P. E., Oksanen, T., and Suominen, O. (2009). Herbivores inhibit climate-driven shrub expansion on the tundra. *Glob. Chang. Biol.* 15 (11), 2681–2693. doi:10.1111/j.1365-2486.2009.01935.x

Olofsson, J., and Post, E. (2018). Effects of large herbivores on tundra vegetation in a changing climate, and implications for rewilding. *Phil. Trans. R. Soc. B* 373, 20170437. doi:10.1098/rstb.2017.0437

Olofsson, J. (2006). Short- and long-term effects of changes in reindeer grazing pressure on tundra heath vegetation. *J. Ecol.* 94 (2), 431–440. doi:10.1111/j.1365-2745.2006.01100.x

Olofsson, J., Stark, S., and Oksanen, L. (2004). Reindeer influence on ecosystem processes in the tundra. *Oikos* 105 (2), 386–396. doi:10.1111/j.0030-1299.2004.13048.x

Palmtag, J., Hugelius, G., Lashchinskiy, N., Tamstorf, M. P., Richter, A., Elberling, B., et al. (2015). Storage, landscape distribution, and burial history of soil organic matter in contrasting areas of continuous permafrost. *Arct. Antarct. Alp. Res.* 47 (1), 71–88. doi:10.1657/AAAR0014-027

Phillips, C. A., and Wurzburger, N. (2019). Elevated rates of heterotrophic respiration in shrub-conditioned arctic tundra soils. *Pedobiologia* 72, 8–15. doi:10.1016/j.pedobi.2018.11.002

RCoreTeam (2021). *R: A language and environment for statistical computing*. Vienna, Austria: R Foundation for Statistical Computing.

Regmi, P., Grosse, G., Jones, M. C., Jones, B. M., and Anthony, K. W. (2012). Characterizing post-drainage succession in thermokarst lake basins on the seward peninsula, Alaska with TerraSAR-X backscatter and landsat-based NDVI data. *Remote Sens.* 4 (12), 3741–3765. doi:10.3390/rs4123741

Reimer, P. J., Austin, W. E. N., Bard, E., Bayliss, A., Blackwell, P. G., Bronk Ramsey, C., et al. (2020). The IntCal20 northern hemisphere radiocarbon age

calibration curve (0–55 cal kBP). *Radiocarbon* 62 (4), 725–757. doi:10.1017/RDC.2020.41

Sannel, A. B. K. (2020). Ground temperature and snow depth variability within a subarctic peat plateau landscape. *Permafr. Periglac. Process.* 31 (2), 255–263. doi:10.1002/ppp.2045

Schirrmeister, L., Grosse, G., Wetterich, S., Overduin, P. P., Strauss, J., Schuur, E. A. G., et al. (2011). Fossil organic matter characteristics in permafrost deposits of the northeast Siberian Arctic. *J. Geophys. Res.* 116, G00M02. doi:10.1029/2011JG001647

Schuur, E. A. G., Bockheim, J., Canadell, J. G., Euskirchen, E., Field, C. B., Goryachkin, S. V., et al. (2008). Vulnerability of permafrost carbon to climate change: Implications for the global carbon cycle. *BioScience* 58 (8), 701–714. doi:10.1641/B580807

Schuur, E. A. G., McGuire, A. D., Schädel, C., Grosse, G., Harden, J. W., Hayes, D. J., et al. (2015). Climate change and the permafrost carbon feedback. *Nature* 520, 171–179. doi:10.1038/nature14338

Shmelev, D., Cherbunina, M., Rogov, V., Opfergelt, S., Monhonval, A., and Strauss, J. (2021). Reconstructing permafrost sedimentological characteristics and post-depositional processes of the yedoma stratotype duvanny yar, Siberia. *Front. Earth Sci. (Lausanne).* 9, 961. doi:10.3389/feart.2021.727315

Skarin, A., Verdonen, M., Kumpula, T., Macias-Fauria, M., Alam, M., Kerby, J. T., et al. (2020). Reindeer use of low Arctic tundra correlates with landscape structure. *Environ. Res. Lett.* 15, 115012. doi:10.1088/1748-9326/abbf15

Strauss, J., Abbott, B. W., Hugelius, G., Schuur, E., Treat, C., Fuchs, M., et al. (2021). *9. Permafrost. Recarbonizing global soils–A technical manual of recommended management practices: Volume 2–Hot spots and bright spots of soil organic carbon* Rome: FAO, 130.

Strauss, J., Schirrmeister, L., Wetterich, S., Borchers, A., and Davydov, S. P. (2012). Grain-size properties and organic-carbon stock of Yedoma Ice Complex permafrost from the Kolyma lowland, northeastern Siberia. *Glob. Biogeochem. Cycles* 26, 2011GB004104. doi:10.1029/2011GB004104

Stuenzi, S. M., Boike, J., Gädeke, A., Herzschuh, U., Kruse, S., Pestryakova, L. A., et al. (2021). Sensitivity of ecosystem-protected permafrost under changing boreal forest structures. *Environ. Res. Lett.* 16 (8), 084045. doi:10.1088/1748-9326/ac153d

Stuiver, M., Reimer, P. J., and Reimer, R. W. (2021). CALIB 8.2 [WWW program]. Available at: http://calib.org/calib/calib.html (Accessed April 9, 2021).

Sundqvist, M. K., Moen, J., Björk, R. G., Vowles, T., Kytöviita, M.-M., Parsons, M. A., et al. (2019). Experimental evidence of the long-term effects of reindeer on Arctic vegetation greenness and species richness at a larger landscape scale. *J. Ecol.* 107 (6), 2724–2736. doi:10.1111/1365-2745.13201

Suominen, O., and Olofsson, J. (2000). Impacts of semi-domesticated reindeer on structure of tundra and forest communities in fennoscandia: A review. *Ann. Zool. Fenn.* 37 (4), 233–249.

te Beest, M., Sitters, J., Ménard, C. B., and Olofsson, J. (2016). Reindeer grazing increases summer albedo by reducing shrub abundance in Arctic tundra. *Environ. Res. Lett.* 11 (12), 125013. doi:10.1088/1748-9326/aa5128

Turetsky, M. R., Abbott, B. W., Jones, M. C., Anthony, K. W., Olefeldt, D., Schuur, E. A. G., et al. (2020). Carbon release through abrupt permafrost thaw. *Nat. Geosci.* 13 (2), 138–143. doi:10.1038/s41561-019-0526-0

Turetsky, M. R., Abbott, B. W., Jones, M. C., Walter Anthony, K., Olefeldt, D., Schuur, E. A. G., et al. (2019). Permafrost collapse is accelerating carbon release. *Nature* 569, 32–34. doi:10.1038/d41586-019-01313-4

Veremeeva, A., Nitze, I., Günther, F., Grosse, G., and Rivkina, E. (2021). Geomorphological and climatic drivers of thermokarst lake area increase trend (1999–2018) in the Kolyma lowland yedoma region, north-eastern Siberia. *Remote Sens.* 13 (2), 178. doi:10.3390/rs13020178

Verma, M., Schulte to Bühne, H., Lopes, M., Ehrich, D., Sokovnina, S., Hofhuis, S. P., et al. (2020). Can reindeer husbandry management slow down the shrubification of the Arctic? *J. Environ. Manag.* 267, 110636. doi:10.1016/j.jenvman.2020.110636

Walker, D. A., Jia, G. J., Epstein, H. E., Raynolds, M. K., Chapin, F. S., III, Copass, C., et al. (2003). Vegetation-soil-thaw-depth relationships along a low-arctic bioclimate gradient, Alaska: Synthesis of information from the ATLAS studies. *Permafr. Periglac. Process.* 14 (2), 103–123. doi:10.1002/ppp.452

Wang, P., Mommer, L., van Ruijven, J., Berendse, F., Maximov, T. C., and Heijmans, M. M. P. D. (2016). Seasonal changes and vertical distribution of root standing biomass of graminoids and shrubs at a Siberian tundra site. *Plant Soil* 407 (1), 55–65. doi:10.1007/s11104-016-2858-5

Wilcox, E. J., Keim, D., Jong, T., Walker, B., Sonnentag, O., Sniderhan, A. E., et al. (2019). Tundra shrub expansion may amplify permafrost thaw by advancing snowmelt timing. *Arct. Sci.* 5 (4), 202–217. doi:10.1139/as-2018-0028

Windirsch, T., Grosse, G., Ulrich, M., Forbes, B. C., Göckede, M., Zimov, N., et al. (2021). *Large herbivores affecting terrestrial permafrost in northeastern Siberia: Biogeochemical and sediment characteristics under different grazing intensities.* Bremen, Germany: PANGAEA.

Windirsch, T., Grosse, G., Ulrich, M., Schirrmeister, L., Fedorov, A. N., Konstantinov, P. Y., et al. (2020). Organic carbon characteristics in ice-rich permafrost in alas and Yedoma deposits, central Yakutia, Siberia. *Biogeosciences* 17 (14), 3797–3814. doi:10.5194/bg-17-3797-2020

Ylänne, H., Olofsson, J., Oksanen, L., and Stark, S. (2018). Consequences of grazer-induced vegetation transitions on ecosystem carbon storage in the tundra. *Funct. Ecol.* 32 (4), 1091–1102. doi:10.1111/1365-2435.13029

Zhang, W., Miller, P. A., Smith, B., Wania, R., Koenigk, T., and Döscher, R. (2013). Tundra shrubification and tree-line advance amplify arctic climate warming: Results from an individual-based dynamic vegetation model. *Environ. Res. Lett.* 8 (3), 034023. doi:10.1088/1748-9326/8/3/034023

Zimov, N. (2020). Pleistocene park. Available at: https://pleistocenepark.ru/ (Accessed March 30, 2021).

Zimov, N. S., Zimov, S. A., Zimova, A. E., Zimova, G. M., Chuprynin, V. I., and Chapin, F. S., III (2009). Carbon storage in permafrost and soils of the mammoth tundra-steppe biome: Role in the global carbon budget. *Geophys. Res. Lett.* 36 (2). doi:10.1029/2008GL036332

Zimov, S. A. (2005). Pleistocene park: Return of the mammoth's ecosystem. *Science* 308 (5723), 796–798. doi:10.1126/science.1113442

Zimov, S. A., Zimov, N. S., Tikhonov, A. N., and Chapin, F. S. (2012). Mammoth steppe: A high-productivity phenomenon. *Quat. Sci. Rev.* 57, 26–45. doi:10.1016/j.quascirev.2012.10.005

frontiers | Frontiers in Environmental Science

TYPE Original Research
PUBLISHED 08 September 2022
DOI 10.3389/fenvs.2022.948367

OPEN ACCESS

EDITED BY
Wenxin Zhang,
Faculty of Science, Lund University, Sweden

REVIEWED BY
Xiaowen Ji,
University of Saskatchewan, Canada
Hanuman Singh Jatav,
Sri Karan Narendra Agriculture University, India

*CORRESPONDENCE
Vyacheslav Polyakov,
slavon6985@gmail.com

SPECIALTY SECTION
This article was submitted to Environmental Informatics and Remote Sensing, a section of the journal Frontiers in Environmental Science

RECEIVED 19 May 2022
ACCEPTED 18 August 2022
PUBLISHED 08 September 2022

CITATION
Polyakov V, Kartoziia A, Nizamutdinov T, Wang W and Abakumov E (2022), Soil-geomorphological mapping of Samoylov Island based on UAV imaging. *Front. Environ. Sci.* 10:948367. doi: 10.3389/fenvs.2022.948367

Soil-geomorphological mapping of Samoylov Island based on UAV imaging

Vyacheslav Polyakov[1,2]*, Andrei Kartoziia[3,4,5], Timur Nizamutdinov[1], Wenjuan Wang[1] and Evgeny Abakumov[1]

[1]Department of Applied Ecology, Faculty of Biology, St. Petersburg State University, Saint Petersburg, Russia, [2]Arctic and Antarctic Research Institute, Saint Petersburg, Russia, [3]V. S. Sobolev Institute of Geology and Mineralogy, Siberian Branch of the Russian Academy of Sciences, Novosibirsk, Russia, [4]A. A. Trofimuk Institute of Petroleum Geology and Geophysics, Siberian Branch of the Russian Academy of Sciences, Novosibirsk, Russia, [5]Department of Geology and GeophysicsNovosibirsk State University, Novosibirsk, Russia

Soil-geomorphological mapping is a reliable tool for analyzing the patterns of soil distribution in various parts of Earth's surface. Cryogenic and watershed areas are the most dynamic landscapes with relatively rapid transformation under the influence of climate change and river activity. The soil-geomorphological map obtained by unmanned aerial vehicle (UAV) imaging, classical soil sections, geomorphological observation, and determination of the main chemical parameters of soils are presented. Mapping of the spatial distribution was performed using QGIS 3.22, SAGA GIS 7.9.1, and ArcGIS 10.6 software. The investigation of soil cover was performed according to WRB soil classification. From the obtained data, four types of soils were identified due to their position in the relief and chemical parameters. The dominant soil type is Folic Cryosol (Siltic) (41.1%) which is formed on the periglacial landscape of wet polygons on Samoylov Island. The application of high-resolution UAV imaging to construct soil-geomorphological maps is the most relevant method for analyzing soils formed in cryogenic, watershed, and mountainous landscapes. Based on SOC distribution, it was found that the highest SOC content corresponds to Holocene terrace (Cryosol and Histosol soil types), in areas that are not subject to the flooding process. According to the analysis of the chemical composition of soils, it was found that the main elements accumulating in the soil are SiO_2, Al_2O_3, CaO, and K_2O, which have a river origin. The soil-geomorphological maps can be used to analyze the reserves and contents of organic and inorganic components with high accuracy.

KEYWORDS

Lena River Delta, Samoylov Island, remote sensing, UAV, soil-geomorphological map

Abbreviations: UAV, unmanned aerial vehicle; SOM, soil organic matter; SOC, soil organic carbon; ON, organic nitrogen; UNCCD, united nations convention to combat desertification; GIS, geographic information system; PCA, principal component analysis; DEM, digital elevation model.

Introduction

Soil organic carbon (SOC) is the organic remains in the soil after the partial decomposition of any material produced by microorganisms and plant remnants (Jones et al., 2010). The SOM supports the key functions of the soil, as it is crucial for stabilizing the structure of the soil, retaining and releasing nutrients for plants, and ensuring the penetration of water and its storage in the soil (Schepaschenko et al., 2013). Soils represent the largest surface reservoir of organic carbon (Schuur et al., 2015). Due to the local geology, climatic conditions, and land use and management (among other environmental factors), soils retain a different amount of SOC (Lefèvre et al., 2017). It is estimated that the largest amount of SOC is stored in the northern permafrost region with over 1024 Pg (1 Pg = 1×10^{13} kg) of organic carbon in the soil in a layer of up to 3 m, as well as 34 Pg of nitrogen (Zubrzycki et al., 2013; Zubrzycki et al., 2014), mainly in Histosol. The permafrost-affected zone occupies an area of more than 8.6 million km^2, which is about 27% of soil cover above 50°N (Jones et al., 2010). They accumulate in themselves a huge amount of organic carbon, so they are considered one of the most important elements of the cryosphere (Zubrzycki et al., 2014). There, carbon is accumulated in soils in huge quantities due to low temperatures, leading to low biological activity and slow decomposition of SOM. The presence of permafrost and long-term freezing of soils has a strong influence on the processes of ion exchange, the water-physical regime, the solubility of nutrients and their availability for plants, and bioproductivity in general (Polyakov and Abakumov, 2020).

The Arctic is the most poorly investigated zone in the world. In Russia, the Murmansk region (Evdokimova and Mozgova, 2001; Dvornikov et al., 2021), the Yamal Nenets Autonomous Okrug (Ji et al., 2019; Nizamutdinov et al., 2021), some areas of Yakutia (Desyatkin et al., 2021; Polyakov et al., 2021) are well studied. The Canadian and American Arctic have local studies of natural permafrost systems (Bölter and Wetzel, 2006; Ping et al., 2008; Tarnocai and Bockheim, 2011). The Svalbard archipelago is well studied (Iavid et al., 2018; Hanaka et al., 2019), but the Russian northern islands are practically uninvestigated (Bogorodskii et al., 2018). Arctic zone research is aimed at studying anthropogenically transformed landscapes (cities and industrial zones) (Dymov et al., 2013). This is due to certain difficulties in logistical operations in the North, as well as severe weather conditions. However, based on the distribution of organic matter, the largest reserves are concentrated in the northern regions of the world (Zubrzycki et al., 2014). The northern regions, in addition to the presence of high reserves of organic matter, are characterized by complex topography and a network of large rivers and channels, which makes it difficult to carry out fieldwork in these regions. A large hydrographic network leads to the development of erosion processes, and degradation of permafrost and soil cover (Ardelean et al., 2020). Soil mapping based on landscape elements and the geological structure of Quaternary rocks, which began back in 1940–1960, showed that this is a powerful mechanism for studying soil cover and soil formation features (Nauman et al., 2022).

The founders of soil mapping were Dokuchaev in 1899 and Jenny in 1941 (Florinsky, 2016). Dokuchaev presented the method of soil mapping based on the soil organic content of the European part of Russia at a scale of 1: 4.2 million. In the 1990s, several researchers (Moore et al., 1993; Gessler et al., 1995) proposed to use in the mapping of soils the combination of soil attributes and soil-forming factors, or environmental factors. With the development of computers and statistical methods processing, it was possible to predict soil parameters with an autocorrelation error. The method is based on the assumption that from a relatively small, but statistically representative sample of measurements of a soil characteristic, it is possible to restore the behavior of characters within a certain territory (field, island, catchment) (McBratney et al., 2003; Scull et al., 2003). The objects of forecasting are the morphological, physical, chemical, and biological properties of soils. The presence of a statistical relationship between soil and morphometric characteristics can be explained by the fact that the quantitative characteristics of the relief affect the course and direction of many natural processes (Moore et al., 1991; Florinsky, 1998). A high correlation of a particular soil characteristic with the curvature of the earth's surface may indicate that this soil characteristic depends on the degree of convergence of surface and subsoil flows of moisture and substances dissolved or suspended in it.

On a global scale, there is growing interest in assessing and mapping the SOC pool and its potential for altering carbon sequestration at lower spatial resolutions and large geographic scales (Lamichhane et al., 2019). In addition, the United Nations Convention to Combat Desertification (UNCCD), which is an indicator of the goal of the Sustainable Development Agency 15.3.1, recognized the SOC reserve map as an indicator for assessing the area of degraded land in the context of achieving neutral land degradation (IUCN, 2015). Soil mapping has long been widely used all over the world, and with the development of GIS technologies, the development of digital mapping has leaped forward (Castaldi et al., 2019; Lupachev et al., 2020; Padilha et al., 2020). However, such maps describe and predict SOM stocks rather well on large areas of land, while local heterogeneities are left without due attention (Scull et al., 2003; Lamichhane et al., 2019).

The identification of soil areas based on geomorphological units is a powerful mechanism for refining existing soil and geomorphological maps (Nauman et al., 2022). For the Arctic, this research method is especially relevant, because the difficult accessibility of many regions hinders research activities (Ardelean et al., 2020). For example, in the Lena River Delta, only the central part has been well studied, while the northern part remains practically inaccessible to researchers (Knoblauch

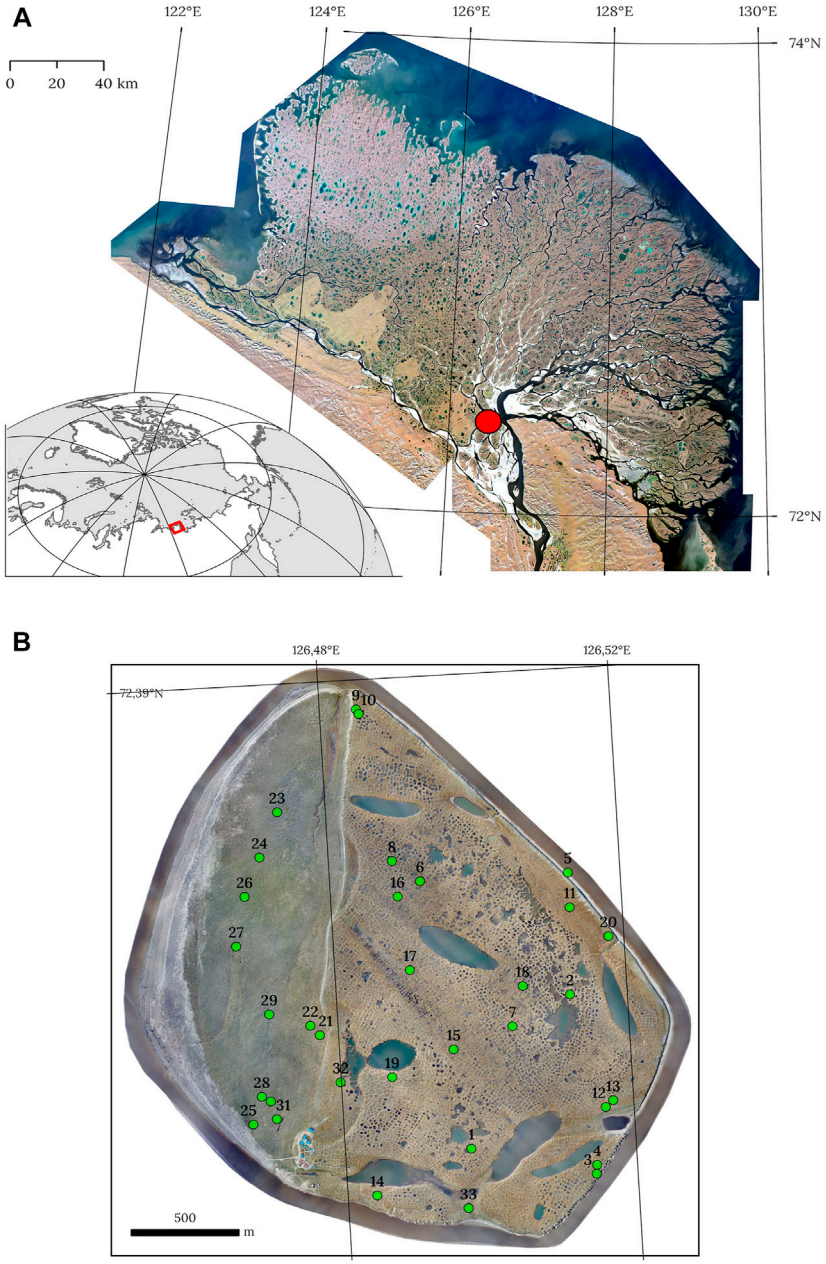

FIGURE 1
Study area. **(A)** Location of Samoylov Island (red square) in a mosaic of satellite Sentinel-2 images of the Lena Delta; **(B)** orthophoto map mosaic of Samoylov Island with observation points.

et al., 2013; Zubrzycki et al., 2014). The use of unmanned aerial vehicles for surveying the terrain, the allocation of geomorphological units together with soil studies in a landscape setting similar in structure will make it possible to create soil-geomorphological maps of high accuracy. Meanwhile, the determination of the main chemical parameters of soils will make it possible to predict the stocks of various chemicals. Here, we have proposed a soil-geomorphological map, which is based on geomorphological characteristics using UAV orthophoto maps and a digital elevation model. A further comparison of landscape units and soil observation with analyzing soil chemical parameters will make it possible with a high degree of probability to determine soil cover in the most dynamic areas of the land (Lupachev et al., 2020). This research method is most relevant in mountainous, watersheds, as well as landscapes exposed to the influence of permafrost and active erosion processes. Thus, this

work aims to provide a soil-geomorphological map of Samoylov Island, the Lena River Delta.

Materials and methods

Study area

The Lena River Delta is the largest northern delta in the world, which is located in the Arctic zone and has an area of about 30.00 km^2 (Kravtsova and Mit'kinykh, 2011). Due to such a huge area and location, it has a significant impact on the water regime of the Arctic Ocean, since a large amount of freshwater flows from the delta into the least salty ocean on our planet (Figure 1). The delta was formed as a result of river activity: sediment removal, erosion, and abrasion under the influence of sea level fluctuations and the movement of the earth's crust (Bolshiyanov et al., 2013).

The Lena River Delta is located in a zone with an Arctic continental climate. The average annual air temperature is −13°C, the average January temperature drops to −32°C, and the average July temperature is 6.5°C. Annual precipitation is 190 mm. The Lena River Delta is covered with various types of tundra vegetation. The main components are lichens, mosses, grasses (cereals and sedges), and some types of shrubs (Kutzbach et al., 2004; Schneider et al., 2009; Boike et al., 2013; Boike et al., 2019).

The key area of work is Samoylov Island (N 72.370 E 126.467), which is located in the area of the first terrace and is periodically flooded by river waters. The island covers an area of about 5 km^2. The western part is formed by recent alluvial processes. The eastern part is represented by small thermokarst lakes, ponds, and polygonal tundra. The parent rocks on the island are Holocene alluvial sands.

Sampling strategy

Soil sampling took place as part of the Lena Delta expedition 2018–2021. The soils were selected based on their position in the landscape, the water content in the area, and the change in vegetation cover. The selection and description of soils were carried out according to the international soil classification WRB (2015). On Samoylov Island, according to the previously proposed geomorphological map and the identification of the main geomorphological units, soil samples were taken (Kartoziia, 2019). To clarify the boundaries of soil areas, soil pits were made for which the analysis of chemical indicators was not carried out; therefore, they were not included in Figure 1. Thus, it was possible to cover a significant area of the island and refine the geomorphological map. To analyze the main physicochemical parameters, 33 soil samples were collected from different landscape positions. More than 60 soil test pits were made to clarify the boundaries of the soil ranges. Upper soil horizons A 5 (10)-30 (35) cm were used to analyze physicochemical parameters. The upper organogenic horizon O was not used in the analysis of physicochemical parameters. The color analysis was carried out according to the international classification Soil color chart (Munsell, 2010), and morphological parameters were determined according to the international classification Guidelines for soil description (WRB, 2015). The redox potential was taken into account by the color features of soil horizons and the presence of liquid suprapermafrost moisture. The studied soils are presented in Figure 2.

Laboratory analysis

The chemical soil parameters were analyzed on fine earth of soil after being passed through a 2 mm sieve. The chemical analyses were performed using classical methods: C and N contents were determined using an element analyzer (EA3028-HT EuroVector, Pravia PV, Italy) and pH in water and in salt suspension (soil-dissolvent ratios 1:2.5 in case of mineral horizons and 1:25 in case of organomineral horizons) suspensions using a pH meter (pH-150 M Teplopribor, Moscow, Russia). To determine the chemical composition of the studied soils, we used the X-ray fluorescence analysis on Energy Dispersive X-ray Fluorescence Spectrometer (EDX-800P, Shimadzu, Japan). The particle-size distribution of soils was determined by the Kachinsky method, a Russian analog of the analysis proposed by Bowman and Hutka (2002). Mapping of the spatial distribution was performed using QGIS 3.22 and SAGA GIS 7.9.1 software. Statistical processing was conducted using Statistica 10.0 software, with a principal component analysis (PCA) module.

Unmanned aerial vehicle imaging and soil-geomorphological mapping

We have analyzed remote sensing (RS) data from a UAV for the recognition of landforms with presumed and determined different soil characteristics. Orthophoto maps, digital elevation models (DEM), and morphometry schemes served as a basis for our analysis. UAV-based imaging was described in detail in (Kartoziia, 2019). It was conducted at the end of July 2016 using Supercam S 250 UAV manufactured by "Unmanned Systems". This UAV was equipped with a geodetic-class GPS receiver and a Sony Alpha 6000 24.7 MP APS-C digital camera. All 3743 images were captured at an altitude of about 150 m above ground level and covered 4.4 km^2 of Samoylov Island. As a result of using specialized software for photogrammetry: Agisoft PhotoScan (Professional Edition, Version 1.2.5) from Geoscan Ltd. and Photomod package (version 5.0) from JSC Racurs, we received 29 georeferenced

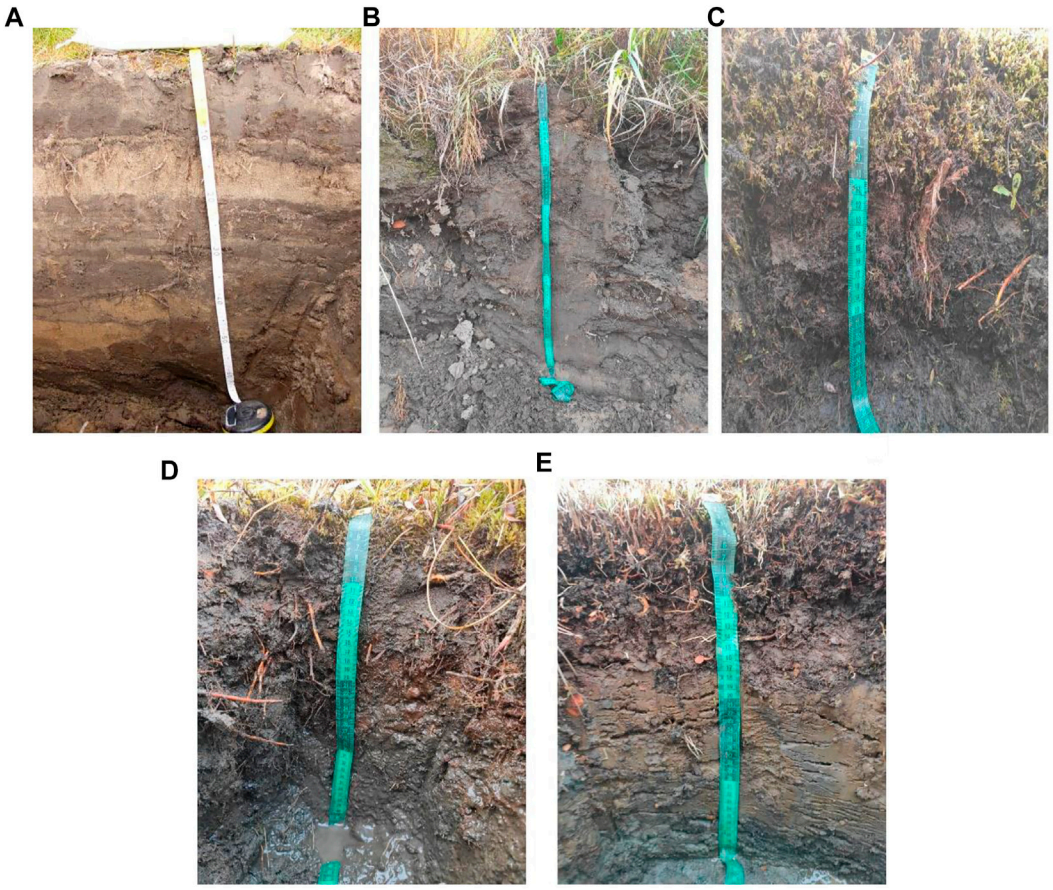

FIGURE 2
Soil distribution in the Samoylov isl. **(A)** Subaquatic Fluvisol (Arenic); **(B)** Folic Podzol (Oxyaquic); **(C)** Epicryic Histosol; **(D)** Reductaquic Cryosol (Siltic); **(E)** Folic Cryosol (Siltic).

orthophoto map tiles with a 0.05 m/px resolution and a DEM presented using a height matrix. Obtained DEM has a horizontal resolution of 0.5 m/px and vertical accuracy of 0.2 m.

We analyzed RS data in the GIS software package ArcGIS 10.6 from ESRI CIS Limited and in QGIS 3.22. We have used ArcGIS and QGIS tools for the creation of several land morphometry schemes. Then we recognized landforms and manually mapped soil map units. In some cases, we know that revealed landforms have different soil characteristics. In other cases, we presume differences in soil parameters of landforms due to their obvious distinction in topography, vegetation cover, and other visible features.

To be more precise, we have taken into account the following features during manual mapping: land microtopography from DEM and morphometry schemes, surface photo tones from orthophoto maps, as well as obtained soil characteristics of different island terrains. We characterized all mapped soil map units further in results and discussion. The use of maps based on the UAV method makes it possible to identify spatial inhomogeneities of the relief, such maps are most convenient to use in areas subject to active external influences (river action, active cryogenic, and erosion processes). Since we have obtained the soil map manually, we can presume, that map error corresponds to a horizontal resolution of morphometry schemes, which is 0.5 m. However, it should be noticed, that some borders between soil map units were visible in orthophoto maps. In these cases, mapping accuracy achieved 0.05 m. Thus, UAV data resolution provides a high level of mapping accuracy.

Results

On Samoylov isl., a lot of work was carried out related to the study of the soil cover (Kutzbach et al., 2004; Zubrzycki et al., 2013; Antcibor et al., 2014; Zubrzycki et al., 2014; Polyakov et al., 2019; Polyakov and Abakumov, 2020). Most of the work is represented by the study of soil organic matter (Zubrzycki et al., 2013), greenhouse gas emissions (Kutzbach et al., 2004),

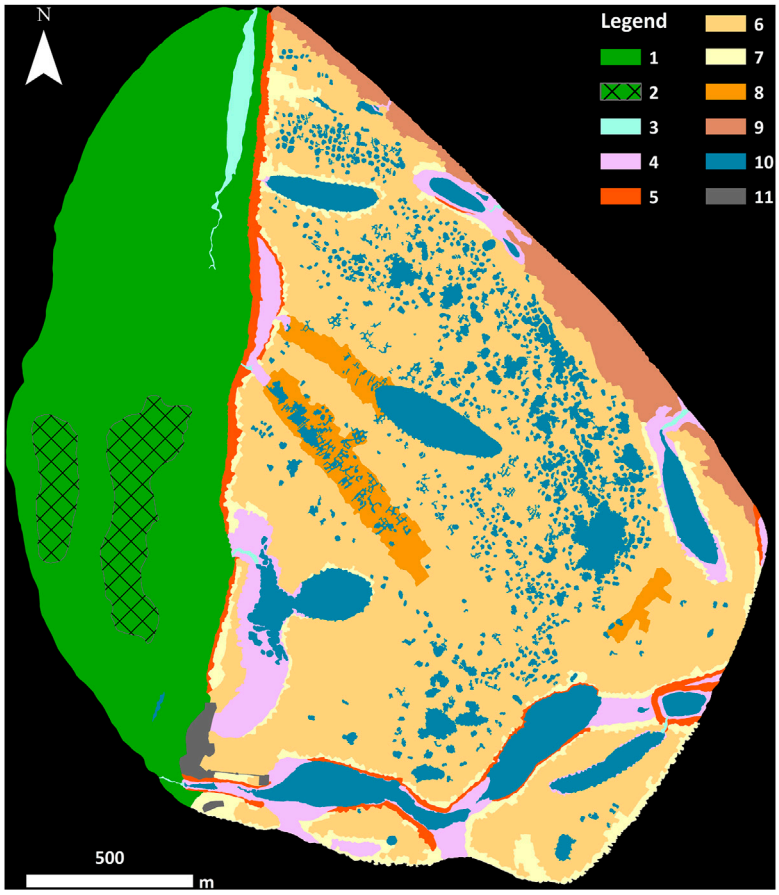

FIGURE 3
Soil-geomorphological map of the Samoylov isl., Lena River Delta. Scale Mapping units are explained in Table 1.

as well as the vegetation cover of Samoylov isl (Boike et al., 2013; Boike et al., 2019). Several studies were also carried out to study the geomorphological features of the structure of the island (Schwamborn et al., 2002; Bolshiyanov et al., 2013; Kartoziia, 2019). Based on the data collected by Pfeiffer et al. (2000) and Pfeiffer et al. (2002) compare Sanders et al. (2010) and presented by Zubrzycki et al. (2013), the first soil map of the island was created and obtained in which 8 soil types were considered according to US taxonomy. In addition, based on data obtained by Boike et al. (2013) the land cover classes on the Samoylov Island map were obtained with six land cover classes. According to geological and geomorphological studies, Samoylov isl. was found to consist of various geological bodies formed by organomineral mass (a stratified mass of organic remains and sand). The northwestern part of the island is flooded every year by high water and is composed of sands and silts from the surface, representing high and low floodplain terraces, gradually decreasing to the Olenekskaya channel. The clear border between the two parts of the island runs northeastward. The surface of the terrace to the east border of the island is a polygonal tundra with thermokarst lakes, which in the southern part of the island are annually flooded with flood waters and at this time constitute a strait. Based on UAV data obtained by Kartoziia (2019), a detailed digital geomorphological model of Samoylov isl. was obtained, on which eight types of land units with eight subtypes were identified. Thus, based on previously obtained data by other researchers and our own, we have provided a soil-geomorphological map of Samoylov isl. based on UAV imaging. The Soil Map is presented in Figure 3. The Soil Legend is presented in Table 1.

Fluvisol

Floodplain (ID 1 in the Figure 3) is one of the largest surfaces of the island that occupies its western half. It is easily recognizable due to its slightly inclined topography and distinctive vegetation. Floodwater overlaps it every spring season. The transitions between floodplain plants and sandy beach, and the first terrace's slope and flat surface are the visible borders of the

TABLE 1 Legend for the soil-geomorphological map of the Samoylov isl., Lena River Delta.

Mapping unit	Environmental characteristic	Soil horizons*	Soil name**	Area	
				km²	%
Fluvisol					
1	Slightly inclined and poorly drained territory; characterized by the presence of wood brought by the river, the vegetation cover is represented by dwarf-shrubs tundra	Ah-C-Abh-C-W	Subaquatic Fluvisol (Arenic)	0.97	24.3
2	Floodplain scroll bars, low ridges, and vegetation are represented by shrubs tundra up to 2 m high	Ah-AB-C-Abh-C	Folic Fluvisol (Arenic)	0.14	3.7
Brooks					
3	The streams are the place where water flows from the upper terrace of the island, as well as from large and network of small islands	-	-	0.03	0.7
Histosol					
4	Flooded areas are characterized by waterlogged conditions, peat accumulation, wet tundra	Hi_1-He_2	Epicryic Histosol	0.18	4.7
Podzol					
5	Valley's slopes, formed as a result of land degradation by cryogenic processes	Oe-Bs-C	Folic Podzol (Oxyaquic)	0.08	2
Cryosol					
6	Periglacial landscape with wet polygons, typical tundra landscape, dry tundra	Oi-B@-C	Oxyaquic Cryosol (Siltic)	0.16	4
7	Periglacial landscape with high and low-centered polygons, dry tundra	Oe-B@-C	Folic Cryosol (Siltic)	1.64	41.1
8	Drainage valleys, formed as a result of the thermal-erosion activity of water drainage	Oi-Br@-C	Reductaquic Cryosol (Siltic)	0.11	2.5
Soil formed under the aeolian impact					
9	Smoothed polygonal landscape, covered with sand under the influence of the aeolian process	C-Obe-B@-C	Folic Cryosol (Aridic)	0.12	3.1
Waterbody					
10	Lakes, large ponds of merged polygons, and water-filled troughs if they eroded more than half of adjacent polygons	-	-	0.54	13.6
Soils formed under the technogenic impact					
11	The territory of the station, vehicle roads	C	Transportic Technosols	0.02	0.4

*Guides of soil description (Jahn et al., 2006).
**FAO WRB (2015).

mapped unit. Furthermore, we revealed two floodplain scroll bars, which are expressed in topography as low ridges (ID 2 in the Figure 3). Moreover, more sandy ground is typical for scroll bars.

Fluvisols are formed on the annually deposited material (during the flooding process). The formation of Fluvisol takes place in areas that are subject to the flooding process and, accordingly, by the fresh river mineral material. The soils are characterized by a stratified mass, which consists of organomineral (Ah) and mineral (C) horizons (Jahn et al., 2006). The thickness of the soil profile, depending on its position in the relief, ranges from 60 cm (in depressions) and up to 100 cm (at low ridges) to the border with the permafrost. No traces of gleying processes were noted, which are associated with sandy materials and lateral movement of moisture along the permafrost boundary towards the river. The vegetation cover here is represented by willow shrubs, various flowering plants, as well as in waterlogged areas—cotton grass and sedge. The vegetation cover is not continuous. The absence of a continuous vegetation cover, in particular of moss-lichen communities, creates conditions for active heat exchange between the soil and the atmosphere. Light particle-size distribution with a predominance of sand fraction (about 80%) prevents the accumulation of gravitational and sorbed moisture, which is associated with the active cryogenic processes. In this regard, the activity of cryogenic processes in Fluvisols is poorly developed, which is reflected in the transformation of the relief.

The main difference between Subaquatic Fluvisol (Arenic) and Folic Fluvisol (Arenic) is the presence of moisture in the Subaquatic Fluvisol (Arenic) soil profile at a depth of up to 100 cm, as well as the more developed Ah-AB horizons in the Folic Fluvisol (Arenic) profile. Folic Fluvisol (Arenic) soil stays less time in flood conditions because formed at low ridges.

The third mapped unit is brooks which are also easily recognizable due to their topography and water presence in

orthophoto maps (ID 3 in the Figure 3). It needs to be marked that brooks locate both island halves.

Histosol

Flooded terrains are annually covered by floodwater (ID 4 in the Figure 3). They subside due to annual flood erosional activity. Generally, these surfaces are flat, and are located below 6 m a.s.l. Thus, their mapping is simple in the DEM. Only flat bottoms concern this unit in the case of distinctive valleys.

These soils are formed under conditions of excessive moisture since they are located in depressions. Under conditions of a high level of hydromorphism and a relatively high level of occurrence of permafrost in soils, the level of microbiological activity decreases, which leads to the accumulation of poorly decomposed plant residues. This is the reason for the formation of Epicryic Histosol.

Podzol

Valley's slopes belong to another unit on the map (ID 5 in the Figure 3). Moreover, we mapped the first terrace's slope. Generally, slope surfaces have more than 10° angle and specific solifluction micro-landforms.

A characteristic feature of these soils is the presence of the Bs horizon, which has an ocher color due to ferruginous films on the surface of mineral grains. The thickness of such soils reaches up to 40–60 cm. The Bs horizon can form a significant part of the soil profile. Here, the accumulation of iron and aluminum oxides is noted. The particle-size distribution of the soils is represented by a sandy fraction (about 70%). The vegetation cover is represented by mosses and lichens.

Cryosol

Ice wedge polygons occupy most territory of the first terrace surface. We have divided them into two different units. The first one consists of the usual periglacial landscape wet polygons (ID six in the Figure 3). The second one differs by water absence in the polygon center. In fact, a major of them concern with high-centered polygons (Kartoziia, 2019). We also attributed walled and low-centered polygons to this unit if all polygon parts are inclined (ID 7 in the Figure 3). Due to inclination, they are drained and have the same vegetation cover along with the polygon profile.

The development of cryogenic soils occurs in areas not subject to the active influence of the river. These soils contain a Bat horizon. The upper horizon is represented by a moss cover with weak signs of decomposition of organic remains and is underlain by permafrost. The depth of permafrost is up to 40 cm in well-drained areas, in depressions of the relief, the depth of the active layer can be up to 20 cm. The characteristic features of cryogenic soils are the development of cryoturbation processes in the form of vortex patterns, as well as the presence of frost cracks. The main difference between Oxyaquic Cryosol (Siltic) and Folic Cryosol (Siltic) is the saturation of Oxyaquic Cryosol (Siltic) with oxygenated waters (by the liquid precipitation). The development of anaerobic conditions is not observed in these soils. Folic Cryosol (Siltic) forming on high and low-centered polygons have a developed Oe horizon, which indicates the transformation of plant residues and a relatively high microbiological activity of these soils, the thickness of the active layer in these soils is much higher [on average, 20 cm more than in Oxyaquic Cryosol (Siltic)]. Isolation of dry and wet polygons is possible using the UAV method (Figure 4).

The increase in the active layer in Folic Cryosol (Siltic) may also be due to the erosion of the permafrost as a result of the movement of suprapermafrost moisture into the nearest water bodies. For example, into lakes, brooks, as well as into ponds above ice wedges, and into ponds in ice wedge polygons' centers. The outflow of suprapermafrost moisture occurs in the nearest water bodies. Due to the movement of relatively warm suprapermafrost water (especially above ice wedges), permafrost degradation near water bodies occurs. These processes of soil erosion and thermokarst are described in the literature, in particular in (Liljedahl et al., 2016). Since the resolution of DEM enables revealing even the smallest topography amplitudes, we have identified these processes' results in landscapes.

Moreover, we have identified drainage valleys in the polygonal landscape (ID 8 in the Figure 3). These surfaces are generally recognizable on the aspect scheme, which was derived from DEM averaging with a moving window of 30 m. Elongated square ice wedge polygons with water in troughs locate in valleys with a 20–40 cm depth. Polygons' long axes are perpendicular to revealed valleys' thalwegs. We can presume that surface subsidence processes occurred here owning to the thermal-erosion activity of water drainage in the inner part of the island. Waterlogged Reductaquic Cryosol (Siltic) is formed under these conditions. A characteristic feature of these soils is reducing conditions due to continued contact with water.

According to the UAV analysis, it is possible to identify these soil types with high reliability (Figure 5).

The next type of soil was distinguished due to the development of active aeolian processes in the eastern part of the island. There is a flat surface with incipient polygons on the eastern edge of the island (ID 9 in Figure 3). The smoothed polygonal landscape is the main distinguishing feature of this unit. We found the overlapping of the first terrace geological body by a bed of river sand here. Sands transport towards the

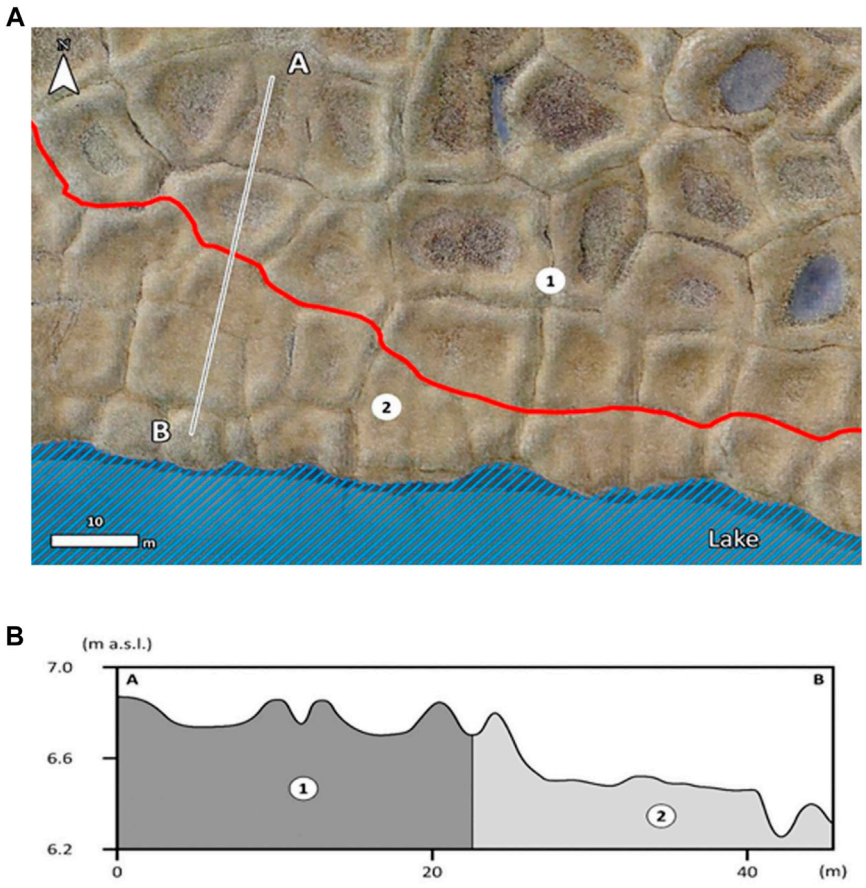

Figure 4
Wet (1) and dried (2) polygons on an orthophoto map that is mixed with a grey shaded relief (GSR) map **(A)**. The red line is a border between mapped polygon types. The topography profile **(B)** was obtained by using ArcGIS and shows small hollows' presence in wet polygons' centers. In addition, it shows the surface general inclination in the case of dried polygons terrain. This inclination conditions water absence.

island's center due to the aeolian process. They smooth polygons and make superficial ground sandier. As a result of changes in the water level in the river, in the eastern part of the island, the sand spit periodically drains, which is further destroyed by the wind, the place of accumulation of this sand is the soils of Samoylov isl. Therefore, we have identified a separate subtype of Folic Cryosol (Aridic).

Based on Kartoziia (2019), we mapped lakes, large ponds of merged polygons, and water-filled troughs if they eroded more than half of adjacent polygons (ID 10 in Figure 3). Ponds that are located in a center of single polygons were not mapped.

Technosol

The last mapped unit is a territory of Samoylov research station (ID 11 in Figure 3). Most of the soil has been radically transformed. There are also wooden decks around the station, serving as a road.

Physicochemical characteristics of soils from the samoylov isl., lena river delta

The data obtained show that in studied soils, the leading elements that accumulate in soils are SiO_2, Fe_2O_3, and Al_2O_3 (Supplementary Table SA1). In connection with the development of cryogenic and gley processes in soils, migration of iron and aluminum oxides occurs. In summer, organomineral compounds migrate down the soil profile, forming humus streaks. The processes of humification of organic matter and the activity of cryogenic processes result in a redistribution of organic matter in soils. We have previously considered the processes of migration and accumulation of soil organic matter in the soils of the Lena River Delta (Zubrzycki et al., 2013; Polyakov and Abakumov, 2021a). Depending on the position in the relief and the activity of cryogenic processes, three types of accumulation can be distinguished. In the first type, which is associated with flooded areas, stratified soils are formed, in which

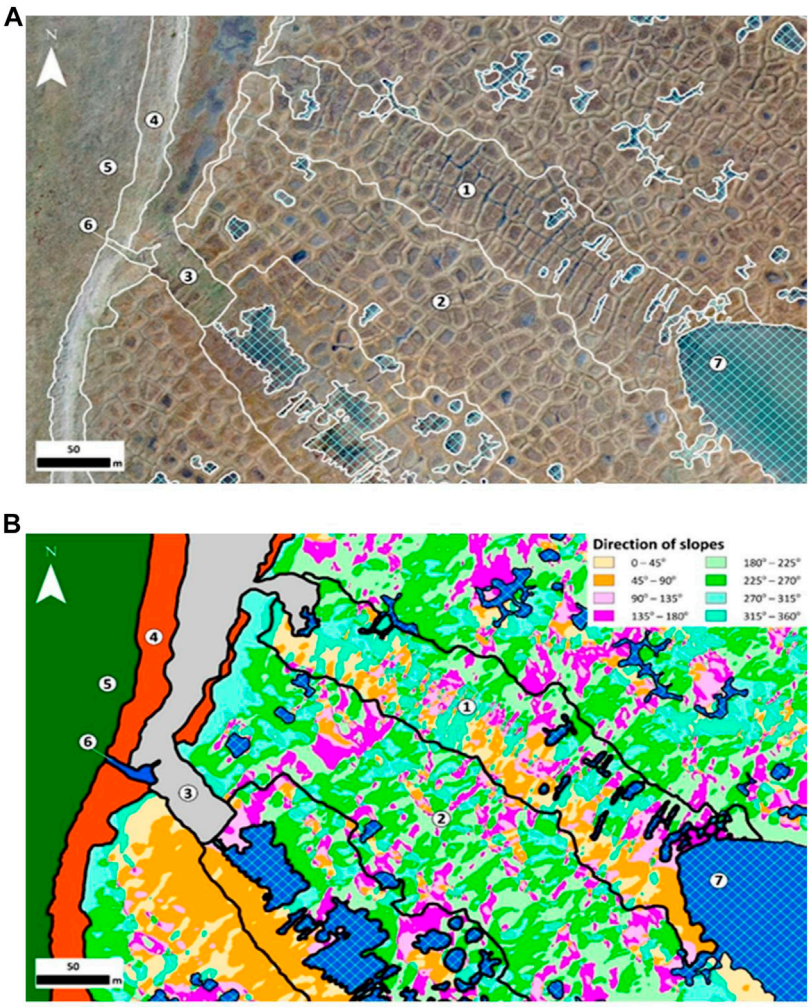

FIGURE 5
Elongated terrains of drainage valleys in the Samoylov Island central part on an orthophoto map that is mixed with a GSR map **(A)** and on an aspect map **(B)**. Legend: 1—drainage valleys; 2—both types of polygons; 3—flooded terrains; 4—slopes; 5—floodplain; 6—brooks. Colors 1 and 2 on **(B)** signify the slopes' direction.

accumulation of soil organic matter occurs in layers, with organomineral horizons overlapping with fresh mineral material. Therefore, in such soils, one can observe several peaks of organic carbon throughout the soil profile. The second and third types are associated with areas that are not subjected to flooding. In the second type, there is the accumulation of organic material in the upper soil horizon (5–20 cm) and decreases with depth. In the third type, there is an accumulation of organic material in the upper soil horizon as well as at the boundary with frozen rocks. The relatively high content of iron and aluminum oxides is the result of the formation of various micas (muscovite, biotite), hydromicas (illite, vermiculite, and glauconite), aluminosilicates (feldspars) (Polyakov and Abakumov, 2021b). In the studied soils, the predominant mineral is quartz, which is largely due to the riverine origin of the delta complex of the Lena River. The low variability of the content of chemical elements among the studied soils indicates a weak influence of exogenous processes on the accumulation of chemical elements in the studied soils (the influence of the sea/river). The spatial distribution of the dominant chemical elements (SiO_2 and Fe_2O_3) on Samoylov isl. is shown in Figure 6.

From the data obtained, we can note that the accumulation of SiO_2 is associated with the influence of the river since the highest concentrations of this mineral are found in the flooded areas of Samoylov isl. At the same time, the accumulation of Fe_2O_3 occurs predominantly in non-flooded soils, but in areas with excessive moisture.

During the statistical processes of the data on the content of chemical compounds in the soil and their relationship with the

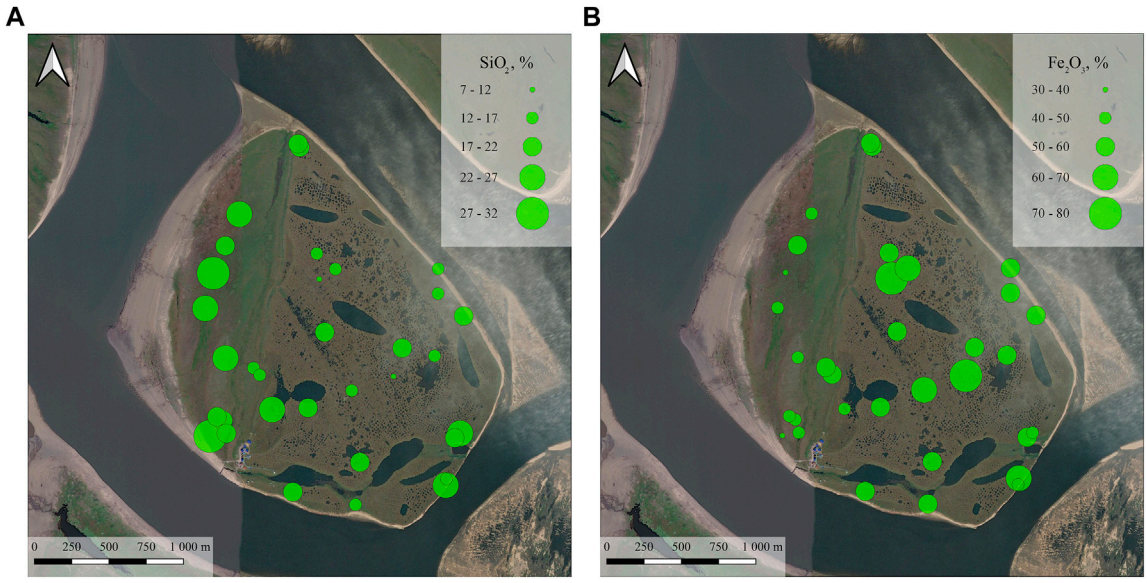

FIGURE 6
Spatial distribution of chemical compounds in study soils. **(A)** SiO_2; **(B)** Fe_2O_3.

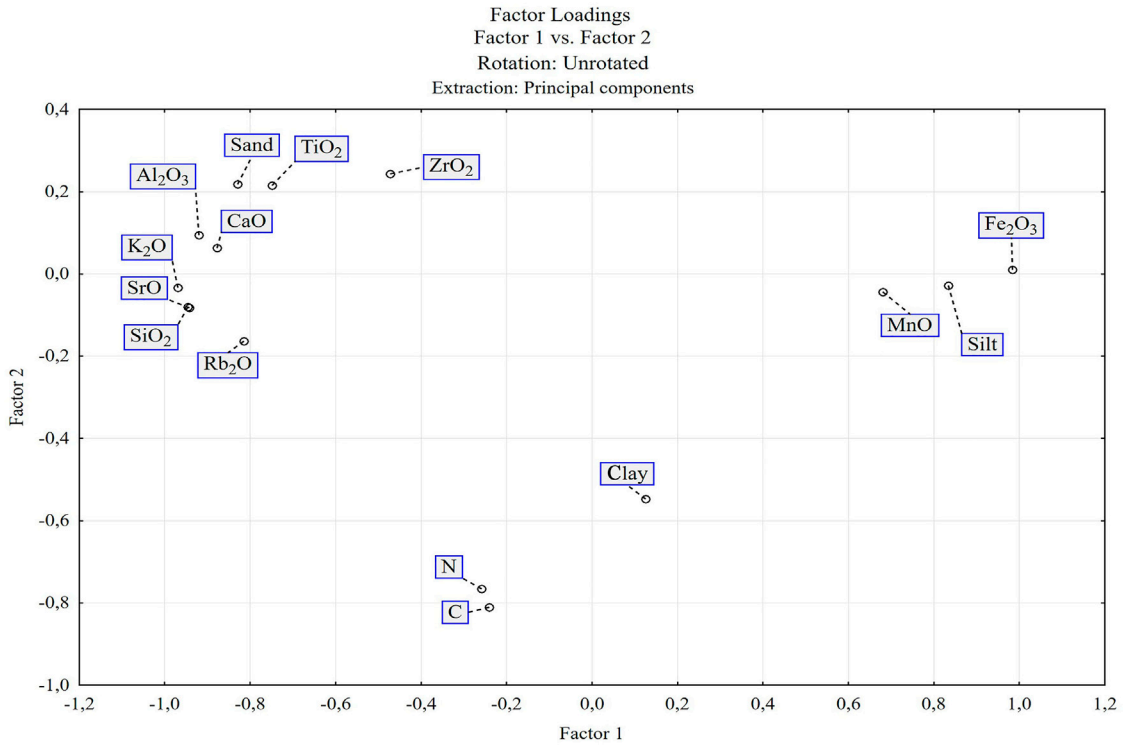

FIGURE 7
PCA analysis for the main chemical compounds and particle-size distribution in soils.

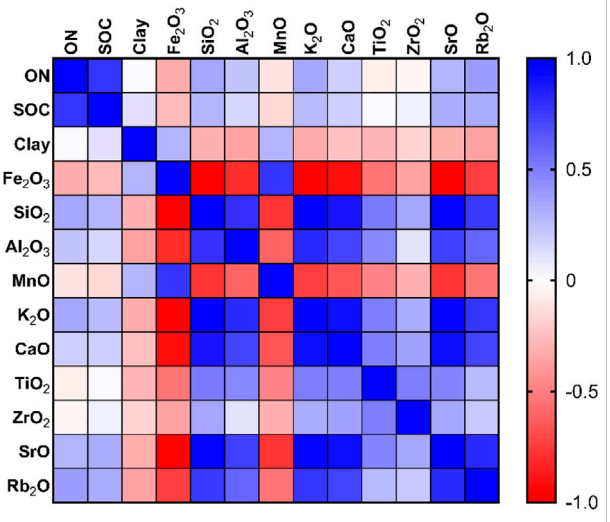

FIGURE 8
Correlation matrix (Spearman r) of main chemical compounds.

particle-size distribution, it was noted that most of the studied compounds are associated with the accumulation of the sand fraction (Figure 7).

Thus, we can conclude that most of the chemical elements are introduced into the delta along with the river waters. Furthermore, under the conditions of weathering of soil primary and secondary minerals, the accumulation of iron and manganese oxides occurs in the soils, while the accumulation of organic carbon and nitrogen, according to statistical analysis, is associated with the silt fraction. The correlation matrix is shown in Figure 8.

The Spearmen r correlation indicates the relationship between the processes of the ON and SOC accumulation ($r = 0.77$, $p < 0.05$). Also significant ($p < 0.05$) correlation coefficients were obtained between the major oxides (Fe_2O_3 and Al_2O_3 $r = -0.81$) and silicon oxide (SiO_2: Fe_2O_3 $r = -0.99$; SiO_2: Al_2O_3 $r = 0.78$). The above oxides are often connected, as their parallel removal or accumulation is determined by the processes of chemical and physical weathering.

An analysis of the spatial distribution of SOC and organic nitrogen (ON) on Samoylov isl. was carried out (Figure 9).

From the obtained Figure 9, we can conclude that the highest SOC content is observed on the Holocene terrace, in areas that are not subject to the flooding process. The sites with the highest SOC content are confined to the formation of Cryosol and Histosol, where SOC accumulates at low temperatures and close occurrence of permafrost. In Fluvisol, a smaller amount of SOC accumulates on the flooded area of the island, which may be associated with the stratification of soil horizons and overlapping of the upper humus horizons with river mineral material.

The ON content is more related to the flooded areas of the island, this may be due to the more varied vegetation cover in the flooded areas and the formation of cereal and flowering plant communities. At the same time, in areas that are not subject to seasonal flood processes, the nitrogen content is not so high.

Discussion

Traditional soil mapping methods are an integral part of modern territory analysis (Florinsky, 2016). These methods are widely used around the world, and most of the existing soil maps have been made by analysis of soil sections and creating a network of soil pits. Based on such data, a soil map of Zubrzycki et al. (2013) was previously obtained. The map we obtained is generally consistent with the previous data, while our data are based on both soil analyzes and the geomorphological structure of the island. Modern methods of soil mapping are aimed at the remote analysis of the territory (Lamichhane et al., 2019). These methods are used to generate the maps needed to calculate soil organic carbon stocks (Lefèvre et al., 2017; Lamichhane et al., 2019). Our proposed UAV-based mapping method is a reliable and accurate tool for the analysis of heterogeneous landscapes because is able to take into account a large number of heterogeneities in the relief, while maps based on satellite images cannot estimate such heterogeneities. Therefore, the use of the UAV method is a promising and necessary tool for analyzing landscapes undergoing active changes (cryogenic, watershed, mountainous landscapes).

Nowadays, the UAV method has been used in the calculation of organic carbon sinks in agriculture (Guo et al., 2020). Regression models are widely used to build digital soil maps of the distribution of organic carbon in various regions of the world were created (Zeng et al., 2016). However, the formation of regression models requires a large database to generate a model with a low error rate. In regions where long-term monitoring studies are carried out, such data are available, in the Arctic regions such data are minimal or absent at all. Due to the complexity of the landscape and the degradation of permafrost, erosional and thermokarst processes (Ardelean et al., 2020) is quite difficult to obtain such data. A similar conclusion was found by Alpine soil researchers who combined remote sensing and traditional soil survey methods (Baruck et al., 2016). However, they came to the problem that the study of the Alps, which are located in different states of Europe, is complicated by the correlation of soil nomenclatures, which have significant differences in different countries. Therefore, a unified soil cover classification, e.g. WRB, should be used. The study of the Canadian Arctic and SOM stocks uses long-term satellite data, DEM, soil depth, and temperature data, and achieves 83% accuracy in the investigation of soil cover (Sothe et al., 2022). A lot of other examples of successful using UAV data in geosciences are described in the literature, particularly in

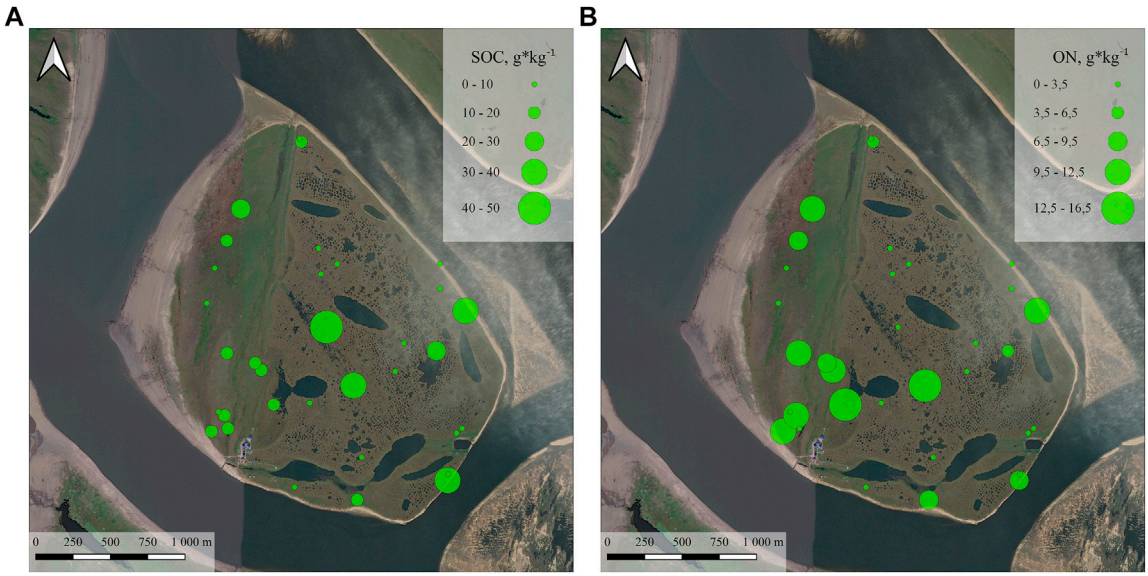

FIGURE 9
Spatial distribution of SOC **(A)** and ON **(B)** in soils of the Lena River Delta.

(Lewis et al., 2022). Therefore, the method proposed by us, based on a DEM, in combination with traditional methods of investigation of the soil cover, makes it possible to obtain reliable data on the formation of the soil cover depending on the landscape situation. For hard-to-reach regions, such as the Arctic, and mountainous areas, the use of soil-geomorphological maps based on UAV surveys can be an effective mechanism for monitoring and studying the soil cover. Thus, when identifying reference landforms and soils that form on them together with an assessment of the chemical parameters of soils, we can extrapolate the data obtained to areas inaccessible to traditional soil studies. This study is the first step for the formation of reference landforms and their corresponding soils, thus the development of this area of mapping will enable creation of soil-geomorphological maps of high accuracy. The obtained data, together with the conducted studies of the physicochemical parameters of soils, can be used as reference values for specific natural zones and used to calculate the reserves of various organic and inorganic substances.

Conclusion

The soil cover of Samoylov isl. is characterized by high diversity. We have identified 8 soil types. Their formation is due to the different positions in the landscape and the conditions of a territory flooding. Most of the territory is represented by the periglacial landscape with high and low-centered polygons and the forming Folic Cryosol (Siltic) (41.1%), as well as slightly inclined and poorly drained territory, on which the Subaquatic Fluvisol (Arenic) is formed (24.3%). As a result of using classical methods of soil investigations and GIS analysis of UAV data, we have obtained a digital soil-geomorphological map of Samoylov isl. We have identified three subtypes of Cryosols (Oxyaquic Cryosol, Folic Cryosol, and Reductaquic Cryosol) based on the soil-geomorphological model. The formation of different Cryosol types here is associated with geomorphological conditions and the hydromorphism degree. We have identified the Folic Podzol (Oxyaquic) type forming valley's slopes, which occupies about 2% of the island's territory, as well as the Cryic Histosol type (4.7%), which is characterized by the accumulation of peat in the humid landscape depressions of the island. Based on the physic-chemical analysis of soils, it was revealed that most of the chemical compounds (SiO_2, Al_2O_3, CaO, K_2O, and others) enter the soil as a result of the activity of the river. In areas outside the annual flooding, Fe_2O_3 and MnO accumulate, and the accumulation of organic components (SOC and ON) is associated with the silt fraction. We suppose that the use of high-resolution soil-geomorphological maps based on GIS analysis of UAV data is a reliable tool for the examination of heterogeneous areas of the earth's surface. This method of analysis will make it possible to reliably determine soil types in conditions of the high variability of the watershed and cryogenic landscapes. Moreover, that method together with the analysis of organic and inorganic components is able to determine soil's content in the most dynamic areas of the landscape. The quantity of soil sampling sites should be

chosen to depend on landscapes and presumed soil types variety which is located in the study area, and also according to classical soil mapping methods. Directly, the determination of soil types should be based on chemical analysis. However, accurate mapping of their distribution and especially their borders are goals for GIS analysis of UAV data. Specific instructions for the soil-geomorphological mapping method could be developed after additional investigations.

Data availability statement

The original contributions presented in the study are included in the article/Supplementary Material; further inquiries can be directed to the corresponding author.

Author contributions

VP and AK: conceptualization, methodology, supervision, and funding acquisition; VP and AK: data curation, writing—original draft, and formal analysis; TN: data curation and visualization; EA: review and editing and supervision; and WW: review and editing.

Funding

This work was supported by the Ministry of Science and Higher Education of the Russian Federation in accordance with agreement No. 075-15-2022-322 date 22.04.2022 on providing a grant in the form of subsidies from the Federal budget of Russian Federation. The grant was provided for state support for the creation and development of a World-class Scientific Center "Agrotechnologies for the Future," and this work was carried out on the state assignment of VS Sobolev Institute of Geology and Mineralogy, Siberian Branch of the Russian Academy of Sciences.

Acknowledgments

The authors thank the Chemical Analysis and Materials Research Center of St. Petersburg State University for assistance in the analysis of chemicals in the studied soils.

Conflict of interest

The authors declare that the research was conducted in the absence of any commercial or financial relationships that could be construed as a potential conflict of interest.

Publisher's note

Supplementary material

The Supplementary Material for this article can be found online at: https://www.frontiersin.org/articles/10.3389/fenvs.2022.948367/full#supplementary-material

References

Antcibor, I., Eschenbach, A., Zubrzycki, S., Kutzbach, L., Bolshiyanov, D., and Pfeiffer, E. M. (2014). Trace metal distribution in pristine permafrost-affected soils of the Lena River delta and its hinterland, northern Siberia, Russia. *Biogeosciences* 11 (1), 1–15. doi:10.5194/bg-11-1-2014

Ardelean, F., Onaca, A., Cheţan, M.-A., Dornik, A., Georgievski, G., Hagemann, S., et al. (2020). Assessment of spatio-temporal landscape changes from VHR images in three different permafrost areas in the western Russian arctic. *Remote Sens.* 12 (23), 3999. doi:10.3390/rs12233999

Baruck, J., Nestroy, O., Sartori, G., Baize, D., Traidl, R., Vrščaj, B., et al. (2016). Soil classification and mapping in the Alps: The current state and future challenges. *Geoderma* 264, 312–331. doi:10.1016/j.geoderma.2015.08.005

Bogorodskii, P. V., Makshtas, A. P., Kustov, V. Y., and Movchan, V. V. (2018). The dynamics of seasonal thawing of permafrost in the region of research station "ice base "cape baranov" (bolshevik island, severnaya zemlya archipelago). *Probl. Arktiki. I. Antarkt.* 64 (1), 16–30. doi:10.30758/0555-2648-2018-64-1-16-30

Boike, J., Kattenstroth, B., Abramova, K., Bornemann, N., Chetverova, A., Fedorova, I., et al. (2013). Baseline characteristics of climate, permafrost and land cover from a new permafrost observatory in the Lena River Delta, Siberia (1998–2011). *Biogeosciences* 10 (3), 2105–2128. doi:10.5194/bg-10-2105-2013

Boike, J., Nitzbon, J., Anders, K., Grigoriev, M., Bolshiyanov, D., Langer, M., et al. (2019). A 16-year record (2002–2017) of permafrost, active-layer, and meteorological conditions at the Samoylov island arctic permafrost research site, Lena River delta, northern siberia: An opportunity to validate remote-sensing data and land surface, snow, and permafrost models. *Earth Syst. Sci. Data* 11 (1), 261–299. doi:10.5194/essd-11-261-2019

Bolshiyanov, D. Y., Makarov, A. S., Schneider, V., and Stoof, G. (2013). *Origin and development of the delta Lena River*. St. Petersburg: AARI.

Bölter, M., and Wetzel, H. (2006). Properties, formation, classification and ecology of arctic soils: Results from the tundra northwest expedition 1999 (nunavut and northwest territories, Canada). *Polarforschung* 73, 89–101. doi:10.2312/polarforschung.73.2-3.89

Bowman, G., and Hutka, J. (2002). "Particle size analysis," in *Soil physical measurment and interpritation for land evaluation*. Editors N. McKezie, K. Coughlan, and H. Cresswell (Victoria: CSIRO Publishing), 224–239.

Castaldi, F., Hueni, A., Chabrillat, S., Ward, K., Buttafuoco, G., Bomans, B., et al. (2019). Evaluating the capability of the Sentinel 2 data for soil organic carbon prediction in croplands. *ISPRS J. Photogrammetry Remote Sens.* 147, 267–282. doi:10.1016/j.isprsjprs.2018.11.026

Desyatkin, R., Filippov, N., Desyatkin, A., Konyushkov, D., and Goryachkin, S. (2021). Degradation of arable soils in central Yakutia: Negative consequences of global warming for yedoma landscapes. *Front. Earth Sci. (Lausanne).* 9, 683730. doi:10.3389/feart.2021.683730

Dvornikov, Y. A., Vasenev, V. I., Romzaykina, O. N., Grigorieva, V. E., Litvinov, Y. A., Gorbov, S. N., et al. (2021). Projecting the urbanization effect on soil organic

carbon stocks in polar and steppe areas of European Russia by remote sensing. *Geoderma* 399, 115039. doi:10.1016/j.geoderma.2021.115039

Dymov, A. A., Kaverin, D. A., and Gabov, D. N. (2013). Properties of soils and soil-like bodies in the Vorkuta area. *Eurasian Soil Sc.* 46 (2), 217–224. doi:10.1134/S1064229313020038

Evdokimova, G., and Mozgova, N. P. (2001). Comparative characterization of microbial biomass in Al-Fe-humus podzols of the kola peninsula. *Eurasian Soil Sci.* 34, 1305–1312.

Florinsky, I. (1998). Combined analysis of digital terrain models and remotely sensed data in landscape investigations. *Prog. Phys. Geogr. Earth Environ.* 22, 33–60. doi:10.1177/030913339802200102

Florinsky, I. V. (2016). *Digital terrain analysis in soil science and geology*. London, England: Elsevier.

Gessler, P. E., Moore, I. D., McKenzie, N. J., and Ryan, P. J. (1995). Soil-landscape modelling and spatial prediction of soil attributes. *Int. J. Geogr. Inf. Syst.* 9 (4), 421–432. doi:10.1080/02693799508902047

Guo, L., Fu, P., Shi, T., Chen, Y., Zhang, H., Meng, R., et al. (2020). Mapping field-scale soil organic carbon with unmanned aircraft system-acquired time series multispectral images. *Soil Tillage Res.* 196, 104477. doi:10.1016/j.still.2019.104477

Hanaka, A., Plak, A., Zagórski, P., Ozimek, E., Rysiak, A., Majewska, M., et al. (2019). Relationships between the properties of Spitsbergen soil, number and biodiversity of rhizosphere microorganisms, and heavy metal concentration in selected plant species. *Plant Soil* 436 (1), 49–69. doi:10.1007/s11104-018-3871-7

Iavid, E., Kondakova, V., Polyakov, V., and Abakumov, E. (2018). Diversity and main properties of soils of the Gronfjord area (Svalbard archipelago). *Czech Polar Rep.* 8, 43–59. doi:10.5817/CPR2018-1-4

IUCN (2015). *International union for consrvation of nature*. Gland, Switzerland: Icun.

Jahn, R., Blume, H. P., Spaargaren, O., and Schad, P. (2006). *Guidelines for soil description*. Rome, Italy: Food and agriculture organization of the united nations.

Ji, X., Abakumov, E., and Polyakov, V. (2019). Assessments of pollution status and human health risk of heavy metals in permafrost-affected soils and lichens: A case-study in yamal peninsula, Russia arctic. *Hum. Ecol. Risk Assess. Int. J.* 25 (8), 2142–2159. doi:10.1080/10807039.2018.1490887

Jones, A., Stolbovoy, V., Tarnocai, C., Broll, G., Spaargaren, O., and Montanarella, L. (2010). *Soil atlas of the northern circumpolar region, European commission*. Luxembourg: Publications Office of the European Union, 144.

Kartoziia, A. (2019). Assessment of the ice wedge polygon current state by means of UAV imagery analysis (Samoylov island, the Lena delta). *Remote Sens.* 11 (13), 1627. doi:10.3390/rs11131627

Knoblauch, C., Beer, C., Sosnin, A., Wagner, D., and Pfeiffer, E. M. (2013). Predicting long-term carbon mineralization and trace gas production from thawing permafrost of Northeast Siberia. *Glob. Chang. Biol.* 19 (4), 1160–1172. doi:10.1111/gcb.12116

Kravtsova, V. I., and Mit'kinykh, N. S. (2011). Mouths of world rivers in the atlas of space images. *Water Resour.* 38 (1), 1–17. doi:10.1134/S0097807811010064

Kutzbach, L., Wagner, D., and Pfeiffer, E.-M. (2004). Effect of microrelief and vegetation on methane emission from wet polygonal tundra, Lena Delta, Northern Siberia. *Biogeochemistry* 69 (3), 341–362. doi:10.1023/B:BIOG.0000031053.81520.db

Lamichhane, S., Kumar, L., and Wilson, B. (2019). Digital soil mapping algorithms and covariates for soil organic carbon mapping and their implications: A review. *Geoderma* 352, 395–413. doi:10.1016/j.geoderma.2019.05.031

Lefèvre, C., Rekik, F., Alcantara, V., and Wiese, L. (2017). *Soil organic carbon - the hidden potential*. Rome, Italy: FAO.

Lewis, Q., Konsoer, K., and Leitner, M. (2022). "How sUAS has pushed forward on-demand low altitude remote sensing in Geography," in *sUAS applications in Geography*. Editors K. Konsoer, M. Leitner, and Q. Lewis (Cham: Springer International Publishing), 1–12.

Liljedahl, A. K., Boike, J., Daanen, R. P., Fedorov, A. N., Frost, G. V., Grosse, G., et al. (2016). Pan-Arctic ice-wedge degradation in warming permafrost and its influence on tundra hydrology. *Nat. Geosci.* 9 (4), 312–318. doi:10.1038/ngeo2674

Lupachev, A. V., Abakumov, E. V., Goryachkin, S. V., and Veremeeva, A. A. (2020). Soil cover of the fildes peninsula (king george island, west Antarctica). *CATENA* 193, 104613. doi:10.1016/j.catena.2020.104613

McBratney, A. B., Mendonça Santos, M. L., and Minasny, B. (2003). On digital soil mapping. *Geoderma* 117 (1), 3–52. doi:10.1016/S0016-7061(03)00223-4

Moore, I. D., Gessler, P., Nielsen, G. A. E., and Peterson, G. (1993). Soil attribute prediction using terrain analysis. *Soil Sci. Soc. Am. J.* 57, 443–452. doi:10.2136/sssaj1993.03615995005700020058x

Moore, I. D., Grayson, R. B., and Ladson, A. R. (1991). Digital terrain modelling: A review of hydrological, geomorphological, and biological applications. *Hydrol. Process.* 5 (1), 3–30. doi:10.1002/hyp.3360050103

Munsell, C. (2010). Munsell soil color charts : With genuine Munsell color chips. *2009 year revised*. Grand Rapids, MI: Munsell Color.

Nauman, T., Burch, S., Humphries, J., Knight, A., and Duniway, M. (2022). A quantitative soil-geomorphic framework for developing and mapping ecological site groups</sup&gt. *Rangel. Ecol. Manag.* 81 (1), 9–33. doi:10.1016/j.rama.2021.11.003

Nizamutdinov, T., Morgun, E., Pechkin, A., Kostecki, J., Greinert, A., and Abakumov, E. (2021). Differentiation of trace metal contamination level between different urban functional zones in permafrost affected soils (the example of several cities in the yamal region, Russian arctic). *Miner. (Basel).* 11 (7), 668. doi:10.3390/min11070668

Padilha, M. C. D. C., Vicente, L. E., Demattê, J. A. M., dos Santos Wendriner Loebmann, D. G., Vicente, A. K., Salazar, D. F. U., et al. (2020). Using Landsat and soil clay content to map soil organic carbon of oxisols and Ultisols near São Paulo, Brazil. *Geoderma Reg.* 21, e00253. doi:10.1016/j.geodrs.2020.e00253

Pfeiffer, E.-M., Wagner, D., Kobabe, S., Kutzbach, L., Kurchatova, A., Stoof, G., et al. (2002). Modern processes in permafrost affected soils. *Rep. Polar Mar. Res.* 426, 21–41.

Pfeiffer, E. M., Wagner, D., Becker, H., Vlasenko, A., Kutzbach, L., Boike, J., et al. (2000). Modern processes in permafrost affected soils. *Geoscience* 22, 54.

Ping, C.-L., Michaelson, G. J., Jorgenson, M. T., Kimble, J. M., Epstein, H., Romanovsky, V. E., et al. (2008). High stocks of soil organic carbon in the North American Arctic region. *Nat. Geosci.* 1 (9), 615–619. doi:10.1038/ngeo284

Polyakov, V., and Abakumov, E. (2021a). Assessments of organic carbon stabilization using the spectroscopic characteristics of humic acids separated from soils of the Lena River delta. *Separations* 8 (6), 87. doi:10.3390/separations8060087

Polyakov, V., and Abakumov, E. (2021b). Micromorphological characteristic of different-aged Cryosols from the east part of Lena River delta, siberia, Russia. *Geosci. (Basel).* 11 (3), 118. doi:10.3390/geosciences11030118

Polyakov, V., and Abakumov, E. (2020). Stabilization of organic material from soils and soil-like bodies in the Lena River Delta (13C-NMR spectroscopy analysis). *Span. J. Soil Sci.* 10 (2), 170–190. doi:10.3232/SJSS.2020.V10.N2.05

Polyakov, V. I., Chegodaeva, N. A., and Abakumov, E. V. (2019). Molecular and elemental composition of humic acids isolated from selected soils of the Russian Arctic. *Tomsk. State. Univ. J. Biol.* 47, 6–21. doi:10.17223/19988591/47/1

Polyakov, V., Nizamutdinov, T., Abakumov, E., and Morgun, E. (2021). Soil diversity and key functional characteristics of yakutsk city: Largest urbanized cryogenic world's Ecosystem. *Energies (Basel).* 14 (13), 3819. doi:10.3390/en14133819

Sanders, T., Fiencke, C., and Pfeiffer, E. M. (2010). Small-scale variability of dissolved inorganic nitrogen (DIN), C/N ratios and ammonia oxidizing capacities in various permafrost affected soils of Samoylov Island, Lena River Delta, Northeast Siberia. *Polarforschung* 80, 23–35. doi:10.2312/polarforschung.80.1.23

Schepaschenko, D. G., Mukhortova, L. V., Shvidenko, A. Z., and Vedrova, E. F. (2013). The pool of organic carbon in the soils of Russia. *Eurasian Soil Sc.* 46 (2), 107–116. doi:10.1134/S1064229313020129

Schneider, J., Grosse, G., and Wagner, D. (2009). Land cover classification of tundra environments in the Arctic Lena Delta based on Landsat 7 ETM+ data and its application for upscaling of methane emissions. *Remote Sens. Environ.* 113 (2), 380–391. doi:10.1016/j.rse.2008.10.013

Schuur, E. A. G., McGuire, A. D., Schädel, C., Grosse, G., Harden, J. W., Hayes, D. J., et al. (2015). Climate change and the permafrost carbon feedback. *Nature* 520 (7546), 171–179. doi:10.1038/nature14338

Schwamborn, G., Rachold, V., and Grigoriev, M. N. (2002). Late quaternary sedimentation history of the Lena delta. *Quat. Int.* 89 (1), 119–134. doi:10.1016/S1040-6182(01)00084-2

Scull, P., Franklin, J., Chadwick, O., and McArthur, D. (2003). Predictive soil mapping: A review. *Prog. Phys. Geogr. Earth Environ.* 27, 171–197. doi:10.1191/0309133303pp366ra

Sothe, C., Gonsamo, A., Arabian, J., and Snider, J. (2022). Large scale mapping of soil organic carbon concentration with 3D machine learning and satellite observations. *Geoderma* 405, 115402. doi:10.1016/j.geoderma.2021.115402

Tarnocai, C., and Bockheim, J. (2011). Cryosolic soils of Canada: Genesis, distribution, and classification. *Can. J. Soil Sci.* 91 (5), 749–762. doi:10.4141/cjss10020

Wrb, F. (2015). IUSS working group WRB world reference base for soil resources 2014, update 2015. Report.

Zeng, C., Yang, L., Zhu, A. X., Rossiter, D. G., Liu, J., Liu, J., et al. (2016). Mapping soil organic matter concentration at different scales using a mixed geographically weighted regression method. *Geoderma* 281, 69–82. doi:10.1016/j.geoderma.2016.06.033

Zubrzycki, S., Kutzbach, L., and Pfeiffer, E. M. (2014). Permafrost-affected soils and their carbon pools with a focus on the Russian Arctic. *Solid earth.* 5 (2), 595–609. doi:10.5194/se-5-595-2014

Zubrzycki, S., Kutzbach, L., Grosse, G., Desyatkin, A., and Pfeiffer, E. M. (2013). Organic carbon and total nitrogen stocks in soils of the Lena River Delta. *Biogeosciences* 10 (6), 3507–3524. doi:10.5194/bg-10-3507-2013

Advantages of publishing in Frontiers

OPEN ACCESS
Articles are free to read for greatest visibility and readership

FAST PUBLICATION
Around 90 days from submission to decision

HIGH QUALITY PEER-REVIEW
Rigorous, collaborative, and constructive peer-review

TRANSPARENT PEER-REVIEW
Editors and reviewers acknowledged by name on published articles

Frontiers
Avenue du Tribunal-Fédéral 34
1005 Lausanne | Switzerland

Visit us: www.frontiersin.org
Contact us: frontiersin.org/about/contact

REPRODUCIBILITY OF RESEARCH
Support open data and methods to enhance research reproducibility

DIGITAL PUBLISHING
Articles designed for optimal readership across devices

FOLLOW US
@frontiersin

IMPACT METRICS
Advanced article metrics track visibility across digital media

EXTENSIVE PROMOTION
Marketing and promotion of impactful research

LOOP RESEARCH NETWORK
Our network increases your article's readership